Springer Proceedings in Physics 321

Olena Fesenko
Leonid Yatsenko *Editors*

Functional Nanomaterials, Nanocatalysts, Nanotechnologies, and Their Applications

Selected Proceedings of the 12th International Conference on Nanotechnology and Nanomaterials (NANO-2024), August 21–24, 2024, Ukraine

Springer

Springer Proceedings in Physics

Volume 321

Indexed by Scopus

The series Springer Proceedings in Physics, founded in 1984, is devoted to timely reports of state-of-the-art developments in physics and related sciences. Typically based on material presented at conferences, workshops and similar scientific meetings, volumes published in this series will constitute a comprehensive up to date source of reference on a field or subfield of relevance in contemporary physics. Proposals must include the following:

- Name, place and date of the scientific meeting
- A link to the committees (local organization, international advisors etc.)
- Scientific description of the meeting
- List of invited/plenary speakers
- An estimate of the planned proceedings book parameters (number of pages/articles, requested number of bulk copies, submission deadline).

Please contact:

For Americas and Europe: Dr. Zachary Evenson; zachary.evenson@springer.com
For Asia, Australia and New Zealand: Dr. Loyola DSilva; loyola.dsilva@springer.com

Olena Fesenko · Leonid Yatsenko
Editors

Functional Nanomaterials, Nanocatalysts, Nanotechnologies, and Their Applications

Selected Proceedings of the 12th International Conference on Nanotechnology and Nanomaterials (NANO-2024), August 21–24, 2024, Ukraine

Springer

Editors
Olena Fesenko
Institute of Physics
National Academy of Sciences of Ukraine
Kiev, Ukraine

Leonid Yatsenko
Institute of Physics
National Academy of Sciences of Ukraine
Kiev, Ukraine

ISSN 0930-8989 ISSN 1867-4941 (electronic)
Springer Proceedings in Physics
ISBN 978-3-031-99135-6 ISBN 978-3-031-99136-3 (eBook)
https://doi.org/10.1007/978-3-031-99136-3

This Springer imprint is published by the registered company Springer Nature Switzerland AG
The registered company address is: Gewerbestrasse 11, 6330 Cham, Switzerland

Preface

This book highlights some of the latest advances in nanotechnology and nanomaterials contributed by leading researchers from Ukraine, Europe, and beyond. It features papers from participants of the 12th International Conference on Nanotechnology and Nanomaterials (NANO-2024), which took place in Uzhhorod, Ukraine, on August 21–24, 2024. The conference was organized by the Institute of Physics of the National Academy of Sciences of Ukraine, Uzhhorod National University, University of Tartu (Estonia), University of Turin (Italy), and Pierre and Marie Curie University (France).

Internationally recognized experts from a wide range of universities and research institutes shared their knowledge and key results in the areas of nanocomposites and nanomaterials, nanostructured surfaces, microscopy of nano-objects, nanophotonics, nanoplasmonics, nanochemistry, and nanocatalysis.

A special emphasis of this book is placed on functional nanomaterials, namely on materials deliberately engineered to exhibit tailored properties and multifunctionality. These include nanostructures with enhanced catalytic, electronic, magnetic, optical, or biochemical performance, which open up opportunities for applications in smart sensors, targeted drug delivery, energy storage and conversion, and environmental remediation. By combining novel synthesis strategies with state-of-the-art characterization methods, researchers are now able not only to create nanomaterials with unique physical and chemical properties but also to fine-tune their functionality for real-world applications.

Today, nanotechnology remains one of the fastest-developing and most promising fields of science. Numerous studies are already producing practical outcomes that can be applied across diverse domains of human activity, from advanced technologies and engineering to medicine and pharmacology. The aim of this book is to present recent achievements in various areas of nanoscience and to stimulate new interest in such important topics as nanomaterials, nanocomposites, nanostructured surfaces, and their wide-ranging applications.

The book is divided into two Volumes. The topics covering advanced nanomaterials, nanocatalysis, sensors, nanochemistry, environmental and biochemical nanotechnologies can be found in Volume II: Nanoengineering, Nanobiotechnology, Nanochemistry, and Their Applications.

The contributions published in this volume fall under the broad categories of nanomaterial preparation and characterization, functional nanomaterials, nanodevices and quantum structures, spectroscopy, and nanocatalysis. We hope that this collection will be equally useful and inspiring for young researchers and PhD students as well as for established scientists.

Kiev, Ukraine

Olena Fesenko
Leonid Yatsenko

Contents

Contributors

O. M. Alekseev Physical Faculty, Taras Shevchenko National University of Kyiv, Kyiv, Ukraine

S. O. Alekseev Faculty of Chemistry, Taras Shevchenko National University of Kyiv, Kyiv, Ukraine

Lyudmila Andriyko Chuiko Institute of Surface Chemistry of NASU, Kyev, Ukraine

D. A. Andrusenko Physical Faculty, Taras Shevchenko National University of Kyiv, Kyiv, Ukraine

L. I. Ardanova Minnesota State University, Mankato, MN, USA

Nadiia Artyukhova Bratislava University of Economics and Business, Bratislava, Slovakia;
Sumy State University, Sumy, Ukraine

Artem Artyukhov Sumy State University, Sumy, Ukraine;
WSEI University, Lublin, Poland

Ilkhom Ashurov Arifov Institute of Ion-Plasma and Laser Technologies of Academy of Sciences, Tashkent, Uzbekistan

N. Atamas Taras Shevchenko National University of Kyiv, Kyiv, Ukraine

Akbar Avvalboev Arifov Institute of Ion-Plasma and Laser Technologies of Academy of Sciences, Tashkent, Uzbekistan;
National University of Uzbekistan, Tashkent, Uzbekistan

N. V. Babkina Institute of Macromolecular Chemistry, National Academy of Sciences of Ukraine, Kyiv, Ukraine

Mariia Baran V.P. Kukhar Institute of Bioorganic Chemistry and Petrochemistry, NAS of Ukraine, Kyiv, Ukraine

A. O. Bilotska G.V. Kurdyumov Institute for Metal Physics of the N.A.S. of Ukraine, Kyiv, Ukraine

O. M. Bondaruk Institute of Macromolecular Chemistry, National Academy of Sciences of Ukraine, Kyiv, Ukraine

Usmon Choriev Arifov Institute of Ion-Plasma and Laser Technologies of Academy of Sciences, Tashkent, Uzbekistan

V. Chornovol Department of Chemistry, Kyiv National University of Construction and Architecture, Ave of Air Forces, Kyiv, Ukraine

M. V. Danylchuk Department of Corrosion and Corrosion Protection, Karpenko Physico-Mechanical Institute of the NAS of Ukraine, Lviv, Ukraine

O. O. Dan'kiv Drohobych Ivan Franko State Pedagogical University, Drohobych, Ukraine

I. I. Demchik G.V. Kurdyumov Institute for Metal Physics of the N.A.S. of Ukraine, Kyiv, Ukraine

Tetiana Dontsova National Technical University of Ukraine "Igor Sikorsky Kyiv Polytechnic Institute", Kyiv, Ukraine

Markiian Dziadyk Lviv Polytechnic National University, Lviv, Ukraine

Liliya Frolova Ukrainian State University of Science and Technologies, Dnipro, Ukraine

E. I. Get'man Vasyl' Stus Donetsk National University, Vinnytsia, Ukraine

I. Grechanyuk Department of Chemistry, Kyiv National University of Construction and Architecture, Ave of Air Forces, Kyiv, Ukraine

M. Grechanyuk Department of Abrasion—and Corrosion-Resistant Powder Construction, Materials Institute for Problems of Material Sciences NAS of Ukraine, Kyiv, Ukraine

V. Grechanyuk Department of Chemistry, Kyiv National University of Construction and Architecture, Ave of Air Forces, Kyiv, Ukraine;
E.O. Paton Electric Welding Institute of the National Academy of Sciences, Kyiv, Ukraine

N. M. Gregirchak National University of Food Technologies of Ukraine, Kyiv, Ukraine

Taras Yu. Gromovy Chuiko Institute of Surface Chemistry of National Academy of Sciences of Ukraine, Kyiv, Ukraine

Olha Haidai V.P. Kukhar Institute of Bioorganic Chemistry and Petrochemistry, NAS of Ukraine, Kyiv, Ukraine

Khrystyna Hutsul Igor Sikorsky Kyiv Polytechnic Institute, Kyiv, Ukraine

M. I. Ilashchuk Department of Electronics and Power Engineering, Yuriy Fedkovych Chernivtsi National University, Chernivtsi, Ukraine

Roman Iurkevych Hetman Petro Sahaidachnyi National Army Academy, Lviv, Ukraine

Iryna Ivasenko Karpenko Physico-Mechanical Institute of the NASU, Lviv, Ukraine;
Lviv Polytechnic National University, Lviv, Ukraine

Dmytro Kamenskyh V.P. Kukhar Institute of Bioorganic Chemistry and Petrochemistry, NAS of Ukraine, Kyiv, Ukraine;
V. Bakul Institute for Superhard Materials, NAS of Ukraine, Kyiv, Ukraine

L. V. Karabanova Institute of Macromolecular Chemistry, National Academy of Sciences of Ukraine, Kyiv, Ukraine

P. F. Kholod Department of Building Constructions and Bridges, Lviv Polytechnic National University, Lviv, Ukraine

Galyna Khovanets' Department of Physical Chemistry of Fossil Fuels of the Institute of Physical-Organic Chemistry and Coal Chemistry named after L. M. Lytvynenko of the National Academy of Sciences of Ukraine, Lviv, Ukraine

O. V. Kiziun Institute for Sorption and Problems of Endoecology, National Academy of Sciences of Ukraine, Kyiv, Ukraine

V. V. Klepko Department of Physics of Polymers, Institute of Macromolecular Chemistry of the National Academy of Sciences of Ukraine, Kyiv, Ukraine

H. Klym Lviv Polytechnic National University, Lviv, Ukraine

V. M. Korendiy Department of Technical Mechanics and Engineering Graphics, Lviv Polytechnic National University, Lviv, Ukraine

Bohdan Korinenko V.P. Kukhar Institute of Bioorganic Chemistry and Petrochemistry, NAS of Ukraine, Kyiv, Ukraine

Yu. Kostiv Lviv Polytechnic National University, Lviv, Ukraine

Ihor Koval'chuck Karpenko Physico-Mechanical Institute of the NASU, Lviv, Ukraine

T. M. Kovbasiuk Department of Materials Science and Engineering, Lviv Polytechnic National University, Lviv, Ukraine

I. G. Kovzun F.D. Ovcharenko Institute of Biocolloidal Chemistry of NAS of Ukraine, Kyiv, Ukraine

D. P. Koziarskyi Department of Electronics and Power Engineering, Yuriy Fedkovych Chernivtsi National University, Chernivtsi, Ukraine

I. P. Koziarskyi Department of Electronics and Power Engineering, Yuriy Fedkovych Chernivtsi National University, Chernivtsi, Ukraine

Jan Krmela Alexander Dubcek University of Trencin, Puchov, Trencin, Slovakia

V. V. Kulyk Department of Materials Science and Engineering, Lviv Polytechnic National University, Lviv, Ukraine

A. I. Kuntii Department of Criminal Proceedings and Criminology, Lviv State University of Internal Affairs, Lviv, Ukraine

Mirtemir Kurbanov Arifov Institute of Ion-Plasma and Laser Technologies of Academy of Sciences, Tashkent, Uzbekistan

Viktor Kurylenko National Technical University of Ukraine "Igor Sikorsky Kyiv Polytechnic Institute", Kyiv, Ukraine

Oksana Kurylets Lviv Polytechnic National University, Lviv, Ukraine

Nataliya Kuskova Institute of Pulse Processes and Technologies, NAS of Ukraine, Mykolaiv, Ukraine

O. V. Kuzyk Drohobych Ivan Franko State Pedagogical University, Drohobych, Ukraine

Svitlana Kyrii National Technical University of Ukraine "Igor Sikorsky Kyiv Polytechnic Institute", Kyiv, Ukraine

M. M. Lazarenko Physical Faculty, Taras Shevchenko National University of Kyiv, Kyiv, Ukraine;
Faculty of Biotechnology and Environmental Control, Taras Shevchenko National University of Kyiv, Kyiv, Ukraine

M. V. Lazarenko Faculty of Biotechnology and Environmental Control, Taras Shevchenko National University of Kyiv, Kyiv, Ukraine

Tetiana A. Len Department of Physics, Taras Shevchenko National University of Kyiv, Kyiv, Ukraine

Ya. I. Lepikh Odesa I. I. Mechnikov National University, Odesa, Ukraine

Marta Litynska Igor Sikorsky Kyiv Polytechnic Institute, Kyiv, Ukraine

S. V. Lizunova G.V. Kurdyumov Institute for Metal Physics of the N.A.S. of Ukraine, Kyiv, Ukraine

V. V. Lizunov G.V. Kurdyumov Institute for Metal Physics of the N.A.S. of Ukraine, Kyiv, Ukraine

P. Y. Lyutyy Department of Materials Science and Engineering, Lviv Polytechnic National University, Lviv, Ukraine

E. V. Maistruk Department of Electronics and Power Engineering, Yuriy Fedkovych Chernivtsi National University, Chernivtsi, Ukraine

Antonina Maizelis National Technical University “Kharkiv Polytechnic Institute”, Kharkiv, Ukraine

L. I. Makarenko G.V. Kurdyumov Institute for Metal Physics of the N.A.S. of Ukraine, Kyiv, Ukraine

A. Makhinia Vienna University, Vienna, Austria

Olena Makido Department of Physical Chemistry of Fossil Fuels of the Institute of Physical-Organic Chemistry and Coal Chemistry named after L. M. Lytvynenko of the National Academy of Sciences of Ukraine, Lviv, Ukraine

Antonina Malyushevskaya Institute of Pulse Processes and Technologies, NAS of Ukraine, Mykolaiv, Ukraine

O. Yu. Mariichak Vasyl’ Stus Donetsk National University, Vinnytsia, Ukraine

O. Matsenko Department of Chemistry, Kyiv National University of Construction and Architecture, Ave of Air Forces, Kyiv, Ukraine

Lyudmila Yu. Matzui Department of Physics, Taras Shevchenko National University of Kyiv, Kyiv, Ukraine

Yurii Yu. Moiseienko Department of Physics, Taras Shevchenko National University of Kyiv, Kyiv, Ukraine

V. B. Molodkin G.V. Kurdyumov Institute for Metal Physics of the N.A.S. of Ukraine, Kyiv, Ukraine

V. V. Molodkin G.V. Kurdyumov Institute for Metal Physics of the N.A.S. of Ukraine, Kyiv, Ukraine

O. O. Mosia Educational Scientific Institute of High Technologies, Taras Shevchenko National University of Kyiv, Kyiv, Ukraine

S. D. Nesin Department of Physics of Polymers, Institute of Macromolecular Chemistry of the National Academy of Sciences of Ukraine, Kyiv, Ukraine

S. V. Nichyi Department of Electronics and Power Engineering, Yuriy Fedkovych Chernivtsi National University, Chernivtsi, Ukraine

O. M. Nikipelova Engineering and Technology Institute “Biotechnika” of NAAS of Ukraine, Odes’ka Oblast, Ukraine

G. I. Nizkova G.V. Kurdyumov Institute for Metal Physics of the N.A.S. of Ukraine, Kyiv, Ukraine

I. G. Orletskyi Department of Electronics and Power Engineering, Yuriy Fedkovych Chernivtsi National University, Chernivtsi, Ukraine

Valeriia M. Ovdenko Institute of Physics of National Academy of Sciences of Ukraine, Kyiv, Ukraine;

Department of Macromolecular Chemistry, Taras Shevchenko National University of Kyiv, Kyiv, Ukraine

Iryna V. Ovsiienko Department of Physics, Taras Shevchenko National University of Kyiv, Kyiv, Ukraine

V. M. Palyukh Department of Strength of Materials and Structural Mechanics, Lviv Polytechnic National University, Lviv, Ukraine

A. V. Panko F.D. Ovcharenko Institute of Biocolloidal Chemistry of NAS of Ukraine, Kyiv, Ukraine

O. Pertko V.P. Kukhar Institute of Bioorganic Chemistry and Petrochemistry of the National Academy of Sciences of Ukraine, Kyiv, Ukraine

Anna Ploshchyk Yuriy Fedkovych Chernivtsi National University, Chernivtsi, Ukraine

Iryna Pohrelyuk Karpenko Physico-Mechanical Institute of the NASU, Lviv, Ukraine

Serhii I. Pokutnii Chuiko Institute of Surface Chemistry of National Academy of Sciences of Ukraine, Kyiv, Ukraine;
Institute of Physics of National Academy of Sciences of Ukraine, Kyiv, Ukraine

Ruslan Politanskyi Yuriy Fedkovych Chernivtsi National University, Chernivtsi, Ukraine

Volodymyr Posuvailo Karpenko Physico-Mechanical Institute of the NASU, Lviv, Ukraine

V. Povazhnyi V.P. Kukhar Institute of Bioorganic Chemistry and Petrochemistry of the National Academy of Sciences of Ukraine, Kyiv, Ukraine

Volodymyr Povazhnyi V.P. Kukhar Institute of Bioorganic Chemistry and Petrochemistry, NAS of Ukraine, Kyiv, Ukraine

V. A. Prokopenko F.D. Ovcharenko Institute of Biocolloidal Chemistry of NAS of Ukraine, Kyiv, Ukraine

S. V. Radio Vasyl' Stus Donetsk National University, Vinnytsia, Ukraine

I. Rovetskii Lviv State University of Life Safety, Lviv, Ukraine

Serhii Ruban LLC RPE «RD PRODUCTION GROUP», Kyiv, Ukraine

Ye. Sheludko V.P. Kukhar Institute of Bioorganic Chemistry and Petrochemistry of the National Academy of Sciences of Ukraine, Kyiv, Ukraine

Liudmyla Shmeleva Taras Shevchenko National University of Kyiv, Kyiv, Ukraine

Vladyslav Sokol V.P. Kukhar Institute of Bioorganic Chemistry and Petrochemistry, NAS of Ukraine, Kyiv, Ukraine

M. O. Sosnovska Physical Faculty, Taras Shevchenko National University of Kyiv, Kyiv, Ukraine

A. I. Stolyarchuk Drohobych Ivan Franko State Pedagogical University, Drohobych, Ukraine

I. D. Stolyarchuk Drohobych Ivan Franko State Pedagogical University, Drohobych, Ukraine

Anatol Suprun Taras Shevchenko National University of Kyiv, Kyiv, Ukraine

G. Taranyik International European University, Kyiv, Ukraine

Tetiana Tkachenko V.P. Kukhar Institute of Bioorganic Chemistry and Petrochemistry, NAS of Ukraine, Kyiv, Ukraine

A. M. Trostianchyn Department of Materials Science and Engineering, Lviv Polytechnic National University, Lviv, Ukraine

Tatiana L. Tsaregradskaya Department of Physics, Taras Shevchenko National University of Kyiv, Kyiv, Ukraine

Sardor Tulaganov Arifov Institute of Ion-Plasma and Laser Technologies of Academy of Sciences, Tashkent, Uzbekistan

Oleh V. Turkov Department of Physics, Taras Shevchenko National University of Kyiv, Kyiv, Ukraine

A. V. Varukha Physical Faculty, Taras Shevchenko National University of Kyiv, Kyiv, Ukraine

Viktor Vasiichuk Lviv Polytechnic National University, Lviv, Ukraine

B. D. Vasyliv Department of Materials Science and Engineering, Lviv Polytechnic National University, Lviv, Ukraine

Y. V. Vasylyk G.V. Kurdyumov Institute for Metal Physics of the N.A.S. of Ukraine, Kyiv, Ukraine

V. I. Vavrukh Department of Materials Science and Engineering, Lviv Polytechnic National University, Lviv, Ukraine

V. V. Vira Department of Strength of Materials and Structural Mechanics, Lviv Polytechnic National University, Lviv, Ukraine

Maria Vistak Danylo Halytsky Lviv National Medical University, Lviv, Ukraine

T. P. Vladimirova G.V. Kurdyumov Institute for Metal Physics of the N.A.S. of Ukraine, Kyiv, Ukraine

O. Yu Voitenko F.D. Ovcharenko Institute of Biocolloidal Chemistry of NAS of Ukraine, Kyiv, Ukraine

Yu. Voloshyna V.P. Kukhar Institute of Bioorganic Chemistry and Petrochemistry of the National Academy of Sciences of Ukraine, Kyiv, Ukraine

Lyudmila L. Vovchenko Department of Physics, Taras Shevchenko National University of Kyiv, Kyiv, Ukraine

K. S. Yablochkova Physical Faculty, Taras Shevchenko National University of Kyiv, Kyiv, Ukraine

Olena Yanushevska National Technical University of Ukraine "Igor Sikorsky Kyiv Polytechnic Institute", Kyiv, Ukraine

Vitalii Yevdokymenko V.P. Kukhar Institute of Bioorganic Chemistry and Petrochemistry, NAS of Ukraine, Kyiv, Ukraine

Ye. V. Zabolotnii Institute for Sorption and Problems of Endoecology, National Academy of Sciences of Ukraine, Kyiv, Ukraine

I. M. Zabolotnyy G.V. Kurdyumov Institute for Metal Physics of the N.A.S. of Ukraine, Kyiv, Ukraine

V. O. Zazhigalov Institute for Sorption and Problems of Endoecology, National Academy of Sciences of Ukraine, Kyiv, Ukraine

Chapter 1
Intergranular Changes in the Microstructure of Ceramics Based on Transition Metal Oxides

H. Klym and Yu. Kostiv

Abstract The transformation of defects and pores within spinel-type ceramics is a multifaceted process influenced by the incorporation of supplementary phases. This transformation follows the dual pathways of a two-component decomposition mechanism, where the interplay between structural modifications and defect dynamics drives the evolution of the ceramic material. Detailed investigations have demonstrated that increasing the concentration of supplementary phases within the ceramic matrix initiates the gradual fragmentation of voids. These fragmented voids subsequently undergo agglomeration, a process propelled by the influence of temporal and thermodynamic forces. This agglomeration leads to significant alterations in the microstructure, impacting the material's overall properties. The supplementary phases, particularly those extracted in close proximity to intergranular boundaries, play a critical role in defining the ceramic's characteristics. These extracted phases serve as active sites for the emergence of unique regions within the material. These regions exhibit a remarkable ability to trap and confine positrons, forming highly localized positron trapping centers. The presence of such centers is crucial for understanding the internal nanostructure of the ceramics, as they provide valuable information about the defect landscape and phase interactions at an atomic level. The creation of these positron trapping sites is facilitated by the supplementary phases' ability to segregate at grain boundaries, where they influence the local microenvironment. These emergent sites are particularly effective in capturing positrons, highlighting their significance in the material's behavior. The intricate balance between void fragmentation, agglomeration, and the formation of trapping centers underscores the complex interplay of compositional and structural factors in spinel-type ceramics. This process not only enhances the functional properties of the material but also provides a deeper understanding of the role of supplementary phases in modifying ceramic microstructures. The findings highlight the importance of controlling the concentration and distribution of these phases to optimize the material for advanced applications, where defect control and nanostructuring are critical for performance.

H. Klym (✉) · Yu. Kostiv
Lviv Polytechnic National University, Lviv, Ukraine
e-mail: halyna.i.klym@lpnu.ua

O. Fesenko and L. Yatsenko (eds.), *Functional Nanomaterials, Nanocatalysts, Nanotechnologies, and Their Applications*, Springer Proceedings in Physics 321,
https://doi.org/10.1007/978-3-031-99136-3_1

1.1 Introduction

Materials with diverse functional applications, such as crystals, nanostructures, and nanofilms, have gained considerable attention due to their potential to transform various technological domains [1–5]. Among these, ceramic materials with a spinel structure are particularly promising. Spinel-type ceramics have become a focal point of scientific research owing to their exceptional properties and wide-ranging applicability in different fields [6–10]. Notably, temperature-sensitive ceramics of the composition $Cu_{0.1}Ni_{0.8}Co_{0.2}Mn_{1.9}O_4$, which belong to this class, find applications in devices such as negative temperature coefficient (NTC) thermistors, precise temperature sensors, and in-rush current limiters, among others [11–13]. Their multifunctional capabilities have positioned these ceramics as a subject of extensive study, with researchers striving to optimize their properties and expand their potential applications.

A critical aspect influencing the performance and reliability of these ceramics is the temperature–time sintering process, which governs the formation and distribution of secondary phases within the bulk and surface of ceramic samples [14–16]. Earlier studies have highlighted the significant impact of this process on the structural and functional properties of spinel ceramics [17, 18]. One particularly intriguing finding emerged when the NiO phase content in these ceramics was reduced, leading to a notable decrease in thermal aging effects [17]. Specifically, the relative resistance changes were limited to less than 3%, underscoring the complexity of these materials and the potential to tailor their properties through precise compositional adjustments.

To address the challenges associated with degradation in ceramics, researchers often employ chemical modification strategies. These involve the introduction of metallic additives during the preparation stage, strategically targeting intergranular regions near grain boundaries [19, 20]. Such modifications play a vital role in suppressing thermally-induced aging phenomena by stabilizing the cationic distribution within ceramic grains. As a result, chemically modified ceramics exhibit superior stability compared to their unmodified counterparts, showcasing the importance of understanding the intricate interplay of chemistry and material science in enhancing the durability and performance of these materials.

Despite these advancements, the structural complexity of spinel-type ceramics, encompassing grains, intergranular boundaries, and pores, continues to pose significant challenges for researchers [21, 22]. To overcome these obstacles, the development and application of advanced characterization techniques are essential. Positron annihilation lifetime (PAL) spectroscopy, a relatively novel method for studying fine-grained functional materials, has emerged as a valuable tool in this regard [23–25]. This technique is highly sensitive to regions of low electron density, enabling the detection of void species within the structural framework of ceramics [26–29]. However, interpreting PAL spectroscopy results in the context of ceramics remains a challenging task due to the intricate influence of crystallographic characteristics of individual grains and structural irregularities at intergranular contacts [21, 26].

The present study aims to explore the structural intricacies of high-reliability transition-metal manganite ceramics with the composition $Cu_{0.1}Ni_{0.8}Co_{0.2}Mn_{1.9}O_4$, focusing specifically on the interactions between grains and pores. A comprehensive approach combining PAL spectroscopy with traditional structural characterization methods will be employed to achieve this goal. By unraveling the structural and functional mechanisms underlying these ceramics, this study seeks to enhance our understanding of their performance and stability, paving the way for their integration into a broad spectrum of technological innovations.

1.2 Experimental

High-purity carbonate salts were precisely measured and subjected to thorough quality control before being processed. The salts were meticulously wet-mixed to ensure homogeneity and then thermally decomposed under ambient air conditions at a temperature of 700 °C for 4 h [17, 18]. The resulting decomposed powders underwent milling to achieve uniform particle sizes, followed by blending with an organic binder. These prepared powders were then carefully pressed into disks, each approximately 10 mm in diameter and 1 mm thick. The blanks were divided into four distinct batches, with each batch sintered following specific time–temperature profiles described in [17], which outlines the sintering processes for $Cu_{0.1}Ni_{0.8}Co_{0.2}Mn_{1.9}O_4$ ceramics.

The sintering process was strategically designed to create optimal conditions that minimize degradation and stabilize the ceramic structure [11]. A notable aspect of this process was the formation of an additional NiO phase with a NaCl-type structure, which significantly influenced the final microstructure of the ceramics. These ceramics were identified as Ni-deficient compared to the stoichiometric baseline composition of $Cu_{0.1}Ni_{0.8}Co_{0.2}Mn_{1.9}O_4$, used as the reference in disproportionality calculations.

The four batches of ceramics prepared contained varying NiO phase proportions, ranging from 1 to 12%. The differences in NiO content were directly linked to the thermal energy absorbed during the sintering process. Specifically, the batches were characterized as follows: sample No. 1 contained 1% NiO, sample No. 2 had 8% NiO, sample No. 3 included 10% NiO, and sample No. 4 contained 12% NiO. The amount of energy transferred during sintering was calculated numerically as the area above the baseline temperature of 920 °C (the temperature at which single-phase $Cu_{0.1}Ni_{0.8}Co_{0.2}Mn_{1.9}O_4$ ceramics are formed) on the temperature–time curve [17].

Microstructural characterization via X-ray diffractometry revealed slight increases in the lattice constant of the primary spinel phase, which ranged from 8.38Å to 8.41 Å. Meanwhile, the NiO phase lattice parameter remained consistent at approximately 4.18 Å, regardless of the variation in NiO content (1%, 8%, 10%, and 12%).

To further investigate the microstructural properties of the sintered ceramics, electron microscopy was performed using a JSM-6700F scanning electron microscope. Cross-sectional morphological analyses were conducted on samples extracted from

both the surface and central regions of the ceramic disks, providing a comprehensive view of their structural uniformity and grain distribution [17].

Additionally, positron annihilation lifetime (PAL) spectroscopy was employed to analyze the defects within the ceramic microstructure. Measurements were conducted using an ORTEC spectrometer with a ^{22}Na positron source sandwiched between two ceramic samples [17, 26]. The obtained data were analyzed using the LT software package [30, 31], applying a two-component fitting method to achieve precise parameter estimation. Key trapping parameters, such as the positron lifetime in defect-free bulk material (τ_b), average positron lifetime ($\tau_{av.}$), and defect trapping rate (κ_d), were calculated from the short and long positron lifetimes (τ_1 and τ_2) and their respective intensities (I_1 and I_2, where $I_1 + I_2 = 1$) [32, 33].

Furthermore, the difference between the long positron lifetime (τ_2) and bulk lifetime (τ_b) served as a quantitative measure of the size of extended defects where positrons were trapped [17]. Through this detailed analysis, the study offers a deeper understanding of the influence of sintering conditions and NiO phase variation on the microstructure and defect characteristics of $Cu_{0.1}Ni_{0.8}Co_{0.2}Mn_{1.9}O_4$ ceramics.

1.3 Results and Discussion

To provide a comprehensive understanding of the phenomena under investigation, a detailed microstructural analysis of the prepared ceramic samples was carried out. As shown in Fig. 1.1, the microstructural features of the ceramic samples reveal significant variations in their grain-pore structures, which can be attributed to differences in fabrication conditions and material properties [17].

Sample 1 exhibits a microstructure characterized by fine grains with an average size of approximately 2 μm. Numerous intergranular pores are distributed throughout the sample, with dimensions generally not exceeding 2 μm. These pores are irregularly shaped and appear interconnected to some extent. Additionally, scattered patches of a white film, identified as an additional phase of NiO, are prominently observed. This NiO phase is mainly localized near the intergranular boundaries and, in some cases, partially fills the pores. The presence of this phase suggests incomplete sintering or chemical reactions leading to the segregation of NiO during the processing stage.

Sample 2 shows a marked increase in grain size compared to Sample 1. The grains in this sample typically range between 6 μm and 9–10 μm. The microstructure indicates a transition towards more compact grain arrangements, with reduced porosity compared to Sample 1. The NiO phase is again observed as a white film, although it is primarily concentrated near the grain boundaries. This selective localization of the NiO film may indicate its role in influencing grain boundary properties and potentially contributing to the overall ceramic performance.

In Sample 3, the microstructure demonstrates a further evolution, with a noticeable transformation in the grain arrangement. The grains appear more interconnected, giving the material a monolithic appearance. The porosity is significantly reduced,

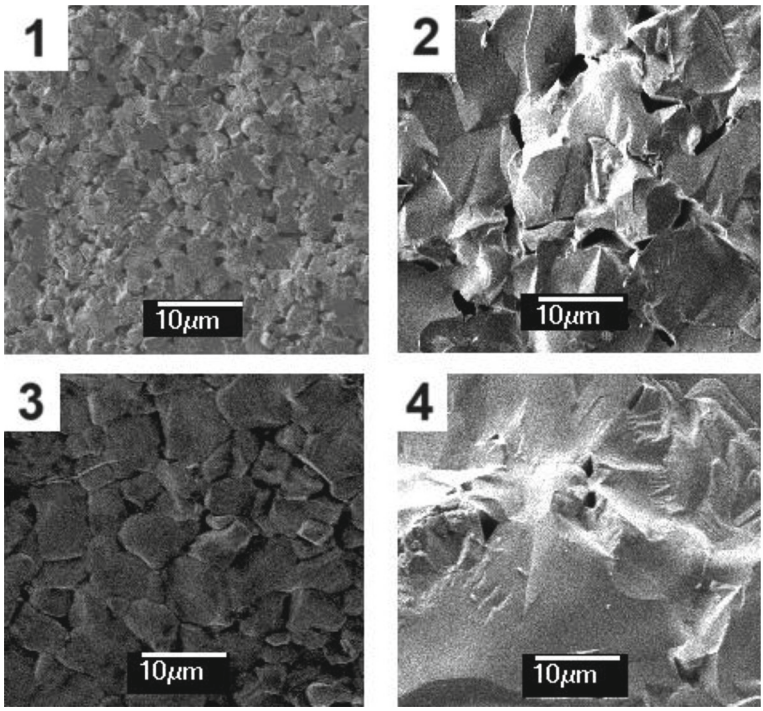

Fig. 1.1 Microstructure of the $Cu_{0.1}Ni_{0.8}Co_{0.2}Mn_{1.9}O_4$ ceramics

with only isolated pores observed, typically around 2 μm in size. A distinguishing feature of this sample is the formation of a bright, continuous NiO layer measuring approximately 10–11 μm in thickness. This layer uniformly coats the grain surfaces, indicating enhanced phase separation and a possible redistribution of NiO during the sintering process.

Sample 4 represents the culmination of the structural transformations, displaying a fully merged grain structure. The grains are densely packed, with minimal porosity. The few remaining pores are larger, measuring around 4 μm in diameter. The NiO phase forms a uniform and continuous layer over the entire ceramic surface. Interestingly, the distribution of the NiO phase is non-uniform within the bulk of the material, with a higher concentration near intergranular boundaries. This non-uniform distribution suggests that the NiO phase acts as a trapping site for positrons migrating through the ceramic matrix, which may have implications for the material's electronic and mechanical properties.

Overall, the progressive changes in grain size, porosity, and the distribution of the NiO phase across the four samples highlight the impact of processing conditions on the microstructural and functional characteristics of the ceramics. These variations underscore the importance of optimizing sintering parameters to achieve desired material properties for specific applications [17].

By employing a two-state model for positron trapping [22, 34–36], the analysis provides insights into the interactions of positrons within the ceramic structure. In this model, the first spectral component corresponds to the primary spinel structure of the material, while the second spectral component is associated with extended free-volume defects located near intergranular boundaries, in close proximity to the additional NiO phases. The intensities of these components, I_1 and I_2, serve as indicators of the material's composition: I_1 reflects the relative abundance of the primary spinel phase, while I_2 correlates with the presence of the NiO phase near grain boundaries.

For Sample 1, the observed positron lifetimes, τ_1 and τ_2, are characteristic of manganite ceramics with the composition $Cu_{0.1}Ni_{0.8}Co_{0.2}Mn_{1.9}O_4$. The measured lifetimes are 0.19 ns for τ_1 and 0.38 ns for τ_2, as depicted in Fig. 1.2. These values provide critical information about the trapping sites within the ceramic. The influence of the additional NiO phase, constituting 1% of the material, on positron trapping is evident in the positron capture rate (κ_d), which is calculated to be 0.48 ns^{-1} (Fig. 1.3). This parameter quantifies the efficiency of positron trapping at defects, demonstrating the role of NiO in modifying the material's microstructure and defect characteristics.

In Sample 2, a distinct processing approach involving prolonged annealing is employed. The ceramics undergo an 8-h annealing process at a sintering temperature of 920 °C, significantly lower than the sintering temperature for monophasic ceramics (1200 °C). The reduced temperature, achieved by a controlled cooling rate of 100 °C per hour during the final synthesis stage, facilitates the formation of an additional phase containing 8% NiO. This phase is predominantly concentrated along the grain boundaries. The reduction in sintering temperature alters the positron trapping dynamics, as evidenced by changes in the fitting parameters.

For this sample, the lifetime of the first spectral component, τ_1, decreases slightly to 0.17 ns, reflecting modifications in the primary spinel structure. Concurrently, the intensity of the second component, I_2, increases slightly, accompanied by an elongation of the second lifetime, τ_2. These changes suggest a growing influence of the NiO phase and its associated defects on the positron trapping process. Most notably, the positron capture rate κ_d rises significantly to 0.62 ns^{-1}, representing an increase of nearly 30% compared to Sample 1.

The adjustments in the second spectral component's parameters, particularly the increase in τ_2 and I_2, provide further evidence of microstructural changes. These observations indicate the initial fragmentation of voids within the ceramic matrix, followed by their subsequent agglomeration as the concentration of the NiO phase increases. This behavior highlights the critical role of the additional phase in modifying defect structures and influencing positron behavior.

These findings underscore the strong correlation between processing parameters, microstructural evolution, and positron trapping characteristics in ceramics. The deliberate adjustment of synthesis conditions, such as sintering temperature and NiO content, provides a valuable pathway for tailoring the properties of these materials for specific applications.

In Sample 3, the concentration of the additional NiO phase increases significantly, reaching 10%. This notable rise in NiO content exerts a pronounced influence on

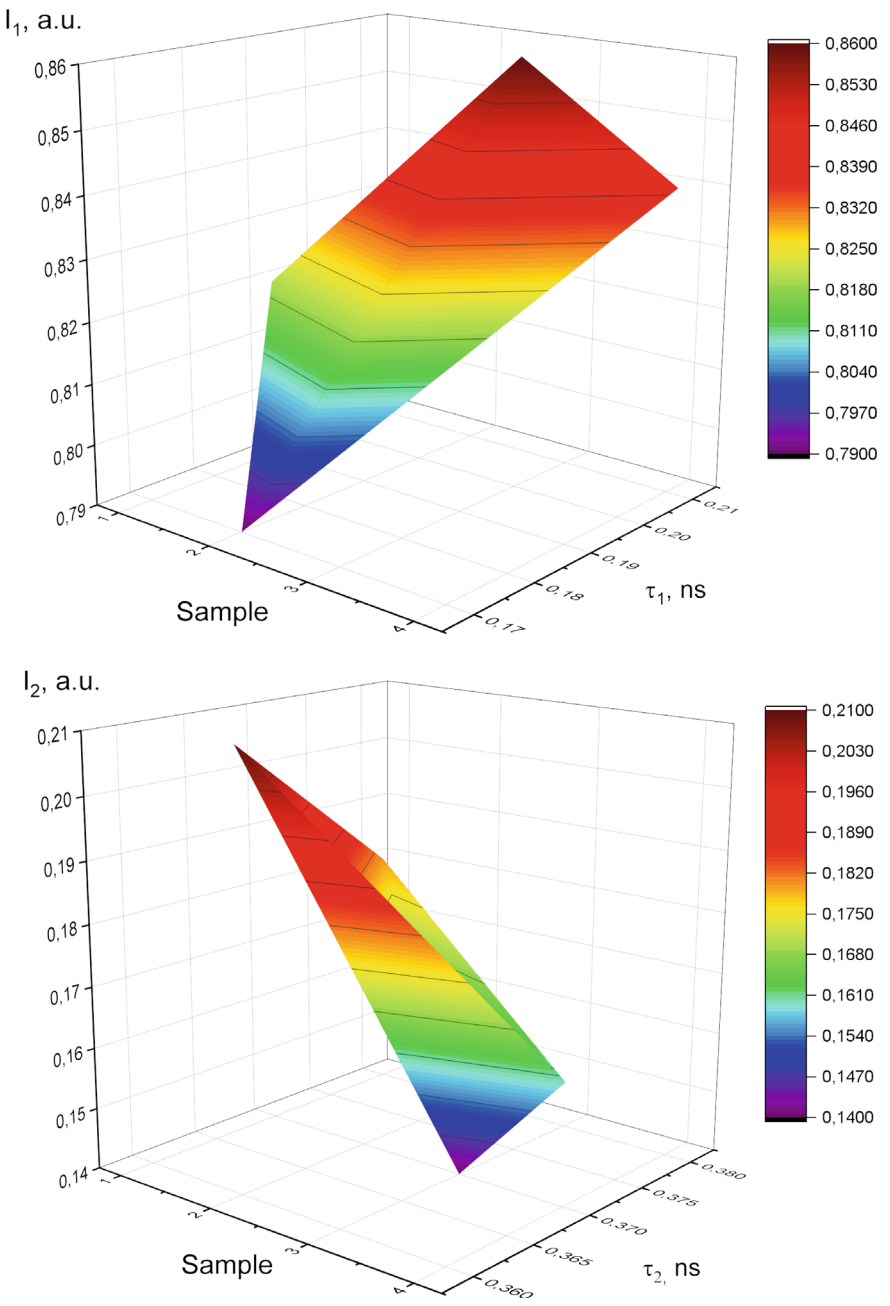

Fig. 1.2 Lifetimes and intensities of the first and the second PAL components

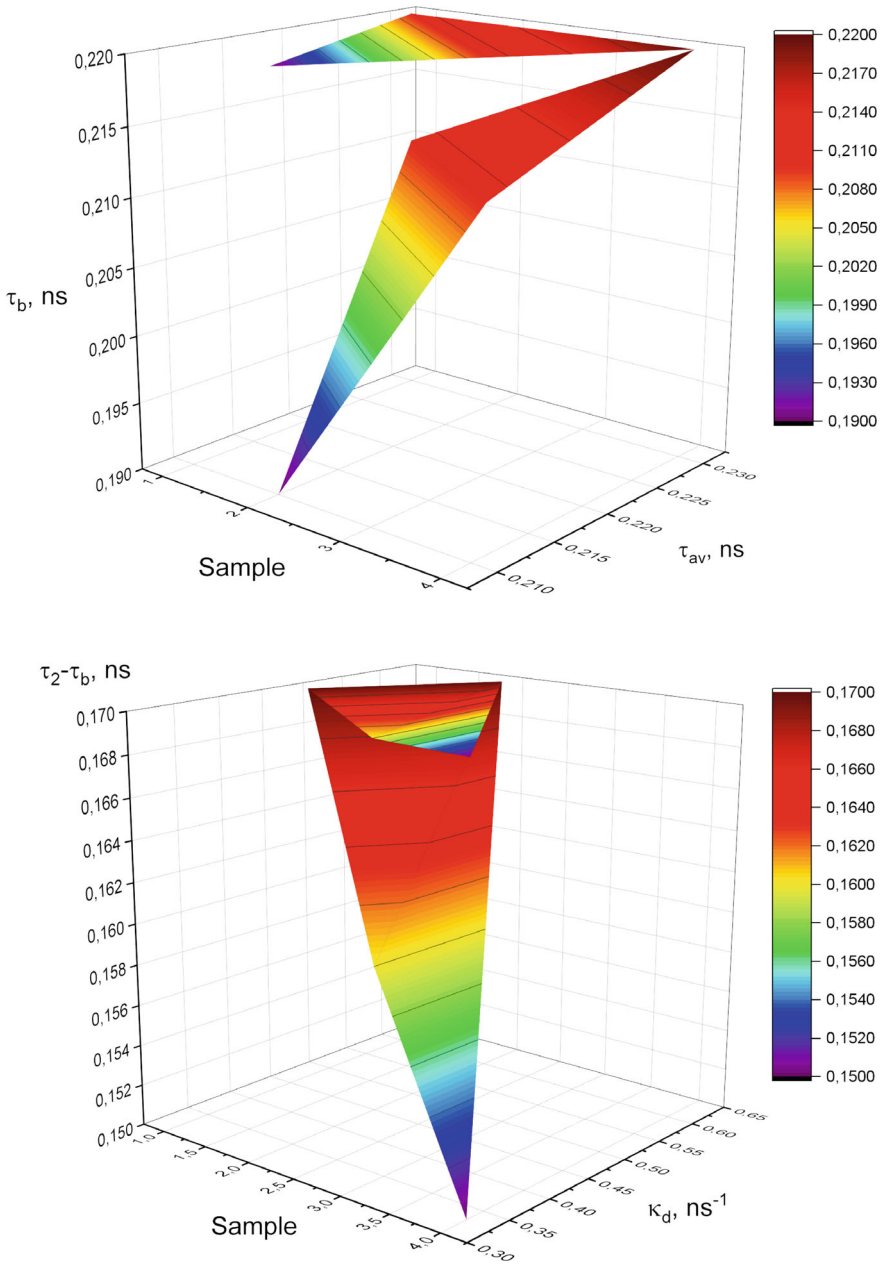

Fig. 1.3 Positron trapping modes for $Cu_{0.1}Ni_{0.8}Co_{0.2}Mn_{1.9}O_4$ ceramic

the ceramic's microstructure and its positron trapping characteristics. The elevated presence of NiO disrupts the structural integrity of the spinel phase, as evidenced by an increase in the lifetime parameter τ_1, which rises to 0.20 ns. This increase indicates a higher degree of free-volume defects within the primary spinel matrix. At the same time, the positron capture rate experiences a decline, dropping to 0.34 ns^{-1}. This reduction in κ_d suggests a diminished efficiency in positron trapping by defects, possibly due to alterations in the defect density or changes in the defect environment caused by the additional phase.

As the NiO content is further increased from 10 to 12%, more pronounced merging phenomena are observed within the ceramic structure. This intensified merging can be attributed to the higher NiO concentration, which enhances phase segregation and facilitates a closer packing of the grains. Interestingly, despite this structural evolution, the key parameters, τ_1 and κ_d, remain relatively stable, showing no significant changes beyond the 10% threshold. This stability highlights the saturation effect, where further increases in NiO content beyond a certain point no longer substantially influence the positron trapping characteristics.

The structural and trapping behavior is also influenced by the thermal energy imparted to the ceramic during the sintering process. As the sintering temperature is raised from 1200 to 1300 °C, the thermal energy transferred to the ceramic intensifies, leading to further changes in the spinel structure. This increase in sintering temperature amplifies the overbaking effect, resulting in a slight degradation of the spinel's perfection. Consequently, the lifetime parameter τ_1 increases slightly from 0.20 to 0.21 ns, reflecting additional structural distortions.

Interestingly, despite the changes in τ_1, the positron trapping behavior associated with bulk defects remains largely unaffected. The second lifetime component τ_2, and the positron capture rate κ_d show minimal variation. Similarly, average lifetime τ_{av} and the difference $(\tau_2 - \tau_b)$ do not exhibit substantial changes, further emphasizing the relative stability of these parameters under the given conditions (Fig. 1.3).

The increase in NiO content and the elevation of sintering temperature have a complex impact on the ceramics. While the higher NiO concentration triggers enhanced merging of the ceramic grains and disrupts the spinel structure, the positron trapping characteristics reach a point of stability beyond the 10% NiO threshold. The interplay between material composition, thermal energy, and structural integrity underscores the delicate balance required to optimize ceramics for desired properties. These findings provide valuable insights into the design and processing of ceramics with tailored microstructures and functional attributes.

A notable aspect of the ceramic microstructural evolution is the shift in the type of positron capture centers during the monolithization process, particularly when transitioning from Sample 2 to Sample 3 and from Sample 2 to Sample 4. This transformation is clearly evidenced by a sharp reduction in the parameter κ_d, which decreases from 1.9 to 1.7—a 10% decline. Despite this change, the fundamental nature of positron capture by defects remains consistent across all samples. The size of bulk defects near the grain boundaries, derived from the difference $(\tau_2 - \tau_b)$, is estimated to correspond to one or two atomic vacancies [17].

The internal nanostructuring of $Cu_{0.1}Ni_{0.8}Co_{0.2}Mn_{1.9}O_4$ ceramics evolves in response to the content of the additional NiO phase and its distribution at grain boundaries. When the NiO content along grain boundaries is elevated to 8%, there is a notable increase in the number of defects or voids that act as positron capture centers. However, these defects undergo a reduction in size, resulting in void fragmentation. This fragmentation process significantly enhances the positron capture rate κ_d, as more efficient trapping sites are created within the ceramic microstructure.

When the NiO content is further increased to 10%, the behavior of the material changes significantly. The number of positron trapping centers and the parameter κ_d experience a marked decline. This reduction can be attributed to the redistribution of the additional NiO phase. At this concentration, a substantial portion of NiO is no longer confined to the grain boundaries but instead migrates to the ceramic surface. This redistribution correlates with the expansion of the ceramic grains and the formation of a monolithic structure. As the grains merge, the number of grain boundaries decreases, reducing the regions where NiO was initially segregated and, consequently, the number of positron trapping centers.

Increasing the NiO content to 12% signals the saturation of the defect formation process. At this stage, positron capture parameters such as κ_d exhibit minimal changes, indicating that the system has reached a stable state regarding defect and void formation.

The evolution of the internal volumetric nanostructure of the $Cu_{0.1}Ni_{0.8}Co_{0.2}Mn_{1.9}O_4$ ceramics, particularly with respect to defect and void formation, suggests that the optimal NiO phase content is 10%. This concentration achieves a balance between defect generation and structural integrity, supporting efficient positron trapping without significant degradation of the spinel matrix. Changes in the positron capture rate κ_d serve as a sensitive metric for understanding the ceramic structure's progression during sintering.

In Sample 2, the greater presence of grain boundaries and pores results in intensified positron trapping. This is evidenced by a higher positron capture rate due to the increased density of defects in the ceramic matrix. The reduction in thermal energy transfer during the sintering process plays a role in sustaining these defects and influencing the trapping behavior. Conversely, as the sintering temperature increases and the NiO phase segregates more prominently to the grain boundaries and surfaces, the ceramic structure undergoes significant changes, leading to variations in κ_d and the monolithization of the material.

The relationship between thermal energy transfer during sintering, defect formation, and nanostructuring is further illustrated in Fig. 1.4, which provides a breakdown of the component contributions to the positron trapping process. These findings highlight the intricate interplay between material composition, defect dynamics, and structural evolution in determining the functional properties of ceramics.

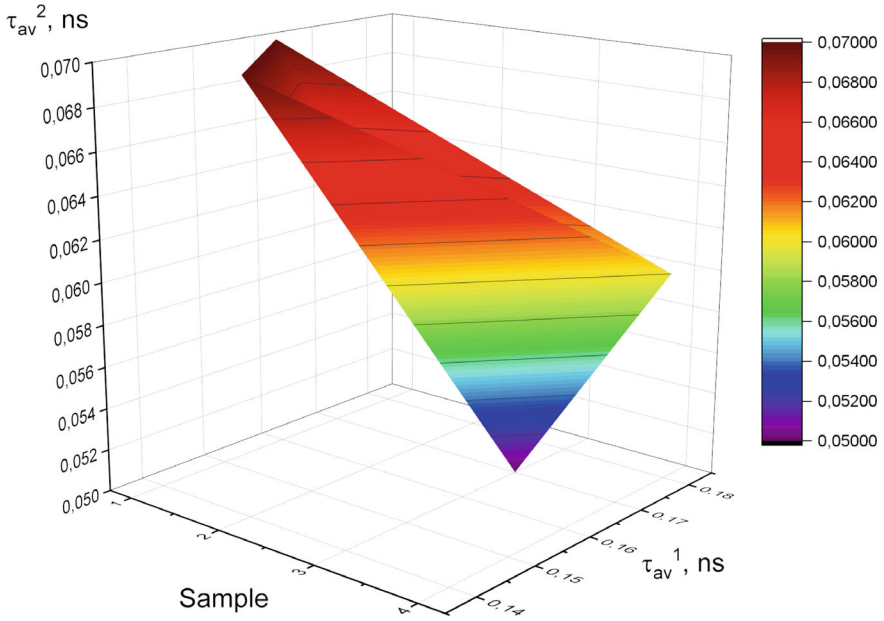

Fig. 1.4 Inputs of the first and the second components

1.4 Conclusions

In conclusion, the results derived from positron annihilation lifetime measurements provide compelling evidence for the occurrence of interphase processes within the mixed transition-metal manganite $Cu_{0.1}Ni_{0.8}Co_{0.2}Mn_{1.9}O_4$ ceramics. These processes are closely linked to the structural transformations induced by the merging phenomena observed during technological modifications, as well as the influence of an optimal concentration of the additional NiO phase.

The PAL findings reveal how changes in NiO content and sintering conditions impact the ceramic's nanostructure, particularly in terms of defect formation, void fragmentation, and grain merging. These transformations highlight the delicate interplay between material composition, defect distribution, and structural integrity, providing a detailed understanding of the mechanisms underlying the observed changes.

Notably, the PAL results align closely with the insights obtained through complementary microstructural characterization techniques such as X-ray diffractometry and electron microscopy. These methods confirm the structural alterations identified in the PAL measurements, further demonstrating that the observed changes in the ceramics are a direct consequence of the technological modification process. The consistency across these techniques underscores the reliability of the findings and emphasizes the importance of a multi-faceted analytical approach.

By integrating evidence from PAL measurements, X-ray diffractometry, and electron microscopy, this study provides a comprehensive picture of the intricate relationship between microstructural evolution and processing interventions in $Cu_{0.1}Ni_{0.8}Co_{0.2}Mn_{1.9}O_4$ ceramics. This combined methodology not only validates the observed phenomena but also offers valuable insights into the underlying mechanisms driving these transformations. Such an approach is critical for optimizing the design and processing of advanced ceramics with tailored microstructures and functional properties, contributing to the development of materials for specialized technological applications.

Acknowledgements Authors would like to thanks the Ministry of Education and Science of Ukraine for providing support. H.K. also thanks Prof. O. Shpotyuk for valuable discussions.

References

1. X. Rong, D. Zhao, C. He, N. Zhao, Recent progress in aluminum matrix composites reinforced by in situ oxide ceramics. J. Mater. Sci. **59**(22), 9657–9684 (2024). https://doi.org/10.1007/s10853-023-09120-z
2. X. Yang, X. Gao, S. Zhang, J. Zhao, X. Zhang, X. Song, X. Hao, Anomalous photovoltaic effect in $Na_{0.5}Bi_{0.5}TiO_3$-based ferroelectric ceramics based on domain engineering. J. Mater. **10**(5), 975–983 (2024). https://doi.org/10.1016/j.jmat.2023.10.010
3. S.V. Luniov, P.F. Nazarchuk, O.V. Burban, Parameters of the high-energy Δ1-minimum of the conduction band in n-Ge. J. Phys. Stud. **17**(3), 3702 (2013). https://doi.org/10.30970/jps.17.3702
4. S.V. Luniov, A.I. Zimych, P.F. Nazarchuk, V.T. Maslyuk, I.G. Megela, Specific features of electron scattering in uniaxially deformed n-Ge single crystals in the presence of radiation defects. Radiat. Eff. Defects Solids **171**(11–12), 855–868 (2016)
5. S.V. Luniov, Calculation of electron mobility for the strained germanium nanofilm. J. Nano Electron. Phys. **11**(2), 02023–02031 (2019)
6. X. Yang, Y. Lai, Y. Zeng, F. Yang, F. Huang, B. Li, H. Su, Spinel-type solid solution ceramic $MgAl_2O_4$-Mg_2TiO_4 with excellent microwave dielectric properties. J. Alloy. Compd. **898**, 162905 (2022). https://doi.org/10.1016/j.jallcom.2021.162905
7. L. Fan, J. Yao, Y. Tuo, A. Chang, Z. Chen, J. Wang, Aging properties of spinel-type high-entropy oxides $(Co_{.2}Cr_{.2}Fe_{.2}Mn_{.2}Zn_{.2})_3O_4$ for thermistors. Int. J. Appl. Ceram. Technol. **21**(6), 3990–4000 (2024). https://doi.org/10.1111/ijac.14866
8. M. Zhu, J. Cao, X. Chen, D. Ma, Y. Meng, Synthesis and thermoelectric properties of a new high-entropy spinel ferrite $(Mn_{0.2}Co_{0.2}Cu_{0.2}Zn_{0.2}Mo_{0.2})Fe_2O_4$. Ceramics Int. **50**(24), 55589–55597 (2024). https://doi.org/10.1016/j.ceramint.2024.10.420
9. S. Lin, T. Zhang, Research progress in preparation and application of spinel-type metallic oxides (M≥2). J. Alloy. Compd. 171117 (2023). https://doi.org/10.1016/j.jallcom.2023.171117
10. I. Rudavskyi, H. Klym, Y. Kostiv, I. Karbovnyk, I. Zhydenko, A. Popov, M. Konuhova, Utilizing an Arduino Uno-based system with integrated sensor data fusion and filtration techniques for enhanced air quality monitoring in residential spaces. Appl. Sci. **14**(19), 9012 (2024). https://doi.org/10.3390/app14199012
11. H. Klym, I. Hadzaman, O. Shpotyuk, M. Brunner, Integrated thick-film nanostructures based on spinel ceramics. Nanoscale Res. Lett. **9**(1), 149 (2014). https://doi.org/10.1186/1556-276X-9-149

12. C. Teichmann, J. Toepfer, Sintering and electrical properties of Cu-substituted Zn-Co-Ni-Mn spinel ceramics for NTC thermistors thick films. J. Eur. Ceram. Soc. **42**(5), 2261–2267 (2022). https://doi.org/10.1016/j.jeurceramsoc.2021.12.078
13. N. Acharya, R. Sagar, Structure and electrical properties characterization of $NiMn_2O_4$ NTC ceramics. Inorg. Chem. Commun. **132**, 108856 (2021). https://doi.org/10.1016/j.inoche.2021.108856
14. I. Karbovnyk, I. Borshchyshyn, Y. Vakhula, I. Lutsyuk, H. Klym, I. Bolesta, Impedance characterization of Cr^{3+}, Y^{3+} and Zr^{4+} activated forsterite nanoceramics synthesized by sol–gel method. Ceram. Int. **42**(7), 8501–8504 (2016). https://doi.org/10.1016/j.ceramint.2016.02.075
15. Z. Shi, X. Zhang, Z. Zheng, X. Feng, Z. Fang, B. Tang, Phase compositions, microstructures, and microwave dielectric properties of novel high-entropy spinel-structured MAl_2O_4 ceramics. J. Alloy. Compd. **1004**, 175714 (2024). https://doi.org/10.1016/j.jallcom.2024.175714
16. B. Wang, J. Yao, J. Wang, A. Chang, Enhanced structural and aging stability in cation-disordered spinel-type entropy-stabilized oxides for thermistors. ACS Appl. Electron. Mater. **4**(3), 1089–1098 (2022). https://doi.org/10.1021/acsaelm.1c01222
17. H. Klym, A. Ingram, O. Shpotyuk, J. Filipecki, I. Hadzaman, Structural studies of spinel manganite ceramics with positron annihilation lifetime spectroscopy. J. Phys. Conf. Ser. **289**(1), 012010) (2011). https://doi.org/10.1088/1742-6596/289/1/012010
18. H. Klym, I. Hadzaman, Y. Kostiv, S. Yatsyshyn, B. Stadnyk, Free-volume defects/nanopores conversion of temperature-sensitive $Cu_{0.1}Ni_{0.8}Co_{0.2}Mn_{1.9}O_4$ ceramics caused by addition phase and monolithization process. Appl. Nanosci. **12**, 1347–1354 (2022). https://doi.org/10.1007/s13204-021-01963-9
19. H. Klym, A. Ingram, I. Hadzaman, O. Shpotyuk, Evolution of porous structure and free-volume entities in magnesium aluminate spinel ceramics. Ceram. Int. **40**(6), 8561–8567 (2014). https://doi.org/10.1016/j.ceramint.2014.01.070
20. H. Klym, I. Karbovnyk, A. Luchechko, Y. Kostiv, V. Pankratova, A.I. Popov, Evolution of free volumes in polycrystalline $BaGa_2O_4$ ceramics doped with Eu^{3+} ions. Crystals **11**(12), 1515 (2021). https://doi.org/10.3390/cryst11121515
21. H. Klym, I. Hadzaman, V. Gryga, Combined study of internal nanovoids in $Cu_{0.1}Ni_{0.1}Co_{1.6}Mn_{1.2}O_4$-based thick-film layers formed near grain boundaries. Appl. Nanosci. **12**, 1257–1262 (2022). https://doi.org/10.1007/s13204-021-01801-y
22. H. Klym, I. Hadzaman, R. Vila, A.I. Popov, Extended positron–positronium trapping defects in the $MgAl_2O_4$ spinel ceramics. Physica status solidi (b). **259**(8), 2100473 (2022). https://doi.org/10.1002/pssb.202100473
23. F.A. Selim, Positron annihilation spectroscopy of defects in nuclear and irradiated materials-a review. Mater Charact **174**, 110952 (2021). https://doi.org/10.1016/j.matchar.2021.110952
24. J.V. Logan, S.W. McAlpine, P.T. Webster, C.P. Morath, M.P. Short, Positron annihilation lifetime spectroscopy: when is it feasible to decompose the spectrum? J. Appl. Phys. **130**(14) (2021). https://doi.org/10.1063/5.0049304
25. I. Makkonen, F. Tuomisto, Perspective on defect characterization in semiconductors by positron annihilation spectroscopy. J. Appl. Phys. **135**(4) (2024). https://doi.org/10.1063/5.0180024
26. H. Klym, I. Karbovnyk, S. Piskunov, A.I. Popov, Positron annihilation lifetime spectroscopy insight on free volume conversion of nanostructured $MgAl_2O_4$ ceramics. Nanomaterials **11**(12), 3373 (2021). https://doi.org/10.3390/nano11123373
27. P. Husband, I. Bartošová, V. Slugeň, F.A. Selim, Positron annihilation in transparent ceramics. J. Phys. Conf. Ser. **674**(1), 012013) (2016). https://doi.org/10.1088/1742-6596/674/1/012013
28. M. Ghasemifard, M. Ghamari, Probing the influence of temperature on defects in oxy-hydroxide ceramics by positron annihilation lifetime and coincidence Doppler broadening spectroscopy. Appl. Phys. A **128**(3), 180 (2022). https://doi.org/10.1007/s00339-022-05323-4
29. M. Ghasemifard, M. Ghamari, S. Samarin, J.F. Williams, Porosity evaluation and positron annihilation study of mesoporous aluminum oxy-hydroxide ceramics. Appl. Phys. A **126**, 1–11 (2020). https://doi.org/10.1007/s00339-020-03657-5
30. D. Giebel, J. Kansy, A new version of LT program for positron lifetime spectra analysis. Mater. Sci. Forum **666**, 138–141 (2011). https://doi.org/10.4028/www.scientific.net/MSF.666.138

31. J. Kansy, D. Giebel, Study of defect structure with new software for numerical analysis of PAL spectra. J Phys. Conf. Series **265**(1), 012030 (2011). https://doi.org/10.1088/1742-6596/265/1/012030
32. H. Klym, A. Ingram, O. Shpotyuk, O. Hotra, A.I. Popov, Positron trapping defects in free-volume investigation of Ge–Ga–S–CsCl glasses. Radiat. Meas. **90**, 117–121 (2016). https://doi.org/10.1016/j.radmeas.2016.01.023
33. H. Klym, A. Ingram, O. Shpotyuk, Free-volume nanostructural transformation in crystallized GeS_2–Ga_2S_3–CsCl glasses. Materialwissenschaft und Werkstofftechnik **47**(2–3), 198–202 (2016). https://doi.org/10.1002/mawe.201600476
34. B. Oberdorfer, R. Würschum, Positron trapping model for point defects and grain boundaries in polycrystalline materials. Phys. Rev. B Condensed Matter Mater. Phys. **79**(18), 184103 (2009). https://doi.org/10.1103/PhysRevB.79.184103
35. H. Klym, Y. Kostiv, Exploring nanovoids in spinel ceramics using positron–positronium trapping model. Mol. Cryst. Liq. Cryst. **768**(16), 849–857 (2024). https://doi.org/10.1080/15421406.2024.2366062
36. A. Yabuuchi, M. Tanaka, A. Kinomura, Short positron lifetime at vacancies observed in electron-irradiated tungsten: experiments and first-principles calculations. J. Nucl. Mater. **542**, 152473 (2020). https://doi.org/10.1016/j.jnucmat.2020.152473

Chapter 2
Hydrogen Evolution on Nanoscale Ni–Zn–Cu Alloy Films

Antonina Maizelis

Abstract The study is devoted to comparing the properties of nanosized Ni–Zn–Cu alloy films, which (Ni–Zn–Cu)/(M–M(OH)$_2$)]$_n$ multilayer coating consists of, in hydrogen evolution reaction. It is shown that the voltammograms of dissolution of the ternary alloy films contain oxidation peaks of the β-phase of the Zn–Ni alloy, the α-phase of the Cu–Zn alloy, and the alloys of "solid solutions" of Ni in Cu and Cu and Zn in Ni. The advantage of the bilayer deposited in the two-pulse potentiostatic mode over the single-layer film deposited at a potential that is average between the deposition potentials of the bilayer layers is revealed: after additional treatment, the kinetics parameters of the hydrogen evolution reaction in an alkaline medium on its surface are significantly better compared to those on a single-layer film.

2.1 Introduction

Nanostructured coatings are of increasing interest in many types of human activity. Alkaline water electrolysis is no exception. In alkaline media, unlike acidic media, the use of a wide range of electrode materials is allowed due to corrosion resistance in this media. The synthesis of nickel-based electrocatalysts is one of the main areas of research in the field of "green" energy [1]. To increase the efficiency of electrolysis, it is necessary to reduce the overvoltage of the hydrogen evolution reaction (HER) [2]. The main strategy for reducing the HER overvoltage is to increase (a) catalytic activity of electrode materials, (b) active surface area, (c) electrical conductivity, and (d) transport of gas bubbles. An increase in these characteristics is observed, e.g., on nanoporous hydrophilic surfaces [3]. To increase the surface area of the electrode, various variants of Raney nickel are used, and electrochemical methods for obtaining 3D structures, including multilayer coatings, are increasingly being used [4].

Among non-platinum metals Ni has a hydrogen atom adsorption energy close to it, which determines its high activity in HER [5]. However, Ni does not show

A. Maizelis (✉)
National Technical University "Kharkiv Polytechnic Institute", Kharkiv, Ukraine
e-mail: a.maizelis@gmail.com

O. Fesenko and L. Yatsenko (eds.), *Functional Nanomaterials, Nanocatalysts, Nanotechnologies, and Their Applications*, Springer Proceedings in Physics 321,
https://doi.org/10.1007/978-3-031-99136-3_2

sufficiently high activity in alkaline environments [6]. That is why its alloying is used, oxidation to NiO or $Ni(OH)_2$, increasing active surface [7–9]. Copper-containing materials are used in water splitting [10] due to their high electrical conductivity and excellent catalytic activity [11]. As electrode materials alloys of Ni–Zn–Cu system are considered: Cu-Ni [12, 13], Cu–Zn [14], Ni–Zn [15–17], Zn–Ni–Cu [18] both in initial state, and as material for further obtaining materials of Ni-Renai type. E.g. current exchange of HER in 1 mol L^{-1} KOH on steel electrode with Ni/NiZn two-layer coating after leaching in alkaline solution increases as compared to Ni from 0.58 mA cm^{-2} to 6.38 mA cm^{-2}, but when it is Pt-modified ((MS)/Ni/NiZn-Pt electrode)—up to 19.86 mA cm^{-2} [19]. Decreasing of HER overvoltage and when Zn in dealoyed from CuZn on graphite [20]. In [21] the conclusion about decreasing HER overvoltage due to increasing hydrogen adsorbtion on surface of ε-phase which is $CuZn_5$ intermetallide, that can be electrochemically abtained under lower Zn content, than stoichiometric.

The Zn-Ni-Cu ternary alloy is used as a material for further selective leaching of the less stable component, zinc, to obtain a porous material [22]. The resulting porous matrix has a more positive potential. Alkaline leaching is used for electrode material for alkaline water electrolysis [23]. Ni-enriched Zn-Ni-Cu coating are obtained by chemical and electrochemical deposition for formation of electrode materials [24]. Porous coatings are also obtained by galvanic substitution, when the more active component of the coating dissolves, and ions of the more electropositive metal present in the solution are deposited on the electrode surface [25].

Activity of electrodes can be increased by hybride materials, e.g. by modification of $Ni(OH)_2$ [26–29]. E.g. the porous $Ni(OH)_2$/NiCu electrode is proposed, that is obtained by brush plating, cyclic voltammetry (CV) treatment, electrochemical dealloying and hydrolysis [30].

Therefore, research of new cheap materials with increased catalytic activity for use as cathodes in the hydrogen evolution reaction during water electrolysis in an alkaline environment, including multilayer coatings in which nano- and micro-sized layers of alloys of the Zn–Ni–Cu system and mixtures of metals with hydroxides alternate, is relevant and promising [31].

2.2 Experimental

Coatings were deposited from ammonia-glycinate electrolytes (Table 2.1), made using distilled water and chemicals of purified grade. pH 8.5 of solutions was monitored using a CT-6020A pH-meter.

Phase composition was determined by stripping voltammetry (ALSV). Solutions for ALSV contained either 0.5 mol L^{-1} Gly, 0.5 mol L^{-1} NH_4Cl, pH 10.5, either 0.5 mol L^{-1} Na_2SO_4.

Three-electrode was used for electrochemical study. The working electrode was made of platinum (surface area was 1 cm^2). Before each experiment, the platinum electrode was anodically treated in sulfuric acid and cathodically treated in a sodium

Table 2.1 Electrolyte composition

Component	Content in solution, mol L^{-1}			
	"CuZnNi"	"CuZn"	"ZnNi"	"CuNi"
Zn^{2+}	0.015	0.024	0.024	–
Ni^{2+}	0.225	–	0.240	0.240
Cu^{2+}	0.001	0.002	–	0.002
NH_4^+	1.550	0.278	1.702	1.570
Gly^-	0.425	0.047	0.470	0.435

sulfate solution. The counter electrode was also made of platinum plate. An Ag/AgCl reference electrode with saturated KCl solution was used (all the potentials are vs Ag/AgCl). The cell with electrolyte and a beaker with saturated KCl solution and reference electrode were connected by a salt bridge.

All the electrochemical studies were carried out using MTech SPG-500L potentiostat.

Exchange current density was calculated out of Tafel equation. Corrosion current was calculated out of extrapolation of linearized cathodic branch to the corrosion potential. The aim of the study is to compare the kinetic parameters of the hydrogen evolution reaction on nanosized Ni-Zn-Cu alloy films that alternate in a 3D-structured [(Ni-Zn-Cu)/(M-M$(OH)_2$)]n multilayer coating.

2.3 Experimental Results and Discussion

For Ni–Zn–Cu alloy films deposition, which form a multilayer metal hydroxide coating $[(Ni–Zn–Cu)/(M–M(OH)_2)]_n$, a weakly alkaline ammonia-glycinate electrolyte is used. The first cathodic wave on the cyclic voltammogram (CVA) (Fig. 2.1) in this electrolyte (at a potential of approximately – 0.2 V) belongs the process of reduction of oxygen dissolved in the electrolyte. At a potential of – 0.3 V, metals begin to be sequentially deposit. First copper deposits and with further polarization nickel is gradually added to its deposition at the limiting current with the formation of a "solid solution" type alloy. Starting from a potential of – 1 V, due to depolarization during alloy formation with Cu and Ni, Zn also appears in the cathodic deposit. The presence of a crossover (see inset) on the cathode branch of the CVA indicates the presence of a nucleation overvoltage during the formation of a new alloy phase at a potential of − 1 V. The current growth begins with a fairly wide, from a potential of − 1.15 V to a potential of − 1.25 V, area of the limiting current of 50 mA cm^{-2}. The last section of the cathode course of the CVA belongs to the process of alloy deposition simultaneously with intensive hydrogen evolution.

The complex shape of the anode branch of the CVA indicates the oxidation of the multiphase alloy deposit accumulated during the production of the cathode part of the CVA. More electronegative phases are oxidized the first (at more negative potentials).

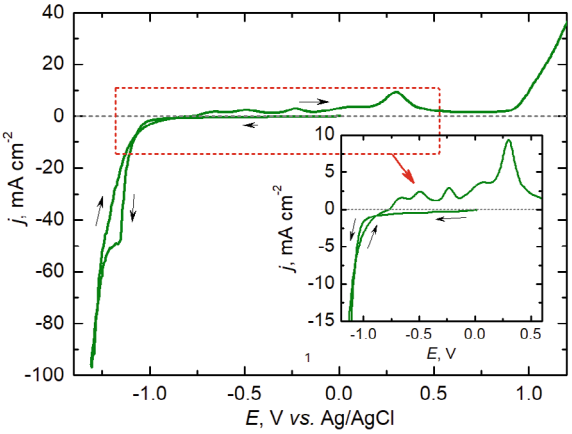

Fig. 2.1 Cyclic voltammogram (main panel) showing the change in current density (j, mA cm^{-2}) during a linear potential scan (E, V) at a rate of 10 mV s^{-1}. The scan starts from open circuit potential (approximately 0 V) in the cathodic direction (downward arrow along the lower brunch of the curve). After that the potential is scanned in the anodic direction (upward arrow on the upper, cathodic, brunch which further becomes anodic branch). The CVA was obtained on Pt in ammonia-glycinate electrolyte for Ni-Zn-Cu alloy deposition (see the composition in Table 2.1). The CVA region indicated by the red dotted line is shown in the inset at an enlarged scale

Thus, the first double anode peak belongs to the oxidation of Zn-enriched phases. Then, in the peak at a potential of − 0.2 V, Cu-enriched phases are oxidized. The last anode peaks belong in an alkaline medium to the oxidation of Ni-enriched phases.

The chronoamperograms of potentiostatic deposition of alloy films at the values of the potentials of the beginning of the main wave (− 1.1 V) on the cathode branch of the CVA (the "− 1.1" coating), the beginning of the limiting current (− 1.15 V), the film "− 1.15", and its middle (− 1.2 V), the film "− 1.2", until the charge of 0.6 C cm^{-2} for deposition of films with a thickness of around 100 nm is reached, are shown in the inset of the Fig. 2.2a. All dependences have peaks of nucleation (at 28 s, 12 s and 3 s, respectively). In the chronoamperogram of deposition at a potential of − 1.2 V after secondary nucleation, the beginning of self-oscillations characteristic of metal deposition at the limiting current is observed (curve 3).

The identification of peaks on the CVA is complicated by the multicomponent nature of the deposit obtained during the cathodic period, the possibility of contact exchange reactions in the electrolyte containing ions of 3 metals, and the incomplete dissolution of the Ni-containing deposit in a weakly alkaline environment. Therefore, the composition of Ni–Zn–Cu films, deposited potentiostatically, was estimated based on the analysis of the anodic voltammograms of their dissolution in a more alkaline ammonium-glycinate electrolyte that does not contain metal ions.

To compare films composition, the voltammograms of their dissolution were reduced to the same charge of 0.3 C cm^{-2} (Fig. 2.2(b)), using coefficients to the current values (Fig. 2.2, panel (b)). Unlike the anodic branch of the CVA (Fig. 2.1), the voltammograms have fewer peaks, and they are more selective. Additionally, the

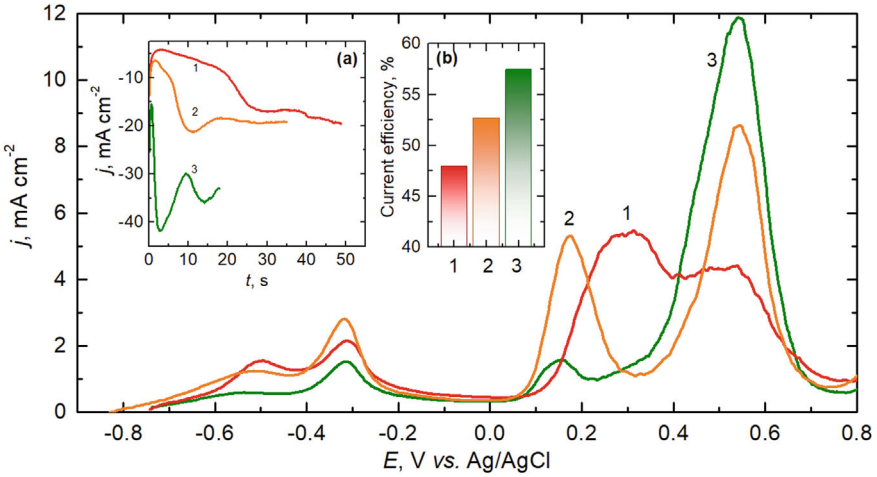

Fig. 2.2 Normalized anodic voltammograms (dependences of j, mA cm-2 on E, V) of dissolution of Ni-Zn-Cu alloy films in alkaline ammonium-glycinate electrolyte. These films were deposited in potentiostatic mode at different potential values: red line − 1.1 V (1), orange line − 1.15 V (2) and green line − 1.2 V (3). Chronoamperograms showing the change in current density j with time t during deposition are shown in the figure in inset **a**. The diagram in inset **b** shows the values of cathodic current efficiency (CE, %) during deposition of the films

deposits dissolve in this solution completely. The current efficiency of films deposition (inset (b) to Fig. 2.2) indicates a significant contribution of side reactions during their deposition: at lower polarization, this is Zn dissolution, at higher polarization, this is hydrogen evolution.

To identify the peaks in the anodic voltammograms of the Cu–Ni–Zn alloy dissolution, we compare the voltammograms of its dissolution (Fig. 2.3, panel (a)) in two electrolytes: in alkaline ammonium-glycinate, in which peaks of binary alloys of the Cu–Ni–Zn system [32–36] were identified, and in Na_2SO_4 solution, in which peaks of the dissolution of the Cu–Zn alloy [37] were identified. If the voltammogram of dissolution in ammonium-glycinate solution has 4 peaks, and the largest is in the region of the most positive potential values (curve 1), then the voltammogram of dissolution of the same film in sodium sulfate solution has only 2 small peaks (curve 1′). That is, we expect that the Ni-enriched phases do not dissolve in the latter electrolyte no containing Cl^- ions.

The voltammogram of the Cu–Zn–Ni alloy dissolution in Na_2SO_4 sodium is compared with the voltammograms of the dissolution of binary alloys deposited at a potential of − 1.15 V from ammonium-glycinate electrolytes containing ions of the corresponding metal pairs (Fig. 2.3 panel (b)). We see that the potential region of the first peak of the voltammogram (curve 1′) matches the potential region of the peaks of oxidation of the β-phase of the Zn–Ni alloy (curve 2′), the β-phase of the Cu–Zn alloy (curve 3′) and the "solid solution" alloy of Ni in Cu (curve 4′). The right shoulder of the first peak may contain the peak of oxidation of the α-phase of the

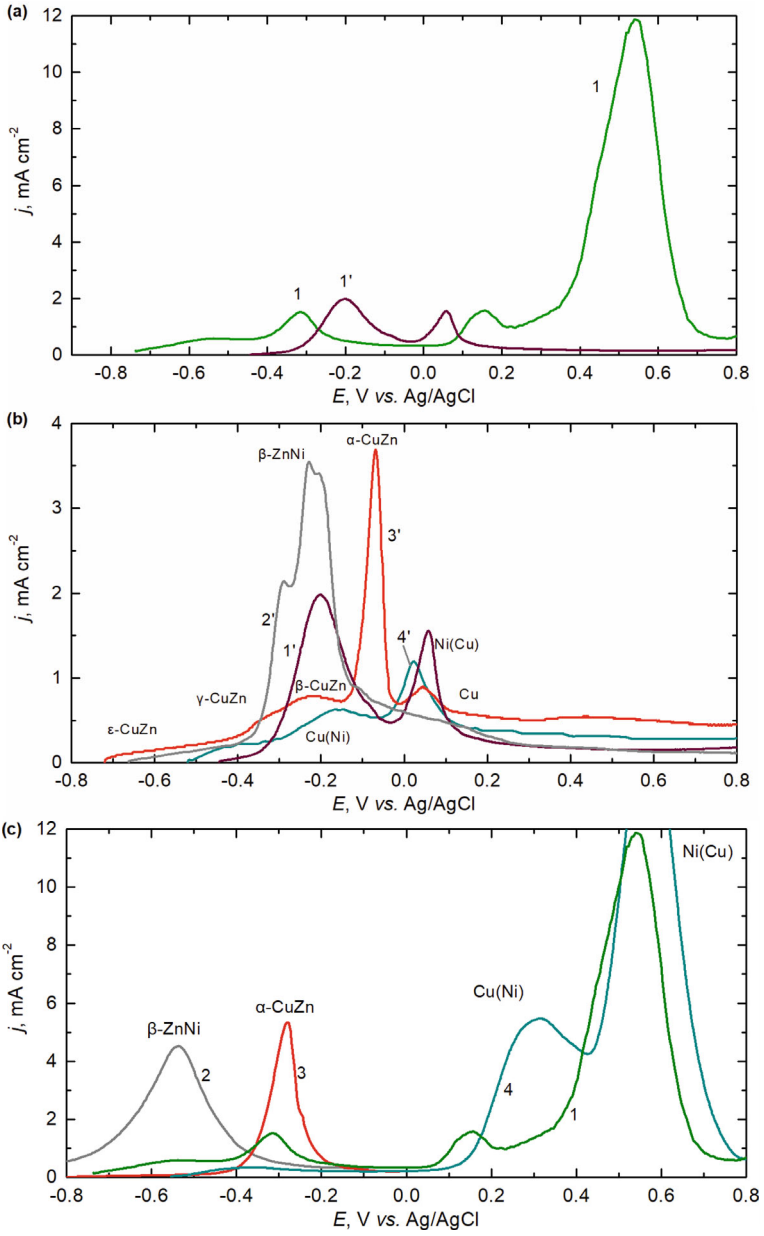
(a)
j, mA cm-2
E, V vs. Ag/AgCl
1
1'
(b)
j, mA cm-2
E, V vs. Ag/AgCl
β-ZnNi
α-CuZn
3'
2'
1'
4'
Ni(Cu)
β-CuZn
γ-CuZn
Cu
ε-CuZn
Cu(Ni)
(c)
j, mA cm-2
E, V vs. Ag/AgCl
Ni(Cu)
Cu(Ni)
α-CuZn
β-ZnNi
2
3
4
1

◀**Fig. 2.3** Normalized anodic voltammograms of dissolution of ternary and binary alloys. Panel (**a**) shows the curves for Ni–Zn–Cu alloy in different electrolytes: ammonia-glycinate (green line 1) and sulphate 0.5 mol L NaSO4 (violet line 1′). Panel (**b**) compares the same curve 1′ (shown in larger scale) with curves for binary alloys in the same sulphate 0.5 mol L NaSO4: Zn–Ni (gray line 2′), Cu-Zn (red line 3′) and Cu-Ni (blue line 4′). Panel (**c**) compares the curve 1 from panel (**a**) with the curves for the same binary alloys (shown by the same colors as in panel (**b**) and marked by the same number without primes) in ammonia-glycinate electrolyte. The inscriptions above the peaks of the voltammograms show which phases of the alloys dissolve are oxidized in this potential region in the corresponding electrolytes. The composition of electrolytes for alloys deposition is given in Table 2.1

Cu–Zn alloy. The potential region of the second peak of the voltammogram (curve 1′) matches the potential region of the further oxidation of the Zn–Ni alloy deposit (curve 2′), copper (curve 3′) and the alloy of "solid solution" of Cu in Ni (curve 4′). That is, the Na_2SO_4 solution does not allow the phases of the ternary alloy to be dissolved selectively.

We will also compare the voltammogram of Cu–Ni–Zn alloy dissolution in the alkaline ammonium-glycinate electrolyte with the voltammograms of the dissolution of binary alloys in it (Fig. 2.3 panel (c)).

The potential region of the first peak of the voltammogram (curve 1) matches potential region of the peaks of β–Zn–Ni phase oxidation (curve 2), the potential region of the second peak (curve 1) matches the potential region of the peaks of α–Cu–Zn phase oxidation (curve 3), the potential region of the third and fourth peaks (curve 1) matches the potential region of the peaks of oxidation of the alloys "solid solution" of Ni in Cu and "solid solution" of Cu in Ni, respectively (curve 4). Thus, the analysis of more selective dissolution of alloy films in an ammonia-glycinate solution with confirmation of the dissolution of some phases in a sulfate solution revealed that the anodic voltammogram of the dissolution of Cu–Zn–Ni alloy contains peaks of oxidation of the following binary alloy phases: β-phases of the Zn–Ni alloy, α-phases of the Cu–Zn alloy, and Cu-Ni alloys, which form a continuous series of "solid solutions". These phases are not necessarily present in the initial films, they can also be formed as residues during the anodic oxidation of more negative phases in the previous peaks.

Figure 2.4 panel (a) compares the voltammograms of dissolution of single-layer films "− 1.1" and "− 1.2" of the Ni–Zn–Cu alloy deposited at a potential of − 1.1 V (curve 1) and − 1.2 V (curve 3), with the voltammogram of dissolution of the "− 1.1/− 1.2" bilayer (curve 2), which is a part of multilayer coatings $[(Ni–Zn–Cu)/(M–M(OH)_2)]_n$. At a potential of − 1.1 V, the alloy is deposited at the limiting current of Cu deposition. At a potential of − 1.2 V, the hydroxo compounds of these metals are included to a greater extent in the deposit at the limiting current of all metals. The bilayer deposition chronoamperogram (Fig. 2.4, inset in panel (a)) shows that the deposition current of the second layer of such a bilayer, at a potential of − 1.2 V, is greater than the deposition current of "− 1.2" single-layer film (curve 3, Fig. 2.2, inset (a)) due to the development of the surface of the first layer, at a potential of − 1.1 V. The voltammogram of bilayer dissolution (curve 2) has a significantly smaller oxidation peak of the phase of "solid solution" of Ni in Cu and the peak of oxidation

of the phase of "solid solution" Cu in Ni, which is located at less positive potential values. Considering that the multilayer coating, which consists of 50 such bilayers, has an elemental composition of 55 wt.% Ni, 39.8 wt. % Zn and 5.2 wt. % Cu, i.e. contains a fraction of Zn that exceeds the contribution of the first two Zn-containing peaks to the voltammogram of dissolution of Cu–Zn–Ni alloy, it should be concluded that the last peak, enriched in nickel, is a "solid solution" alloy in Ni not only Cu, but also more negative Zn with a Zn content not higher than its content in the equilibrium α-phase of the Zn–Ni alloy (which contains 30 wt. % zinc), the oxidation peak of which in the ammonia-glycinate electrolyte is at more negative potential values than the oxidation peak of the β-phase of the Zn–Ni alloy [33].

Compared to voltammogram for single layer deposited at potential (Fig. 2.4, panel b), e.g. at a potential of − 1.15 V (curve 4), which is the average value between the deposition potentials of the bilayer layers, − 1.1 V and − 1.2 V, the bilayer dissolution voltammogram (curve 2) also differs in the dissolution peak of a more homogeneous deposit of the "solid solution" of Cu and Zn in Ni, in contrast to the 2 peaks in the film "− 1.15" dissolution voltammogram.

In 1 mol L^{-1} NaOH solution, which is used in alkaline water electrolysis with the hydrogen evolution (Fig. 2.5, panel a), these films also dissolve differently: the "− 1.15" single-layer film (curve 2) has a larger second peak than that of the bilayer (curve 1). Their corrosion diagrams (Fig. 2.5, panel b), obtained after exposure to an alkaline solution at open circuit potential for 30 min, indicate approximately the same corrosion rate in an alkaline solution (curves 1, 2; 50.1 μA cm^{-2} and 47.7 mA cm^{-2}, respectively) and a more positive corrosion potential than the beginning of the anodic dependences in Fig. 2.5 panel a.

After additional treatment (AT) by holding the samples at a potential of -0.7 V, to increase the corrosion resistance by removing electronegative phases from the films, the corrosion potential of "− 1.1/− 1.2-AT" bilayer significantly shifted towards positive potential values (curve 1′), the corrosion potential of "− 1.15-AT" single-layer film (curve 2′) shifted slightly (the phase that is oxidized in the second peak of curve 2, Fig. 2.5a, remained). The corrosion current becomes the same for both films after treatment, 40.7 μA cm^{-2}.

Cathodic polarization dependences of hydrogen evolution on these Ni–Zn–Cu alloy films are shown in Fig. 2.6a. It is interesting to note that hydrogen evolution on the bilayer film (curve 2) is more difficult than on the single-layer film (curve 1), however, after additional processing, the advantage of the bilayer (curves 1′ and 2′) was revealed. In Tafel coordinates, taking into account ohmic losses (Fig. 2.6b), this difference is even more obvious.

The kinetic parameters of the hydrogen evolution reaction (HER) on the alloy films are given in Table 2.2. The Tafel coefficients a and b and the exchange current density i_0 of HER on both initial films are close. However, after additional treatment, all parameters of the single-layer film become worse, and those of the bilayer improve. The deterioration of all HER parameters on the single-layer film is probably due to the negative influence of the residue from the dissolution of the negative phase on the surface of the deposit after treatment. Since the coefficient b for the HER on the bilayer after processing decreased slightly, it is possible to assume that the roughness

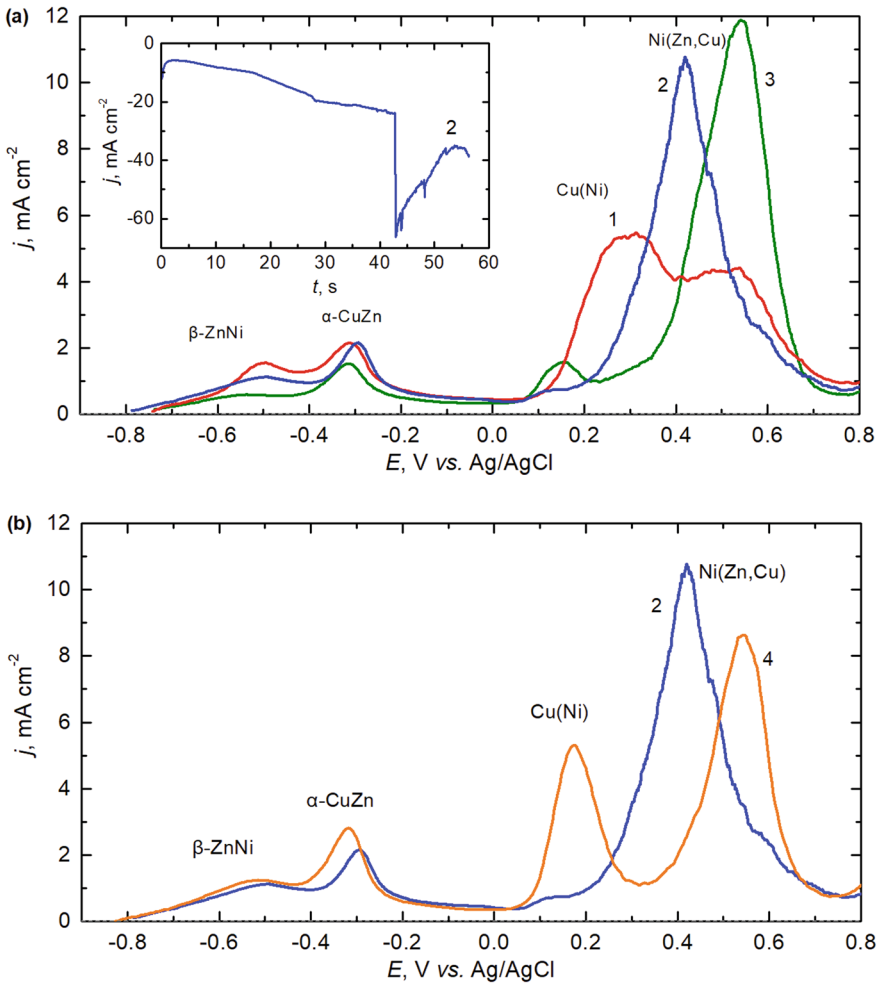

Fig. 2.4 Normalized anodic voltammogram of dissolution of the bilayer film in comparison with the curves for single-layer films in ammonia-glycinate electrolyte. Panel (**a**) compares the curve for bilayer (blue line 2) with the curves for single-layer films, deposited at potentials: -1.1 V (red line 1) and − 1.2 V (green line 3), which are the sublayers of the bilayer. Inset in panel b shows chronoamperogram j-E of bilayer deposition. Panel (**b**) compares the curve for the bilayer with curve for single-layer film deposited at − 1.15 V (orange line 4), which is between the potentials for the sublayers. The inscriptions above the peaks of the voltammograms show which phases of the alloys are oxidized in this potential region in the corresponding electrolytes. The composition of electrolytes for alloys deposition is given in Table 2.1

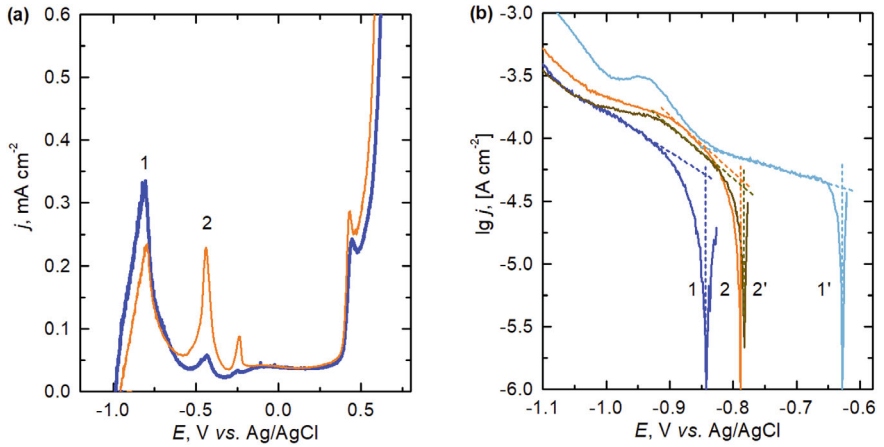

Fig. 2.5 Anodic polarization j-E curves (panel **a**) and corrosion diagrams lg j-lgE (panel **b**) of the bilayer (lines 1 and 1') and single-layer films (lines 2 and 2') films in 1 mol L NaOH solution. Curves 1 and 2 were obtained for the initial films while curves 1' and 2' were obtained after additional treating of the films in 1 mol L NaOH

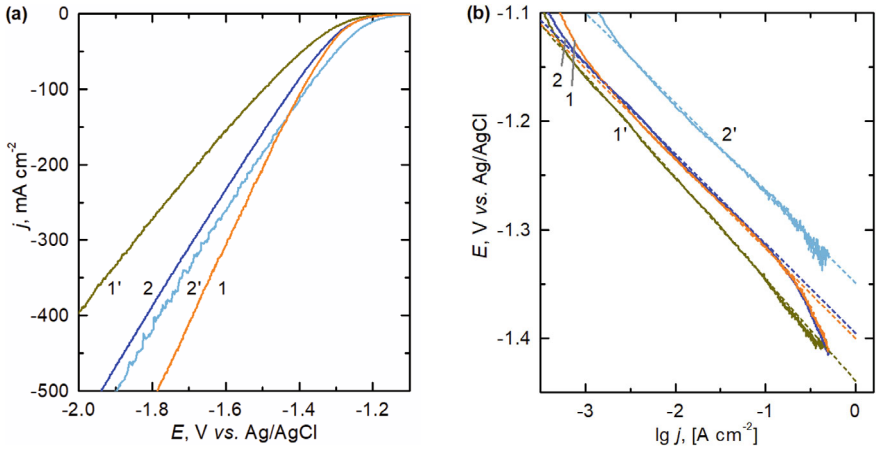

Fig. 2.6 Cathodic polarization j-E curves without iR correction (panel **a**) and semi-logarithmic lg j-E Tafel plots with iR correction (panel **b**) in 1 mol L NaOH. Dependences 1 and 2 were obtained on the initial bilayer film (blue line 2) and single-layer film deposited at the potential -1.15 V (orange line 1). Dependences 1' and 2' were obtained on the films after their additional treatment. Potential scan rate is 1 mV s-1

factor of the bilayer surface increased due to the dissolution of the negative phase during treatment.

Table 2.2 Tafel parameters of hydrogen evolution reaction

Kinetic parameter	Initial		After treatment	
	«– 1.15»	«– 1.1/– 1.2»	«– 1.15»	«– 1.1/– 1.2»
a, mV	– 374	– 369	– 413	– 323
b, mV	83	82	94	83
i_o, μA cm^{-2}	31	33	39	128

2.4 Conclusions

The properties of nanoscale Ni–Zn–Cu alloy films, which are multilayer coating Ni–Zn–Cu)/(M–M(OH)$_2$)]$_n$ consist of, were compared. The alloy films were deposited from a weakly alkaline ammonia-glycinate electrolyte at the potentials of the beginning of the main wave (–1.1 V) on the cathode branch of the CVA (film "– 1.1"), the beginning of the limiting current (– 1.15 V), "– 1.15" film, and its middle (– 1.2 V), "– 1.2" film, with "– 1.1/– 1.2" bilayer.

It was shown that the dissolution voltammograms of the ternary alloy films contain oxidation peaks of the β-phase of the Zn–Ni alloy, the α-phase of the Cu–Zn alloy and the alloys of "solid solutions" of Ni in Cu and Cu and Zn in Ni.

Comparison of the properties of the bilayer and the single-layer film "– 1.2", deposited at a potential of – 1.2 V, the average potential between the potential values of the bilayer layers "– 1.1/– 1.2", in the hydrogen evolution reaction showed that they have approximately the same corrosion rate in alkaline solution, 50.1 μA cm^{-2} and 47.7 μA cm^{-2}, respectively. After additional treatment by holding the samples at a potential of – 0.7 V, the corrosion current of the films becomes the same, 40.7 μA cm^{-2}. The kinetic parameters of the HER on both initial films are close. However, after additional treatment, the advantage of the bilayer was revealed, the exchange current density of HER on the surface of which increases by 3.9 times. Taking into account the insignificant change in the Tafel coefficient, it is assumed that during additional treatment the roughness factor of the bilayer surface increases due to the dissolution of the most negative phase.

References

1. Q. Cao, Y. Shen, J. Bai, Q. Liu, Z. Zhao, T. Lei, A.S. Dhmees, H. Zhang, Mild formation of Ni(OH)$_2$ dense nanosheets array for ultra-efficient electrocatalytic hydrogen evolution. Int. J. Hydrogen Energy **77**, 15–22 (2024)
2. Q. Liu, W. Erdong, S. Gongquan, Layered transition-metal hydroxides for alkaline hydrogen evolution reaction. Chin. J. Catal. **41**(4), 574–591 (2020)
3. R. Solmaz, Electrochemical preparation, characterization, and application of a novel cathode material, mild Steel/Ni/NiZn–Pt, for alkaline water electrolysis. Energy Sources Part A Recover. Util. Environ. Eff. **36**(11), 1212–1218 (2024)
4. A. Maizelis, *Electrochemical Formation of Multilayer Coatings: Copper-Nickel Alloys and Oxo-hydroxides: Monograph.* Lambert Academic Publishing (2021)

5. J. Greeley, T.F. Jaramillo, J. Bonde, I.B. Chorkendorff, J.K. Nørskov, Computational high-throughput screening of electrocatalytic materials for hydrogen evolution. Nat. Mater. **5**(11), 909–913 (2006)
6. N. Danilovic, R. Subbaraman, D. Strmcnik, K.C. Chang, A.P. Paulikas, V.R. Stamenkovic, N.M. Markovic, Enhancing the alkaline hydrogen evolution reaction activity through the bifunctionality of $Ni(OH)_2$/metal catalysts. Angewandte Chemie International Edition **51**(50), 12495–12498 (2012)
7. Y. Kuang, G. Feng, P. Li, Y. Bi, Y. Li, X. Sun, Single-crystalline ultrathin nickel nanosheets array from in situ topotactic reduction for active and stable electrocatalysis. Angew. Chem. **128**(2), 703–707 (2016)
8. L. Zhang, K. Xiong, Y. Nie, X. Wang, J. Liao, Z. Wei, Sputtering nickel-molybdenum nanorods as an excellent hydrogen evolution reaction catalyst. J. Power. Sources **297**, 413–418 (2015)
9. R. Kavian, S.I. Choi, J. Park, T. Liu, H.C. Peng, N. Lu, S.W. Lee, Pt–Ni octahedral nanocrystals as a class of highly active electrocatalysts toward the hydrogen evolution reaction in an alkaline electrolyte. J. Mater. Chem. A **4**(32), 12392–12397 (2016)
10. M.B. Gawande, A. Goswami, F.X. Felpin, T. Asefa, X. Huang, R. Silva, X. Zou, R. Zboril, R.S. Varma, Cu and Cu-based nanoparticles: synthesis and applications in catalysis. Chem. Rev. **116**(6), 3722–3811 (2016)
11. J. Zhang, M.D. Baró, E. Pellicer, J. Sort, Electrodeposition of magnetic, superhydrophobic, non-stick, two-phase Cu–Ni foam films and their enhanced performance for hydrogen evolution reaction in alkaline water media. Nanoscale **6**(21), 12490–12499 (2014)
12. S. Mojabi, S. Sanjabi, Decorated fractal Ni-Cu foam with Pd nanoparticles as a high-performance electrocatalyst toward hydrogen evolution reaction. Thin Solid Films **758**, 139415 (2022)
13. B. Huener, N. Demir, M.F. Kaya, Electrodeposition of NiCu bimetal on 3D printed electrodes for hydrogen evolution reactions in alkaline media. Int. J. Hydrogen Energy **47**(24), 12136–12146 (2022)
14. S.T. Döşlü, A. Döner, R. Yıldız, Electrocatalysis property of CuZn electrode with Pt and Ru decoration. Int. J. Hydrogen Energy **46**(43), 22409–22421 (2021)
15. F. Ganci, B. Buccheri, B. Patella, E. Cannata, G. Aiello, P. Mandin, R. Inguanta, Electrodeposited nickel–zinc alloy nanostructured electrodes for alkaline electrolyzer. Int. J. Hydrogen Energy **47**(21), 11302–11315 (2022)
16. Y.X. Li, H.X. Yang, Q.P. Zhang, T.Z. Jian, C.X. Xu, Q.X. Zhou, In-situ building of multiscale porous NiFeZn/NiZn-Ni heterojunction for superior overall water splitting. Trans. Nonferrous Metals Soc. China **34**(9), 2972–2986 (2024)
17. F. Ganci, B. Patella, E. Cannata, V. Cusumano, G. Aiello, C. Sunseri, P. Mandin, R. Inguanta, Ni alloy nanowires as high efficiency electrode materials for alkaline electrolysers. Int. J. Hydrogen Energy **46**(72), 35777–35789 (2021)
18. H. Ashassi-Sorkhabi, S. Abolghasemi-Fakhri, B.R. Moghadam, H. Javan, One step electrochemical route to the fabrication of highly ordered array of cylindrical nano porous structure and its electrocatalytic performance toward efficient hydrogen evolution. J. Colloid Interface Sci. **515**, 189–197 (2018)
19. R. Solmaz, Electrochemical preparation, characterization, and application of a novel cathode material, mild Steel/Ni/NiZn-Pt, for alkaline water electrolysis. Energy Sources Part A Recover. Util. Environ. Eff. **36**(11), 1212–1218 (2014)
20. E. Telli, Copper-Zinc and Copper-İron Binary Electrode for Hydrogen Evolution Reaction. Sakarya Univ. J. Sci. **22**(3), 945–951 (2018)
21. J.C. Ballesteros, C. Gómez-Solís, L.M. Torres-Martínez, I. Juárez-Ramírez, Electrodeposition of Cu-Zn intermetallic compounds for its application as electrocatalyst in the hydrogen evolution reaction. Int. J. Electrochem. Sci. **10**(4), 2892–2903 (2015)
22. N.C. Lo, I.W. Sun, P.Y. Chen, Electrochemical preparation of porous ZnCuNi by electrodeposition in ethaline deep eutectic solvent followed by anodic or cathodic dealloying in alkaline aqueous solutions for higher nitrate reduction activity. J. Electroanal. Chem. **890**, 115256 (2021)

23. R. Solmaz, A. Döner, G. Kardaş, Preparation, characterization and application of alkaline leached CuNiZn ternary coatings for long-term electrolysis in alkaline solution. Int. J. Hydrogen Energy **35**(19), 10045–10049 (2010)
24. B. Liu, Z. Li, Electrochemical treating of a smooth Cu–Ni–Zn surface into layered microchips of rice grain-like Cu/$Ni(OH)_2$ nanocomposites as a highly sensitive enzyme-free glucose sensor. J. Electroanal. Chem. **855**, 113493 (2019)
25. N.C. Lo, C.L. Yu, P.Y. Chen, Characterization of nanowire-constructed porous CuZn and CuNiZn nitrate-active electrodes prepared via galvanic displacement on electrodeposited Zn Templates in ionic liquids. J. Electron. Mater. **52**(5), 2995–3007 (2023)
26. Z. Yin, F. Chen, Electrochemically fabricated hierarchical porous Ni (OH) 2/NiCu electrodes for hydrogen evolution reaction. Electrochim. Acta **117**, 84–91 (2014)
27. H. Yuan, R.R. Lunt, J.I. Thompson, R.Y. Ofoli, Electrodeposition of Ni/Ni (OH) 2 catalytic films for the hydrogen evolution reaction produced by using cyclic voltammetry. ChemElectroChem **4**(2), 241–245 (2017)
28. S. Tao, F. Yang, J. Schuch, W. Jaegermann, B. Kaiser, Electrodeposition of nickel nanoparticles for the alkaline hydrogen evolution reaction: correlating electrocatalytic behavior and chemical composition. Chemsuschem **11**(5), 948–958 (2018)
29. N. Danilovic, R. Subbaraman, D. Strmcnik, K.C. Chang, A.P. Paulikas, V.R. Stamenkovic, N.M. Markovic, Enhancing the alkaline hydrogen evolution reaction activity through the bifunctionality of $Ni(OH)_2$/metal catalysts. Angew. Chem. Int. Ed. **51**(50), 12495–12498 (2012)
30. Z. Yin, F. Chen, Electrochemically fabricated hierarchical porous $Ni(OH)_2$/NiCu electrodes for hydrogen evolution reaction. Electrochim. Acta **117**, 84–91 (2014)
31. A. Maizelis, B. Bairachniy, Formation of multilayer metal-hydroxide electrode with developed surface for alkaline water electrolysis. Mater. Today Proc. **6**, 227–231 (2019)
32. A.A. Maizelis, Voltammetric analysis of phase composition of Zn–Ni alloy thin films electrodeposited under different electrolyze modes, in *2017 IEEE 7th International Conference Nanomaterials: Application and Properties (NAP)* (IEEE, 02NTF13-1, 2017)
33. A. Maizelis, Z. Kolupaieva, Quantitative analysis of chemical and phase composition of Zn−Ni alloy coating by potentiodynamic stripping. Electroanalysis **33**(2), 515–525 (2021)
34. A. Maizelis, I. Patsay, Dissolution of zinc-enriched phases during layer-by-layer deposition of Cu–Zn thin films, in *2020 IEEE 40th International Conference on Electronics and Nanotechnology (ELNANO)* (IEEE, 2020), pp. 311–314
35. A. Maizelis, Stripping voltammetry of nanoscale films of Zn–Ni alloy. Appl. Nanosci. (Switzerland) **12**(3), 735–740 (2022)
36. A. Maizelis, Stripping voltammetry of nanoscale films of Cu–Zn, Cu–Sn, Zn–Ni alloys. Springer Proc. Phys. **263**, 323–336 (2021)
37. J. Stevanović, L.J. Skibina, M. Stefanović, A. Despić, V.D. Jovi, Phase-structure analysis of brass by anodic linearsweep voltammetry. J. Appl. Electrochem. **22**, 172–178 (1992)

Chapter 3
Injection Currents in *p*-$MnCo_2O_4$/*n*-CdTe Anisotypic Heterojunctions

I. G. Orletskyi, M. I. Ilashchuk, I. P. Koziarskyi, E. V. Maistruk, D. P. Koziarskyi, and S. V. Nichyi

Abstract Anisotype *p*-$MnCo_2O_4$/*n*-CdTe heterojunctions with rectifying properties were fabricated by spray-pyrolysis of a mixture of 0.1 M aqueous solutions of $MnCl_2 \cdot 4H_2O$ and $CoCl_2 \cdot 6H_2O$ salts onto *n*-CdTe crystalline substrates. The temperature dependences of the *I*-*V*-characteristics ($T = 295$–346 K) were analyzed and it was found that at forward and reverse ($V \geq -0.5$ V) biases, the current flow through the heterojunction is determined by the processes of injection of the main charge carriers into the high-resistance *n*-CdTe contact region, which is formed during the manufacture of the structures. Based on the theory of space charge-limited currents, the main electrical parameters of the high-resistance part of the base are determined. The features of the *C*-*V*-characteristics in the range $f = 1.0$–100 kHz are explained based on the equivalent electrical circuit of the structure with a high-resistance layer in the base, taking into account its capacitance. The light *I*-*V*-characteristics indicate the possibility of practical use of the fabricated *p*-$MnCo_2O_4$/*n*-CdTe heterojunctions as visible radiation photodetectors.

3.1 Introduction

Manganese cobaltite nanomaterials $MnCo_2O_4$ and solid solutions based on them are the object of intensive research aimed at studying their electrical, magnetic, optical, dielectric and catalytic properties, which determine their practical use in devices for various purposes. The study of the electrochemical properties of manganese cobaltite spinel $MnCo_2O_4$ led to the use of this material in lithium-ion batteries to obtain a carbon-free anode, and later to manufacture a cathode [1, 2]. Many scientific articles have investigated the use of $MnCo_2O_4$ in supercapacitors [3, 4]. Supercapacitors obtained on the basis of nanostructured films of manganese cobaltite heterostructure

I. G. Orletskyi · M. I. Ilashchuk · I. P. Koziarskyi (✉) · E. V. Maistruk · D. P. Koziarskyi · S. V. Nichyi
Department of Electronics and Power Engineering, Yuriy Fedkovych Chernivtsi National University, Chernivtsi, Ukraine
e-mail: i.koziarskyi@chnu.edu.ua

O. Fesenko and L. Yatsenko (eds.), *Functional Nanomaterials, Nanocatalysts, Nanotechnologies, and Their Applications*, Springer Proceedings in Physics 321,
https://doi.org/10.1007/978-3-031-99136-3_3

$MnCo_2O_4$/PPy (Polypyrrole), in which these composites are used for the manufacture of both positive and negative electrodes, showed high energy density (78.5 W h kg^{-1} at 1121 W kg^{-1}) and high stability (94.3% capacitance retention after 5000 cycles at 20 A g^{-1}) [5]. The optical properties of $MnCo_2O_4$ have shown that they can be used as photocatalysts for hydrogen production and in optical gas sensors for ethanol and acetone [6–8]. As part of the $MnCo_2O_4$@$NiCo_2O_4$ heterostructure, manganese cobaltite is used in dye-sensitized solar cells (DSSCs) as their main component—the counter electrode (CE) with excellent electrochemical properties, providing a high photoelectric conversion efficiency of 9.58%, which is much higher than traditional Pt FTO CE (8.0%) [9].

Thin films of manganese cobaltite $MnCo_2O_4$ belong to direct-gap semiconductor materials with an optical band gap E_g = 1.3–1.5 eV [6, 8, 10, 11], which is in the optimal energy range (1.1 eV < E_g < 1.6 eV) for photovoltaic energy conversion [12].

In scientific works that investigate the electrical properties of both $MnCo_2O_4$ nanocomposites [8, 13, 14] and $Mn_{3-x}Co_xO_4$ solid solutions [13, 15], it is reported that these semiconductors, as a rule, exhibit *p*-type conductivity with low resistivity. The value of the resistivity ρ of the specified materials slightly depends on the method of manufacturing thin films: spray pyrolysis method—ρ = 530 Ω cm [8], sintered classically ρ = 387 Ω cm and by spark plasma sintering ρ = 387 Ω cm [15] (the values of ρ are given at room temperature). The conductivity activation energy determined from the temperature dependences $\rho = \rho_0 exp(E_a/kT)$ was E_a = 0.31–0.36 eV for $MnCo_2O_4$ films and solid solutions based on them, obtained by various methods [8, 13, 16]. The conductivity mechanism of spinel oxides was explained by the presence of manganese atoms with different valences Mn^{3+} and Mn^{4+} in the octahedral lattice sites. Conductivity has a jump-like character and is caused by the transitions of charge carriers between neighboring ions, which thus change their valence [13–15]. According to [8], thin films of $MnCo_2O_4$ exhibit thermal stability in the temperature range of electrical characteristics measurement 293 K < T < 383 K.

Thin films of cobaltite exhibit strong absorption of solar radiation [11, 13]. The absorption spectrum of $Mn_{3-x}Co_xO_4$ ($0 \le x < 3$) nanocomposites, obtained in the wavelength range λ = 300–1100 nm, is characterized by high absorption in the UV region and some linear decrease in the visible and in the specified IR range [11]. Thin films of $M_xMnCo_{2-x}O_4$ (M = Ni, Cu, Zn; x = 0, 0.15, 0.30, 0.60) showed an absorption value exceeding 90% in the entire range of UV and visible radiation, which practically covers the main part of the solar spectrum [13].

Cadmium telluride is one of the most promising semiconductors that is effectively used in solar energy as a material that actively absorbs solar radiation (absorption coefficient in the visible region of the spectrum $\alpha \approx 10^5 см^{-1}$). In addition, its band gap $E_g \approx$ 1.5 eV, similar to $MnCo_2O_4$, is in the energy range 1.1 eV < E_g < 1.6 eV, which corresponds [12] to the optimal photovoltaic conversion of solar energy.

Due to the above-mentioned electrical and optical properties, as well as the value of the band gap, manganese cobaltite $MnCo_2O_4$ can be used as an alternative to *p*-CdTe in homogeneous semiconductor *p*-*n*-junctions based on cadmium telluride, which can have practical use as photoconverters and photodetectors of optical radiation. The

advantages of this use are due to the reduction in the band gap width of $MnCo_2O_4$ thin films obtained by spray pyrolysis ($E_g = 1.3$ eV) [8], compared to CdTe, and a rather high absorption in the near-IR region [11], which significantly expands the spectral range of solar radiation absorption. In addition, it is possible to avoid the complexity of obtaining ohmic contacts to p-CdTe, which requires additional technological operations [17, 18]. It is known that low-resistance p-CdTe, unlike $MnCo_2O_4$, exhibits instability of electrical parameters in the temperature range quite close to room temperature ($T > 325$ K) [19]. The use of manganese cobaltite $MnCo_2O_4$ in the above barrier structures will reduce toxic cadmium, which will increase their environmental friendliness.

The paper presents studies of the electrical and photoelectric properties of anisotype heterojunctions p-$MnCo_2O_4$/n-CdTe, fabricated by depositing thin films of $MnCo_2O_4$ on single-crystal cadmium telluride substrates by spray pyrolysis.

3.2 Experiment Details

To produce thin $MnCo_2O_4$ films by spray pyrolysis, mixtures of aqueous solutions of cobalt(II) chloride hexahydrate $CoCl_2 \cdot 6H_2O$ and manganese(II) chloride tetrahydrate $MnCl_2 \cdot 4H_2O$ salts with a concentration of 0.1 M at a component ratio of Co/Mn = 2 were used. The pyrolysis temperature was $T_S = 390$ °C. The thickness of the films, measured by a Linnik MII-4 micro-interferometer, was ~ 0.3 μm. The resistivity of $MnCo_2O_4$ films was measured by the four-probe method. Its value at room temperature $T = 293$ K was $\rho \approx 530\ \Omega$ cm. The type of charge carriers in the film was determined by the polarity of the thermo emf. According to research data, $MnCo_2O_4$ films had p-type conductivity.

CdTe crystals were grown by the vertical Bridgman method under low Cd vapor pressure. The electronic conductivity of the crystals is due to the doping of CdTe with a Cl impurity during the growth process, the concentration of which in the melt was $N_{Cl}^0 = 5 \cdot 10^{18}\ \text{cm}^{-3}$. Kinetic parameters of the crystals: specific electrical conductivity $\sigma = 5.6\ \Omega^{-1}\ \text{cm}^{-1}$, electron concentration and their Hall mobility $n = 3.6 \cdot 10^{16}\ \text{cm}^{-3}$ and $\mu_H = 980\ \text{cm}^2\ \text{V}^{-1}\ \text{s}^{-1}$, respectively.

The external contacts of the anisotype heterojunctions p-$MnCo_2O_4$/n-CdTe were made on the side of the low-resistance film using a conductive paste based on silver, and on the side of the n-type CdTe substrates by fusion of indium.

The I-V-characteristics of the studied p-$MnCo_2O_4$/n-CdTe heterojunctions were measured using a hardware-software complex implemented on the basis of the Arduino platform, an Agilent 34410A digital multimeter, and a Siglent SPD3303X programmable power supply, which were controlled by a personal computer using software created by the authors in the LabView environment. The measurements of capacitance–voltage (C-V) characteristics of structures in a wide frequency range of the alternating signal under investigation were carried out by a LCR Meter BR2876. The light-voltage characteristics were measured under illumination with integral light using the "FIBEROPTIC HEIM" device.

3.3 Results and Discussion

The current–voltage (I-V) characteristics of anisotype heterojunctions p-$MnCo_2O_4$/n-CdTe, measured at forward and reverse voltages in a wide temperature range T = 295–346 K (Fig. 3.1), indicate their diode properties. The rectification ratio of the studied structures at $T = 295$ K and $V = 1.5$ V is $\approx 10^2$.

A feature of the I-V-characteristics of p-$MnCo_2O_4$/n-CdTe heterostructures was the small values of direct currents, which were measured in microamperes even at fairly high voltages (for example, $I = 11.6$ μA at $V = 2$ V). It can be assumed that this property of the heterojunctions under study is due to the presence of a high-resistance layer in their base region, which is formed during the manufacturing process of the structure. To establish the structural features of the obtained heterojunctions and clarify the main mechanisms of current transfer through the potential barrier in the region of forward biases, an analysis of the $I = f(V)$ dependences plotted in different coordinates was performed. It was established that the linearization of the I-V-characteristics of the structures is observed in the coordinates $lnI = f(lnV)$, with a different angle of inclination to the voltage axis in different measurement ranges (Fig. 3.2). Therefore, in the region of forward biases, the I-V-dependences of p-$MnCo_2O_4$/n-CdTe heterojunctions are described by the power law $I \sim V^m$, characteristic of space charge limited currents (SCLC) [20]. Such currents typically occur in high-resistance semiconductors and dielectrics and are caused by the injection of main charge carriers. In this case, the SCLC arise due to the injection of electrons from the low-resistance part of the base into the high-resistance part, which is formed in the surface region of CdTe during the technological operations of manufacturing the structure.

Indeed, as was established in many works [21, 22], when a CdTe substrate is heated to low temperatures (T_s = 250–300 °C) in the surface layer, due to the sublimation of mainly cadmium atoms, intrinsic point defects of the acceptor type of cadmium

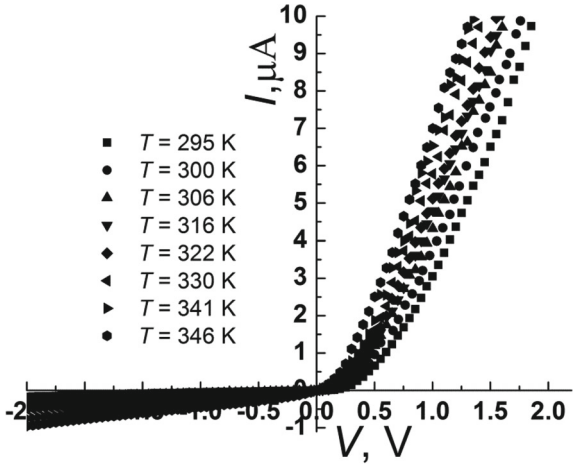

Fig. 3.1 I-V-characteristics of anisotype heterojunctions p-$MnCo_2O_4$/n-CdTe at forward and reverse biases

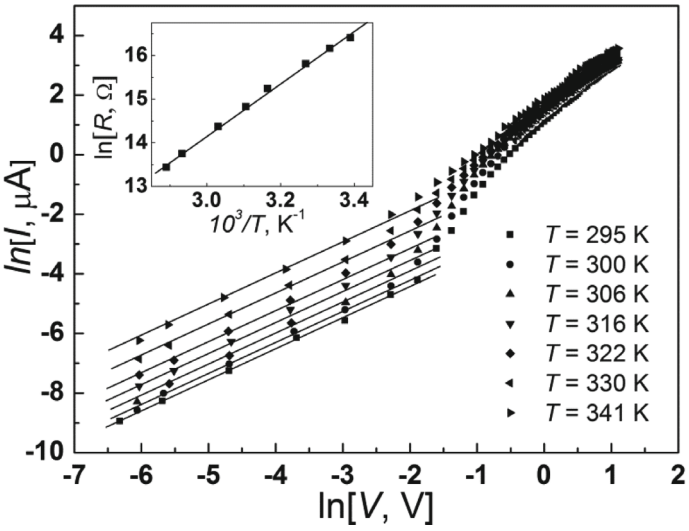

Fig. 3.2 I-V-characteristics of anisotypic heterostructures p-$MnCo_2O_4$/n-CdTe at positive biases, plotted on a logarithmic scale. The inset shows the temperature dependence of the resistance of the high-resistance base layer

vacancy—V_{Cd}^{-}, V_{Cd}^{-2} are formed. Since the main point defects that determine the electronic conductivity of the base material are Cl_{Te}^{+}, when V_{Cd}^{-}, V_{Cd}^{-2} appear, their interaction will occur with the formation of electrically active and neutral complexes $\left(V_{Cd}^{-2}Cl_{Te}^{+}\right)^{-}$, $(V_{Cd}^{-2}2Cl_{Te}^{+})$, $\left(V_{Cd}^{-}Cl_{Te}^{+}\right)^{0}$. Such processes lead to the formation of a compensating material with high resistance [23].

The study of injection currents makes it possible to detect the presence of both shallow and deep local states in the material used, which can trap free charge carriers, and to determine some of their parameters. In addition, from the analysis of the SCLC, information can be obtained about the properties of the semiconductor itself. That is why, in the work, a detailed analysis of the I-V-characteristics of the studied p-$MnCo_2O_4$/n-CdTe structures was carried out.

As can be seen from Fig. 3.3, the I-V-characteristics of p-$MnCo_2O_4$/n-CdTe structures are characterized by the presence of three sections, which are in good agreement with the theory of the SCLC [20]. The linear section of the I-V-characteristic in the region of small voltages $V = V_{TFL} \leq 0.15$ V is characterized by the power index $m = 1$. That is, the dependence $I = f(V)$ at small values of the applied voltage is described by Ohm's law, which is due to the presence of thermally generated charge carriers n_0 in the semiconductor, if their concentration exceeds the concentration of the injected ones. The presence of a linear section $m = 1$ on the dependences $lnI = f(lnV)$ in the temperature range $T = 295$–346 K (Fig. 3.2) makes it possible to determine the resistance value of the high-resistance layer at different temperatures and to construct its temperature dependence (Fig. 3.2, inset). The calculated value of the resistance R_b at $T = 295$ K was $1.7 \cdot 10^7\,\Omega$. The determined depth of the energy level

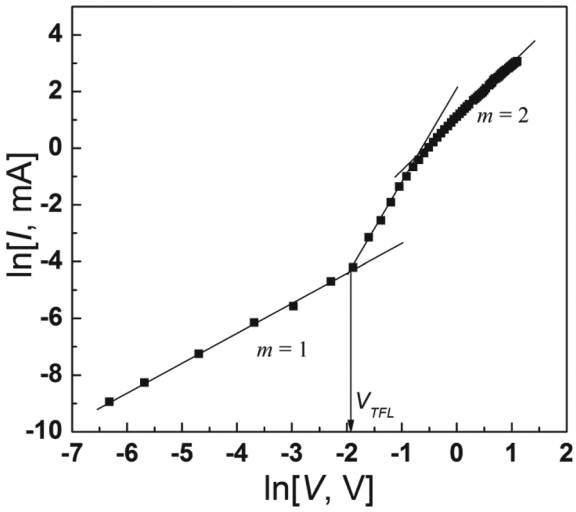

Fig. 3.3 *I-V*-characteristic of the *p*-$MnCo_2O_4$/*n*-CdTe heterostructure at positive biases, plotted on a logarithmic scale at $T =$ 295 K

ΔE, which determines the equilibrium conductivity of the high-resistance part of the base, is $\Delta E = 0.52$ eV, which, as a rule, manifests itself in semi-insulating CdTe:Cl crystals and corresponds to complexes with the participation of intrinsic defects and uncontrolled impurities [23]. Taking into account the geometric dimensions of the substrate and the thickness of the high-resistance layer, which was determined from the analysis of the *C-V*-characteristics and was $d = 65$ μm, we calculated its resistivity $\rho = 5.15 \cdot 10^8\ \Omega$ cm.

According to the SCLC theory, the presence of a linear region with $m = 1$ at low voltages is characteristic of semiconductors that contain deep traps, the energy levels of which are located below the Fermi level. In the region of the specified voltages, the injected charge carriers are captured by traps, forming a stationary space charge and do not participate in the transfer of current through the sample. The voltage V_{TFL} corresponds to the voltage of complete filling of the traps. As the voltage $V > V_{TFL}$ increases, the current begins to increase sharply, as the number of injected electrons increases, which are no longer captured by traps. The change in the slope of the dependences $lnI = f(lnV)$, observed after a significant increase in current ($V > 0.53$ V), according to the theory of the *I-V*-characteristic of the SCLC, is explained by the transition to a trap-free quadratic law, since all local states are already filled with electrons [20]. Indeed, the value of the power exponent $m = 2$ is determined in the specified voltage interval (Fig. 3.3).

If the monoenergetic traps contained in the semiconductor are deep, the expression for the voltage of their complete filling will be:

$$V_{TFL} = \frac{q(N_t - n_{t0})L^2}{2\varepsilon\varepsilon_0}, \tag{3.1}$$

where: q is the electron charge; N_t is the trap concentration; n_{t0} is the concentration of traps filled with electrons; L is the thickness of the semiconductor; ε is the relative permittivity of the semiconductor; $\varepsilon_0 = 8.85 \cdot 10^{-12}\,\mathrm{F\,m^{-1}}$ is the electric constant. The calculated value of $N_t - n_{t0}$, which determines the concentration of unfilled electron traps, was equal to $N_t - n_{t0} = 4.2 \cdot 10^{10}\,\mathrm{cm^{-3}}$. The concentration of equilibrium electrons in the high-resistance part of the base was determined based on the ratio [20]:

$$I(2V_{TFL})/I(V_{TFL}) = N_t - n_{t0}/n_0. \tag{3.2}$$

The calculated value of the equilibrium electron concentration in the high-resistance part of the base n_0 was $n_0 = 3.5 \cdot 10^9\,\mathrm{cm^{-3}}$. Taking into account the obtained value of n_0 and the value of the resistivity calculated above, the determined effective electron mobility was equal to $\mu_n = 5.6\,\mathrm{cm^2\ V^{-1}\ s^{-1}}$, which is practically two orders of magnitude less than in n-type CdTe crystals. The underestimated value of the charge carrier mobility is explained by the presence of an uncompensated negative charge of electrons concentrated on the traps, the electric field of which opposes their further injection.

The reverse branches of the I-V-characteristic in the region of small biases ($V \leq 0.4$ V at $T = 295$ K) are well described by the power law $I \sim V^m$ with the exponent $m = 1$ (Fig. 3.4). That is, the I-V-characteristic in this case, similarly to forward biases, obeys Ohm's law and can be explained within the framework of the model of currents limited by space charge. The injection of electrons into the high-resistance part of the base occurs from the conduction band of the film, where these carriers are minority.

The resistance values of the high-resistance layer, determined at the same voltage value for different temperatures according to Ohm's law, correlate well with those determined from the analysis of the forward branches of the I-V-characteristic. For example, at $T = 295$ K, the calculated value of the resistance R_b at reverse and forward biases was $1.8 \cdot 10^7\,\Omega$ and$1.7 \cdot 10^7\,\Omega$, respectively. In addition, the depth of the energy level determined from the temperature dependence of R_b (Fig. 3.4, inset)—equal to $\Delta E = 0.54$ eV—coincides with the corresponding value calculated when analyzing the forward branches of the I-V-characteristic.

With increasing reverse bias voltage in the studied p-$MnCo_2O_4$/n-CdTe heterojunctions, the current transfer mechanism changes. The voltage value at which the specified change occurs decreases with increasing temperature (Fig. 3.4). The I-V-characteristics in this case are well described by the formula for the tunnel current [24]:

$$I = a_0 \exp\left(-b_0(\phi_k - V)^{-1/2}\right) \tag{3.3}$$

where a_0 is a parameter whose value depends on the probability of filling energy levels with electrons participating in the tunneling process, b_0 is a parameter determined by the rate of change of current from voltage. The linearity of the I-V-characteristic of the studied heterojunctions in the coordinates $lnI_t = f((\varphi_\kappa - V)^{-1/2})$ (Fig. 3.5) agrees

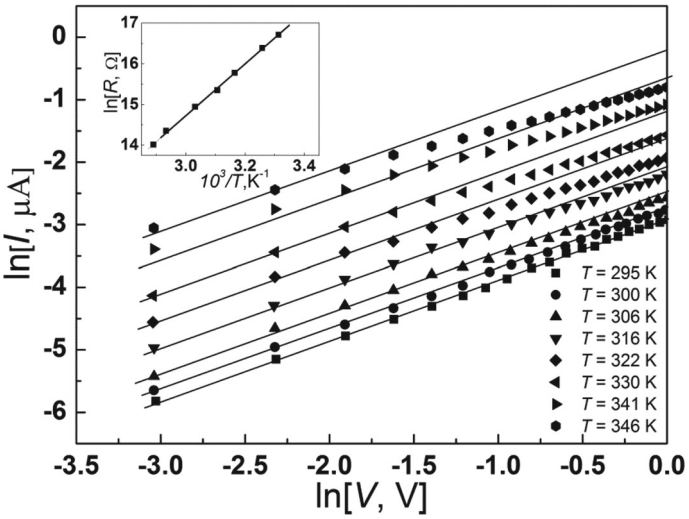

Fig. 3.4 Reverse branches of the *I-V*-characteristic of *p*-$MnCo_2O_4$/*n*-CdTe heterojunctions on a logarithmic scale in the temperature range $T = 295$–346 K. The inset shows the temperature dependence of the high-resistance part of the base

well with expression (3.3). The value of the contact potential difference φ_κ at T = 295 K is determined from the *C-V*-characteristics $\varphi_\kappa \approx 0.8$ V. The coefficient of temperature change of the potential barrier height, for determining the dependence $\varphi_\kappa = f(T)$, is taken from work [25], which investigated the electrical properties of barrier structures based on *n*-CdTe $d(q\varphi_\kappa/dT) = -2.8 \cdot 10^{-3}$ eV K^{-1}.

The constructed temperature dependence of the parameter a_0 in the coordinates $lna_0 = f(10^3/T)$ for the studied heterojunctions *p*-$MnCo_2O_4$/*n*-CdTe is well approximated by a straight line (Fig. 3.5, inset). The value of lna_0 was determined by approximating the linear sections of the dependences $lnI_t = f((\varphi_\kappa - V)^{-1/2})$ to the current axis. Therefore, the probability of filling energy levels with electrons from which they tunnel is determined by Fermi–Dirac statistics. Given the polarity of the external bias, it can be assumed that these levels are located in the band gap of the $MnCo_2O_4$ film, and the reverse current is formed due to the tunneling of electrons from them into the conduction band of CdTe. The energy distribution of the indicated energy levels in the band gap of manganese cobaltite, determined from the dependences $lna_0 = f(10^3/T)$, was 0.23 eV. The manifestation of tunnel current at higher voltages is due to its exponential dependence on the voltage value, in contrast to the power-law dependence of the current limited by space charge.

Measurements of the *C-V*-characteristics of the studied $MnCo_2O_4$/*n*-CdTe heterostructures were carried out in a wide frequency range $f = 1.0$–100 kHz (Fig. 3.6).

Characteristic for the *C-V*-characteristics of the obtained heterojunctions is their frequency dependence in the low frequency range ($f = 1$–60 kHz) and its absence at *f*

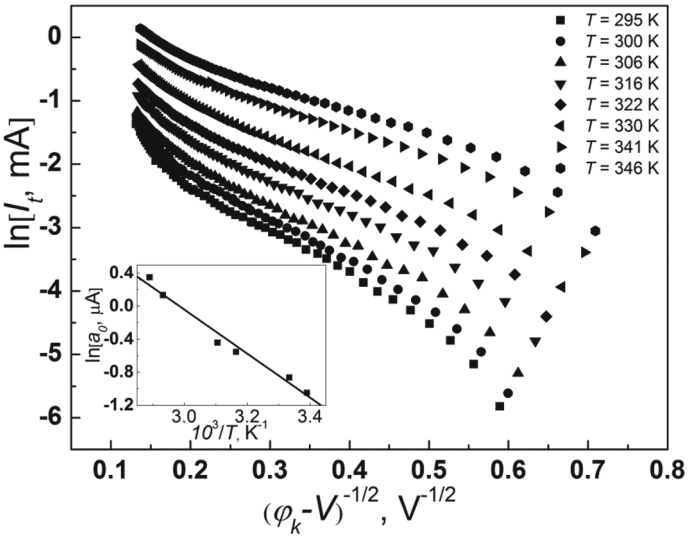

Fig. 3.5 Linear dependence of the reverse I-V-characteristics of p-$MnCo_2O_4$/n-CdTe heterojunctions for tunnel current. Inset—temperature dependence of the parameter a_0

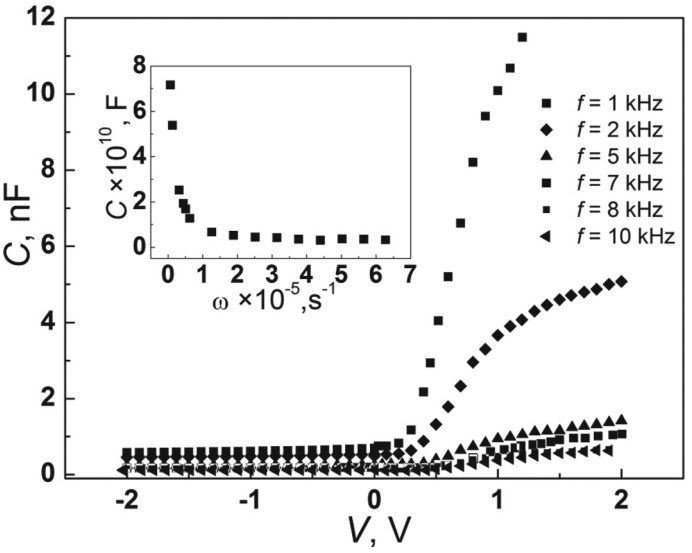

Fig. 3.6 C-V-characteristics of the $MnCo_2O_4$/n-CdTe structure in the frequency range $f = 1$–10 kHz. The inset shows the frequency dependence of the measured capacitance of the structure in the range $f = 1$–100 kHz (the given values of the quantity C correspond to $V = 0$ V)

> 60 kHz in the range of reverse and small forward voltages. For the studied structures, in the range of no dependence of the measured capacitance on frequency, its value reached a minimum value and was $C \approx 35$ pF. In addition, there is also a practical independence of the measured capacitance value at reverse voltages and its rather sharp increase when the polarity of the external bias changes. The absence of the dependence $C = f(V)$ in the reverse bias region is inconsistent with the dependence $C \sim \sqrt{\phi_k - \mathrm{qV}}$ characteristic of sharp barrier structures, which is observed when the capacitance changes with voltage due to a change in the width of the space charge region [26].

Taking into account the presence of a high-resistance layer in the base region of the structure, established from the analysis of the *I*-*V*-characteristics of the studied *p*-$MnCo_2O_4$/*n*-CdTe structures, which determines the injection currents during forward biases, the established features of the *C*-*V*-characteristics can be explained on the basis of a model of a structure with a series resistance in the base, the value of which R_b changes at the forward bias [27].

For this type of structure, the analysis of *C*-*V*-characteristics must be carried out using an equivalent circuit, which, in addition to the base resistance, also takes into account its capacitance (Fig. 3.7).

In the case when the value of the series resistance R_b is quite significant, the equivalent circuit of the structure is usually represented as a parallel *RC* circuit with a series-connected resistance. Then the measured capacitance is determined through the parameters of the equivalent circuit by the following ratio

$$C_M = \frac{C_d}{(1 + R_b/R_d) + \omega^2 R_b^2 C_d^2}, \tag{3.4}$$

where: C_M is the measured capacitance of the system; C_d and R_d are the capacitance and resistance of the space charge region; R_b is the series resistance of the structure; $\omega = 2\pi f$ is the cyclic frequency of the alternating signal when measuring the capacitance. Correct measurements are possible in the range of frequencies and series resistances when the ratio holds

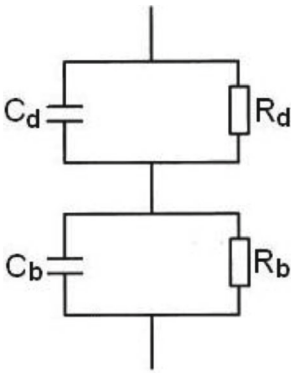

Fig. 3.7 Equivalent diagram of the structure taking into account the presence of a thin high-resistance layer

$$(\omega R_b C_d)^2 << 1. \tag{3.5}$$

As shown in works [27, 28], a characteristic sign of non-fulfillment of condition (3.5) is the appearance of a dependence of the measured capacitance on frequency, which leads to a parallel shift of the dependences $C_M^{-2} = f(V)$ and an increase in the cutoff value on the voltage axis. However, the dependence of the measured capacitance on the external bias $C \sim \sqrt{\phi_k - qV}$ remains.

It is usually assumed that $R_b << R_d$, therefore, in the case when $(\omega R_b C_d)^2 > 1$, expression (3.4) takes the form

$$C_M \approx C_d/(\omega R_b C_d)^2. \tag{3.6}$$

Analysis of expression (3.6) shows that with increasing measurement frequency, the capacitance of the C_M should approach zero proportional to ω^{-2}. However, for the studied p-$MnCo_2O_4$/n-CdTe structures, the minimum capacitance value is $C \approx 35$ pF and the dependence of the C_M value in the region of reverse and small forward biases at $f > 60$ kHz was absent (Fig. 3.6). This indicates that in this case it is necessary to use a more complex equivalent scheme of the structure, which would allow for a more accurate explanation of the experimental C-V-characteristics. For this, in the case of a large base resistance, an equivalent circuit is used that takes into account the base capacitance (Fig. 3.7).

Assuming that at reverse and small forward voltages the resistances of the high-resistance layer R_b and the depleted region of the structure R_d are approximately equal to each other $R_b \cong R_d$, taking into account that $(\omega R_b C_d)^2 >> 1$ for the total capacitance of the system, the authors [26] obtained the expression:

$$C_M \cong \frac{C_d C_b}{C_d + C_b}, \tag{3.7}$$

that is, the total capacitance of the system consists of the series-connected capacitances of the high-resistance layer C_b and the space charge of the heterojunction C_d.

Since at $V < 0$ a high barrier capacitance of the electrical junction $C_d >> C_b$ is observed, expression (3.7) takes the form $C_M \cong C_b$, i.e. the absolute value of the quantity C_M approaches the capacitance of the high-resistance layer C_b, i.e. the capacitance equal to $C \approx 35$ pF. In this case, the frequency dependence of the capacitance is not observed.

In the case of forward biases, a significant increase in the C_M value is observed with increasing voltage, which is explained by a sharp decrease in the resistance of the high-resistance base layer due to the injection of charge carriers. The significant increase in current observed on the forward branches of the I-V- characteristics even at low voltages ($V \approx 0.15$ V) (Fig. 3.3) confirms the modulation of the high-resistance part of the base by injected charge carriers. In this case, $R_b < R_d$, and to describe the dependence $C_M = f(V)$, we can use the expression for the equivalent circuit of the structure in the form of a parallel RC chain with a series-connected resistance [29].

$$C_M = \frac{C_d}{1 + \omega^2 [R_b(V)]^2 C_d^2}. \tag{3.8}$$

It is believed that each voltage value will correspond to its own R_b value. Another reason for the sharp increase in capacitance is the narrowing of the space charge region of the heterojunction.

A sharp decrease in the value of R_b will lead to the fact that the measured capacitance of the C_M structure in a certain range of forward biases will change from C_b to C_d, which is confirmed by the presence of straight-line sections on the dependences $C_M^{-2} = f(V)$ (Fig. 3.8). It can be assumed that when $V \to V_C$, where V_C is the cutoff voltage determined by extrapolation of the straight-line sections of the $C_M^{-2} = f(V)$ characteristics to the abscissa axis, then $C_M \to C_d$. The value of V_C is 0.8 V, which is quite realistic for this type of barrier structures based on CdTe.

The increase in capacitance in the positive bias region depends on the ability of the injected charge carriers to keep up with the change in the signal on which the measurements are made. If this condition is not met, which may occur in the high-frequency region, an increase in capacitance at $V > 0$ may not be observed [26].

Since the value of the measured capacitance $C_M \approx 35$ pF of the studied *p*-$MnCo_2O_4$/*n*-CdTe structures is interpreted as the capacitance of the high-resistance base layer, its thickness was estimated using the formula for a flat capacitor:

$$C = \frac{\varepsilon_0 \varepsilon S}{d}, \tag{3.9}$$

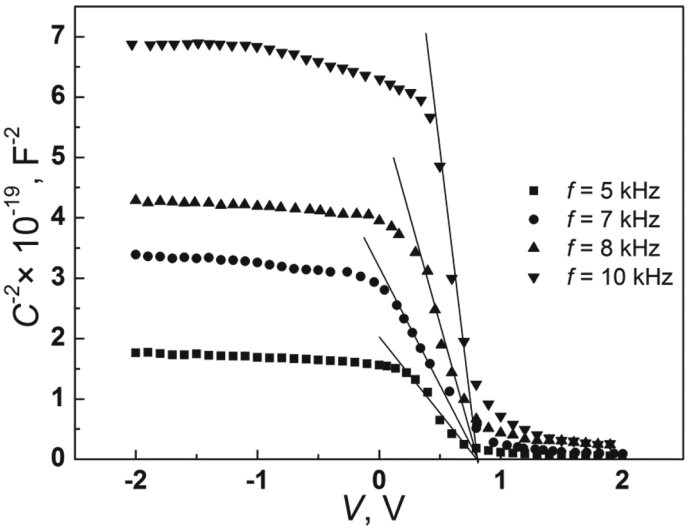

Fig. 3.8 *C-V*-characteristics of the $MnCo_2O_4$/*n*-CdTe heterojunction, plotted in the coordinates $C_M^{-2} = f(V)$

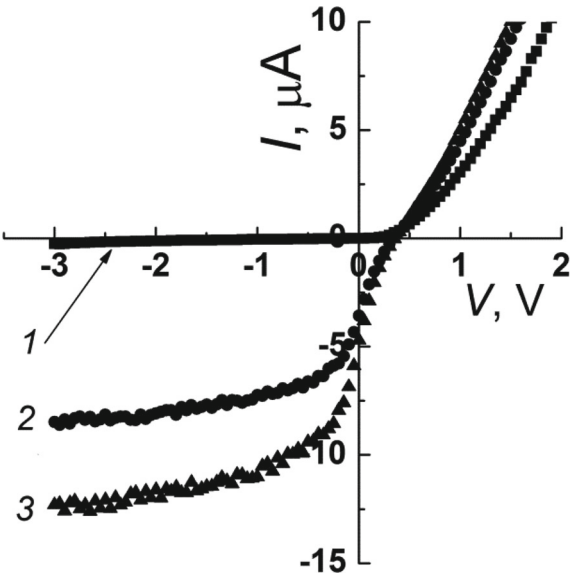

Fig. 3.9 I-V-characteristics of the p-$MnCo_2O_4$/n-CdTe heterostructure, unilluminated (curve 1) and illuminated at photoexcitation intensities of 25,000 lx (curve 2) and 40,000 lx (curve 3)

where S is the area of the heterojunction, d is the width of the space charge region, $\varepsilon_0 = 8.85 \cdot 10^{-12}$ F m^{-1} is the electric constant; $\varepsilon = 10.6$ is the relative dielectric constant of CdTe. The calculated value was d = 65 μm.

The photovoltaic properties of the obtained p-$MnCo_2O_4$/n-CdTe heterojunctions were studied. It was found that when illuminated from the side of the manganese cobaltite film with integral light, the structures exhibited fairly good photosensitivity in the region of reverse voltages (Fig. 3.9). Practical independence of the photocurrent from the applied voltage was observed.

3.4 Conclusions

Anisotype heterojunctions p-$MnCo_2O_4$/n-CdTe with diode properties were obtained by spray-pyrolysis of thin films of manganese cobaltite $MnCo_2O_4$ on the surface of crystalline n-CdTe at a substrate temperature of $T_S = 390$ °C.

The features of the electrical properties of the studied structures are determined by the presence of a high-resistance layer, which is formed in the contact area of the base during their manufacture. The emergence of the high-resistance region is explained by the processes of compensation of the main impurity defects of the base material Cl_{Te}^{+} by electrically active intrinsic defects of the acceptor type cadmium vacancies V_{Cd}^{-}, V_{Cd}^{-2} due to the formation of electrically active and neutral complexes $\left(V_{Cd}^{-2}Cl_{Te}^{+}\right)^{-}$, $(V_{Cd}^{-2}2Cl_{Te}^{+})$, $\left(V_{Cd}^{-}Cl_{Te}^{+}\right)^{0}$. The increase in the concentration of V_{Cd}^{-}, V_{Cd}^{-2} in the near-surface region of CdTe occurs due to the sublimation of its surface upon heating.

The *I-V*-characteristics of the fabricated anisotype heterojunctions *p*-$MnCo_2O_4$/*n*-CdTe at forward and small reverse (*V*³ 0.5 V) biases are determined by the processes of electron injection into the high-resistance near-contact part of *n*-CdTe, from the low-resistance region of the base and the $MnCo_2O_4$ film at forward and reverse voltages, respectively. Based on the theory of space charge-limited currents, which well describes the *I-V*-characteristics, the presence of deep traps in the high-resistance region that capture injected charge carriers was established, and its main electrical parameters were calculated: resistivity $\rho = 5.15 \cdot 10^8\ \Omega\,\text{cm}$; equilibrium charge carrier concentration$n_0 = 3.5 \cdot 10^9\ \text{cm}^{-3}$, their effective Hall mobility *m*$_n = 5.6\ \text{cm}^2\ \text{V}^{-1}\ \text{s}^{-1}$, and a deep energy level that determines the equilibrium conductivity—$\Delta E = 0.52$ eV. The *C-V*-characteristics of the studied heterojunctions are in good agreement with the model of surface-barrier structures with a high-resistance layer, the resistance of which decreases under forward biases due to the injection of majority charge carriers. The height of the potential barrier, which determines the rectifying properties of the structure, $q\varphi_k \approx 0.8$ eV and the thickness of the high-resistance region $d = 65$ μm were determined.

The photosensitivity of *p*-$MnCo_2O_4$/*n*-CdTe heterojunctions in the negative bias region and the practical independence of the reverse current from the voltage determine their practical use as visible radiation photodetectors.

References

1. R.S. Kalubarme, H.S. Jadhav, D.T. Ngo, G. Park, J.G. Fisher, Y. Choi et al., Simple synthesis of highly catalytic carbon-free $MnCo_2O_4$@Ni as an oxygen electrode for rechargeable Li–O_2 batteries with long-term stability. Sci. Rep. **5**, 13266 (2015). https://doi.org/10.1038/srep13266
2. K. Song, L. Yuan, Z. Li, Y. Lv, B. Yang, Y. Yu et al., Tuning $MnCo_2O_4$ nanowire arrays on carbon cloth as an efficient cathode catalyst for Li–O2 batteries. Electrochim. Acta **353**, 136572 (2020). https://doi.org/10.1016/j.electacta.2020.136572
3. Y. Dong, Y. Wang, Y. Xu, C. Chen, Y. Wang, L. Jiao et al., Facile synthesis of hierarchical nanocage $MnCo_2O_4$ for high performance supercapacitor. Electrochim. Acta **225**, 39–46 (2017). https://doi.org/10.1016/j.electacta.2016.12.109
4. L.Q. Fan, J.L. Huang, Y.L. Wang, C.L. Geng, S.J. Sun, Y.F. Huang et al., High-capacity $MnCo_2O_4$ supported by reduced graphene oxide as an anode for lithium-ion capacitors. J. Energy Storage **30**, 101427 (2020). https://doi.org/10.1016/j.est.2020.101427
5. R. BoopathiRaja, M. Parthibavarman, Hetero-structure arrays of $MnCo_2O_4$ nanoflakes@nanowires nanoflakes@nanowires grown on Ni foam: Design, fabrication and applications in electrochemical energy storage. J. Alloy. Compd. **811**, 152084 (2019). https://doi.org/10.1016/j.jallcom.2019.152084
6. J.A. Jiménez-Miramontes, J.L. Domínguez-Arvizu, F.A. Gaxiola-Cebreros, B.C. Hernández-Majalca, J.C. Pantoja-Espinoza, J.M. Salinas-Gutiérrez, V.H. Collins-Martínez, A. López-Ortiz, Effect of the synthesis method on the $MnCo_2O_4$ towards the photocatalytic production of H_2. Rev. Adv. Mater. Sci. **61**, 654–672 (2022). https://doi.org/10.1515/rams-2022-0263
7. S. Vadivel, G. Balaji, S. Rathinavel, High performance ethanol and acetone gas sensor based nanocrystalline $MnCo_2O_4$ using clad-modified fiber optic gas sensor. Opt. Mater. **85**, 267–274 (2018). https://doi.org/10.1016/j.optmat.2018.08.067
8. I.G. Orletskyi, I.P. Koziarskyi, D.P. Koziarskyi, E.V. Maistruk, Optical, electrical and gas sensing properties of the $MnCo_2O_4$ thin films, in *2024 IEEE 14th International Conference*

"Nanomaterials: Applications & Properties" (IEEE NAP-2024, Riga, Latvia, 2024), pp. 1–5. https://doi.org/10.1109/NAP62956.2024.10739681
9. Z. Li, S. Liu, L. Li, W. Qi, W. Lai, L. Li, X. Zhao, Y. Zhang, W. Zhang, In situ grown $MnCo_2O_4$@$NiCo_2O_4$ layered core-shell plexiform array on carbon paper for high efficiency counter electrode materials of dye-sensitized solar cells. Sol. Energy Mater. Sol. Cells **220**, 110859 (2021). https://doi.org/10.1016/j.solmat.2020.110859
10. T.L. Le, S. Guillemet-Fritsch, P. Dufour, C. Tenailleau, Microstructural and optical properties of spinel oxide $MxCo_{2-x}MnO_4$ (M= Ni, Zn or Cu; $0 < x < 1$) thin films prepared by inorganic polycondensation and dip-coating methods. Thin Solid Films **612**, 14–21 (2016). https://doi.org/10.1016/j.tsf.2016.05.030
11. G. Salek, P. Dufour, S. Guillemet-Fritsch, C. Tenailleau, Sustainable low temperature preparation of $Mn_{3-x}Co_xO_4$ ($0 \leq x < 3$) spinel oxide colloidal dispersions used for solar absorber thin films. Mater. Chem. Phys. **162**, 252–262 (2015). https://doi.org/10.1016/j.matchemphys.2015.05.065
12. I.M. Dharmadasa, A.E. Alam, A.A. Ojo, O.K. Echendu, Scientific complications and controversies noted in the field of CdS/CdTe thin film solar cells and the way forward for further development. J. Mater. Sci. Mater. Electron. **30**, 20330–20344 (2019). https://doi.org/10.1007/s10854-019-02422-6
13. T.L. Le, Preparation of transition metal oxide thin films used as solar absorbers. Materials, Université Paul Sabatier—Toulouse III (2016). https://theses.hal.science/tel-01578163
14. A. Zaouali, A. Dhahri, A. Bougharriou, E. Dhahri, R. Barille, B.F.O. Costa, K. Khirouni, High electrical conductivity at room temperature of $MnCo_2O_4$ cobaltite spinel prepared by sol–gel method. J. Mater. Sci. Mater. Electron. **32**, 1221–1232 (2021). https://doi.org/10.1007/s10854-020-04895-2
15. H. Bordeneuve, S. Guillemet-Fritsch, A. Rousset, S. Schuurman, V. Poulain, Structure and electrical properties of single-phase cobalt manganese oxide spinels $Mn_{3-x}Co_xO_4$ sintered classically and by spark plasma sintering (SPS). J. Solid State Chem. **182**, 396–401 (2009). https://doi.org/10.1016/j.jssc.2008.11.004
16. P.L. Meena, K. Sreenivas, R. Kumar, Conduction mechanism in cobalt rich $Co_{3-x}Mn_xO_4$ ($0.1 \leq x \leq 1.0$) spinel oxide ceramics. Appl. Sci. Lett. **1**, 110–114 (2015). https://doi.org/10.17571/appslett.2015.01025
17. E.V. Maistruk, M.I. Ilashchuk, I.G. Orletskyi, I.P. Koziarskyi, P.D. Marianchuk, H.P. Parkhomenko, D.P. Koziarskyi, S.V. Nichyi, Electric and photoelectric properties of vacuum-deposited ZnO:Al/CdS/p-$Cd_{1-x}Zn_xTe$ heterojunctions. Optik **241**, 167246 (2021). https://doi.org/10.1016/j.ijleo.2021.167246
18. I.P. Koziarskyi, M.I. Ilashchuk, I.G. Orletskyi, D.P. Koziarskyi, L.A. Myroniuk, D.V. Myroniuk, A.I. Ievtushenko, E.V. Maistruk, The influence of manufacturing modes on the electrical and energy parameters of graphene/p-CdTe Schottky diodes. Physica B **667**, 415151 (2023). https://doi.org/10.1016/j.physb.2023.415151
19. A.V. Savitsky, M.I. Ilashchuk, O.A. Parfenyuk, K.S. Ulyanytsky, V.R. Burachek, R. Ciach, Z. Swiatek, Z. Kuznicki, Thermostability of physical properties of cadmium telluride crystals. Thin Solid Films **361–362**, 203–207 (2000). https://doi.org/10.1016/S0040-6090(99)00794-4
20. M.A. Lampert, P. Mark, Current injection in solids (Academic Press, 1970) [ISBN: 9780124353503]
21. I.G. Orletskyi, M.I. Ilashchuk, I.P. Koziarskyi, M.V. Koval, E.V. Maistruk, D.P. Koziarskyi, Electrical Properties of Photosensitive $MnFe_2O_4$/n-CdTe Heterojunctions, in *Nanooptics and Nanoelectronics, Nanobiotechnology, and Their Applications. NANO 2023*, ed by O. Fesenko, L. Yatsenko (Springer Proceedings in Physics, 2024), pp. 151–164. https://doi.org/10.1007/978-3-031-67527-0_12
22. I.G. Orletskyi, M.I. Ilashchuk, E.V. Maistruk, I.P. Koziarskyi, D.P. Koziarskyi, Electrical properties of the *n*-NiS_2/*n*-CdTe isotype heterojunction fabricated by spray pyrolysis. Acta Physica Polonica Series A **142**, 615–620 (2022). https://doi.org/10.12693/APhysPolA.142.615
23. K.R. Zanio, Cadmium telluride. in *Semiconductors and Semimetals*, vol. 13 (Academic Press, New York, San Francisko, London, 1978), p. 256

24. B.L. Sharma, R.K. Purohit, Semiconductor heterojunctions (Pergamon Press, 1974) [ISBN:9781483280868]
25. E.V. Maistruk, I.G. Orletskyi, M.I. Ilashchuk, I.P. Koziarskyi, D.P. Koziarskyi, ZnO:Al/ZnS/*n*-CdTe heterojunctions' electric and photoelectric properties. Optik **276**, 170663 (2023). https://doi.org/10.1016/j.ijleo.2023.170663
26. S.M. Sze, K.N. Kwok, *Physics of Semiconductor Devices* (Wiley, New York, 2007)
27. A.M. Goodman, Metal—semiconductor barrier height measurement by the differential capacitance method—one carrier system. J. Appl. Phys. **34**, 329–338 (1963). https://doi.org/10.1063/1.1702608
28. A.S. Kavasoglu, N. Kavasoglu, S. Oktik, Simulation for capacitance correction from Nyquist plot of complex impedance–voltage characteristics. Solid-State Electron. **52**, 990–996 (2008). https://doi.org/10.1016/j.sse.2008.02.004
29. A.A. Lebedev, A.A. Lebedev, D.V. Davydov, Capacitance measurements for diodes in the case of a strong dependence of the series resistance of the diode base on the applied voltage. Semiconductors **34**, 115–118 (2000). https://doi.org/10.1134/1.1187964

Chapter 4
Geomechanical and Physicochemical Influences on the Movement of Iron-Aluminosilicate Marine Sediments in the Ocean Depths

I. G. Kovzun, A. V. Panko, V. A. Prokopenko, O. Yu Voitenko, and O. M. Nikipelova

Abstract Transformations and interfacial interactions in dissipative natural marine geoecological systems (MGES) of sediments consisting of various iron-aluminosilicates play a significant role in the geoecological behavior of the resulting ocean suspensions, which significantly affects the life of mankind. This impact has recently increased many times over due to the growing pollution of the oceans by more than 350 thousand species of surfactants. The study of environmental behavior under the influence of geomechanical, physicochemical, and other factors has just begun. The simplified scheme of the impact of various factors on MGES and preliminary verification of the information already obtained indicate the growing role of geomechanical and physicochemical processes in open MGES, which allowed us to draw several significant conclusions. For example, the acceleration of sediment bottom layers movement due to the reduction of suspension viscosity by the resulting alkaline solutions of various sodium silicates and the increased role of information exchange of contacting dissipation compounds in the MGES are noteworthy. Simplified scheme of influence on the MGES: Entry into the MGES system: Flows of

I. G. Kovzun · A. V. Panko (✉) · V. A. Prokopenko · O. Y. Voitenko
F.D. Ovcharenko Institute of Biocolloidal Chemistry of NAS of Ukraine, Kyiv, Ukraine
e-mail: phd.wiz@gmail.com

I. G. Kovzun
e-mail: gr.k.ibcc@ukr.net

V. A. Prokopenko
e-mail: prokop_va@ukr.net

O. Y. Voitenko
e-mail: elvoitenko@ukr.net

O. M. Nikipelova
Engineering and Technology Institute "Biotechnika" of NAAS of Ukraine, Odes'ka Oblast, Ukraine
e-mail: olena.nikipelova2020@gmail.com

O. Fesenko and L. Yatsenko (eds.), *Functional Nanomaterials, Nanocatalysts, Nanotechnologies, and Their Applications*, Springer Proceedings in Physics 321,
https://doi.org/10.1007/978-3-031-99136-3_4

information, energy, and substances entering the system → Accumulation of information, energy, and substances in the new system → Export of excess accumulated information, energy, and new substances from the system.

4.1 Introduction

Recently, considerable attention of scientists has been drawn to studies related to the geoecology of the World Ocean (hereinafter referred to as the Ocean), inorganic and biocolloidal transformations of materials of the oceanic and partially coastal continental zones and underwater deposits of ores and dispersed sediments, as well as other related problems [1–26], Figs. 4.1, 4.2, and 4.3. Such research is carried out to obtain fundamental knowledge to reveal the complex processes of sustainable use of various resources of the Ocean, provided that the ecological and biocolloidal balance is maintained in it and the Earthx's biosphere as a whole. This is primarily due to the predominant role of the Ocean in global biosphere processes that maintain the ecological balance between all living organisms and the Ocean as their main habitat on the planet [1–12]. Indeed, the Ocean occupies 70.8% of the Earth's surface area; its maximum depth is 11028 m, and the average depth is about 3800 m. The totality of living organisms inhabiting the world's oceans at all depths has a significant impact, exceeding 80% of the total, on environmental phenomena in the hydrosphere and in the sedimentary shell of the ocean floor, as well as in the Earth's atmosphere. They are governed by complex equilibrium processes, which are studied by marine geoecology, ocean chemistry, biocolloidal chemistry, and physicochemical geomechanics [1, 2]. Compared to such processes, similar processes on the solid surface of the Earth have a much smaller impact, not exceeding 18–20%. However, during the twentieth century, the negative impact of the anthropogenic technological factor on the equilibrium processes in the biosphere has grown exponentially and continues to grow. Thus, in 1900, the world's population was 1.6 billion, in 1988 it was about 3 billion, and by 2021 it reached 8 billion people, which had a corresponding impact on environmental pollution. Therefore, at the current stage of scientific and technological progress, it is clear that to solve such problems, it is necessary to rapidly improve the system of knowledge about the biosphere, taking into account the achievements of various geological, chemical, colloid-chemical, biocolloidal and related disciplines.

In the 70 s of the twentieth century, a new scientific field, marine engineering geology, emerged to study and solve problems caused by anthropogenic activities, including technogenic impact on the bottom sediments of the seas and oceans [9]. This area developed in parallel with physicochemical geomechanics [10] and mechanics [11] as branches of colloidal chemistry, as well as with soil mechanics [1, 2] and engineering geology [9]. At the same time, insufficient attention has been paid to the problems associated with the impact of microbial metabolism in soils, sediments, and bottom sediments in the offshore zone, on coastal and underwater slopes, and even more so on the beds and dips of the abyssal plains of the seas and oceans. The processes themselves in such systems have not been considered in terms of

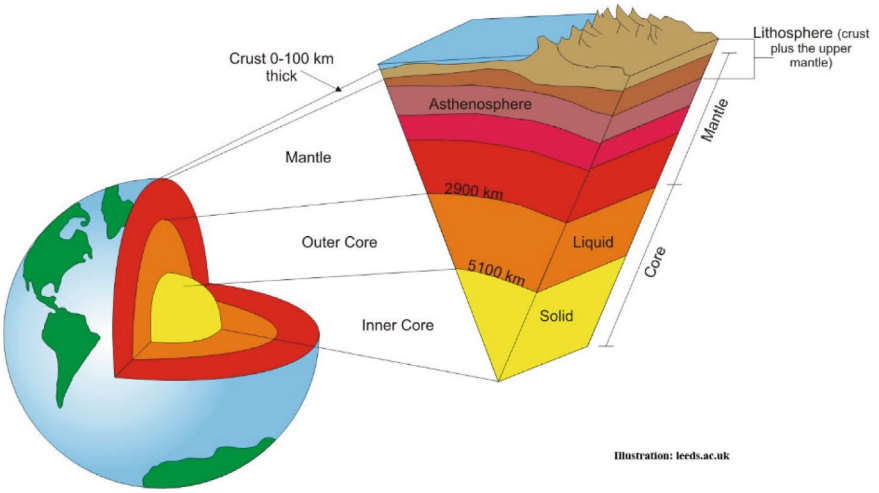

Fig. 4.1 Cross-sectional structure of the Earth

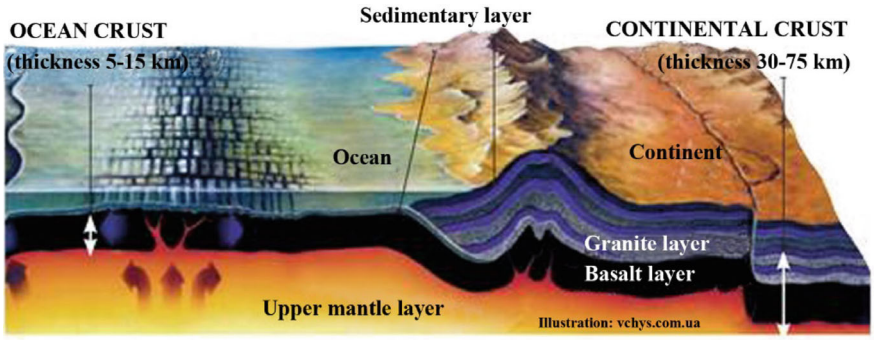

Fig. 4.2 Scheme of oceanic and coastal continental zones and submarine volcanic activity

Fig. 4.3 Cross-sectional diagram of continental and oceanic zones and the distribution of coastal and deep-sea sediments and ore deposits

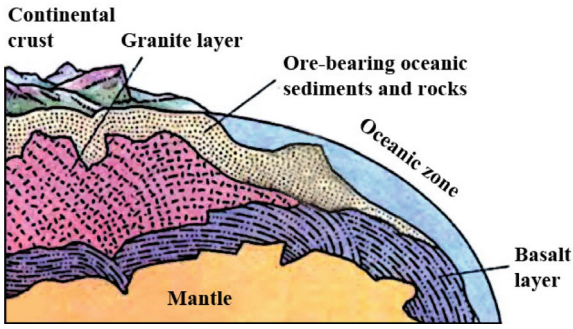

their impact on the preservation of the environment and marine resources, as well as the impact on ecological balance [8]. Recent interdisciplinary research in the fields of nanochemistry, biocolloidal chemistry, and physicochemical geomechanics has allowed us to obtain new data, develop new concepts and views on the problems of ecology, development, and changes in the Ocean resource base [1, 2], which correlate with the views of various branches of geological sciences (Earth physics, marine chemistry, marine geology, biology, and hydraulic engineering, oceanography, and others) [1]. The deterioration in the quality of the natural environment has necessitated the development of environmental problems related to traditional geological and related sciences (colloidal and biocolloidal chemistry, physicochemical mechanics and geomechanics, nanoscience in general, and its sections—nanochemistry, nanophysics, biocolloidal and colloidal nanoscience). As a result, new areas in chemical and geological sciences (marine biocolloidal geoecology and physicochemical geomechanics) emerged and began to develop. The evolution of traditional areas in geology, chemistry, and physics has led to the emergence of new and interdisciplinary concepts and concepts that are also beginning to develop rapidly. Thus, the part of the lithosphere whose surface is covered by the Ocean waters has been considered as one of the main abiotic and biotic structures of the biosphere ecological system (biocenoses, biogeocenoses). At the same time, the theoretical and methodological basis for studying and solving many problems caused by anthropogenic activities that affect the multifunctional properties and characteristics of the Ocean is formed by the biosphere-ecological concept, ecosystem, and model-target approaches to solving problems of marine geoecology, physicochemical geomechanics, and biocolloidal chemistry [1–26].

4.1.1 Theoretical Concepts of the MGES

The fundamental and practical conclusions and analytical findings have shown that without solving terminological, methodological and conceptual issues of general importance, it is difficult to effectively develop many specific geological, colloidal, biocolloidal, engineering and environmental problems of regulating the Ocean resource base. Moreover, it is challenging to establish new economic complexes in marine, coastal, and nearshore areas, as well as at great depths.

The growing global scale of marine and oceanic pollution by human waste is a matter of concern to the scientific community at the interdisciplinary level. The reason for this is a decrease in the bioproductivity and quality of products and ore deposits extracted from the sea depths, suitable for food and use in industrial production. The quality of mineral resources is also deteriorating, while their extraction in coastal and deep-sea areas of the seas and oceans continues to increase, further disrupting the dynamic ecological and industrial balance of the Ocean, which has been forming over hundreds of millions of years. Therefore, there is a need to accelerate the study of the complex nature of the phenomena that regulate the balance of water areas at all levels, from the shelf zone, sloping and steep slopes to the deep

abyssal plains of the oceans and abysses up to 11,000 m. This can be based on the theoretical and practical knowledge accumulated in previous research in the fields of marine chemistry, biochemistry, colloidal and biocolloidal chemistry, nanochemistry and physicochemical geomechanics on the one hand, and on the other hand in the fields of geology, oceanology, biology, ecology, hydraulic engineering, and other scientific and technical fields. In this sense, the further accelerated development of such new complex scientific areas as the basics of marine geoecology [1], as well as aspects of marine biocolloidal geoecology and physicochemical geomechanics [2] is undoubtedly timely and highly necessary.

Thus, the monograph [1] highlights the development of the theoretical and methodological foundations of a new synthetic scientific field—marine geoecology (MG). The conceptual approaches to the study of bottom sediments of the seas and oceans as marine geological ecosystems (MGES) are considered. New concepts have been proposed and substantiated that cover not only the ideology and direction of marine geoecological research but also the material component of their object. In the example of the study of the Black Sea and the Guinea sector of the Tropical Atlantic, it is shown that the theoretical and methodological basis of marine geoecology is the doctrine of the place of the MGES in the structure of the biosphere and ecosphere. Even though MG is at the initial stage of its formation as a branch of Earth and environmental science, it is focused on the study of bottom sediments and their components, including living organisms as components of the MGES, their component composition, properties, functions, as well as the development of their resources. All of this is interesting for humanity not only in terms of acquiring new knowledge but also in connection with the need to survive in the unstable conditions of the ecosphere, the balance of which is disturbed primarily by the negative anthropogenic impact on it. Therefore, a fundamentally new approach to the study of the Ocean bottom sediments is being developed, which has not been used by other sciences before [1]. The bottom sediments are considered as a subsystem ecosphere, i.e., the MGES. At the same time, it is assumed that both the MGES and the ecosphere are phenomena of a geological nature. The principles of classification of MGES and factors of disturbance of sediment geoecosystems are also presented. The Black Sea sediments were zoned using appropriate criteria and recommendations for the preservation of the geoecosystem of such sediments were developed and partially implemented in the substantiation of local hydrotechnical practical solutions, as well as in the preparation of a diagnosis and forecast of the ecological state of the Burgas Bay. In general, the theoretical and methodological knowledge and practical experience in marine geoecology indicate a significant development of this new scientific field, as well as the need to develop knowledge about the mechanisms of complex processes in MGES and, first of all, about the mechanisms of creation, movement and subsequent transformation of an important component of such systems—disperse bottom turbidite-pelagic sediments, considered in the monograph [2] and in many scientific publications of recent decades [1, 2, 13–18, 20, 21, 23]. They indicate the beginning of the formation of another modern scientific direction—the basics of biocolloidal marine geoecology and physicochemical geomechanics (BG and PCGM). This area not only complements the concepts of marine geoecology in the traditional sense [1]

but also significantly expands them. Thus, by now, according to the achievements of BG and PCGM [2], the concepts of polymineral, nano- and microdisperse iron-aluminosilicate systems and materials (IAS) widespread in the Earth's crust have been developed. Colloid-chemical studies of such systems and materials based on iron ores, soils, clays, marine and coastal lake sediments (muds), and sands of various origins have always received great attention [1, 2, 13–23]. In the last decade, they have been increasingly studied not only in terms of the influence of the laws of colloidal chemistry, nanochemistry, and physicochemical geomechanics on their properties [2, 13–18, 20, 21], but also to elucidate the mechanisms of complex biocolloidal interactions, which can be considered as interfacial colloid-chemical and nanochemical transformations of IAS and similar disperse systems under the influence of microbial metabolic products [1, 2, 8, 13–18, 20, 21]. However, the determination of such impacts on polymineral IAS due to the complexity of multifaceted physicochemical, geomechanical, colloid-chemical, and biocolloidal methods of their study and the ambiguity of the relevant conclusions, in many specific cases remains either unclear or not yet completed.

To date, it is generally known that physicomechanical, colloid-chemical, nanochemical transformations and contact interfacial interactions in IAS and clay-containing pelagic sediments (PS) with the participation of microbiological processes in biogeocenoses lead to the emergence of new disperse polymineral nanostructured materials with new properties. The composition of materials such as IAS and PS consists mainly of iron, aluminum and silicon oxides, as well as many other inorganic and organic components in smaller quantities, the role of which in many cases has not yet been fully clarified. These disperse systems and materials, which are widely used in scientific research and practice, include sedimentary iron oxide-aluminosilicate ores, iron-bearing clays, pelitic sea and lake sediments, coastal and shelf sands, other sedimentary and solid nano- and microstructured ore deposits, as well as soils of various origins. Many of them have been transformed in the course of their geological history under the influence of primary physicomechanical, microbiological, and mechanochemical processes of dispersion of dense rocks and secondary colloidal, nanochemical, and tectonic processes of further dispersion or compaction of dispersed materials with the transition to sedimentary rocks. For example, it has recently been established that solid microcrystalline iron quartzites (jaspelites), which are the basis of the main iron ore deposits, began to form 2 billion years ago, initially with the formation of finely dispersed polymineral compositions, their enrichment due to the activity of microorganisms, followed by the compaction of the resulting enriched iron-iron-aluminosilicate disperse formations [2].

As the practical significance of both IAS and PS and the nanostructured materials extracted from them is constantly growing, so is the attention of both technologists and researchers studying the fundamental mechanisms of transformation of IAS and other relevant materials. Therefore, such studies of problematic issues are relevant. They can be formulated as follows:

- The understanding of the role of physicochemical mechanics and geomechanics, as a section of colloidal and biocolloidal chemistry, in the dispersion, transformation, and subsequent secondary contact interfacial nanostructuring and subsequent compaction of sedimentary deposits of iron-aluminosilicate and iron oxide-hydroxide materials is not sufficiently developed.
- The mechanisms of secondary contact compaction of IAS and the coagulation-crystallization processes of their further transformation are not sufficiently studied.
- The influence of microbiological processes on the above-mentioned mechanisms of dispersion and subsequent restructuring and transformation of IAS and their constituent minerals is known only in general terms; therefore, such processes require further research.
- The nanochemical, mechanochemical, and nanostructural transformations of the components of the IAS, primarily iron oxides and hydroxides, as well as silicate minerals and quartz, have been studied rather superficially; these transformations of the IAS in individual inorganic iron oxide-hydroxide-aluminosilicate systems and in the composition of biogenic-abiotic materials are still being studied both from the point of view of theoretical consideration of the relevant processes and their experimental confirmation.
- The development of ideas about the corresponding complex mechanisms of transformation of the IAS and PS as subsystems of the MGES also requires the creation of new colloid-chemical, biocolloidal, and physico-geomechanical views on stress (phenomenal) and volcanic phenomena in the coastal crust and in marine sediments of different depths.
- Recommendations for the creation of scientifically based effective ecogeotechnological solutions for the practical use of IAS and PS and the prevention of phenomenal processes occurring on marine slopes and in natural and technogenic barriers and dams involving highly disperse iron-aluminosilicate nanostructured complex mineral sediments need further generalization.

Thus, the above considerations indicate the considerable urgency of the problematic issues and the need to address them by conducting appropriate long-term systematic experimental and theoretical studies of iron-aluminosilicate systems and materials to generalize them and form stable views on biocolloidal, colloid-chemical, nanochemical, mechanical and geomechanical transformations in them with the participation of nano-, ultra- and microdisperse particles and nanostructures.

4.2 Results and Discussion

4.2.1 Analysis of Interfacial Interactions in IAS

Many processes in the IAS are explained by the manifestations of non-standard ultra-anomalous flow of concentrated sediments with a moisture content of 60–34% located on slopes and in deep abyssal plains and dips of seas and oceans. Additional study of these issues will improve the views on the features of ultra-anomalous flow since the movement of iron-aluminosilicate sediments and suspensions on the slopes of the Ocean and in its large abyssal plains and deep dips is explained by a non-standard anomaly (ultra-anomaly) of viscosity (Fig. 4.4), which is associated with the contact effect on the rheological processes in the IAS of micro- and nanoparticles in the zones of mechanochemical and nanochemical transformation of coagulation-condensation contacts [2–10, 12–23]. Rheological data (Fig. 4.4) and the diffractogram of the model sample (Fig. 4.5) indicate an amorphous, highly dispersed structure of the sediments. They include goethite, saponite, quartz, sulfides, nanodispersed impurities of phosphates, and arsenates of aluminum and iron, which are of microbiological origin (Table 4.1).

Sorption isotherms indicate similarities in the mineralogical composition and dispersion of both shallow and deep marine sediments and suspensions (Table 4.1, Figs. 4.4, 4.5 and 4.6). The most developed pores are in the 2 nm range. Thus, the millennia-long deposition of sediments leads to a reduction in pore size and a 9–tenfold increase in their specific surface area, from 60–70 m^2/g to 580–600

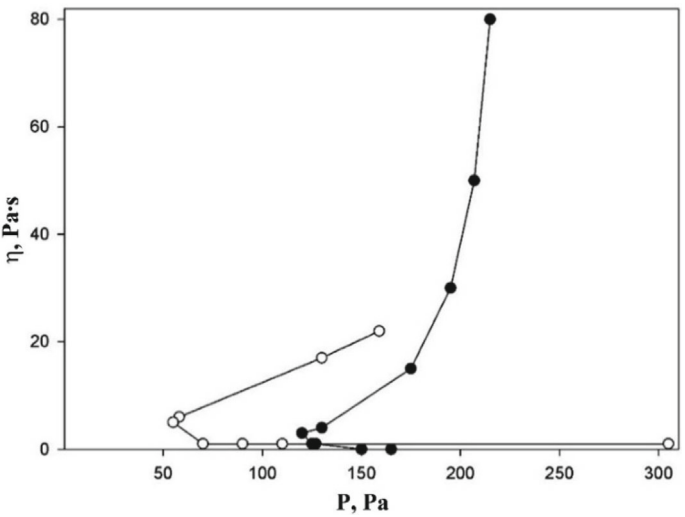

Fig. 4.4 Dependence of viscosity (η) on shear stress (P) of the Black Sea sediment of biocolloidal origin. The moisture content of the suspension is 46%. (●)—"forward" and (○)—"reverse" curves

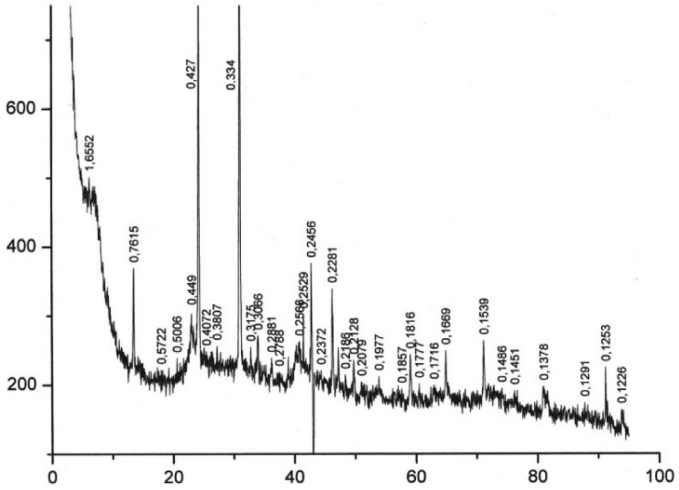

Fig. 4.5 XRD of the Black Sea sediment of biocolloidal origin

Table 4.1 Minerals of the Black Sea (1), Kuyalnik (2), and Azov Sea (3) pelagic sediments

Pelagic sediment sample, No.	Mineral composition
1	Quartz, mica, glauconite, chlorite, kaolinite, feldspar, montmorillonite and other
2	Quartz, mica, glauconite, chlorite, kaolinite, feldspar, montmorillonite and other
3	Quartz, mica, glauconite, chlorite, kaolinite, feldspar, montmorillonite and other

m^2/g, resulting in a corresponding increase in their adsorption-contact capacity for toxic substances entering the Ocean from industrial zones of the Earth, which are consequently caused by anthropogenic activities [24–26].

It was also shown, using the achievements of physicochemical geomechanics, and experimentally confirmed, using XRD, SEM, rheological and chemical methods, laser correlation spectroscopy and biomedical testing methods, concepts of the role of chemical transport of carbonates in the contact zones of mineral particles of dispersed carbonate-iron oxide-aluminosilicate systems (IAS), which is accompanied by accelerated isothermal distillation of ultrafine carbonates in the conditions of their interaction with carbonic acid in the presence of sodium chloride solution and laminar flow. Or, in the conditions of mineral separation, chemical transport of colloidal carbonate microparticles in contact zones in the dispersion medium in the form of ultrafine particles under conditions of the intense (turbulent) flow of the IAS and in the presence of air carbon dioxide and sodium chloride dissolved in the dispersion medium, according to the scheme (Fig. 4.7).

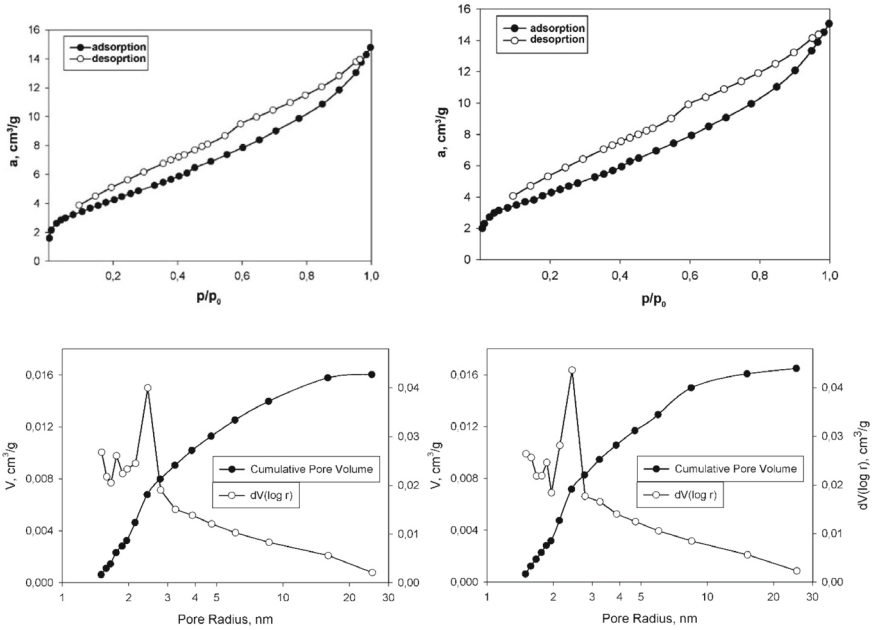

Fig. 4.6 Nitrogen sorption isotherms (a – p/p_0) and pore size dependence (V – r, dV(logr) – r) for two samples of Black Sea pelagic sediments (a and b) collected at different remote sites

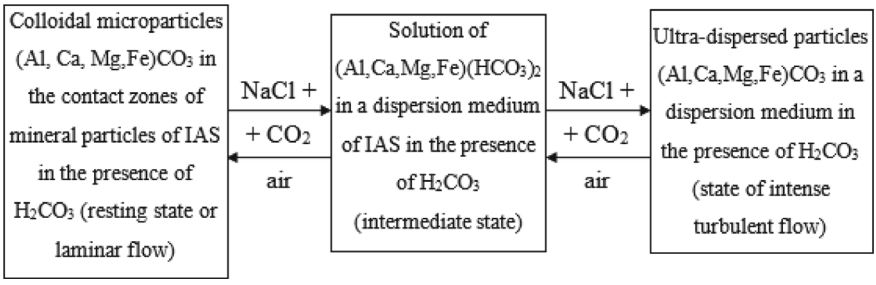

Fig. 4.7 Scheme of interfacial transformations in mixtures of iron-aluminosilicate minerals in IAS: (→)—the direction of enhanced formation, due to chemical transport, of ultrafine particles in the conditions of intensified state of intense (turbulent) flow of IAS; (←)—the direction of enhanced formation, due to isothermal distillation, of colloidal microparticles in the conditions of enhanced state of rest or laminar flow of IAS

Thus, the analysis of the literature data from the studies of other authors and additional analysis of the published experimental and theoretical results of the co-authors of this work, as well as the latest experimental results and new models of processes, allowed us to draw clarifying conclusions about the mechanisms of processes and their conditions (Fig. 4.7). It has been shown that the strength of contact interfacial interactions between nano-, micro-, and colloidal particles and

aggregates in dispersions and suspensions of clayey iron-aluminosilicate materials is primarily due to nanophase nanostructural bonds between clay minerals and iron oxide-hydroxide compounds. The siloxane or siloxane-carbonate bonds of Ca or Mg ions in these interactions are of secondary importance and are more characteristic of composite materials with an additional aluminosilicate-carbonate mineral composition. In general, all three types of interfacial bonds are caused at the final stages of their formation by biocolloidal processes that affect the change in the rheological properties of dispersions and suspensions of clay-containing iron-aluminosilicates. Such processes and phenomena are activated by mechanical (gravitational) flow, which begins with laminar elastic–plastic deformation of the dispersion and deposits of clay-containing iron-aluminosilicate muds (oozes) and soils. Under various mechanical factors (gravity, earthquakes, tsunamis, etc.), the initial elastic deformation under laminar conditions is transformed by the dilution of the suspension with water, first into an ultra-fast and then into an ultra-anomalous flow at the beginning of the suspension settling. Over time, the flow rate under the influence of mechanical stresses increases due to a decrease in concentration with a simultaneous rapid increase in the viscosity of the mud (ooze) material, and the flow transforms from laminar to turbulent, passing through the dilatant, rheopex and thixotropic stages of non-Newtonian flow, gradually dampening. Thus, gigantic masses of sediments and soils move, creating avalanche-like underwater flows that quickly reach deep oceanic abyssal plains and dips where they eventually create sedimentary deposits that gradually separate (Fig. 4.8). Avalanche-like flows are controlled by nanocontact nanostructured interfacial interactions in dispersions caused not only by colloidal nanochemical and geomechanical processes but also, to a large extent, at the final stage, by biocolloidal biotic phenomena caused by bacterial and biochemical reactions that form amphiphilic peptide-type surfactants [2]. Such surfactants are involved in the accelerated dispersion of sediments to micro-nanoscale and in increasing their sorption volume.

Chemical models of the main processes in Figs. 4.8 and 4.9:

1. Contact interactions under conditions of ultra-anomalous viscosity effect:

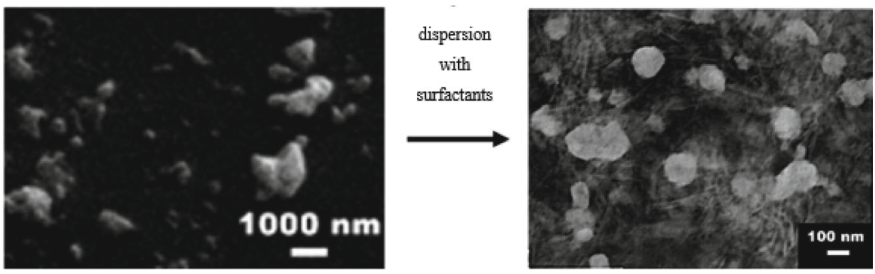

Fig. 4.8 SEM images of the products of hydrochemical autodispersion and separation of IAS minerals in the presence of surfactants of biocolloidal origin

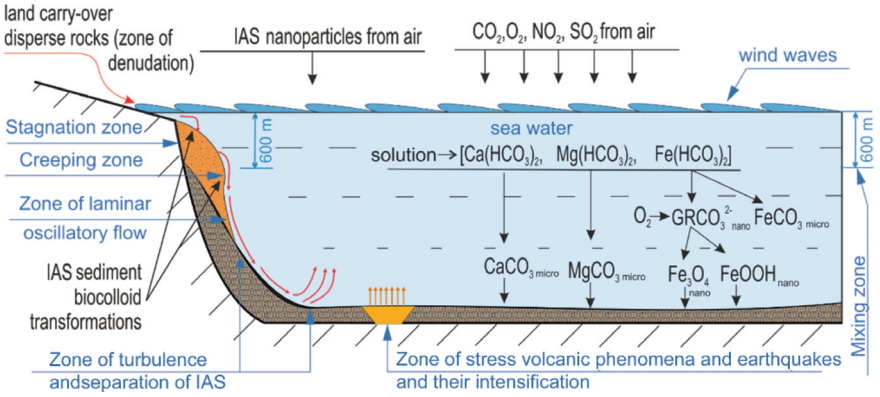

Fig. 4.9 Model of geomechanical, colloid-chemical and biocolloidal factors influence on the separation of IAS on slopes and intensification of volcanic phenomena in the Ocean bed

$$\left[\equiv\left[\begin{matrix}O\\O\\O\end{matrix}\right\rangle SiOH\right]_n + Si(OH)_4{}_n + {}_n\left[HOSi\left\langle\begin{matrix}O\\O\\O\end{matrix}\right]\equiv\right] \longrightarrow \left[\equiv\left[\begin{matrix}O\\O-Si-O-\\O\end{matrix}\right\rangle\begin{matrix}OH\\Si\\OH\end{matrix}\left\langle\begin{matrix}O\\-O-Si-O-\\O\end{matrix}\right]\equiv\right]_n + nH_2O \tag{4.1}$$

2. Biocolloidal reduction–oxidation of iron compounds in IAS:

$$Fe(OH)_{3\ 3n} \rightarrow \begin{matrix} Fe(OH)_{2\ n} \\ \rightarrow Fe(OH)_{3\ 2n} \end{matrix} \xrightarrow[(ШПГ)]{+CO_2} GRCO_3 \xrightarrow{+O_2} Fe_3O_{4\ 1,5n} + \alpha - FeOOH_{\ 1,5n} \tag{4.2}$$

where GR—Green Rust, LDH—layered structures with iron.

3. Thermomechanical effect of Fe and Fe_3O_4 separation from aluminosilicates:

$$[Al_2O_3 \cdot SiO_2 \cdot Fe_2O_3] + C \xrightarrow{700-1000^\circ C} Fe_3O_4 + Al_2O_3 \cdot SiO_2 + CO; \quad Fe_3O_4 + C \xrightarrow{700-1200^\circ C} Fe_{\text{sponge iron}} + CO;$$
$$\text{ultrafine carbon}$$
$$Fe_3O_4 + C \xrightarrow{700-1200^\circ C} Fe_3C + CO; \quad Fe_3C \rightleftarrows Fe + C_{nano} \tag{4.3}$$

Thus, for the first time, it was established that in the processes of additional biocolloidal transformation of IAS with the participation of surface-active peptide products of microorganisms' metabolism, the processes of hydration and thermal autodispersion of ASW minerals with the formation of nanostructured high-viscosity elastic–plastic compositions are accelerated by orders of magnitude [Figs. 4.7, 4.8 and 4.9, schemes (4.1)–(4.3)], which, using model representations (Fig. 4.9) and experimental data, demonstrate that geomechanochemical, colloid-chemical, and

biocolloidal factors significantly affect the production, transformation, purification, and separation of nanostructured phases and compositions of iron oxide-hydroxide-aluminosilicate or polymetallic carbide containing iron and other dispersed systems (IAS) (Figs. 4.7, 4.8 and 4.9).

Preliminary ideas are given (Fig. 4.9) about phenomenal processes on the slopes of the coastline of seas and oceans (under conditions of gravitational laminar-turbulent movement of pelitic sediments according to the laws of physicochemical geomechanics and laws of elastic–plastic viscosity changes). The colloidal-chemical, nanochemical, biocolloidal, and geomechanical concepts of the mechanisms of non-standard phenomena in the Ocean are developed and it is shown that the processes in iron-aluminosilicate clayey minerals are carried out by the mechanism of their auto-hydration dispersion in saline seawater. Under certain conditions, biotic processes controlled by complexes of microorganisms in the biogeocenosis, which also contain autochthonous bacteria, are even faster than with individual types of bacteria. Such processes should be taken into account in complex studies of the movement of clayey iron-aluminosilicates and soils under various conditions, including elevated temperatures and at great depths with a significant increase in the size of the specific surface, which can increase from 70 to 580–600 m^2/g, which requires additional special studies beyond the scope of this work.

4.3 Conclusions

A generalizing model of mechanochemical and hydrochemical dispersion and transformation phenomena in polymineral iron-aluminosilicate ore materials (IAS) is proposed and it is shown that nanochemical transformations in the processes of mechanical and magnetic effects on iron-aluminosilicate structures occur with the participation of polysilicate nanoclusters of alkali metals. It has been shown that the chemical and mineralogical composition of IAS, the composition of alkaline impurities, the pH of the medium, and the conditions of their heat treatment significantly affect the processes of dispersion, movement, and separation of micro- and nanoparticles forming under the simultaneous action of chemical and mechanical forces. It has been established that heat treatment of IAS at temperatures close to 1000–1200°C under reducing conditions (model of underwater deep volcanic phenomena) leads to the formation of mineral micro-layers in which nanoparticles of silicate, phosphate, arsenate, sulfur, and other impurities are located, which allowed to effectively separate nanoparticles during their mechanical processing in bench conditions, modeling green chemistry processes near underwater volcanoes. The processes of mechanochemical separation of melts in a liquid medium have been improved by preliminary thermo-mechanochemical dispersion of IAS at temperatures up to 1000 °C. The scientific basis of nanotechnologies for the extraction of cast iron or steel-based composites from polymineral thermally reduced structures of ZAS with their simultaneous purification from impurities of silicates, phosphates,

arsenates, sulfur compounds, and excess carbon in the form of nanoporous carbon-silicate sorbents and activating additives to binders have been developed. Using elements of nanotechnology. They are protected by patents in Ukraine, Australia, and China. Methods for producing magnetite concentrates and high-purity iron powders have been developed. Based on the results of iron ore reduction with nanocarbon to produce sponge iron and subsequent alkaline iron purification, it was concluded that such purification is the most effective way to separate non-metallic impurities from the metal. The paper shows the importance of nanochemical reactions accompanying the purification process in substantiating the optimal method of grinding metal-containing impurities of nanoparticles of wustite (FeO), carbon, cementite (Fe_3C), as well as microparticles of silicates, phosphates, arsenates, sulfides, etc. using natural 'green chemistry'.

References

1. V.A. Emel'janov, Basics of marine geoekology (Osnovy morskoj geoekologii) (in Russian). Naukova dumka, Kyiv (2003)
2. I.G. Kovzun, Z.R. Ulberg, A.V. Panko et al, Nanochemical, nanostructural and biocolloidal aspects of transformations in dispersions of iron-aluminosilicate minerals. Kyiv: PH 'Akademperiodyka' (2020). https://doi.org/10.15407/akademperiodyka.416.188
3. V.I. Vernadsky, *The Biosphere.* (Copernicus/Springer-Verlag, New York, 1998)
4. V.S. Krisachenko, *Human and the Biosphere [in Ukrainian].* (Zapovit, Kyiv, 1998), p. 668
5. S.A. Moroz, *History of Earth's Biosphere: In 2 Books [in Ukrainian].* Book 1 (Zapovit, Kyiv, Book 2, 1996), p. 422
6. E.P. Odum, G.W. Barrett, *Fundamentals of Ecology*, 5th edn. (Brooks/Cole, Belmont, CA, 2005)
7. E.P. Odum, *Basic Ecology* (Saunders College Publishing, Philadelphia, 1983)
8. R.A. Horne, *Marine Chemistry: The Structure of Water and the Chemistry of the Hydrosphere* (Wiley-Interscience, New York, 1969)
9. L.B. Rozovsky, On a new direction in engineering geology—marine engineering geology [in Russian], in *Geology of the Coasts and Bottom of the Black and Azov Seas within the Borders of the Ukrainian SSR* (Kyiv University Press, Kyiv, 1972), pp. 137–142
10. N.V. Pertsov, Rebinder effect in Earth crust (Physicochemical Geomechanics). Colloid J. **60**(5), 629–640 (1998)
11. E.D. Shchukin, A.V. Pertsov, E.A. Amelina, *Colloid and Surface Chemistry* (Cambridge International Science Publishing, Cambridge, 2001)
12. O.M. Adamenko, G.M. Rudko, *Ecological Geology [in Ukrainian]* (Manuskript, Kyiv, 1998), p. 350
13. A.V. Panko, I.G. Kovzun, V.A. Prokopenko et al., Catastrophic phenomena on marine slopes and in artificial dams in a presence of nanostructured iron-aluminosilicates, in *Nanomaterials and Nanocomposites, Nanostructure Surfaces, and Their Applications. Springer Proceedings in Physics*, vol. 246ed. by O. Fesenko, L. Yatsenko (Springer, Cham, 2021), pp. 381–395. https://doi.org/10.1007/978-3-030-51905-6_28
14. C. Gomes, M.-I. Carretero, M. Pozo et al., Peloids and pelotherapy: historical evolution, classification and glossary. Appl. Clay Sci. **75–76**, 28–38 (2013)
15. M.I. Carretero, Clays in pelotherapy: a review. Part I: mineralogy, chemistry, physical and physicochemical properties. Appl. Clay Sci. **189**, 105526 (2020). https://doi.org/10.1016/j.clay.2020.105526

16. A.V. Panko, I.G. Kovzun, Z.R. Ulberg et al., Colloid-chemical modification of peloids with nano- and microparticles of natural minerals and their practical use, in *Nanophysics, Nanophotonics, Surface Studies and Applications*, vol. 183 (Springer International Publishing Switzerland, 2016), pp. 163–177. https://doi.org/10.1007/978-3-319-30737-4_14
17. A.V. Panko, I.G. Kovzun, O.M. Nikipelova et al., Nanostructural effects in iron oxide silicate materials of the Earth's crust, in *Nanophysics, Nanophotonics, Surface Studies and Applications*, vol. 221 (Springer Nature Switzerland AG, 2019), pp. 367–386. https://doi.org/10.1007/978-3-030-17759-1_25
18. A.V. Panko, I.G. Kovzun, O.M. Nikipelova et al., Nanostructural and nanochemical processes in peloid sediments aided with biogeocenosis, in *Nanophysics, Nanophotonics, Surface Studies and Applications*, vol. 214 (Springer International Publishing AG, 2018), pp. 215–230. https://doi.org/10.1007/978-3-319-92567-7_13
19. Y. Tarasevich, F.D. Ovcharenko, *Adsorption on Clay Minerals [in Russian]* (Naukova Dumka, Kyiv, 1975), p. 351
20. I.G. Kovzun, Z.R. Ulberg, A.V. Panko et al., Colloid-chemical and nanochemical processes in peloids on basis of ferrous clay minerals, in *Nanoplasmonics, Nano-Optics, Nanocomposites and Surface Studies. Springer Proceedings in Physics*, vol. 167 ed. by O. Fesenko, L. Yatsenko (Springer, Cham, 2015), pp. 233–243. https://doi.org/10.1007/978-3-319-18543-9_15
21. A.V. Panko, I.G. Kovzun, V.A. Prokopenko et al., Nano- and microdisperse structures in processes of metamorphism, reduction sintering, and component separation of iron-oxide-silicate materials, in *Nanophysics, Nanophotonics, Surface Studies and Applications*, vol. 195 (Springer International Publishing AG, 2017), pp. 743–755. https://doi.org/10.1007/978-3-319-54422-7_57
22. I. Voitenko Yu, Synergetics of geological mediums and its impact on the effectiveness of the exploitation and exploration for mineral deposits. *Мінеральні ресурси України* (3):15–21 (2019). https://doi.org/10.31996/mru.2019.3.15-21
23. O.M. Nikipelova, *Colloid-chemical and biocolloidal properties of mud sulfide peloid systems [in Ukrainian]*. Dissertation. F. D. Ovcharenko Institute of Biocolloidal Chemistry NAS of Ukraine (2011)
24. R. Lohmann, J. Dachs, Chapter 15—polychlorinated biphenyls in the global ocean, in *World Seas: An Environmental Evaluation*, 2nd edn. C. Sheppard (Academic Press, Elsevier, 2019), pp. 269–282. ISBN 9780128050521. https://doi.org/10.1016/B978-0-12-805052-1.00017-6
25. Astenosfera (Asthenosphere) [in Ukrainian]//Velyka ukrainska entsyklopediia (Great Ukrainian Encyclopedia). Available at: https://vue.gov.ua/Астеносфера
26. E.R.R. Moody, S. Álvarez-Carretero, T.A. Mahendrarajah et al., The nature of the last universal common ancestor and its impact on the early Earth system. Nature Ecol Evol **8**, 1654–1666 (2024). https://doi.org/10.1038/s41559-024-02461-1

Chapter 5
Evolution of the Phase Composition and Microstructure of Fine-Grained Si_3N_4–Y_2O_3 Ceramics Due to Changes in the Sintering Mode

B. D. Vasyliv, V. V. Kulyk, P. Y. Lyutyy, V. V. Vira, P. F. Kholod, T. M. Kovbasiuk, V. M. Palyukh, V. I. Vavrukh, and M. V. Danylchuk

Abstract Silicon nitride based ceramics are widely used in the chemical industry and high-temperature applications due to their chemical inertness under specific harsh conditions. Their mechanical properties, meanwhile, remain almost unchanged. This work aimed to study the effects of the sintering mode, namely, the sintering temperature and isothermal holding time on the evolution of the phase composition and formation of fine-grained microstructure of Si_3N_4–Y_2O_3 ceramics. The initial Si_3N_4 and Y_2O_3 powders were used to fabricate ceramic samples. The percentage of Y_2O_3 powder was chosen to be 10 wt% for all the studied modes. The samples were undergone conventional sintering in a nitrogen atmosphere. The sintering temperatures were set as 1650, 1700, and 1750 °C, whereas values of the isothermal holding time for the sintering temperature of 1700 °C were set as 2 and 5 h. The sintered samples possessed different densities and porosities. Accordingly, their phase compositions changed significantly with the sintering temperature and isothermal holding time changes. This, in turn, affected the mechanical behavior of the materials. In particular, the optimum combination of hardness, fracture toughness, and strength was found for the Si_3N_4–Y_2O_3 ceramic samples sintered at 1700 °C for 5 h. Based on

B. D. Vasyliv (✉) · V. V. Kulyk · P. Y. Lyutyy · T. M. Kovbasiuk · V. I. Vavrukh
Department of Materials Science and Engineering, Lviv Polytechnic National University, Lviv, Ukraine
e-mail: mechengin1111@gmail.com

V. V. Vira · V. M. Palyukh
Department of Strength of Materials and Structural Mechanics, Lviv Polytechnic National University, Lviv, Ukraine

P. F. Kholod
Department of Building Constructions and Bridges, Lviv Polytechnic National University, Lviv, Ukraine

M. V. Danylchuk
Department of Corrosion and Corrosion Protection, Karpenko Physico-Mechanical Institute of the NAS of Ukraine, Lviv, Ukraine

O. Fesenko and L. Yatsenko (eds.), *Functional Nanomaterials, Nanocatalysts, Nanotechnologies, and Their Applications*, Springer Proceedings in Physics 321,
https://doi.org/10.1007/978-3-031-99136-3_5

the results of this study, prerequisites for the formation of fine-grained Si_3N_4–Y_2O_3 ceramic microstructure with improved mechanical characteristics were substantiated.

5.1 Introduction

Silicon nitride based ceramics are widely used as material for critical parts in many industry branches, in particular, for high-temperature and chemical equipment, as they exhibit high chemical inertness and stability of mechanical properties under specific harsh conditions. However, these high-temperature properties can be deteriorated due to an intergranular glass phase present in the sintered ceramics. The devitrification of the glass during heat treatments results in silicon nitride based composite microstructures comprising chemically compatible crystalline phases [1].

Silicon oxynitride (Si_2N_2O) with a needle- or plate-like grain morphology is a particular example of such secondary phase [2, 3]. Such morphology can provide the mechanism of crack wake bridging for toughening silicon nitride based ceramics [4].

Duan et al. [5] studied the in situ formed Si_3N_4–Si_2N_2O–TiN composites by hot-pressing the mixtures of Si_3N_4, TiO_2, and TiN powders at 1650 °C. Composites containing various Si_3N_4-, Si_2N_2O-, and TiN volume fractions were obtained and the effect of elevated temperatures (up to 1400 °C) on the composite microstructure was investigated. The intergranular glass phases and the main crystalline phase were stable up to 1400 °C. In the reducing atmosphere (N_2 or vacuum), the silicon oxynitride phase and amorphous intergranular phase were formed in the sample surface layer. Material with such phase composition is not usable, as the silicon oxynitride phase is non-stable at temperatures above 1300 °C in the presence of a substantial amount of amorphous intergranular phase. The authors performed hardness and fracture toughness tests using the indentation method [6–16] to select a composite for further development. They showed that a high-Si_2N_2O/high-TiN/β-Si_3N_4 composite can be considered the most promising.

Yan et al. [17] analyzed the sintered silicon nitride ceramics that underwent the grinding experiment and determined corresponding parameters. They also explored various methods for mechanical testing of ceramics [18–30] and revealed the peculiarities of changes in longitudinal crack propagation depth and surface residual stress.

Duan et al. [31] investigated silicon nitride based composites. During hot pressing of mixtures of Si_3N_4, 6 wt% Y_2O_3, and up to 63 wt% TiO_2 powders under vacuum (0.1 Pa) at 1650 °C for 1 h under a mechanical pressure of 28 MPa, TiO_2 was converted to TiN and Si_2N_2O was formed. TiO_2 was found to promote the α to β-Si_3N_4 conversion in the sintering process. It was revealed that thermal expansion of the unit cell parameters a and c of the β-Si_3N_4 phase decreased with increasing amounts of TiO_2. The conclusion was drawn that the formed microstructure and resulting mechanical properties of the ceramics are strongly related to the TiO_2

content. Similar peculiarities were found by other authors for various types of ceramic materials [32–44].

Zalite et al. [45] fabricated ceramic materials based on fine Si_3N_4 powders. They showed a strong relation between sintering modes and formed microstructure of the materials.

Duan et al. [46] studied the effect of TiC, TiN, and TiO_2 additives on microstructure of Si_3N_4-based ceramics. They showed that such compounds do not promote the formation of intergranular glass pockets but have different effects on the change in the internal friction with temperature. The TiO_2 and TiN additives promote the α to β-silicon nitride transformation [45, 47–56] and, as a result, cause changes in mechanical properties of the ceramics.

He et al. [56] used three homologous binary sintering aids, namely, Y_2O_3-Al_2O_3, $Y_2Si_2O_7$, and $Y_2Si_2O_7$-$Al_6Si_2O_{13}$, where the content of $Y_2Si_2O_7$ compound varied from 5 to 20 wt%, to manufacture various Si_3N_4-based ceramics. They thoroughly investigated the impact of the liquid phase formation temperature and content of the sintering aid on the shrinkage, density, phase balance, and microstructure of Si_3N_4 ceramics.

Several researchers have developed novel toughening methods to improve fracture toughness and wear resistance of Si_3N_4 ceramics [57–61].

In terms of mechanical behavior, flexural strength, hardness, and fracture toughness may be considered as the most appropriate characteristics of the ceramics under study. For this purpose, various ceramic microstructures should be examined and various test methods can be applied [62–73].

This work aims to study the effects of the sintering temperature and isothermal holding time on the evolution of the phase composition and formation of the fine-grained microstructure of Si_3N_4–Y_2O_3 ceramics, which resulted in high hardness, flexural strength, and fracture toughness.

5.2 Materials and Methods

A mixture of Si_3N_4 and Y_2O_3 ceramic powders in Si_3N_4–10 wt% Y_2O_3 composition (Table 5.1) was prepared by plasma-chemical method [45, 74] due to adding yttria powder during the synthesis of silicon nitride powder. The initial Y_2O_3 and Si_3N_4 powders exhibited specific surfaces of 20–24 m^2/g and 40–46 m^2/g, respectively. Beam samples $4.5 \times 3.5 \times 36$ mm^3 in size were fabricated by conventional sintering in an argon atmosphere according to the specified modes (Table 5.1).

A series of sintered samples were ground and polished using a polishing machine to prepare metallographic surfaces. According to the requirements of the corresponding ISO standard [75], the final cross-sectional dimensions of samples were set as follows: the thickness was $b = (3.0 \pm 0.2)$ mm and the width was $w = (4.0 \pm 0.2)$ mm. Samples for metallographic studies were etched in 40% hydrofluoric acid for 30 min as recommended in the work [76].

Table 5.1 Sintering modes, physical, and mechanical properties of the studied materials

Variant	Sintering mode		Density, g/cm^3	Porosity, %	Hardness HV_{20}, GPa	σ_f, MPa	K_{Ic}, MPa m$^{1/2}$
	Temperature, °C	Time, h					
1	1650	2	3.14	8.99	15.7	211	3.4
2	1700	2	3.33	3.48	18.1	250	3.1
3	1700	5	3.39	1.74	18.7	276	4.1
4	1750	2	3.41	1.16	18.7	219	4.4

Note Average values of density, porosity, hardness HV_{20}, flexural strength σ_f, and fracture toughness K_{Ic} are given

Hardness of the polished samples was determined on a NOVOTEST TC-БРВ hardness tester by the standards [77, 78]. The indentation load was 20 kg. The Vickers hardness (HV_{20}) values were calculated using the equation [78]:

$$H = 0.0018544\left(\frac{P}{d^2}\right) \tag{5.1}$$

where P is the indentation load (N) and d is the average length of the imprint diagonals (mm).

The geometry of imprints was determined with an optical microscope Neophot-21. Five indentations were made on the surface of each sample, and the average HV_{20} value for each material was calculated.

Fracture toughness and flexural strength of the ceramic samples were estimated on a testing machine UIT STM 050 under three-point bending.

The above-mentioned beam samples were used for both tests. Using the fracture load and geometry parameters of a sample and the support, flexural strength (σ_f) was calculated by the following equation as recommended in the works [75, 79, 80]:

$$\sigma_f = \frac{1.5 \cdot P \cdot l}{w \cdot b^2} \tag{5.2}$$

where P is the fracture load (N), l is the span between the supporting rollers (30 mm), and b and w are the thickness and width (mm) of the beam sample, respectively.

Five samples of each variant were tested and the average σ_f value for each material was determined.

In fracture mechanics, there are well-known methods for estimating fracture toughness of materials [81–93]. The critical stress intensity factor (SIF) K_{Ic} [94–105] as a measure of fracture toughness can be calculated using the equations presented in some articles and standards [106–117]. In several articles, equations for calculating K_{Ic} values are given, which incorporate data from the Vickers indentation test method [118–127].

In this work, the critical SIF of material was determined according to [75] based on the single-edge notch beam (SENB) samples of cross-section geometry mentioned

above. In such a sample, a 0.1 mm wide notch was cut with a thin diamond saw. The notch front was oriented along the sample thickness dimension. The samples were tested under three-point bending. The span between the supporting rollers was 30 mm. Five samples of each variant were examined and the average K_{Ic} value for each material was calculated.

Mechanical testing of the materials under study was performed at 20 °C in air.

An X-ray diffractometer (Malvern Panalytical) in Cu K_α radiation mode was used for X-ray diffraction (XRD) analysis.

Microstructure and fracture surfaces of the material samples were analyzed with a scanning electron microscope (SEM) Carl Zeiss EVO-40XVP. The back-scattered diffraction (BSD) imaging mode was used for microstructure images, whereas the secondary electron (SE) imaging mode was utilized for the fracture surface images. An energy-dispersive X-ray (EDX) microanalysis of the studied ceramics was performed using an INCA Energy 350 system.

5.3 Results and Discussion

The evolution of phase compositions and microstructure of the Si_3N_4–Y_2O_3 ceramics sintered in various modes were analyzed for their flexural strength, hardness, and fracture toughness.

5.3.1 Phase Balance in the Si_3N_4–Y_2O_3 Ceramics

Based on the XRD patterns, the following phases were revealed in the studied Si_3N_4–Y_2O_3 ceramics: β-Si_3N_4, SiO_2, $Ca_3Y_2(Si_3O_9)_2$, $Y_3Ca_2(SiO_4)_3(OH)$, $YSiNO_2$, and $Y_2Si_3N_4O_3$ (Fig. 5.1). A clear difference between phase compositions of variants of the ceramics is observed (Table 5.2).

The phase fractions for variant 1 were estimated as follows (Table 5.2): β-Si_3N_4 phase (56.03 wt%), SiO_2 phase (2.89 wt%), and $Ca_3Y_2(Si_3O_9)_2$ phase (41.08 wt%). Phase compositions of the ceramics of variants 3 and 4 are quite similar to variant 1. Namely, the ceramic of variant 3 exhibited the following phase fractions (Table 5.2): β-Si_3N_4 phase (66.24 wt%), $Ca_3Y_2(Si_3O_9)_2$ phase (23.18 wt%), and $YSiNO_2$ phase (10.58 wt%). The phase fractions for variant 4 were estimated as follows (Table 5.2): β-Si_3N_4 phase (59.12 wt%), $Ca_3Y_2(Si_3O_9)_2$ phase (15.8 wt%), and $Y_2Si_3N_4O_3$ phase (25.08 wt%). Specifically, the $Y_3Ca_2(SiO_4)_3(OH)$ phase (35.44 wt%) was detected in the ceramic of variant 2, in addition to the β-Si_3N_4 phase (64.56 wt%). The formation of the $Y_3Ca_2(SiO_4)_3(OH)$ phase is probably related to the plasticizer content, which in the ceramic of variant 2 was two times higher as compared to that in all other compositions (10 wt% versus 5 wt%). Besides, only the ceramic of variant 1 contained the SiO_2 phase.

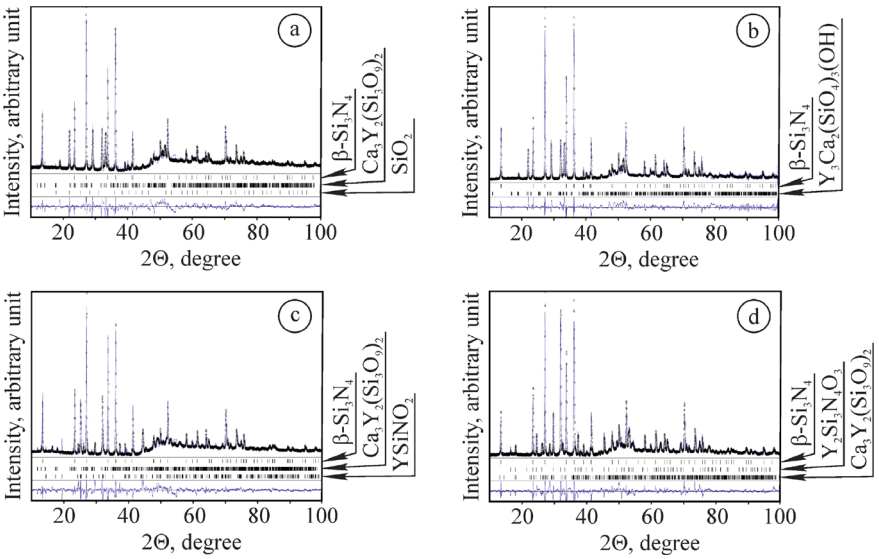

Fig. 5.1 XRD patterns of Si_3N_4–Y_2O_3 ceramics in **a** series 1, **b** 2, **c** 3, and **d** 4 (Table 5.1). The arrows indicate **a** the β-Si_3N_4, $Ca_3Y_2(Si_3O_9)_2$, SiO_2, **b** β-Si_3N_4, $Y_3Ca_2(SiO_4)_3(OH)$, **c** β-Si_3N_4, $Ca_3Y_2(Si_3O_9)_2$, $YSiNO_2$, and **d** β-Si_3N_4, $Y_2Si_3N_4O_3$, $Ca_3Y_2(Si_3O_9)_2$ phases, respectively

Table 5.2 Phase composition of the studied materials

Phase	Phase fractions for series			
	1	2	3	4
β-Si_3N_4	56.03	64.56	66.24	59.12
SiO_2	2.89	–	–	–
$Ca_3Y_2(Si_3O_9)_2$	41.08	–	23.18	15.80
$Y_3Ca_2(SiO_4)_3(OH)$	–	35.44	–	–
$YSiNO_2$	–	–	10.58	–
$Y_2Si_3N_4O_3$	–	–	–	25.08

Note Values of phase fractions are given in wt%

5.3.2 *Microstructure, Physical, and Mechanical Properties of the Si_3N_4–Y_2O_3 Ceramics*

The low density of the ceramic of variant 1 (Table 5.1) and, as a consequence, its high porosity (about 9%) are related to low sintering temperature not providing a perfect densification of the material. SEM microstructure images of this ceramic (Fig. 5.2a, b) show separate pores 2–5 μm in size and multiple nano-sized pores. Besides, incomplete recrystallization of the initial powder is proved by its separate clusters (light-color areas of the irregular shape, 1–3 μm in size). The β-Si_3N_4 phase

nanograins (particles of light color observed in Fig. 5.2b) are nucleated, but their growth is confined. The same concerns the dark-gray grains of the $Ca_3Y_2(Si_3O_9)_2$ phase formed in this sintering mode. The SiO_2 phase (nanoareas of dark color), given its small amount in the material, is distributed more or less uniformly at the interface of microstructural components of both these phases. Such morphology of the components does not provide a sufficient structural integrity of the material. Therefore, its hardness is about 15% lower on average than that of other variants of ceramics (Table 5.1). Flexural strength of this material is about 210 MPa, whereas fracture toughness is 3.4 MPa·$m^{1/2}$ (Table 5.1). Quite low levels of these characteristics can be related to the fracture surface of the ceramic sample tested for fracture toughness. Intergranular fracture along the boundaries of fine grains of the β-Si_3N_4 and $Ca_3Y_2(Si_3O_9)_2$ phases is peculiar to this material evidencing thus a low cohesion strength between grains of these phases (Fig. 5.3a, b).

The higher density (by 6%) of the ceramic of variant 2 compared to that of variant 1 (Table 5.1) and its comparatively low porosity (about 3.5%) prove better densification of the ceramic. Microstructure images of this material (Fig. 5.2c, d) exhibit the β-Si_3N_4 matrix phase (64.56 wt%, see Table 5.2). Besides, the $Y_3Ca_2(SiO_4)_3(OH)$ phase detected by XRD-analysis is probably present in crystals about 0.3–1.2 μm in size and tiny 100–300 nm light-colored particles observed in the images. Due to the presence of hard and brittle $Y_3Ca_2(SiO_4)_3(OH)$ phase colonies, which surround the β-Si_3N_4 phase grains, the ceramic possesses high hardness but low fracture toughness (Table 5.1). Flexural strength of this ceramic is about 250 MPa. Although this level of strength is moderate compared to those of other ceramics, the fracture toughness test showed the domination of brittle cleavage of the $Y_3Ca_2(SiO_4)_3(OH)$ phase, as well as delamination along the boundaries between the β-Si_3N_4 and $Y_3Ca_2(SiO_4)_3(OH)$ phase grains (Fig. 5.3c, d). This confirms the implementation of a low energy-consuming fracture micromechanism in this ceramic. The unsatisfactory fracture toughness of the ceramic creates a limitation for the further implementation of this production mode.

Quite high density (3.39 g/cm^3) and low porosity (1.74%) of the ceramic of variant 3 compared to those characteristics of two previous variants resulted in a fine microstructure of this material (Fig. 5.2e, f). In the SEM images, the dominance of dark-gray β-Si_3N_4 phase grains 1–3 μm in size can be noted. Nano-grains of the $Ca_3Y_2(Si_3O_9)_2$ phase 200–300 nm in size (light-gray particles embedded in the β-Si_3N_4 phase matrix) and the $YSiNO_2$ phase 50–100 nm in size (separated light-gray particles) can also be observed. Grain aggregates about 10–20 μm in size comprising all the detected phases, which were formed in this sintering mode due to the prolonged sintering time of 5 h, provided comparatively high fracture toughness (4.1 MPa·$m^{1/2}$, see Table 5.1) and the highest flexural strength of the material (276 MPa). Therefore, such microstructure of uniformly distributed the $Ca_3Y_2(Si_3O_9)_2$ and $YSiNO_2$ phases in the β-Si_3N_4 phase matrix has provided high cohesive strength between adjoining grains and, as a result, the best strength of the ceramic. This also allowed reaching the highest hardness of 18.7 GPa. In the SEM image of sample fracture surface taken at low magnification (Fig. 5.3e), crack growth along the boundaries of grain aggregates can be observed, whereas the SEM image taken at high magnification shows the

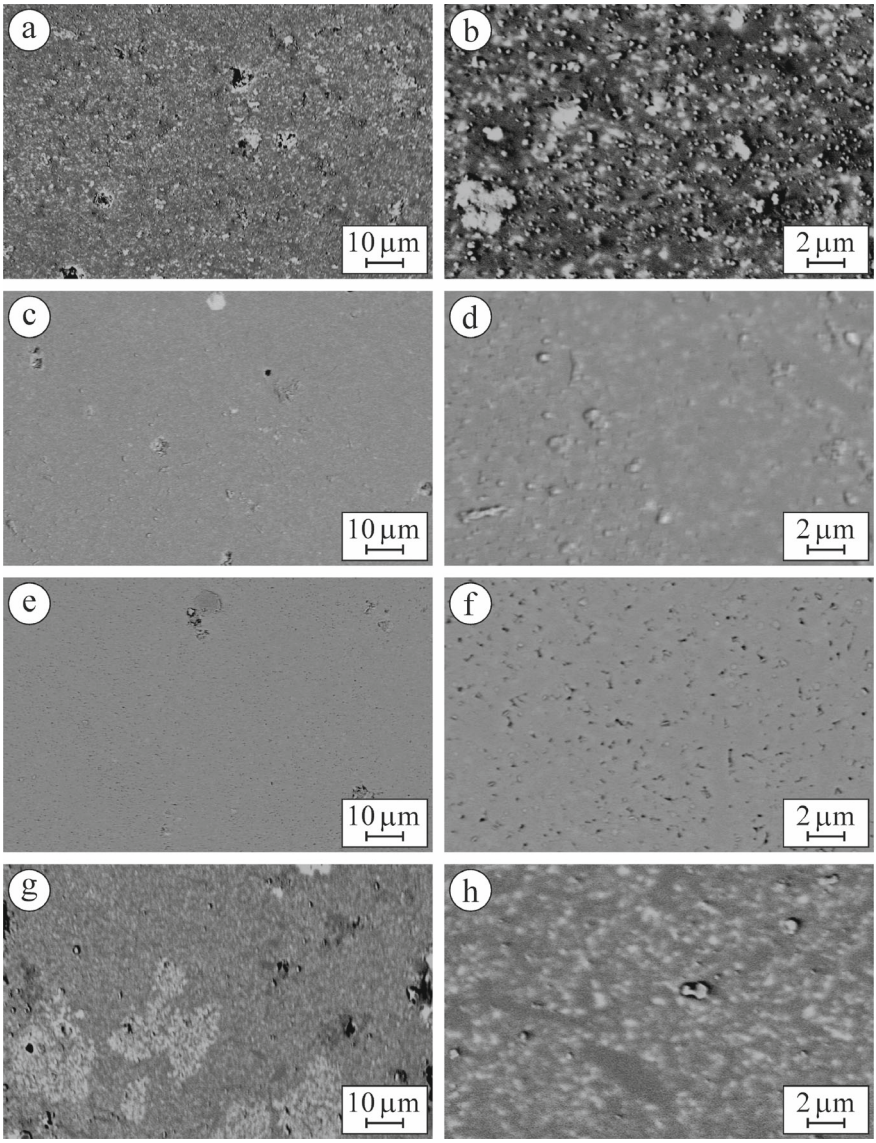

Fig. 5.2 SEM microstructures in BSD mode of Si_3N_4–Y_2O_3 ceramics of **a, b** variant 1, **c, d** 2, **e, f** 3, and **g, h** 4 (Table 5.1) taken at **a, c, e, g** low and **b, d, f, h** high magnification

intergranular fracture along the elongated β-Si_3N_4 grains about 3–6 μm in size and round-shaped $Ca_3Y_2(Si_3O_9)_2$ and $YSiNO_2$ grains of several hundred nanometers in size (Fig. 5.3f). This confirms the domination of a high energy-consuming fracture micromechanism in this ceramic. As a result, the high fracture toughness of the material was reached.

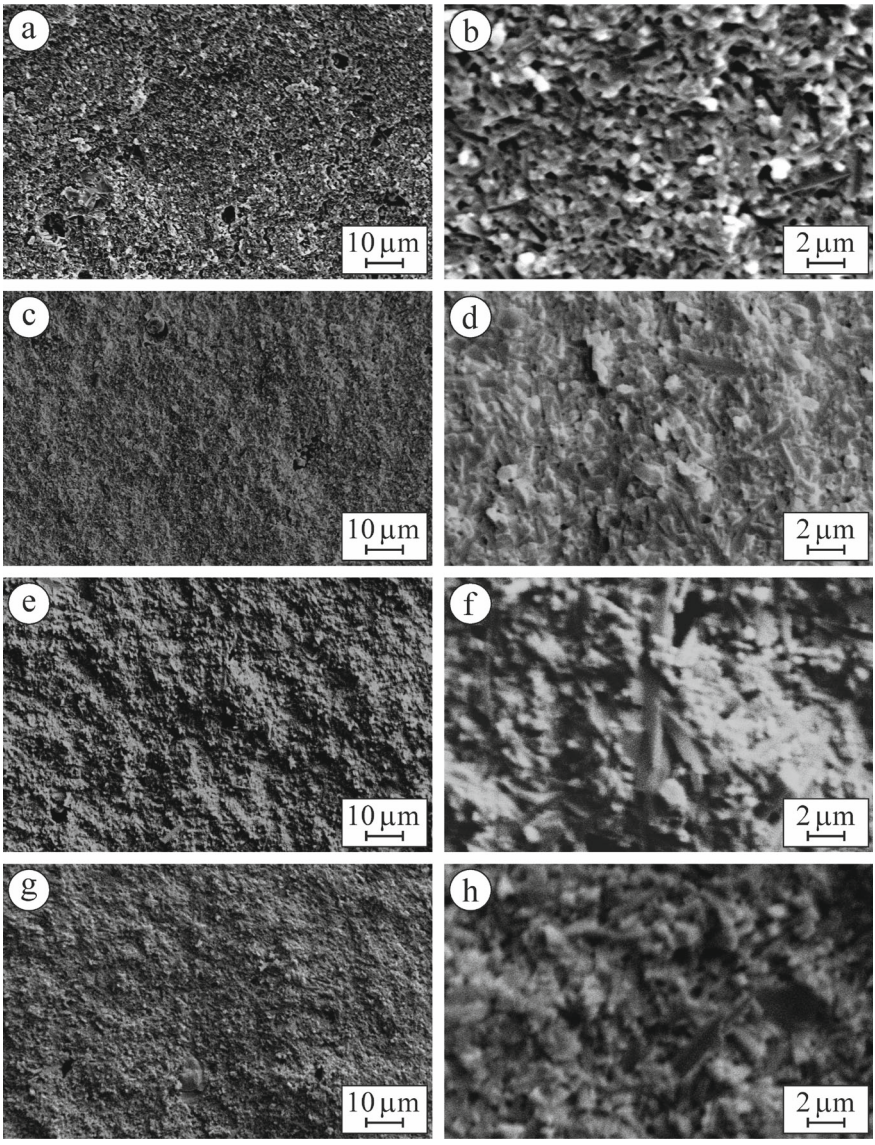

Fig. 5.3 SEM fractography in SE mode of Si_3N_4–Y_2O_3 ceramics samples of **a, b** variant 1, **c, d** 2, **e, f** 3, and **g, h** 4 (Table 5.1) taken at **a, c, e, g** low and **b, d, f, h** high magnification

It is worth mentioning that an increase in the sintering temperature to 1750 °C did not cause a significant difference in both the density and porosity of the ceramic of variant 4 compared to those of variant 3 (Table 5.1). The maximum hardness revealed for variant 4, i.e. the same as for variant 3 (Table 5.1), also evidences slight changes in densification of the material. Such dense microstructure was formed due to the intense

grain growth at 1750 °C. It should be mention the well-observed inverse relationship between the $Ca_3Y_2(Si_3O_9)_2$ phase fraction and fracture toughness of the materials of variants 1, 3, and 4 (Table 5.1). However, the presence of about 25 wt% $Y_2Si_3N_4O_3$ phase affected negatively the structural integrity of the material and, as a result, its flexural strength. It is supposed that 200–400 nm aggregates of particles of light color observed in the SEM images (Fig. 5.2g, h) correspond to this phase. Therefore, the $Y_2Si_3N_4O_3$ phase caused a decrease in flexural strength of the ceramic of variant 4 due to the formation of aggregates of grains. However, this material exhibited the highest fracture toughness (Table 5.1). The reason for this is, at first, the lower fraction of the $Ca_3Y_2(Si_3O_9)_2$ phase and, secondly, the complete recrystallization of the initial powders and formation of the perfect elongated β-Si_3N_4 grains about 1–3 μm in size visible in fracture surface images (Fig. 5.3g, h). The uniform distribution of these grains among the grains of other phases made it possible to implement a whisker toughening micromechanism during crack initiation and growth [4]. Therefore, this material presents a microstructure-related balance between strength at a mesolevel and fracture toughness at a microlevel.

In general, the materials of variants 3 and 4 may be considered for applications in structural components of critical equipment for various industry branches.

5.4 Conclusions

1. The Si_3N_4–10 wt% Y_2O_3 ceramics that underwent different sintering modes contained mainly the β-Si_3N_4 matrix phase and variety of other phases: SiO_2, $Ca_3Y_2(Si_3O_9)_2$, $Y_3Ca_2(SiO_4)_3(OH)$, $YSiNO_2$, and $Y_2Si_3N_4O_3$. The ceramic containing the $Y_3Ca_2(SiO_4)_3(OH)$ phase situated on the boundaries of the β-Si_3N_4 matrix phase grains exhibited low fracture toughness, which can be explained by the excessive brittleness of the first one. In contrast, the low fraction of the $Ca_3Y_2(Si_3O_9)_2$ phase in combination with complete recrystallization of the initial powders with the formation of elongated β-Si_3N_4 grains had a strong positive effect on crack growth resistance providing a high level of fracture toughness in the ceramic sintered at 1750 °C for 2 h.
2. The Si_3N_4–Y_2O_3 ceramic sintered at 1700 °C for 5 h is characterized by fine-grained microstructure. The phase balance of this ceramic, namely, the β-Si_3N_4, $Ca_3Y_2(Si_3O_9)_2$, and $YSiNO_2$ phases in relation of 66.24:23.18:10.58 wt% provided the optimum combination of hardness (18.7 GPa), flexural strength (276 MPa), and fracture toughness (4.1 MPa·$m^{1/2}$) of the material.

Acknowledgements The authors are thankful to the staff of the Scientific Equipment Collective Use Center "Laboratory of Advanced Technologies, Creation and Physicochemical Analysis of New Substances and Functional Materials" at Lviv Polytechnic National University (https://lpnu.ua/ckkno) for their kind help in performing X-ray diffraction studies.

References

1. M.J. Hoffmann, A. Geyer, R. Oberacker, Potential of the sinter-HIP-technique for the development of high-temperature resistant Si_3N_4-ceramics. J. Eur. Ceram. Soc. **19**(13–14), 2359–2366 (1999). https://doi.org/10.1016/S0955-2219(99)00106-5
2. M.B. Trigg, K.H. Jack, Solubility of aluminium in silicon oxynitride. J. Mater. Sci. Lett. **6**, 407–408 (1987). https://doi.org/10.1007/BF01756778
3. W. Braue, R. Pleger, W. Luxem, Nucleation and growth of Si_2N_2O in Si_3N_4 materials employing different sintering additives. Key Eng. Mater. **89–91**, 483–488 (1994). https://doi.org/10.4028/www.scientific.net/KEM.89-91.483
4. R.O. Ritchie, Mechanisms of fatigue-crack propagation in ductile and brittle solids. Int. J. Fract. **100**(1), 55–83 (1999). https://doi.org/10.1023/A:1018655917051
5. R.-G. Duan, G. Roebben, J. Vleugels et al., Thermal stability of in situ formed Si_3N_4–Si_2N_2O–TiN composites. J. Eur. Ceram. Soc. **22**(14–15), 2527–2535 (2002). https://doi.org/10.1016/S0955-2219(02)00110-3
6. H. Charalambous, M.H. Jancich, P.W.F. Evans et al., Processing and characterization of the homologous $Zr_xTa_2O_{2x+5}$ series. Ceram. Int. **50**(9), 15848–15855 (2024). https://doi.org/10.1016/j.ceramint.2024.02.064
7. S.G. Giniyatova, A.L. Kozlovskiy, R.I. Shakirzyanov et al., Structural, dielectric, and mechanical properties of high-content cubic zirconia ceramics obtained via solid-state synthesis. Appl. Sci. **13**(19), 10989 (2023). https://doi.org/10.3390/app131910989
8. M.B. Hanif, S. Rauf, Z.U. Abadeen et al., Proton-conducting solid oxide electrolysis cells: Relationship of composition-structure-property, their challenges, and prospects. Matter **6**(6), 1782–1830 (2023). https://doi.org/10.1016/j.matt.2023.04.013
9. V. Kulyk, Z. Duriagina, B. Vasyliv et al., Effect of sintering temperature on crack growth resistance characteristics of yttria-stabilized zirconia. Acta Phys. Pol. A **141**(4), 323–327 (2022). http://przyrbwn.icm.edu.pl/APP/PDF/141/app141z4p18.pdf
10. S. Liu, J. Zhang, Y. Tian et al., Preparation of Bi_2O_3–YSZ and YSB–YSZ composite powders by a microemulsion method and their performance as electrolytes in a solid oxide fuel cell. Materials **16**(13), 4673 (2023). https://doi.org/10.3390/ma16134673
11. S.N. Almohammed, B. Alshorman, L.A. Abu-Naba'a, Mechanical properties of five esthetic ceramic materials used for monolithic restorations: a comparative in vitro study. Ceramics **6**(2), 1031–1049 (2023). https://doi.org/10.3390/ceramics6020061
12. T.F. Alghazzawi, G.M. Janowski, H. Ning et al., Qualitative SEM analysis of fracture surfaces for dental ceramics and polymers broken by flexural strength testing and crown compression. J. Prosthodont. **32**(5) (2023). https://doi.org/10.1111/jopr.13659
13. V.G. Efremenko, Y.G. Chabak, V.I. Fedun et al., Formation mechanism, microstructural features and dry-sliding behaviour of "Bronze/WC carbide" composite synthesised by atmospheric pulsed-plasma deposition. Vacuum **185**, 110031 (2021). https://doi.org/10.1016/j.vacuum.2020.110031
14. N.C. Golota, Z.P. Fredin, D.P. Banks et al., Diamond rotors. J. Magn. Reson. **352**, 107475 (2023). https://doi.org/10.1016/j.jmr.2023.107475
15. K. Tanaka, Elastic/plastic indentation hardness and indentation fracture toughness: the inclusion core model. J. Mater. Sci. **22**(4), 1501–1508 (1987). https://doi.org/10.1007/BF01233154
16. X. Fu, F. Zhang, W. Zhu et al., Mechanical properties and toughening mechanisms of promising Zr-Y-Ta-O composite ceramics. Coatings **13**(5), 855 (2023). https://doi.org/10.3390/coatings13050855
17. H. Yan, F. Deng, Z. Qin et al., Effects of grinding parameters on the processing temperature, crack propagation and residual stress in silicon nitride ceramics. Micromachines **14**(3), 666 (2023). https://doi.org/10.3390/mi14030666
18. T.G.T. Nindhia, T. Lube, Single edge precrack V-notched beam (SEPVNB) fracture toughness testing on silicon nitride. Mater. Sci. Forum **962**, 205–209 (2019). https://doi.org/10.4028/www.scientific.net/MSF.962.205

19. B.D. Vasyliv, A procedure for the investigation of mechanical and physical properties of ceramics under the conditions of biaxial bending of a disk specimen according to the ring–ring scheme. Mater. Sci. **45**(4), 571–575 (2009). https://doi.org/10.1007/s11003-010-9215-2
20. S.S. Savka, D.I. Popovych, A.S. Serednytski, Molecular dynamics simulations of the formation processes of zinc oxide nanoclusters in oxygen environment, in *Nanophysics, Nanomaterials, Interface Studies, and Applications*, vol. 195 (Springer Proceedings in Physics, 2017), pp. 145–156. https://doi.org/10.1007/978-3-319-56422-7_11
21. B. Alfahed, A. Alayad, The effect of sintering temperature on Vickers microhardness and flexural strength of translucent multi-layered zirconia dental materials. Coatings **13**(4), 688 (2023). https://doi.org/10.3390/coatings13040688
22. O.P. Ostash, L.I. Muravs'kyi, T.I. Voronyak et al., Determination of the size of the fatigue prefracture zone by the method of phase-shifting interferometry. Mater. Sci. **46**, 781–788 (2011). https://doi.org/10.1007/s11003-011-9353-1
23. K. Hoggas, S. Benaissa, A. Cherouana et al., Mechanical behavior of transparent spinel fabricated by spark plasma sintering. Ceramics **6**(2), 1191–1209 (2023). https://doi.org/10.3390/ceramics6020072
24. Y.G. Chabak, K. Shimizu, V.G. Efremenko et al., Microstructure and phase elemental distribution in high-boron multi-component cast irons. Int. J. Miner. Metall. Mater. **29**, 78–87 (2022). https://doi.org/10.1007/s12613-020-2135-8
25. Y. Li, H. Sun, J. Song et al., Effect of two-step sintering on the mechanical and electrical properties of 5YSZ and 8YSZ ceramics. Materials **16**(5), 2019 (2023). https://doi.org/10.3390/ma16052019
26. S. Liu, J. Wang, Y. Chen et al., Tetragonal nanosized zirconia: hydrothermal synthesis and its performance as a promising ceramic reinforcement. Inorganics **11**(5), 217 (2023). https://doi.org/10.3390/inorganics11050217
27. V. Korendiy, O. Kachur, V. Zakharov et al., Experimental study of the lap motion trajectory of vibratory finishing machine. Vib. Proced. **46**, 1–7 (2022). https://doi.org/10.21595/vp.2022.23002
28. H. Miyazaki, H. Hyuga, K. Hirao et al., Comparison of fracture resistance as measured by the indentation fracture method and fracture toughness determined by the single-edge-precracked beam technique using silicon nitrides with different microstructures. J. Eur. Ceram. Soc. **27**, 2347–2354 (2007). https://doi.org/10.1016/j.jeurceramsoc.2006.09.002
29. V.V. Kulyk, B.D. Vasyliv, Z.A. Duriagina et al., The effect of water vapor containing hydrogenous atmospheres on the microstructure and tendency to brittle fracture of anode materials of YSZ–NiO(Ni) system. Arch. Mater. Sci. Eng. **108**(2), 49–67 (2021). https://doi.org/10.5604/01.3001.0015.0254
30. J. Lankford, Indentation microfracture in the Palmqvist crack regime: implications for fracture toughness evaluation by the indentation method. J. Mater. Sci. Lett. **1**(11), 493–495 (1982). https://doi.org/10.1007/BF00721938
31. R.-G. Duan, G. Roebben, J. Vleugels et al., In situ formation of Si_2N_2O and TiN in Si_3N_4-based ceramic composites. Acta Mater. **53**(9), 2547–2554 (2005). https://doi.org/10.1016/j.actamat.2005.01.021
32. G.P. Alparone, D. Penney, E. Jewell et al., The effect of sliding speed on the tribological properties of ceramic materials. Materials **16**(23), 7252 (2023). https://doi.org/10.3390/ma16237252
33. P. Uasuwan, N. Juntavee, A. Juntavee, Flexural strength of novel glass infiltrated monochrome and multilayer high yttrium oxide containing zirconia upon various sintered cooling rates. J. Prosthodont. **33**(S1), 47–59 (2024). https://doi.org/10.1111/jopr.13872
34. V. Korendiy, O. Kachur, Dynamic behavior of a vibratory plate compactor working on a horizontal elastic-viscous-plastic surface, in *InterPartner 2022: Advanced Manufacturing Processes IV*, ed. by V. Tonkonogyi et al. Lecture Notes in Mechanical Engineering (2023), pp. 434–443. https://doi.org/10.1007/978-3-031-16651-8_41
35. V. Podhurska, B. Vasyliv, Influence of NiO reduction on microstructure and properties of porous Ni–ZrO_2 substrates, in *Proceedings of the 3rd international conference on oxide*

materials for electronic engineering (OMEE-2012) (Lviv, Ukraine, 2012), pp 293–294. https://doi.org/10.1109/OMEE.2012.6464761
36. P. Jeevankumar, P. Rose, A. Rajanikanth et al., Net-shaping of advanced ceramic composites by gelcasting into precision molds made by rapid-prototyping. Int. J. Appl. Ceram. Technol. **21**(2), 664–674 (2024). https://doi.org/10.1111/ijac.14568
37. O.M. Romaniv, I.V. Zalite, V.M. Simin'kovych et al., Effect of the concentration of zirconium dioxide on the fracture resistance of Al_2O_3–ZrO_2 ceramics. Mater. Sci. **31**(5), 588–594 (1996). https://doi.org/10.1007/BF00558793
38. G. Sokolowski, A. Szczesio-Wlodarczyk, M.I. Szynkowska-Jóźwik et al., The shear bond strength of resin-based luting cement to zirconia ceramics after different surface treatments. Materials **16**(15), 5433 (2023). https://doi.org/10.3390/ma16155433
39. T.F. Alghazzawi, A comparison of failure loads for polycrystalline zirconia ceramics with varying amounts of yttria, glass-ceramics and polymers in two different test conditions. Polymers **15**(23), 4506 (2023). https://doi.org/10.3390/polym15234506
40. V. Kulyk, B. Vasyliv, Z. Duriagina et al., The effect of sintering temperature on phase-related peculiarities of the microstructure, flexural strength, and fracture toughness of fine-grained ZrO_2–Y_2O_3–Al_2O_3–CoO–CeO_2–Fe_2O_3 ceramics. Crystals **14**(2), 175 (2024). https://doi.org/10.3390/cryst14020175
41. I. Sanchez, D. Axinte, Z. Liao et al., The effect of high strain rate impact in Yttria stabilized zirconia. Mater. Des. **229**, 111908 (2023). https://doi.org/10.1016/j.matdes.2023.111908
42. O.P. Ostash, I.M. Andreiko, V.V. Kulyk et al., Influence of braking on the microstructure and mechanical behavior of railroad wheel steels. Mater. Sci. **48**, 569–574 (2013). https://doi.org/10.1007/s11003-013-9539-9
43. V.G. Efremenko, A.G. Lekatou, Y.G. Chabak et al., Micromechanical, corrosion and wet sliding wear behaviours of Co-28Cr-6Mo alloy: wrought vs. LPBF. Mater. Today Commun. **35**, 105936 (2023). https://doi.org/10.1016/j.mtcomm.2023.105936
44. K.W. Jeong, J.S. Han, G.U. Yang et al., Influence of preaging temperature on the indentation strength of 3Y–TZP aged in ambient atmosphere. Materials **14**, 2767 (2021). https://doi.org/10.3390/ma14112767
45. I. Zalite, M. Herrmann, J. Grabis, Materials on the basis of finely dispersed Si_3N_4 powders. Key Eng. Mater. **132–136**, 1018–1021 (1997)
46. R.-G. Duan, G. Roebben, J. Vleugels et al., Effect of TiX(X = C, N, O) additives on microstructure and properties of silicon nitride based ceramics. Scr. Mater. **53**(6), 669–673 (2005). https://doi.org/10.1016/j.scriptamat.2005.05.024
47. Y.S. Romario, C. Bhat, M. Ramezani et al., Fabrication of translucent graded dental crown using zirconia-yttrium multi-slurry tape casting 3D printer. J. Mech. Behav. Biomed. Mater. **152**, 106406 (2024). https://doi.org/10.1016/j.jmbbm.2024.106406
48. D. Cao, K. Lv, Y. Bao et al., Thickness effect of an alumina-zirconia-mullite composite coating on the properties of zirconia. RSC Adv. **13**(4), 2736–2744 (2023). https://doi.org/10.1039/D2RA07549K
49. I. Izonin, R. Tkachenko, M. Gregus et al., Hybrid classifier via PNN-based dimensionality reduction approach for biomedical engineering task. Procedia Comput. Sci. **191**, 230–237 (2021). https://doi.org/10.1016/j.procs.2021.07.029
50. Y. Wang, W. Qin, Z. Deng et al., High strength Y_2O_3-stabilized zirconia continuous fibers up to 1500 °C: crystalline phase and microstructure evolution as well as grain growth kinetics. J. Alloys Compd. **976**, 173165 (2024). https://doi.org/10.1016/j.jallcom.2023.173165
51. P. Uasuwan, N. Juntavee, A. Juntavee, Flexural strength of high yttrium oxide-doped monochrome and multilayered fully stabilized zirconia upon various sintered cooling rates. J. Prosthodont. **32**(6), (2023). https://doi.org/10.1111/jopr.13692
52. J.-M. Jung, G.-N. Kim, Y.-H. Koh et al., Manufacturing and characterization of dental crowns made of 5-mol% yttria stabilized zirconia by digital light processing. Materials **16**(4), 1447 (2023). https://doi.org/10.3390/ma16041447
53. V. Kulyk, Z. Duriagina, A. Kostryzhev et al., Effects of sintering temperature and yttria content on microstructure, phase balance, fracture surface morphology, and strength of yttria-stabilized zirconia. Appl. Sci. **12**(22), 11617 (2022). https://doi.org/10.3390/app122211617

54. K. Nonaka, M. Teramae, G. Pezzotti, Evaluation of the effect of high-speed sintering and specimen thickness on the properties of 5 mol% yttria-stabilized dental zirconia sintered bodies. Materials **15**(16), 5685 (2022). https://doi.org/10.3390/ma15165685
55. H. Li, W. Qian, Z. Zhang et al., The phase stability of t-ZrO_2 realized by grain size at cryogenic temperature in ZrO_2/TiO_2 composite. Mater. Des. **239**, 112741 (2024). https://doi.org/10.1016/j.matdes.2024.112741
56. L. He, N. Huang, D. Lu et al., A study on the effects of liquid phase formation temperature and the content of sintering aids on the sintering of silicon nitride ceramics. Crystals **13**(7), 1099 (2023). https://doi.org/10.3390/cryst13071099
57. G. Cui, T. Li, Z. Wang et al., In-situ formation reinforcement phase for Si_3N_4 ceramics with high toughness and wear resistance. Mater. Today Commun. **40**, 110081 (2024). https://doi.org/10.1016/j.mtcomm.2024.110081
58. H. Xiong, B. Li, X. Xi et al., Preparation of graded silicon nitride ceramics with high mechanical performance using β-Si_3N_4 seeds. Ceram. Int. **49**(22), 36528–36535 (2023). https://doi.org/10.1016/j.ceramint.2023.08.336
59. S. Huang, Y. Li, P. Yang et al., Cure behaviour and mechanical properties of Si_3N_4 ceramics with bimodal particle size distribution prepared using digital light processing. Ceram. Int. **49**(8), 12166–12172 (2023). https://doi.org/10.1016/j.ceramint.2022.12.068
60. K. Matsuura, T. Ohji, T. Takahashi et al., Effects of rare-earth oxides on grain boundary strength of silicon nitride ceramics. J. Eur. Ceram. Soc. **44**(14), 116672 (2024). https://doi.org/10.1016/j.jeurceramsoc.2024.116672
61. C.C. Ye, K. Ma, H.M. Chen et al., Effect of texture on the thermal conductivity and mechanical properties of silicon nitride ceramic. Ceram. Int. **50**(2), 4014–4021 (2024). https://doi.org/10.1016/j.ceramint.2023.11.170
62. M. Alghauli, A.Y. Alqutaibi, S. Wille et al., 3D-printed versus conventionally milled zirconia for dental clinical applications: trueness, precision, accuracy, biological and esthetic aspects. J. Dent. **144**, 104925 (2024). https://doi.org/10.1016/j.jdent.2024.104925
63. A.K. Lakshya, K.K. Jha, C. Bhardwaj et al., Attaining translucency in binder/additive-free, nanograined, tetragonal 1.5 mol.% yttria-stabilized zirconia ceramics. Materialia **34**, 102075 (2024). https://doi.org/10.1016/j.mtla.2024.102075
64. Y. Yue, Y. Zhu, Z. Li, Preparation and cutting performance study of YSZ-toughened PcBN superhard tools. RSC Adv. **13**(23), 15616–15623 (2023). https://doi.org/10.1039/D3RA02079G
65. M.M.H. Parvez, M.A. Daud, Effects of TiO_2 on the mechanical and physical properties of Fe_2O_3-doped yttria-stabilized zirconia for electrolyte of solid oxide fuel cells. Results Surf. Interfaces **16**, 100239 (2024). https://doi.org/10.1016/j.rsurfi.2024.100239
66. Z.-G. Wang, W.-D. Chen, S.-F. Yan et al., Direct fabrication and characterization of zirconia thick coatings on zirconium hydride as a hydrogen permeation barrier. Coatings **13**(5), 884 (2023). https://doi.org/10.3390/coatings13050884
67. T.M. Lenkovskiy, V.V. Kulyk, Z.A. Duriagina et al., Mode I and mode II fatigue crack growth resistance characteristics of high tempered 65G steel. Arch. Mater. Sci. Eng. **84**(1), 34–41 (2017). https://doi.org/10.5604/01.3001.0010.3029
68. I.G. Alhindawy, H. Gamal, A.A. Zaher et al., La/Nd-doped zirconium oxide: Impact of zirconia phase transition on gamma-ray shielding properties. J. Phys. Chem. Solids **187**, 111828 (2024). https://doi.org/10.1016/j.jpcs.2023.111828
69. W. Huang, H. Qiu, Y. Zhang et al., Microstructure and phase transformation behavior of Al_2O_3–ZrO_2 under microwave sintering. Ceram. Int. **49**(3), 4855–4862 (2023). https://doi.org/10.1016/j.ceramint.2022.09.376
70. B.V. Efremenko, K. Shimizu, N. Espallargas et al., High-temperature solid particle erosion of Cr–Ni–Fe–C arc cladded coatings. Wear **460–461**, 203439 (2020). https://doi.org/10.1016/j.wear.2020.203439
71. O.P. Ostash, A.D. Ivasyshyn, B.D. Vasyliv et al., Influence of the structure and asymmetry of loading cycles on the cyclic crack resistance of Ti–Si composites. Mater. Sci. **38**(1), 55–61 (2002). https://doi.org/10.1023/A:1020120714703

72. F. Inchingolo, A.D. Inchingolo, I.A. Charitos et al., Inchingolo, ceramic biomaterials in dentistry: chemical structure and biosafety—a review and a bibliometric visual mapping on Scopus database. Eur. Rev. Med. Pharmacol. Sci. **28**(4), 1242–1258 (2024). https://doi.org/10.26355/eurrev_202402_35446
73. F. Mayinger, R. Buser, M. Laier et al., Impact of the material and sintering protocol, layer thickness, and thermomechanical aging on the two-body wear and fracture load of 4Y-TZP crowns. Clin. Oral Investig. **26**(11), 6617–6628 (2022). https://doi.org/10.1007/s00784-022-04616-5
74. B.D. Vasyliv, O.M. Romaniv, I.V. Zalite et al., Correction to: Enhancement of the crack resistance of $Si_36N_4-Y_2O_3$ ceramics and its structural and metallurgical aspects. Mater. Sci. **33**(3), 323–330 (1997). https://doi.org/10.1007/BF02539086. Mater. Sci. **56**(4), 583 (2021). https://doi.org/10.1007/s11003-021-00467-9
75. ISO 6872, Dentistry–Ceramic Materials. International Organization of Standardization: Geneva, Switzerland (2015)
76. Q. Flamant, F. García Marro, J.J. Roa Rovira et al., Hydrofluoric acid etching of dental zirconia. Part 1: Etching mechanism and surface characterization. J. Eur. Ceram. Soc. **36**, 121–134 (2015). https://doi.org/10.1016/j.jeurceramsoc.2015.09.021
77. ASTM E 384-11, Standard test method for Knoop and Vickers hardness of materials. ASTM Int. (2011). https://doi.org/10.1520/E0384-11
78. ASTM C 1327-03, Standard test method for Vickers indentation hardness of advanced ceramics. ASTM Int. (2003). https://doi.org/10.1520/C1327-03
79. O.M. Romaniv, B.D. Vasyliv, Some features of formation of the structural strength of ceramic materials. Mater. Sci. **34**(2), 149–161 (1998). https://doi.org/10.1007/BF02355530
80. J.M. Gere, S.P. Timoshenko, *Mechanics of Materials*, 4th edn. (PWS Publishing Company, Boston, MA, USA, 1997), p. 912
81. B.R. Lawn, M.V. Swain, Microfracture beneath point indentations in brittle solids. J. Mater. Sci. **10**(1), 113–122 (1975). https://doi.org/10.1007/BF00541038
82. R.H. Purba, K. Kusumoto, K. Shimizu et al., Influence of tempering temperature on abrasive-wear performance of high-chromium-based multicomponent white cast iron. Lubricants **11**(7), 285 (2023). https://doi.org/10.3390/lubricants11070285
83. O.P. Ostash, A.D. Ivasyshyn, B.D. Vasyliv et al., High-temperature and cyclic corrosion crack resistance of alloys of the Ti–Si–Al–Zr system. Mater. Sci. **42**(3), 330–343 (2006). https://doi.org/10.1007/s11003-006-0087-4
84. Q. Yao, Y. Chen, Z. Wang et al., Evaluations on ceramic fracture toughness measurement by edge chipping. Coatings **12**, 1146 (2022). https://doi.org/10.3390/coatings12081146
85. S. Begand, S. Spintzyk, J. Geis-Gerstorfer et al., Fracture toughness of 3Y-TZP ceramic measured by the chevron-notch beam method: a round-robin study. Dent. Mater. **38**(7), 1128–1139 (2022). https://doi.org/10.1016/j.dental.2022.05.001
86. V.Y. Podhurs'ka, B.D. Vasyliv, O.P. Ostash et al., Structural transformations in the NiO-containing anode of ceramic fuel cells in the course of its reduction and oxidation. Mater. Sci. **49**(6), 805–811 (2014). https://doi.org/10.1007/s11003-014-9677-8
87. Y. Zhang, C. Ren, J. Zhou et al., Influence of microwave heating on grain growth behavior and phase stability of nano Y_2O_3/La_2O_3 co-doped ZrO_2 ceramics. Ceram. Int. **50**(6), 8733–8741 (2024). https://doi.org/10.1016/j.ceramint.2023.12.190
88. X. Zhu, G. Hou, J. Ma et al., Effect of Y_2O_3 doping content on phase composition, mechanical properties and cavitation erosion performance of ZrO_2 ceramics. Ceram. Int. **50**(9), 14718–14730 (2024). https://doi.org/10.1016/j.ceramint.2024.01.385
89. O.P. Ostash, I.M. Andreiko, V.V. Kulyk et al., Influence of the mode of thermal treatment and load ratio on the cyclic crack-growth resistance of wheel steels. Mater. Sci. **45**, 211–219 (2009). https://doi.org/10.1007/s11003-009-9177-4
90. S. Ozkan, S.J. Kim, D.N. Miller et al., A new approach to fuel cell electrodes: Lanthanum aluminate yielding fine Pt nanoparticle exsolution for oxygen reduction reaction. Adv. Energy Mater. **14**(15), 2303025 (2024). https://doi.org/10.1002/aenm.202303025

91. A. Moradkhani, H. Baharvandi, M. Tajdari et al., Determination of fracture toughness using the area of micro-crack tracks left in brittle materials by Vickers indentation test. J. Adv. Ceram. **2**, 87–102 (2013). https://doi.org/10.1007/s40145-013-0047-z
92. R.F. Cook, G.M. Pharr, Direct observation and analysis of indentation cracking in glasses and ceramics. J. Am. Ceram. Soc. **73**(4), 787–817 (1990). https://doi.org/10.1111/j.1151-2916.1990.tb05119.x
93. T.M.B. Campos, C. Dos Santos, L.M.M. Alves et al., Minimally processed recycled yttria-stabilized tetragonal zirconia for dental applications: Effect of sintering temperature on glass infiltration. J. Mech. Behav. Biomed. Mater. **150**, 106311 (2024). https://doi.org/10.1016/j.jmbbm.2023.106311
94. G.R. Anstis, P. Chantikul, B.R. Lawn et al., A critical evaluation of indentation techniques for measuring fracture toughness: I, Direct crack measurement. J. Am. Ceram. Soc. **64**(9), 533–538 (1981). https://doi.org/10.1111/j.1151-2916.1981.tb10320.x
95. V. Kulyk, I. Izonin, V. Vavrukh et al., Prediction of hardness, flexural strength, and fracture toughness of ZrO_2 based ceramics using ensemble learning algorithms. Acta Metall. Slovaca **29**(2), 93–103 (2023). https://doi.org/10.36547/ams.29.2.1819
96. O. Kachur, V. Korendiy, Dynamic behavior of vibratory screening conveyor equipped with crank-type exciter, in *DSMIE 2023: Advances in Design, Simulation and Manufacturing VI*, ed. by V. Ivanov et al. Lecture Notes in Mechanical Engineering (2023), pp. 44–53. https://doi.org/10.1007/978-3-031-32774-2_5
97. A.G. Evans, E.A. Charles, Fracture toughness determinations by indentation. J. Am. Ceram. Soc. **59**(7–8), 371–372 (1976). https://doi.org/10.1111/j.1151-2916.1976.tb10991.x
98. I.M. Andreiko, V.V. Kulyk, O.P. Ostash, Resistance of steels of railroad wheels to corrosion-fatigue fracture. Mater. Sci. **47**, 608–612 (2012). https://doi.org/10.1007/s11003-012-9434-9
99. S. Wu, S. Liu, Y. Chen et al., Optimization of the structure and morphology of monoclinic phase nanoscale zirconium dioxide. MRS Commun. **14**(4), 646–652 (2024). https://doi.org/10.1557/s43579-024-00578-9
100. M.A. Ali Bash, S.A. Ajeel, R.A. Abbas et al., A direct laser sintering approach for the electrophoretic deposition overlay of yttria-stabilized zirconia on the surface of a thermal barrier coating system. Coatings **13**(10), 1695 (2023). https://doi.org/10.3390/coatings13101695
101. B.D. Vasyliv, A.D. Ivasyshyn, O.P. Ostash et al., Kinetics of corrosion-fatigue cracks in Ti–Si cermet composite. Mater. Sci. **38**(2), 220–224 (2002). https://doi.org/10.1023/A:1020990103898
102. J.C.C.A. Diaz, E.N.D.S. Muccillo, R. Muccillo, Porous 8YSZ ceramics prepared with alkali halide sacrificial additives. Materials **16**(9), 3509 (2023). https://doi.org/10.3390/ma16093509
103. B.R. Vaishnavi Krupa, C. Ghosh, S.K. Sinha et al., Reverse transition of ball milling induced m-Y_2O_3 nano-crystallites during in-situ annealing. Ceram. Int. **49**(14), 23522–23530 (2023). https://doi.org/10.1016/j.ceramint.2023.04.185
104. Y. Kharchenko, Z. Blikharskyy, V. Vira et al., Nanostructural changes in a Ni/NiO cermet during high-temperature reduction and reoxidation, in *Nanomaterials and Nanocomposites, Nanostructure Surfaces, and Their Applications*, vol. 246 (Springer Proceedings of Physics, 2021), pp. 219–229. https://doi.org/10.1007/978-3-030-51905-6_17
105. H. Yoo, J. Kim, H. Lee et al., Phase formation and stabilization behavior of Ca-PSZ by post-heat treatment II: CaO*x*-ZrO_2(1–x) (x = 5–10 mol%). Metals **13**(10), 1659 (2023). https://doi.org/10.3390/met13101659
106. ASTM E 399-20a, Standard test method for linear-elastic plane-strain fracture toughness of metallic materials. ASTM Int. (2020). https://doi.org/10.1520/E0399-20A
107. ASTM C 1421-18, Standard test methods for determination of fracture toughness of advanced ceramics at ambient temperature. ASTM Int. (2018). https://doi.org/10.1520/C1421-18
108. B. Vasyliv, V. Podhurska, O. Ostash, Preconditioning of the YSZ-NiO fuel cell anode in hydrogenous atmospheres containing water vapor. Nanoscale Res. Lett. **12**, 265 (2017). https://doi.org/10.1186/s11671-017-2038-4

109. H. Peng, Y. Yu, T. Shi et al., Effects of induction plasma spheroidization on properties of yttria-stabilized zirconia powders for thermal barrier coating applications. Materials **17**(7), 1518 (2024). https://doi.org/10.3390/ma17071518
110. Y. Wang, X. Liu, S. Pan et al., Local structure regulation and spectroscopy study of blue cubic zirconia. CrystEngComm **25**(11), 1582–1588 (2023). https://doi.org/10.1039/D2CE01674E
111. J. Kübier, Fracture toughness of ceramics using the SEVNB method: From a preliminary study to a standard test method, in *Fracture Resistance Testing of Monolithic and Composite Brittle Materials*, ed. by J. Salem et al. (ASTM International, 2002), pp. 93–106. https://doi.org/10.1520/STP10473S
112. B. Vasyliv, J. Milewski, V. Podhurska et al., Study of the degradation of a fine-grained YSZ–NiO anode material during reduction in hydrogen and reoxidation in air. Appl. Nanosci. **12**, 965–975 (2022). https://doi.org/10.1007/s13204-021-01768-w
113. A. Shearer, M. Montazerian, B. Deng et al., Zirconia-containing glass-ceramics: from nucleating agent to primary crystalline phase. Int. J. Ceram. Eng. Sci. **6**(2), e10200 (2024). https://doi.org/10.1002/ces2.10200
114. H. Shao, J. Zhu, X. Zhao et al., Additive manufacturing of magnesium-doped calcium silicate/zirconia ceramic scaffolds with projection-based 3D printing: sintering, mechanical and biological behavior. Ceram. Int. **50**(6), 9280–9292 (2024). https://doi.org/10.1016/j.ceramint.2023.12.244
115. H. Gujjaramma, B.S. Krishna, K. Gurushantha et al., Phyllantus acidus mediated combustion method synthesised yttria stabilized zirconia, its application as photocatalyst and antibacterial agent. Desalin. Water Treat. **317**, 100301 (2024). https://doi.org/10.1016/j.dwt.2024.100301
116. L. Du, J. Yang, X. Zhong et al., Synthesized by coprecipitation method for controlled phase structures of 5YSZ. J. Mater. Res. Technol. **29**, 5473–5483 (2024). https://doi.org/10.1016/j.jmrt.2024.02.222
117. A. Unnadkat, L. Kirby, S. Kulanthaivel et al., The effect of sintering on zirconia manufactured via suspension-enclosing projection stereolithography for dental applications: an in vitro study. Materials **17**(1), 14 (2023). https://doi.org/10.3390/ma17010014
118. K. Niihara, A fracture mechanics analysis of indentation-induced Palmqvist crack in ceramics. J. Mater. Sci. Lett. **2**(5), 221–223 (1983). https://doi.org/10.1007/BF00725625
119. T.A. Prikhna, O.P. Ostash, A.S. Kuprin et al., A new MAX phases-based electroconductive coating for high-temperature oxidizing environment. Compos. Struct. **277**, 114649 (2021). https://doi.org/10.1016/j.compstruct.2021.114649
120. G.A. Gogotsi, S.N. Dub, E.E. Lomonova et al., Vickers and Knoop indentation behaviour of cubic and partially stabilized zirconia crystals. J. Eur. Ceram. Soc. **15**(5), 405–413 (1995). https://doi.org/10.1016/0955-2219(95)91431-M
121. H.-S. Lee, H. Ko, K. Heo et al., Dispersion control via crystal-phase modulation of yttrium-doped ZrO_2 nanoparticle sol. Colloids Surf A Physicochem Eng Asp **670**, 131476 (2023). https://doi.org/10.1016/j.colsurfa.2023.131476
122. B.D. Vasyliv, V.Y. Podhurska, O.P. Ostash et al., Effect of a hydrogen sulfide-containing atmosphere on the physical and mechanical properties of solid oxide fuel cell materials, in *Nanochemistry, Biotechnology, Nanomaterials, and Their Applications* (Springer Proceedings of Physics, 2018), pp. 475–485. https://doi.org/10.1007/978-3-319-92567-7_30
123. P. Gothwal, F. Singh, V. Chauhan et al., Effects of lithium ion irradiation on yttria-stabilized zirconia thin films: structural and optical investigations. J. Electron. Mater. **53**(9), 5204–5211 (2024). https://doi.org/10.1007/s11664-024-11230-6
124. J.-H. Yun, Y.-J. Jeon, M.-S. Kang, Analysis of elastic properties of polypropylene composite materials with ultra-high molecular weight polyethylene spherical reinforcement. Materials **15**(16), 5602 (2022). https://doi.org/10.3390/ma15165602
125. V. Korendiy, O. Kachur, V. Gursky et al., Kinematic and dynamic analysis of three-mass oscillatory system of vibro-impact plate compactor with crank excitation mechanism. Vib. Proced. **40**, 14–19 (2022). https://doi.org/10.21595/vp.2022.22393
126. J.P. Winczewski, S. Zeiler, S. Gabel et al., Additive manufacturing of 3D yttria-stabilized zirconia microarchitectures. Mater. Des. **238**, 112701 (2024). https://doi.org/10.1016/j.matdes.2024.112701

127. H. Sun, P. Tabrizian, A. Qambrani et al., Bio-inspired nacre-like zirconia/PMMA composites for chairside CAD/CAM dental restorations. Dent. Mater. **40**(2), 307–317 (2024). https://doi.org/10.1016/j.dental.2023.11.017

Chapter 6
Substantiation of the Effect of Fine-Grained Microstructure of Silicon Nitride Based Ceramics on the Protective Properties of Metal-Ceramic Macrocomposite Plates

B. D. Vasyliv, V. V. Kulyk, V. V. Vira, P. Y. Lyutyy, P. F. Kholod, A. M. Trostianchyn, and V. M. Palyukh

Abstract Silicon nitride (Si_3N_4) based ceramics attract the attention of manufacturers and researchers due to their high strength to weight, fracture toughness to weight, and hardness to weight ratios enabling them as promising sources for the creation of state-of-the-art macrocomposite protective plates used in the arms industry. In this work, sintering mode-related physical and mechanical properties of fine-grained Si_3N_4–10 wt%Y_2O_3 ceramics were studied to reveal an optimum combination of strength, fracture toughness, and hardness. Initial Si_3N_4 and Y_2O_3 powders with high specific surface areas were synthesized by the plasma-chemical method. In the process of synthesis of Si_3N_4 powder, Y_2O_3 powder was introduced into the plasma jet forming thus a powder mixture. The content of Y_2O_3 powder in all the studied compositions was 10 wt% which provided the preparation of relatively dense materials by conventional sintering at the set temperatures in a nitrogen atmosphere. Based on the results of mechanical tests and fracture surface analysis, the effect of fine-grained microstructure of Si_3N_4–Y_2O_3 ceramics on the protective properties of metal-ceramic macrocomposite plates was substantiated. The ceramic material sintered at 1700 °C for 5 h exhibited an optimal combination of porosity,

B. D. Vasyliv (✉) · V. V. Kulyk · P. Y. Lyutyy · A. M. Trostianchyn
Department of Materials Science and Engineering, Lviv Polytechnic National University, Lviv, Ukraine
e-mail: mechengin1111@gmail.com

V. V. Vira · V. M. Palyukh
Department of Strength of Materials and Structural Mechanics, Lviv Polytechnic National University, Lviv, Ukraine

P. F. Kholod
Department of Building Constructions and Bridges, Lviv Polytechnic National University, Lviv, Ukraine

O. Fesenko and L. Yatsenko (eds.), *Functional Nanomaterials, Nanocatalysts, Nanotechnologies, and Their Applications*, Springer Proceedings in Physics 321,
https://doi.org/10.1007/978-3-031-99136-3_6

hardness, strength, and fracture toughness. However, the highest strength and fracture toughness were found in the ceramic sintered at 1700 °C for 2 h, in which the plasticizer content was 2 wt%. Peculiarities of fracture surface morphology of Si_3N_4–Y_2O_3 ceramics were also studied. It was shown that nanometric silicon nitride particles are mostly agglomerated in the ceramic materials sintered at 1700 °C for 2 h and 5 h ensuring thus the high-energy consuming fracture micromechanism in the fracture toughness test. Such mechanical behavior evidences that Si_3N_4–Y_2O_3 ceramic material sintered in the appropriate mode is promising for application in protective metal-ceramic macrocomposite layers.

6.1 Introduction

Among ceramics for high-temperature and chemical industry branches, silicon nitride based ceramics have advantages in high mechanical stability under harsh conditions and high chemical inertness. However, it is known that the intergranular glass phase available in these ceramics causes deterioration of their high-temperature mechanical stability. To solve this issue, silicon nitride based ceramics can be heat-treated after sintering. As a result, chemically compatible crystalline phases are formed in the Si_3N_4-based ceramics [1, 2].

The Si_2N_2O compound known as silicon oxynitride can be formed in silicon nitride based ceramics as the secondary phase when the appropriate composition of initial powders in the powder mixture is provided [3]. This phase is characterized by a needle or plate-like grain morphology. Due to such morphology, significant toughening of silicon nitride based ceramics can be achieved by implementing the crack bridging mechanism [4].

In the work [5], mixtures of silicon nitride powder with up to 63 wt% TiO_2 and 6 wt% Y_2O_3 powders were hot pressed under 28 MPa in vacuum at 1650 °C for 1 h to obtain silicon nitride based composites. In the presence of the TiO_2 compound, TiN and Si_2N_2O were formed, and α to β-Si_3N_4 conversion was improved. It should be noted that other types of ceramic materials [6–17] exhibited similar relationships between their microstructure and mechanical behavior.

The authors of the study [18] developed silicon nitride based ceramics manufactured with adding $Y_2Si_2O_7$, Y_2O_3–Al_2O_3, and $Y_2Si_2O_7$–$Al_6Si_2O_{13}$ binary sintering aids. In these ceramic compositions, the $Y_2Si_2O_7$ percentage varied in the range of 5–20 wt%. Physical properties of Si_3N_4 ceramics such as density, shrinkage, phase composition, and microstructure were thoroughly studied about the sintering aid content and peculiarities of the liquid phase formation.

The in situ formed Si_3N_4–Si_2N_2O–TiN composites studied in the work [19] were hot pressed at 1650 °C from mixtures of silicon nitride powder with TiN and TiO_2 powders. Various, TiN and Si_2N_2O volume fractions were achieved in the sintered Si_3N_4-based composites. It was found that the main crystalline phase and the intergranular glass phases were stable at temperatures up to 1400 °C. While holding samples in the nitrogen atmosphere or vacuum, the microstructure of the sample

surface layer changed forming the silicon oxynitride phase and amorphous intergranular phase. This deteriorated mechanical properties and high-temperature stability of material containing the silicon oxynitride phase and amorphous intergranular phase. A high-Si_2N_2O/high-TiN/β-Si_3N_4 composite was proposed as the most promising for further development based on the hardness and fracture toughness tests by the indentation method [20–31].

In the work [32], ceramic materials based on fine silicon nitride powder were sintered and their physical properties were thoroughly studied. The authors related peculiarities of material microstructure to corresponding sintering modes.

The work [33] studied the effects of various additives (TiN, TiO_2, and TiC) on the intergranular glass phase formation in silicon nitride based ceramic materials. The authors revealed the change in the internal friction with the temperature of the ceramics related to the additive fractions. They found that the TiN and TiO_2 compounds promoted the α to β-silicon nitride transformation [32, 34–43]. Such an increased amount of the needle-shaped β-Si_3N_4 phase grains resulted in significant improvement of crack growth resistance of the ceramics [44–54].

In the study [55], longitudinal crack propagation depth and surface residual stress were chosen as the main parameters to analyze the behavior of sintered silicon nitride ceramics in the grinding process. Different mechanical testing methods [56–67] were utilized to assess the applicability of the studied ceramics in various industry areas.

The mechanical reliability of ceramic products is estimated based on the main mechanical properties of the materials, such as hardness, flexural strength, and fracture toughness. For this reason, the mentioned properties of the ceramics under study were chosen as the most appropriate. Besides, according to several works [68–72], novel toughening methods may be implemented to improve wear resistance and fracture toughness of silicon nitride ceramics.

This work aims to study the effect of the microstructure of silicon nitride based ceramics on their mechanical behaviors, for possible application of the materials in metal-ceramic macrocomposite plates.

6.2 Materials and Methods

A powder mixture of Si_3N_4–Y_2O_3 ceramic composition [32, 73] was prepared by introducing Y_2O_3 powder in plasma jets in the process of synthesis of Si_3N_4 powder. The fraction of Y_2O_3 was set as 10 wt% (Table 6.1). The specific surfaces of Si_3N_4 and Y_2O_3 initial powders were measured as 42–46 m^2/g and 22–24 m^2/g, respectively. Bar specimens approximately $4.5 \times 3.5 \times 42$ mm^3 in size were produced by conventional sintering according to the set modes (Table 6.1) and then ground and polished to use for microstructural and mechanical testing. The width of the prepared specimens was $w = (4.0 \pm 0.2)$ mm and their thickness was $b = (3.0 \pm 0.2)$ mm satisfying thus the requirements of the corresponding ISO standard [74]. Cross-sectional surfaces of specimens prepared for metallographic studies were etched in 40% hydrofluoric acid (HF) for 30 min according to the proposed technique [75].

Table 6.1 Sintering modes, physical, and mechanical properties of the investigated Si_3N_4–Y_2O_3 ceramics

Series	Sintering mode			Density, g/cm^3	Porosity, %	Hardness HV_{20}, GPa	σ_f, MPa	K_{Ic}, MPa·m$^{1/2}$
	Temperature, °C	Time, h	C_p, wt%					
1	1700	0.5	5	2.91	15.65	14.1	178	3.75
2	1700	2	2	3.31	4.35	17.8	285	5.12
3	1700	2	10	3.32	3.46	18.1	252	3.07
4	1700	5	5	3.38	1.73	18.6	275	4.14

Note Average values of density, porosity, hardness HV_{20}, flexural strength σ_f, and fracture toughness K_{Ic} are given. C_p is the content of plasticizer

All mechanical tests were carried out in air at 20 °C.

The hardness measurements were performed according to the relevant standards [76, 77] under the indentation load of 20 kg using a NOVOTEST TC-БРВ hardness tester. The values of Vickers hardness (HV_{20}) were calculated by the formula [77]:

$$H = 0.0018544\left(\frac{P}{d^2}\right) \tag{6.1}$$

where P is the indentation load (N) and d is the average length of the imprint diagonals (mm).

The imprint sizes were measured with a Neophot-21 optical microscope. The hardness values of the studied ceramics were calculated using the results of five indentations.

For estimating both the flexural strength and fracture toughness of the studied ceramics, a UIT STM 050 testing machine with a loading unit for three-point test at a cross-head speed of 10^{-2} mm/s was used.

To determine the material strength in flexure, bar specimens of the above-mentioned geometry were used. The values of flexural strength (σ_f) were calculated by the equation presented in the works [74, 78, 79] using the "load–flexure" test data:

$$\sigma_f = \frac{1.5 \cdot P \cdot l}{w \cdot b^2} \tag{6.2}$$

where P is the fracture load (N), l is the span between the supporting rollers (mm), and w and b are the width and thickness (mm) of the bar specimen, respectively. The span between the supporting rollers was set to 30 mm.

The average flexural strength value for each material series was calculated based on the data from five specimens.

To estimate fracture toughness of materials, various methods of fracture mechanics can be used [80–93]. In this work, the main parameter for measuring fracture toughness known as the critical stress intensity factor (SIF) K_{Ic} [94–104]

was estimated. Corresponding formulas for the critical SIF determination in materials can be found in the standards and articles [105–116]. In some of them, the parameters measured by the Vickers indentation test method were used [117–127]. In our work, single-edge notch beam (SENB) specimens of the same cross-section geometry as for the flexural test were used. A straight notch 0.1 mm in width with its front along the specimen thickness dimension was made by a 0.08 mm thick diamond wheel. The specimens were tested under three-point bending with the span between the supporting rollers of 30 mm, and values of K_{Ic} were calculated according to [74] based on the specimen geometry and the "load–flexure" test data. For each material series, the average K_{Ic} value of five specimens was calculated.

To prepare X-ray diffraction (XRD) patterns, a Malvern Panalytical X-ray diffractometer operated in Cu K_α radiation mode was utilized.

A scanning electron microscope (SEM) Carl Zeiss EVO-40XVP was used for analyses of microstructure and fracture surfaces of the studied specimens. SEM microstructure images were prepared in the back-scattered diffraction (BSD) imaging mode, whereas SEM images of specimen fracture surfaces were made in the secondary electron (SE) imaging mode. An INCA Energy 350 system was utilized for an energy-dispersive X-ray (EDX) microanalysis of the studied materials.

6.3 Results and Discussion

The phase compositions and microstructure of the Si_3N_4–Y_2O_3 ceramic series were analyzed and their hardness, flexural strength, and fracture toughness were examined.

6.3.1 Evaluation of Phase Compositions of the Si_3N_4–Y_2O_3 Ceramic Series

According to the XRD patterns of the Si_3N_4–Y_2O_3 ceramics, six different phases were detected in these materials: β-Si_3N_4, SiO_2, $Y_3Ca_2(SiO_4)_3(OH)$, $Ca_3Y_2(Si_3O_9)_2$, Si_2N_2O, and $YSiNO_2$ (Fig. 6.1).

Series 1 ceramic exhibited the following phase fractions (Table 6.2): β-Si_3N_4 phase (82 wt%), SiO_2 phase (2.5 wt%), and $Y_3Ca_2(SiO_4)_3(OH)$ phase (15.5 wt%). The phase fractions for series 2 ceramic were estimated as follows (Table 6.2): β-Si_3N_4 phase (50.3 wt%), $Ca_3Y_2(Si_3O_9)_2$ phase (34.6 wt%), and Si_2N_2O phase (15.1 wt%). Similarly to series 1, series 3 ceramic exhibited the phase fractions as follows (Table 6.2): β-Si_3N_4 phase (64.6 wt%) and $Y_3Ca_2(SiO_4)_3(OH)$ phase (35.4 wt%). However, in the latter, no signs of the SiO_2 phase were detected. Series 4 ceramic exhibited the following phase balance (Table 6.2): β-Si_3N_4 phase (66.2 wt%), $Ca_3Y_2(Si_3O_9)_2$ phase (23.2 wt%), and $YSiNO_2$ phase (10.6 wt%). Thus, all the ceramics contain more than 50 wt% β-Si_3N_4. Series 2 ceramic shows the lowest

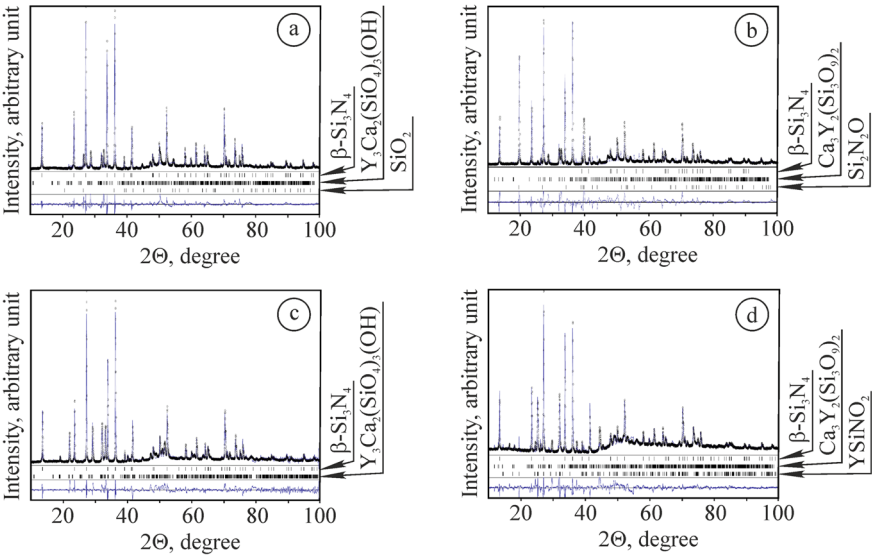

Fig. 6.1 XRD patterns of Si_3N_4–Y_2O_3 ceramics in **a** series 1, **b** 2, **c** 3, and **d** 4 (Table 6.1). The arrows indicate **a** the β-Si_3N_4, $Y_3Ca_2(SiO_4)_3(OH)$, SiO_2, **b** β-Si_3N_4, $Ca_3Y_2(Si_3O_9)_2$, Si_2N_2O, **c** β-Si_3N_4, $Y_3Ca_2(SiO_4)_3(OH)$, and **d** β-Si_3N_4, $Ca_3Y_2(Si_3O_9)_2$, $YSiNO_2$ phases, respectively

percentage of this phase. Both series 1 and 3 contain the $Y_3Ca_2(SiO_4)_3(OH)$ phase. The formation of this phase is probably related to the sintering mode and the plasticizer content. Series 1 ceramic was sintered for 0.5 h, and this sintering time is quite short. Series 3 ceramic was prepared using a five times higher plasticizer percentage (10 wt%) than that added to series 2 ceramic (Table 6.1).

Table 6.2 Phase composition of the investigated materials

Phase	Phase fractions for series			
	1	2	3	4
β-Si_3N_4	82.0	50.3	64.6	66.2
SiO_2	2.5	–	–	–
$Y_3Ca_2(SiO_4)_3(OH)$	15.5	–	35.4	–
$Ca_3Y_2(Si_3O_9)_2$	–	34.6	–	23.2
Si_2N_2O	–	15.1	–	–
$YSiNO_2$	–	–	–	10.6

Note Values of phase fractions are given in wt%

6.3.2 Microstructural Features of the Si_3N_4–Y_2O_3 Ceramics

According to a SEM microstructure image of series 1 ceramic (Fig. 6.2a), this material contains nano-sized particles of light color of two size ranges: (1) 20–100 nm; (2) 200–800 nm. Based on the above XRD analysis, it can be assumed that the particles in the second range belong to the β-Si_3N_4 phase, which dominates in the material (the phase fraction is 82 wt%). Foggy areas of dark-gray color surrounding these particles probably belong to the $Y_3Ca_2(SiO_4)_3(OH)$ and SiO_2 phases. These phases were formed due to inappropriate sintering conditions (i.e., the sintering time and the plasticizer content). Against the background of these phases, nuclei of the β-Si_3N_4 phase are seen, which belong to the first size range.

SEM microstructure image of series 2 ceramic (Fig. 6.2c) shows the dark-gray matrix probably consisting of the β-Si_3N_4 phase as the dominant one (50.3 wt%, see Table 6.2). On the boundaries of grains of this phase about 1.0–1.5 μm in size, particles of light color appear, which probably belong to both the $Ca_3Y_2(Si_3O_9)_2$ and Si_2N_2O phases. The size of these particles ranges from 20 to 600 nm.

The microstructure image of series 3 ceramic (Fig. 6.2e) probably exhibits the β-Si_3N_4 phase matrix, as the fraction of this phase is comparatively high (64.6 wt%, see Table 6.2). In the image, colonies of crystals about 0.2–1.0 μm in size probably belonging to the $Y_3Ca_2(SiO_4)_3(OH)$ phase can be observed. In this material, the SiO_2 phase was not detected. Therefore, small particles of light color 200–300 nm in size distributed uniformly in the matrix also belong to the $Y_3Ca_2(SiO_4)_3(OH)$ phase.

SEM microstructure image of series 4 ceramic (Fig. 6.2g) shows the dark-gray matrix probably consisting of the β-Si_3N_4 phase, as the fraction of this phase is comparatively high (66.2 wt%). It is supposed that the particles of light-gray color 100–400 nm in size segregated on the boundaries of the β-Si_3N_4 phase grains belong to the $Ca_3Y_2(Si_3O_9)_2$ and $YSiNO_2$ phases.

6.3.3 Physical and Mechanical Properties of the Si_3N_4–Y_2O_3 Ceramics

The studied Si_3N_4–Y_2O_3 ceramics exhibited a gradual increase in density and a steep decrease in porosity while increasing the sintering time from 0.5 to 2 h (Table 6.1). With a further increase in the sintering time to 5 h, a slight increase in density but still a significant decrease in porosity of the ceramics was revealed.

Sintering modes significantly affected the mechanical behavior of the Si_3N_4–Y_2O_3 ceramics. Fracture toughness (the average K_{Ic} value) of 3.75 MPa·$m^{1/2}$ estimated for series 1 ceramic (Table 6.1) presents a moderate level characteristic of silicon nitride based ceramics. Flexural strength of this ceramic is 178 MPa and its hardness is 14.1 GPa, which presents quite low levels of strength and hardness for such material. The fracture surface of a specimen of this ceramic examined for fracture toughness exhibits a complicated pattern (Fig. 6.2b). Grains of light-gray color of various shapes

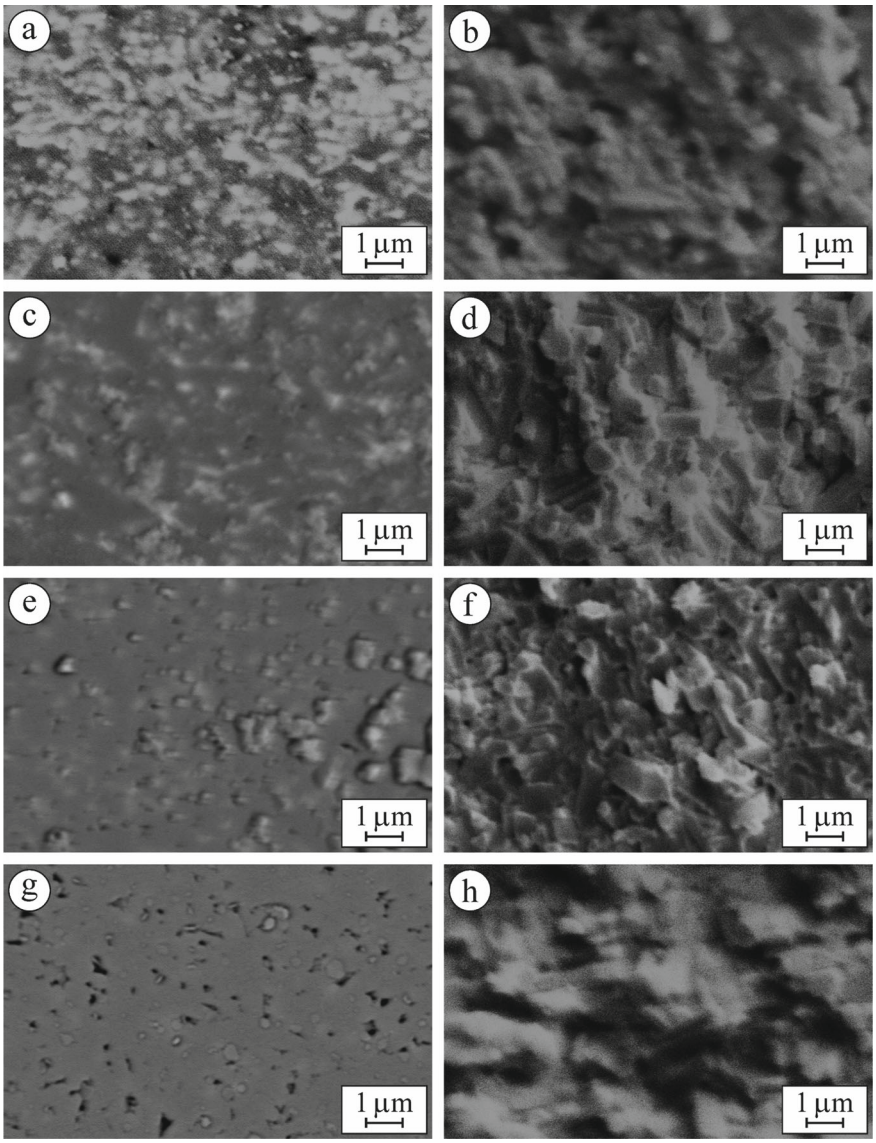

Fig. 6.2 SEM microstructures **a, c, e, g** in BSD mode and fractography **b, d, f, h** in SE mode of specimen series of Si_3N_4–Y_2O_3 ceramics (Table 6.1)

and sizes, with blurred contours surrounded with a substance of dark-gray color, are observed in the image. Some elongated grains are probably recrystallized β-Si_3N_4 phase grains, whereas others are smaller rounded β-Si_3N_4 phase grains formed in this sintering mode due to quite short holding time (0.5 h). The mentioned substance is probably a mixture of the $Y_3Ca_2(SiO_4)_3(OH)$ and SiO_2 phases. During the fracture

toughness test, a crack advanced along the boundaries of the β-Si_3N_4 phase grains fracturing areas of the $Y_3Ca_2(SiO_4)_3(OH)$ and SiO_2 phases. In such a way, a low energy-consuming fracture micromechanism was implemented in this ceramic.

It should be noted that flexural strength of 252 MPa of series 3 ceramic is higher by 41.6% and hardness is higher by 28.4% than those estimated for series 1 ceramic (Table 6.1). However, series 3 ceramic exhibited lower by 18.1% fracture toughness (3.07 MPa·$m^{1/2}$, see Table 6.1). The reason for fracture toughness reduction is probably too high a percentage of plasticizer (10 wt%) added in the preparation process, which promoted the formation of brittle $Y_3Ca_2(SiO_4)_3(OH)$ phase colonies (Fig. 6.2f) surrounding the β-Si_3N_4 phase grains. The signs of delamination of the $Y_3Ca_2(SiO_4)_3(OH)$ phase along the boundaries of β-Si_3N_4 grains and brittle cleavage areas of this phase both confirm a brittle low energy-consuming fracture micromechanism implemented in this ceramic.

Series 4 ceramic sintered for 5 h exhibited the highest hardness of 18.6 GPa and increases in flexural strength by 54.5% and fracture toughness by 10.4% compared to series 1 ceramic sintered for 0.5 h (Table 6.1). These results proved a positive effect of prolonged holding time on the quality of sintered Si_3N_4–Y_2O_3 ceramics. A specific fracture surface pattern was observed in a specimen of series 4 ceramic. Here, high energy-consuming fracture along the boundaries of elongated β-Si_3N_4 grains neighboring the rectangle particles of the unidirectional solidified $Ca_3Y_2(Si_3O_9)_2$ phase dominates (Fig. 6.2h), as no signs of transgranular fracture are observed. In contrast, the $YSiNO_2$ phase available in this ceramic, which has an orthorhombic structure, probably weakens the bond strength between the grains of the β-Si_3N_4 and $Ca_3Y_2(Si_3O_9)_2$ phases due to multiple cleavage planes promoting the nucleation of microcracks.

Special attention should be paid to series 2 ceramic prepared by adding only 2 wt% plasticizer and sintered for 2 h. Although this ceramic contains the lowest percentage of the β-Si_3N_4 phase (50.3 wt%) compared to other studied series, high percentages of the $Ca_3Y_2(Si_3O_9)_2$ and Si_2N_2O phases (34.6 wt% and 15.1 wt%, respectively) provided its best mechanical characteristics, namely, the average K_{Ic} value of 5.12 MPa·$m^{1/2}$ and flexural strength of 285 MPa, along with moderate hardness of 17.8 GPa (Table 6.1). The fracture surface of a specimen of this ceramic exhibits needle-shaped β-Si_3N_4 phase grains about 1.0–1.5 μm in size (Fig. 6.2d). Round-shaped fine particles of both the $Ca_3Y_2(Si_3O_9)_2$ and Si_2N_2O phases 20–600 nm in size are situated on the boundaries of grains of the β-Si_3N_4 phase. A limited number of cleavage facets are observed, whereas fracture along interfaces of β-Si_3N_4 phase grains dominates. Such a high energy-consuming fracture micromechanism provided the highest level of fracture toughness of this ceramic.

The sintered in the appropriate mode Si_3N_4–Y_2O_3 ceramic is promising in terms of the mechanical behavior, microstructure, and peculiarities of crack growth for various applications, in particular, in metal-ceramic macrocomposite layers of armor for protecting the body.

6.4 Conclusions

1. The studied Si_3N_4–10 wt% Y_2O_3 ceramics exhibited different phase compositions depending on the sintering mode. Six different phases were detected in these materials: β-Si_3N_4, SiO_2, $Y_3Ca_2(SiO_4)_3(OH)$, $Ca_3Y_2(Si_3O_9)_2$, Si_2N_2O, and $YSiNO_2$. The $Y_3Ca_2(SiO_4)_3(OH)$ phase deteriorated the microstructure and mechanical properties of the ceramics, whereas the $Ca_3Y_2(Si_3O_9)_2$ phase exhibited a strong positive effect on these properties.
2. The studied ceramics showed a gradual increase in density and a steep decrease in porosity while increasing the sintering time from 0.5 to 2 h.
3. The ceramic of Si_3N_4–10 wt% Y_2O_3 composition with adding 2 wt% plasticizer, which was sintered at 1700 °C for 2 h, exhibited high percentages of the $Ca_3Y_2(Si_3O_9)_2$ and Si_2N_2O phases (34.6 wt% and 15.1 wt%, respectively). Even though this ceramic contains the lowest percentage of the β-Si_3N_4 phase (50.3 wt%) compared to other studied series, such a phase balance provided its best mechanical characteristics, namely, the average K_{Ic} value of 5.12 MPa·$m^{1/2}$ and flexural strength of 285 MPa, along with moderate hardness of 17.8 GPa. The highest level of fracture toughness was provided due to the implementation of a high energy-consuming fracture micromechanism, namely, the fracture along interfaces of β-Si_3N_4 phase grains.
4. The Si_3N_4–Y_2O_3 ceramic sintered in such an appropriate mode can be successfully used in metal-ceramic macrocomposite layers of armor.

Acknowledgements The authors are thankful to the staff of the Scientific Equipment Collective Use Center "Laboratory of Advanced Technologies, Creation and Physicochemical Analysis of New Substances and Functional Materials" at Lviv Polytechnic National University (https://lpnu.ua/ckkno) for their kind help in performing X-ray diffraction studies.

References

1. W. Braue, R. Pleger, W. Luxem, Nucleation and growth of Si_2N_2O in Si_3N_4 materials employing different sintering additives. Key Eng. Mater. **89–91**, 483–488 (1994). https://doi.org/10.4028/www.scientific.net/KEM.89-91.483
2. M.J. Hoffmann, A. Geyer, R. Oberacker, Potential of the sinter-HIP-technique for the development of high-temperature resistant Si_3N_4-ceramics. J. Eur. Ceram. Soc. **19**(13–14), 2359–2366 (1999). https://doi.org/10.1016/S0955-2219(99)00106-5
3. M.B. Trigg, K.H. Jack, Solubility of aluminium in silicon oxynitride. J. Mater. Sci. Lett. **6**, 407–408 (1987). https://doi.org/10.1007/BF01756778
4. R.O. Ritchie, Mechanisms of fatigue-crack propagation in ductile and brittle solids. Int. J. Fract. **100**(1), 55–83 (1999). https://doi.org/10.1023/A:1018655917051
5. R.-G. Duan, G. Roebben, J. Vleugels et al., In situ formation of Si_2N_2O and TiN in Si_3N_4-based ceramic composites. Acta Mater. **53**(9), 2547–2554 (2005). https://doi.org/10.1016/j.actamat.2005.01.021

6. K.W. Jeong, J.S. Han, G.U. Yang et al., Influence of preaging temperature on the indentation strength of 3Y–TZP aged in ambient atmosphere. Materials **14**, 2767 (2021). https://doi.org/10.3390/ma14112767
7. I. Sanchez, D. Axinte, Z. Liao et al., The effect of high strain rate impact in yttria stabilized zirconia. Mater. Des. **229**, 111908 (2023). https://doi.org/10.1016/j.matdes.2023.111908
8. V. Podhurska, B. Vasyliv, Influence of NiO reduction on microstructure and properties of porous Ni–ZrO_2 substrates, in *Proceedings of the 3rd International Conference on Oxide Materials for Electronic Engineering (OMEE-2012)* (Lviv, Ukraine, 2012), pp. 293–294. https://doi.org/10.1109/OMEE.2012.6464761
9. V.G. Efremenko, A.G. Lekatou, Y.G. Chabak et al., Micromechanical, corrosion and wet sliding wear behaviours of Co-28Cr-6Mo alloy: wrought versus LPBF. Mater. Today Commun. **35**, 105936 (2023). https://doi.org/10.1016/j.mtcomm.2023.105936
10. O.M. Romaniv, I.V. Zalite, V.M. Simin'kovych et al., Effect of the concentration of zirconium dioxide on the fracture resistance of Al_2O_3–ZrO_2 ceramics. Mater. Sci. **31**(5), 588–594 (1996). https://doi.org/10.1007/BF00558793
11. P. Uasuwan, N. Juntavee, A. Juntavee, Flexural strength of novel glass infiltrated monochrome and multilayer high yttrium oxide containing zirconia upon various sintered cooling rates. J. Prosthodont. **33**(S1), 47–59 (2024). https://doi.org/10.1111/jopr.13872
12. O.P. Ostash, I.M. Andreiko, V.V. Kulyk et al., Influence of braking on the microstructure and mechanical behavior of railroad wheel steels. Mater. Sci. **48**, 569–574 (2013). https://doi.org/10.1007/s11003-013-9539-9
13. G. Sokolowski, A. Szczesio-Wlodarczyk, M.I. Szynkowska-Jóźwik et al., The shear bond strength of resin-based luting cement to zirconia ceramics after different surface treatments. Materials **16**(15), 5433 (2023). https://doi.org/10.3390/ma16155433
14. V. Korendiy, O. Kachur, Dynamic behavior of a vibratory plate compactor working on a horizontal elastic-viscous-plastic surface, in *InterPartner 2022: Advanced Manufacturing Processes IV*, ed. by V. Tonkonogyi et al. Lecture Notes in Mechanical Engineering (2023), pp. 434–443. https://doi.org/10.1007/978-3-031-16651-8_41
15. G.P. Alparone, D. Penney, E. Jewell et al., The effect of sliding speed on the tribological properties of ceramic materials. Materials **16**(23), 7252 (2023). https://doi.org/10.3390/ma16237252
16. V. Kulyk, B. Vasyliv, Z. Duriagina et al., The effect of sintering temperature on phase-related peculiarities of the microstructure, flexural strength, and fracture toughness of fine-grained ZrO_2–Y_2O_3–Al_2O_3–CoO–CeO_2–Fe_2O_3 ceramics. Crystals **14**(2), 175 (2024). https://doi.org/10.3390/cryst14020175
17. P. Jeevankumar, P. Rose, A. Rajanikanth et al., Net-shaping of advanced ceramic composites by gelcasting into precision molds made by rapid-prototyping. Int. J. Appl. Ceram. Technol. **21**(2), 664–674 (2024). https://doi.org/10.1111/ijac.14568
18. L. He, N. Huang, D. Lu et al., A study on the effects of liquid phase formation temperature and the content of sintering aids on the sintering of silicon nitride ceramics. Crystals **13**(7), 1099 (2023). https://doi.org/10.3390/cryst13071099
19. R.-G. Duan, G. Roebben, J. Vleugels et al., Thermal stability of in situ formed Si_3N_4–Si_2N_2O–TiN composites. J. Eur. Ceram. Soc. **22**(14–15), 2527–2535 (2002). https://doi.org/10.1016/S0955-2219(02)00110-3
20. X. Fu, F. Zhang, W. Zhu et al., Mechanical properties and toughening mechanisms of promising Zr-Y-Ta-O composite ceramics. Coatings **13**(5), 855 (2023). https://doi.org/10.3390/coatings13050855
21. T.F. Alghazzawi, G.M. Janowski, H. Ning et al., Qualitative SEM analysis of fracture surfaces for dental ceramics and polymers broken by flexural strength testing and crown compression. J. Prosthodont. **32**(5) (2023). https://doi.org/10.1111/jopr.13659
22. N.C. Golota, Z.P. Fredin, D.P. Banks et al., Diamond rotors. J. Magn. Reson. **352**, 107475 (2023). https://doi.org/10.1016/j.jmr.2023.107475

23. V.G. Efremenko, Y.G. Chabak, V.I. Fedun et al., Formation mechanism, microstructural features and dry-sliding behaviour of "Bronze/WC carbide" composite synthesised by atmospheric pulsed-plasma deposition. Vacuum **185**, 110031 (2021). https://doi.org/10.1016/j.vacuum.2020.110031
24. S. Liu, J. Zhang, Y. Tian et al., Preparation of Bi_2O_3–YSZ and YSB–YSZ composite powders by a microemulsion method and their performance as electrolytes in a solid oxide fuel cell. Materials **16**(13), 4673 (2023). https://doi.org/10.3390/ma16134673
25. I. Izonin, R. Tkachenko, M. Gregus et al., Hybrid classifier via PNN-based dimensionality reduction approach for biomedical engineering task. Procedia Comput. Sci. **191**, 230–237 (2021). https://doi.org/10.1016/j.procs.2021.07.029
26. M.B. Hanif, S. Rauf, Z.U. Abadeen et al., Proton-conducting solid oxide electrolysis cells: relationship of composition-structure-property, their challenges, and prospects. Matter **6**(6), 1782–1830 (2023). https://doi.org/10.1016/j.matt.2023.04.013
27. H. Charalambous, M.H. Jancich, P.W.F. Evans et al., Processing and characterization of the homologous $Zr_xTa_2O_{2x+5}$ series. Ceram. Int. **50**(9), 15848–15855 (2024). https://doi.org/10.1016/j.ceramint.2024.02.064
28. K. Tanaka, Elastic/plastic indentation hardness and indentation fracture toughness: the inclusion core model. J. Mater. Sci. **22**(4), 1501–1508 (1987). https://doi.org/10.1007/BF01233154
29. O.N. Grigoriev, V.B. Vinokurov, T.V. Mosina et al., Kinetics of shrinkage, structurization, and the mechanical characteristics of zirconium boride sintered in the presence of activating additives. Powder Metall. Met. Ceram. **55**(11–12), 676–688 (2017). https://doi.org/10.1007/s11106-017-9855-y
30. S.N. Almohammed, B. Alshorman, L.A. Abu-Naba'a, Mechanical properties of five esthetic ceramic materials used for monolithic restorations: a comparative in vitro study. Ceramics **6**(2), 1031–1049 (2023). https://doi.org/10.3390/ceramics6020061
31. S.G. Giniyatova, A.L. Kozlovskiy, R.I. Shakirzyanov et al., Structural, dielectric, and mechanical properties of high-content cubic zirconia ceramics obtained via solid-state synthesis. Appl. Sci. **13**(19), 10989 (2023). https://doi.org/10.3390/app131910989
32. I. Zalite, M. Herrmann, J. Grabis, Materials on the basis of finely dispersed Si_3N_4 powders. Key Eng. Mater. **132–136**, 1018–1021 (1997)
33. R.-G. Duan, G. Roebben, J. Vleugels et al., Effect of TiX(X = C, N, O) additives on microstructure and properties of silicon nitride based ceramics. Scr. Mater. **53**(6), 669–673 (2005). https://doi.org/10.1016/j.scriptamat.2005.05.024
34. J.-M. Jung, G.-N. Kim, Y.-H. Koh et al., Manufacturing and characterization of dental crowns made of 5-mol% yttria stabilized zirconia by digital light processing. Materials **16**(4), 1447 (2023). https://doi.org/10.3390/ma16041447
35. H. Li, W. Qian, Z. Zhang et al., The phase stability of t-ZrO_2 realized by grain size at cryogenic temperature in ZrO_2/TiO_2 composite. Mater. Des. **239**, 112741 (2024). https://doi.org/10.1016/j.matdes.2024.112741a
36. S.S. Savka, D.I. Popovych, A.S. Serednytski, Molecular dynamics simulations of the formation processes of zinc oxide nanoclusters in oxygen environment, in *Nanophysics, Nanomaterials, Interface Studies, and Applications*, vol. 195 (Springer Proceedings of Physics, 2017), pp. 145–156. https://doi.org/10.1007/978-3-319-56422-7_11
37. S. Liu, J. Wang, Y. Chen et al., Tetragonal nanosized zirconia: hydrothermal synthesis and its performance as a promising ceramic reinforcement. Inorganics **11**(5), 217 (2023). https://doi.org/10.3390/inorganics11050217
38. V. Kulyk, Z. Duriagina, A. Kostryzhev et al., Effects of sintering temperature and yttria content on microstructure, phase balance, fracture surface morphology, and strength of yttria-stabilized zirconia. Appl. Sci. **12**(22), 11617 (2022). https://doi.org/10.3390/app122211617
39. D. Cao, K. Lv, Y. Bao et al., Thickness effect of an alumina-zirconia-mullite composite coating on the properties of zirconia. RSC Adv. **13**(4), 2736–2744 (2023). https://doi.org/10.1039/D2RA07549K

40. Y.S. Romario, C. Bhat, M. Ramezani et al., Fabrication of translucent graded dental crown using zirconia-yttrium multi-slurry tape casting 3D printer. J. Mech. Behav. Biomed. Mater. **152**, 106406 (2024). https://doi.org/10.1016/j.jmbbm.2024.106406
41. K. Nonaka, M. Teramae, G. Pezzotti, Evaluation of the effect of high-speed sintering and specimen thickness on the properties of 5 mol% yttria-stabilized dental zirconia sintered bodies. Materials **15**(16), 5685 (2022). https://doi.org/10.3390/ma15165685
42. P. Uasuwan, N. Juntavee, A. Juntavee, Flexural strength of high yttrium oxide-doped monochrome and multilayered fully stabilized zirconia upon various sintered cooling rates. J. Prosthodont. **32**(6) (2023). https://doi.org/10.1111/jopr.13692
43. Y. Wang, W. Qin, Z. Deng et al., High strength Y_2O_3-stabilized zirconia continuous fibers up to 1500 °C: crystalline phase and microstructure evolution as well as grain growth kinetics. J. Alloys Compd. **976**, 173165 (2024). https://doi.org/10.1016/j.jallcom.2023.173165
44. Z.-G. Wang, W.-D. Chen, S.-F. Yan et al., Direct fabrication and characterization of zirconia thick coatings on zirconium hydride as a hydrogen permeation barrier. Coatings **13**(5), 884 (2023). https://doi.org/10.3390/coatings13050884
45. M.M.H. Parvez, M.A. Daud, Effects of TiO_2 on the mechanical and physical properties of Fe_2O_3-doped yttria-stabilized zirconia for electrolyte of solid oxide fuel cells. Results Surf. Interfaces **16**, 100239 (2024). https://doi.org/10.1016/j.rsurfi.2024.100239
46. Y. Yue, Y. Zhu, Z. Li, Preparation and cutting performance study of YSZ-toughened PcBN superhard tools. RSC Adv. **13**(23), 15616–15623 (2023). https://doi.org/10.1039/D3RA02079G
47. O.P. Ostash, A.D. Ivasyshyn, B.D. Vasyliv et al., Influence of the structure and asymmetry of loading cycles on the cyclic crack resistance of Ti–Si composites. Mater. Sci. **38**(1), 55–61 (2002). https://doi.org/10.1023/A:1020120714703
48. A.K. Lakshya, K.K. Jha, C. Bhardwaj et al., Attaining translucency in binder/additive-free, nanograined, tetragonal 1.5 mol.% yttria-stabilized zirconia ceramics. Materialia **34**, 102075 (2024). https://doi.org/10.1016/j.mtla.2024.102075
49. M. Alghauli, A.Y. Alqutaibi, S. Wille et al., 3D-printed versus conventionally milled zirconia for dental clinical applications: trueness, precision, accuracy, biological and aesthetic aspects. J. Dent. **144**, 104925 (2024). https://doi.org/10.1016/j.jdent.2024.104925
50. B.V. Efremenko, K. Shimizu, N. Espallargas et al., High-temperature solid particle erosion of Cr–Ni–Fe–C arc cladded coatings. Wear **460–461**, 203439 (2020). https://doi.org/10.1016/j.wear.2020.203439
51. I.G. Alhindawy, H. Gamal, A.A. Zaher et al., La/Nd-doped zirconium oxide: Impact of zirconia phase transition on gamma-ray shielding properties. J. Phys. Chem. Solids **187**, 111828 (2024). https://doi.org/10.1016/j.jpcs.2023.111828
52. F. Mayinger, R. Buser, M. Laier et al., Impact of the material and sintering protocol, layer thickness, and thermomechanical aging on the two-body wear and fracture load of 4Y-TZP crowns. Clin. Oral Investig. **26**(11), 6617–6628 (2022). https://doi.org/10.1007/s00784-022-04616-5
53. F. Inchingolo, A.D. Inchingolo, I.A. Charitos et al., Inchingolo, Ceramic biomaterials in dentistry: chemical structure and biosafety—a review and a bibliometric visual mapping on Scopus database. Eur. Rev. Med. Pharmacol. Sci. **28**(4), 1242–1258 (2024). https://doi.org/10.26355/eurrev_202402_35446
54. W. Huang, H. Qiu, Y. Zhang et al., Microstructure and phase transformation behavior of Al_2O_3–ZrO_2 under microwave sintering. Ceram. Int. **49**(3), 4855–4862 (2023). https://doi.org/10.1016/j.ceramint.2022.09.376
55. H. Yan, F. Deng, Z. Qin et al., Effects of grinding parameters on the processing temperature, crack propagation and residual stress in silicon nitride ceramics. Micromachines **14**(3), 666 (2023). https://doi.org/10.3390/mi14030666
56. H. Miyazaki, H. Hyuga, K. Hirao et al., Comparison of fracture resistance as measured by the indentation fracture method and fracture toughness determined by the single-edge-precracked beam technique using silicon nitrides with different microstructures. J. Eur. Ceram. Soc. **27**, 2347–2354 (2007). https://doi.org/10.1016/j.jeurceramsoc.2006.09.002

57. Y. Li, H. Sun, J. Song et al., Effect of two-step sintering on the mechanical and electrical properties of 5YSZ and 8YSZ ceramics. Materials **16**(5), 2019 (2023). https://doi.org/10.3390/ma16052019
58. V. Korendiy, O. Kachur, V. Zakharov et al., Experimental study of the lap motion trajectory of vibratory finishing machine. Vib. Proced. **46**, 1–7 (2022). https://doi.org/10.21595/vp.2022.23002
59. B.D. Vasyliv, A procedure for the investigation of mechanical and physical properties of ceramics under the conditions of biaxial bending of a disk specimen according to the ring–ring scheme. Mater. Sci. **45**(4), 571–575 (2009). https://doi.org/10.1007/s11003-010-9215-2
60. B. Alfahed, A. Alayad, The effect of sintering temperature on Vickers microhardness and flexural strength of translucent multi-layered zirconia dental materials. Coatings **13**(4), 688 (2023). https://doi.org/10.3390/coatings13040688
61. O.P. Ostash, L.I. Muravs'kyi, T.I. Voronyak et al., Determination of the size of the fatigue prefracture zone by the method of phase-shifting interferometry. Mater. Sci. **46**, 781–788 (2011). https://doi.org/10.1007/s11003-011-9353-1
62. Y.G. Chabak, K. Shimizu, V.G. Efremenko et al., Microstructure and phase elemental distribution in high-boron multi-component cast irons. Int. J. Miner. Metall. Mater. **29**, 78–87 (2022). https://doi.org/10.1007/s12613-020-2135-8
63. V.V. Kulyk, B.D. Vasyliv, Z.A. Duriagina et al., The effect of water vapor containing hydrogenous atmospheres on the microstructure and tendency to brittle fracture of anode materials of YSZ–NiO(Ni) system. Arch. Mater. Sci. Eng. **108**(2), 49–67 (2021). https://doi.org/10.5604/01.3001.0015.0254
64. J. Lankford, Indentation microfracture in the Palmqvist crack regime: implications for fracture toughness evaluation by the indentation method. J. Mater. Sci. Lett. **1**(11), 493–495 (1982). https://doi.org/10.1007/BF00721938
65. T.M. Lenkovskiy, V.V. Kulyk, Z.A. Duriagina et al., Mode I and mode II fatigue crack growth resistance characteristics of high tempered 65G steel. Arch. Mater. Sci. Eng. **84**(1), 34–41 (2017). https://doi.org/10.5604/01.3001.0010.3029
66. T.G.T. Nindhia, T. Lube, Single edge precrack V-notched beam (SEPVNB) fracture toughness testing on silicon nitride. Mater. Sci. Forum **962**, 205–209 (2019). https://doi.org/10.4028/www.scientific.net/MSF.962.205
67. K. Hoggas, S. Benaissa, A. Cherouana et al., Mechanical behavior of transparent spinel fabricated by spark plasma sintering. Ceramics **6**(2), 1191–1209 (2023). https://doi.org/10.3390/ceramics6020072
68. C.C. Ye, K. Ma, H.M. Chen et al., Effect of texture on the thermal conductivity and mechanical properties of silicon nitride ceramic. Ceram. Int. **50**(2), 4014–4021 (2024). https://doi.org/10.1016/j.ceramint.2023.11.170
69. K. Matsuura, T. Ohji, T. Takahashi et al., Effects of rare-earth oxides on grain boundary strength of silicon nitride ceramics. J. Eur. Ceram. Soc. **44**(14), 116672 (2024). https://doi.org/10.1016/j.jeurceramsoc.2024.116672
70. S. Huang, Y. Li, P. Yang et al., Cure behaviour and mechanical properties of Si_3N_4 ceramics with bimodal particle size distribution prepared using digital light processing. Ceram. Int. **49**(8), 12166–12172 (2023). https://doi.org/10.1016/j.ceramint.2022.12.068
71. H. Xiong, B. Li, X. Xi et al., Preparation of graded silicon nitride ceramics with high mechanical performance using β-Si_3N_4 seeds. Ceram. Int. **49**(22), 36528–36535 (2023). https://doi.org/10.1016/j.ceramint.2023.08.336
72. G. Cui, T. Li, Z. Wang et al., In-situ formation reinforcement phase for Si_3N_4 ceramics with high toughness and wear resistance. Mater. Today Commun. **40**, 110081 (2024). https://doi.org/10.1016/j.mtcomm.2024.110081
73. B.D. Vasyliv, O.M. Romaniv, I.V. Zalite et al., Correction to: enhancement of the crack resistance of $Si_36N_4-Y_2O_3$ ceramics and its structural and metallurgical aspects. Mater. Sci. 33, 3, 323–330 (1997). 10.1007/BF02539086. Mater. Sci. 56(4), 583 (2021). 10.1007/s11003-021-00467-9

74. ISO 6872, Dentistry–Ceramic Materials. International Organization of Standardization: Geneva, Switzerland (2015)
75. Q. Flamant, F. García Marro, J.J. Roa Rovira et al., Hydrofluoric acid etching of dental zirconia. Part 1: Etching mechanism and surface characterization. J. Eur. Ceram. Soc. **36**, 121–134 (2015). https://doi.org/10.1016/j.jeurceramsoc.2015.09.021
76. ASTM E 384-11, Standard test method for Knoop and Vickers hardness of materials. ASTM Int. (2011). https://doi.org/10.1520/E0384-11
77. ASTM C 1327-03, Standard test method for Vickers indentation hardness of advanced ceramics. ASTM Int. (2003). https://doi.org/10.1520/C1327-03
78. J.M. Gere, S.P. *Timoshenko, Mechanics of Materials*, 4th edn. (PWS Publishing Company, Boston, MA, USA, 1997), p. 912
79. O.M. Romaniv, B.D. Vasyliv, Some features of formation of the structural strength of ceramic materials. Mater. Sci. **34**(2), 149–161 (1998). https://doi.org/10.1007/BF02355530
80. S. Begand, S. Spintzyk, J. Geis-Gerstorfer et al., Fracture toughness of 3Y-TZP ceramic measured by the chevron-notch beam method: a round-robin study. Dent. Mater. **38**(7), 1128–1139 (2022). https://doi.org/10.1016/j.dental.2022.05.001
81. X. Zhu, G. Hou, J. Ma et al., Effect of Y_2O_3 doping content on phase composition, mechanical properties and cavitation erosion performance of ZrO_2 ceramics. Ceram. Int. **50**(9), 14718–14730 (2024). https://doi.org/10.1016/j.ceramint.2024.01.385
82. V.Y. Podhurs'ka, B.D. Vasyliv, O.P. Ostash et al., Structural transformations in the NiO-containing anode of ceramic fuel cells in the course of its reduction and oxidation. Mater. Sci. **49**(6), 805–811 (2014). https://doi.org/10.1007/s11003-014-9677-8
83. B.R. Lawn, M.V. Swain, Microfracture beneath point indentations in brittle solids. J. Mater. Sci. **10**(1), 113–122 (1975). https://doi.org/10.1007/BF00541038
84. Y. Zhang, C. Ren, J. Zhou et al., Influence of microwave heating on grain growth behavior and phase stability of nano Y_2O_3/La_2O_3 co-doped ZrO_2 ceramics. Ceram. Int. **50**(6), 8733–8741 (2024). https://doi.org/10.1016/j.ceramint.2023.12.190
85. O.P. Ostash, A.D. Ivasyshyn, B.D. Vasyliv et al., High-temperature and cyclic corrosion crack resistance of alloys of the Ti–Si–Al–Zr system. Mater. Sci. **42**(3), 330–343 (2006). https://doi.org/10.1007/s11003-006-0087-4
86. T.M.B. Campos, C. Dos Santos, L.M.M. Alves et al., Minimally processed recycled yttria-stabilized tetragonal zirconia for dental applications: effect of sintering temperature on glass infiltration. J. Mech. Behav. Biomed. Mater. **150**, 106311 (2024). https://doi.org/10.1016/j.jmbbm.2023.106311
87. R.H. Purba, K. Kusumoto, K. Shimizu et al., Influence of tempering temperature on abrasive-wear performance of high-chromium-based multicomponent white cast iron. Lubricants **11**(7), 285 (2023). https://doi.org/10.3390/lubricants11070285
88. A. Moradkhani, H. Baharvandi, M. Tajdari et al., Determination of fracture toughness using the area of micro-crack tracks left in brittle materials by Vickers indentation test. J. Adv. Ceram. **2**, 87–102 (2013). https://doi.org/10.1007/s40145-013-0047-z
89. I.M. Andreiko, V.V. Kulyk, O.P. Ostash, Resistance of steels of railroad wheels to corrosion-fatigue fracture. Mater. Sci. **47**, 608–612 (2012). https://doi.org/10.1007/s11003-012-9434-9
90. S. Ozkan, S.J. Kim, D.N. Miller et al., A new approach to fuel cell electrodes: Lanthanum aluminate yielding fine Pt nanoparticle exsolution for oxygen reduction reaction. Adv. Energy Mater. **14**(15), 2303025 (2024). https://doi.org/10.1002/aenm.202303025
91. R.F. Cook, G.M. Pharr, Direct observation and analysis of indentation cracking in glasses and ceramics. J. Am. Ceram. Soc. **73**(4), 787–817 (1990). https://doi.org/10.1111/j.1151-2916.1990.tb05119.x
92. O.P. Ostash, I.M. Andreiko, V.V. Kulyk et al., Influence of the mode of thermal treatment and load ratio on the cyclic crack-growth resistance of wheel steels. Mater. Sci. **45**, 211–219 (2009). https://doi.org/10.1007/s11003-009-9177-4
93. Q. Yao, Y. Chen, Z. Wang et al., Evaluations on ceramic fracture toughness measurement by edge chipping. Coatings **12**, 1146 (2022). https://doi.org/10.3390/coatings12081146

94. A.G. Evans, E.A. Charles, Fracture toughness determinations by indentation. J. Am. Ceram. Soc. **59**(7–8), 371–372 (1976). https://doi.org/10.1111/j.1151-2916.1976.tb10991.x
95. O. Kachur, V. Korendiy, Dynamic behavior of vibratory screening conveyor equipped with crank-type exciter, in *DSMIE 2023: Advances in Design, Simulation and Manufacturing VI*, ed. by V. Ivanov et al. Lecture Notes in Mechanical Engineering (2023), pp. 44–53. https://doi.org/10.1007/978-3-031-32774-2_5
96. M.A. Ali Bash, S.A. Ajeel, R.A. Abbas et al., A direct laser sintering approach for the electrophoretic deposition overlay of yttria-stabilized zirconia on the surface of a thermal barrier coating system. Coatings **13**(10), 1695 (2023). https://doi.org/10.3390/coatings13101695
97. V. Kulyk, I. Izonin, V. Vavrukh et al., Prediction of hardness, flexural strength, and fracture toughness of ZrO_2 based ceramics using ensemble learning algorithms. Acta Metall. Slovaca **29**(2), 93–103 (2023). https://doi.org/10.36547/ams.29.2.1819
98. G.R. Anstis, P. Chantikul, B.R. Lawn et al., A critical evaluation of indentation techniques for measuring fracture toughness: I, direct crack measurement. J. Am. Ceram. Soc. **64**(9), 533–538 (1981). https://doi.org/10.1111/j.1151-2916.1981.tb10320.x
99. B.R. Vaishnavi Krupa, C. Ghosh, S.K. Sinha et al., Reverse transition of ball milling induced m-Y_2O_3 nano-crystallites during in-situ annealing. Ceram. Int. **49**(14), 23522–23530 (2023). https://doi.org/10.1016/j.ceramint.2023.04.185
100. B.D. Vasyliv, A.D. Ivasyshyn, O.P. Ostash et al., Kinetics of corrosion-fatigue cracks in Ti–Si cermet composite. Mater. Sci. **38**(2), 220–224 (2002). https://doi.org/10.1023/A:1020990103898
101. S. Wu, S. Liu, Y. Chen et al., Optimization of the structure and morphology of monoclinic phase nanoscale zirconium dioxide. MRS Commun. **14**(4), 646–652 (2024). https://doi.org/10.1557/s43579-024-00578-9
102. H. Yoo, J. Kim, H. Lee et al., Phase formation and stabilization behavior of Ca-PSZ by post-heat treatment II: CaO*x*-ZrO_2(1–x) (x = 5–10 mol%). Metals **13**(10), 1659 (2023). https://doi.org/10.3390/met13101659
103. Y. Kharchenko, Z. Blikharskyy, V. Vira et al., Nanostructural changes in a Ni/NiO cermet during high-temperature reduction and reoxidation, in *Nanomaterials and Nanocomposites, Nanostructure Surfaces, and Their Applications*, vol. 246 (Springer Proceedings of Physics, 2021), pp. 219–229. https://doi.org/10.1007/978-3-030-51905-6_17
104. J.C.C.A. Diaz, E.N.D.S. Muccillo, R. Muccillo, Porous 8YSZ ceramics prepared with alkali halide sacrificial additives. Materials **16**(9), 3509 (2023). https://doi.org/10.3390/ma16093509
105. ASTM E 399-20a, Standard test method for linear-elastic plane-strain fracture toughness of metallic materials. ASTM Int. (2020). https://doi.org/10.1520/E0399-20A
106. ASTM C 1421-18, Standard test methods for determination of fracture toughness of advanced ceramics at ambient temperature. ASTM Int. (2018). https://doi.org/10.1520/C1421-18
107. Y. Wang, X. Liu, S. Pan et al., Local structure regulation and spectroscopy study of blue cubic zirconia. CrystEngComm **25**(11), 1582–1588 (2023). https://doi.org/10.1039/D2CE01674E
108. B. Vasyliv, J. Milewski, V. Podhurska et al., Study of the degradation of a fine-grained YSZ–NiO anode material during reduction in hydrogen and reoxidation in air. Appl. Nanosci. **12**, 965–975 (2022). https://doi.org/10.1007/s13204-021-01768-w
109. H. Gujjaramma, B.S. Krishna, K. Gurushantha et al., Phyllantus acidus mediated combustion method synthesised yttria stabilized zirconia, its application as photocatalyst and antibacterial agent. Desalin. Water Treat. **317**, 100301 (2024). https://doi.org/10.1016/j.dwt.2024.100301
110. J. Kübier, Fracture toughness of ceramics using the SEVNB method: From a preliminary study to a standard test method, in *Fracture Resistance Testing of Monolithic and Composite Brittle Materials*, ed. by J. Salem et al. ASTM International 93–106 (2002). https://doi.org/10.1520/STP10473S
111. B. Vasyliv, V. Podhurska, O. Ostash, Preconditioning of the YSZ-NiO fuel cell anode in hydrogenous atmospheres containing water vapor. Nanoscale Res. Lett. **12**, 265 (2017). https://doi.org/10.1186/s11671-017-2038-4

112. H. Peng, Y. Yu, T. Shi et al., Effects of induction plasma spheroidization on properties of yttria-stabilized zirconia powders for thermal barrier coating applications. Materials **17**(7), 1518 (2024). https://doi.org/10.3390/ma17071518
113. A. Unnadkat, L. Kirby, S. Kulanthaivel et al., The effect of sintering on zirconia manufactured via suspension-enclosing projection stereolithography for dental applications: an in vitro study. Materials **17**(1), 14 (2023). https://doi.org/10.3390/ma17010014
114. L. Du, J. Yang, X. Zhong et al., Synthesized by coprecipitation method for controlled phase structures of 5YSZ. J. Mater. Res. Technol. **29**, 5473–5483 (2024). https://doi.org/10.1016/j.jmrt.2024.02.222
115. T.F. Alghazzawi, A comparison of failure loads for polycrystalline zirconia ceramics with varying amounts of yttria, glass-ceramics and polymers in two different test conditions. Polymers **15**(23), 4506 (2023). https://doi.org/10.3390/polym15234506
116. A. Shearer, M. Montazerian, B. Deng et al., Zirconia-containing glass-ceramics: from nucleating agent to primary crystalline phase. Int. J. Ceram. Eng. Sci. **6**(2), e10200 (2024). https://doi.org/10.1002/ces2.10200
117. V. Kulyk, Z. Duriagina, B. Vasyliv et al., Effect of sintering temperature on crack growth resistance characteristics of yttria-stabilized zirconia. Acta Phys. Pol. A **141**(4), 323–327 (2022). http://przyrbwn.icm.edu.pl/APP/PDF/141/app141z4p18.pdf
118. B.D. Vasyliv, V.Y. Podhurska, O.P. Ostash et al., Effect of a hydrogen sulfide-containing atmosphere on the physical and mechanical properties of solid oxide fuel cell materials, in *Nanochemistry, Biotechnology, Nanomaterials, and Their Applications*, vol. 214 (Springer Proceedings of Physics, 2018), pp. 475–485. https://doi.org/10.1007/978-3-319-92567-7_30
119. P. Gothwal, F. Singh, V. Chauhan et al., Effects of lithium ion irradiation on yttria-stabilized zirconia thin films: structural and optical investigations. J. Electron. Mater. **53**(9), 5204–5211 (2024). https://doi.org/10.1007/s11664-024-11230-6
120. V. Korendiy, O. Kachur, V. Gursky et al., Kinematic and dynamic analysis of three-mass oscillatory system of vibro-impact plate compactor with crank excitation mechanism. Vib. Proced. **40**, 14–19 (2022). https://doi.org/10.21595/vp.2022.22393
121. H. Shao, J. Zhu, X. Zhao et al., Additive manufacturing of magnesium-doped calcium silicate/zirconia ceramic scaffolds with projection-based 3D printing: sintering, mechanical and biological behavior. Ceram. Int. **50**(6), 9280–9292 (2024). https://doi.org/10.1016/j.ceramint.2023.12.244
122. J.-H. Yun, Y.-J. Jeon, M.-S. Kang, Analysis of elastic properties of polypropylene composite materials with ultra-high molecular weight polyethylene spherical reinforcement. Materials **15**(16), 5602 (2022). https://doi.org/10.3390/ma15165602
123. H. Sun, P. Tabrizian, A. Qambrani et al., Bio-inspired nacre-like zirconia/PMMA composites for chairside CAD/CAM dental restorations. Dent. Mater. **40**(2), 307–317 (2024). https://doi.org/10.1016/j.dental.2023.11.017
124. T.A. Prikhna, O.P. Ostash, A.S. Kuprin et al., A new MAX phases-based electroconductive coating for high-temperature oxidizing environment. Compos. Struct. **277**, 114649 (2021). https://doi.org/10.1016/j.compstruct.2021.114649
125. J.P. Winczewski, S. Zeiler, S. Gabel et al., Additive manufacturing of 3D yttria-stabilized zirconia microarchitectures. Mater. Des. **238**, 112701 (2024). https://doi.org/10.1016/j.matdes.2024.112701
126. H.-S. Lee, H. Ko, K. Heo et al., Dispersion control via crystal-phase modulation of yttrium-doped ZrO_2 nanoparticle sol. Colloids Surf A Physicochem Eng Asp **670**, 131476 (2023). https://doi.org/10.1016/j.colsurfa.2023.131476
127. K. Niihara, A fracture mechanics analysis of indentation-induced Palmqvist crack in ceramics. J. Mater. Sci. Lett. **2**(5), 221–223 (1983). https://doi.org/10.1007/BF00725625

Chapter 7
Application of "Nano + Micro"-Grained Alumina Based Ceramics for Improving the Functionality of the State-of-the-Art Protective Macrocomposite Plates

B. D. Vasyliv, V. V. Kulyk, P. Y. Lyutyy, V. V. Vira, A. I. Kuntii, and V. M. Korendiy

Abstract Alumina (Al_2O_3) based ceramics have great potential in attaining outstanding mechanical properties due to the superior hardness of this kind of ceramics. With the setting of appropriate sintering modes and doping aids, the fracture toughness and flexural strength of alumina can be greatly improved. Therefore, alumina based ceramic material sintered in the proper mode can be considered promising for application in protective metal-ceramic macrocomposite layers. A model of a macrocomposite protective plate was considered in this work. The dynamics of a body moving through the plate were assessed. A change in the velocity of the body was calculated using the energy spent to fracture ceramic inserts as a part of the total energy dissipated by the protective macrocomposite plate. Based on the calculation data and results of mechanical tests and fracture surface analysis, it was revealed that flexural strength, hardness, and fracture toughness are crucial for attaining high energy dissipation values in ceramics. Revealing the optimum combination of these mechanical properties enabled us to develop an improved geometry of ceramic inserts forming a layer of the protective metal-ceramic macrocomposite. A concept of "nano + micro"-grained alumina based ceramics for improving

B. D. Vasyliv (✉) · V. V. Kulyk · P. Y. Lyutyy
Department of Materials Science and Engineering, Lviv Polytechnic National University, Lviv, Ukraine
e-mail: mechengin1111@gmail.com

V. V. Vira
Department of Strength of Materials and Structural Mechanics, Lviv Polytechnic National University, Lviv, Ukraine

A. I. Kuntii
Department of Criminal Proceedings and Criminology, Lviv State University of Internal Affairs, Lviv, Ukraine

V. M. Korendiy
Department of Technical Mechanics and Engineering Graphics, Lviv Polytechnic National University, Lviv, Ukraine

O. Fesenko and L. Yatsenko (eds.), *Functional Nanomaterials, Nanocatalysts, Nanotechnologies, and Their Applications*, Springer Proceedings in Physics 321,
https://doi.org/10.1007/978-3-031-99136-3_7

the functionality of the state-of-the-art protective macrocomposite plates was also developed.

7.1 Introduction

In fabricating armor for protecting the body (individual protection), ceramic materials, along with conventional metallic materials and polymers, are widely used. Alumina based ceramics can be considered promising for their application in protective metal-ceramic macrocomposite layers [1–5]. To improve the reliability and extend the lifetime of the individual components of protective macrocomposites, it is important to know the mechanical characteristics of the corresponding ceramic material. Among these, flexural strength [6–15], hardness [16–26], and fracture toughness [27–35] may be chosen as the most important characteristics of the ceramics. For the examination, various alumina based ceramics should be considered.

To reach a positive effect of changes in chemical composition and sintering technique of ceramics on their hardness, strength, and fracture toughness, various ceramics have been explored by many research institutions. Shearer A. et al. [36] performed a thorough review of ZrO_2-containing glass–ceramics and relevant glass–ceramic matrix composites. They exhibited main toughening mechanisms (the transformation toughening and others [37–48]) implemented in such materials for reaching high fracture toughness. They also showed that ZrO_2 contributes to improved stability and mechanical properties of sintered and glass–ceramic matrix composites.

Uasuwan et al. [49] fabricated novel glass-infiltrated monolayer and multilayer 5 mol% yttria-partially stabilized zirconia (5Y-PSZ) and studied their flexural strength related to cooling rates in the sintering process. They showed that glass infiltration significantly enhanced strength through elastic gradience. Fast cooling reduced grain size, impaired grain boundary integration, and increased the tetragonal to monoclinic phase transition [50–54]. In the case of traditional sintering [55–59], this is followed by a significant decrease in flexural strength of 5Y-PSZ ceramic. In the case of glass-infiltrated 5Y-PSZ, reduced processing time followed by fast cooling was recommended, as this mode enhanced strength [60]. In the work [61], flexural strength of high yttria-doped monolayer and multilayered fully stabilized zirconia upon various sintered cooling rates was estimated. The authors showed that slow and normal cooling provided significantly higher flexural strength than fast cooling. The first two sintering modes were recommended to achieve the optimum strength for 5Y-PSZ. An increase in the cooling rate during the sintering of 5Y-PSZ ceramic is followed by the smaller grain size, which, along with weaker grain boundary integration [62–72] and more intensive t-m transformation [73–82], led to lower strength.

Winczewski et al. [83] introduced additive manufacturing of 3D yttria-stabilized zirconia microarchitectures. After printing, thermal processing of microarchitecture samples at 600–1200 °C for 1 and 2 h in air was carried out to reach the crystallization

of the YSZ phase. The authors revealed yellowish-green emission upon UV excitation related to defects of YSZ microarchitectures, namely, intrinsic and extrinsic centers. This was found to correlate with the charge compensation due to Y^{3+} doping. The authors also observed the highest strength under compression for micropillars processed at 600 °C, and their strength lowered with an increase in the treatment temperature. The Hall–Petch strengthening mechanism [84–89] responsible for the gradual change from ductile to brittle-like fracture behavior was recognized during micropillar deformation.

Vaishnavi Krupa et al. [90] investigated the reverse transition of ball milling-induced m-Y_2O_3 nano-crystallites during in-situ annealing. The m-Y_2O_3 has been prepared by high-energy ball milling of the c-Y_2O_3. The authors performed a detailed crystallite size analysis of monoclinic to cubic (m → c) phase transition [91–98], compared the data with those reported earlier for the milling-induced c → m transition, and found that during annealing, the m- and c-phases of Y_2O_3 coexist up to ~ 850 °C. At 1000 °C, the phase is completely c-Y_2O_3.

Golota et al. [99] explored the possibility of using diamonds to fabricate micro-rotors. They assessed the resistance to fracture of diamond rotors by comparing it with various materials, including YSZ ceramics. They also showed that diamond offers the advantage of improved fracture toughness and reduced density relative to YSZ. Fracture toughness of YSZ varies in a range of 3–8 MPa•$m^{1/2}$ as a function of yttria content. Although natural diamond has a comparatively low fracture toughness of 4–5 MPa•$m^{1/2}$, some types of Ib diamond have fracture toughness in the range of 10 ± 2 MPa•$m^{1/2}$, while CVD diamond doped with nitrogen or boron reaches fracture toughness of about 34 MPa•$m^{1/2}$ [100–107].

Jeevankumar et al. [108] reported the net-shaping of advanced ceramic composites by gelcasting into precision molds made by rapid prototyping. The process was extended to fabricate composites of alumina and YSZ with α-alumina platelet particles, which exhibited enhanced fracture toughness. The components have shown uniform density across the body of large and complex-shaped parts, uniform microstructures, and good mechanical properties. This process also enables uniform distribution of second phases.

Yue et al. [109] reported a new type of polycrystalline cubic boron nitride (PcBN) superhard tool prepared by introducing 8YSZ powder under high pressure and temperature (5.5 GPa, 1500 °C). The material containing 5 wt% YSZ exhibited the maximum values of the flexural strength and fracture toughness of 637.77 MPa and 7.18 MPa $m^{1/2}$, respectively, along with the maximum value of the tool cutting life of 2615.81 m. The maximum hardness of 43.62 GPa was reached in the material containing 2.5 wt% YSZ.

Huang et al. [110] studied the microstructure and phase transformation behavior of Al_2O_3–ZrO_2 under microwave sintering. They reached the lowering of the phase transition temperature using the microwave sintering technique. This promoted the transformation between the m-ZrO_2 and t-ZrO_2, improving the crystallinity and microstructural characteristics of the specimens. The particle size of the material decreased with the temperature increase. In the studied temperature range of

800–1200 °C, the optimized sintering effect was revealed at 1000 °C for Al_2O_3–ZrO_2 powders. Under the optimized sintering mode, the best grain morphology was obtained.

It was essential to use the above research results on various ceramic microstructures for improving the mechanical properties of the material of individual macrocomposite components.

This work aims at studying the mechanical behavior of alumina based ceramics with formed nano- and micro-grained microstructures for their application in state-of-the-art protective macrocomposite plates.

7.2 Materials and Methods

Three different chemical compositions of alumina based ceramics containing small amounts of MgO, SiO_2, Fe_2O_3, Ga_2O_3, ZrO_2, PdO, and HfO_2 were studied (Table 7.1).

Ceramic plates of the set chemical compositions were produced by slip casting [111]. The cast plates were sintered according to the specified modes (Table 7.1). After sintering, they were cut into 3.6 × 4.6 × 38 mm^3 samples. Samples were prepared for flexural strength and fracture toughness tests by grinding their side surfaces. For the microhardness test and microstructure analysis, a few samples of each ceramic variant were polished. The final dimensions (thickness × width) of processed samples were (3.0 ± 0.2) mm × (4.0 ± 0.2) mm as per the ISO standard [15]. Etching samples for the microstructure analysis were carried out in 40% HF acid for 30 min according to the work [112].

All the mechanical tests were carried out in air at 20 °C. The Vickers microhardness (HV_1) of the ceramics was measured with a NOVOTEST TC-MKB1 tester under the indentation load of 9.81 N by the standards [18, 19]. A Neophot-21 optical microscope was used to measure the dimensions of imprints and cracks. These dimensions, along with the value of the indentation load, were used for calculating the values of Vickers microhardness by the equation given in [19]. For each material, the microhardness value was calculated as an average of five measurements.

Table 7.1 Sintering modes and physical properties of the studied materials

Variant	Sintering mode		Density, g/cm^3	Porosity, %	HV_1, GPa	σ_f, MPa	K_{Ic}, MPa·m$^{1/2}$
	Temperature, °C	Time, h					
1	1850	1	3.99	0.05	10.5 ± 2.7	175 ± 5	3.3 ± 0.3
2	1850	1	3.89	2.36	13.7 ± 1.1	248 ± 15	3.3 ± 0.3
3	1850	1	3.91	1.91	13.0 ± 0.8	249 ± 9	2.8 ± 0.1

Note Average values of density and porosity are given

A UIT STM 050 testing machine was used for fracture toughness and flexural strength tests. A loading unit providing a three-point bend scheme of a beam sample was installed on the machine. Flexural strength (σ_f) of ceramics was estimated based on parameters such as the dimensions of a sample, the distance between supporting rollers (30 mm), and the fracture load according to the equation given in [15, 113]. The flexural strength value for each material was calculated based on the measurements of five samples.

The critical stress intensity factor (SIF) K_{Ic} [114, 115] as a measure of fracture toughness is traditionally used to estimate the crack growth resistance of materials. In this work, the single-edge notch beam (SENB) method [15] as one of the well-known methods of fracture mechanics was applied to assess the fracture toughness of the studied ceramics. The main advantage of this method over other methods [35, 89, 114–124] is its simplicity which does not require much time and cost to perform the test. Only the method that is as easy as this one is the Vickers indentation method widely used for assessing fracture toughness of ceramics [25–27].

A series of SENB samples were prepared from those mentioned above, by producing a 0.1 mm wide notch along the sample thickness dimension. The loading unit with a distance between the supporting rollers of 30 mm was used for the three-point bending of samples. The average K_{Ic} value for each material was estimated based on five measurements.

A Malvern Panalytical X-ray diffractometer in Cu K_α irradiation mode was used for X-ray diffraction (XRD) analysis.

For microstructure and fractography studies, a scanning electron microscope (SEM) Carl Zeiss EVO-40XVP was utilized. Images of microstructure in the back-scattered diffraction (BSD) imaging mode and fractography images in the secondary electron (SE) imaging mode were thoroughly analyzed. An INCA Energy 350 system was utilized for an energy-dispersive X-ray (EDX) microanalysis of the studied ceramics.

7.3 Results and Discussion

7.3.1 The Modeling of Mechanical Behavior of the Macrocomposite Constituents

The design of the ceramic inserts for protective metal-ceramic macrocomposite plates has been developed. These inserts as constituents of the macrocomposite serve as the second-level structure for energy dissipation (for safety purposes), whereas metallic constituents serve as the front (first-level) structure. To assess the effectiveness of the developed protective macrocomposite, a model of a macrocomposite plate was considered. The dynamics of a body moving through the plate were analyzed due to a change in the body velocity, given the elastic characteristics of the macrocomposite constituents, namely, ceramic inserts and stainless steel building platform.

The velocity was calculated using the energy spent to fracture ceramic inserts as a part of the total energy dissipated by the protective macrocomposite plate.

A linear change in the velocity of the moving body is assumed, as it travels a distance of several millimeters in a short time interval (about 0.01 s). The total displacement of a layer in the direction of the moving body is assumed to be 4 mm.

The principle of parallel elastic components was used to solve the task of damping the energy of the moving body. For this purpose, the equation of dynamics was applied, which describes the total stiffness factor of the components [125]:

$$\sum_{i=1}^{n} k_i = \frac{m\left(v_{j-1}^2 - v_j^2\right)}{u_n^2} \tag{7.1}$$

where n is the number of parallel elastic components; k_i ($i = 1$ *to* n) is the stiffness of the i-th component; m is the mass of the moving body; v_{j-1} and v_j are velocities of the moving body before and after passing through the j-th layer, respectively; u_n is the total displacement in the direction parallel to the body movement.

For the calculation, the following parameters were used (Table 7.2): mass of the moving body m; total displacement $u_n = 4$ mm; time interval $\Delta t_j = 0.01$ s; velocities of the moving body before ($v_{j\text{-}1}$) and after (v_j) passing through the j-th layer; deceleration of the moving body a_j upon passing through the j-th layer; stiffness k_j of the j-th layer; energy E_j dissipated by the moving body upon passing through the j-th layer. The calculation was performed for a two-layer macrocomposite.

The total energy of the moving body dissipated in the protective macrocomposite plate is 3791 J that is according to the literary data presented for the set dynamic conditions [126, 127].

In terms of fracture toughness, the reliability can be assessed using a well-known equation [128] describing the energy γ_j spent to form a fracture surface:

$$\gamma_j = \frac{K_{Ic}^2}{2E} \tag{7.2}$$

where K_{Ic} is the critical SIF of material of the j-th layer component; E is Young's modulus of the material.

Table 7.2 The data of the calculation of damping parameters

No.	Layer	m, kg	$v_{j\text{-}1}$, m/s	v_j, m/s	a_j, m/s^2	k_j, kg/μm	E_j, J	p_j, number	γ_j, J	n_j, number
1	L1	11.7×10^{-3}	805	505	3×10^4	29	2299.1	24	54.45	1.76
2	L2	11.7×10^{-3}	505	0	5.05×10^4	19	1491.9	24	54.45	1.14
Total							3791.0			2.90

Using the edge flaking approach developed in the study [129] and an average crack length formed under a certain indentation load in alumina based ceramics [1, 58], the parameter p_j was calculated (Table 7.2), which is the flaking distance to the crack length ratio. For the j-th layer, a parallel elastic components number n_j was calculated based on the obtained values of energy E_j dissipated by the moving body upon passing through the j-th layer and the energy γ_j spent to form a unit fracture surface (Table 7.2). It was found that the total number of parallel elastic components should be not less than 2.9.

Preliminary conclusions can be drawn as follows:

(1) *Impact of flexural strength on energy dissipation.* The value n = 200 (number of inserts of size 10 × 10 × 20 mm^3 in a second-level structure of a single macrocomposite block) fits well with the above requirements. This second-level structure provides the complete damping of the retaining energy of the moving body (weight of 11.7 g, initial velocity of 805 m/s) by ceramic inserts having a flexural strength of about 240 MPa.

(2) *Impact of microhardness, edge flaking, and fracture toughness on energy dissipation.* As a result of the above calculations, 3 parallel elastic components, i.e. three layers consisting of ceramic inserts of size 10 × 10 × 20 mm^3 having flexural strength of about 240 MPa and fracture toughness of about 3.3 MPa·$m^{1/2}$ should provide complete dissipation of energy of the moving body.

7.3.2 Phase Balance in the Al_2O_3-based Ceramics as Candidate Materials for the Inserts

The evolution of phase compositions of three variants of Al_2O_3-based ceramics has been analyzed. In general, the tetragonal (t) and monoclinic (m) phases of t-ZrO_2, along with the α-Al_2O_3 phase were detected in these ceramics. The XRD pattern of variant 1 exhibited peaks of the α-Al_2O_3 phase and the t-ZrO_2 phase (Fig. 7.1a). For variant 2, only peaks of the α-Al_2O_3 phase were detected (Fig. 7.1b). In contrast, for variant 3, peaks of the α-Al_2O_3, m-ZrO_2, and t-ZrO_2 phases were identified (Fig. 7.1c). The phase fractions were estimated as follows (Table 7.3): α-Al_2O_3 phase (93.57 wt%) and t-ZrO_2 phase (6.43 wt%) for variant 1; α-Al_2O_3 phase (100 wt%) for variant 2; α-Al_2O_3 phase (96.80 wt%), m-ZrO_2 phase (1.22 wt%), and t-ZrO_2 phase (1.98 wt%) for variant 3. Small amounts of the t-ZrO_2 and m-ZrO_2 phases formed in the ceramics of variants 1 and 3 are related to their initial chemical compositions.

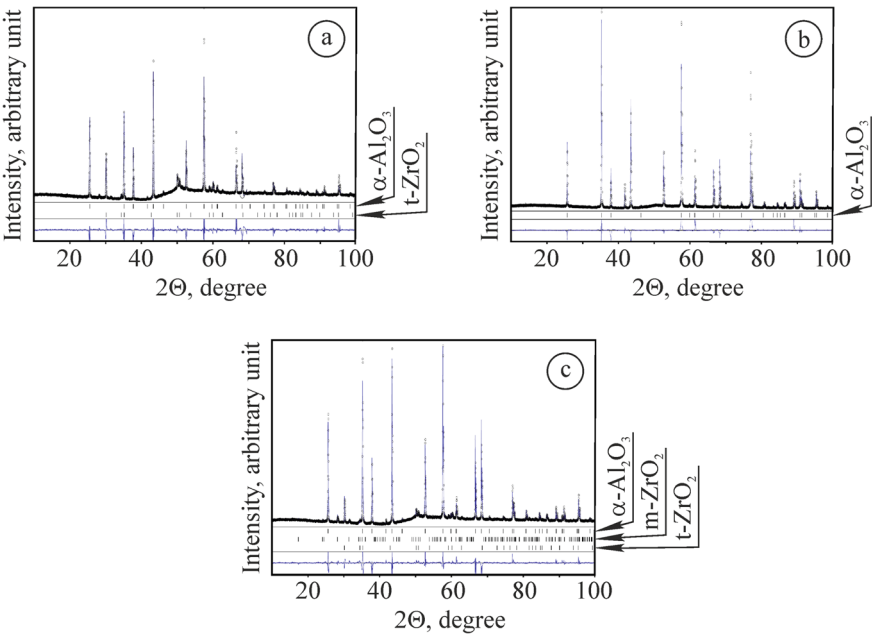

Fig. 7.1 XRD patterns of Al_2O_3 based ceramics of **a** variant 1, **b** 2, and **c** 3 (Table 7.1). The arrows indicate **a** the α-Al_2O_3, t-ZrO_2, **b** α-Al_2O_3, and **c** α-Al_2O_3, m-ZrO_2, t-ZrO_2 phases, respectively

Table 7.3 Phase composition of the studied materials

Phase	Phase fractions for series		
	1	2	3
α-Al_2O_3	93.57	100.00	96.80
t-ZrO_2	6.43	–	1.98
m-ZrO_2	–	–	1.22

Note Values of phase fractions are given in wt%

7.3.3 Microstructure, Physical, and Mechanical Properties of the Al_2O_3-based Ceramics

High sinterability of the ceramic of variant 1 was attained by adding small amounts of MgO, SiO_2, Fe_2O_3, and ZrO_2 as sintering aids. As a result, this ceramic showed density close to the theoretical one [111] and excellent porosity (Table 7.1). The microstructure of the α-Al_2O_3 matrix phase grains of dark-gray color with more or less uniformly distributed round-shaped particles of a second phase of light-gray color, 0.5–4.0 μm in size is characteristic of this ceramic (Fig. 7.2a). These round-shaped particles belong to the t-ZrO_2 phase, which was revealed by XRD analysis

(Table 7.3), as element Zr was detected by EDX analysis only in the mentioned particles (Table 7.4). Besides, elements Mg, Si, and Fe were also detected (Table 7.4).

This ceramic showed quite low levels of microhardness (10.5 ± 2.7 GPa, see Fig. 7.3a) and flexural strength (175 ± 5 MPa, see Fig. 7.3b), but comparatively high fracture toughness (3.3 ± 0.3 MPa·m$^{1/2}$, see Fig. 7.3c).

Rare pores of about 0.5–2.0 μm size were observed in an SEM microstructure image taken at higher magnification (Fig. 7.4a).

Although flexural strength of this ceramic is comparatively low, its high fracture toughness is attained due to the implementation of high-energy fracture micromechanism (Figs. 7.2b and 7.4b). The striations on the large cleavage facets behind the multiple second-phase microparticles, which are oriented perpendicular to the crack growth direction, evidenced quasi-brittle crack relaxation due to its retardation at these sites. However, a low level of flexural strength does not provide sufficient reliability for this ceramic to be applied as material for inserts.

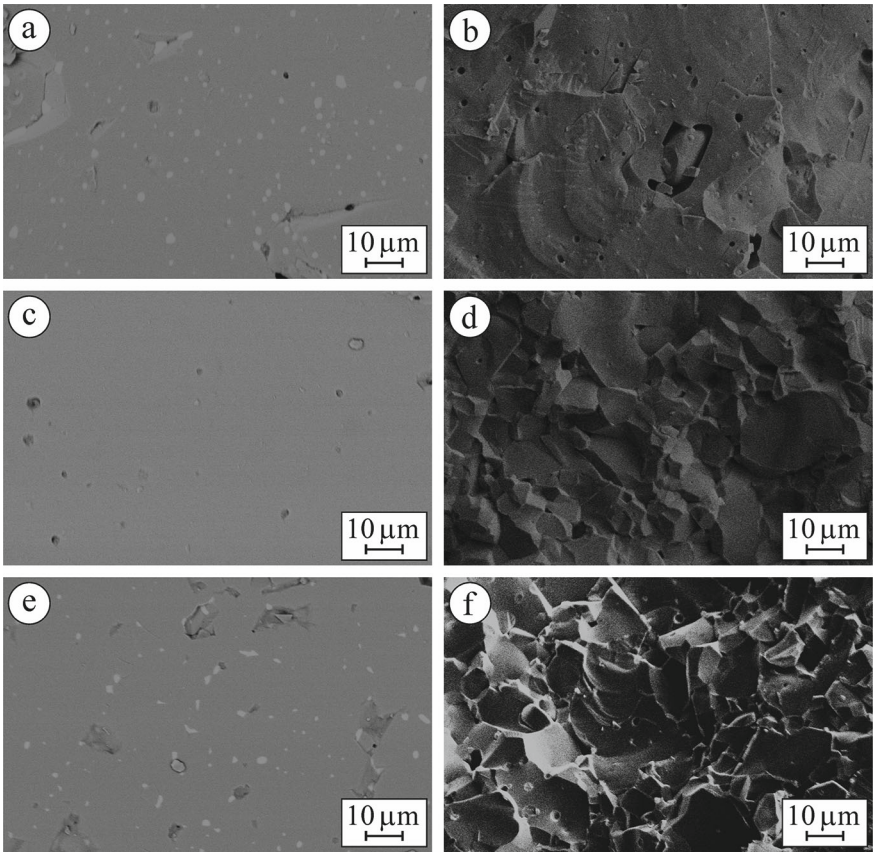

Fig. 7.2 SEM **a, c, e** microstructures (BSD images) and **b, d, f** fractography (SE images) of the Al_2O_3 based ceramic samples of **a, b** variant 1, **c, d** 2, and **e, f** 3 (Table 7.1) taken at low magnification

Table 7.4 The data of the EDX spectra for the ceramics of variants 1–3

Chemical element and X-ray series	Variant					
	1		2		3	
	wt%	at%	wt%	at%	wt%	at%
O K	39.31	52.69	35.24	48.20	32.39	46.77
Mg K	0.26	0.23	0.34	0.31	0.16	0.15
Al K	58.19	46.24	63.12	51.21	59.99	51.39
Si K	0.09	0.07	–	–	–	–
Fe L	1.77	0.68	–	–	–	–
Ga L	–	–	0.09	0.03	–	–
Zr L	0.38	0.09	–	–	5.36	1.36
Pd L	–	–	1.21	0.25	0.58	0.13
Hf M	–	–	–	–	1.52	0.20

The moderate density of the ceramic of variant 2 (3.89 g/cm^3) and corresponding porosity of 2.36% (Table 7.1), which are close to those of high-performance alumina based ceramics [1, 58], were ensured due to the adding of minor amounts of sintering aids such as MgO, Ga_2O_3, and PdO. Elements Mg, Ga, and Pd were detected by EDX analysis (Table 7.4). Here, a concept of the "nano + micro"-grained alumina based ceramic has been developed. A microstructure image of this ceramic (Fig. 7.2c) showed the uniform α-Al_2O_3 matrix phase (Table 7.3) with moderate porosity and rare oxide conglomerates. Such microstructure provided comparatively high levels of microhardness, flexural strength, and fracture toughness (13.7 ± 1.1 GPa, 248 ± 15 MPa, and 3.3 ± 0.3 MPa·m$^{1/2}$, see Fig. 7.3a–c). In a SEM microstructure image taken at higher magnification, oxide conglomerates 0.5–2.0 μm in size were observed (Fig. 7.4a).

The high fracture toughness of the ceramic of variant 2 is likely due to the fine-grained microstructure without visible defects both at grain boundaries and within the grains. As a result, mixed fracture comprising cleavage facets along larger grains and crack growth along the boundaries of small grains and their agglomerates occurs (Figs. 7.2d and 7.4d) confirming thus the implementation of the above concept of the "nano + micro"-grained ceramic. The latter micromechanism as more energy-consuming was found to be dominant. This has provided the corresponding level of fracture toughness of the ceramic and, as a result, its sufficient reliability when applied in the ceramic macrolayers of a protective composite.

Density of the ceramic of variant 3 (3.91 g/cm^3) is close to that of variant 2 (Table 7.1). Corresponding porosity of 1.91% is also close to that of high-performance alumina based ceramics [1, 58]. This was provided by adding small percentages of MgO, ZrO_2, PdO, and HfO_2.

Uniform microstructure of grains of the α-Al_2O_3 matrix phase of dark-gray color with randomly distributed both the particles of a second phase of light-gray color and rare nanosized pores observed in SEM images (Figs. 7.2e and 7.4e) is characteristic

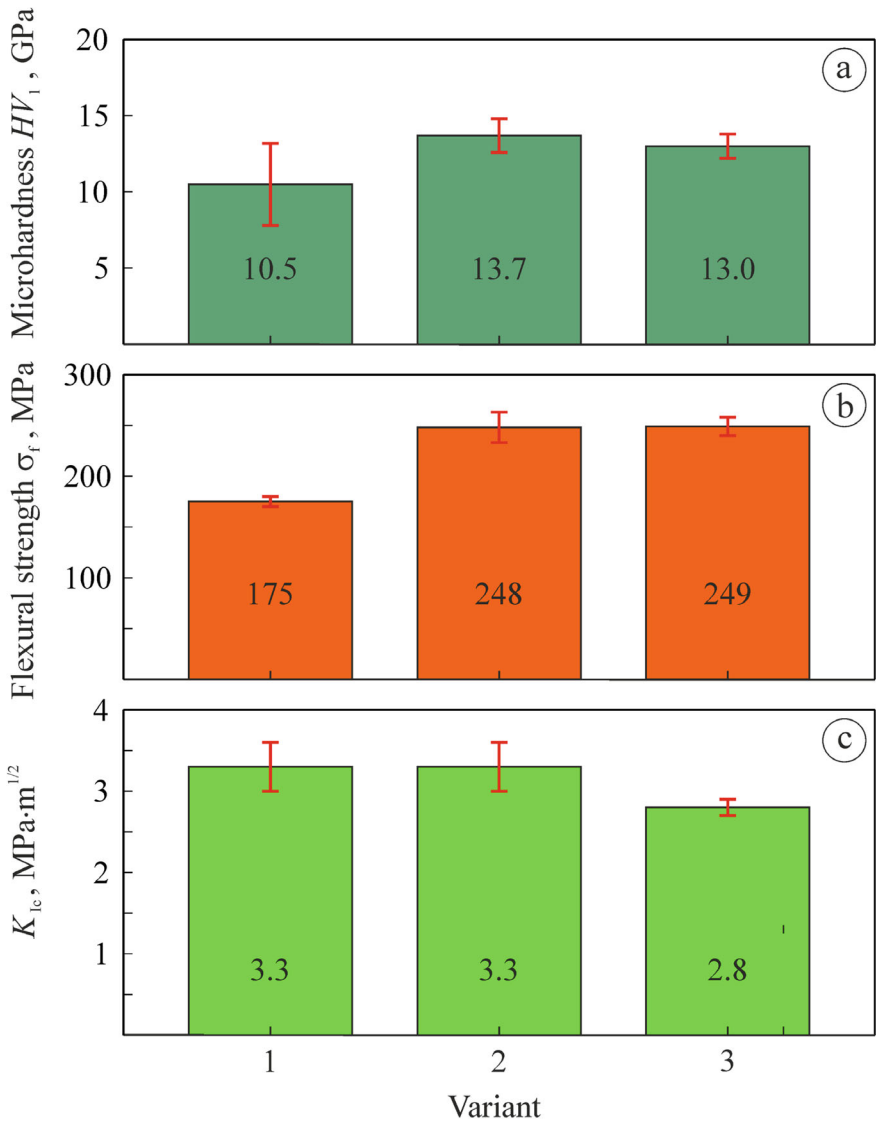

Fig. 7.3 Microhardness HV_1 **a**, flexural strength σ_f **b**, and fracture toughness K_{Ic} **c** of the studied variants of ceramics (Table 7.1). The numbers inside the bars indicate the average values of the corresponding parameters. The red bars show the standard deviation for the corresponding values

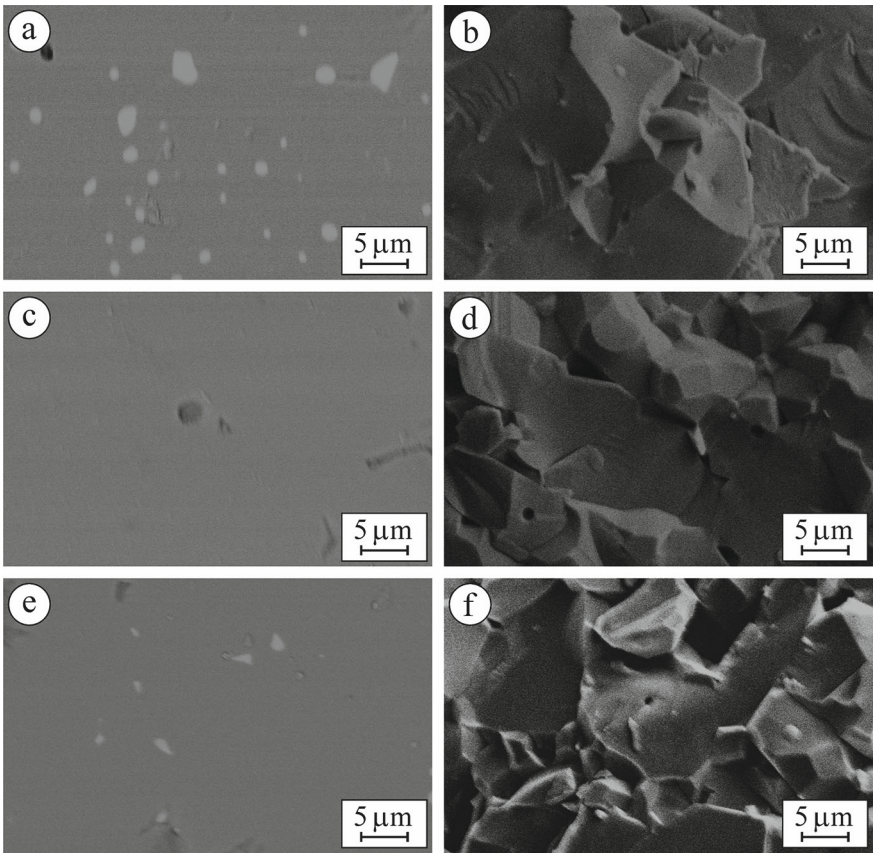

Fig. 7.4 SEM **a, c, e** microstructures (BSD images) and **b, d, f** fractography (SE images) of the Al_2O_3 based ceramic samples of **a, b** variant 1, **c, d** 2, and **e, f** 3 (Table 7.1) taken at high magnification

of the ceramic of this variant. The second phase particles 0.2–2.5 μm in size are of irregular shape, mostly with sharp corners. Small percentages of the m-ZrO_2 and t-ZrO_2 phases were detected in this ceramic by XRD analysis (Table 7.3) and element Zr was revealed by EDX analysis only in these particles. However, it was impossible to distinguish particles of the separate (t-ZrO_2 and m-ZrO_2) phases. Such microstructure provided moderate microhardness and flexural strength of the ceramic (13.0 ± 0.8 GPa and 249 ± 9 MPa, respectively, see Fig. 7.3). However, this material having fracture toughness of 2.8 ± 0.1 MPa·$m^{1/2}$ is inferior to the ceramics of variants 1 and 2 (Fig. 7.3c).

Comparatively low fracture toughness of the ceramic of variant 3 is probably a result of the implemented low-energy fracture micromechanism. As can be seen in the SEM images of the fracture surface of a tested sample, the second phase particles of irregular shape pulled out of the α-Al_2O_3 phase grains during crack

growth evidence its low cohesion to the matrix (Figs. 7.2f and 7.4f). Although a frequent change in cleavage plane orientation observed in the images argues in favor of high-energy fracture micromechanism [37], local weakening around second-phase particles contributes to the losses in fracture toughness of this material.

Given the levels of mechanical characteristics estimated for the ceramic of variant 2, this material may provide appropriate reliability when applied in protective metal-ceramic macrocomposites.

7.4 Conclusions

1. Based on the calculation data and results of mechanical tests and fracture surface analysis, it was revealed that flexural strength, microhardness, edge flaking, and fracture toughness are crucial for attaining high energy dissipation values in the studied Al_2O_3-based ceramics. Revealing the optimum combination of these mechanical properties enabled us to develop an improved geometry of ceramic inserts forming a layer of the protective metal-ceramic macrocomposite.
2. A concept of "nano + micro"-grained alumina based ceramics for improving the functionality of the state-of-the-art protective macrocomposite plates was developed. Therefore, alumina based ceramic material sintered in the appropriate mode can be considered promising for application in protective metal-ceramic macrocomposite layers.

Acknowledgements The authors are thankful to the staff of the Scientific Equipment Collective Use Center "Laboratory of Advanced Technologies, Creation and Physicochemical Analysis of New Substances and Functional Materials" at Lviv Polytechnic National University (https://lpnu.ua/ckkno) for their kind help in performing X-ray diffraction studies.

References

1. J.E. Blendell, The origins of internal stresses in polycrystalline alumina and their effects on mechanical properties. Cambridge (1979). http://hdl.handle.net/1721.1/44234
2. I. Danilenko, G. Lasko, I. Brykhanova et al., The peculiarities of structure formation and properties of zirconia-based nanocomposites with addition of Al_2O_3 and NiO. Nanoscale Res. Lett. **12**, 125 (2017). https://doi.org/10.1186/s11671-017-1901-7
3. A. Nastic, A. Merati, M. Bielawski et al., Instrumented and Vickers indentation for the characterization of stiffness, hardness and toughness of zirconia toughened Al_2O_3 and SiC armor. J. Mater. Sci. Technol. **31**(8), 773–783 (2015). https://doi.org/10.1016/j.jmst.2015.06.005
4. O.M. Romaniv, I.V. Zalite, V.M. Simin'kovych et al., Effect of the concentration of zirconium dioxide on the fracture resistance of Al_2O_3–ZrO_2 ceramics. Mater. Sci. **31**(5), 588–594 (1996). https://doi.org/10.1007/BF00558793
5. M.Y. Smyrnova-Zamkova, O.K. Ruban, O.I. Bykov et al., The influence of the ZrO_2 solid solution amount on the physicochemical properties of Al_2O_3–ZrO_2–Y_2O_3–CeO_2 powders.

Powder Metall. Met. Ceram. **60**(3–4), 129–141 (2021). https://doi.org/10.1007/s11106-021-00222-4
6. Y. Wang, W. Qin, Z. Deng et al., High strength Y_2O_3-stabilized zirconia continuous fibers up to 1500 °C: crystalline phase and microstructure evolution as well as grain growth kinetics. J. Alloys Compd. **976**, 173165 (2024). https://doi.org/10.1016/j.jallcom.2023.173165
7. O.P. Ostash, B.D. Vasyliv, V.Y. Podhurs'ka et al., Optimization of the properties of 10Sc1CeSZ-NiO composite by the redox treatment. Mater. Sci. **46**(5), 653–658 (2011). https://doi.org/10.1007/s11003-011-9337-1
8. V. Kulyk, Z. Duriagina, B. Vasyliv et al., Effect of sintering temperature on crack growth resistance characteristics of yttria-stabilized zirconia. Acta Phys. Pol. A **141**(4), 323–327 (2022). http://przyrbwn.icm.edu.pl/APP/PDF/141/app141z4p18.pdf
9. O.V. Sukhova, Influence of mechanisms of structure formation of interfaces in composites on their properties. Metallofiz. Noveishie Tekhnol. **31**(7), 1001–1012 (2009)
10. F. Mayinger, R. Buser, M. Laier et al., Impact of the material and sintering protocol, layer thickness, and thermomechanical aging on the two-body wear and fracture load of 4Y-TZP crowns. Clin. Oral Investig. **26**(11), 6617–6628 (2022). https://doi.org/10.1007/s00784-022-04616-5
11. V. Korendiy, O. Kachur, V. Zakharov et al., Experimental study of the lap motion trajectory of vibratory finishing machine. Vib. Proced. **46**, 1–7 (2022). https://doi.org/10.21595/vp.2022.23002
12. V.G. Efremenko, Y.G. Chabak, V.I. Fedun et al., Formation mechanism, microstructural features and dry-sliding behaviour of "Bronze/WC carbide" composite synthesised by atmospheric pulsed-plasma deposition. Vacuum **185**, 110031 (2021). https://doi.org/10.1016/j.vacuum.2020.110031
13. K. Nonaka, M. Teramae, G. Pezzotti, Evaluation of the effect of high-speed sintering and specimen thickness on the properties of 5 mol% yttria-stabilized dental zirconia sintered bodies. Materials **15**(16), 5685 (2022). https://doi.org/10.3390/ma15165685
14. B.D. Vasyliv, V.Y. Podhurs'ka, O.P. Ostash et al., Influence of reducing and oxidizing media on the physicomechanical properties of ScCeSZ–NiO and YSZ–NiO ceramics. Mater. Sci. **49**(2), 135–144 (2013). https://doi.org/10.1007/s11003-013-9593-3
15. ISO 6872, Dentistry–Ceramic Materials. International Organization of Standardization: Geneva, Switzerland (2015)
16. B.R. Lawn, A.G. Evans, D.B. Marshall, Elastic/plastic indentation damage in ceramics: the median/radial crack system. J. Am. Ceram. Soc. **63**(9–10), 574–581 (1980). https://doi.org/10.1111/j.1151-2916.1980.tb10768.x
17. V. Kulyk, I. Izonin, V. Vavrukh et al., Prediction of hardness, flexural strength, and fracture toughness of ZrO_2 based ceramics using ensemble learning algorithms. Acta Metall. Slovaca **29**(2), 93–103 (2023). https://doi.org/10.36547/ams.29.2.1819
18. ASTM E 384-11, Standard test method for Knoop and Vickers hardness of materials. ASTM Int. (2011). https://doi.org/10.1520/E0384-11
19. ASTM C 1327-03, Standard test method for Vickers indentation hardness of advanced ceramics. ASTM Int. (2003). https://doi.org/10.1520/C1327-03
20. B.R. Lawn, M.V. Swain, Microfracture beneath point indentations in brittle solids. J. Mater. Sci. **10**(1), 113–122 (1975). https://doi.org/10.1007/BF00541038
21. A.G. Evans, E.A. Charles, Fracture toughness determinations by indentation. J. Am. Ceram. Soc. **59**(7–8), 371–372 (1976). https://doi.org/10.1111/j.1151-2916.1976.tb10991.x
22. R.F. Cook, G.M. Pharr, Direct observation and analysis of indentation cracking in glasses and ceramics. J. Am. Ceram. Soc. **73**(4), 787–817 (1990). https://doi.org/10.1111/j.1151-2916.1990.tb05119.x
23. L.A. Dobrzański, L.B. Dobrzański, A.D. Dobrzańska-Danikiewicz, Additive and hybrid technologies for products manufacturing using powders of metals, their alloys and ceramics. Arch. Mater. Sci. Eng. **102**(2), 59–85 (2020). https://doi.org/10.5604/01.3001.0014.1525
24. T.A. Prikhna, O.P. Ostash, A.S. Kuprin et al., A new MAX phases-based electroconductive coating for high-temperature oxidizing environment. Compos. Struct. **277**, 114649 (2021). https://doi.org/10.1016/j.compstruct.2021.114649

25. J. Lankford, Indentation microfracture in the Palmqvist crack regime: implications for fracture toughness evaluation by the indentation method. J. Mater. Sci. Lett. **1**(11), 493–495 (1982). https://doi.org/10.1007/BF00721938
26. G.R. Anstis, P. Chantikul, B.R. Lawn et al., A critical evaluation of indentation techniques for measuring fracture toughness: I, direct crack measurement. J. Am. Ceram. Soc. **64**(9), 533–538 (1981). https://doi.org/10.1111/j.1151-2916.1981.tb10320.x
27. K. Niihara, A fracture mechanics analysis of indentation-induced Palmqvist crack in ceramics. J. Mater. Sci. Lett. **2**(5), 221–223 (1983). https://doi.org/10.1007/BF00725625
28. B. Vasyliv, V. Kulyk, Z. Duriagina et al., Estimation of the effect of redox treatment on microstructure and tendency to brittle fracture of anode materials of YSZ-NiO(Ni) system. East Eur. J. Enterp. Technol. **108/6**(12):61–71 (2020). https://doi.org/10.15587/1729-4061.2020.218291
29. K.W. Jeong, J.S. Han, G.U. Yang et al., Influence of preaging temperature on the indentation strength of 3Y–TZP aged in ambient atmosphere. Materials **14**, 2767 (2021). https://doi.org/10.3390/ma14112767
30. V.G. Efremenko, A.G. Lekatou, Y.G. Chabak et al., Micromechanical, corrosion and wet sliding wear behaviours of Co-28Cr-6Mo alloy: wrought versus LPBF. Mater. Today Commun. **35**, 105936 (2023). https://doi.org/10.1016/j.mtcomm.2023.105936
31. O.P. Ostash, A.D. Ivasyshyn, B.D. Vasyliv et al., High-temperature and cyclic corrosion crack resistance of alloys of the Ti–Si–Al–Zr system. Mater. Sci. **42**(3), 330–343 (2006). https://doi.org/10.1007/s11003-006-0087-4
32. S. Ozkan, S.J. Kim, D.N. Miller et al., A new approach to fuel cell electrodes: lanthanum aluminate yielding fine Pt nanoparticle exsolution for oxygen reduction reaction. Adv. Energy Mater. **14**(15), 2303025 (2024). https://doi.org/10.1002/aenm.202303025
33. B.D. Vasyliv, A.D. Ivasyshyn, O.P. Ostash et al., Kinetics of corrosion-fatigue cracks in Ti–Si cermet composite. Mater. Sci. **38**(2), 220–224 (2002). https://doi.org/10.1023/A:1020990103898
34. B. Alfahed, A. Alayad, The effect of sintering temperature on Vickers microhardness and flexural strength of translucent multi-layered zirconia dental materials. Coatings **13**(4), 688 (2023). https://doi.org/10.3390/coatings13040688
35. J. Kübier, Fracture toughness of ceramics using the SEVNB method: from a preliminary study to a standard test method, in *Fracture Resistance Testing of Monolithic and Composite Brittle Materials*, ed. by J. Salem et al. (ASTM International, 2002), pp. 93–106. https://doi.org/10.1520/STP10473S
36. A. Shearer, M. Montazerian, B. Deng et al., Zirconia-containing glass-ceramics: from nucleating agent to primary crystalline phase. Int. J. Ceram. Eng. Sci. **6**(2), e10200 (2024). https://doi.org/10.1002/ces2.10200
37. R.O. Ritchie, Mechanisms of fatigue-crack propagation in ductile and brittle solids. Int. J. Fract. **100**(1), 55–83 (1999). https://doi.org/10.1023/A:1018655917051
38. V. Kulyk, B. Vasyliv, Z. Duriagina et al., The effect of sintering temperature on phase-related peculiarities of the microstructure, flexural strength, and fracture toughness of fine-grained ZrO_2–Y_2O_3–Al_2O_3–CoO–CeO_2–Fe_2O_3 ceramics. Crystals **14**(2), 175 (2024). https://doi.org/10.3390/cryst14020175
39. L. Du, J. Yang, X. Zhong et al., Synthesized by coprecipitation method for controlled phase structures of 5YSZ. J. Mater. Res. Technol. **29**, 5473–5483 (2024). https://doi.org/10.1016/j.jmrt.2024.02.222
40. V. Podhurska, B. Vasyliv, O. Ostash et al., Influence of treatment temperature on microstructure and properties of YSZ–NiO anode materials. Nanoscale Res. Lett. **11**, 93 (2016). https://doi.org/10.1186/s11671-016-1306-z
41. J.-H. Yun, Y.-J. Jeon, M.-S. Kang, Analysis of elastic properties of polypropylene composite materials with ultra-high molecular weight polyethylene spherical reinforcement. Materials **15**(16), 5602 (2022). https://doi.org/10.3390/ma15165602
42. A. Unnadkat, L. Kirby, S. Kulanthaivel et al., The effect of sintering on zirconia manufactured via suspension-enclosing projection stereolithography for dental applications: an in vitro study. Materials **17**(1), 14 (2023). https://doi.org/10.3390/ma17010014

43. O.P. Ostash, A.D. Ivasyshyn, B.D. Vasyliv et al., Influence of the structure and asymmetry of loading cycles on the cyclic crack resistance of Ti–Si composites. Mater. Sci. **38**(1), 55–61 (2002). https://doi.org/10.1023/A:1020120714703
44. Y.G. Chabak, K. Shimizu, V.G. Efremenko et al., Microstructure and phase elemental distribution in high-boron multi-component cast irons. Int. J. Miner. Metall. Mater. **29**, 78–87 (2022). https://doi.org/10.1007/s12613-020-2135-8
45. I. Izonin, R. Tkachenko, M. Gregus et al., Hybrid classifier via PNN-based dimensionality reduction approach for biomedical engineering task. Procedia Comput. Sci. **191**, 230–237 (2021). https://doi.org/10.1016/j.procs.2021.07.029
46. A.K. Lakshya, K.K. Jha, C. Bhardwaj et al., Attaining translucency in binder/additive-free, nanograined, tetragonal 1.5 mol.% yttria-stabilized zirconia ceramics. Materialia **34**, 102075 (2024). https://doi.org/10.1016/j.mtla.2024.102075
47. O. Kachur, V. Korendiy, Dynamic behavior of vibratory screening conveyor equipped with crank-type exciter, in *DSMIE 2023: Advances in Design, Simulation and Manufacturing VI*, ed. by V. Ivanov et al. Lecture Notes in Mechanical Engineering (2023), pp. 44–53. https://doi.org/10.1007/978-3-031-32774-2_5
48. S.G. Giniyatova, A.L. Kozlovskiy, R.I. Shakirzyanov et al., Structural, dielectric, and mechanical properties of high-content cubic zirconia ceramics obtained via solid-state synthesis. Appl. Sci. **13**(19), 10989 (2023). https://doi.org/10.3390/app131910989
49. P. Uasuwan, N. Juntavee, A. Juntavee, Flexural strength of novel glass infiltrated monochrome and multilayer high yttrium oxide containing zirconia upon various sintered cooling rates. J. Prosthodont. **33**(S1), 47–59 (2024). https://doi.org/10.1111/jopr.13872
50. I.G. Alhindawy, H. Gamal, A.A. Zaher et al., La/Nd-doped zirconium oxide: impact of zirconia phase transition on gamma-ray shielding properties. J. Phys. Chem. Solids **187**, 111828 (2024). https://doi.org/10.1016/j.jpcs.2023.111828
51. G.P. Alparone, D. Penney, E. Jewell et al., The effect of sliding speed on the tribological properties of ceramic materials. Materials **16**(23), 7252 (2023). https://doi.org/10.3390/ma16237252
52. B.V. Efremenko, K. Shimizu, N. Espallargas et al., High-temperature solid particle erosion of Cr–Ni–Fe–C arc cladded coatings. Wear **460–461**, 203439 (2020). https://doi.org/10.1016/j.wear.2020.203439
53. J.-M. Jung, G.-N. Kim, Y.-H. Koh et al., Manufacturing and characterization of dental crowns made of 5-mol% yttria stabilized zirconia by digital light processing. Materials **16**(4), 1447 (2023). https://doi.org/10.3390/ma16041447
54. R.H. Purba, K. Kusumoto, K. Shimizu et al., Influence of tempering temperature on abrasive-wear performance of high-chromium-based multicomponent white cast iron. Lubricants **11**(7), 285 (2023). https://doi.org/10.3390/lubricants11070285
55. Y. Wang, X. Liu, S. Pan et al., Local structure regulation and spectroscopy study of blue cubic zirconia. CrystEngComm **25**(11), 1582–1588 (2023). https://doi.org/10.1039/D2CE01674E
56. B.D. Vasyliv, V.Y. Podhurska, O.P. Ostash et al., Effect of a hydrogen sulfide-containing atmosphere on the physical and mechanical properties of solid oxide fuel cell materials, in *Nanochemistry, Biotechnology, Nanomaterials, and Their Applications*, vol. 214 (Springer Proceedings of Physics, 2018), pp. 475–485. https://doi.org/10.1007/978-3-319-92567-7_30
57. T.S. Cherepova, H.P. Dmytrieva, O.I. Dukhota et al., Properties of nickel powder alloys hardened with titanium carbide. Mater. Sci. **52**(2), 173–179 (2016). https://doi.org/10.1007/s11003-016-9940-2
58. D. Cao, K. Lv, Y. Bao et al., Thickness effect of an alumina-zirconia-mullite composite coating on the properties of zirconia. RSC Adv. **13**(4), 2736–2744 (2023). https://doi.org/10.1039/D2RA07549K
59. S. Liu, J. Zhang, Y. Tian et al., Preparation of Bi_2O_3–YSZ and YSB–YSZ composite powders by a microemulsion method and their performance as electrolytes in a solid oxide fuel cell. Materials **16**(13), 4673 (2023). https://doi.org/10.3390/ma16134673
60. T.M.B. Campos, C. Dos Santos, L.M.M. Alves et al., Minimally processed recycled yttria-stabilized tetragonal zirconia for dental applications: effect of sintering temperature on glass

infiltration. J. Mech. Behav. Biomed. Mater. **150**, 106311 (2024). https://doi.org/10.1016/j.jmbbm.2023.106311
61. P. Uasuwan, N. Juntavee, A. Juntavee, Flexural strength of high yttrium oxide-doped monochrome and multilayered fully stabilized zirconia upon various sintered cooling rates. J. Prosthodont. **32**(6) (2023). https://doi.org/10.1111/jopr.13692
62. Y. Zhang, C. Ren, J. Zhou et al., Influence of microwave heating on grain growth behavior and phase stability of nano Y_2O_3/La_2O_3 co-doped ZrO_2 ceramics. Ceram. Int. **50**(6), 8733–8741 (2024). https://doi.org/10.1016/j.ceramint.2023.12.190
63. V. Korendiy, O. Kachur, Dynamic behavior of a vibratory plate compactor working on a horizontal elastic-viscous-plastic surface, in *InterPartner 2022: Advanced Manufacturing Processes IV*, ed. by V. Tonkonogyi et al. Lecture Notes in Mechanical Engineering (2023), pp. 434–443. https://doi.org/10.1007/978-3-031-16651-8_41
64. S. Wu, S. Liu, Y. Chen et al., Optimization of the structure and morphology of monoclinic phase nanoscale zirconium dioxide. MRS Commun. **14**(4), 646–652 (2024). https://doi.org/10.1557/s43579-024-00578-9
65. Y. Kharchenko, Z. Blikharskyy, V. Vira et al., Nanostructural changes in a Ni/NiO cermet during high-temperature reduction and reoxidation, in *Nanomaterials and Nanocomposites, Nanostructure Surfaces, and Their Applications*, vol. 246 (Springer Proceedings of Physics, 2021), pp. 219–229. https://doi.org/10.1007/978-3-030-51905-6_17
66. Y.S. Romario, C. Bhat, M. Ramezani et al., Fabrication of translucent graded dental crown using zirconia-yttrium multi-slurry tape casting 3D printer. J. Mech. Behav. Biomed. Mater. **152**, 106406 (2024). https://doi.org/10.1016/j.jmbbm.2024.106406
67. O.P. Ostash, I.M. Andreiko, V.V. Kulyk et al., Influence of braking on the microstructure and mechanical behavior of railroad wheel steels. Mater. Sci. **48**, 569–574 (2013). https://doi.org/10.1007/s11003-013-9539-9
68. Y. Li, H. Sun, J. Song et al., Effect of two-step sintering on the mechanical and electrical properties of 5YSZ and 8YSZ ceramics. Materials **16**(5), 2019 (2023). https://doi.org/10.3390/ma16052019
69. B.D. Vasyliv, Improvement of the electric conductivity of the material of anode in a fuel cell by the cyclic redox thermal treatment. Mater. Sci. **46**(2), 260–264 (2010). https://doi.org/10.1007/s11003-010-9282-4
70. M.B. Hanif, S. Rauf, Z.U. Abadeen et al., Proton-conducting solid oxide electrolysis cells: relationship of composition-structure-property, their challenges, and prospects. Matter **6**(6), 1782–1830 (2023). https://doi.org/10.1016/j.matt.2023.04.013
71. V. Kulyk, Z. Duriagina, A. Kostryzhev et al., Effects of sintering temperature and yttria content on microstructure, phase balance, fracture surface morphology, and strength of yttria-stabilized zirconia. Appl. Sci. **12**(22), 11617 (2022). https://doi.org/10.3390/app122211617
72. Z.-G. Wang, W.-D. Chen, S.-F. Yan et al., Direct fabrication and characterization of zirconia thick coatings on zirconium hydride as a hydrogen permeation barrier. Coatings **13**(5), 884 (2023). https://doi.org/10.3390/coatings13050884
73. X. Zhu, G. Hou, J. Ma et al., Effect of Y_2O_3 doping content on phase composition, mechanical properties and cavitation erosion performance of ZrO_2 ceramics. Ceram. Int. **50**(9), 14718–14730 (2024). https://doi.org/10.1016/j.ceramint.2024.01.385
74. G.A. Gogotsi, S.N. Dub, E.E. Lomonova et al., Vickers and Knoop indentation behaviour of cubic and partially stabilized zirconia crystals. J. Eur. Ceram. Soc. **15**(5), 405–413 (1995). https://doi.org/10.1016/0955-2219(95)91431-M
75. V.V. Kulyk, B.D. Vasyliv, Z.A. Duriagina et al., The effect of water vapor containing hydrogenous atmospheres on the microstructure and tendency to brittle fracture of anode materials of YSZ–NiO(Ni) system. Arch. Mater. Sci. Eng. **108**(2), 49–67 (2021). https://doi.org/10.5604/01.3001.0015.0254
76. K. Tanaka, Elastic/plastic indentation hardness and indentation fracture toughness: the inclusion core model. J. Mater. Sci. **22**(4), 1501–1508 (1987). https://doi.org/10.1007/BF01233154

77. H. Charalambous, M.H. Jancich, P.W.F. Evans et al., Processing and characterization of the homologous $Zr_xTa_2O_{2x+5}$ series. Ceram. Int. **50**(9), 15848–15855 (2024). https://doi.org/10.1016/j.ceramint.2024.02.064
78. M. Alghauli, A.Y. Alqutaibi, S. Wille et al., 3D-printed versus conventionally milled zirconia for dental clinical applications: trueness, precision, accuracy, biological and esthetic aspects. J. Dent. **144**, 104925 (2024). https://doi.org/10.1016/j.jdent.2024.104925
79. B.D. Vasyliv, Initiation of a crack from the edge of a notch with oblique front in specimens of brittle materials. Mater. Sci. **38**(5), 724–728 (2002). https://doi.org/10.1023/A:1024222709514
80. F. Inchingolo, A.D. Inchingolo, I.A. Charitos et al., Inchingolo, ceramic biomaterials in dentistry: chemical structure and biosafety—a review and a bibliometric visual mapping on Scopus database. Eur. Rev. Med. Pharmacol. Sci. **28**(4), 1242–1258 (2024). https://doi.org/10.26355/eurrev_202402_35446
81. H. Gujjaramma, B.S. Krishna, K. Gurushantha et al., Phyllantus acidus mediated combustion method synthesised yttria stabilized zirconia, its application as photocatalyst and antibacterial agent. Desalin. Water Treat. **317**, 100301 (2024). https://doi.org/10.1016/j.dwt.2024.100301
82. H. Peng, Y. Yu, T. Shi et al., Effects of induction plasma spheroidization on properties of yttria-stabilized zirconia powders for thermal barrier coating applications. Materials **17**(7), 1518 (2024). https://doi.org/10.3390/ma17071518
83. J.P. Winczewski, S. Zeiler, S. Gabel et al., Additive manufacturing of 3D yttria-stabilized zirconia microarchitectures. Mater. Des. **238**, 112701 (2024). https://doi.org/10.1016/j.matdes.2024.112701
84. M.A. Ali Bash, S.A. Ajeel, R.A. Abbas et al., A direct laser sintering approach for the electrophoretic deposition overlay of yttria-stabilized zirconia on the surface of a thermal barrier coating system. Coatings **13**(10), 1695 (2023). https://doi.org/10.3390/coatings13101695
85. I. Sanchez, D. Axinte, Z. Liao et al., The effect of high strain rate impact in yttria stabilized zirconia. Mater. Des. **229**, 111908 (2023). https://doi.org/10.1016/j.matdes.2023.111908
86. I.M. Andreiko, V.V. Kulyk, O.P. Ostash, Resistance of steels of railroad wheels to corrosion-fatigue fracture. Mater. Sci. **47**, 608–612 (2012). https://doi.org/10.1007/s11003-012-9434-9
87. P. Gothwal, F. Singh, V. Chauhan et al., Effects of lithium ion irradiation on yttria-stabilized zirconia thin films: structural and optical investigations. J. Electron. Mater. **53**(9), 5204–5211 (2024). https://doi.org/10.1007/s11664-024-11230-6
88. H. Yoo, J. Kim, H. Lee et al., Phase formation and stabilization behavior of Ca-PSZ by post-heat treatment II: CaO*x*-ZrO_2(1–x) (x = 5–10 mol%). Metals **13**(10), 1659 (2023). https://doi.org/10.3390/met13101659
89. P. Khajavi, P.V. Hendriksen, J. Chevalier et al., Improving the fracture toughness of stabilized zirconia-based solid oxide cells fuel electrode supports: effects of type and concentration of stabilizer(s). J. Eur. Ceram. Soc. **40**(15), 5670–5682 (2020). https://doi.org/10.1016/j.jeurceramsoc.2020.05.042
90. B.R. Vaishnavi Krupa, C. Ghosh, S.K. Sinha et al., Reverse transition of ball milling induced m-Y_2O_3 nano-crystallites during in-situ annealing. Ceram. Int. **49**(14), 23522–23530 (2023). https://doi.org/10.1016/j.ceramint.2023.04.185
91. H. Li, W. Qian, Z. Zhang et al., The phase stability of t-ZrO_2 realized by grain size at cryogenic temperature in ZrO_2/TiO_2 composite. Mater. Des. **239**, 112741 (2024). https://doi.org/10.1016/j.matdes.2024.112741
92. S.N. Almohammed, B. Alshorman, L.A. Abu-Naba'a, Mechanical properties of five esthetic ceramic materials used for monolithic restorations: a comparative in vitro study. Ceramics **6**(2), 1031–1049 (2023). https://doi.org/10.3390/ceramics6020061
93. H. Sun, P. Tabrizian, A. Qambrani et al., Bio-inspired nacre-like zirconia/PMMA composites for chairside CAD/CAM dental restorations. Dent. Mater. **40**(2), 307–317 (2024). https://doi.org/10.1016/j.dental.2023.11.017
94. X. Fu, F. Zhang, W. Zhu et al., Mechanical properties and toughening mechanisms of promising Zr-Y-Ta-O composite ceramics. Coatings **13**(5), 855 (2023). https://doi.org/10.3390/coatings13050855

95. K. Hoggas, S. Benaissa, A. Cherouana et al., Mechanical behavior of transparent spinel fabricated by spark plasma sintering. Ceramics **6**(2), 1191–1209 (2023). https://doi.org/10.3390/ceramics6020072
96. S. Liu, J. Wang, Y. Chen et al., Tetragonal nanosized zirconia: hydrothermal synthesis and its performance as a promising ceramic reinforcement. Inorganics **11**(5), 217 (2023). https://doi.org/10.3390/inorganics11050217
97. G. Sokolowski, A. Szczesio-Wlodarczyk, M.I. Szynkowska-Jóźwik et al., The shear bond strength of resin-based luting cement to zirconia ceramics after different surface treatments. Materials **16**(15), 5433 (2023). https://doi.org/10.3390/ma16155433
98. H.-S. Lee, H. Ko, K. Heo et al., Dispersion control via crystal-phase modulation of yttrium-doped ZrO_2 nanoparticle sol. Colloids Surf A Physicochem Eng Asp **670**, 131476 (2023). https://doi.org/10.1016/j.colsurfa.2023.131476
99. N.C. Golota, Z.P. Fredin, D.P. Banks et al., Diamond rotors. J. Magn. Reson. **352**, 107475 (2023). https://doi.org/10.1016/j.jmr.2023.107475
100. T.F. Alghazzawi, G.M. Janowski, H. Ning et al., Qualitative SEM analysis of fracture surfaces for dental ceramics and polymers broken by flexural strength testing and crown compression. J. Prosthodont. **32**(5) (2023). https://doi.org/10.1111/jopr.13659
101. T.F. Alghazzawi, A comparison of failure loads for polycrystalline zirconia ceramics with varying amounts of yttria, glass-ceramics and polymers in two different test conditions. Polymers **15**(23), 4506 (2023). https://doi.org/10.3390/polym15234506
102. H. Shao, J. Zhu, X. Zhao et al., Additive manufacturing of magnesium-doped calcium silicate/zirconia ceramic scaffolds with projection-based 3D printing: Sintering, mechanical and biological behavior. Ceram. Int. **50**(6), 9280–9292 (2024). https://doi.org/10.1016/j.ceramint.2023.12.244
103. S.S. Savka, D.I. Popovych, A.S. Serednytski, Molecular dynamics simulations of the formation processes of zinc oxide nanoclusters in oxygen environment, in *Nanophysics, Nanomaterials, Interface Studies, and Applications*, vol. 195 (Springer Proceedings of Physics, 2017), pp. 145–156. https://doi.org/10.1007/978-3-319-56422-7_11
104. M.M.H. Parvez, M.A. Daud, Effects of TiO_2 on the mechanical and physical properties of Fe_2O_3-doped yttria-stabilized zirconia for electrolyte of solid oxide fuel cells. Results Surf. Interfaces **16**, 100239 (2024). https://doi.org/10.1016/j.rsurfi.2024.100239
105. V. Korendiy, O. Kachur, V. Gursky et al., Kinematic and dynamic analysis of three-mass oscillatory system of vibro-impact plate compactor with crank excitation mechanism. Vib. Proced. **40**, 14–19 (2022). https://doi.org/10.21595/vp.2022.22393
106. P. Prysyazhnyuk, D. Di Tommaso, The thermodynamic and mechanical properties of Earth-abundant metal ternary boride $Mo_2(Fe, Mn)_B2$ solid solutions for impact- and wear-resistant alloys. Mater. Adv. **4**, 3822–3838 (2023). https://doi.org/10.1039/D3MA00313B
107. J.C.C.A. Diaz, E.N.D.S. Muccillo, R. Muccillo, Porous 8YSZ ceramics prepared with alkali halide sacrificial additives. Materials **16**(9), 3509 (2023). https://doi.org/10.3390/ma16093509
108. P. Jeevankumar, P. Rose, A. Rajanikanth et al., Net-shaping of advanced ceramic composites by gelcasting into precision molds made by rapid-prototyping. Int. J. Appl. Ceram. Technol. **21**(2), 664–674 (2024). https://doi.org/10.1111/ijac.14568
109. Y. Yue, Y. Zhu, Z. Li, Preparation and cutting performance study of YSZ-toughened PcBN superhard tools. RSC Adv. **13**(23), 15616–15623 (2023). https://doi.org/10.1039/D3RA02079G
110. W. Huang, H. Qiu, Y. Zhang et al., Microstructure and phase transformation behavior of Al_2O_3–ZrO_2 under microwave sintering. Ceram. Int. **49**(3), 4855–4862 (2023). https://doi.org/10.1016/j.ceramint.2022.09.376
111. G. Savage, H. Newman, *An Illustrated Dictionary of Ceramics* (Thames & Hudson, 1985), p. 265
112. Q. Flamant, F. García Marro, J.J. Roa Rovira et al., Hydrofluoric acid etching of dental zirconia. Part 1: Etching mechanism and surface characterization. J. Eur. Ceram. Soc. **36**, 121–134 (2015). https://doi.org/10.1016/j.jeurceramsoc.2015.09.021

113. J.M. Gere, S.P. Timoshenko, *Mechanics of Materials*, 4th edn. (PWS Publishing Company, Boston, MA, USA, 1997), p. 912
114. ASTM E 399-20a, Standard test method for linear-elastic plane-strain fracture toughness of metallic materials. ASTM Int. (2020). https://doi.org/10.1520/E0399-20A
115. ASTM C 1421-18, Standard test methods for determination of fracture toughness of advanced ceramics at ambient temperature. ASTM Int. (2018). https://doi.org/10.1520/C1421-18
116. A. Moradkhani, H. Baharvandi, M. Tajdari et al., Determination of fracture toughness using the area of micro-crack tracks left in brittle materials by Vickers indentation test. J. Adv. Ceram. **2**, 87–102 (2013). https://doi.org/10.1007/s40145-013-0047-z
117. T.M. Lenkovskiy, V.V. Kulyk, Z.A. Duriagina et al., Mode I and mode II fatigue crack growth resistance characteristics of high tempered 65G steel. Arch. Mater. Sci. Eng. **84**(1), 34–41 (2017). https://doi.org/10.5604/01.3001.0010.3029
118. Q. Yao, Y. Chen, Z. Wang et al., Evaluations on ceramic fracture toughness measurement by edge chipping. Coatings **12**, 1146 (2022). https://doi.org/10.3390/coatings12081146
119. OP. Ostash, V.V. Kulyk, V.D. Poznyakov et al., Influence of the modes of heat treatment on the strength and cyclic crack-growth resistance of 65G steel. Mater. Sci. **54**, 776–782 (2019). https://doi.org/10.1007/s11003-019-00263-6
120. S. Begand, S. Spintzyk, J. Geis-Gerstorfer et al., Fracture toughness of 3Y-TZP ceramic measured by the chevron-notch beam method: a round-robin study. Dent. Mater. **38**(7), 1128–1139 (2022). https://doi.org/10.1016/j.dental.2022.05.001
121. T.G.T. Nindhia, T. Lube, Single edge precrack V-notched beam (SEPVNB) fracture toughness testing on silicon nitride. Mater. Sci. Forum **962**, 205–209 (2019). https://doi.org/10.4028/www.scientific.net/MSF.962.205
122. O.P. Ostash, V.V. Panasyuk, I.M. Andreiko et al., Methods for the construction of the diagrams of fatigue crack-growth rate of materials. Mater. Sci. **43**, 479–491 (2007). https://doi.org/10.1007/s11003-007-0056-6
123. M. Guazzato, M. Albakry, S.P. Ringer et al., Strength, fracture toughness and microstructure of a selection of all-ceramic materials. Part II. Zirconia-based dental ceramics. Dent. Mater. **20**, 449–456 (2004). https://doi.org/10.1016/j.dental.2003.05.003
124. H. Miyazaki, H. Hyuga, K. Hirao et al., Comparison of fracture resistance as measured by the indentation fracture method and fracture toughness determined by the single-edge-precracked beam technique using silicon nitrides with different microstructures. J. Eur. Ceram. Soc. **27**, 2347–2354 (2007). https://doi.org/10.1016/j.jeurceramsoc.2006.09.002
125. G.W. Housner, D.E. Hudson, *Applied Mechanics. Dynamics*, 2nd edn. (California Institute of Technology, Pasadena, CA, USA, 1959), p. 392
126. https://www.sellierbellot.us/products/rifle-ammunition/
127. http://www.wolfammo.com/
128. R.P. Wei, *Fracture Mechanics: Integration of Mechanics, Materials Science and Chemistry* (Cambridge University Press & Assessment, Cambridge CB2 8EA, United Kingdom, 2014), p. 232
129. G.A. Gogotsi, V.I. Galenko, S.P. Mudrik et al., Fracture resistance estimation of elastic ceramics in edge flaking: EF baseline. J. Eur. Ceram. Soc. **30**(6), 1223–1228 (2010). https://doi.org/10.1016/j.jeurceramsoc.2009.12.002

Chapter 8
Metamaterials with Structures of Nanometre and Submicron Sizes

Ruslan Politanskyi, Maria Vistak, and Anna Ploshchyk

Abstract In this paper, the properties of a metasurface formed by magnetic dipoles arranged in the form of a periodic structure are investigated. The studies were carried out using the method of moments (MoM) and the principle of equivalence of electric and magnetic fields. The application of the equivalence principle allows us to reduce the complex problem of calculating the properties of a metasurface formed by ordered magnetic dipoles to a simpler problem of electric dipoles. The resonant properties of the reflection and absorption coefficients of a metasurface formed by magnetic dipoles in a given direction (the effect of a phased antenna array) are revealed on the basis of the developed model. The revealed properties of the meta-surface can be used in modern telecommunication systems that use MIMO technologies. Also, the studied effects can be used to design RIS (reconfigurable intelligence surface), which makes it possible to overcome the effects of multipath signal propagation, increasing the signal-to-noise ratio, reducing the power consumption for transmitting one bit of information, which is especially important for Internet of Things technology, autonomous cyber-physical systems and unmanned aerial vehicles (UAV). Using the method of moments, it was possible to overcome the limitations of antenna system modelling programs and study devices with elements of nano- and submicron size (meta-atoms).

R. Politanskyi · A. Ploshchyk (✉)
Yuriy Fedkovych Chernivtsi National University, Chernivtsi, Ukraine
e-mail: ploshchyk.anna@chnu.edu.ua

R. Politanskyi
e-mail: r.politansky@chnu.edu.ua

M. Vistak
Danylo Halytsky Lviv National Medical University, Lviv, Ukraine
e-mail: vistak_maria@ukr.net

O. Fesenko and L. Yatsenko (eds.), *Functional Nanomaterials, Nanocatalysts, Nanotechnologies, and Their Applications*, Springer Proceedings in Physics 321,
https://doi.org/10.1007/978-3-031-99136-3_8

8.1 Development of Metamaterial Technologies: From Periodic Structures to Meta-Atoms

At the initial stage of metamaterial development, the basic elements used for their fabrication were periodic structures composed of resonant elements in the form of circular or rectangular designs [1]. Further studies of the properties and possible applications of metamaterials are associated with significant progress in manufacturing technologies, in particular additive manufacturing (creating an object by building it one layer at a time) [2]: optical 3D printing, advanced lithography technologies, multi-photon 4D printing, and nano-printing technologies [3, 4]. This has significantly expanded the possible areas of their application: from the first applications in optics to electromagnetic energy harvesting [5], sensor manufacturing, biomedical applications, automotive and aerospace industries, and artificial intelligence technologies (speech recognition, signal processing). Modern research shows that the functional properties of materials can be a starting point for determining their structure. A number of methods are used for this purpose. One of the first was a method based on the equivalent representation of metastructure elements by the parameters of a certain oscillatory circuit (RLC circuit) [1]. The limitations of the macroscopic approach in modeling metamaterial properties are defined by the size constraints of periodic inclusions, often referred to as meta-atoms. These inclusions must be sufficiently small compared to the wavelength or constitute only a specific fraction of the wavelength:

$$L \ll \lambda \tag{8.1}$$

where L is the geometric size of the cell, and λ is the length of the electromagnetic wave. A model that represents the interface in the form of a plane of metaatoms are presented in [6].

One of the methods for designing a metasurface is solving the inverse problem of determining the boundary conditions for the integral equation of the electric field [7]. This equation is obtained by decomposing the equivalent impedance of the metasurface (which is unknown a priori) into a series of Fourier–Bessel basis functions. Two approaches are used for this purpose. The first approach means that a priori the shape of the metasurface impedance has a discrete azimuthal symmetry, and thus certain conditions are imposed on the set of solutions, which gives rise to the existence of solutions in the form of multiple beams when supplying power in the form of sources located along the azimuthal lines. The second approach does not make any a priori assumptions about the surface impedance profile, but the systems of equations describing each ray are combined and solved simultaneously in the sense of the least-squares criterion. This approach can also be used to obtain the polarization properties of the generated rays. Such a solution can also help determine the design of a beam system with continuous scanning properties. This is achieved by generating two sets in the azimuthal window with opposite phase tilts, followed by the continuous phase shift of two points where power is supplied. The conducted research is relevant for

the design of multi-channel antenna devices that find application in Internet of Things (IoT) devices, cyber-physical systems, and unmanned aerial vehicles (UAV) [8–10].

8.2 Mathematical Apparatus of the Method of Moments

The essence of the method of moments is that the current distribution on the antenna surface is approximated by a linear combination of known basis functions with unknown coefficients:

$$\vec{J}(x, y, z) = \sum_{n}^{N_{max}} I_n \cdot \vec{J}_n(x, y, z), \tag{8.2}$$

where $\vec{J}_n(x, y, z)$—basis functions in cartesian space, I_n—unknown coefficients that determine a certain distribution of currents on the radiating surface.

Then the electric field of the resulting wave $\vec{E}^s(x, y, z)$ is defined as a linear combination of electric fields $\vec{E}_n^s(x, y, z)$, generated by known base currents:

$$\vec{E}^s(x, y, z) = \sum_{n}^{N_{max}} I_n \cdot \vec{E}_n^s(x, y, z) \tag{8.3}$$

Next, we assume that the normal component of the electric field on the radiating surface is zero, and the problem is reduced to the matrix equation:

$$[Z] \times [I] + \left[V^{ex}\right] = [0], \tag{8.4}$$

where the matrix elements are defined as follows:

$$Z_{mn} = \iint\limits_{S_m} \vec{E}_n^s(x, y, z) \cdot \vec{J}_m(x, y, z) dS, \tag{8.5}$$

$$V_m^{ex} = \iint\limits_{S_m} \vec{E}^{ex}(x, y, z) \cdot \vec{J}_m(x, y, z) dS \tag{8.6}$$

The method of moments is described in more detail in [7].

8.3 Results Obtained

8.3.1 Application of the Method of Moments to the Problem of Electric Dipole Radiation

In general, the calculation of matrix coefficients is complex, requires the use of computational methods, and may be accompanied by the occurrence of non-convergence points (the so-called singularities). Consider an example of a calculation for a thin cylindrical antenna directed along the z-axis (Fig. 8.1).

As the functions of the basic functions, we choose piecewise constant functions:

$$J_{zm}(z) = \begin{cases} 1, z_{m-1} < z < z_{m+1}, \\ 0, \text{інакше} \end{cases} \tag{8.7}$$

where $m = 1, 2, \ldots, N_{max}$.

Problem (8.5) is transformed from two-dimensional to one-dimensional (8.7) due to the presence of symmetry properties of the radiating surface (Fig. 8.1). In this case, the problem can be solved analytically:

$$F = \left(1 + \frac{1}{(2\pi f/c)^2}\frac{\partial^2}{\partial z^2}\right)\frac{e^{-j2\pi f/c\cdot\sqrt{a^2+z^2}}}{4\pi\sqrt{a^2+z^2}}, \tag{8.8}$$

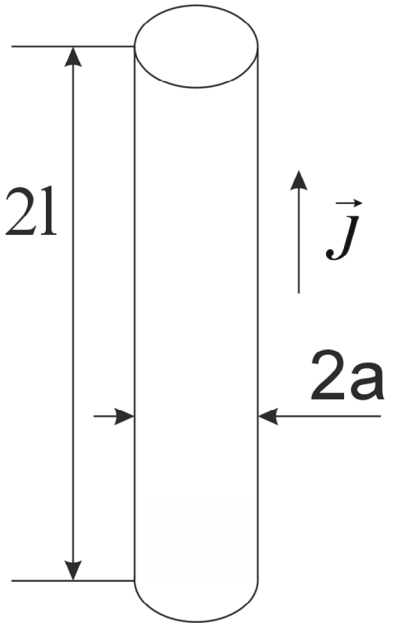

Fig. 8.1 A cylindrical wire antenna of length 2l and diameter 2a centered at the origin, directed along the z-axis

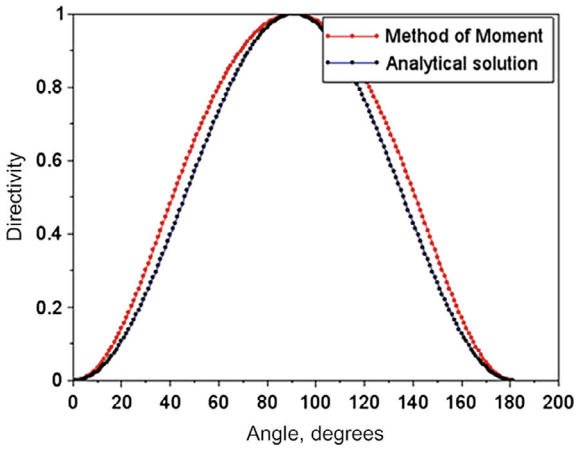

Fig. 8.2 Comparison of the directivity of a half-wave dipole antenna calculated by the method of moments (red line) and the analytical method (blue line)

where $c = 3 \cdot 10^8$ м/с—light speed, f—frequency of the wave.

In order to validate the method, the directional coefficient of radiation formed by a single dipole are calculated and compared with the known analytical solution:

$$F(\theta, \varphi) = \sin^2 \theta \tag{8.9}$$

The comparison results are shown on Fig. 8.2.

A significant advantage of the method of moments (MoM) is the ability to easily find solutions to the problem in the case of multiple (multi-port) signals being fed to the radiating device. To do this, it is enough to set non-zero values of the input potentials of the vector $\vec{V}^{ex}$ in the matrix equation ($[Z] \times [I] + [V^{ex}] = [0]$, (8.4).

8.3.2 *Application of the Method of Moments to the Problem of Radiation from a Planar Array of Magnetic Dipoles*

The results obtained are applied to flat surfaces on which periodic circular structures which conduct currents. The simplest of these is a surface on which currents flow along annular tracks, which can be regarded as magnetic dipoles if they have a sufficiently small radius (Fig. 8.3). In this case, the dimensions of the plane can be commensurate with the dimensions of microwave antennas, and the dimensions of the dipoles themselves can be nanometre or submicron scales, depending on the design of the antennas.

From the point of view of the equations of electrodynamics, magnetic and electric dipoles are interchangeable if magnetic currents and charges are introduced into Maxwell's equations. Therefore, to solve the problem of radiation of a surface with magnetic dipoles, the results of the problem of radiation of an electric dipole can be used. But in this case, the electric and magnetic fields are reversed, and the sign (phase

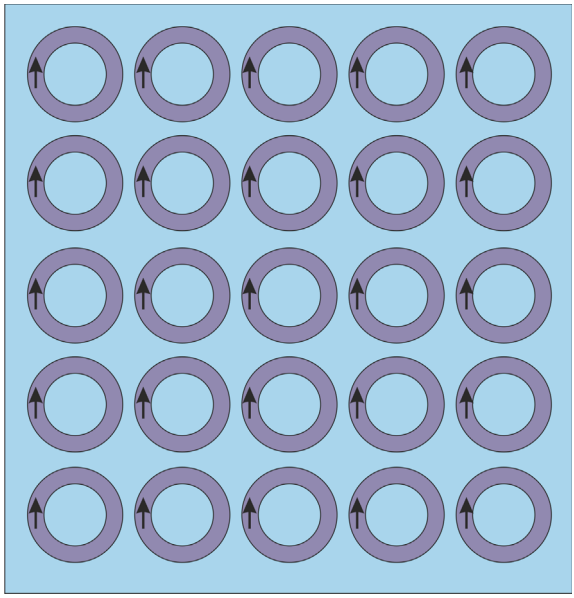

Fig. 8.3 Planar array of magnetic dipoles (phased array antenna)

change) of the electric field is reversed. Obviously, this does not affect the radiation power. In this formulation of the problem, to determine the field, it is necessary to specify the distribution of voltages along the antenna axis, which will determine the phases and amplitudes of the input signals. Then, using the method of moments, you need to determine the distribution of currents on the antenna surface for the given input signals. Having the current distribution at the top, it is possible to determine the radiation field of the antenna in the far field.

The radiation of an array of elementary dipoles can be determined by the superposition principle if the electromagnetic interaction between the dipoles is negligible compared to the dipole radiation. If the dipoles have different radiation characteristics and different amplitudes of the received signals, the general radiation pattern of the planar array of dipoles (Fig. 8.3) can be in general form [7]:

$$S(u, v) = \sum_{k=1}^{K} \sum_{l=1}^{L} |a_{kl}| f_{kl}(u, v) e^{jk_0[(k-1)d_x(u-u_0)+(l-1)d_y(v-v_0)]}, \tag{8.10}$$

where $f_{kl}(u, v)$—radiation characteristic (directivity coefficient) of one dipole, a_{kl}—dipole emission amplitudes that are directly proportional to the input signal, u, v—variables that depend on angular coordinates θ (convergence angle), φ—azimuth angle in the spherical coordinate system: $u = \sin\theta \cdot \cos\varphi$, $v = \sin\theta \cdot \sin\varphi$; d_x and d_y—distances between array elements along the x, y coordinates of the cartesian coordinate system; u_0, v_0—direction of the main beam: $u_0 = \sin\theta_0 \cdot \cos\varphi_0$, $v_0 = \sin\theta_0 \cdot \sin\varphi_0$.

One of the applications of the results obtained for an electric dipole is the analysis of the problem of electronic beam steering, which is solved by means of a planar array of magnetic dipoles (Fig. 8.3). To modeling the dynamic change of the beam pattern of the entire lattice, which can achieve the effect of electronic beam control, you can set different values of the amplitudes of individual elementary radiators. By grouping the amplitudes into a matrix, the research is reduced to finding the optimal coefficient matrix for a given lattice intensity distribution $A = a_{kl}$.

8.3.3 *Results of Calculations of a 5 × 5 Array*

To simplify the problem, we consider only binary matrices A: if an element of the matrix is equal to «1», then the corresponding emitter is switched on, and if «0», then it is not involved, the radiation characteristic of one dipole $f_{kl}(u, v)$ are chosen on the basis of solutions to problem $F(\theta, \varphi) = \sin^2\theta$ (8.9). Next, let us consider the simulation of a rectangular array of magnetic dipoles with dimensions 5 × 5. Figure 8.4 shows the results of the radiation simulation when all dipoles are switched on ($a_{kl} \equiv 1$). Diagrams displayed in polar coordinates of the azimuthal angle θ for the following values of the meridional angle φ: 0°, 45° i 90°.

According to results presented on the Fig. 8.4, the main lobe is in the direction of the $\theta = 90°$and $\varphi = 0°$. The radiation diagrams show that the planar array of dipoles forms a set of narrowly directed beams, which make it possible to implement

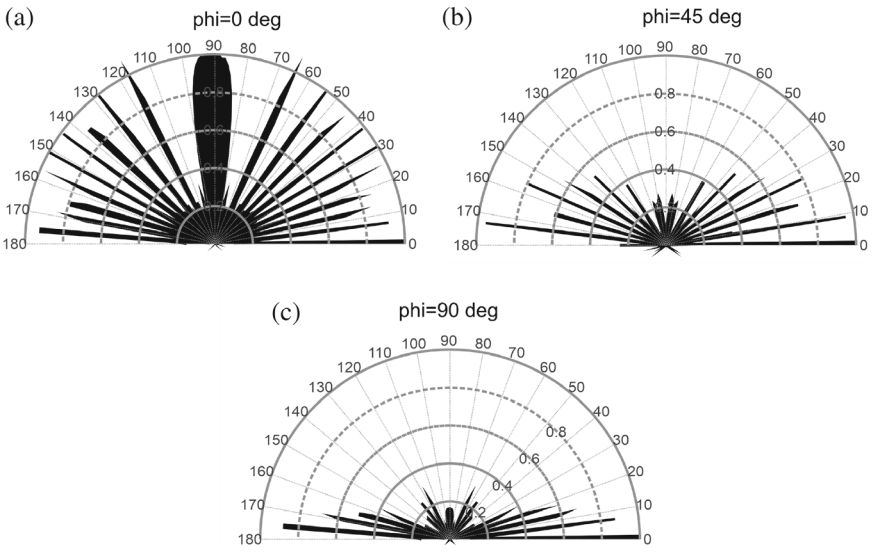

Fig. 8.4 Radiation patterns of a 5 × 5, magnetic dipole array when all dipoles are included for the angles $\varphi = 0°$ (**a**), $\varphi = 45°$ (**b**), $\varphi = 90°$ (**c**)

antenna devices with spatial channel separation, which is used in systems that use MIMO channel formation. In this case, in the direction of the greatest gain at the angle $\varphi = 0°$, 20 beams with almost the same gain coefficient are formed, which are equidistant from each other by an angular distance $\Delta\theta = 10°$, with the exception of the main lobe ($\theta = 90°$), which is distant from the others by $\Delta\theta = \pm 20°$. For other values φ, there is a significant attenuation of all rays except those directed at angles $\theta = 0°, 180°$.

8.4 Discussion of Results and Conclusions

An algorithm for calculating radiation patterns of a planar array of magnetic dipoles is developed in this paper. The algorithm is based on the principle of equivalence of magnetic and electric charges, which is often used to solve electrodynamics problems. The problem of radiation from a single dipole is solved by the method of moments, which makes it easy to find solutions in the case of multi-port signal supply. The method of emissivity studies based on the dipole inclusion/exclusion binary matrix is proposed. The results for an array of size 5×5 demonstrate the possibility of forming narrowly directed electron beams, the directions of which depend on the values of the elements of the inclusion matrix. The developed method makes it possible to implement electron beam control algorithms, which are important in today's MIMO technologies and are being actively developed. Using the method of moments, it was possible to overcome the limitations of antenna system modelling programs and study devices with elements of nano- and submicron size (meta-atoms).

References

1. M.M. Bait-Suwailam, Electromagnetic field interaction with metamaterials. IntechOpen (2019). https://doi.org/10.5772/intechopen.84170
2. A.O. Krushynska, S. Janbaz, J.H. Oh et al., Fundamentals and applications of metamaterials: breaking the limits. Appl. Phys. Lett. **123**, 240401 (2023). https://doi.org/10.1063/5.0189043
3. A. Nazir, O. Gokcekaya, K.M.M. Billah et al., Multi-material additive manufacturing: a systematic review of design, properties, applications, challenges, and 3D Printing of materials and cellular metamaterials. Mater. Des. **226**, 111661 (2023). https://doi.org/10.1016/j.matdes.2023.111661
4. X. Zhou, L. Ren, Z. Song et al., Advances in 3D/4D printing of mechanical metamaterials: from manufacturing to applications. Compos. Part B-Eng. **254**, 110585 (2023). https://doi.org/10.1016/j.compositesb.2023.110585
5. H. Xiong, X. Ma, H. Liu et al., Research on electromagnetic energy absorption and conversion device with four-ring multi-resistance structure. Appl. Phys. Lett. **123**, 153902 (2023). https://doi.org/10.1063/5.0170827
6. M. Bodehou, E. Martini, S. Maci et al., Multibeam and beam scanning with modulated metasurfaces. IEEE Trans. Antennas Propag. **68**, 1273–1281 (2020). https://doi.org/10.1109/TAP.2019.2944554

7. A. Smolders, H. Visser, U. Johannsen, *Modern Antennas and Microwave Circuits—A Complete Master-Level Course* (2019). https://doi.org/10.48550/arXiv.1911.08484
8. A. Ploshchyk, R. Politanskyi, S. Haliuk, Analysis of antenna system S-parameters in wireless communication networks using HFSS: role and significance in Wi-Fi and 5G, in *IEEE 17th International Conference on Advanced Trends in Radioelectronics, Telecommunications and Computer Engineering, TCSET 2024—Proceedings* (2024), pp. 560–563. https://doi.org/10.1109/TCSET64720.2024.10755706
9. R. Politanskyi, S. Haliuk, A. Ploshchyk, et al., Study of information flows in a network based on exact solutions, in *5th IEEE International Conference on Advanced Information and Communication Technologies, AICT 2023—Proceedings* (2023), pp. 15–17. https://doi.org/10.1109/AICT61584.2023.10452673
10. C. Dharmendra, A. Patel, A. Vala, et al., Microstrip antenna for Internet of Things (IOT) applications, in *Internet of Things Enabled Antennas for Biomedical Devices and Systems*(2023), pp.129–142. https://doi.org/10.1007/978-981-99-0212-5_11

Chapter 9
Predicting Isomorphous Substitution Limits and Thermodynamic Stability of Nanoscale Solid Solutions of $(Y_{1-x}Ln_x)_2SiO_5$, Ln = La–Lu

E. I. Get'man, O. Yu. Mariichak, L. I. Ardanova, and S. V. Radio

Abstract Within the framework of Urusov's crystal energy theory of isomorphous substitutions, the mixing energies (interaction parameters) in $(Y_{1-x}Ln_x)_2SiO_5$ systems, where Ln represents rare-earth elements (REEs), have been calculated. It has been demonstrated that the mixing energy during the substitution of yttrium by REEs from the cerium subgroup is determined mainly by the size differences of the substituting structural units. At the same time, the yttrium subgroup is primarily influenced by the differences in the degree of ionicity of the chemical bonds of the system's components. The solid solutions' decomposition (stability) temperatures were calculated, and based on these, thermodynamic stability diagrams for all systems and decomposition domes for each system were constructed. These diagrams allow for predicting the equilibrium substitution limits (x) as a function of temperature or the decomposition temperature based on specified substitution limits and the areas of thermodynamic stability. The results of this work can help choose the component ratios in matrices and the amount of activator (dopant) in new luminescent, scintillation, and other materials based on REEs oxyorthosilicate solid solutions of the composition $(Y_{1-x}Ln_x)_2SiO_5$ with the space group $P2_1/c$.

9.1 Introduction

Yttrium oxyorthosilicate, composed of Y_2SiO_5 and doped with rare-earth elements (REEs), can be used as a material for photoluminescence, cathodoluminescence [1], scintillation [2], and other applications.

E. I. Get'man · O. Yu. Mariichak · S. V. Radio (✉)
Vasyl' Stus Donetsk National University, Vinnytsia, Ukraine
e-mail: radio@donnu.edu.ua

L. I. Ardanova
Minnesota State University, Mankato, MN, USA
e-mail: lyudmyla.stackpool@mnsu.edu

O. Fesenko and L. Yatsenko (eds.), *Functional Nanomaterials, Nanocatalysts, Nanotechnologies, and Their Applications*, Springer Proceedings in Physics 321,
https://doi.org/10.1007/978-3-031-99136-3_9

Yttrium oxyorthosilicate solid solutions doped with praseodymium can be used for nitrobenzene photodegradation in wastewater, achieving a degradation rate of 97.14% in 6 h [3]. Currently, there is also intensive research being conducted on the effects of composition, structure, and synthesis conditions on the electrophysical, luminescent, and other properties of so-called "mixed" oxyorthosilicates, which incorporate other REEs into the matrix composition alongside yttrium, such as $(Y_{1-x}Gd_x)_2SiO_5:Tb^{3+}$ [4].

Since successful synthesis strictly depends on the thermodynamic stability of the solid solution, it is crucial to predict the substitution limits and thermodynamic stability of such solid solutions across a wide range of compositions and temperatures. This capability is critical for determining the practically important properties of the materials.

However, the physicochemical foundations for synthesizing "mixed" REE oxyorthosilicate solid solutions—such as phase diagrams and the solubility ranges of solid solutions based on REE oxyorthosilicates and their thermodynamic stability—remain largely unexplored. As a result, researchers studying the properties of "mixed" REE oxyorthosilicates are often compelled to select the composition of matrices and activators either by analogy with related systems or through a "trial-and-error" approach.

Moreover, it is not always considered that solid solutions synthesized at high temperatures are prone to decomposition during cooling in the region of thermodynamic instability, leading to changes in phase composition and properties [5, 6]. This can result in the degradation of materials based on these solid solutions during practical applications and in the irreproducibility of their properties. Therefore, before synthesizing and studying the properties of such solid solutions, it is advisable to evaluate the limits of isomorphous substitutions and the thermodynamic stability within the relevant systems under synthesis, operation, and expected storage conditions. The experimental determination of substitution limits and stability regions of solid solutions synthesized by the "annealing and hardening" method using X-ray phase (diffraction) analysis (XRD) is complicated by the difficulty of achieving equilibrium at low temperatures due to the slow diffusion rates in the solid phase and the possibility of partial decomposition during cooling from high temperatures.

Moreover, XRD may provide limited information when dealing with isostructural components with very similar sizes of substituting structural units, during spinodal decomposition of the solid solution [5, 6], or with nanoscale particles of the studied samples due to the broadening and overlapping of X-ray reflections. Therefore, it is rational to use experimental methods and computational approaches that are free from these disadvantages to determine substitution limits and stability regions of solid solutions. For example, works [7, 8] employed computational results using the mathematical apparatus of the crystal energy theory of isomorphous substitutions for the $Y_{1-x}Sc_xPO_4$ system, as described in [9], to select sample synthesis conditions.

Considering the above, the objective of this study was to predict the substitution limits and thermodynamic stability regions of yttrium oxyorthosilicate solid solutions $(Y_{1-x}Ln_x)_2SiO_5$, where Ln = REEs, with the space group $P2_1/c$ (X1). Since substitution limits are predicted based on 1 mol of substituting cation according to [5]

and considering that the anionic sublattice of oxyorthosilicates contains SiO_4^{4-} and O^{2-} anions not bonded to the Si atom, the composition of yttrium oxyorthosilicate in calculations will be represented as a pseudobinary compound $Y[(SiO_4)_{0.5}O_{0.5}]$. Solid solutions based on this will be defined as $(Y_{1-x}Ln_x)[(SiO_4)_{0.5}O_{0.5}]$ while maintaining the traditional formula for yttrium oxyorthosilicate Y_2SiO_5 in the text of the article.

9.2 Calculation Methodology and Initial Data

In the crystal energy theory of isomorphous miscibility developed by Urusov [5, 6], the main problem in determining the isomorphous substitution limits is finding the mixing energy. Once this energy is known, the substitution limit (x) can be calculated for a given decomposition temperature (T_d) of the solid solution, or the decomposition (stability) temperature can be determined for a specified substitution limit. The thermodynamic stability regions can be identified using Becker's equation (Eq. 9.1) in the approximation of regular solid solutions [10]:

$$-(1-2x)/\ln[x/(1-x)] = R_g T_d/Q, \tag{9.1}$$

The critical decomposition (stability) temperatures, T_{cr}, were calculated using Eq. (9.2) [5]:

$$T_{cr} = Q/2\,\mathrm{kN}, \tag{9.2}$$

where Q is the mixing energy; R_g is the universal gas constant; k is the Boltzmann constant; and N is Avogadro's number. In both cases, the value of Q was expressed in calories [5].

Becker's equation can be used if the size parameter does not exceed 0.1 [5, 6]. The size parameter was calculated based on the unit cell volumes (Eq. 9.3) [5]:

$$\delta = \left(V_{Ln2SiO5}^{1/3} - V_{min}^{1/3}\right)/V_{min}^{1/3}, \tag{9.3}$$

where V_{min} is the volume of the smaller unit cell for each system, and since the value of the size parameter was less than 0.054 (see Table 9.1), Becker's equation is appropriate. The calculation using unit cell volumes is due to the lack of interatomic distance data in the available literature on the synthesis and properties of Ln_2SiO_5, such as [11–13]. Additionally, the authors of [11], who described Ln_2SiO_5 with the $P2_1/c$ space group, do not provide unit cell parameters for Lu_2SiO_5. Therefore, the volume of the unit cell for the low-temperature modification of Lu_2SiO_5 (approximately 384 Å^3) was determined by us [14] through the extrapolation of the relationship between the unit cell volumes of low-temperature modifications of Ln_2SiO_5 and the ionic radii of REEs according to Shannon [15].

Table 9.1 Data for calculating the mixing energies of yttrium oxyorthosilicates $(Y_{1-x}Ln_x)_2SiO_5$, Ln = La–Lu, of structural type $P2_1/c$ (X1)

Ln	V (Å^3)	δ	Q_δ (kJ/mol)	χ_{Ln}	ε	Δε	Q_ε (kJ/mol)	Q (kJ/mol)
La	465.2	0.05390	38.27	1.327	0.724	0.002	0.03	38.30
Ce*	455.2	0.04629	28.23	1.348	0.720	0.002	0.03	28.26
Pr	445.1	0.03850	19.53	1.374	0.716	0.006	0.24	19.77
Nd	439.3	0.03397	15.20	1.382	0.714	0.008	0.43	15.64
Pm*	431.9	0.02814	10.43	1.391	0.712	0.010	0.68	11.11
Sm	424.4	0.02215	6.46	1.410	0.708	0.014	1.33	7.79
Eu	417.9	0.01690	3.76	1.433	0.704	0.018	2.20	5.96
Gd	414.0	0.013732	2.48	1.386	0.712	0.010	0.68	3.16
Tb	409.2	0.009800	1.26	1.410	0.708	0.014	1.33	2.596
Dy	404.0	0.005505	0.3992	1.426	0.706	0.016	1.74	2.14
Ho	397.5	0.0000838	$\approx 10^{-5}$	1.433	0.704	0.018	2.20	2.20
Er	395.6	0.001514	0.030	1.438	0.703	0.019	2.45	2.48
Tm	389.7	0.006542	0.564	1.455	0.700	0.022	3.29	3.85
Yb	387.0	0.008799	1.02	1.479	0.695	0.027	4.95	5.97
Lu	384.0	0.011498	1.74	1.431	0.705	0.017	1.96	3.70
Y	397.4	0.008877		1.340	0.722			

**Note* The unit cell volumes of cerium and promethium oxyorthosilicates were determined as the arithmetic mean of the unit cell volumes of lanthanum and praseodymium oxyorthosilicates, as well as neodymium and samarium oxyorthosilicates, respectively

Since the components of the systems under consideration are isostructural [11], the formula for calculating the mixing energy (Q) consists of two contributions: one due to the difference in the sizes of substituting structural units (Q_δ) and the other due to the difference in the degree of ionicity of the chemical bonds of the components (Q_ε) [5]. In this case, the mixing energy can be calculated using Eq. (9.4):

$$Q = Q_\delta + Q_\varepsilon = Cmnz_m z_x \delta^2 + 1390 m z_m z_x \alpha (\Delta\varepsilon)^2/(2R), \text{ kJ/mol}. \quad (9.4)$$

Since at temperatures above 1173–1373 K, both components of the systems under consideration are not isostructural (the space group $P2_1/c$ is characteristic for a series of REEs oxyorthosilicates from La to Tb, while the space group B2/b is characteristic for a series from Dy to Lu) [11], when calculating the decomposition temperatures in the systems with REEs oxyorthosilicates of the Dy–Lu series at $T >$ (1173–1373) K, it is necessary to also consider the contributions to the mixing energy due to the enthalpy of polymorphic transitions $P2_1/c \rightarrow$ B2/b [5], the values of which are unknown.

In Eq. (9.4), the constant C is equal to 112.6 kJ, calculated from the expression $C = 20(2\Delta\chi + 1)$ [6], where $\Delta\chi$ is the difference in electronegativities between the

cations [16] and the anion [17] in the pseudobinary approximation of the structure. The choice of the scale [16], as opposed to other authors' scales, was because the values of χ vary with regular periodicity, increasing in the cerium subgroup of REEs from La^{3+} to Eu^{3+} from 1.327 to 1.433 and in the yttrium subgroup from Gd^{3+} to Yb^{3+} from 1.386 to 1.479, with a sharp decrease during transitions from Eu^{3+} to Gd^{3+} (from 1.433 to 1.386) and from Yb^{3+} to Lu^{3+} (from 1.479 to 1.431), which is attributed to the specific filling of the electron shells of the REEs.

The 4f shell is half-filled (7 electrons) for europium and gadolinium, while it is filled (14 electrons) for ytterbium and lutetium. During the transition from europium to gadolinium and from ytterbium to lutetium, the first electron appears in the 5d sublevel. The value of m is the number of formula units in the pseudobinary approximation of the structure $Ln[(SiO_4)_{0.5}O_{0.5}]$ [18], calculated per mole of the substituting structural unit ($1 + 0.5 + 0.5 = 2$). The value of n is the coordination number of the substituting structural unit in the pseudobinary approximation of the structure: in the first cationic position ($n = 7$), there are 6 SiO_4^{4-} tetrahedra and one O^{2-} ion, and in the second ($n = 6$), there are 3 SiO_4^{4-} tetrahedra and three O^{2-} ions [18], giving an average of $n = 6.5$.

z_m and z_x are the formal charges of the substituting and common structural units in the components: $z_m = 3$, $z_x = 4 \times 0.5 + 2 \times 0.5 = 3$;

δ is the size parameter, calculated for each system based on the unit cell volumes provided in [11, 18];

α is the reduced Madelung constant, equal to 1.9, calculated using Hoppe's formula [19]: $(\alpha / n)^2 + \alpha = 1.81$;

ε is the degree of ionicity of the chemical bond, determined by the difference in electronegativity (χ) between the anion and the REEs cations, with values provided in [16, 17]. The electronegativity (χ) of the SiO_4^{4-} radical was taken as equal to the χ of the oxide anion, 3.7, according to the recommendation in [20].

R is the average "cation–anion" interatomic distance in the pseudobinary approximation, calculated for one of the previously studied structures of this structural type, $Gd[(SiO_4)_{0.5}O_{0.5}]$ [18]. The distances considered were the "cation-tetrahedral anion" distances, which include the sum of the (Gd–O + Si–O) distances, and the "cation-oxygen" distance (Gd–O) for oxygen not bonded to silicon, for two gadolinium positions [18]. For the first position, the cation is surrounded by 6 tetrahedra and 1 oxygen, with an average distance of $[6 \times (2.49 + 1.63) + 2.35]/7 = 3.86$ Å; for the second position, the cation is surrounded by 3 tetrahedra and 3 oxygens, with an average distance of $[3 \times (2.39 + 1.63) + 3 \times 2.30)]/6 = 3.15$ Å. The average distance for the two cation positions is $R = 3.5$ Å. The error in the calculation of T_{cr} was ± 100 K [5].

9.3 Results of Calculations and Discussion

9.3.1 Mixing Energies of Solid Solutions

Some initial data and results of the mixing energy calculations are summarized in Table 9.1 and depicted in Fig. 9.1a. As shown, with increasing REEs atomic number, the contributions to the total mixing energy due to differences in the sizes of substituting structural units (Q_δ) vary smoothly across the series from $(Y_{1-x}La_x)_2SiO_5$ to $(Y_{1-x}Ho_x)_2SiO_5$, significantly decreasing from 38.27 kJ/mol to nearly 0, and then slightly increasing to 1.74 kJ/mol in the series of solid solutions from $(Y_{1-x}Ho_x)_2SiO_5$ to $(Y_{1-x}Lu_x)_2SiO_5$.

This variation in the mixing energy Q_δ is because in the series of systems with La–Ho oxyorthosilicates, the differences between the ionic radii of the rare-earth elements (1.300–1.155 Å) and yttrium (1.16 Å) decrease, whereas in the series of systems with Ho–Lu oxyorthosilicates (1.155–1.117 Å), they increase. This is because the ionic radius of yttrium (1.16 Å) is very close to that of holmium (1.155 Å).

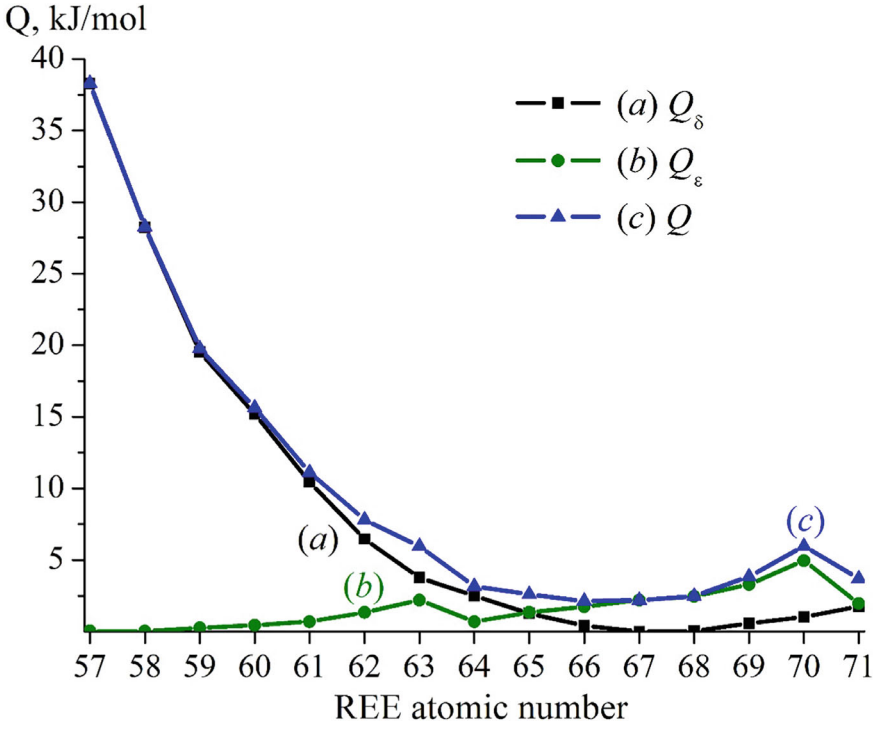

Fig. 9.1 Dependences of the calculated contributions to the mixing energies of solid solutions Q_δ (curve *a*), Q_ε (curve *b*), and Q (curve *c*) for the systems $(Y_{1-x}Ln_x)_2SiO_5$ on the atomic numbers of the REEs

The crystal ionic radii of the cations were taken from [15] for a coordination number of 8.

The contributions to the mixing energy due to differences in the degree of ionicity of the chemical bonds Q_ε (Table 9.1 and Fig. 9.1b) increase slightly with the atomic number of the REEs in each of the REEs subgroup. Two maxima are observed at $(Y_{1-x}Eu_x)_2SiO_5$ and $(Y_{1-x}Yb_x)SiO_5$, which are attributed to the aforementioned electronic shell structures of the REEs.

According to [5], generally, if the differences in the degree of ionicity of the chemical bonds in the components of the systems are less than 0.05, the value of Q_ε will be insignificant and can be neglected. In this case, these differences range from 0.002 to 0.027 (Table 9.1), and the values of Q_ε are significantly smaller (Fig. 9.1b) than Q_δ for systems with oxyorthosilicates of the cerium subgroup.

For the remaining systems (from Dy to Yb), the values of Q_ε are somewhat larger than Q_δ. In such cases, considering the magnitude of Q_ε is necessary, as indicated in [5]. Therefore, we did not neglect the values of Q_ε for any of the systems.

It should also be noted that when substituting yttrium with REEs from the cerium and yttrium subgroups, the total mixing energies Q change differently (Table 9.1, Fig. 9.1c). In the case of the cerium subgroup REEs, the mixing energies systematically decrease in the series from $(Y_{1-x}La_x)_2SiO_5$ to $(Y_{1-x}Gd_x)_2SiO_5$. In contrast, when substituting yttrium cations with REEs cations from the yttrium subgroup, the energies increase slightly in the series from $(Y_{1-x}Dy_x)_2SiO_5$, with a peak for the system $(Y_{1-x}Yb_x)_2SiO_5$. This change in total mixing energies Q is explained by the fact that for systems with cerium subgroup REEs, the values are mainly determined by the differences in the sizes of the substituting structural units. In contrast, systems with yttrium subgroup REEs are influenced by differences in the degree of ionicity of the chemical bonds. The peak value for the system $(Gd_{1-x}Yb_x)_2SiO_5$, as with Q_ε, is due to the specific electronic configuration of ytterbium. In the case of the system $(Y_{1-x}Eu_x)_2SiO_5$, the analogous maximum in Q_ε is less pronounced, so this maximum in the dependence of Q on the atomic number of the REEs appears as an inflection.

9.3.2 *Limits of Substitution and Thermodynamic Stability Ranges of the Yttrium Oxyorthosilicates $(Y_{1-x}Ln_x)_2SiO_5$*

Decomposition (stability) temperatures for limited ranges of solid solutions were calculated for the given substitution limits $x = 0.01; 0.03; 0.09; 0.20$ using Eq. (9.1), and for unlimited solid solutions (for $x = 0.50$) using Eq. (9.2) (see Table 9.2).

Based on the calculated values of the decomposition temperatures, their dependencies on the REEs atomic numbers were plotted (Fig. 9.2). These dependencies allow for a graphical determination of the equilibrium substitution limits x for a limited

Table 9.2 Decomposition temperatures (K) of solid solutions of oxyorthosilicates $(Y_{1-x}Ln_x)_2SiO_5$ for $x = 0.01$, 0.03, 0.09, 0.20, and 0.50 (T_{cr})

Ln	T_d (K) at the x values				
	$x = 0.01$	$x = 0.03$	$x = 0.09$	$x = 0.20$	$x = 0.50$ (T_{cr}*)
La	975	1237	1573	1956	2290
Ce	720	912	1160	1460	1690
Pr	504	638	837	1022	1180
Nd	398	505	662	808	930
Pm	283	359	470	574	660
Sm	198	252	330	403	470
Eu	152	193	252	308	360
Gd	81	102	134	163	190
Tb	66	84	119	134	160
Dy	54	69	90	119	130
Ho	56	71	93	114	130
Er	63	80	102	128	150
Tm	98	124	163	199	230
Yb	152	193	253	309	360
Lu	94	120	157	191	220

**Note* Critical decomposition temperatures at $x = 0.5$ are rounded

series of solid solutions at given decomposition temperatures T_d or the decomposition temperatures at given substitution limits for yttrium oxyorthosilicate doped with REEs from La to Lu [21]. The intersection points of the isotherm, drawn from the specified decomposition temperature, with the vertical line drawn from the REE atomic number allow for estimating the composition range within which the substitution limit is found. In contrast, interpolating this vertical segment between the two nearest curves provides for determining the substitution limit. Solid solutions with values of $x = 0.01$, 0.03, 0.09, 0.20, and 0.50 in the ranges above the curves (*a*), (*b*), (*c*), (*d*), and (*e*) are thermodynamically stable and unstable below them.

The substitution limit can be refined by plotting, for a specific system, the dependence of the decomposition temperatures calculated using Becker's equation on the given composition (the decomposition dome).

The critical decomposition temperatures of the unlimited solid solution series for the systems under consideration were calculated for $x = 0.50$ (Table 9.2, Fig. 9.2e) using Eq. (9.2). These temperatures vary with the atomic numbers of the REEs, corresponding to changes in the total mixing energy. They can be used to determine the stability range of continuous solid solution series. For instance, at $T > T_{cr}$ (curve *e*), the continuous solid solutions are thermodynamically stable for all systems across the entire concentration range $0 \leq x \leq 1$. In the region below curve *e*, at $T < T_{cr}$, the continuous solid solutions become unstable and may decompose into phases with limited solubility if the diffusion rate and time are sufficient for their formation [21].

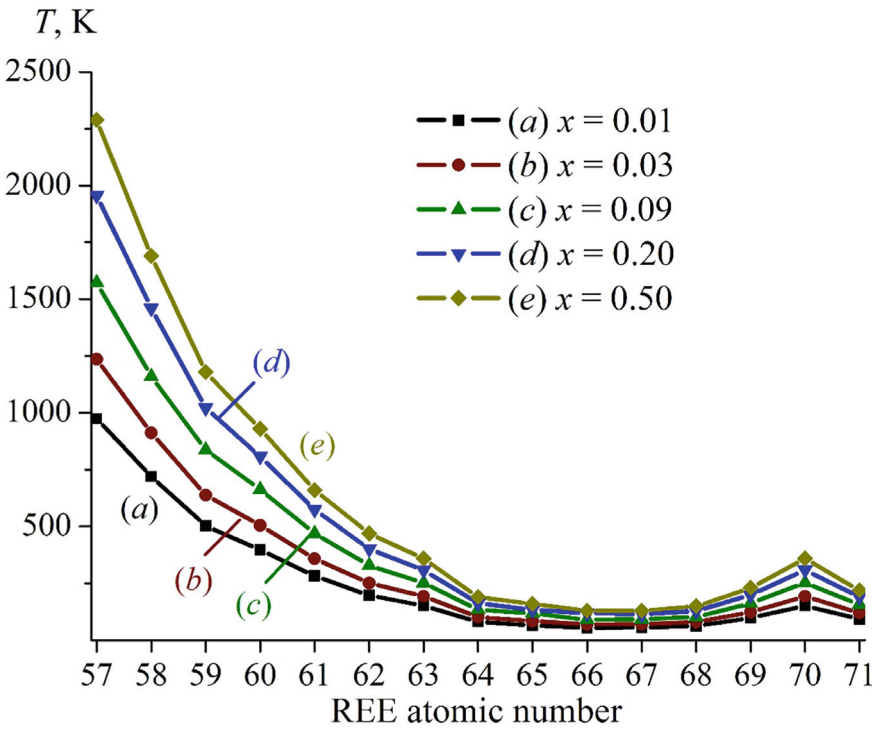

Fig. 9.2 Dependencies of the calculated decomposition (stability) temperatures of the solid solutions $(Y_{1-x}Ln_x)_2SiO_5$ on the REEs atomic numbers (thermodynamic stability diagram) for substitution limits $x = 0.01$ (**a**), $x = 0.03$ (**b**), $x = 0.09$ (**c**), $x = 0.20$ (**d**), and $x = 0.50$ (**e**)

It should be noted that the solid solutions in the $(Y_{1-x}Ln_x)_2SiO_5$ systems have very low critical decomposition (stability) temperatures, with 7 out of 15 systems showing T_{cr} even below room temperature. Consequently, if low-temperature modifications of solid solutions are stabilized by doping up to high temperatures, they may remain stable over a wide temperature range from room temperature up to the melting temperatures, 2170–2320 K for the REE oxyorthosilicates [22]. This fact may indicate a particular advantage of materials based on the $(Y_{1-x}Ln_x)_2SiO_5$ oxyorthosilicate solid solutions in terms of stability and reproducibility of properties compared to similar materials based on other REE oxyorthosilicate solid solutions, such as those mentioned in [23].

As the temperature decreases, the mobility of the structural units in a solid solution diminishes due to reduced diffusion rates, leading to a narrowing of the solubility range [5]. This continues until the diffusion rate becomes so low that the reduction in solubility ranges practically stops, resulting in spontaneous quenching and the solid solutions becoming metastable. Assuming that the quenching temperature is close to the minimum temperature at which component interaction begins in the solid

phase to form a solid solution, one can estimate the quenching temperature and the metastability range in the system [24, 25].

Synthesis of REE orthosilicates and their solid solutions using the solid-state method is typically carried out over a wide temperature range up to 1773 K, using oxides of the corresponding elements as starting materials [26]. However, more accurately determining the temperature at which the interaction of the system components begins can be achieved with the sol–gel synthesis method. For example, it is known that in [27], amorphous solid samples of Y_2SiO_5:Eu were synthesized at 1123 K, which became crystalline after heating at 1173 K. It can be assumed that upon cooling solid solutions below the average temperature of approximately 1148 K, the mobility of structural units may be insufficient for thermodynamically unstable solid solutions to decompose, meaning they would become metastable.

Therefore, in the $(Y_{1-x}Ln_x)_2SiO_5$ systems with REEs from La to Pr, solid solutions that are thermodynamically stable at temperatures above the critical ones (2290–1180 K) become thermodynamically unstable when the temperature decreases to the range between the critical temperature and approximately 1148 K. In this range, they may decompose if the diffusion rate and time are sufficient to form and grow stable nuclei of a new phase. At temperatures lower than approximately 1148 K, the solid solutions might not decompose, meaning they could undergo spontaneous quenching and become metastable.

In systems with REEs from Nd to Lu, solid solutions will be thermodynamically stable at temperatures higher than the critical temperatures (in the range of 930–1300 K). At lower temperatures, they will become metastable and may not decompose.

For all systems $(Y_{1-x}Ln_x)_2SiO_5$, decomposition temperatures were also calculated across the entire composition range $1.0 > x > 0$ with a step of $x = 0.05$, and decomposition domes were plotted (Fig. 9.3a–d). These allow for a more precise graphical determination of the thermodynamic stability regions, decomposition temperature for a given composition limit of the solid solution, or its equilibrium composition limit for a specified decomposition temperature.

9.3.3 Comparison of Calculation Results with Literature Data

The literature lacks data regarding the thermodynamic stability, substitution limits, and critical decomposition temperatures of solid solutions in the $(Y_{1-x}Ln_x)_2SiO_5$ systems. This certainly complicates the assessment of the accuracy of the calculations performed. However, data are available for the synthesis temperatures of solid solutions in several $(Y_{1-x}Ln_x)_2SiO_5$ systems (see Table 9.3).

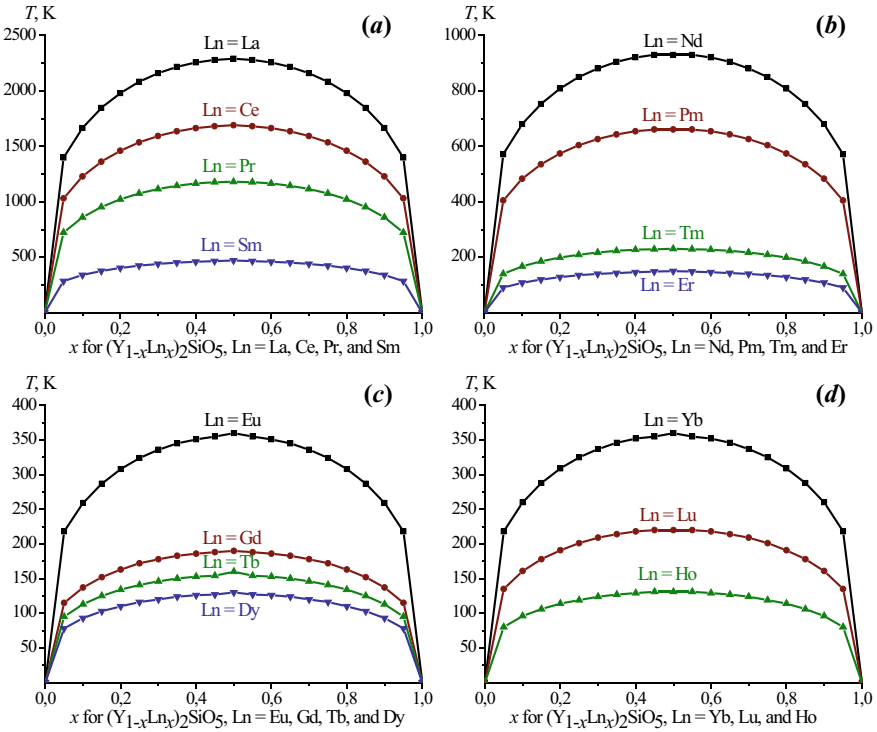

Fig. 9.3 Decomposition domes of solid solutions of oxyorthosilicates $(Y_{1-x}Ln_x)_2SiO_5$: **a** Ln = La, Ce, Pr, and Sm; **b** Ln = Nd, Pm, Tm, and Er; **c** Ln = Eu, Gd, Tb, and Dy; **d** Ln = Yb, Lu, and Ho

9.3.3.1 Thermodynamic Stability Regions of Solid Solutions

Synthesis of solid solutions in the systems described in [27, 29, 32–38, 40] was carried out in the temperature range of 1023–1773 K (Table 9.3), which is significantly higher than the critical temperatures (148–1180 K), i.e., in the regions of thermodynamic stability. A continuous series of solid solutions may be stable in the indicated systems in this temperature range.

The synthesis of the solid solutions described in [26, 30, 36, 40] was carried out at temperatures of 1773, 1273, 1023–1223, and 1473 K, which are significantly lower than the critical temperatures of 2287, 1687, 1687, and 2287 K, respectively, but still higher than the decomposition dome temperatures for compositions with $x <$ 0.5, i.e., within the thermodynamically stable regions (see Fig. 9.4). However, in the system $(Ce_xY_{1-x})_2SiO_5$ [36], decomposition of the $(Ce_{0.05}Y_{0.95})_2SiO_5$ solid solution is possible, as its synthesis temperature does not differ from the decomposition temperature within the calculation method error (±100 K).

The solid solutions of the $(Y_{1-x}Pr_x)_2SiO_5$ systems described in [3, 28, 31, 39] were synthesized at temperatures of 1223, 1173, 1173, and 1173 K, respectively,

Table 9.3 Comparison of T_{cr} calculation results for solid solutions of oxyorthosilicates $(Y_{1-x}Ln_x)_2SiO_5$ with space group $P2_1/c$ with literature data

Composition*, ref	x, unit or percentage	Synthesis method, product characterization	$T_{synthesis}$ (K)	T_{cr} (K)
$Y_2SiO_5:Pr^{3+}$ [3]	0.47, 0.77, 0.96, 2.95, and 4.93%	Sol–gel, nanomaterials	1223	1180
$(Y_{1-x}La_x)_2SiO_5:Ce_{0.01}$ [26]	< 0.05	Solid phase	1523	2287
Y_2SiO_5:Eu [27]	100% (?)	Sol–gel and solid phase	1173** 1773**	356
$Y_2SiO_5:Pr^{3+}$ [28]	1, 2, 4, 10%	Sol–gel, nanomaterials	1173	1180
$Y_2SiO_5:Sm^{3+}$ [29]	1–9%	By ultrasonic treatment, nanophosphorus	1373–1573	465
Y_2SiO_5:Ce [30]	0.25, 0.5, 0.75, 1, 2, 4, 6, and 8%	Solution combustion synthesis (SCS), nanoscintillator	1273	1687
$Y_2SiO_5:Pr^{3+}$ [31]	0.5–2%	Sol–gel, nanomaterials	1173	1180
$Y_{2-x}Tb_xSiO_5$ [32]	0.02, 0.04, 0.06, 0.08, 0.10, 0.12, 0.16, and 0.20	Sol–gel, nanomaterials	1173	155
$Y_{2-x}Tb_xSiO_5$ [33]	$5\bullet10^{-4}$ – $5\bullet10^{-1}$	Solid phase	1573	155
$Er_xY_{2-x}SiO_5$ [34]	0, 0.26, 1,5, 10, 18 and 25%	Centrifugation of solutions in ethanol, nanomaterials	1173	148
$Y_{1.92-x}Gd_xSiO_5:Ce_{0.08}$ [35]	0.00, 0.25, 0.50, and 0.75	Solid phase	1373	188
$(Eu_xY_{1-x})_2SiO_5$ [36]	0.005, 0.01, 0.02, 0.03, and 0.05	Sol–gel, thin films	1023	356
$(Tb_xY_{1-x})_2SiO_5$ [36]	0.005, 0.01, 0.02, 0.03, and 0.05	Sol–gel, thin films	1023	155
$(Ce_xY_{1-x})_2SiO_5$ [36]	0.005, 0.01, 0.02, 0.03, and 0.05	Sol–gel, thin films	1023	1687
$Eu_{0.25}Y_{1.75}SiO_5$ [37]	0.25	Metallorganic decomposition (MOD)	1323	356
$Tb_{0.13}Y_{1.87}SiO_5$ [37]	0.13	Metallorganic decomposition (MOD)	1323	155
$Sm_{0.05}Y_{1.95}SiO_5$ [37]	0.05	Metallorganic decomposition (MOD)	1323	465

(continued)

Table 9.3 (continued)

Composition*, ref	x, unit or percentage	Synthesis method, product characterization	$T_{synthesis}$ (K)	T_{cr} (K)
$Y_2SiO_5:Pr^{3+}$ (X1 с примесью X2 и $Y_2Si_2O_7$, SiO_2) [38]***	0.1, 1, 2, 3, 4%	Electrophoretic film deposition	1473	1180
$Y_2SiO_5:Pr^{3+}$ [39]	0.01, 0.1, 0,5, 1.0, 2.0, 4.0, 10.0%	Sol–gel, nanomaterials	1173	1180
$(Y_{0.995-x}Gd_xCe_{0.005})_2SiO_5$ [40]	0.05, 0.1, 0.15, 0.20, 0.25, 0.30, 0.35, and 0.40	MS&Sol–gel method + calcination	1473	188
$(Y_{0.995-x}La_xCe_{0.005})_2SiO_5$ [40]	0.01, 0.02, 0.03, 0.04, and 0.05	MS&Sol–gel method + calcination	1473	2287

Notes *The composition of the solid solutions is given according to formulae from the original articles

**Nanocrystalline $Y_{2-x}Eu_xSiO_5$ [27] with a particle size of 50 nm, obtained by the sol–gel method at 1173 K, has an extinction concentration of $x = 0.6$, whereas the solid-state synthesized sample at 1773 K with a particle size of 2 μm has an extinction concentration of $x = 0.2$. Additionally, the nanomaterial exhibits higher luminescence intensity

***As shown in [38], the X1 phase with X2, $Y_2Si_2O_7$, and SiO_2 impurities may form in systems with REEs from the cerium subgroup at low dopant contents (up to 4%)

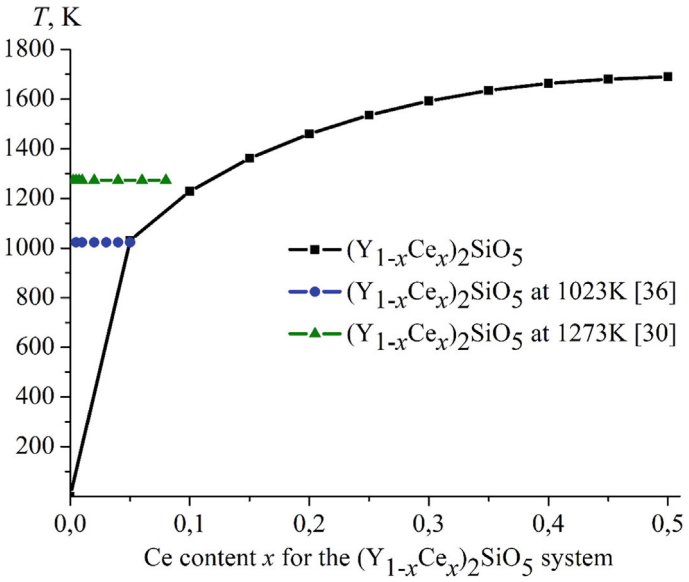

Fig. 9.4 Fragment of the decomposition dome (T_{cr} = 1687 K) for the solid solution of the $(Y_{1-x}Ce_x)_2SiO_5$ system and experimental data for the synthesis temperatures of samples for the systems Y_2SiO_5:Ce at 1273 K [30] and $(Ce_xY_{1-x})_2SiO_5$ at 1023 K [36]. For the samples from [36], the lower limit of the synthesis temperature range used (1023–1223 K) is shown

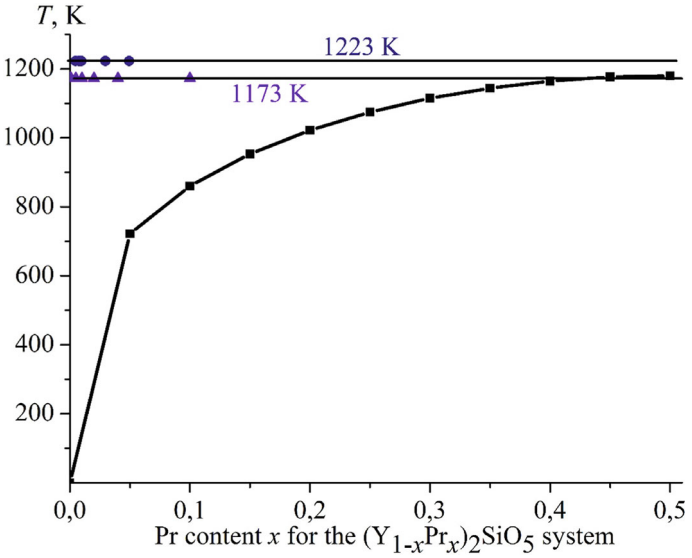

Fig. 9.5 A fragment of the decomposition dome for the solid solution in the $(Y_{1-x}Pr_x)_2SiO_5$ system ($T_{cr} = 1180$ K) and experimental data on the synthesis temperatures of samples at 1223 K [3], 1173 K [28, 31, 39]

which differ from the critical temperature (1180 K) within the calculation method error (±100 K). Therefore, it is impossible to assess these solid solutions' thermodynamic stability based only on the critical temperature. However, considering their composition ($x \leq 0.10$) and synthesis temperatures (1223 K [3], 1173 K [28, 31, 39]), which exceed the corresponding decomposition dome temperatures ($\leq$ 860 K, see Fig. 9.5), it can be assumed that they were synthesized in the region of thermodynamic stability.

9.3.3.2 Limits of Isomorphous Substitutions

To our knowledge, the substitution limit has only been experimentally established for the $(Y_{0.995-x}La_xCe_{0.005})_2SiO_5$ system, where at 1473 K, it is equal to $x = 0.05$ [40]. This result agrees with our calculated value of $x = 0.06$ for this temperature (Fig. 9.6). The calculated decomposition temperature for the composition of $x = 0.05$ is 1398 K, differing by 75 K from the experimental temperature of 1473 K, within the calculation error of ± 100 K.

In [26], for nearly the same system, $(Y_{1-x}La_x)_2SiO_5$:$Ce_{0.01}$, it was found that the possible substitution limit at 1773 K is less than 0.05. The higher temperature in [26] and the formation of a non-single-phase sample at $x = 0.05$ are likely due to using the solid-state synthesis method from oxides. In contrast, the study [40] employed

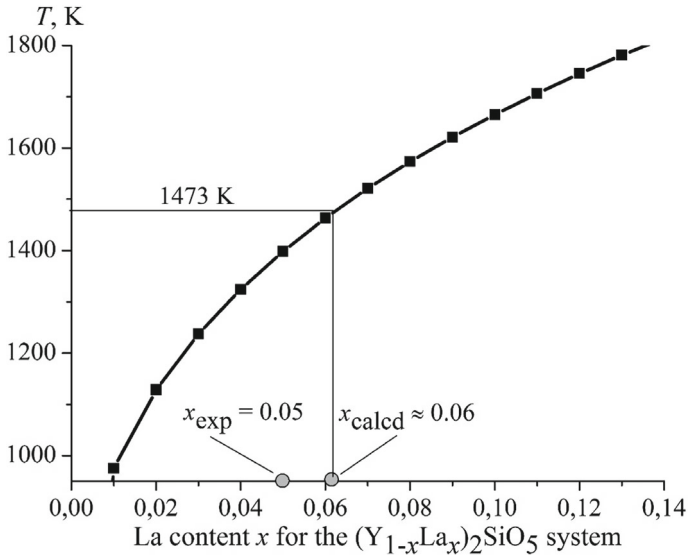

Fig. 9.6 Fragment of the decomposition dome for the solid solution system $(Y_{1-x}La_x)_2SiO_5$: calculated (0.06) and experimentally found (0.05 [40]) limits of isomorphous substitution of yttrium by lanthanum at 1473 K.

the MS&Sol–gel method, which achieves a greater degree of chemical equilibrium than the solid-state synthesis method from oxides.

Thus, the calculation results do not contradict the experimental literature data in the sense that the synthesis of solid solutions for most $Y_{1-x}Ln_xSiO_5$ systems, except for $(Ce^{3+}{}_xY_{1-x})_2SiO_5$ ($x = 0.05$) [36], was carried out within the thermodynamically stable regions predicted by us. Moreover, the calculated substitution limit of yttrium by lanthanum in the system $(Y_{1-x}La_x)_2SiO_5$:$Ce_{0.01}$, equal to 0.06, agrees with the limit of 0.05 (Fig. 9.6) found experimentally in the study [40].

9.4 Conclusions

1. The contributions of Q_ε to the total mixing energy Q, due to differences in the ionicity of the chemical bonds of the system components, increase with the REEs atomic number increasing in both the cerium and yttrium subgroups similarly and reach maxima in the cases of $(Y_{1-x}Eu_x)_2SiO_5$ and $(Y_{1-x}Yb_x)_2SiO_5$, respectively, and then decrease. The peculiarities of the f-electron orbital filling of the REE atoms explain this behavior.
2. The contributions Q_δ to the total mixing energy Q, due to the differences in the sizes of the substituting structural units, vary across the systems from $(Y_{1-x}La_x)_2SiO_5$ to $(Y_{1-x}Ho_x)_2SiO_5$. These contributions decrease significantly

from 28.23 kJ/mol to nearly zero and then slightly increase to 1.74 kJ/mol in the series from $(Y_{1-x}Ho_x)_2SiO_5$ to $(Y_{1-x}Lu_x)_2SiO_5$. This variation is explained by the proximity of the crystal ionic radii of yttrium and holmium.

3. The total mixing energies and critical decomposition temperatures for substituting yttrium with REEs from the cerium subgroup are mainly determined by the differences in the sizes of the substituting structural units. In contrast, these parameters for the yttrium subgroup are determined by the differences in the degree of ionicity of the chemical bonds in the system components.
4. Thermodynamic stability diagrams and decomposition domes for the $(Y_{1-x}Ln_x)_2SiO_5$ systems are presented, which allow for the graphical prediction of decomposition temperatures of solid solutions based on given substitution limits, equilibrium substitution limits at a specified temperature and the assessment of thermodynamic stability regions.
5. Most systems with REEs from the yttrium subgroup (except for $(Y_{1-x}Yb_x)_2SiO_5$) have critical decomposition temperatures below room temperature. Therefore, they exhibit a broad temperature range of thermodynamic stability. Additionally, these materials could be preferentially used for nanomaterials production, as nanomaterials are typically synthesized at relatively low temperatures.
6. The results of the calculations are consistent with experimental literature data in that the synthesis of solid solutions in the systems $(Y_{1-x}Ln_x)_2SiO_5$ in most studies (19 out of 21 cited sources) was carried out within the thermodynamically stable regions predicted by us. Additionally, the calculated substitution limit in the system $(Y_{1-x}La_x)_2SiO_5$ at 1473 K ($x = 0.06$) is almost identical to the previously experimentally determined value ($x = 0.05$).

Acknowledgements The research was carried out within the framework of the Fundamental Research Programme of the Ministry of Education and Science of Ukraine (Research Project No. 0122U000762).

References

1. H. Jiao, F. Liao, S. Tian, X. Jing, Influence of rare Earth Sc and La to the luminescent properties of FED blue phosphor Y_2SiO_5:Ce. J. Electrochem. Soc. **151**(7), J39–J42 (2004). https://doi.org/10.1149/1.1757463
2. C.M. Michail, G.P. Fountos, S.L. David, I.G. Valais, A.E. Toutountzis, N.E. Kalyvas, I.S. Kandarakis, G.S. Panayiotakis, A comparative investigation of Lu_2SiO_5: Ce and G_d2_O2S: Eu powder scintillators for use in x-ray mammography detectors. Meas. Sci. Technol. **20**(10), 104008 (2009). https://doi.org/10.1088/0957-0233/20/10/104008
3. Y. Yang, Ch. Liu, P. Mao, L.-J. Wang, Upconversion luminescence and photodegradation performances of Pr doped Y_2SiO_5 nanomaterials. J. Nanomater. 427370 (2013). https://doi.org/10.1155/2013/427370
4. J. Reichardt, M. Stiebler, R. Hirrle, S. Kemmler-Sack, Cathodo- and photoluminescence in oxyorthosilicates of X1 and X2 Type: system $Y_{2-x}Gd_xSiO_5$:Tb^{3+}. Phys. Status Solidi **119**(2), 631–642 (1990). https://doi.org/10.1002/pssa.2211190227

5. V.S. Urusov, *Teoriia izomorfnoi smesimosti* [Theory of isomorphous miscibility] (Nauka, Moskva, 1977) (in Russian)
6. V.S. Urusov, V.L. Tauson, V.V. Akimov, *Geokhimiya tverdogo tela* [Geochemistry of solid state] (GEOS, Moskva, 1997) (in Russian)
7. D. Spassky, A. Vasil'ev, V. Nagirnyi, I. Kudryavtseva, D. Deyneko, I. Nikiforov, I. Kondratyev, B. Zadneprovski, Bright UV-C phosphors with excellent thermal stability—$Y_{1-x}Sc_xPO_4$ solid solutions. Materials **15**, 6844 (2022). https://doi.org/10.3390/ma15196844
8. V.S. Voznyak-Levushkina, A.A. Arapova, D.A. Spassky, I.V. Nikiforov, B.I. Zadneprovski, Luminescent properties of Yttrium-Scandium phosphate solid solutions doped with Europium ions. Phys. Solid State **64**(11), 567–575 (2022). https://doi.org/10.1134/S1063783422110130
9. E.I. Get'man, S.V. Radio, L.I. Ardanova, Predicting the phase stability of $Sc_{1-x}Ln_xPO_4$ (Ln = Gd–Lu, Y) Zircon-structured solid solutions. Inorg. Mater. **54**(6), 596–600 (2018). https://doi.org/10.1134/S0020168518060031
10. R. Becker, Über den Aufbau binarer Legierungen. *Z. Metallkunde*, vol. 29 (1937), pp. 245–249 (in German)
11. J. Wang, S. Tian, G. Li, F. Liao, X. Jing, Preparation and X-ray characterization of low-temperature phases of R_2SiO_5 (R = rare earth elements). Mater. Res. Bull. **36**(10), 1855–1861 (2001). https://doi.org/10.1016/S0025-5408(01)00664-X
12. E.G. Yukihara, L.G. Jacobsohn, M.W. Blair, B.L. Bennett, S.C. Tornga, R.E. Muenchausen, Luminescence properties of Ce-doped oxyorthosilicate nanophosphors and single crystals. J. Lumin. **130**(12), 2309–2316 (2010). https://doi.org/10.1016/j.jlumin.2010.07.010
13. R.E. Muenchausen, E.A. McKigney, L.G. Jacobsohn, M.W. Blair, B.L. Bennett, D.W. Cooke, Science and application of oxyorthosilicate nanophosphors. IEEE Trans. Nucl. Sci. **55**(3), 1532–1535 (2008). https://doi.org/10.1109/TNS.2008.922844
14. E.I. Get'man, Yu.A. Oleksii, S.V. Radio, L.I. Ardanova, Determining the phase stability of luminescent materials based on the solid solutions of oxyorthosilicates $(Lu_{1-x}Ln_x)[(SiO_4)_{0.5}O_{0.5}]$, where Ln = La−Yb. Tonkie Khimicheskie Tekhnologii **15**(5), 54–62 (2020). https://doi.org/10.32362/2410-6593-2020-15-5-54-62
15. R.D. Shannon, Revised effective ionic radii and systematic studies of interatomic distances in halides and chalcogenides. Acta Cryst. **A32**(5), 751–767 (1976). https://doi.org/10.1107/S0567739476001551
16. K. Li, D. Xue, Estimation of electronegativity values of elements in different valence states. J. Phys. Chem. A **110**(39), 11332–11337 (2006). https://doi.org/10.1021/jp062886k
17. S.S. Batsanov, *Strukturnaya khimiya. Fakty i zavisimosti* [Structural chemistry. Facts and dependencies] (Dialog-MGU, Moskva, 2000) (in Russian)
18. J. Felsche, The crystal chemistry of the rare-earth silicates, in *Rare Earths. Structure and Bonding*, vol. 13 (Springer, Heidelberg, 1973), pp. 99–197. https://doi.org/10.1007/3-540-06125-8_3
19. R. Hoppe, Madelung constants as a new guide to the structural chemistry of solids. Adv. Fluor. Chem. **6**, 387–438 (1970)
20. S.S. Batsanov, The concept of electronegativity. Conclusions and prospects. Russ. Chem. Rev. **37**(5), 332–351 (1968). https://doi.org/10.1070/RC1968v037n05ABEH001639
21. E.I. Get'man, S.V. Radio, Mixing energies (interaction parameters) and decomposition temperatures in solid solutions of monazites of rare earth elements with structure $La_{1-x}Ln_xPO_4$. Inorg. Mater. **53**(7), 718–721 (2017). https://doi.org/10.1134/S0020168517070044
22. B. Grynyov, V. Ryzhikov, J.K. Kim, M. Jae, *Scintillator Crystals, Radiation Detectors & Instruments on Their Base* (Kharkiv, Ukraine, 2004). http://functmaterials.org.ua/contents/book/Ryzhikov-2004.pdf
23. E.I. Get'man, S.V. Radio, Predicting the substitution of rare-earth elements with cerium in the solid solutions based on nanoscale Ln_2SiO_5 (Ln = Tb–Lu, Y). Nanosistemi, Nanomateriali, Nanotehnologii **17**(4), 701–710 (2019). https://doi.org/10.15407/nnn.17.04.701
24. E.I. Get'man, S.V. Radio, L.B. Ignatova, L.I. Ardanova, Energies of mixing (interaction parameters), substitution limits, and phase stability of solid solutions $Lu_{1-x}Ln_xVO_4$ (Ln = Ce–Yb, Sc, Y). Russ. J. Inorg. Chem. **64**(1), 118–124 (2019). https://doi.org/10.1134/S0036023619010091

25. S.V. Radio, E.I. Get'man, L.I. Ardanova, Substitution limits and thermodynamic stability of solid solutions in HTSC based on iron and yttrium oxyarsenides. Low Temp. Phys. **49**(2), 197–203 (2023). https://doi.org/10.1063/10.0016895
26. J. Wang, S. Tian, G. Li, F. Liao, X. Jing, Influence of rare earth elements (Sc, La, Gd, and Lu) to the luminescent properties of FED blue phosphor Y_2SiO_5:Ce. J. Electrochem. Soc. **148**(6), H61–H66 (2001). https://doi.org/10.1149/1.1369376
27. W. Zhang, P. Xie, C. Duan, K. Yan, M. Yin, L. Lou, S. Xia, J.-C. Krupa, Preparation and size effect on concentration quenching of nanocrystalline Y_2SiO_5:Eu. Chem. Phys. Lett. **292**(1–2), 133–136 (1998). https://doi.org/10.1016/S0009-2614(98)00656-3
28. A.A. Masalov, A.V. Sorokin, S.L. Yefimova, I.Yu. Kuril'chenko, Yu.V. Malyukin, Osobennosti lyuminestsentsii v nanodispersnykh materialakh [Features of luminescence in nanodispersed materials]. Nanostrukturnoye materialovedeniye 1, 3–15 (2011). http://dspace.nbuv.gov.ua/handle/123456789/62747 (in Russian)
29. M. Mangala Gowri, G.P. Darshan, Y.V. Naik, H.B. Premkumar, D. Kavyashree, S.C. Sharma, H. Nagabhushana, Phase dependent photoluminescence and thermoluminescence properties of $Y_2SiO_5:Sm^{3+}$ nanophosphors and its advanced forensic applications. Opt. Mater. **96**, 109282 (2019). https://doi.org/10.1016/j.optmat.2019.109282
30. A. Dickey, Nano-Scintillators as Next Generation Tools for Optogenetics. A Dissertation Presented to the Graduate School of Clemson University. All Dissertations, 2966 (2020). https://tigerprints.clemson.edu/all_dissertations/2966
31. V.V. Seminko, A.A. Masalov, Yu.I. Boyko, Yu.V. Malyukin, Strong segregation of doped ions in $Y_2SiO_5:Pr^{3+}$ nanocrystals. J. Lumin. **132**(9), 2443–2446 (2012). https://doi.org/10.1016/j.jlumin.2012.04.056
32. H. Huang, B. Yan, Sol-gel preparation and luminescence properties of nanophosphors $Y_{2-x}Tb_xSiO_5$ derived from in situ assembling hybrid precursors. J. Non-Cryst. Solids **351**(6–7), 618–621 (2005). https://doi.org/10.1016/j.jnoncrysol.2005.01.048
33. Y.Y. Choi, K.-S. Sohn, H.D. Park, S.Y. Choi, Luminescence and decay behaviors of Tb-doped yttrium silicate. J. Mater. Res. **16**(3), 881–889 (2001). https://doi.org/10.1557/JMR.2001.0116
34. K. Suh, J.H. Shin, S.-J. Seo, B.-S. Bae, Er^{3+} luminescence and cooperative upconversion in $Er_xY_{2-x}SiO_5$ nanocrystal aggregates fabricated using Si nanowires. Appl. Phys. Lett. **92**(12), 121910 (2008). https://doi.org/10.1063/1.2890414
35. P. Thiyagarajan, B. Tiwari, M. Kottaisamy, N. Rama, M.S. Ramachandra Rao, UV excitable $Y_{2-x-y}Gd_ySiO_5:Ce_x$ phosphors for cool white light emission. Appl. Phys. A **94**, 607–612 (2009). https://doi.org/10.1007/s00339-008-4861-z
36. Q.Y. Zhang, K. Pita, S. Buddhudu, C.H. Kam, Luminescent properties of rare-earth ion doped yttrium silicate thin film phosphors for a full-colour display. J. Phys. D Appl. Phys. **35**(23), 3085 (2002). https://doi.org/10.1088/0022-3727/35/23/308
37. Y. Liu, C.N. Xu, K. Nonaka, H. Tateyama, Strong blue, green and red light emission at elevated temperatures from Y_2SiO_5 doped by the rare-earth ions. J. Mater. Sci. **36**(18), 4361–4364 (2001). https://doi.org/10.1023/A:1017953913334
38. T. Kang, UVC Electroluminescence in $Y_2SiO_5:Pr^{3+}$ Powder and Film Phosphors. Thesis for the Degree of Doctor of Philosophy. The Graduate School, Pukyong National University (2020). http://surl.li/emulxd
39. A. Masalov, O. Viagin, I. Ganina, Yu. Malyukin, Strong quenching of praseodymium f-f luminescence induced by a surface of $Y_2SiO_5:Pr^{3+}$ nanocrystal. J. Lumin. **129**(12), 1695–1697 (2009). https://doi.org/10.1016/j.jlumin.2009.01.037
40. Q. Wu, X. Jing, H. Jiao, Preparation of La^{3+} and Gd^{3+} doped Y_2SiO_5: Ce phosphors by the MS&Sol-gel method. Opt. Mater. **31**(8), 1123–1127 (2009). https://doi.org/10.1016/j.optmat.2008.12.004

Chapter 10
Influence of γ-Radiation on Optical Characteristics Coordination Associations of Germanium

Ya. I. Lepikh

Abstract The influence of the ionizing agent was studied γ- about radiation on optical characteristics and coordination compounds of germanium (CCG). It was established that for CCG with H_4 OEDPH, a complex compound of germanium with tartaric acid and zinc, as well as CCG with tartaric acid and sodium under the influence of γ-rays for the 450 nm band almost complete transmission of incident light is observed for all samples. Absorption stability at a specific wavelength ionizing gamma radiation makes it possible to use CCG to build a γ-radiation sensor.

10.1 Introduction

A significant improvement in the characteristics of microelectronics devices and creation their new classes can be achieved, in particular, by using new functional materials [1–3]. In this connection, coordination compounds of germanium attract considerable attention [4–8]. A rather urgent issue is the study of the impact of ionizing radiation on the change in the physical characteristics of such materials for the purpose of further use materials of this new class, in particular, as active elements of ionizing radiation sensors or functional elements of devices based on them that work under conditions of exposure to radiation.

When studying radiation effects for semiconductors, the so-called irreversible (residual) and reversible (transient) effects are usually distinguished. Reversible disturbances are a consequence of the transition of electrons or holes into a non-equilibrium state, which usually leads to ionization. To irreversible disturbances include the rearrangement of atoms in lattices (formation vacancies, internodes in, dislocations), that is, the occurrence of so-called radiation defects. The interaction of γ-quanta with matter consists of three main processes: the photoeffect, Compton scattering, and the formation of electron–positron pairs. In fact, during the primary

Ya. I. Lepikh (✉)
Odesa I. I. Mechnikov National University, Odesa, Ukraine
e-mail: ndl_lepikh@onu.edu.ua

O. Fesenko and L. Yatsenko (eds.), *Functional Nanomaterials, Nanocatalysts, Nanotechnologies, and Their Applications*, Springer Proceedings in Physics 321,
https://doi.org/10.1007/978-3-031-99136-3_10

impact of γ- quanta on materials, rapid Compton photoelectrons, which in the future cause the atoms of the crystal lattice to shift from their equilibrium positions.

All changes occurring in semiconductor structures and devices based on them are associated with the formation of secondary electrons, lattice defects, and ionization of the medium due to the influence of γ-quanta. Analyzing the known materials, it is possible to conclude that the increase in radiation resistance is achieved by the complication of the atomic composition of substances. In this connection is increasing attention allocate complex compounds germanium.

The paper investigated the effect of γ-irradiation on the optical characteristics of coordination compounds of OEDPH with Ge(IV) – Zn and with Na.

10.2 Film Production Technology

Hexanuclear cyclic complex anions form the basis of the structure of germanium complex compounds Ge6(μ - OH)6(μ - OEDPH)6]6- [5]. Atoms Germanium in structures are combined in pairs hydroxyl and oxyethylenediphosphonate bridges. Everyone Ge coordinated along the vertices of the octahedron two oxygen atoms two hydroxogroup and four oxygen atoms phosphonic groups.

- Films for optical of research complex compounds germanium grown on glass linings (subject glass) by the so-called "flowing" method. To receive film was used isothermal evaporation (at a temperature of 20–25 °C) of an aqueous solution corresponding sample
- Solutions obtained by mixing 1 mol of distilled water from 0.2 g required complex compounds. Samples were well dissolved in water, solutions went out are uniform and transparent.
- Films obtained by this method were 1 μm thick, did not crack and had smooth the surface to increase thickness film throughout the application procedure repeated two or three more times.
- Irradiation was carried out with γ-quanta from the Co60 source. Irradiation was carried out in two stages: prepared samples from each material were irradiated at a dose of 1000 Gy, then measurements of selected parameters were carried out. After that, the samples were irradiated a second time at a dose of 50,000 Gy.
- Samples of OEDPH films, OEDPH with tartaric acid and zinc, OEDF with tartaric acid and sodium were studied.

10.3 Research Results and Their Discussion

Optical density spectra of CCG films before and after irradiation were obtained. The results of the measurements are represented by graphical dependences of the optical density spectra of each of the samples before and after irradiation (Figs. 10.1, 10.2 and 10.3).

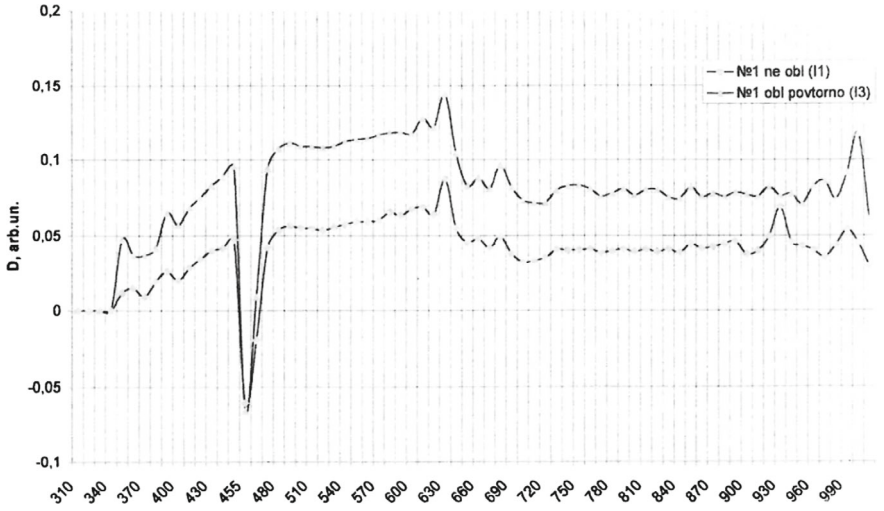

Fig. 10.1 Optical density spectrum based on oxyethylenediphosphonategermanic acid: 1—before irradiation, 2—after irradiation (dose 1000 Gy)

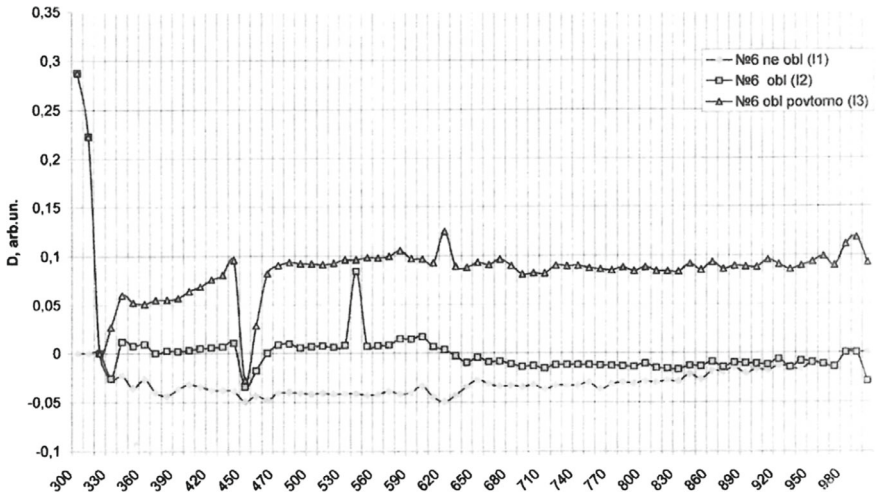

Fig. 10.2 Optical density spectrum of films based on CCG with tartaric acid and zinc: 1—before irradiation, 2—after irradiation (dose 1000 Gy), C—after repeated irradiation (dose 51,000 Gy)

It was established that for KSG with H_4 0e dph most clearly stand out two bands: at a wavelength of 650 nm (2 eV) and at 450 nm (2.74 eV). After exposure data stripes are preserved even when increasing absorbed doses they are found more intensive. A number of bands in Fig. 10.1, that have not bright pronounced the nature of the post influence of γ-quanta are found more clearly.

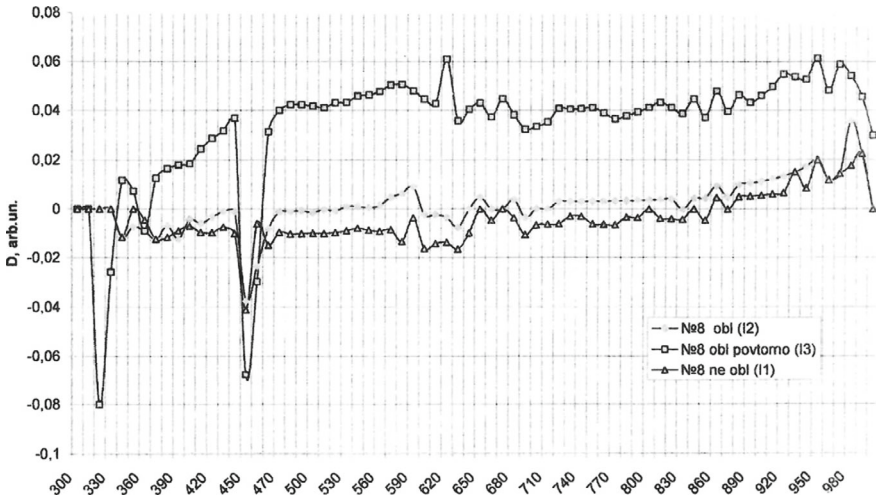

Fig. 10.3 Optical density spectrum of films based on CCG with tartaric acid and sodium: 1—before irradiation, 2—after irradiation (dose 1000 Gy), 3—after repeated irradiation (dose 51,000 Gy)

For the complex compound of germanium with tartaric acid and zinc (Fig. 10.2), it was established that under the influence of irradiation, the 650 nm (2 eV) band is smoothed out, while the 450 nm (2.74 eV) transmission band increases in intensity. It should be noted that the value of the dielectric constant under the influence of γ-irradiation on this complex compound increases. An absorbed radiation dose of 51,000 Gray corresponds to a 25% increase in dielectric constant.

For CCG with tartaric acid and sodium (Fig. 10.3), the value of the optical density for 2.74 eV keeps its value of 0.009 rel. unit independent of the absorbed dose of radiation. At this point, there is almost complete transmission of incident light. The 2.05 eV band at the first irradiated is smoothed out, and when repeated completely is disappearing. Others line after exposure are stored.

Analysis received experimental data allows do the following assumptions about physical mechanisms impact γ-irradiation. If consider complex compounds as cyclic polymers, then it is possible for them select two possible ones processes impact ionizing irradiation is a process stitching—formation chemical connections between individual macromolecules and destruction—breaking of the main chain polymer, separation fragments into macromolecules. Stitching and destruction polymers—irreversible radiation-chemical processes that lead to the most significant x changes physical structure and chemical polymer constructions materials.

Because complex compounds are closed structural units, then the process stapling is unlikely. So, quite the process is possible destruction. For given the assumption says the same thing as in complex formation germanium reveals coordination number 6 (while his valence is equal to 4), that is gap coordination connections most likely when exposed about radiation.

Analyzing all received spectral dependencies optical density from doses impact γ-op romination, it is impossible not to notice lane 450 nm (2.75 eV). Moreover, beyond dependence from the composition of the complex, this strip it turns out enough clearly and stably. It is obvious that it is due to the very structure of the complex compounds.

10.4 Conclusion

Based on the results of research, the following was established.

1. Out of three studied complex compounds of germanium OEDF at a dose of γ-irradiation of 51,000 Gy, a significant increase in the intensity of the bands detected on the optical density spectrum is observed. The value of the absorption coefficient for the 2.74 eV band retains its value of 0.03 relative to unit regardless of the absorbed radiation dose.
2. In CCG with tartaric acid and zinc at a dose of γ-irradiation of 1000 A significant increase in the intensity of the 2.74 eV band is observed in the optical density spectrum of Gy. When the radiation dose increases to 51,000 Gy, the 2 eV band is smoothed out.
3. At a dose of γ-irradiation of 1000 Gy on CCG with tartaric acid and sodium, a smoothing of the 2.05 eV band is observed, and when the dose is increased to 51,000 Gy, this band disappears. The absorption coefficient for the 2.74 eV band retains its value of 0.009 relative to unit regardless of the absorbed radiation dose. At this point, almost complete transmission of incident light is observed.
4. From the received spectra optical density, it can be seen that for the band 2.74 eV for all samples observed almost complete transmission falling of light Stable pass the ability to give length waves due to the structure of the complex itself.
5. Thus, γ-irradiation some materials class complexes of germanium with OEDF leads to substantial and stable with mines and spectral characteristics that can be used to create sensors ionizing radiation, as well as taking into account such an impact of ionizing radiation on the characteristics of devices built on the basis of CCG.

References

1. Ya.I. Lepikh, S.V. Lienkov, V.H. Melnyk, S.V. Dziadevych, Mikroelektronni datchyky dlia informatsiinykh (intelektualnykh) system spetsialnoho pryznachennia. Nauka i oborona №3, S.54–55 (2010). https://shron1.chtyvo.org.ua/Nauka_i_oborona/2010_N3.pdf?PHPSESSID=2d9n4lq632g68bdrbsd45u4mi3
2. Ya.I. Lepikh, S.V. Lenkov, A.A. Druzhinin, Detektory ioniziruyushih izluchenij dlya sistem radiacionnoj bezopasnosti. Suchasna specialna tehnika №2(21), C. 86–99 (2010). https://suchasnaspectehnika.com/

3. Ya.I. Lepikh, V. Machulin, V. Lytovchenko, O. Stronskyi, V. Smyntyna, Sensoryka – perspektyvnyi napriam rozvytku suchasnykh intelektualnykh informatsiinykh system. Visnyk NAN Ukrainy, №11, S. 27–29 (2010). http://dspace.nbuv.gov.ua/handle/123456789/27754
4. Ya.I. Lepikh, S.V. Lienkov, A.A. Yevtukh, S.V. Dziadevych, V.Iu.Protsenko, Doslidzhennia novoho klasu materialiv kompleksnykh spoluk hermaniiu z bahatoosnovnymy orhanichnymy kyslotamy. Zb. nauk. prats Viiskovoho in-tu Kyivskoho nats. un-tu im. T. Shevchenka, Vyp. №30.-Kyiv, S.55–61 (2011)
5. I.I. Sejfullina, E.E. Marcinko, G.G. Aleksandrov, V.S. Sergienko, Sintez, svojstva i stroenie poliyadernyh oksietilidendifosfonatogermanatov: kristallicheskaya i molekulyarnaya struktura dvuh solej na ih osnove. Zhurn. Neorg. Himii. T.46, №6, S.928–937 (2004). https://eposlink.com/ru/catalog/library/elibrary/book/zhurnal_neorganicheskoy_himii-1987/publication/126272/
6. Ya.I. Lepikh, Physical properties of the thin films based he germanium compounds with a supramolecular structure, in *Abstract Book of International Research and Practice Conference "Nanotechnology and nanomaterials" (NANO-2023)*, 16–19 Aug 2023, Bukovel, Ukraine, p. 363 (2023). https://eenukraine.com/wp-content/uploads/nano/nano23/
7. Ya.I. Lepikh, Electruphysical properties transport mechanisms in semiconductor complex compounds with supramolecular structure, in *Nanooptics and Nanoelectronics, Nanobiotechnology, end Their Applications. Selected proceeding of the 11th International Conference on Nanotechnology and Nanomaterials (NANO 2023)* 16–19 Aug 2023, Bukovel, Ukraine, Springer Proceeding in Physics, vol. 312, pp. 484–494 (2023). https://doi.org/10.1007/978-3-031-67527-0_33
8. Ya.I. Lepikh, Influence of ionized radiation on optical characteristics og Ge coordinate compounds, in *Abstract Book of International Research and Practice Conference "Nanotechnology and Nanomaterials" (NANO-2024)*, 21–24 Aug 2024, Uzhhorod, Ukraine, p. 47 (2024). http://nano-conference.iop.kiev.ua/assets/files/program2024.pdf

Chapter 11
Composite Catalysts in the Processing of Secondary Raw Materials for ABS Plastic Production

Viktor Kurylenko, Olena Yanushevska, and Tetiana Dontsova

Abstract This study examines the potential for producing ABS plastic from secondary raw materials. The selection of secondary raw materials is based on their availability in Ukraine, which presents novel opportunities to develop alternative catalytic technologies for the production of ABS plastic precursors that are independent of oil prices. In order to achieve this objective, it is of particular importance to create selective and highly active catalysts. Currently, catalysts are understood to be composites comprising aluminosilicates, various carriers with an extensive range of modifiers, and the so-called PNNL catalysts. Accordingly, the aim of this study was to review existing catalytic technologies and promising catalysts for processing secondary raw materials (technical glycerol, bioethanol, and PS plastic waste) into monomers (acrylonitrile, butadiene, and styrene) for the subsequent synthesis of ABS plastic. The analysis of existing literature indicates that the production of acrylonitrile from glycerol represents a promising avenue for the advancement of environmentally sustainable organic synthesis technologies. Furthermore, the utilization of water-containing ethanol as a raw material for butadiene production offers a dual advantage in terms of financial and environmental considerations. The production of styrene from polystyrene using natural clinoptilolite presents significant advantages, offering an economically beneficial alternative for processing polymer waste into fuel-like products. It has been established that developing catalytic technologies for synthesizing ABS plastic precursors from secondary raw materials represents a promising direction, offering alternative, economical, and ecological technologies for their production.

V. Kurylenko (✉) · O. Yanushevska · T. Dontsova
National Technical University of Ukraine "Igor Sikorsky Kyiv Polytechnic Institute", Kyiv, Ukraine
e-mail: vi.kurylenko@kpi.ua

O. Fesenko and L. Yatsenko (eds.), *Functional Nanomaterials, Nanocatalysts, Nanotechnologies, and Their Applications*, Springer Proceedings in Physics 321,
https://doi.org/10.1007/978-3-031-99136-3_11

11.1 ABS Plastic Production

11.1.1 Introduction

Acrylonitrile–butadiene–styrene (ABS) copolymer is a well-known thermoplastic elastomer with rubber-like properties. It possesses several attractive characteristics, including impact strength, solvent resistance, and processability. Given its extensive range of applications in engineering, the technologies employed in the synthesis of ABS remain a topic of considerable interest in both industrial and academic research laboratories.

The primary method for producing ABS plastic is the bulk/emulsion copolymerization of styrene and acrylonitrile monomers in the presence of polybutadiene [1]. Consequently, the precursors for ABS plastic synthesis are acrylonitrile, butadiene, and styrene, which are obtained via catalytic technologies using various composite catalysts.

Catalysts currently under consideration for use in catalytic synthesis include composite aluminosilicate catalysts of both natural (Ukrainian zeolite and other Ukrainian raw materials) and synthetic origin [2], a wide range of modifiers (vanadium, molybdenum, antimony, nickel, cobalt, etc.) on various carriers (aluminum oxide, silicon oxide, zirconium oxide, etc.) [3], and the so-called PNNL catalysts (based on molybdenum phosphides) [4].

An analysis of the raw materials required for the catalytic synthesis of acrylonitrile, butadiene, and styrene indicates that the use of secondary raw materials, specifically, technical glycerol, bioethanol, and PS plastic waste is both promising and rational, given their sufficient availability in Ukraine.

Figure 11.1 illustrates the general scheme for obtaining ABS plastic from secondary material resources available in Ukraine, emphasizing the potential and relevance of developing catalytic technologies for synthesizing the precursors (acrylonitrile, butadiene, and styrene) of ABS plastic.

This can only be achieved through the utilization of highly active and selective composite catalysts. Accordingly, the objective of this study is to provide a comprehensive analysis of existing catalytic technologies and promising catalysts for processing secondary raw materials (technical glycerol, bioethanol, and PS plastic waste) into monomers (acrylonitrile, butadiene, and styrene) for subsequent synthesis into ABS plastic.

11.1.2 Acrylonitrile

Acrylonitrile has a wide range of applications, including the production of acrylic fibers for textiles, synthetic rubber, polymer plastics, and the synthesis of dyes, medicines, insecticides, and other products.

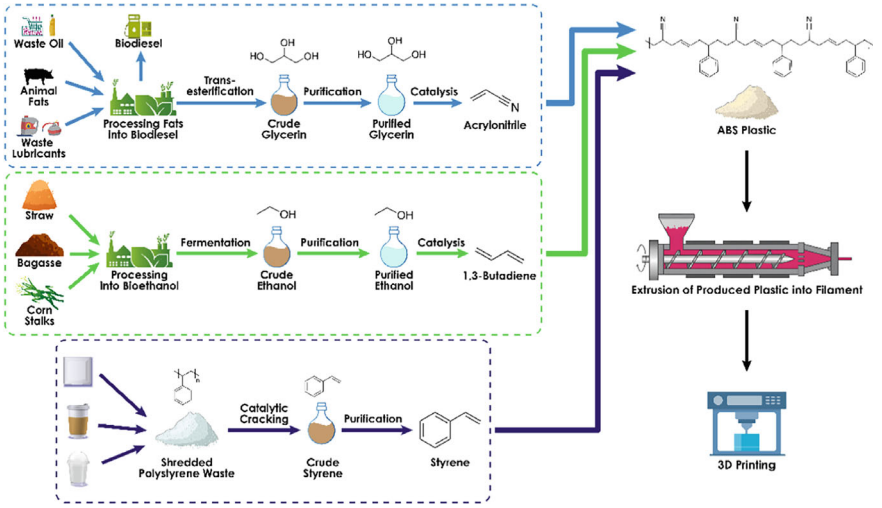

Fig. 11.1 General scheme for obtaining ABS plastic from secondary material resources available in Ukraine

The first synthesis of acrylonitrile was achieved by Charles Moureu in 1893; however, the technology was not widely adopted due to its high cost and complexity. A significant advancement in the production of acrylonitrile occurred in the late 1950s. Research conducted by SOHIO in the field of selective catalytic oxidation resulted in a notable reduction in the costs associated with the synthesis of acrylonitrile and its subsequent commercialization [5].

The developed technology, responsible for producing at least 90% of acrylonitrile today, employs propylene, air, and ammonia as raw materials. The process operates under a pressure of 0.3–2 bar at temperatures of 400–510 °C, utilizing catalysts such as oxides of tellurium, cerium, and molybdenum deposited on silica particles. A noteworthy benefit of this process is the high conversion of reagents in a single reactor pass with a residence time of only a few seconds. However, the persistent rise in propylene costs has resulted in elevated acrylonitrile production expenses, prompting the pursuit of alternative avenues in acrylonitrile synthesis. One such avenue is the substitution of conventional raw materials with secondary mineral raw materials, such as technical glycerol—a biodiesel production by-product—which could markedly reduce acrylonitrile synthesis costs.

Glycerol is an inexpensive by-product of biodiesel production, and its utilization has become increasingly relevant globally. Instead of disposal, crude glycerol can be transformed into other valuable products. Given its bioavailability, renewability, and distinctive structure, glycerol is an especially appealing starting material for the synthesis of a diverse array of specialized compounds, including acrylonitrile [6].

It has been demonstrated that acrylonitrile can be successfully obtained via the indirect ammoxidation of glycerol, with intermediate acrolein formation in two stages: dehydration and ammoxidation. In the initial stage of the process, whereby

glycerol is dehydrated to acrolein, a WO_3/TiO_2 catalyst is employed. In the subsequent ammoxidation stage, catalysts such as Sb–V–O or Sb–Fe–O are utilized. Notably, the Sb–Fe–O catalyst has demonstrated high selectivity, achieving an overall acrylonitrile yield of up to 40% [7].

Another study describes the synthesis of acrylonitrile from renewable raw materials through gas-phase ammoxidation of glycerol [8]. The synthesis can be achieved in a single stage (direct ammoxidation) or in two stages with preliminary dehydration (indirect ammoxidation).

In conclusion, the production of acrylonitrile from glycerol is still in its infancy but represents a promising avenue of research in the development of environmentally sustainable organic synthesis technologies. This approach permits the processing of secondary material resources and the production of ABS plastic from more cost-effective raw materials.

11.1.3 1,3-Butadiene

1,3-Butadiene (1,3-BD) is a diene of considerable importance, serving as a foundation for a wide range of organic syntheses, including the production of polymers such as synthetic rubbers, polymer resins, and plastics. The global demand for butadiene is gradually increasing due to growth in the tire industry, mechanical engineering, and civil construction, where styrene-butadiene rubber is actively used [9, 10]. However, the instability of raw material prices, particularly for butadiene, which depends on oil prices—represents a significant obstacle to market expansion.

Traditionally, butadiene is obtained through dehydrogenation of n-butane and n-butenes, which are extracted from C_4 streams during oil cracking at ethylene plants. This method is costly due to the necessity of extraction and distillation, resulting in a selectivity of only 4–5% [11]. Consequently, the ethanol-based method of producing butadiene from renewable raw materials, involving bioethanol derived from Thus, there are three main ways to produce butadiene: from the steam cracking of petroleum products, as a by-product of ethylene production, to obtain crude butadiene [12, 13]; from the catalytic dehydrogenation of n-butane and 1-butene, sequentially or separately [12]; from ethanol, the so-called “ethanol route”.

In the process of steam cracking of hydrocarbon feedstocks (ethane, propane, butane, oil, condensate or gas oil), which accounts for over 95% of world butadiene production, butadiene is one of the by-products of ethylene production (the process takes place in a pyrolysis furnace at a temperature of 790–830 °C). Steam cracking produces a pyrolysate with the following composition: ethylene, propylene, butadiene, hydrogen and several by-products. After removal of the high-boiling components (C_5 and above), the remaining products are pyrolysis crude gasoline (hydrogen and C_1–C_4), which is further processed to separate hydrogen, methane, ethylene and propylene. Crude butadiene is then left in the crude fraction [12].

Heavy crackers use crude oil, condensate or gas oils as feedstock and produce much larger quantities of butadiene and by-products. Light (ethane) crackers produce

8 times less butadiene, so most light crackers do not have butadiene recovery facilities. As a result, it is either returned to the cracker or collected in separate tanks for transfer to the regeneration stage. Depending on the operation of the plant and the feedstock used, the butadiene content of the crude butadiene is typically between 40 and 50%. The crude butadiene is purified by extractive distillation, which is necessary due to the formation of azeotropic mixtures by the components of the crude butadiene. This complex process involves one or two stages of extractive distillation followed by one or two stages of conventional distillation, which makes the technology very complex, costly and cumbersome. Thus, it can be concluded that the method of producing butadiene from steam cracking products is not acceptable for Ukraine, as it requires scarce oil resources, large and complex technologies, and the implementation of such processes requires disproportionate investment of money and human resources.

Oxidative catalytic dehydrogenation produces butadiene, water and CO, while non-oxidative dehydrogenation produces butadiene and H_2. In addition to the dehydrogenation reactions, several side reactions take place: CO_2 can react with H_2 (produced during the reaction) to form H_2O and CO, 1-butene can undergo isomerisation to cis- or trans-butene, and polymerisation of olefins or adsorbed intermediates can lead to the formation of coke.

Cr catalysts on various carriers such as SiO_2, ZrO_2, Al_2O_3, TiO_2 and silica materials are considered the most promising [14]. Studies on the synthesis of 1-butene to 1,3 butadiene in a CO_2 atmosphere on Cr–SiO_2 catalysts with Cr contents ranging from 0.5% to 9% showed a correlation between the yield of 1,3-BD (34% at 600 °C) and the amount of Cr^{6+}; the higher the Cr^{6+} content, the higher the yield of butadiene. In work [15], the developed ferric-based catalyst allowed to achieve 49% selectivity for 1,3-BD in a CO_2 atmosphere. The increase in selectivity was shown to be influenced by acid Lewis sites on the catalyst surface. Similar conclusions were reached by the authors of [16], where Fe_2O_3/γ-Al_2O_3 catalysts were modified with acid and alkalis (H_2SO_4, LiOH, NaOH and KOH): Li-Fe_2O_3/γ-Al_2O_3 > S-Fe_2O_3/γ-Al_2O_3 > Fe_2O_3/γ-Al_2O_3 >

K-Fe2O3/γ-Al_2O_3 > Na-Fe_2O_3/γ-Al_2O_3.

The oxidative dehydrogenation of n-butane to butadiene is carried out using a wide range of vanadium-based catalysts applied by different methods to a wide range of supports: TiO_2, ZrO_2 i Al_2O_3, SiO_2, CeO_2, γ-Al_2O_3, α-Al_2O_3, zeolites such as USY, NaY. In [3], a Ni-Bi-O-silica catalyst was used which was prepared by impregnating mesoporous silica supports (MCM-41, SBA-15 and silica foam) with nickel and bismuth salts (20% Ni and 30% Bi in the final catalyst).

The catalyst on the SBA-15 support showed the best efficiency (selectivity for butadiene 47.5% with n-butane conversion of 28.9%).

From the above parameters of n-butane and 1-butene dehydrogenation technologies, it can be concluded that, firstly, synthesis by dehydrogenation requires a feedstock base of n-butane and 1-butene, which for obvious reasons implies the same hydrocarbon production. Secondly, the process of dehydrogenating n-butane and 1-butene is no less cumbersome and complex, with a large number of by-products, than the process of purifying crude butadiene. It should be noted that the price of

1,3-butadiene has recently been volatile, which is not acceptable in the long term for industrial users of this important precursor.

The increase in the cost of production of 1,3-butadiene is explained by the rise in the price of crude oil and the so-called "shale gas" surge in Europe and the United States (shale gas contains ethane, which, when dehydrated to ethylene, serves as a feedstock for the synthesis of 1,3-butadiene). The increase in the cost of production of 1,3-butadiene is explained by the increase in the price of crude oil and the rise of so-called "shale gas" in Europe and the United States (shale gas contains ethane which, when dehydrated to ethylene, serves as a feedstock for the synthesis of 1,3-butadiene). The growing dependence on shale gas as a source of cheap natural gas may have negative effects and make society dependent on fossil resources alone, as technological progress should be aimed at developing a sustainable society that produces its energy, chemicals and materials in a more advanced, environmentally friendly and economical way [17]. For this reason, the chemical industry is constantly trying to find a sustainable and safe way to produce important chemical products that could fully match the quality characteristics of analogues derived from fossil raw materials, while at the same time finding ways to synthesise such substances in an efficient, cost-effective and, above all, environmentally friendly way, using secondary materials and waste. Achieving a circular economy in the chemical industry is a pressing and urgent task today.

The desire to replace or significantly reduce dependence on oil as the main source of 1,3-butadiene production is prompting a return to some renewable resources, in particular bioethanol produced from biomass. The production of 1,3-BD from ethanol has been a well-known industrial process from the 1920s to the early 1960s [18], and is now attracting renewed attention from researchers due to the above factors and the growth in global bioethanol production as an alternative fuel. The well-known process of ethanol conversion to butadiene is described by a sequence of reactions: dehydration, aldol condensation, Meerwein-Pondorf-Verley reduction and dehydration [19].

It is known that mixed metal oxides, including major components such as MgO and ZnO, are active catalysts for the conversion of ethanol to 1,3-BD with selectivities for BD below 80% in most of them [13, 18]. Paper [20] reports on the production of 1,3-butadiene from ethanol using zirconia and magnesium catalysts based on ash. The highest ethanol conversion, yield and selectivity of 1,3-butadiene were obtained using the Ash: MgO–ZrO_2 catalyst. At 350 °C, the ethanol conversion was 78% and the selectivity for 1,3-butadiene was 90.8%. These results indicate that the addition of zirconia increases the selectivity for 1,3-butadiene and is explained by the ability of ZrO_2 in the Ash: MgO–ZrO_2 catalyst to catalyse the dehydrogenation and aldol condensation steps. The authors explain this assumption by the fact that on the surface of zirconium(IV) oxide in monoclinic and tetragonal syngonies there are acid and basic Lewis sites that can interact with the hydrogen of the ethanol methyl group, allowing the formation of H–H bonds that facilitate dehydrogenation. At the same time, the ash provides redox catalytic sites and acidic Brønsted sites on the SiO_2 surface, accelerating the conversion of the aldol to 1,3-butadiene.

A number of interesting catalysts (Nb_2O_5/ZrO_2, Cu–Nb_2O_5/ZrO_2 and Ag–Nb_2O_5/ZrO_2) in the process of ethanol conversion to valuable products have been investigated in [21]. The addition of niobium(V) oxide to the catalyst resulted in the formation of a surface layer of crystalline Nb_2O_5 nanoparticles and increased the density of acid centres. The impregnation method allowed to obtain highly dispersed Ag and CuO nanoparticles on the surface of Nb_2O_5/ZrO_2, the presence of which, together with a reduction of the process temperature, significantly improved the ethanol dehydrogenation process. In addition, the selectivity for 1,3-butadiene and ethyl acetate increased with increasing contact time of the reagents with the catalyst.

The use of metal oxides (MgO, ZrO_2, Nb_2O_5, TiO_2, Al_2O_3, ZrO_2) as promoters deposited on a silica carrier allows high selectivity for 1,3-BD to be achieved.

The authors in [22] used the $4Ag/4ZrO_2/SBA-16$ catalyst prepared by impregnation. Promoters were also added, namely Li_2O, Na_2O, K_2O, Cs_2O, and silica was used as a carrier. Selectivity was achieved on the $0.5Na/4Ag/4ZrO_2/SBA-16$ catalyst. The formation of 1,3-butadiene from ethanol on the $Ag/ZrO_2/SiO_2$ zirconia catalyst was carried out [23] with the participation of two catalytic steps: dehydrogenation of ethanol to acetaldehyde on Ag/Si–OH sites and conversion of acetaldehyde or ethanol on acidic zirconia Lewis sites.

In [24], two-component Zn-Y clusters on the zeolite surface were synthesised and studied as catalysts for the conversion of ethanol to butadiene with a selectivity of ~63%. According to the authors, it was the influence of the structural confinement of the zeolite on the conversion of ethanol to 1,3-BD that provided the higher selectivity for butadiene. The study compares the effect of catalysts with two-component 5%Zn–5%Y clusters deposited on different matrices (zeolite H-beta, MCM-41 and SiO_2) and shows that the highest yield of 1,3-BD was achieved with 5%Zn–5%Y/beta. The authors suggest that close contact between different functional sites (acidic and basic) is more conducive to acetaldehyde condensation. The highest yield of 1,3-BD, namely 75%, was obtained at an ethanol conversion of 100% over a 2%Zn–8%Y/beta catalyst at 350 °C.

Specific to the practical production of 1,3-butadiene from ethanol is the presence of water in ethanol [13], which is derived from biomass. The conversion of ethanol to butadiene can take place in the presence of water, in contrast to the use of bioethanol as a fuel, which requires it to be anhydrous. Therefore, the use of ethanol with water as a feedstock for butadiene production is both financially and environmentally advantageous as it does not require costly drying steps.

11.1.4 Styrene

Styrene or vinylbenzene is one of the most common monomers used in the synthesis of polymers such as polystyrene, acrylonitrile–butadiene–styrene (ABS) plastic, styrene-butadiene rubber and other copolymers. It is used in the manufacture of packaging materials, insulation, automotive parts and various consumer goods.

Traditionally, the styrene is manufactured through the catalytic dehydrogenation of ethylbenzene at high temperatures (550–650 °C) in the presence of potassium-promoted iron oxide catalysts [25]. This process is energy intensive and requires significant energy consumption, stimulating the search for alternative styrene production methods.

With the growing amount of polystyrene (PS) waste, which has a negative impact on the environment due to its low biodegradability, the issue of its recovery and recycling is becoming increasingly important. One of the most promising methods is the pyrolysis of polystyrene to produce styrene, which not only reduces the amount of polymer waste, but also returns the valuable monomer to the production cycle [26, 27].

Catalytic pyrolysis of polystyrene has advantages over thermal pyrolysis in that it allows lower process temperatures, increased selectivity and higher styrene yields [28, 29]. Natural aluminosilicates, such as zeolites and bentonites, and their modifications with metal oxides can be used as catalysts [2]. The use of natural catalysts is cost-effective and environmentally friendly, especially considering the availability of significant reserves of zeolites and bentonites in Ukraine. According to current data, Ukraine has significant reserves of zeolites, represented by clinoptilolite with a content of up to 96%, concentrated mainly in the Zakarpattia region. The main deposits—Sokyrnytske, Saryginske and Zelenokamiane—have total reserves of over 125 million tones. More than 100 deposits and occurrences of bentonite clays with total reserves of over 60 million tones have also been discovered in the country [30]. Bentonite clays in Ukraine have a high montmorillonite content (up to 95%), with the main deposits being Cherkasy, Horbivske and Hryhorivske.

The literature indicates that bentonite clays are effective catalysts in the pyrolysis of polystyrene, increasing the selectivity for styrene and the overall yield of liquid products. In [31], the catalytic pyrolysis of polystyrene was carried out at 400 °C for 60 min using bentonite at 25% by weight of the polystyrene. The results showed that the yield of liquid products was 85.2%, of which the selectivity for styrene was 30.2%. This indicates that the presence of bentonite promotes the depolymerisation of polystyrene due to its acidic sites.

In another study [32], authors investigated the effect of changing the amount of catalyst on the pyrolysis process. They reduced the amount of bentonite to 20% by weight of polystyrene, keeping the temperature (400 °C) and reaction time (60 min) unchanged. It was found that the yield of liquid products decreased to 74.6%, but the selectivity for styrene increased to 35.4%. This indicates that reducing the amount of catalyst reduces the degree of secondary reactions leading to the formation of unwanted products, thereby increasing the selectivity for styrene.

The natural zeolite clinoptilolite was also investigated as a catalyst in the pyrolysis of polystyrene. The effect of clinoptilolite on the pyrolysis process at 400 °C for 120 min was investigated in [33]. The selectivity for styrene was 48.1%. Compared to bentonite, clinoptilolite gave higher selectivity at a longer reaction time. This may be due to the more porous structure and higher acidity of clinoptilolite, which contributes to a more efficient depolymerisation of polystyrene to styrene.

Study [34] compared the efficiency of natural zeolite and synthetic zeolite type Y in the pyrolysis of polystyrene. The experiments were carried out at an elevated temperature of 450 °C for 75 min. The natural zeolite gave a liquid product yield of 54% with a styrene selectivity of 7.6%, while the synthetic zeolite gave a yield of 50% with a styrene selectivity of 15.8%. The higher selectivity of the synthetic zeolite is due to its more homogeneous porous structure and higher acidity, which contributes to a more efficient degradation of polystyrene to styrene and reduces side reactions.

Study [35] investigated the thermal and catalytic decomposition of mixtures of high density polyethylene (HDPE) and polystyrene using different catalysts: zeolite ZSM-5 and clinoptilolite. The mixture consisted of 90% HDPE and 10% PS and the experiments were carried out at temperatures of 410–450 °C. As a result, the yield of naphtha-like fraction was obtained: 62.4% (fresh) and 63.1% (activated) on ZSM-5 catalyst; 59.7% (fresh) and 60.5% (activated) on clinoptilolite. At the same time, the selectivity for styrene in the gasoline fraction was 29–30% and 26–27% for ZSM-5 catalyst and clinoptilolite, respectively.

The study showed that synthetic zeolite ZSM-5 is a more efficient catalyst in the thermal decomposition of a mixture of HDPE and PS compared to natural clinoptilolite. ZSM-5 zeolite provides a higher yield of gasoline fraction, increases the content of light aliphatic hydrocarbons and increases the selectivity for styrene. However, clinoptilolite, as a natural and more readily available catalyst, also gives satisfactory results and can be used as a cost-effective alternative in the processing of polymer waste into fuel-like products.

11.1.5 Analysis of Catalytic Activity of Catalysts in the Processes of Acrolein, 1,3-Butadiene and Styrene Production

Table 11.1 shows the data on the yield and selectivity of catalysts in the processes of acrolein, 1,3-butadiene and styrene production. The analysis of these data indicates that the development of catalytic production of ABS plastic precursors, namely acrylonitrile, 1,3-butadiene and styrene, from secondary raw materials such as industrial glycerine, bioethanol and PS plastic waste is quite promising. The already existing high selectivities (up to 75%) and yields (up to 85%) of the monomers indicate a high potential for the use of recycled materials for the production of ABS plastics (Table 11.2).

Thus, an analysis of the existing literature shows that the development of catalytic technologies for the synthesis of ABS plastic precursors from recycled materials is a promising area that will provide alternative, economical and environmentally friendly technologies for their production. The challenge remains to obtain highly active and selective catalysts based on composites with the participation of aluminosilicates, various modifiers and carriers, and PNNL catalysts.

Table 11.1 Catalyst yield and selectivity data for acrylonitrile and 1,3-butadiene processes

№	Feedstock	Catalyst	Synthesis parameters, Yield (Y)/selectivity (S) of main product	Source
Production of acrolein				
1	Glycerol	Stage I: WO_3/TiO_2, Stage II: Sb-Fe–O	Indirect amoxidation, Stage I: 270–300 °C, Stage II: 400–500 °C, 40% (Y)	[7]
2	Glycerol	Stage I: WO_3/TiO_2 Stage II: W/Nb/Ti/Ta/Al_2O_3	Indirect amoxidation Stage I: 300 °C, Stage II: 420 °C, 60% (Y)	[8]
Production of 1,3-butadiene				
4	1-Butene	Cr-SiO_2	Fixed catalyst bed, atmospheric pressure, 600 °C, 34% (Y)	[14]
5	1-Butene	Li-Fe_2O_3/γ-Al_2O_3	Isothermal reactor, fixed catalyst bed, atmospheric pressure, 600 °C, 45% (S)	[16]
6	n-Butane	Ni-Bi-O/(MCM-41/SBA-15/foam) SiO_2	Automated reactor, fixed bed catalyst, atmospheric pressure, 400–500 °C, 47.5% (S)	[3]
7	Ethanol	Ash: MgO-ZrO_2	Fixed bed reactor, constant pressure, nitrogen atmosphere, 350 °C, 70% (Y)	[20]
8	Ethanol	0.5Na/4Ag/4ZrO_2/SBA-16	Fixed-bed catalyst, pressure 1 atm, 325°C, 75% (S)	[22]
9	Ethanol	2%Zn–8%Y/beta	Fixed bed catalyst reactor, atmospheric pressure, 350 °C, 63% (S)	[24]

11.2 Conclusions

The article shows the prospects for the production of ABS plastic from recycled raw materials, the choice of which is based on their availability in Ukraine, which opens new opportunities for the development of alternative catalytic technologies for the production of ABS plastic precursors.

The analysis of literature data shows that the production of acrylonitrile from glycerol is a promising direction in the development of "green" technologies for organic synthesis, and the use of hydrous ethanol as a raw material for the production of butadiene will allow the development of an economically feasible and environmentally friendly technology for its production. It is also noted that the production of styrene from polystyrene using natural clay pellets has significant advantages that will allow the development of an economically viable alternative technology for the

Table 11.2 Catalyst yield and selectivity data for styrene production processes

Production of styrene				
10	Polystyrene	Bentonite (25%)	400 °C, reaction time 60 min, 85.20% (Y), 30.19% (S)	[30]
11	Polystyrene	Bentonite (25%)	400 °C, reaction time 60 min, 74.55% (Y), 35.43% (S)	[31]
12	Polystyrene	Protonated clinoptilolite (HNZ)	400 °C, reaction time 120 min, 48.1% (S)	[32]
13	Polystyrene	Natural zeolite	450 °C, reaction time 75 min, 54% (Y), 7.6% (S)	[33]
14	Polystyrene	Synthetic zeolite	450 °C, reaction time 75 min, 50% (Y), 15.8% (S)	[33]
15	90% HDPE, 10% PS	ZSM-5	410–450 °C, 62.4% (Y), 29.88% (S)	[34]
16	90% HDPE, 10% PS	Clinoptilolite	410–450 °C, 59.7% (Y), 26.03% (S)	[34]

synthesis of styrene. Thus, it has been established that the development of catalytic technologies for the synthesis of ABS plastic precursors from recycled raw materials is a promising direction that will allow obtaining alternative, economical and environmentally friendly technologies for their production.

Composites based on aluminosilicates, using modifiers and supports, and the so-called PNNL catalysts have been found to be promising catalysts. The challenge today is to further increase the activity and selectivity of the composite catalysts under consideration.

References

1. Y. Hu, Z. Jia, Y. Li, L. Chang, Y. Wang, Synthesis and impact properties of in situ bulk made ABS resins toughened by high cis-1,4 polybutadiene. Mater. Sci. Eng. A **528**, 6667–6672 (2011). https://doi.org/10.1016/j.msea.2011.05.061
2. J. Aguado, D.P. Serrano, J.M. Escola, Fuels from waste plastics by thermal and catalytic processes: a review. Ind. Eng. Chem. Res. **47**, 7982–7992 (2008). https://doi.org/10.1021/ie800393w
3. G. Tanimu, A. Palani, S. Asaoka, S. Al-Khattaf, Pore structure effect of support in Ni-Bi-O/mesoporous silica catalyst on oxidative dehydrogenation of n-butane to butadiene. Catal. Today **324**, 97–105 (2019). https://doi.org/10.1016/J.CATTOD.2018.06.014
4. D.C. Phillips, S.J. Sawhill, R. Self, M.E. Bussell, Synthesis, characterization, and hydrodesulfurization properties of silica-supported molybdenum phosphide catalysts. J. Catal. **207**, 266–273 (2002). https://doi.org/10.1006/JCAT.2002.3524

5. Sohio Acrylonitrile Process, https://www.acs.org/education/whatischemistry/landmarks/acrylonitrile.html. Last accessed 2024/12/14
6. N. Yadav, G. Yadav, M. Ahmaruzzaman, Catalytic conversion and mechanism of glycerol into various value-added products: a critical review. Ind. Crops Prod. **210**, 117999 (2024). https://doi.org/10.1016/j.indcrop.2023.117999
7. C. Liebig, S. Paul, B. Katryniok, C. Guillon, J.-L. Couturier, J.-L. Dubois, F. Dumeignil, W.F. Hoelderich, Glycerol conversion to acrylonitrile by consecutive dehydration over WO_3/TiO_2 and ammoxidation over Sb-(Fe, V)-O. Appl. Catal. B **132–133**, 170–182 (2013). https://doi.org/10.1016/j.apcatb.2012.11.035
8. J.-L., Dubois, *Method for the Synthesis of Acrylonitrile from Glycerol* (2010). https://patents.google.com/patent/US20100048850A1/en
9. Butadiene Styrene Rubber Market Research (2021). https://pro-consulting.ua/ua/issledovanie-rynka/issledovanie-rynka-butadien-stirolnogo-kauchuka-kontinentalnaya-evropa-i-strany-sng-2021-god. Last accessed 2024/12/14
10. K. Iffländer, R. Eckelt, H. Lund, C. Kreyenschulte, S. Bartling, A. Wotzka, N. Steinfeldt, Dehydrogenation of 1-butene with CO_2 over VO_x supported catalysts. Appl. Catal. A **602**, 117648 (2020). https://doi.org/10.1016/j.apcata.2020.117648
11. E.V. Makshina, M. Dusselier, W. Janssens, J. Degrève, P.A. Jacobs, B.F. Sels, Review of old chemistry and new catalytic advances in the on-purpose synthesis of butadiene. Chem. Soc. Rev. **43**, 7917–7953 (2014). https://doi.org/10.1039/C4CS00105B
12. W.C. White, Butadiene production process overview. Chem. Biol. Interact. **166**, 10–14 (2007). https://doi.org/10.1016/J.CBI.2007.01.009
13. G. Pomalaza, P. Arango Ponton, M. Capron, F. Dumeignil, Ethanol-to-butadiene: the reaction and its catalysts. Catal. Sci. Technol. **10**, 4860–4911 (2020). https://doi.org/10.1039/D0CY00784F
14. B. Gao, Y. Luo, C. Miao, Y. Yue, W. Yang, W. Hua, Z. Gao, Oxidative dehydrogenation of 1-Butene to 1,3-Butadiene using CO_2 over Cr-SiO_2 catalysts prepared by sol-gel method. Chem. Res. Chin. Univ. **34**, 609–615 (2018). https://doi.org/10.1007/s40242-018-8063-8
15. B. Yan, L. Wang, Q. Chen, H. Dou, C. Liu, J. Li, T. Jiang, Highly selective conversion of 1-Butene to 1,3-Butadiene under CO_2 atmosphere over an alumina-supported iron-based catalyst: the role of Brønsted acids and Lewis acids. ChemistrySelect **5**, 11237–11241 (2020). https://doi.org/10.1002/SLCT.202003195
16. Y. Gao, B. Wang, B. Yan, J. Li, F. Alam, Z. Xiao, T. Jiang, Catalytic oxidative dehydrogenation of 1-butene to 1,3-butadiene with CO_2 over Fe_2O_3/γ-Al_2O_3 catalysts: the effect of acid or alkali modification. Reac. Kinet. Mech. Cat. **122**, 451–462 (2017). https://doi.org/10.1007/s11144-017-1205-z
17. P.C.A. Bruijnincx, B.M. Weckhuysen, Shale gas revolution: an opportunity for the production of biobased chemicals? Angew. Chem. Int. Ed. **52**, 11980–11987 (2013). https://doi.org/10.1002/ANIE.201305058
18. D. Sun, Y. Li, C. Yang, Y. Su, Y. Yamada, S. Sato, Production of 1,3-butadiene from biomass-derived C_4 alcohols. Fuel Process. Technol. **197**, 106193 (2020). https://doi.org/10.1016/J.FUPROC.2019.106193
19. M.D. Jones, Catalytic transformation of ethanol into 1,3-butadiene. Chem. Cent. J. **8**, 1–5 (2014). https://doi.org/10.1186/S13065-014-0053-4/SCHEMES/3
20. A.A. Bojang, H.S. Wu, 1,3-butadiene production using ash-based catalyst. Catalysts **13**, 258 (2023). https://doi.org/10.3390/CATAL13020258/S1
21. V.G.F. Pereira, C.R. Moreira, C.P. Rodrigues, F.S. Toniolo, Influence of active sites and the reaction conditions on the ethanol upgrading over Nb_2O_5/ZrO_2 based multifunctional catalysts. Braz. J. Chem. Eng. **40**, 1039–1054 (2023). https://doi.org/10.1007/S43153-022-00287-7/METRICS
22. A.D. Winkelman, V.L. Dagle, T.L. Lemmon, L. Kovarik, Y. Wang, R.A. Dagle, Effect of alkali metal addition on catalytic performance of Ag/ZrO_2/SBA-16 catalyst for single-step conversion of ethanol to butadiene. Catal. Sci. Technol. **13**, 975–983 (2023). https://doi.org/10.1039/D2CY01722A

23. F. Zeng, K.L. Hohn, Catalytic conversion of biomass-derived compounds to C_4 chemicals. Catalysis **31**, 1–36 (2019). https://doi.org/10.1039/9781788016971-00001
24. W. Dai, S. Zhang, Z. Yu, T. Yan, G. Wu, N. Guan, L. Li, Zeolite structural confinement effects enhance one-pot catalytic conversion of ethanol to butadiene. ACS Catal. **7**, 3703–3706 (2017). https://doi.org/10.1021/ACSCATAL.7B00433/SUPPL_FILE/CS7B00433_SI_001.PDF
25. J.J.H.B. Sattler, J. Ruiz-Martinez, E. Santillan-Jimenez, B.M. Weckhuysen, Catalytic dehydrogenation of light alkanes on metals and metal oxides. Chem. Rev. **114**, 10613–10653 (2014). https://doi.org/10.1021/CR5002436/ASSET/CR5002436.FP.PNG_V03
26. S.M. Al-Salem, P. Lettieri, J. Baeyens, Recycling and recovery routes of plastic solid waste (PSW): a review. Waste Manage. **29**, 2625–2643 (2009). https://doi.org/10.1016/J.WASMAN.2009.06.004
27. O. Yanushevska, T. Dontsova, G. Krymets, S. Kyrii, O. Krasuliak, K. Dorozhko, Prospects for the catalytic conversion of plastic waste, in *Nanooptics and Photonics, Nanochemistry and Nanobiotechnology, and Their Applications*, ed. by O. Fesenko, L. Yatsenko (Springer International Publishing, Cham, 2023), pp. 73–82. https://doi.org/10.1007/978-3-031-18104-7_5
28. J. Scheirs, W. Kaminsky, *Feedstock Recycling and Pyrolysis of Waste Plastics: Converting Waste Plastics into Diesel and Other Fuels* (2006), pp. 1–785. https://doi.org/10.1002/0470021543
29. D.O. Pavlovskyi, H.V. Krymets, O.I. Yanushevska, I.A. Levandovskyi, T.A. Dontsova, Perspectives of low-temperature atmospheric pressure catalytic decomposition of polystyrene. J. Chem. Technol. **32**, 276–283 (2024). https://doi.org/10.15421/jchemtech.v32i2.286999
30. B.G. Shabalin, O.M. Lavrynenko, P.O. Kosorukov, S.P. Bugera, The perspectives of the natural Smectite Clay application for the creation of a geological repository of radioactive waste in Ukraine. Mineralogical J. **40**, 65–78 (2018). https://doi.org/10.15407/mineraljournal.40.04.065
31. Dewangga, P.B., Rochmadi, Purnomo, C.W.: Pyrolysis of polystyrene plastic waste using bentonite catalyst. IOP Conference Series: Earth and Environmental Science. 399, 012110 (2019). https://doi.org/10.1088/1755-1315/399/1/012110.
32. Pramudia, B.D., Rochmadi, Chandra, W.P.: Styrene Recovery from the Pyrolysis of Polystyrene Waste Using Bentonite and Natural Zeolite Catalyst. Key Engineering Materials. 849, 84–89 (2020). https://doi.org/10.4028/WWW.SCIENTIFIC.NET/KEM.849.84.
33. S.Y. Lee, J.H. Yoon, J.R. Kim, D.W. Park, Degradation of polystyrene using clinoptilolite catalysts. J. Anal. Appl. Pyrol. **64**, 71–83 (2002). https://doi.org/10.1016/S0165-2370(01)00171-1
34. R. Miandad, M.A. Barakat, M. Rehan, A.S. Aburiazaiza, I.M.I. Ismail, A.S. Nizami, Plastic waste to liquid oil through catalytic pyrolysis using natural and synthetic zeolite catalysts. Waste Manage. **69**, 66–78 (2017). https://doi.org/10.1016/J.WASMAN.2017.08.032
35. Miskolczi, N., Bartha, L., Deák, Gy.: Thermal degradation of polyethylene and polystyrene from the packaging industry over different catalysts into fuel-like feed stocks. Polymer Degradation and Stability. 91, 517–526 (2006). https://doi.org/10.1016/j.polymdegradstab.2005.01.056.

Chapter 12
Effective Dielectric Constant of a Water-Protein Mixture for an Optical Sensor Based on Plasmon Resonance

Anatol Suprun and Liudmyla Shmeleva

Abstract The permittivity was calculated for an optical sensor based on surface plasmon resonance (SPR), in which the receptor-analyte layer is an aqueous mixture of protein microinclusions. These microinclusions together with water form the effective permittivity of the mixture, which depends on the concentration of the inclusions. Also, the effective permittivity of the mixture significantly accounting the dependence of the permittivity of water on temperature and wavelength of radiation. The complex nature of the dielectric properties of a protein molecular inclusion is also accounting. In this case, the imaginary part of the refractive index of a protein molecular inclusion depends on the length of the molecular chain, as well as on the wavelength of radiation. In this study, the effect on the effective dielectric permittivity of the mixture of all the factors listed above (concentration of protein-type inclusions, protein-type chain length, radiation wavelength at normal temperature) was calculated.

12.1 Introduction

Recently, there has been an intensive search for optical sensors based on surface plasmon resonance (SPR) with improved characteristics such as sensitivity, resolution, accuracy, cost reduction, speed, miniaturization, etc. This leads to the consideration of various technical solutions for sensors [1–7]. The construction of most sensors is based on the Kretschmann scheme [1]. However, various modifications of it are used [2–7]. A typical Kretschmann scheme (Fig. 12.1) consists of an input optical prism, on one face of which a metal, most often gold, nanolayer of several tens of nanometers (usually from 10 to 50) is deposited. A dielectric nanolayer is attached

A. Suprun · L. Shmeleva (✉)
Taras Shevchenko National University of Kyiv, Kyiv, Ukraine
e-mail: lshmel@univ.kiev.ua

O. Fesenko and L. Yatsenko (eds.), *Functional Nanomaterials, Nanocatalysts, Nanotechnologies, and Their Applications*, Springer Proceedings in Physics 321,
https://doi.org/10.1007/978-3-031-99136-3_12

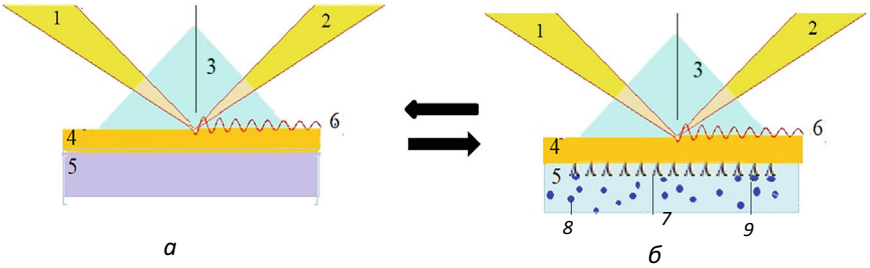

Fig. 12.1 Sensor diagram for Kretschmann configuration: 1—excitation light; 2—reflected light; 3—dielectric prism with high refractive index; 4—metal nanolayer (here gold nanolayer); 5—dielectric layer in Fig. 12.1a, or the medium being analyzed (analyte) in Fig. 12.1b; 6—surface plasmon; 7—receptor (or adsorbent); 8—ligand (or adsorbed molecular structure); 9—captured analyte

to the gold nanolayer (Fig. 12.1a) and this entire structure (prism–gold nanolayer–dielectric) is called a chip. SPR occurs on the surface of the gold nanolayer that borders the dielectric.

On the other hand, the dielectric is adjacent to the analyte, which is usually an aqueous mixture of molecular inclusions (Fig. 12.1b). In this case, the molecular inclusions are called the ligand, and the dielectric layer of the mixture is called the receptor.

Regarding the structural modifications of sensors on the SPR, for example, in [2] a sensor was studied in which the refractive index of the receptor (dielectric layer) and, accordingly, its dielectric permittivity had a periodic modulation along the direction of light propagation. In [3] a transverse (to the direction of light propagation) periodic structure in the form of metal strips deposited on the surface of a dielectric or semiconductor was considered. In [4] a receptor formed by several ordered layers of a liquid crystal is considered.

In [1, 5, 6], a sensor is studied in which a layer (or several layers) of graphene is placed between a gold nanolayer and a receptor. Recently, sensors with a chip structure are being actively considered, where a multilayer periodic structure of the type of a one-dimensional photonic crystal with alternating layers is placed between the input prism and the gold nanolayer [7]. Original constructive solutions of the sensor itself are also considered, for example, in the form of an optical fiber with a segment of the outer shell replaced by a gold nanolayer and a receptor nanolayer [8], or sensors based on dynamic scattering [9].

In this article, we will consider a Kretschmann-type sensor, but with a simplified chip construction: “input prism – gold nanolayer”. At the same time, an aqueous mixture of protein molecules is considered as the receptor-analyte layer, for which the effective permittivity is determined. The simplest method for determining the effective permittivity of an aqueous mixture is considered in [10].

12.2 Effective Permittivity ε of an Aqueous Mixture with Arbitrary Molecular Inclusions

In this section an optical sensor based on surface plasmon resonance (SPR) without a receptor layer and with analyte in the form of an aqueous mixture with arbitrary inclusions is discusses. Detailed attention was paid to the influence on the effective dielectric permittivity of the receptor-analyte layer (as the main sensitive sensor element) of various factors related to the physical properties of the mixture components—water and molecular inclusions.

The effective permittivity ε of a single-component aqueous mixture is determined by the formula [11]:

$$\varepsilon = \varepsilon_0 + 3\varepsilon_0 \frac{f_1 \frac{\varepsilon_1 - \varepsilon_0}{\varepsilon_1 + 2\varepsilon_0}}{1 - f_1 \frac{\varepsilon_1 - \varepsilon_0}{\varepsilon_1 + 2\varepsilon_0}} \tag{12.1}$$

Here ε_0 is the permittivity of water; ε_1 is the permittivity of molecular inclusions in the aqueous mixture, and f_1 is their partial volume fraction (hereinafter concentration), which is determined by the ratio:

$$f_1 = \frac{V_1}{V_0 + V_1},$$

where V_1 is the partial volume of molecular inclusions in the mixture, and V_0 is the partial volume of water in the mixture.

Next, we will use expression (12.1) in a more compact form:

$$\varepsilon = \varepsilon_0 \frac{\varepsilon_1 + 2\varepsilon_0 + 2f_1(\varepsilon_1 - \varepsilon_0)}{\varepsilon_1 + 2\varepsilon_0 - f_1(\varepsilon_1 - \varepsilon_0)} \tag{12.2}$$

Since one of the sensor factors is the wavelength of the SPR, it is necessary to take into account the dependence of the elements of the sensor under consideration on the wavelength. First, this is the permittivity of molecular inclusions ε_1, which here are protein molecules. The permittivity for protein molecules was considered in detail in [12]. Second, this is the dielectric permittivity of water ε_0, considered in detail in [13]. It is worth noting that, according to [12], the permittivity of protein molecular inclusions ε_1, in addition to the wavelength, also depends on their parameters, in particular, on the number of amino acid residues, which can be a controlling factor for plasmon resonance. According to [13], the dielectric properties of water also depend on temperature.

12.3 Dielectric Permittivity ε_1 of Protein Molecules

In this section, we will briefly reproduce the procedure for calculating the permittivity of protein molecules, since it may be useful in other similar cases.

In general, the dielectric properties of a medium can be determined if its specific conductivity is known, which is related to the imaginary part of the complex permittivity $\tilde{\varepsilon}_1$ by the relation:

$$\mathrm{Im}(\tilde{\varepsilon}_1) = \frac{4\psi}{\omega} \equiv \frac{2\lambda\sigma}{C}, \tag{12.3}$$

where σ is the specific conductivity, in this case, of the protein chain; ω and λ are the frequency and wavelength of the incident radiation; C is the speed of light. In the following, the speed of light, in numerical implementations, will be conveniently used in non-standard units: $C = 2.998 \times 10^{17}$ nm/s. This is due to the fact that the wavelength λ is conveniently used in nanometers. The last relation and all the following ones are formulated in the CGS system, in which they have the simplest form, and estimated numerical values, if necessary, will also be given in the SI system.

As follows from definition (12.3), to determine the imaginary part of the dielectric constant of a material, it is necessary to determine its specific conductivity σ. In this case, we are talking about the specific conductivity of protein molecules, which can be directly determined by the relation:

$$j = \sigma E,$$

where j is the current density, and E is the electrostatic field strength that causes the current. So now we need to find the current created by the metabolic electron. Considerable attention has been paid to this issue [14–18] and it was found that the density of the metabolic current, caused by amino acid heterogeneity, in all studied cases for a metabolic electron injected into a zone with the main quantum number $n = 2$, orbital quantum number $l = 1$ and arbitrary azimuthal quantum number m, can ultimately be specified to the form:

$$j_{21m} = \sigma E.$$

Here, the effective electrostatic field E, due to the amino acid heterogeneity of proteins, is determined by the relation:

$$E = \frac{z^3}{3000}\frac{R_0}{a_B}\exp\left(-\frac{zR_0}{a_B}\right)\frac{e}{R_0^2}, \tag{12.4}$$

and the specific conductivity σ can be expressed by the expression:

$$\sigma = \frac{\sigma_0}{N^2}, \tag{12.5}$$

where

$$\sigma_0 = \frac{\varepsilon_R}{\hbar}\left(\frac{R_0}{a_B}\right)^3, \tag{12.6}$$

The quantities included in the relations (12.4), (12.6) have the following definitions and physical meanings: $z = 7$ is the average charge number of atoms of a protein molecule according to the nitrogen model of the protein [19]; $\varepsilon_R = \frac{m_e e^4}{2\hbar^2} = 13.6\,\text{eV}$ is the Rydberg energy, in which $m_e = 9.1 \times 10^{-28}\,\text{g}\,\left(\equiv 9.1 \times 10^{-31}\,\text{kg}\right)$ is the electron mass, $e = 4.8 \times 10^{-10}\sqrt{\text{erg} \cdot \text{sm}}\left(\equiv 1.6 \times 10^{-10}\,\text{C}\right)$ is the electron charge; $\hbar = 6.58 \times 10^{-16}\,\text{eV} \cdot s\left(\equiv 1.055 \times 10^{-34}\,\text{J}\,\text{s}\right)$ is the Planck constant; $a_B = \frac{\hbar^2}{m_e e^2} = 0.53\,\mathring{\text{A}} \equiv 0.053\,\text{nm}$ is the Bohr radius. (12.4)–(12.6) also include the quantities: $R_0 = 1.44\,\mathring{\text{A}} \equiv 0.144\,\text{nm}$ is the distance between amino acid residues along the primary structure of the protein, and N is the number of amino acid residues in the denatured fragment of the protein molecule.

Based on these numerical values, an estimate can be made for the specific conductivity σ of protein chains: $\sigma_0 = 4.144 \times 10^{17}\,\text{s}^{-1}\left(\equiv 4.605 \times 10^7\,\Omega^{-1}\,\text{m}^{-1}\right)$.

Now we can find the imaginary part of the complex permittivity $\tilde{\varepsilon}_1$ of the protein chain. Substituting (12.5) into (12.3), we find:

$$\text{Im}(\tilde{\varepsilon}_1) = \frac{2\lambda\sigma_0}{CN^2}.$$

On the other hand, based on the general definition:

$$\tilde{\varepsilon}_1 = \tilde{n}^2 = (n + i\kappa)^2 = n^2 - \kappa^2 + i2n\kappa, \tag{12.7}$$

it is seen that:

$$\text{Im}(\tilde{\varepsilon}_1) = 2n\kappa. \tag{12.8}$$

Here n is the refractive index of the protein, and κ is its absorption coefficient.

So now we can find the absorption coefficient:

$$\kappa = \frac{\text{Im}(\tilde{\varepsilon}_1)}{2n} = \frac{\lambda\sigma_0}{nCN^2}, \tag{12.9}$$

and also, the full definition of the complex refractive index of the protein receptor:

$$\tilde{n} = n + i\frac{\lambda\sigma_0}{nCN^2}. \tag{12.10}$$

The real part of the dielectric constant: $\varepsilon_1 \equiv \text{Re}(\tilde{\varepsilon}_1)$, we find as follows:

$$\varepsilon_1 = n^2 - \frac{\lambda^2}{n^2 \lambda_0^2 N^4}. \tag{12.11}$$

where $\lambda_0 \equiv C/\sigma_0 = 0.7235$ nm.

Further, for the refractive index of the protein, the value $n = 1.375$ [12] will be used, which is the average between the values 1.37 for glutamic acid and 1.38 for lysine. This makes relation (12.11) fully defined for numerical implementation.

12.4 Permittivity of Water ε_0

The refractive index of water n_w is determined by the relation in which this coefficient is a function of the wavelength λ (nm) and the temperature t (°C) [13]:

$$n_w(\lambda, t) = A(t) + \frac{B(t)}{\lambda^2} + \frac{C(t)}{\lambda^4} + \frac{D(t)}{\lambda^6}, \tag{12.12}$$

where

$$A(t) = 1.3208 - 1.2325 \times 10^{-5}\,\mathrm{t} - 1.8674 \times 10^{-6}\,\mathrm{t}^2 + 5.0233 \times 10^{-9} \times t^3;$$

$$B(t) = 5208.2413 - 0.5179 \times \mathrm{t} - 2.284 \times 10^{-2}\,\mathrm{t}^2 + 6.9608 \times 10^{-5} \times \mathrm{t}^3;$$

$$C(t) = -2.5551 \times 10^8 - 18341.336\,\mathrm{t} - 917.2319\,\mathrm{t}^2 + 2.7729\,\mathrm{t}^3;$$

$$D(t) = 9.3495 + 1.7855 \times 10^{-3}\,\mathrm{t} + 3.6733 \times 10^{-5}\,\mathrm{t}^2 - 1.2932 \times 10^{-7}\,\mathrm{t}^3.$$

Next, we will consider normal conditions, assuming $t = 25\,°\mathrm{C}$. Then all coefficients: $A(t), B(t), C(t), D(t)$, become defined as:

$$A(25) = 1.319; \quad B(25) = 5182\ \mathrm{nm}^2;$$

$$C(25) = -2.565 \times 10^8\ \mathrm{nm}^4; \quad D(25) = 9.415\ \mathrm{nm}^6.$$

and expression (12.12) takes the form:

$$n_w(\lambda) = 1.319 + \frac{5182}{\lambda^2} - \frac{2.565 \times 10^8}{\lambda^4} + \frac{9.415}{\lambda^6}. \tag{12.13}$$

It is obvious that $\varepsilon_0(\lambda)$ is determined by the relation:

$$\varepsilon_0(\lambda) = n_w^2(\lambda). \tag{12.14}$$

Here we will not give an explicit expression for $\varepsilon_0(\lambda)$, since further this dielectric constant will be used only in graphical-numerical algorithms, for which the definitions (12.13), (12.14) are sufficient.

12.5 Graphical-Numerical Analysis of the Effective Permittivity E

Now let us return to the definition (12.2) and consider it in the form of a general calculation algorithm:

$$\varepsilon(\lambda, N, f_1, t) = \varepsilon_0(\lambda, t)\frac{\varepsilon_1(\lambda, N) + 2\varepsilon_0(\lambda, t) + 2f_1(\varepsilon_1(\lambda, N) - \varepsilon_0(\lambda, t))}{\varepsilon_1(\lambda, N) + 2\varepsilon_0(\lambda, t) - f_1(\varepsilon_1(\lambda, N) - \varepsilon_0(\lambda, t))}. \quad (12.15)$$

It is obvious that such a four-parameter dependence causes difficulties even at the stage of graphical-numerical analysis. Therefore, let us discuss certain simplifications of the general calculation algorithm (12.15).

The first simplification will concern temperature. Namely, we will determine the change in permittivity at a constant normal temperature $t = 25\,^{\circ}\mathrm{C}$. Thus, one of the four parameters in algorithm (12.15) disappears as a varied variable, and the algorithm itself takes the form:

$$\varepsilon(\lambda, N, f_1, t) = \varepsilon_0(\lambda, t)\frac{\varepsilon_1(\lambda, N) + 2\varepsilon_0(\lambda, t) + 2f_1(\varepsilon_1(\lambda, N) - \varepsilon_0(\lambda, t))}{\varepsilon_1(\lambda, N) + 2\varepsilon_0(\lambda, t) - f_1(\varepsilon_1(\lambda, N) - \varepsilon_0(\lambda, t))}. \quad (12.16)$$

where $\varepsilon_0(\lambda)$ is determined by relations (12.13), (12.14), and $\varepsilon_1(\lambda, N)$ is determined by equality (12.11).

In the three-parameter dependence (12.16), the wavelength λ should obviously play the role of an independent variable, since it is one of the main sensory characteristics. The number of amino acid residues N will be considered here as the main parameter affecting the wavelength of the SPR, and the concentration of protein molecular inclusions f_1 in the graphical-numerical implementation of dependence (12.16) will take four actual values:

$$f_1 = \{0.1; 0.2; 0.3; 0.4\} \quad (12.17)$$

In the algorithm (12.11), (12.13), (12.14), (12.16), for the refractive index of the protein, we will use the value: $n = 1.375$ [12].

We will begin the graphical-numerical analysis of this algorithm by analyzing the denominator of expression (12.16) for the possibility of realizing a situation when it can turn to zero. Equating this denominator to zero and considering the explicit form (12.11) for the permittivity ε_1, which now, in the notation of algorithm (12.16), has the form:

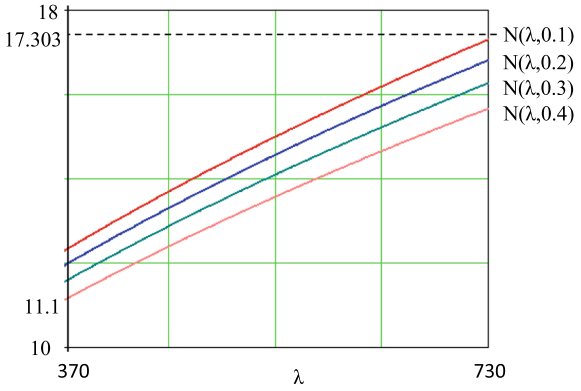

Fig. 12.2 The connected set of values of the number of amino acid residues N in a protein molecule, the wavelength of radiation λ and the concentration of protein molecular inclusions $f_1 = \{0, 1; 0, 2; 0, 3; 0, 4\}$, at which the strict equality of the denominator to zero in the right-hand side of (12.16) is ensured

$$\varepsilon_1(\lambda, N) = n^2 - \frac{\lambda^2}{n^2 \lambda_0^2 N^4},$$

after some transformations, we obtain the algorithm:

$$N(\lambda, f_1) = \frac{\sqrt{\lambda}}{\sqrt{n\lambda_0}\left(n^2 + \frac{f_1+2}{1-f_1}\varepsilon_0(\lambda)\right)^{1/4}},$$

to find the connected set of values of N, λ and f_1, which ensures strict equality of the denominator of the right-hand side of (12.16) to zero. An explicit view of this dependence is shown in Fig. 12.2.

From Fig. 12.2 it is seen that only the optical range from 370 to 730 nm is considered for the wavelength λ. This is due to two circumstances. First, this range is the most relevant (at least, the preferred) for the considered sensory studies. And, secondly, the element of the algorithm (12.13), (12.14) is quite correctly defined in this range.

The functional dependencies themselves, shown in the graphs (Fig. 12.2), reproduce the forbidden, from the point of view of the equality of the denominator to zero in (12.16), set of values N, λ for each of the four values of the concentration f_1, given in (12.17). Analyzing the results shown in Fig. 12.2, we can conclude that for a guaranteed absence of singularities in the denominator in (12.16) at any values of the wavelength λ, the value of the number of amino acid residues N must be either significantly greater than 18 (this is the maximum value for the family of dependencies), or significantly less than 11 (this is their minimum value).

Therefore, to ensure the unconditional "workability" of the algorithm used, we further excluded from consideration the length of protein molecular inclusions approximately in the range $3 \leq N \leq 60$. This limitation is associated with the algorithm used and applies only to computational (not experimental) studies. Since the "length" of typical proteins most often exceeds the value of $N = 60$ amino acid residues, we will continue to work in the range $N \geq 60$.

The dependences (12.16) for the effective dielectric permittivity ε on the wavelength λ and the length of the molecular chain N for the four values of the inclusion concentration f_1 given in (12.17) are presented in Fig. 12.3.

From these figures, we can immediately draw the first conclusion: with a decrease in the concentration f_1 from 0.4 to 0.1, the entire system of graphs for different values of the number $N = \{60, 70, 90, 120, 300\}$ of amino acid residues in the protein chain narrows and generally shifts towards lower values of the effective permittivity ε. That is, the concentration is an important sensory indicator, the change of which leads to a change in the permittivity ε, which will automatically lead to a change in the SPR wavelength and the resonant angle of incidence.

The second conclusion is that an equally important sensory indicator is the number of amino acid residues in the protein chain N, but it is most pronounced at high

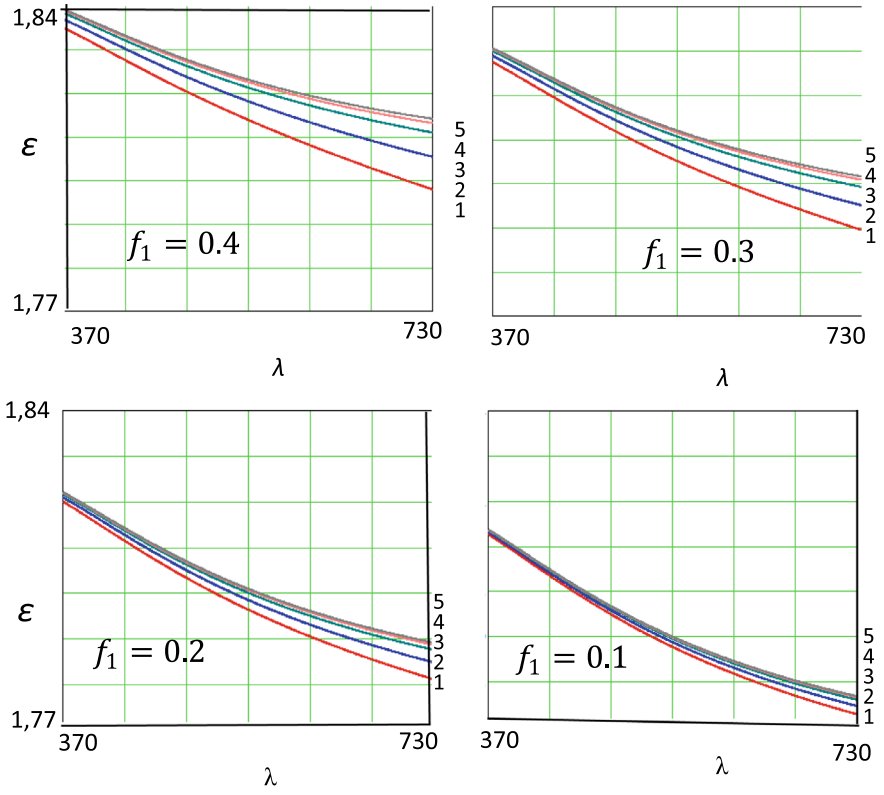

Fig. 12.3 Dependence of the effective dielectric constant ε on the wavelength λ for five values of the molecular chain length N (in the range of 60–300 amino acid residues) at the concentration of molecular inclusions $f_1 = \{0, 1; 0, 2; 0, 3; 0, 4\}$. Curve 1 corresponds to $N = 60$, curve 2 corresponds to $N = 70$, curve 3 corresponds to $N = 90$, curve 4 corresponds to $N = 120$, curve 5 corresponds to $N = 300$

concentrations f_1 (see Fig. 12.3). It is advisable to analyze the direct dependence of ε on N at a fixed wavelength, for example, at the wavelength of the SPR.

And, finally, the third conclusion: the dependence of ε on N is significant in the range from $N = 60$ to $N = 90$. And starting from $N = 120$ this dependence is weak and, most likely, cannot be used to analyze the influence of N on ε. On the other hand, it is clear that according to the parameter N, the most appropriate sensory inclusions of the protein type are proteins ($60 < N < 100$).

12.6 Conclusions

The article discusses the scheme of an optical sensor based on SPR, in which the layer. directly adjacent to the gold nanolayer, is an aqueous mixture of microinclusions from protein molecules. Since the main parameters of PPR—the resonant wavelength and the resonant angle of incidence—significantly depend on the effective permittivity of the protein mixture, then in this study the main attention was paid to the analysis of the effective permittivity.

The physical characteristics of water were significantly taken into account—the dependence of its permittivity on the wavelength λ and temperature t—and the physical characteristics of protein-type molecules—the dependence of the real part of their permittivity also on the wavelength λ and the number of amino acid residues N in the chain. In addition, the algorithm itself also depends on the volume concentration f_1 of protein-type chains. That is, the effective permittivity ε turned out to be a function of four parameters, which required some assumptions regarding their reduction. First of all, temperature was actually excluded from consideration, since the entire consideration was carried out at a fixed normal temperature $t = 25\,^{\circ}\mathrm{C}$. Of the three remaining parameters, the wavelength of radiation λ was chosen as an independent variable ($370\,\mathrm{nm} \leq \lambda \leq 730\,\mathrm{nm}$), the number of amino acid residues N was chosen as the main parameter ($N \geq 60$), and the volume concentration of protein-type inclusions $f_1 = \{0, 1; 0, 2; 0, 3; 0, 4\}$ was selected as an additional parameter.

The following results were obtained.

The typical algorithm, which is usually used to calculate the effective permittivity of mixtures, in the case of inclusions of protein-type molecules, can also be used for protein-type chains, the length of which is not less than 60 amino acid residues.

With a decrease in the concentration f_1 from 0.4 to 0.1, the entire system of dependences of the effective permittivity of the mixture ε on the wavelength λ for different values of the number of amino acid residues in the protein-type chain $N = \{60, 70, 90, 120, 300\}$ narrows and generally shifts towards lower values of the effective permittivity ε. That is, the concentration is an important sensory indicator, the change of which leads to a change in the dielectric permittivity ε.

At a fixed wavelength λ, an increase in the number of amino acid residues N leads to an increase in the effective permittivity ε, but already at $N > 120$ its change practically stops.

For all considered values of the variable λ (from 370 to 730 nm), parameters N = {60, 70, 90, 120, 300} and f_1 (from 0.1 to 0.4), the effective permittivity of the mixture ε is positive and can be used in SPR studies.

12.7 Disclosure of Interests

The authors have no competing interests to declare that are relevant to the content of this article.

Acknowledgements The work was supported by the Ministry of Education and Science of Ukraine in the framework of projects, which are performed on the basis of Taras Shevchenko National University of Kyiv.

References

1. S. Szunerits, N. Maalouli, E. Wijaya, J.P. Vilcot, R. Boukherroub, Recent advances in the development of graphene-based surface plasmon resonance (SPR) interfaces. Anal. Bioanal. Chem. **403**, 1435–1443 (2013)
2. V.Y. Reshetnyak, I.P. Pinkevych, T.J. Bunning, D.R. Evans, Influence of rugate filters on the spectral manifestation of tamm plasmon polaritons. Materials **14**(5), 1282 (2021)
3. F.B. Barho, F. Gonzalez-Posada, M.J. Milla-Rodrigo, M. Bomers, L. Cerutti, T. Taliercio, All-semiconductor plasmonic gratings for biosensing applications in the mid-infrared spectral range. Opt. Express **24**(14), 16175–16190 (2016)
4. A. Vahedi, M. Kouhi, Liquid crystal-based surface plasmon resonance biosensor. Plasmonics **15**(1), 61–71 (2020)
5. O. Salihoglu, S. Balci, C. Kocabas, Plasmon-polaritons on graphene-metal surface and their use in biosensors. Appl. Phys. Lett. **100**, 213110 (2012)
6. N.F. Chiu, T.Y. Huang, H.C. Lai, Graphene oxide based surface plasmon resonance biosensors. Advances in Graphene Science. InteachOpen Book Series (2013)
7. E. Buzavaite-Verteliene, I. Plikusiene, T. Tolenis, A. Valavicius, J. Anulyte, A. Ramanavicius, Z. Balevicius, Hybrid Tamm-surface plasmon polariton mode for highly sensitive detection of protein interactions. Opt. Express **28**(20), 29033–29043 (2020)
8. K.M. Mayer, J.H. Hafner, Localized surface plasmon resonance sensors. Chem. Rev. **111**(6), 3828–3857 (2011)
9. J.D. Driskell, C.A. Jones, S.M. Tompkins, R.A. Tripp, One-step assay for detecting influenza virus using dynamic light scattering and gold nanoparticles. Analyst **136**(15), 3083–3090 (2011)
10. A.O. Koval, A.V. Korotun, Yu.A. Kunytskyi, V.A. Tatarenko, I.M. Titov, *Electrodynamics of Plasmon Effects in Nanomaterials* (Naukova Dumka, Kyiv, 2021)
11. A.H. Sihvola, *Electromagnetic Mixing Formulas and Applications*. Electromagnetic Waves Series, Iet (1999)
12. A. Suprun, L. Shmeleva, S. Perepelytsya, Protein biosensor compared to nucleic one, in *2024 IEEE 42nd International Conference on Electronics and Nanotechnology (ELNANO)*, pp. 359–363, Kyiv, Ukraine (2024)
13. A.N. Bashkatov, E.A. Genina, Water refractive index in dependence on temperature and wavelength: a simple approximation. Optical Technol. Biophys. Med. IV. Int. Soc. Optics Photonics **5068**, 393–395 (2003)

14. A.D. Suprun, L.V. Shmeleva, Current in the protein nanowires: quantum calculations of the base states. Nanoscale Res. Lett. **11**(1), 74 (2016)
15. A.D. Suprun, L.V. Shmeleva, Temperature effect on the basis states for charge transfer through a polypeptide fragments of proteins and on the nanocurrent in it, in *Chapter 13 "Nanophysics, Nanomaterials, Surface Studies, and Applications"*. Part of the Springer Proceedings in Physics Book Series, vol. 195 (2017), pp. 175–186
16. A.D. Suprun, L.V. Shmeleva, Control of metabolic current through a protein-like nanowire by means of a magnetic field. Mol. Cryst. Liq. Cryst. **674**(1), 98–109 (2018)
17. L.V. Shmeleva, A.D. Suprun, Mechanism of active electron transfer in a protein-like nanowire under real conditions, in *Chapter 5 in "Nanophysics, Nanomaterials, Surface Studies, and Applications"*. Springer International Publishing AG, Part of Springer Nature, Springer Proceedings in Physics Book Series, vol. 210 (2018), pp. 59–71
18. A. Suprun, L. Shmeleva, Physical fields in proteins as a factor of controlling metabolic nanocurrent, in *2020 IEEE 40th International Conference on Electronics and Nanotechnology (ELNANO)* (IEEE, 2020), pp.409–414
19. A.D. Suprun, L.V. Shmeleva, Primary structure of proteins as a nanowire for metabolic electronic transport. Nanoscale Res. Lett. **10**, 121 (2015)

Chapter 13
Soliton as a Model of a Pulse Heart Wave

Anatol Suprun and Liudmyla Shmeleva

Abstract The paper finds a solution to the dimensional Korteweg-de Vries (KdF) equation for a channel with a circular cross-section. Soliton solutions are obtained. They describe pulse waves that arise during the operation of the cardiovascular system. The results of the solution simulate ordinary pulse waves that describe the operation of a healthy cardiac system without deviations. The asymptotics of the obtained solutions are studied considering real medical data.

13.1 Introduction

The heart is considered an exclusive structure that plays a vital role in the human body. Now, it is well known that the heart is an electromechanical pump that propels oxygenated blood proportionately to the demand and receives deoxygenated blood from all over the body [1].

The function of the heart is to contract and pump oxygenated blood to the body and deoxygenated blood to the lungs. To achieve this goal, a normal human heart must beat regularly and continuously for one's entire life [2]. Heartbeats originate from the rhythmic pacing discharge from the sinoatrial (SA) node within the heart itself. In the absence of extrinsic neural or hormonal influences, the SA node pacing rate would be about 60–100 beats per minute [2, 3].

Therefore, theoretical studies of this issue are necessary for a model representation of vital processes.

A. Suprun · L. Shmeleva (✉)
Taras Shevchenko National University of Kyiv, Kyiv, Ukraine
e-mail: lshmel@univ.kiev.ua

O. Fesenko and L. Yatsenko (eds.), *Functional Nanomaterials, Nanocatalysts, Nanotechnologies, and Their Applications*, Springer Proceedings in Physics 321,
https://doi.org/10.1007/978-3-031-99136-3_13

13.2 Model Description of the Process of Pumping Blood Through the Cardiovascular System

The cardiovascular system, also called the circulatory system, is the organ system that transports blood to and from all the cells of the body. Materials carried by the blood include oxygen from the lungs, nutrients from the digestive system, hormones from the endocrine glands, and waste products from cells throughout the body. The transport of these and many other materials is necessary to maintain homeostasis in the body. The main components of the cardiovascular system are the heart, blood vessels, and blood.

The heart is a muscular organ in the chest cavity. It is composed primarily of cardiac muscle tissue and pumps blood through the blood vessels with repeated, rhythmic contractions. The heart has four internal chambers: the right atrium and ventricle and the left atrium and ventricle. The heart also contains several valves that allow blood to flow only in the proper direction through the heart.

Unlike skeletal muscle, cardiac muscle normally contracts without stimulation from the nervous system. Specialized cells in the cardiac muscle send electrical impulses that stimulate contraction. As a result, the atria and ventricles normally contract at the correct time to maintain efficient pumping of blood through the heart.

The process of pumping blood through the heart can be described by a nonlinear differential equation, which is a universal model for describing one-dimensional media with dispersion and without dissipation, in which the dispersion law for linear waves is described by two terms in the wavenumber expansion.

The dimensional Korteweg-de Vries (KdF) equation for the velocity u(t,x) of a disturbance in a rectangular channel is:

$$u_t + uu_x + \frac{1}{6}u_0 h^2 u_{xxx} = 0. \tag{13.1}$$

Here h is the dimensional depth of the channel. As for the velocity u_0, , which is included in (13.1), there are 2 versions of its physical meaning:

1. This is the velocity of the natural flow in the channel, which is considered a given value. In the case of the cardiovascular system, there is no natural velocity independent of the system itself, therefore this meaning for the velocity u_0 is not suitable.
2. This is the velocity, which is a consequence of the desired velocity $u(t, x)$ and can be interpreted as the capture velocity. It must be determined together with the solution $u(t, x)$ and in this sense is a certain analogue of the eigenvalue. It is this case that we will consider as one that forms the blood flow.

One of the partial solutions of such Eq. (13.1) is the so-called soliton solution of the form:

$$u(t, x) = \frac{A}{\mathrm{ch}^2[b(x - vt)]}, \tag{13.2}$$

where v is the velocity of the soliton wave. In solution (13.2), the parameters A, b, and v are determined by directly substituting (13.2) into (13.1). In this case, A and v have the dimension of velocity, and b has the dimension of the inverse length.

We will model the pulse wave by the soliton solution of the KdF equation. The propagation velocity of the pulse wave depends on both the geometric parameters of the vessel (radius, thickness) and the elastic properties of the vascular wall [4]. Since no one has derived the KdF equation for a channel with a circular cross-section, we will use a simple analogy, as a result of which we can postulate the equation:

$$u_t + uu_x + u_0 S u_{xxx} = 0, \tag{13.3}$$

in which S is the cross-sectional area of the aorta in the immediate vicinity of the heart.

To solve (13.2), we successively find:

$$u_t = 2Abv\frac{\mathrm{sh}[b(x-vt)]}{\mathrm{ch}^3[b(x-vt)]};$$

$$uu_x = -2A^2b\frac{\mathrm{sh}[b(x-vt)]}{\mathrm{ch}^5[b(x-vt)]};$$

$$u_{xxx} = -8Ab^3\frac{\mathrm{sh}[b(x-vt)]}{\mathrm{ch}^3[b(x-vt)]} + 24Ab^3\frac{\mathrm{sh}[b(x-vt)]}{\mathrm{ch}^5[b(x-vt)]}.$$

Substituting the right-hand sides of these three relations into (13.3), we can obtain the equation:

$$\left\{2Abv - 8Ab^3u_0S\right\}\frac{\mathrm{sh}[b(x-vt)]}{\mathrm{ch}^3[b(x-vt)]} + \left\{24Ab^3u_0S - 2A^2b\right\}\frac{\mathrm{sh}[b(x-vt)]}{\mathrm{ch}^5[b(x-vt)]} = 0,$$

which can be satisfied by equating both curly brackets to zero. As a result, we obtain 2 relations:

$$v - 4b^2u_0S = 0; \tag{13.4}$$

$$12b^2u_0S - A = 0, \tag{13.5}$$

which include 4 unknown quantities: A, b, v and u_0. Equation (13.4) allows us to immediately find the blood flow velocity u_0, which is stimulated by the soliton velocity v:

$$u_0 = {}^{v}\!/_{4Sb^2}. \tag{13.6}$$

Substituting this into Eq. (13.5), we can find the amplitude factor A:

$$A = 3v. \tag{13.7}$$

Now only 2 quantities remain undetermined: the soliton pulse velocity v and the parameter b, which determines the soliton width.

As for the parameter b, it is quite obvious from equality (13.6) that in the general case it can be found in the form:

$$b = \beta \Big/ \sqrt{S}, \tag{13.8}$$

where β is a dimensionless uncertain parameter, which can be interpreted as a dimensionless representation of the factor b. Considering (13.8), the relation (13.6) takes the form:

$$u_0 = v \Big/ 4\beta^2. \tag{13.9}$$

It can be seen from equality (13.9) that the parameter β satisfies the condition $\beta > 1/2$, since the blood flow velocity u_0 is always less than the soliton pulse velocity v.

The solution (13.2), considering (13.7), (13.8), takes the form:

$$u(t, x) = 3v \Big/ \mathrm{ch}^2\left(\beta \frac{x - vt}{\sqrt{S}}\right). \tag{13.10}$$

We will determine the remaining two parameters (β and v) based on known physiological facts.

13.3 Estimation of the Parameters of the Constructed Model

The movement of blood through the cardiovascular system is a rather complex phenomenon. The blood vessel has a complex structure, which is a branched system of elastic vessels of various types [4]. The fluid itself—blood—is a complex suspension, the rheological characteristics of which depend on the conditions of its flow. The driving force of blood flow is the pressure difference that occurs at the beginning and end of the tube. The movement of blood through the vascular system is laminar in nature (the movement of blood in separate layers parallel to the axis of the vessel). In this case, the layer adjacent to the vessel wall remains practically motionless, the second layer slides along it, the third one after the second, etc. The "formed" elements of blood (erythrocytes, leukocytes and platelets) make up the central axial flow; plasma moves closer to the walls. It is known that the smaller the diameter of the vessel, the closer the central layers of blood are to the walls and the more they are slowed down. This means that in small vessels the blood flow velocity is lower

than in large ones. Thus, in the aorta it is 0.5 m/s, in the arteries—0.3 m/s, in the capillaries—0.005–0.01 m/s, in the veins—0.05–0.14 m/s, in the vena cava—0.2 m/s [5].

The main kinetic energy required for blood movement is given by the heart during systole (compression, contraction, reduction of the ventricles and atria during the cardiac cycle). At the same time, blood is ejected into the aorta from the left ventricle and the pulmonary artery—from the right. One part of the energy goes to push the blood, the other is converted into potential, which is necessary for stretching the walls of the aorta, large and medium vessels during systole. During relaxation of the ventricles and atria during the cardiac cycle the energy of the walls of the aorta and blood vessels is converted into kinetic energy, promoting the movement of blood through the vessels.

Vessels are also able to actively respond to changes in blood pressure in them. Pulsating blood flow, due to the peculiarities of the aorta and large vessels, is leveled and becomes relatively continuous. Normally, the outflow of blood from the heart corresponds to its inflow. This means that the volume of blood flowing per unit of time through the entire arterial and venous systems of the large and small circles of blood circulation is the same.

The speed of blood flow in the vascular bed is different and depends on the total sum of the area of the lumens of vessels of this caliber in a given area of the body. The aorta has the smallest cross-section, and the speed of blood movement in it is the highest—0.5 to 0.7 m/s. The capillaries have the largest total cross-sectional area—800 times greater than that of the aorta. Accordingly, the speed of blood in them is about 0.0005 m/s. In arteries it is 0.2–0.4 m/s, in arterioles—0.005 m/s.

Pulse is understood as periodic oscillations of the vessel wall associated with the dynamics of their blood filling and pressure in them during one cardiac cycle. At the moment of expulsion of blood from the heart, the pressure in the aorta increases and the wave of this pressure spreads along the arteries to the capillaries, where the pulse wave fades. Accordingly, the pulsating changes in pressure also give rise to a pulsating character in the movement of blood through the arteries: acceleration of blood flow during systole and deceleration during diastole. The amplitude of the pulse wave decays as it moves from the center to the periphery. The speed of propagation of the pulse wave in the human aorta is 5.5–8.0 m/s, in large arteries—6.0 to 9.5 m/s [5].

The circulatory system has active energy sources (ventricles and atria of the heart). Various active physiological processes (mechanisms of reflex changes in vascular tone and cardiac output) change the physiological properties of the circulatory system, and therefore the conditions of blood flow. Any description of hemodynamic processes (from simple cases of blood flow mechanics to complex processes of reflex control of blood circulation) is based on experimental data accumulated over many years of research [1].

Let us consider the pulse wave as a soliton. Then [5] the pulse velocity of the soliton v in the aorta (at the exit from the heart) is $5.5 \div 8$ m/s, while the velocity of the blood flow u_0 in it is 0.4–0.6 m/s [4].

That is, the pulse velocity v at the exit from the heart is $9 \div 20$ times greater than the flow velocity u_0. For certainty, we will use the value $(v/u_0) = 20$, which corresponds to the pulse velocity of the soliton $v = 8\,\text{m/s}$. So, using the formula:

$$\beta = \frac{1}{2}\sqrt{\frac{v}{u_0}},$$

obtained from (13.9), we can find: $\beta \approx 2.24$.

Based on the obtained values, we can represent the dependence (13.10) graphically.

The last thing left to do is to check the results obtained, knowing the normal pulse rate—1 beat per second. This means that between two consecutive pulse waves in the form of a soliton (between two heart beats) the period should be: $T = 1s$. And the check is reduced to the fact that with such a pulse the solitons should not intersect with great accuracy (then the condition of separation of successive soliton pulses is fulfilled). To perform this check, we will use the solution (13.10).

First of all, we will put $x = 0$ in (13.10), on the basis that the point of exit of the aorta from the heart will be considered the origin of coordinates. Then from (13.10) we obtain a special (not arbitrary) soliton-like boundary condition:

$$u(t, 0) = 3v \Big/ \text{ch}^2\left(\frac{\beta v t}{\sqrt{S}}\right), \tag{13.11}$$

which in this consideration is considered to form a physiologically healthy heart rhythm, and any deviations from this boundary condition will lead to arrhythmias.

If we compare Figs. 13.1 and 13.2, we can see that the function $u(t, x)$ has a tendency to narrow the peaks of the solution and demonstrates pulse waves. Thus, it can be stated that the smaller the value of S, the narrower the peaks of the waves. And this is the value that needs to be paid attention to at this stage of the study.

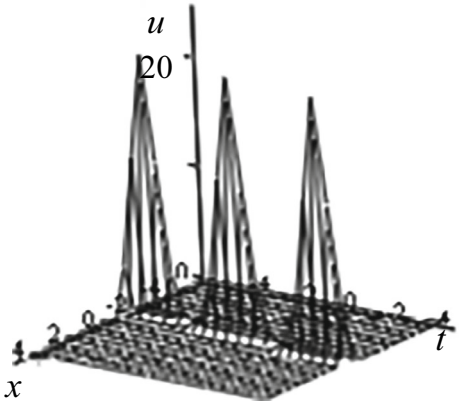

Fig. 13.1 Dependence of $u(t, x)$ in the general case without considering the cross-sectional area of the aorta (formally we assume $S = 1m^2$) in the immediate vicinity of the heart

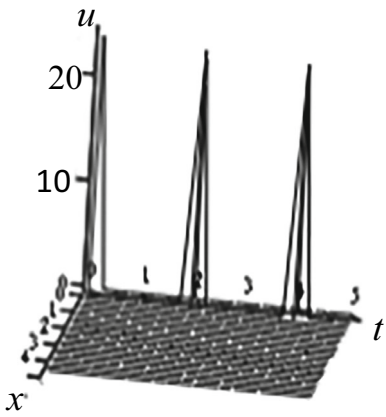

Fig. 13.2 Dependence u(t, 0) at $S = 0.01\,\mathrm{m}^2$

If we put $t = T$ in the argument of this boundary condition, then this argument takes the form:

$$\frac{\beta v T}{\sqrt{S}}. \tag{13.12}$$

The cross-section S of the artery directly at the exit from the heart (at the point $x = 0$) [4] has the value $S \sim 3 \cdot 10^{-4}\ \mathrm{m}^2$ Then the value of argument (13.12) can be estimated by substituting into it the numerical values of all quantities: $\beta \approx 2, 24$, $v = 8\,\mathrm{m/s}$, $T = 1\,\mathrm{s}$, $(v/u_0) = 20$. As a result, we will have:

$$\frac{\beta v T}{\sqrt{S}} = \frac{vT}{2}\sqrt{\frac{v}{Su_0}} = 800\sqrt{\frac{5}{3}} \approx 1033.$$

If we use the analytical or graphical representation of the hyperbolic cosine, it is obvious that with an increase in the value of argument (13.12), the function ch(x) increases proportionally to e^x. That is, for the value obtained here, $ch(1033) \to \infty$, or $1/\left(ch^2(1033) \to 0\right)$. . This means that the solution (13.10) in the form of a sequence of single-soliton pulse waves with the obtained parameters is physically correct, since it ensures the separation of each soliton with a good margin, as well as the blood flow velocity $u_0 = 0.5\,\mathrm{m/s}$ at the beginning of the aorta.

For greater certainty, we consider the lower limit of the impulse velocity v at the exit from the heart, namely $(v/u_0) = 9$. Then $\beta = 1.5$, which also corresponds to the pulse velocity of the soliton $v = 5.5\,\mathrm{m/s}$. The argument of the hyperbolic cosine will then be equal to 476, which also approaches zero $1/\mathrm{ch}^2(476) \to 0$).

If the boundary condition (13.11) is violated, i.e. ceases to be soliton-like, then other solutions of Eq. (13.3) are realized: multi-soliton solutions with different pulse velocities v, or solutions in the form of cnoidal waves. The latter, however, also require a special boundary condition.

All deviations from boundary condition (13.11) within the framework of the considered soliton model of pulse waves look like pathological disorders caused by instability of the heart rhythm (arrhythmia).

13.4 Conclusions

The paper proposes a model that can be used to represent the work of the cardiovascular system, namely the formation of pulse heart waves. The model is based on the dimensional Korteweg-de Vries (KdF) equation with a circular channel for the velocity u(t, x). A partial solution to this equation is the soliton solution.

To verify the applicability of the model, the solution of the KdF equation obtained in the paper was analyzed considering medical data obtained in real life. The asymptotic studies performed show that the model is working and can represent the work of the cardiovascular system without pathologies. A boundary condition is obtained that guarantees the stability of the heart rhythm. Violation of this condition can lead to multi-soliton solutions with different pulse velocities v, or to solutions in the form of cnoidal waves, which will describe the instability of the heart rhythm (arrhythmia).

Disclosure of Interests The authors have no competing interests to declare that are relevant to the content of this article.

References

1. Tiwari, R., Kumar, R., Malik, S., Raj, T, Kumar, P. Analysis of Heart Rate Variability and Implication of Different Factors on Heart Rate Variability. Curr. Cardiol. Rev. 2021;17(5), e160721189770 (2021)
2. R. Gordan, J.K. Gwathmey, L.H. Xie, Autonomic and endocrine control of cardiovascular function. World J. Cardiol. **7**(4), 204–214 (2015)
3. Vesnina, L.E., Sokolenko, V.M., Mishchenko, I.V. Physiology of the cardiovascular system, Ukrainian Medical Stomatological Academy, Poltava, Ukraine (2015)
4. Chaly, O. V., Tsekhmister, Ya. V., Agapov, B. T. and others. Medical and biological physics: Third edition. – Nova Knyga, Vinnytsia: (2017).
5. Fedyukovich N. I., Human Anatomy and Physiology, Feniks, Kiev, Ukraine (2020)

Chapter 14
Preparation of Nanocarbon by the High-voltage Breakdown of Hydrocarbons

Antonina Malyushevskaya and Nataliya Kuskova

Abstract The method of high-voltage breakdown in liquids and gases to obtain various types of nanocarbon with different structures and types of local atomic order is considered. The initial electron configuration of atoms and the structure of molecules in organic liquids—sources of carbon—is the determining factor in preparing the amorphous carbon with different types of local atomic order and specific electrical conductivity. The selectivity of the method of gas processing by high-voltage breakdown is also can be controlled by the choice of the chemical composition and morphology of the substrate material for deposition. The considered data are proposed to be used as a basis for an express method for assessing the type of nanocarbon, obtained as a result of the high-voltage breakdown of liquid and (or) gaseous carbon sources.

14.1 Introduction

The preparation and research of nanoscale materials is one of the most rapidly developing and in-demand areas of modern materials science. Issues related to the nanoscale states of carbon materials are of particular interest to discoverers. Over the past 30 years, carbon nanostructures have proven themselves as the basis of modern functional materials, their fields of application extend from chemistry [1, 2], biology [3], and medicine [4, 5] to the next generation of electronics [6], mechanical engineering [7, 8], and energetic [9, 10].

In the scientific and technical literature, the term "nanocarbon" without additional clarification can denote various nanosized modifications of carbon: fullerenes, carbon nanotubes, nanographite and graphene, nanodiamond, carbon "onions", amorphous nanocarbon, etc. [11–13]. This has become common practice because carbon has the largest number of allotropic modifications known and practically proven, and

A. Malyushevskaya · N. Kuskova (✉)
Institute of Pulse Processes and Technologies, NAS of Ukraine, Mykolaiv, Ukraine
e-mail: Ninutsa.1974@gmail.com

O. Fesenko and L. Yatsenko (eds.), *Functional Nanomaterials, Nanocatalysts, Nanotechnologies, and Their Applications*, Springer Proceedings in Physics 321,
https://doi.org/10.1007/978-3-031-99136-3_14

even more modifications will be discovered soon. The discovery of the era of carbon allotropes is described in the work [14]. The development of methods for low-dimensional carbon materials' synthesizing is closely related to the problem of quantum analysis of nanoscale carbon structures. The classification of carbon allotropic structures, based on the hybridization of atomic orbits, was first proposed in the work [15]. This classification is unique in that it introduces fractional dimensions of carbon structures. They have so far been used only in theoretical work, since the known, practically obtained carbon structures are usually described by discrete sets of atoms and, in essence, do not require fractional dimensions. However, the work [15] became the key one not only because of the classification of structures of various carbon modifications but also because of the development of understanding of the formation of nanocarbon materials. The principles and approaches described in this work served as the basis for a more modern classification proposed in [16]. In recent decades, many modifications of carbon, previously theoretically described in the above-mentioned works, have been experimentally discovered and studied. Among them are spherical and polyhedral forms of fullerenes, cylindrical forms of nanotubes, and sheet forms of graphene and graphane. Larger-scale nanostructures of carbon modifications include nanobuds, fibers, foams, and ribbons, though some modifications of nanocarbon exist only at high temperatures or extreme pressures. Allotropic modifications of carbon radically differ from each other in their properties, from soft to hard, from opaque to transparent, from abrasive to lubricating, etc. This wide range of properties of modifications can be illustrated, for example, by amorphous nanocarbon materials (coal, soot, foam) compared to crystalline ones (nanodiamond, lonsdaleite, graphite, nanotubes, and fullerenes). Thus, the prospects for using nanocarbon of various modifications remain attractive for solving various applied problems.

For example, the use of nanosized forms of carbon in the development of polymer composites based on them has given impetus to new research in the field of materials science and nanotechnology. Characteristic properties of nanosized carbon compounds are high Young's modulus and tensile strength, high electrical and magnetoresistance, and large surface area, in addition, carbon materials have low weight and high corrosion resistance [17, 18].

An important feature of polymer-nanocarbon composites is the low percolation threshold of electrical conductivity due to the high aspect ratio of carbon nanoparticles, which makes it easy to form a continuous electrically conductive cluster in the composite [19, 20]. These properties of carbon materials, when providing a high level of their dispersion in a polymer matrix, open up new possibilities for creating composites with unique functional properties that are not inherent in conventional materials. In nanocarbon composites, it is possible to obtain a sharp increase in permittivity and low dielectric losses near the percolation threshold, which is important for use as capacitors with high energy density and materials for controlling the electric field. Nanocomposites are heterogeneous structures with a large number of interphase boundaries, and studies of electrical and thermal transport in them are of great importance for aeronautics, space, and telecommunications equipment [21]. At the same time, the works of recent years [22–24] show that the most successful

strategy is the use of multicomponent fillers, and the combination of filler particles of different shapes (1D, 2D, 3D morphology) is an effective way to improve the electrical, thermal and mechanical properties of composites. The authors of [25] showed that when using two types of conductive fillers, such as carbon nanotubes and nanoplates, simultaneously, electrical transport can occur in parallel in conductive clusters formed separately by different fillers, this leads to a sharp decrease in the percolation threshold. The combination of fillers of different natures and morphology also improves their dispersion in the composite. Thus, the nanocarbon material in demand is a mixture of particles of different shapes, structures, and surface morphologies. The scale of applicability of such nanocarbon in composite materials for aerospace technologies is extensive, today the potential for application is declared at the level of tons per year [26].

To date, the most successful methods for synthesizing nanocarbon are recognized as [27]: laser ablation method, exfoliation method—mechanical separation of graphene layers from three-dimensional materials such as graphite; chemical vapor deposition (CVD) method, reduction of carbon oxides method—graphite oxide or graphene oxide is reduced to graphene or nanotubes. The listed methods are efficient and accurate, allow obtaining a predetermined required modification of nanocarbon, and almost do not require purification of the material from impurities. However, the methods above are mainly used to obtain materials for laboratory investigations, their scaling up to production needs is impractical. Large-scale production of nanocarbon is hampered by both the high cost of existing technological equipment and the narrow focus of existing methods on the synthesis of only certain modifications. This limits the use of nanocarbon in industry and reduces the economic effect of its use. Therefore, the problem of developing new, highly productive, and energy-efficient methods, as well as increasing the variability of nanocarbon synthesis in a single technological process is relevant. Several demands are made on the methods of nanocarbon synthesis that would satisfy the industry: a diverse qualitative composition of the resulting nanocarbon materials together with the ability to control the phase and (or) component composition of the synthesized material; high productivity of the method; low specific energy costs and raw material consumption; high environmental friendliness. Fulfillment of the entire complex of such requirements becomes possible when using the electric discharge method of influencing the substance. The equipment for its implementation is energy efficient, highly adaptable to technical tasks, and shows high productivity [28, 29]. In our work [30] the mechanisms of nanocarbon formation in the course of high-voltage electrical breakdown of liquid hydrocarbons have been established. It has been shown that high-voltage breakdown leads to a cascade of chemical transformations, as a result, both lower gaseous hydrocarbons are formed due to destruction, and higher ones due to polymerization, as well as various carbon nanostructures appear as a result of dehydrogenation. The possibility of targeted synthesis of various allotropic forms of carbon in the course of high-voltage breakdown of hydrocarbons has been shown. Developing the work [15] the authors found that the key to targeted synthesis is the choice of liquid hydrocarbon—raw material, which allows the structure and composition of the synthesized nanocarbon prediction. Experimental studies confirmed that the

qualitative and quantitative composition of carbon can be varied in a wide range. It was found that the nanocarbon obtained in the course of the electrical breakdown in the mixture of formed gases, depending on the type of material of the deposition surfaces and catalysts, consists mainly of one modification (fullerene-like carbon structures, carbon nanotubes with a diameter of 10 to 50 nm, nanofibers or films). Thus, parallel simultaneous processing by the method of high-voltage breakdown of liquid and formed gaseous hydrocarbons under certain energy input modes, varying catalysts, and initial hydrocarbon raw materials, different by the type of hybridization of carbon atomic orbits in molecules and molecular structure, allows obtaining different types of nanocarbon in one technological process. Undoubtedly, to meet the requirements stated above, it is necessary to study the efficiency of the method depending on various factors and select the range of processing conditions in which the method will be most effective.

The subject of our research is to determine the potential of selective synthesis of allotropic forms of nanocarbon by the high-voltage breakdown and to reveal the interrelations between the electrophysical properties of the obtained materials and the electron configuration of the atoms in the original hydrocarbons.

14.2 Materials and Methods

High-voltage electrical breakdown of hydrocarbons, due to the creation of extreme conditions (high temperatures and pressures), initiate a cascade of chemical transformations—destruction of raw materials molecules with subsequent formation of various types of liquid hydrocarbons and a mixture of gases (hydrogen and lower hydrocarbons). As the result of the destruction, dehydrogenation, dehydrocyclization, and polymerization of liquid hydrocarbon molecules, the synthesis of solid nanocarbon occurs. The conditions for parallel simultaneous electrical breakdown of organic liquids and the resulting gaseous hydrocarbons, different in the degree of hybridization of carbon atoms in molecules and the structure of molecules, can change within wide limits. The main variable parameters are operating voltages (15 … 35 kV) and storage capacities (0.25 … 50 μF) and, accordingly, the energy in a single pulse; energy input mode (type of discharge current pulse, rate of pulse current rise); configuration of discharge chambers and electrode systems; it is possible to use catalysts and precursors. The broad ranges of the listed parameters make it possible to obtain various types of nanocarbon in a single technological process. The materials under study were obtained during the high-voltage breakdown of organic liquids and the resulting gases. The block diagram of the experimental setup for the processing of organic liquids and the resulting gases is shown in Fig. 14.1.

In working chamber 1 high-voltage breakdown of liquid hydrocarbons is processed, resulting in the formation of solid-phase carbon, hydrogen, and a mixture of gaseous hydrocarbons. In the working chamber 2, a high-voltage breakdown of the resulting gas mixture is realized. The breakdown of the liquid was carried out in a working chamber with a coaxial electrode system, and the gases formed in this case

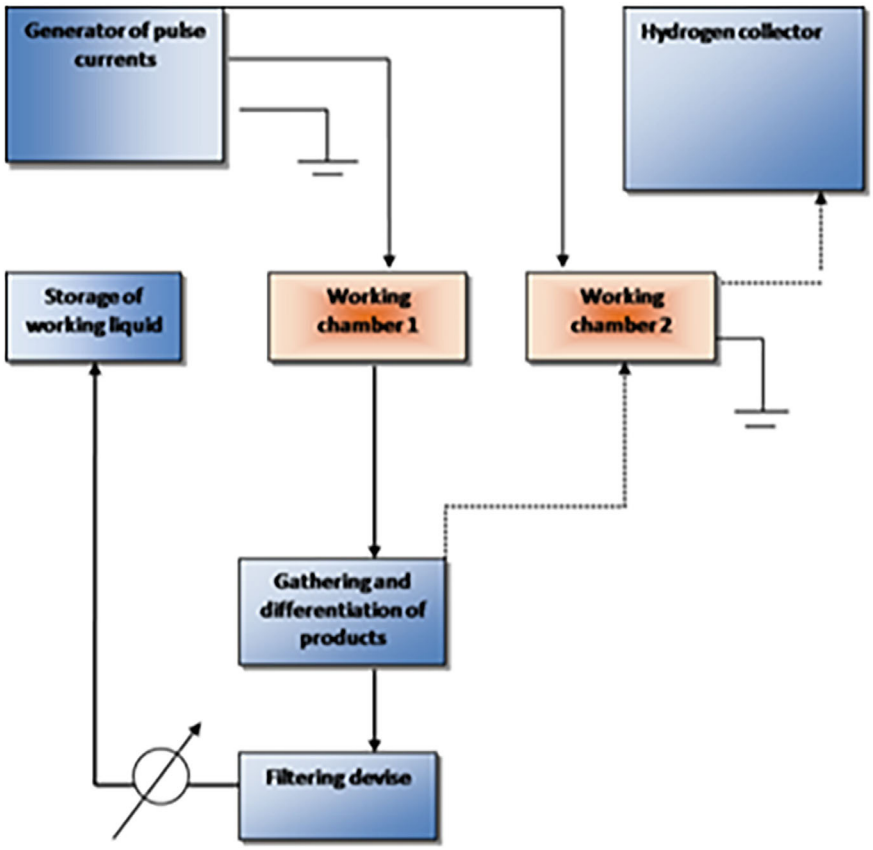

Fig. 14.1 Block diagram of the experimental setup

were processed in a working chamber with a tip-plane electrode system. Both the walls of chamber 2 and quartz and nickel–chromium substrates were used to deposit the products of high-voltage breakdown in gases.

High-voltage breakdown of liquid was realized in hydrocarbons, which differ in the type of hybridization of electrons in carbon atoms and the structure of molecules:

- ethanol (C_2H_6O) – monohydric alcohol (sp3—hybridization of atomic orbits);
- cyclohexanone ($C_6H_{10}O$) – alicyclic ketone (sp3/sp2—hybridization of atomic orbits);
- benzene (C_6H_6) – aromatic compound (sp2—hybridization of atomic orbits in planar ring-shaped molecules);
- pentane (C_5H_{12}), hexane (C_6H_{14}) – alkanes, (sp3—hybridization of atomic orbits);
- cyclopentane (C_5H_{10}) and cyclohexane (C_6H_{12}) —cycloalkanes (sp3—hybridization of atomic orbits in non-planar ring-shaped molecules);

- kerosene TC-1—composition of hydrocarbon (sp2/sp3—hybridization of atomic orbits), mass fraction aromatic hydrocarbons—0,22, gross-formula $C_{7.2107}H_{3.2936}$.

The obtained nanocarbon powders were purified from traces of working liquids with organic solvents (ethyl acetate, acetone), then volatile solvents were removed by filtration and evaporation. After that, the obtained powders were dried in a thermostat at a constant temperature (T = 100° C) to a constant weight. Powders deposited on the internal surfaces of the working chamber or special substrates during gas breakdown were examined immediately after obtaining them.

The obtained materials were studied by methods of electron transmission and scanning microscopy using Hitachi H-800 and LEO Supra 50VP electron microscopes.

Specific electrical conductivity of powder samples of the material was measured. To maintain identical conditions for measuring electrical conductivity and to compare the results for different powder samples, the dependence of electrical conductivity on the density of the powder material was measured in the cylinder under the piston during compression. This allowed us to find the minimum value of the material density at which sufficiently good contacts are formed, ensuring the electrical conductivity of the sample. To measure the specific electrical conductivity, the powders were poured into a loading container, which was closed with a spring-piston system. Then, the sample was gradually compressed using a press with a pressure change of up to 10^7 Pa and a constant temperature. During compression, the circuit between the electrodes, which were the piston and the bottom of the loading container, connected to the MO-62 DC bridge, was closed. The resistance expectedly decreased due to an increase in the total contact area between neighboring particles of material. The bulk density ρ depending on the degree of compaction and the specific electrical conductivity σ of the powders under study was determined based on the results of the electrical resistance R measuring and the height of the powder column h, initially having the mass of sample m, by the formulas:

$$\rho = \frac{4m}{\pi d^2 h} \tag{14.1}$$

$$\sigma = \frac{4h}{R\pi d^2} \tag{14.2}$$

where d—inner diameter of loading container.

The measurements were carried out in triplicate and the arithmetic mean was found; the measurement error of the specific electrical conductivity of nanocarbon powders did not exceed 5%.

14.3 Results and Discussion

14.3.1 High-voltage Breakdown of Liquid Hydrocarbons.

High-voltage breakdown of liquid alkanes and cycloalkanes.

It is known, that alkanes at temperatures above 450 °C disintegrate into hydrocarbons with a smaller number of carbon atoms. The C− C bond can be broken at any random point in the molecule, so a mixture of alkanes (C_pH_{2p+2}) and alkenes (C_mH_{2m}) is formed with a lower molecular weight than the original alkane. The plasma-chemical action of high-voltage breakdown begins with the dissociation of liquid molecules. Dissociation is realized as the ruptures of strong C − C bonds in the central parts of linear molecules, which leads to the formation of carbon clusters C_k, hydrogen, and lower hydrocarbons—gases [30]: $C_nH_{2n+2} = C_k + C_mH_{2m} + C_pH_{2p+2} + kH_2$, where $k + m + p = n$.

During the high-voltage breakdown of cycloalkanes, the molecules of which are ring-shaped, some of the rings do not rupture, and the synthesis of nanocarbon occurs due to dehydrogenation—the hydrogen atom splits off. This can be explained by the fact that the energy of the σ-bond C−C in cycloalkanes is several times higher than the energy of the bond C=C and greater than the energy of the bond C−H. Dehydrogenation and polymerization are the most probable processes of nanocarbon synthesis, and the rupture of the bonds C−C leads to the formation of gaseous alkanes [30].

Individual nanocarbon particles obtained from cyclohexane have a spheroidal shape and "onion-like" structure (Fig. 14.2).

The diameters of conglomerates of spherical carbon particles obtained in the process of high-voltage treatment of cyclohexane were determined by atomic force microscopy and ranged from 27 to 70 nm. After the above-described cleaning with solvents, a 3D image of the layer of obtained carbon particles was obtained (Fig. 14.3a). Based on the section trace 1–2 (Fig. 14.3b) from the section profile (Fig. 14.3c) the sizes of the nanocarbon particles were determined. The diameter of the obtained carbon particles is from 2.5 to 3.0 nm. Individual particles have a diameter of about 1 nm. Thus, the true size of the carbon nanoparticles obtained by high-voltage breakdown of cyclohexane is from 1 to 3 nm.

The similarity of the Raman spectra of nanodiamonds and nanocarbon obtained by the electrical breakdown of cyclohexane indicates a diamond-like type of its local atomic order [31].

It should be noted, that in addition to the electron configuration of the carbon source atoms, the structure of the molecule itself also plays an important role. For example, nanocarbon with a pronounced diamond-like type of local atomic order was obtained only from cyclohexane. It is known, that the molecule of cyclohexane is similar to a ring in the crystal structure of a diamond with strong C–C bonds. When using hexane as a carbon source, a mixed type of local atomic order structure of nanocarbon was obtained (sp3/sp2—hybridization of atomic orbits). The

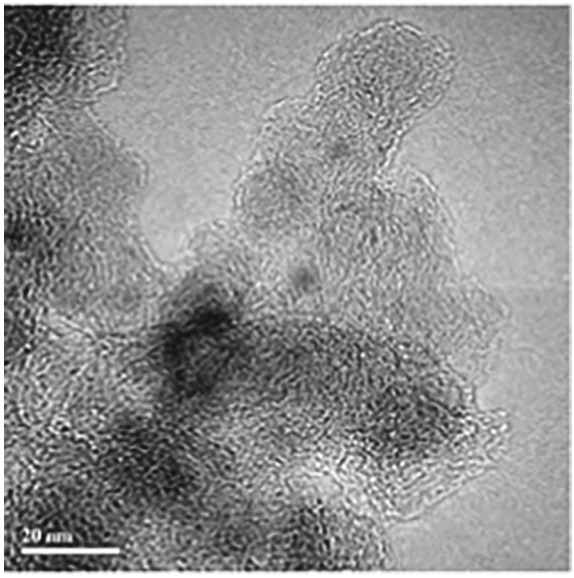

Fig. 14.2 TEM image of carbon nanospheres, carbon source—cyclohexane

results of measuring the dependences of the specific electrical conductivity of the obtained materials on the compaction density (Fig. 14.4) allow us to assume that compacted powders obtained by high-voltage breakdown of cyclohexane can be classified as diamond-type nanocarbon with a predominant sp3 electron configuration. Their specific electrical conductivity does not exceed 0.2 S/m. Studies of the electrical conductivity of nanocarbon formations obtained by high-voltage breakdown of hexane and cyclohexane made it possible to identify significant differences in the obtained materials (Fig. 14.4).

High-voltage breakdown of kerosene and benzene

Amorphous carbon obtained using the high-voltage breakdown of kerosene and benzene is characterized by a small block size, which is practically independent of the type of liquid used with the same energy parameters of synthesis (Fig. 14.5).

To compare known and thoroughly studied modifications of carbon (graphite and diamond) with other carbon materials, it is necessary to know the characteristic bond lengths and valence angles in the molecules of the substance. For graphite, the bond length for the two main polymorphic modifications is 1.418 Å, and the valence angle $\varphi = 120.0$; for diamond, the length of a single bond for the cubic modification is 1.5417 Å, for the hexagonal modification—1.5641 Å, the valence angle $\varphi = 109.50$.

The conducted studies of nanocarbon have shown that the products of the electrical breakdown of benzene and kerosene have a pronounced graphite-like type of local atomic order. In particular, the calculation of the valence angle between bonds for nanocarbon obtained from benzene showed that it varies within the range from 121.9 to 123.1°, which indicates the prevalence of the graphite-like type of local atomic

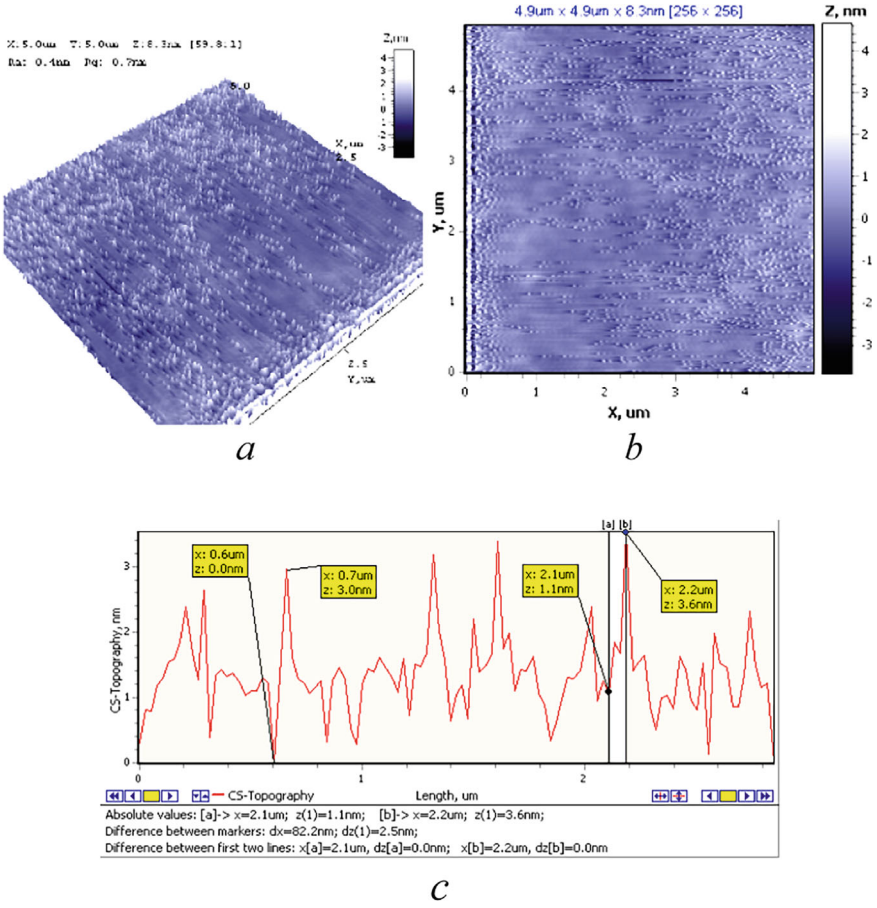

Fig. 14.3. 3D image of carbon particles layer **a** and the surface topography of the layer on quartz glass with section trace **b**, and section profile **c**

order. During the amorphous carbon obtained as the result of the high-voltage breakdown of benzene and kerosene at different energy parameters annealing no significant structural changes occur, i.e. nanocarbon does not graphitize. However, nanocarbon obtained in the course of the high-voltage breakdown of cyclohexane graphitizes already at 1000 °C, which is typical for diamond-like materials [32]. The values of specific electrical conductivity also allow us to validate indirectly the predominant type of sp2-hybridization of atomic orbits in the obtained material (Fig. 14.6).

High-voltage breakdown of oxygen-containing liquids (alcohols, ketones)

High-voltage breakdown of monoatomic alcohols initiates the synthesis of alkenes (C_nH_{2n}). During the dehydrogenation of ethanol, ethylene (gas) forms: $CH_3 - CH_2 - OH \rightarrow CH_2 = CH_2 + H_2O$. The yield of nanocarbon straight as the result of

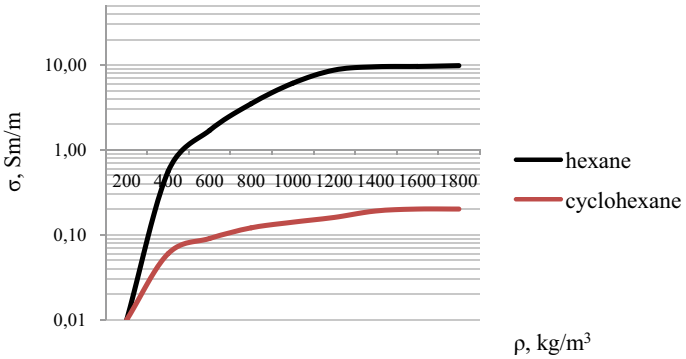

Fig. 14.4 Dependence of specific electrical conductivity of materials obtained by high-voltage breakdown of hexane and cyclohexane on the density of the sample

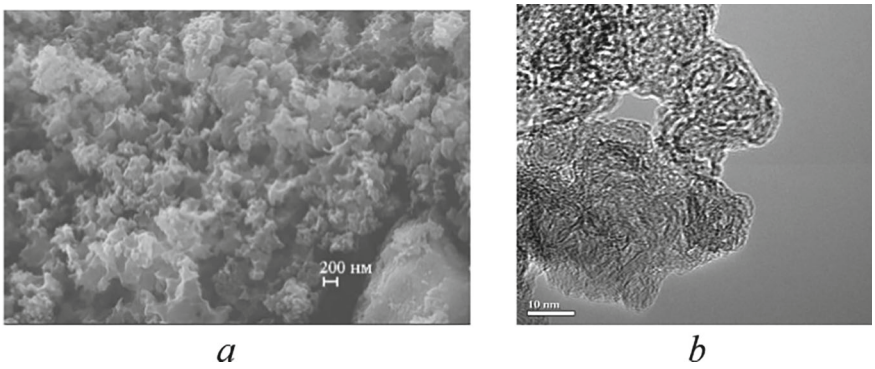

Fig. 14.5 TEM image of high-voltage breakdown products of kerosene (**a**) and benzene (**b**)

the breakdown of ethanol is only 1.21% [30], and the resulting powder (Fig. 14.7) contains impurities of iron and oxygen.

In the course of the high-voltage breakdown in cyclohexanone, "onion-shaped" carbon structures were obtained (Fig. 14.8). However, the maximum specific electrical conductivity of compacted nanocarbon powder obtained during the high-voltage breakdown of cyclohexanone (20 Sm/m) is between the values of specific electrical conductivities of amorphous carbon with diamond-like and graphite-like local atomic order. Thus, the obtained material can be classified as nanocarbon with mixed hybridization of atomic orbits sp3/sp2 (Fig. 14.9).

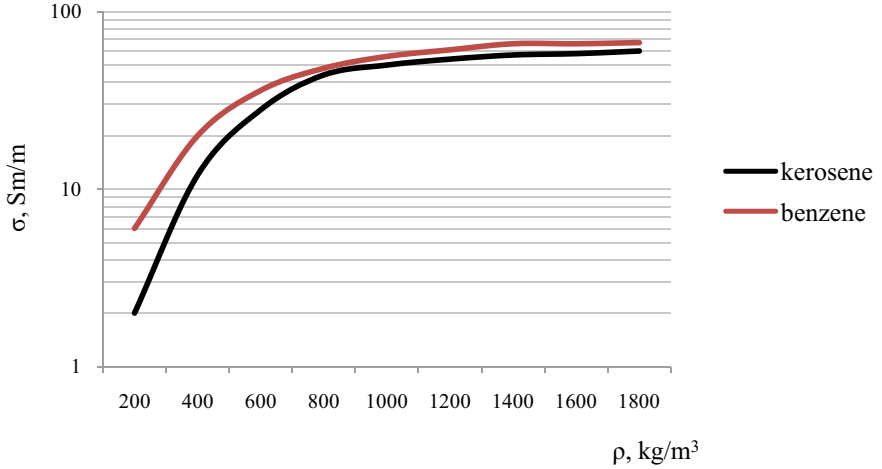

Fig. 14.6 Dependence of specific electrical conductivity of powders obtained by high-voltage breakdown of kerosene and benzene on the sample density

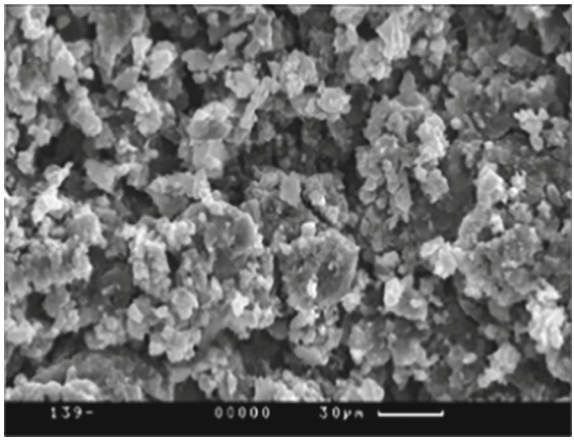

Fig. 14.7 Amorphous nanocarbon obtained by high-voltage breakdown of ethanol

14.3.2 High-voltage Breakdown of Gases Formed During the Breakdown of Liquids

The deposition of nanocarbon synthesized during high-voltage breakdown of the mixture of formed gases, regardless of the initial liquid hydrocarbon, occurs both in the form of films up to 0.1 mm thick on a quartz substrate (Fig. 14.10), and in the form of carbon nanotubes and fibers (Fig. 14.11). The surface of the films facing the substrate contains silicon (up to 5%), and the opposite side contains only carbon.

It was established by electron microscopy that the surface of the synthesized films consists of globules, the diameter of globules varies from 1 to 25 μm (Fig. 14.12).

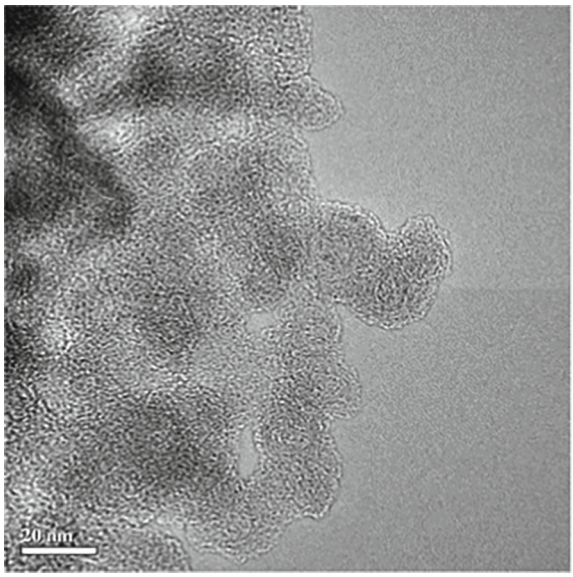

Fig. 14.8 TEM image of nanocarbon, carbon source—cyclohexanone

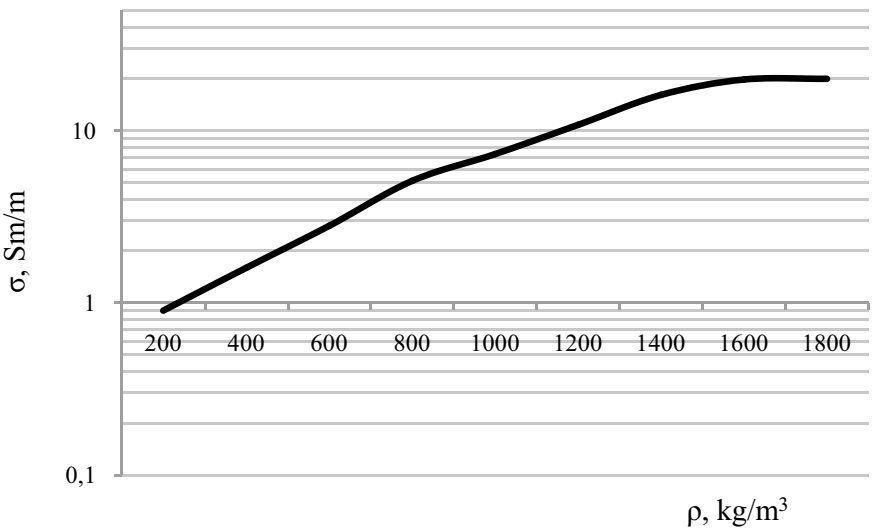

Fig. 14.9 Dependence of the specific electrical conductivity of the powder obtained by high-voltage breakdown of cyclohexanone on the sample density

When processing gases forming during the high-voltage breakdown of kerosene and benzene on a nickel–chromium substrate in the working chamber 2 (Fig. 14.1) carbon nanotubes (Fig. 14.13a) and fibers (Fig. 14.13b) are synthesized. Upon reaching a certain length, the fibers and nanotubes growing on the catalytic surface

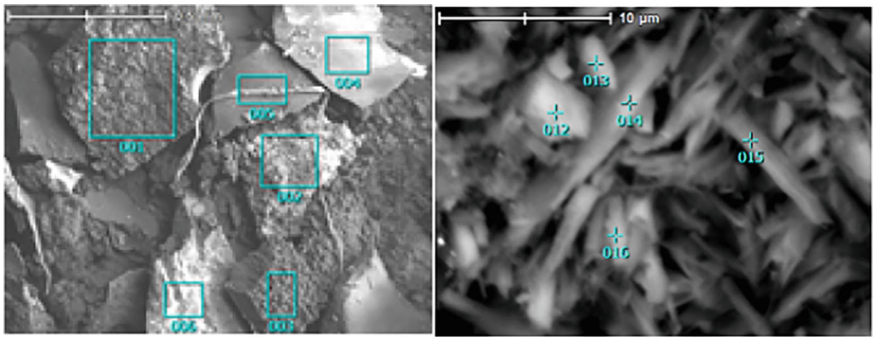

Fig. 14.10 Micrographs of films obtained on a quartz substrate as a result of high-voltage breakdown of gases (primary carbon source—hexane)

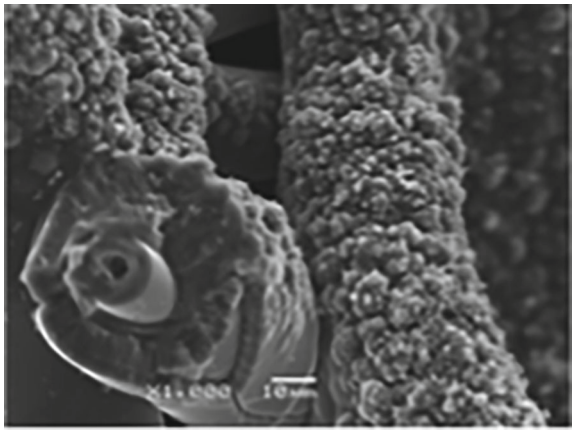

Fig. 14.11 Micrographs of rolled films obtained as a result of high-voltage breakdown of gases (primary carbon source—cyclohexane)

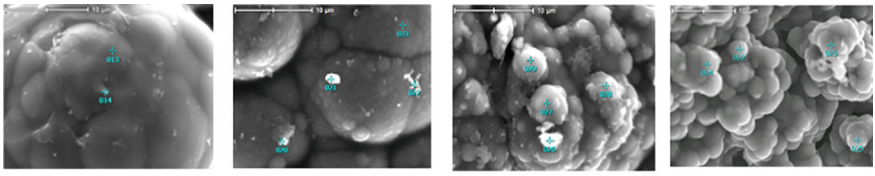

a *b* *c* *d*

Fig. 14.12 Micrographs of the surface of films synthesized as a result of high-voltage breakdown of gases (primary carbon source: **a**—pentane, **b**—hexane, **c**—cyclopentane, **d**—cyclohexane)

crumble in the form of powder, and fibers with a length-to-diameter ratio of more than 100 are obtained. Such powder, as follows from the results of chemical analysis (Table 14.1), contains only traces of the catalyst substance.

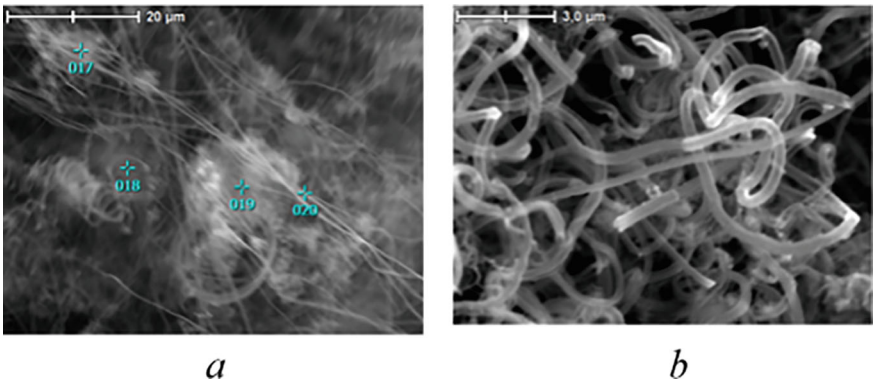

Fig. 14.13 Micrographs of carbon nanotubes and carbon fibers obtained as a result of gas breakdown (primary carbon source: **a**—benzene, **b**—kerosene)

Table 14.1 Chemical composition (mass %) of the sections indicated in Fig. 14.13a

Number of section	C	O	Ni	Total
17	100	0	Traces	100
18	100	0	Traces	100
19	100	0	Traces	100
20	100	0	Traces	100

The energy of the C−H bond in alkene molecules ($\varepsilon_1 = 433$ kJ/mol) is less than the energy of the double bond C=C ($\varepsilon_2 = 588$ kJ/mol), therefore the high-voltage breakdown of gaseous alkenes leads to the synthesis of solid-phase nanocarbon, which has predominantly sp2—hybridization of carbon atomic orbits. High-voltage breakdown in the resulting ethylene, for example, leads to the formation of carbon nanotubes on the catalyst (Fig. 14.14). Carbon nanotubes deposited on a nickel–chromium substrate completely cover its surface. The diameter of the synthesized carbon nanotubes correlates with the dispersion of the substrate material.

The measured values of specific electrical conductivity of nanocarbon obtained in the form of films allow us to conclude that there is a mixed (sp2/sp3) type of hybridization of carbon atomic orbits. In contrast, the carbon material, consisting mainly of nanotubes, shows high values of specific electrical conductivity, which are typical for the graphite-like type of local atomic order (Fig. 14.15).

The data summarizing the influence of the carbon source on the type of local atomic order and the specific electrical conductivity of nanocarbon powders obtained by high-voltage breakdown are summarized in Table 14.2. For comparison, Table 14.2 includes the values of the specific electrical conductivity of nanodiamonds obtained by the detonation method [33] and nanographite obtained by electrical explosion of graphite conductors [34].

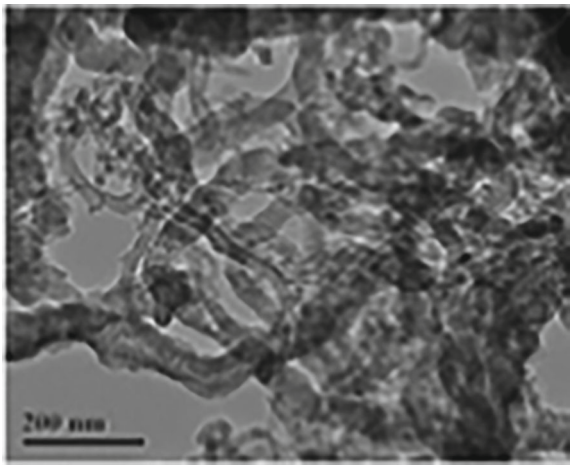

Fig. 14.14 Carbon nanotubes obtained in the process of high-voltage breakdown of ethylene formed during high-voltage breakdown of ethanol

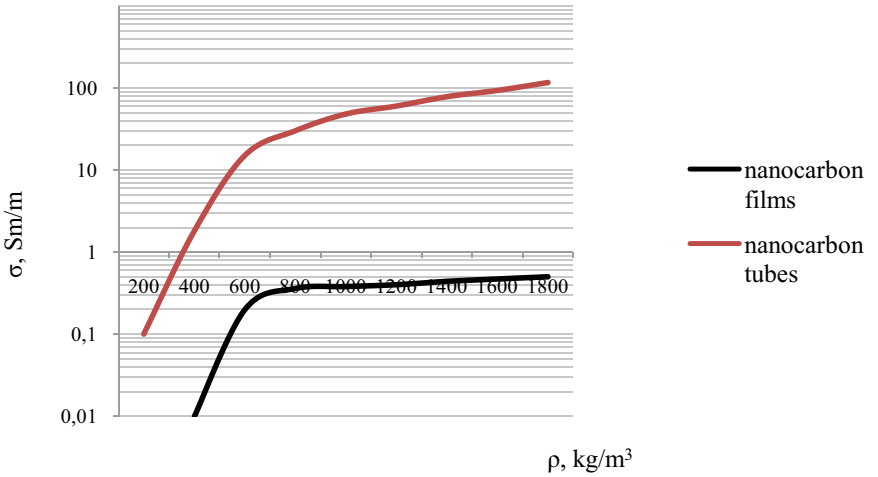

Fig. 14.15 Dependence of the specific electrical conductivity of powders of nanocarbon films and nanotubes obtained in the course of high-voltage breakdown of a gas mixture on the density of the sample

As can be seen from the data presented in Table 14.2, the type of local atomic order and the value of specific electrical conductivity of the obtained nanocarbon materials are associated with the electron configuration of carbon atoms and the structure of the carbon source molecules. However, the effect of high temperatures during the breakdown of alkanes and cycloalkanes leads to a change in the hybridization of some carbon atomic orbits from sp3 to sp2. Then the formation of sp2/sp3 nanocomposites with a diamond-like type of local atomic order occurs, and nanocarbon with a specific electrical conductivity of less than 1 Sm/m is synthesized. Compacted

Table 14.2 Effect of carbon source and type of synthesized nanocarbon on the specific electrical conductivity of nanocarbon powders at compaction density $\rho = 1800$ kg/m^3

Carbon source (type of hybridization of carbon atomic orbits)	Type of local atomic order of the nanocarbon to obtain	Specific conductivity, S/m
Explosives (sp^3) [33]	Nanodiamond	10^{-5}
Cyclohexane (sp^3)	Onion-shaped nanocarbon with diamond-like local atomic order	0,2
Mixture of gaseous alkanes (sp^3)	Nanocarbon films with diamond-like local atomic order	0,5
Hexane (sp^3)	Amorphous nanocarbon with mixed diamond-graphite type of local atomic order	9,8
Cyclohexanone (sp^2/sp^3)	Amorphous nanocarbon with mixed diamond-graphite type of local atomic order	20,0
Kerosene (sp^2/sp^3)	Graphite-like amorphous nanocarbon	60,0
Benzene (sp^2)	Amorphous nanocarbon with graphite-like type of local atomic order	67,0
Mixture of gaseous alkenes (sp^2)	Carbon nanotubes and fibers	116,0
Grafite (sp^2) [34]	Nanografite (sp^2)	104,0

powders with specific electrical conductivity from 1 Sm/m to 20 Sm/m can be classified as amorphous carbon with a mixed diamond-graphite type of local atomic order.

14.4 Conclusions

Thus, the method of high-voltage breakdown in liquids and gases allows us to obtain various types of nanocarbon, differing in structure and type of local atomic order due to pulsed high-energy actions on organic liquids and the resulting gaseous hydrocarbons.

The dependence was revealed of the selectivity of the high-voltage breakdown synthesis of amorphous carbon with different types of local atomic order and specific electrical conductivity on the initial electron configuration of atoms and the structure of molecules in organic liquids—sources of carbon.

The choice of the chemical composition and morphology of the substrate material for deposition also controls the selectivity of the gas processing method by high-voltage breakdown.

It is shown that at powder compaction density of 1800 kg/m^3, the values of specific electrical conductivity of amorphous nanocarbon with a diamond-like type of local atomic order do not exceed 1 Sm/m, and the specific electrical conductivity of nanocarbon with a mixed diamond-graphite type of local atomic order lies in the range from 1 Sm/m to 20 Sm/m. The obtained data are proposed to be used as a basis for an express method for assessing the type of nanocarbon obtained as a result of high-voltage breakdown of liquid and (or) gaseous carbon sources.

References

1. H. Nishihara, Progress in template nanocarbons and related materials chemistry. Carbon **228**, 119279 (2024).https://doi.org/10.1016/j.carbon.2024.119279
2. J. Chen, Z. Ou, H. Chen, Sh. Song, K. Wang, Y. Wang, Recent developments of nanocarbon based supports for PEMFCs electrocatalysts. Chinese J. Catalys. **42**(8), 1297–1326 (2021). https://doi.org/10.1016/S1872-2067(20)63736-6
3. W. Nakanishi, K. Minami, L.K. Shrestha, Q. Ji, J.P. Hill, K. Ariga, Bioactive nanocarbon assemblies: nanoarchitectonics and applications. Nano Today **9**(3), 378–394 (2014). https://doi.org/10.1016/j.nantod.2014.05.002
4. N. Yang, X. Jiang, Nanocarbons for DNA sequencing: a review. Carbon **115**, 293–311 (2017). https://doi.org/10.1016/j.carbon.2017.01.012
5. Gacem, M.A., Gacem, H., Ould-El-Hadj-Khelil, A.: Nanocarbons: antibacterial, antifungal, and antiviral activity and the underlying mechanism. In: Abd-Elsalam K.A. (eds.) Micro and nanotechnologies, carbon nanomaterials for agri-food and environmental applications, pp. 505–533, Elsevier, Amsterdam (2020). https://doi.org/10.1016/B978-0-12-819786-8.00022-0
6. Zhou, C., Zhang, M., Yang, C. (eds.): Nanocarbon electronics. 1st edn. Jenny Stanford Publishing, Singapore (2020). https://doi.org/10.1201/9781003043089
7. Liu, J., Ding, R., Cao, J., Zhan, K., Li, S., Zha, B., et al.: Recent progress in architecture design of nanocarbon-reinforced metal matrix composites and their properties: a review. Carbon, **228**, 119382 (2024). https://doi.org/10.1016/j.carbon.2024.119382
8. Kostaras, C., Pavlou, C., Galiotis, C., Dassios, K.G.: Nanocarbon-based sheets: advances in processing methods and applications. Carbon **221**, 118909 (2024). https://doi.org/10.1016/j.carbon.2024.118909
9. Kumar, D., Abraham, J.E., Varghese, M., George, J., Balachandran, M., Cherusseri, J.: Nanocarbon assisted green hydrogen production: development and recent trends. Int. J. Hydrogen Energy, **50**(B), 118–141 (2024). https://doi.org/10.1016/j.ijhydene.2023.07.257
10. Li, K., Liu, G., Zheng, L., Jia, J., Zhu, Y., Zhang, Y.: Coal-derived carbon nanomaterials for sustainable energy storage applications. New Carbon Mater. **36**(1), 133–154 (2021). https://doi.org/10.1016/S1872-5805(21)60010-0
11. N. Roy, R. Sengupta, A.K. Bhowmick, Modifications of carbon for polymer composites and nanocomposites. Prog. Polym. Sci. **37**(6), 781–819 (2012). https://doi.org/10.1016/j.progpolymsci.2012.02.002
12. I.A. Stepek, M. Nagase, A. Yagi, New paradigms in molecular nanocarbon science. Tetrahedron **123**, 132907 (2022). https://doi.org/10.1016/j.tet.2022.132907
13. N. Saba, M. Jawaid, H. Fouad, O.Y. Alothman, Nanocarbon: preparation, properties, and applications, in *Nanocarbon and its composites*, ed. byA. Khan, M. Jawaid, A.M. Inamuddin, Abdullah Mohamed Asiri, pp. 327–354. Woodhead Publishing, Sawston, Cambridge (2019). https://doi.org/10.1016/B978-0-08-102509-3.00009-2
14. A. Hirsch, The era of carbon allotropes. Nat. Mater. **9**(11), 868–871 (2010). https://doi.org/10.1038/nmat2885

15. R.B. Heimann, S.E. Evsvukov, Y. Koga, Carbon allotropes: a suggested classification scheme based on valence orbital hybridization. Carbon **35** (10), 1654–1658 (1997). https://doi.org/10.1016/s0008-6223(97)82794-7
16. V. Georgakilas, J.A. Perman, J. Tucek, R. Zboril, Broad family of carbon nanoallotropes: classification, chemistry, and applications of fullerenes, carbon dots, nanotubes, graphene, nanodiamonds, and combined superstructures. Chem. Rev. **115**(11), 4744–4822 (2015).https://doi.org/10.1021/cr500304f
17. M. Hasan, A. Islam, M. Rahman, A.K. Kasi, Zh. Jiang, Md.Z. Rahman, Recent advancements in nanocarbon derivatives: from synthesis to applications, in *Comprehensive Materials Processing*, 2nd edn. ed by S. Hashmi, (Elsevier, Amsterdam, 2024), pp. 96–124. https://doi.org/10.1016/B978-0-323-96020-5.00277-6
18. A.D. Rud, N.E. Kornienko, I.M. Kirian, A.N. Kirichenko, O.P. Kucherov, Local heteroallotropic structures of carbon. Mater. Today: Proc. **5**(12–3), 26089–26095 (2018). https://doi.org/10.1016/j.matpr.2018.08.035
19. Plevachuk, Yu., Poverzhuk, V., Svec P. Sr., Svec, P., Janotová, I., Janickovic, D., Rud, A.: Electrical resistivity of lead-free solders reinforced by carbon nanospheres. Int. J. Thermophys. **45**(31) (2024). https://doi.org/10.1007/s10765-023-03326-8
20. I.V. Ovsiienko, T.A. Len, L.Y. Matzui, Y.I. Prylutskyy, U. Ritter, P. Scharff, et al., Resistance of a nanocarbon material containing nanotubes. Molecular Crystals and Liquid Crystals **468**(1), 289/[641]-297/[649] (2007). https://doi.org/10.1080/15421400701231582
21. A. Bianco, Y. Chen, E. Frackowiak, M. Holzinger, N. Koratkar, V. Meunier et al., Carbon science perspective in 2020: current research and future challenges. Carbon **161**, 373–391 (2020). https://doi.org/10.1016/j.carbon.2020.01.055
22. I.V. Ovsiienko, L.L. Vovchenko, L.Y. Matzui, T.L. Tsaregradskaya, T.A. Len, G.V. Saenko, et al.: Conductivity of polymer composites with nanocarbon filler, in *Nanomaterials and Nanocomposites, Nanostructure Surfaces, and Their Applications, Springer Proceedings in Physics*, ed by O. Fesenko, L. Yatsenko, vol. 279. Springer, Cham. https://doi.org/10.1007/978-3-031-18096-5_20
23. T.A. Len, L.Y. Matzui, I.V. Ovsiienko, Y.I. Prylutskyy, I.I. Andrievskii, I.B. Berkutov, et al.: Magnetoresistance of nanocarbon materials based on carbon nanotubes. Low Temp. Phys. **37**(9–10), 1027–1032 (2011). https://doi.org/10.1063/1.3665770
24. A.A. Khurram, S.A. Rakha, P. Zhou, M. Shafi, A. Munir, Correlation of electrical conductivity, dielectric properties, microwave absorption, and matrix properties of composites filled with graphene nanoplatelets and carbon nanotubes. J. Appl. Phys. **118**, 044105 (2015). https://doi.org/10.1063/1.4927617
25. L.L. Vovchenko, O.V. Lozitsky, V.V. Oliynyk, V.V. Zagorodnii, T.A. Len, L.Y. Matzui, Dielectric and microwave shielding properties of three-phase composites graphite nanoplatelets/carbonyl iron/epoxy resin. Appl. Nanosci. **10**, 4781–4790 (2020). https://doi.org/10.1007/s13204-020-01326-w
26. C.J. Shearer, A. Cherevan, D. Eder, Application and future challenges of functional nanocarbon hybrids. Adv. Mater. **26**, 2295–2318 (2014). https://doi.org/10.1002/adma.201305254
27. S. Dhanushree, C. Nithya, Introduction to nanocarbon. in *NanoCarbon: A Wonder Material for Energy Applications. Engineering Materials*, ed by R.K. Gupta (Springer, Singapore, 2024. https://doi.org/10.1007/978-981-99-9935-4_1
28. D. Vinnychenko, N. Nazarova, The high-voltage electrical engineering systems of gaseous hydrocarbons electro-discharge processing design principles. in *IEEE 39th International Conference on Electronics and Nanotechnology (ELNANO) 2019* (2019), pp. 678–683. https://doi.org/10.1109/ELNANO.2019.8783220
29. N. Nazarova, D. Vinnichenko, Electrotechnical control and current protection system of the high-voltage pulse-current generator. *IEEE First Ukraine Conference on Electrical and Computer Engineering (UKRCON)*, pp. 574–577 (2017). https://doi.org/10.1109/UKRCON.2017.8100307
30. N. Kuskova, A. Malyushevskaya, M. Prystash, S. Prystash, Y. Adamchuk, Synthesis of nanocarbon by high-voltage breakdown of hydrocarbons. Eastern-Eur J Enterprise Technol **6**(126), 6–16 (2023). https://doi.org/10.15587/1729-4061.2023.292774

31. A.D. Rud, N.I. Kuskova, L.I. Ivaschuk, A.E. Perekos, Synthesis of carbon nanomaterials using high-voltage electric discharge techniques, in *Nanomaterials*, ed by Rahman, (Tech Open, Rijeka, 2011), pp. 211–230. https://doi.org/10.5772/25819
32. A.D. Rud, N.I. Kuskova, L.I. Ivaschuk, G.M. Zelinskaya, N.M. Biliy, Structure state of carbon nanomaterials produced by high-energy electric discharge techniques. Fullerenes, Nanotubes, Carbon Nanostruct. **19**(1), 120–126 (2011). https://doi.org/10.1080/1536383X.2010.490129
33. Q. Zou, M.Z. Wang, Y.G. Li, Analysis of the nanodiamond particle fabricated by detonation. J. Exp. Nanosci. **5**(4), 319–328 (2010). https://doi.org/10.1080/17458080903531021
34. A.D. Rud, A.E. Perekos, A.P. Shpak, V.N. Uvarov, N.I. Kuskova, V.M. Ogenko, Electrical explosion technology for novel carbon nanomaterials production. in *Hydrogen Materials Science and Chemistry of Carbon Nanomaterials. NATO Security through Science Series A: Chemistry and Biology*, ed. by T.N. Veziroglu et al. Springer, Dordrecht (2007). https://doi.org/10.1007/978-1-4020-5514-0_21

Chapter 15
Fine Treatment of Dairy Wastewater in a Heterogeneous Fenton System

Olena Makido, Galyna Khovanets', Oksana Kurylets, Markiian Dziadyk, and Viktor Vasiichuk

Abstract Wastewater contaminated with organic substances (dye production and food industry) causes great harm to the environment. Among food enterprises, the dairy industry leads in wastewater production. The purpose of this article is to study the use of a heterogeneous Fenton system based on a pre-synthesized nanostructured magnetically separable catalyst $CoFe_2O_4/SiO_2/CuO$ for fine post-treatment of dairy wastewater. The structure of the obtained composite was confirmed by Fourier transform infrared spectroscopy (FTIR). The surface morphology of the particles and the elemental composition were determined using a scanning electron microscope (SEM). The studied catalyst was tested on simulated dairy wastewater. The content of organic compounds was analyzed by chemical oxygen demand (COD), O_2 content, redox potential (ORP) and medium pH. The effect on the oxidation process of organic compounds in the Fenton system of replacing the oxidant hydrogen peroxide with air oxygen was studied. The dependence of the efficiency of the oxidation process on the amount of supplied oxygen was shown. It was established that when using O_2 as an oxidant, the catalyst forms organoperoxide compounds that are responsible for the complete oxidation of organic pollutants. It was determined that for fine treatment of dairy wastewater the optimal system is «dairy wastewater : O_2 : $CoFe_2O_4/SiO_2/CuO$», in which the degree of oxidation of organic pollutants reaches 96%, and the value of chemical oxygen demand (COD) decreases from 115 mgO_2/dm^3 to 10 mgO_2/dm^3. The efficiency and easy extraction of the magnetically separable catalyst allows for the implementation of a cyclic water use scheme and makes the proposed system economically viable and environmentally friendly.

O. Makido · G. Khovanets' (✉)
Department of Physical Chemistry of Fossil Fuels of the Institute of Physical-Organic Chemistry and Coal Chemistry named after L. M. Lytvynenko of the National Academy of Sciences of Ukraine, Lviv, Ukraine
e-mail: khovanetsgalyna@gmail.com

O. Kurylets · M. Dziadyk · V. Vasiichuk
Lviv Polytechnic National University, Lviv, Ukraine
e-mail: oksana.h.kurylets@lpnu.ua

O. Fesenko and L. Yatsenko (eds.), *Functional Nanomaterials, Nanocatalysts, Nanotechnologies, and Their Applications*, Springer Proceedings in Physics 321,
https://doi.org/10.1007/978-3-031-99136-3_15

15.1 Introduction

Today, the pollution of the ecosystem by wastewater is global in nature. Among food enterprises, the dairy industry is considered the largest source of wastewater, where wastewater accounts for up to 80% of the used water [1].

Water is the main technological medium used at all stages of dairy production, equipment cleaning and washing, as well as heating, cooling and disinfection processes [2]. The total amount of wastewater in units of volume can exceed the amount of milk produced by 2.5 times. Of these, contaminated water coming from production processes accounts for 50–80% and only the remaining 20–50% is considered conditionally clean.

Recently, interest in the treatment of dairy wastewater and its possible reuse has increased significantly [3, 4]. Dairy wastewater is characterized by a high content of dissolved and suspended solids (oils, fats, proteins), and may contain ammonia, phosphates, and detergent residues. Although such wastewater does not usually contain toxic chemicals, it can pose a major problem for the surrounding community due to the high concentration of dissolved organic matter and the unpleasant odor caused by its decomposition. To solve these problems, dairy producers use a complex wastewater treatment protocol, which has a significant impact on the economic performance of the enterprise. Wastewater treatment in dairy production is complex and involves the use of various methods: mechanical, physicochemical and biological. Mechanical treatment helps to equalize changes in the volume and mass flow rate of wastewater and reduce the proportion of suspended solids. Various physical and chemical processes are aimed at removing emulsified compounds, but the introduction of reagents into the process significantly increases treatment costs. Another disadvantage is the low removal of the organic component of wastewater, which is characterized by high levels of chemical oxygen demand (COD) and biochemical oxygen demand (BOD) [5].

To reduce the organic load, anaerobic and/or aerobic biological methods are mainly used, which allow to treat wastewater with a high COD and achieve a degree of purification of up to 90% [6]. However, the use of classical biological treatment technology, characterized by the presence of recirculation flows, is associated with relatively high energy consumption for wastewater treatment and the formation of a significant amount of excess biomass. The need to stabilize the resulting sludge requires additional costs, and the need to develop new wastewater treatment technologies is justified by the changing nature and phase-dispersed state of dairy wastewater contaminants. In addition, after biological treatment, the COD of such wastewater reaches up to 125 mgO_2/dm^3, which allows it to be discharged into the general sewerage system, but an additional stage of fine treatment should be implemented to reuse it.

In order to improve the biodegradation of dairy wastewater, some authors have proposed to add pure oxygen as an oxidant to the homogenization pools before traditional physical and chemical treatment [2]. Although the use of pure oxygen as

an oxidant improves the quality of wastewater and reduces treatment costs, oxygen supply systems are hardware complex and require certain measures for safe use.

Advanced oxidation processes (AOPs), based on the formation of strong oxidants – hydroxyl radicals, that destroy organic compounds by oxidizing them to CO_2 and water, are widely used to treat water from persistent organic pollutants. These include the heterogeneous Fenton process, known as a highly efficient process for the oxidation and degradation of a wide range of water pollutants, including those of organic origin [7–9]. The synthesis of hydroxyl radicals in this process occurs as a result of the interaction of a heterogeneous catalyst based on transition metals, such as Fe, Cu, Co, Mn or their combinations, and hydrogen peroxide as an oxidant.

The advantages of using this process include an «environmentally friendly» oxidant—hydrogen peroxide, since after its use there is no secondary water pollution [10], the possibility of using in a wide range of pH and temperatures. In addition, hydrogen peroxide is highly soluble in water and well stored in containers, as its commercial solutions are stable. Thus, the use of the Fenton system for the treatment of dairy wastewater, which contains a large amount of organic pollutants [11] is appropriate and promising. However, the use of heterogeneous catalysts based on transition metals requires complex filtration equipment for their extraction for the next cycle of application, which also increases the cost of the process.

To solve the problem of catalyst extraction from the reaction medium for its reuse, in the Department of Physical Chemistry of Fossil Fuels was synthesized a multilayer core–shell composite consisting of a magnetically sensitive cobalt ferrite core covered with a stabilizing layer of porous silicon oxide, on which copper oxide catalytic centers are located. Preliminary studies on model solutions of organic dyes, in particular, methylene blue, have shown the prospects of using a heterogeneous Fenton system based on the $CoFe_2O_4/SiO_2/CuO$ catalyst for the oxidation of organic compounds [12]. These composites have a developed surface and good adsorption properties, which is one of the important characteristics of the catalyst [13].

This research work is devoted to the study of the possibility of using a synthesized heterogeneous nanostructured magnetically sensitive catalyst based on copper oxide in the Fenton system for the fine treatment of dairy wastewater to return it for technical or other purposes.

However, the use of a heterogeneous catalyst in the Fenton system has its own caveats. The mechanism of oxidation of organic substances in the Fenton and Raffa systems depends on a number of factors, including the chemical structure of substrates, their complexing ability with respect to transition metal ions, in particular, Fe. In addition, some authors [14] showed that the introduction of molecular oxygen into the heterogeneous Fenton system significantly improves the completeness of the conversion of organic compounds. It is assumed that it is oxygen that affects the course of intermediate reactions responsible for the destruction of the structure of organic molecules. Therefore, in this work, the effect of oxygen supply on the process rate and completeness of degradation of organic compounds was studied.

15.2 Experimental Part

15.2.1 Materials and Methods

The copper oxide-based catalyst was synthesized by a multistage technology [12].

The structure of the obtained $CoFe_2O_4/SiO_2/CuO$ composite particles was confirmed on the basis of FTIR spectra taken using a NICOLET 6700 spectrometer (Thermo Fisher Scientific) using the KBr technique (5% of the sample in KBr). Measurements were performed in the range of 400–4000 cm^{-1} with a resolution of 4 cm^{-1}. The surface morphology of the particles and elemental composition of the samples were determined using a scanning electron microscope REMMA 102–02 with an X-ray microanalyzer (EDX) system.

The study was carried out on a dairy wastewater imitation prepared from milk powder (GOST 10,970–87). 1 g of milk powder was added to a 100 mL volumetric flask, diluted with hot water (60 °C), mixed thoroughly, and after cooling, diluted to a COD content of approximately 100 mgO_2/dm^3.

The volume of milk wastewater in all experiments was the same and amounted to 50 mL. The weight of the catalyst was 0.139 g (in terms of CuO—$7.5 \bullet 10^{-4}$ mol). Hydrogen peroxide was introduced into the system in an amount equivalent to the amount of organic matter in the milk wastewater. The flow rate of air bubbled through the solution was 250–500 mL/min.

To conduct the study with the supply of oxygen to the reaction medium, a bubbling apparatus was used—a Schott filter, through which air was passed at a given capacity. The air supply through the glass filter solved two problems at once: the introduction of oxygen into the reaction zone, as well as the effective mixing of the reaction heterogeneous mixture. In addition, the purpose of supplying air to the system was to try to partially replace the oxidant – hydrogen peroxide – with air oxygen, which could lead to a reduction in the cost of the oxidation process.

The reaction mixture was analyzed before, after and during the process for organic pollutants by chemical oxygen demand (COD), O_2 content, redox potential (ORP) and pH.

15.2.2 Results and Discussion

Characterization of the Composite. The elemental analysis of the obtained particles confirmed the structure of the $CoFe_2O_4/SiO_2/CuO$ catalyst and the stoichiometry of its composition (Fig. 15.1, Table 15.1).

The presented SEM image of the $CoFe_2O_4/SiO_2/CuO$ catalyst (Fig. 15.2) shows the catalytic CuO centers located on the porous SiO_2 surface.

The analysis of the obtained peaks on the IR spectrum of the composite confirmed the presence of all the declared phases in the composite (Fig. 15.3). The broad absorption peak at 3384 cm^{-1} is caused by adsorbed water molecules, since nanostructured

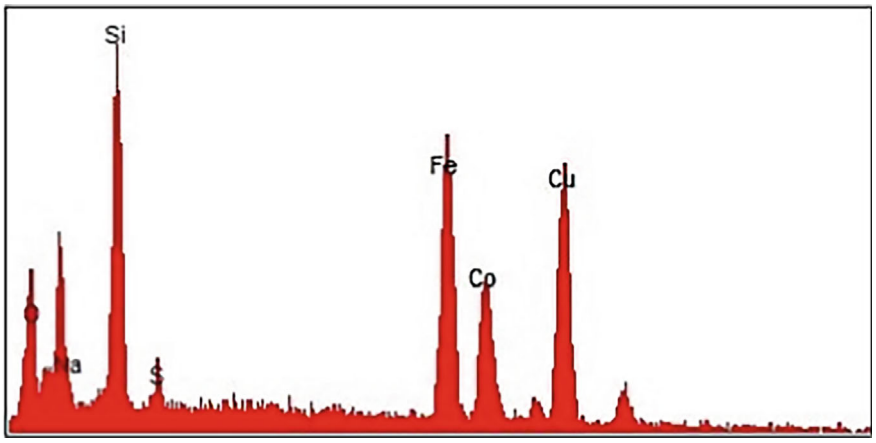

Fig. 15.1 EDX spectra of $CoFe_2O_4/SiO_2/CuO$ composite

Table 15.1 Quantitative determination of elements in the $CoFe_2O_4/SiO_2/CuO$ composite

Element	Sr	Intensity	Concentration	Percent element
O	*	0	0	51.42
Na_2O	K	1158	1.78	1.91
SiO_2	K	19,546	18.35	10.12
SO_3	K	1435	2.66	1.10
FeO	K	19,081	27.88	12.86
CoO	K	8054	12.47	5.52
Cu_2O	K	16,709	36.86	17.08
Summary			100	100

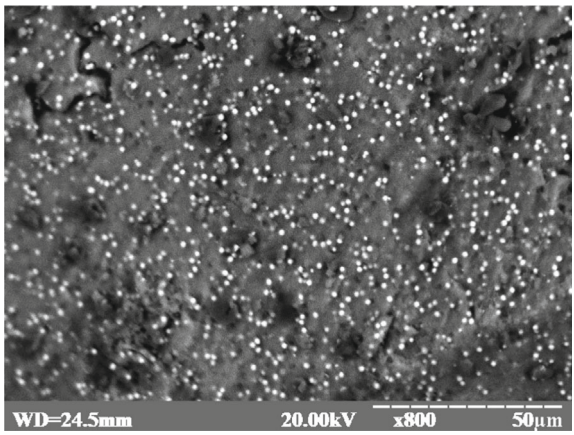

Fig. 15.2 FESEM image of $CoFe_2O_4/SiO_2/CuO$ particles

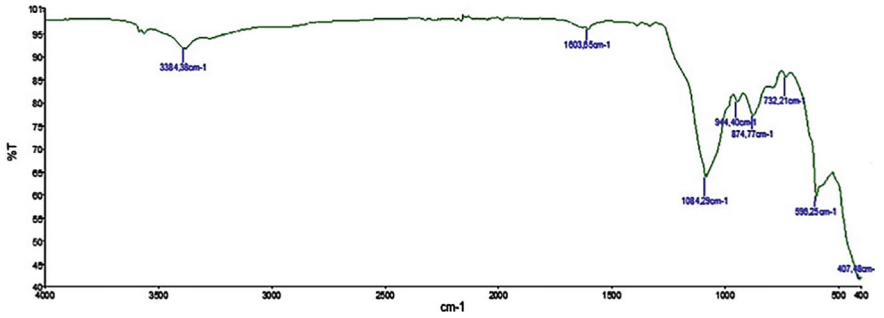

Fig. 15.3 FTIR spectra of $CoFe_2O_4/SiO_2/CuO$ catalyst

materials are characterized by a high surface-to-volume ratio, due to which they easily absorb moisture. The presence of the 1603 cm^{-1} band is due to the Cu–O valence vibrations [15]. The peak at 1084 cm^{-1} corresponds to the valence vibrations of Fe–O–Si, which confirms not only the presence of a SiO_2 layer in the composite but also the formation of a chemical bond between the core ($CoFe_2O_4$) and the protective layer of silicon oxide [16]. The bands at 944 cm^{-1} and 874 cm^{-1} can be attributed to the presence of silanol groups (Si–OH) and symmetrical O–Si–O bonding [17]. The infrared absorption peak at 596 cm^{-1} was attributed to the Cu–O valence vibration in CuO [18], and the peak at 410 cm^{-1} is due to the oscillation of metal oxide in the complex of octahedral Co(II)-O_2 groups and the complex of tetrahedral Fe(III)-O_2 groups of the cobalt ferrite phase [19].

The obtained results confirmed the structure of the catalyst, consisting of three layers: a magnetic core of $CoFe_2O_4$ spinel structure, a protective porous SiO_2 shell and monoclinic CuO catalytic centers located on it.

Investigation of the Oxidation Process of Organic Wastewater. The following systems were chosen to study the oxidation process of organic wastewater: «dairy wastewater : air oxygen : catalyst : hydrogen peroxide» (1), «dairy wastewater : air oxygen» (2), «dairy wastewater : air oxygen : hydrogen peroxide» (3), and «dairy wastewater : air oxygen : catalyst» (4). Such studies provide an understanding of the catalyst's action in the system and the selection of its optimal composition. The results obtained are shown in Figs. 15.4, 15.5 and in Table 15.3.

According to the given graphs (Fig. 15.4), the best results were obtained for the system «dairy wastewater : air oxygen : catalyst» (4). In 30 min, the system achieved a 92% removal rate, and the residual COD was 9.6 mgO_2/dm^3. The catalyst involving oxygen is effective.

The system «dairy wastewater : O_2 : $CoFe_2O_4/SiO_2/CuO$: H_2O_2» (1) also showed a positive result. However, the extreme nature of the COD curve is clearly visible in the system under study (Fig. 15.4, curve 1). After the addition of hydrogen peroxide to the system, an increase in the COD value is observed, which reaches its maximum at 60 min of the process, after which it decreases by 63% (Fig. 15.4, curve 1, Table 15.2).

This anomaly can be explained by the fact that during the COD analysis, the reagent (potassium dichromate) is consumed not only for the oxidation of organic

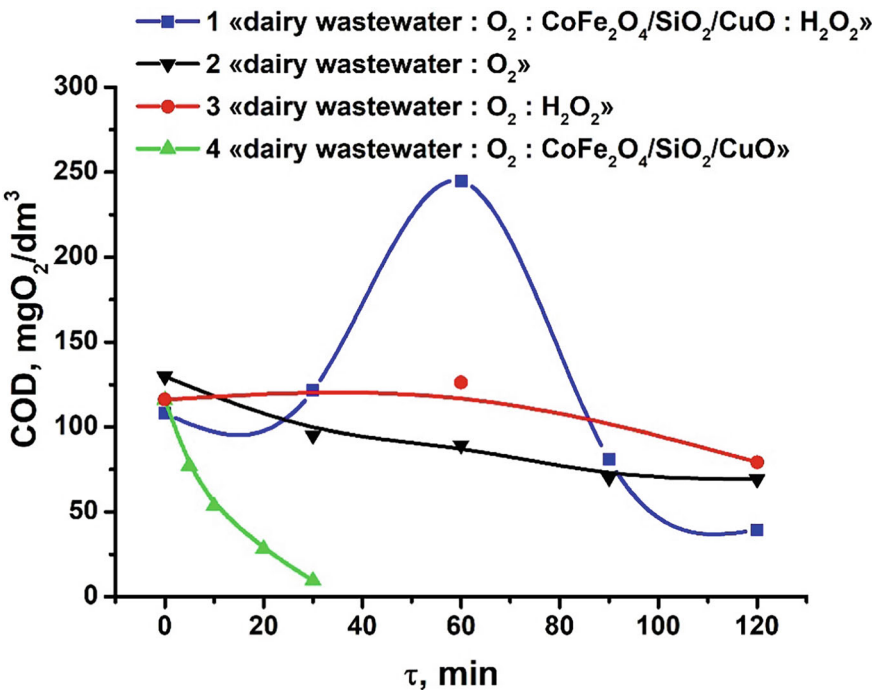

Fig. 15.4 Kinetics of COD change in systems 1, 2, 3, 4

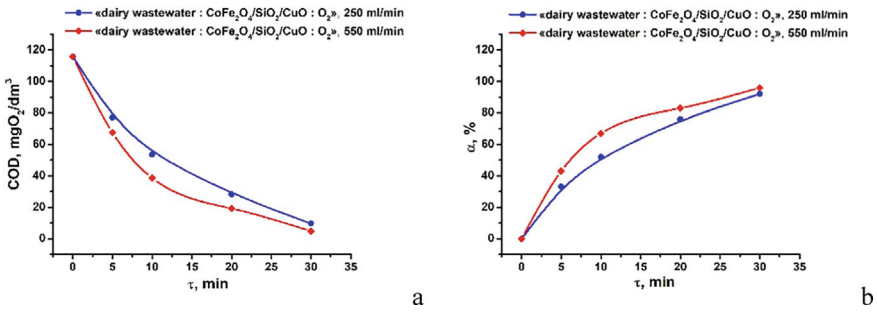

Fig. 15.5 Influence of air flow rate on the change in COD (a) and oxidation rate (b) over time for the system «dairy wastewater : $CoFe_2O_4/SiO_2/CuO : O_2$»

compounds in solution, but also for the oxidation of hydrogen peroxide introduced into the system by reaction:

$$4\,H_2O_2 + K_2Cr_2O_7 + 3\,H_2SO_4 \rightarrow Cr_2(SO_4)_2 + K_2SO_4 + 4\,O_2 + 7\,H_2O \quad (15.1)$$

Table 15.2 Comparative analysis of the results of the systems «dairy wastewater : air oxygen : catalyst : hydrogen peroxide» (1) and «dairy wastewater : air oxygen : catalyst» (4)

The system «dairy wastewater : O_2 : $CoFe_2O_4/SiO_2/CuO$» (4)					The system «dairy wastewater : O_2 : $CoFe_2O_4/SiO_2/CuO$: H_2O_2» (1)				
τ, min	ORP, mV	O_2, %	pH	α, %	τ, min	ORP, mV	O_2, %	pH	α, %
0	368	56.6	6.15	0	0	300	54.7	7.30	0
5	398	65.3	–	33	30	389	65.4	–	−12
10	400	69.8	–	52	60	349	69.8	–	−126
20	398	69.3	–	76	90	368	69.5	–	25
30	407	75.1	3.12	92	120	388	75.1	3.85	63

Table 15.3 Comparative analysis of the results of the systems «dairy wastewater : air oxygen» (2) and «dairy wastewater : air oxygen : hydrogen peroxide» (3)

The system «dairy wastewater : O_2» (2)						The system «dairy wastewater : O_2 : H_2O_2» (3)					
τ, min	ORP, mV	O_2, %	pH	$C_{H_2O_2}$, g/dm^3	α, %	τ, min	ORP, mV	O_2, %	pH	$C_{H_2O_2}$, g/dm^3	α, %
0	289	58.0	5.43	–	0	0	338	54.7	5.80	12.73	0
30	498	62.0	–		26.6	30	432	65.4	–	–	
60	500	65.4	–	–	31.2	60	499	69.8	–	8.50	−6
90	523	61.7	–		45.9	90	450	69.3	–	–	
120	568	58.2	2.85	–	46.3	120	484	75.1	3.30	4.25	33

The conducted analysis of the system for H_2O_2 content using the iodometric method showed that 30 min after the introduction of hydrogen peroxide, an increase in its concentration was observed, which remained practically unchanged until the end of the process. This may indicate the appearance of an additional amount of peroxide compounds that should compensate for the consumption of H_2O_2 for the oxidation of organic components.

As can be seen from the results (Table 15.2), systems (1) and (4), according to the change in the time of ORP, go into an oxidative state, both of them show acidification in the oxidation process, i.e., the pH of the medium decreases, but system (4) without the addition of hydrogen peroxide is more efficient. Probably, the introduction of H_2O_2, which can be a reducing agent, into the system help to slows down the course of the main oxidation reactions of organic compounds.

The effect of air oxygen and H_2O_2 on the oxidation process was studied in the systems «dairy wastewater : air oxygen» (2) and «dairy wastewater : air oxygen : hydrogen peroxide» (3).

As shown by the results for the system «dairy wastewater : air oxygen» (2) (Fig. 15.4, curve 2), when oxygen is supplied to the reaction medium, the oxidation of the organic component of milk is observed to be 27% within 30 min, and

46.3% within 2 h. This result can be explained primarily by the effective supply of active oxidant (O_2) and its contact with the reducing medium due to the successful design of the apparatus.

The increase in the value of the redox potential confirms the oxidation process (Table 15.3). The decrease in COD of the system during the process is almost linear, while the formation of peroxide compounds is not observed.

In the system «dairy wastewater : air oxygen : H_2O_2» (3), according to the results obtained, the COD change graph has an unexpressed extreme dependence (Fig. 15.4, curve 3), while the amount of hydrogen peroxide in the reaction medium decreases over time (Table 15.3). The increase in COD value with a decrease in the H_2O_2 concentration indicates the formation of new compounds in the system, probably of the peroxide type, the presence of which may affect the analysis result. In the further course of the process, COD naturally decreases as a result of oxidation of the organic component, but the degree of conversion after 120 min is only 33.4%, which is significantly lower than the process with oxygen itself (Table 15.3). When comparing the value of the ORP, it can be seen that system (3) has a lower oxidizing capacity than system (4) without the addition of peroxide.

Thus, the most productive system is «dairy wastewater : air oxygen : catalyst» (4), which can be explained by the efficiency of the catalyst for the production of active particles with the participation of air oxygen. Iodometric analysis confirmed the presence of active intermediate peroxide compounds on the surface of the $CoFe_2O_4/SiO_2$/CuO catalyst. Their maximum amount of 0.128 g/dm^3 was observed after 20 min from the beginning of the process and then it slowly decreased to 0.102 g/dm^3, probably due to the costs of the process of oxidation of organic pollutants (Table 15.2). The concentration of the detected peroxide compounds is insignificant, but it is sufficient for the process of oxidation of organic compounds until their complete destruction.

As defined by the authors [20], the action of a peroxide radical on an organic compound can be described by the equation

$$^{\cdot}OH + RH \rightarrow R^{\cdot} + H_2O. \tag{15.2}$$

In the presence of oxygen in the reaction medium, the organic radical is removed [20]

$$R^{\cdot} + O_2 \rightarrow ROO^{\cdot}, \tag{15.3}$$

with the formation of a peroxo-organic radical, which itself can initiate the following reactions [20, 21]

$$ROO^{\cdot} + RH \rightarrow ROOH + R^{\cdot} \tag{15.4}$$

$$ROO^{\cdot} + H_2O \rightarrow ROH + HOO^{\cdot} \tag{15.5}$$

$$HOO^{\cdot} + H_2O_2 \rightarrow OH^{\cdot} + H_2O + O_2. \tag{15.6}$$

This confirms the assumption that the oxidation of organic substances in this system occurs during interacting with peroxide compounds, the appearance of which can be associated with processes occurring on the catalyst surface under the influence of oxygen. At the same time, the presence of hydrogen peroxide in the reaction medium can inhibit the course of reaction (15.5), which slows down the oxidation process (system (3)).

The high degree of conversion and the rate of the process for system (4) (92% in 30 min) significantly exceed the indicators for other systems, and the nature of the change in the degree of purification over time indicates the high activity and efficiency of the copper-containing catalyst at such low concentrations of active peroxide compounds produced.

To test the role of the catalyst in the formation of peroxide compounds, an experiment was conducted without organic compounds in the system «H_2O(dist): O_2: $CoFe_2O_4/SiO_2/CuO$» with the same component consumption. The results obtained showed that the concentration of peroxide compounds ($C_{H_2O_2}$) after 10 min of the process reaches 0.113 g/dm^3, which corresponds to their amount for system (4). Thus, it can be assumed that hydrogen peroxide or other peroxide-type compounds appear in the system in the presence of the $CoFe_2O_4/SiO_2/CuO$ catalyst, water and air oxygen, and their amount is quite sufficient for the effective flow of the catalytic process of oxidation of organic pollutants.

As the results showed, the presence of oxygen in the reaction medium affects the mechanism of the oxidation process, so a study was conducted to determine the dependence of the completeness of the conversion on the amount of oxygen in the system. The parameters of the experiment are identical to the previous ones. Only the air flow rate was a variable factor: 250 mL/min and 550 mL/min. The results (Fig. 15.5) show that a twofold increase in the amount of oxygen in the reaction medium leads to a slight acceleration of the oxidation process (the degree of conversion increases from 92 to 96% after 30 min, and COD decreases from 9.648 to 4.824 mgO_2/dm^3).

Based on the results obtained, it can be concluded that for the effective treatment of dairy wastewater, it is optimal to use the system «dairy wastewater : air oxygen : $CoFe_2O_4/SiO_2/CuO$». The additional introduction of H_2O_2 into the reactor leads to a slowdown in the destruction of organic pollutants, probably due to a shift in the equilibrium of oxidation processes towards the initial reagents.

In addition, the system «dairy wastewater : air oxygen : $CoFe_2O_4/SiO_2/CuO$» is more cost-effective because it does not require additional hydrogen peroxide, which significantly affects the cost of the treatment process, making it available for industrial use.

15.3 Conclusions

It has been determined that the use of the synthesized heterogeneous nanostructured magnetically separable $CoFe_2O_4/SiO_2/CuO$ catalyst in the Fenton system for the fine treatment of dairy wastewater is effective. The high value of the degree of oxidation of organic pollutants (up to 96%), as well as the easy removal of the catalyst from the reaction medium, suggests the possibility of returning wastewater to production, which makes it advisable to use this catalyst for the fine treatment of dairy wastewater. It has been established that when air oxygen is supplied to the reaction medium, the formation of organoperoxide compounds occurs on the catalyst, which are responsible for the complete oxidation of organic pollutants. It has been determined that the system «dairy wastewater : air oxygen : $CoFe_2O_4/SiO_2/CuO$», which is cost-effective and environmentally friendly.

Disclosure of Interests The authors have no competing interests to declare that are relevant to the content of this article.

References

1. V. Andronov, Ye. Makarov, Yu. Danchenko, T. Obizhenko, Research of the regularities of forming and chemical composition of sewage water of a dairy processing company. Tech. Ecol. Safety **7**(1), 13–21 (2020). https://doi.org/10.5281/zenodo.3780011
2. A. Slavov, General characteristics and treatment possibilities of dairy wastewater—a review. Food Technol. Biotech. **55**(1), 14–28 (2017). https://doi.org/10.17113/ftb.55.01.17.4520
3. S. Sinha, A. Srivastava, T. Mehrotra, R. Singh, A review on the dairy industry waste water characteristics, its impact on environment and treatment possibilities, in *Emerging Issues in Ecology and Environmental Science. Springer Briefs in Environmental Science.* (Springer, Cham, 2019), pp. 73–84. https://doi.org/10.1007/978-3-319-99398-0_6
4. O. Kurylets, A. Helesh, V. Vasiichuk, Z. Znak, A. Romaniv, Coagulation treatment of effluent from milk-processing enterprises with waste $FeSO_4$. Eastern-Eur. J. Enterprise Technol. **1**(10(115)), 17–23 (2022). https://doi.org/10.15587/1729-4061.2022.252309
5. A. Srivastava, S. Rana, T. Mehrortra, R. Singh, Characterization and immobilization of bacterial consortium for its application in degradation of dairy effluent. J. Pure Appl. Microbiol. **10**(3), 2199–2208 (2016)
6. S. Martín-Rilo, R. Coimbra, J. Martín-Villacorta, M. Otero, Treatment of dairy industry wastewater by oxygen injection: performance and outplay parameters from full scale implementation. J. Clean. Prod. **86**, 15–23 (2015). https://doi.org/10.1016/j.jclepro.2014.08.026
7. W. Li, V. Nanaboina, Q. Zhou, G. Korshin, Effects of Fenton treatment on the properties of effluent organic matter and their relationships with the degradation of pharmaceuticals and personal care products. Water Res. **46**(2), 403–412 (2012). https://doi.org/10.1016/j.watres.2011.11.002
8. N. Thomas, D. Dionysiou, S. Pillai, Heterogeneous Fenton catalysts: a review of recent advances. J. Hazardous Mater. **404**(Part B), 124082 (2021). https://doi.org/10.1016/j.jhazmat.2020.124082
9. J. Li, A. Pham, R. Dai, Z. Wang, T. Waite, Recent advances in Cu-Fenton systems for the treatment of industrial wastewaters: role of Cu complexes and Cu composites. J. Hazard. Mater. **392**, 122261 (2020). https://doi.org/10.1016/j.jhazmat.2020.122261

10. Y. Deng, R. Zhao, Advanced oxidation processes (AOPs) in wastewater treatment. Current Pollut. Rep. **1**(3), 167–176 (2015). https://doi.org/10.1007/s40726-015-0015-z
11. A. Hyvlyud, Monitoring of wastewater pollution of dairy processing enterprises. Bulletin of the National University of Lviv Polytechnic. Chem., Technol. Substances Appl. **787**, 301–305 (2014). (in Ukrainian)
12. O. Makido, G. Khovanets', V. Kochubei, I. Yevchuk, Nanostructured magnetically sensitive catalysts for the Fenton system: obtaining, research, application. Chem. Chem. Technol. **16**(2), 227–236 (2022). https://doi.org/10.23939/chcht16.02.227
13. O. Makido, Yu. Medvedevskikh, G. Khovanets', Investigation into the adsorption of methylene blue on the surface of a «core-shell» type catalyst for the Fenton system. Voprosy Khimii i Khimicheskoi Tekhnologii **6**, 91–98 (2020). https://doi.org/10.32434/0321-4095-2020-133-6-91-98 (in Ukrainian)
14. N. Zhao et al., The role of dissolved oxygen in Fenton system, in *The 4th International Conference on Water Resource and Environment (WRE 2018), IOP Conference Series: Earth and Environmental Science*, **191**, 012084–102091. IOP Publishing Ltd, Kaohsiung City, Taiwan (2018). https://doi.org/10.1088/1755-1315/191/1/012084
15. M. Sunjuk et al., Adsorption of cationic and anionic organic dyes on SiO_2/CuO composite. Desalin. Water Treat. **169**, 383–394 (2019). https://doi.org/10.5004/dwt.2019.24706
16. S. Alterary, A. AlKhamees, Synthesis, surface modification, and characterization of Fe_3O_4@SiO_2 core@shell nanostructure. Green Proc. Synthesis **10**(1), 384–391 (2021). https://doi.org/10.1515/gps-2021-0031
17. P. Arévalo-Cid, J. Isasi, F. Martín-Hernández, Comparative study of core-shell nanostructures based on amino-functionalized Fe_3O_4@SiO_2 and $CoFe_2O_4$@SiO_2 nanocomposites. J. Alloy. Compd. **766**, 609–618 (2018). https://doi.org/10.1016/j.jallcom.2018.06.246
18. H. Li et al., Regulation of Cu species in CuO/SiO_2 and its structural evolution in ethynylation reaction. Nanomaterials **9**(6), 842–858 (2019). https://doi.org/10.3390/nano9060842
19. M. Habibi, H. Parhizkar, FTIR and UV-vis diffuse reflectance spectroscopy studies of the wet chemical (WC) route synthesized nanostructure $CoFe_2O_4$ from $CoCl_2$ and $FeCl_3$. Spectrochim. Acta Part A Mol. Biomol. Spectrosc. **127**, 102–106 (2014). https://doi.org/10.1016/j.saa.2014.02.090
20. I. Siés, E. Brillas, M. Oturan, M. Rodrigo, M. Panizza, Electrochemical advanced oxidation processes: today and tomorrow. A review. Environ. Sci. Pollut. Res. **21**(14), 8336–8367 (2014). https://doi.org/10.1007/s11356-014-2783-1
21. B. Utset, J. Garcia, J. Casado, X. Domenech, J. Peral, Replacement of H_2O_2 by O_2 in Fenton and photo-Fenton reactions. Chemosphere **41**(8), 1187–1192 (2000). https://doi.org/10.1016/s0045-6535(00)00011-4

Chapter 16
Effect of Additional Carbonization During the Synthesis on the Structure of the Obtained Carbon Material

O. Pertko, Yu. Voloshyna, Ye. Sheludko, and V. Povazhnyi

Abstract In this work, the influence of the synthesis method on the properties of the external surface of the carbon nanomaterial was studied. Namely, it was determined the structure of carbon nanomaterial produced by template synthesis and according to an improved method (with an additional post-carbonization stage). The synthesized samples were studied by X-ray diffraction, Raman spectroscopy, Fourier transform infrared spectroscopy, Atomic force microscopy and Scanning electron microscopy methods. It was shown that the additional carbonization stage contributes to the development of carbon nanomaterial external surface. And also contributes to the addition of disordered structures along with some increase in crystallite size of such material.

16.1 Introduction

Synthetic carbon nanomaterials (SCNMs) are widely studied as sorbents [1–5] and catalysts/carriers [6–11] in many industrially important processes. SNCMs are attractive and competitive materials despite the complexity and high cost of synthesis. Using template synthesis and by varying a template, a wide range of carbonaceous materials can be obtained: micro-, meso-, macroporous, and hierarchically ordered, as well as materials with a disordered porous structure. This is important because SCNMs should have a well-developed specific surface area for placing adsorption/catalytically active centers on it. If there are large adsorbate/reagent molecules in the reaction mixture, the active centers located inside small pores will be inaccessible to them. In this case, interaction will take place only on the open external surface. Therefore, surface development is an urgent task today. It is equally important to obtain SCNMs with a well-ordered crystal structure, as this is the key to their strength and thermal stability, which will affect the duration of their use. In previous

O. Pertko (✉) · Yu. Voloshyna · Ye. Sheludko · V. Povazhnyi
V.P. Kukhar Institute of Bioorganic Chemistry and Petrochemistry of the National Academy of Sciences of Ukraine, Kyiv, Ukraine
e-mail: o.pertko@gmail.com

O. Fesenko and L. Yatsenko (eds.), *Functional Nanomaterials, Nanocatalysts, Nanotechnologies, and Their Applications*, Springer Proceedings in Physics 321,
https://doi.org/10.1007/978-3-031-99136-3_16

work, it was shown that additional post-carbonization has a positive effect on the thermal stability of SCNMs produced by the template synthesis method [12]. It was also shown that such modification of SCNMs reduces the number of micropores that are often inaccessible to adsorbate/reagent molecules. The aim of the work was to determine the structure of SCNM produced by template synthesis and according to an improved method (with an additional post-carbonization stage—acSCNM) as well as the influence of the synthesis method on the properties of the external surface of SCNMs.

16.2 Experimental

16.2.1 Sample Preparation

SCNMs were synthesized by the hard template synthesis method, the details of which were described in a previous work [12]. A schematic representation of the synthesis procedures is shown in Fig. 16.1.

Silica gel ("Silica gel 60" Fluka, cat. no. 60752, 230–400 mesh ASTM 0.04–0.063 mm) was used as the template, which was previously calcined in a corundum crucible in air for 5 h at a temperature of 773 K (the bulk density and the specific surface area after calcination were 0.51 g/cm^3 and 360 m^2/g, respectively).

16.2.2 Sample Characterization

X-ray diffraction (XRD). The phase composition of the samples was determined by X-ray diffraction (MiniFlex600 diffractometer Rigaku) in CuKα-radiation (λ = 0.154178 nm, the step of 0.05 degrees and a rotation speed of 1 degree/min, the accelerating voltage was 40 kV, the anode current was 15 mA). Powdered samples were scanned from 3 to 70° in 2-theta range.

The peak position, integrated intensity (S) and full width at half maximum ($^{1/2}$ h) were calculated from XRD spectrum (Table 16.1). The ratio of aromatic carbon to total carbon ($R^{ar/tot}$) was calculated by the Eq. (16.1) [13]:

$$R^{ar/tot} = S^{(002)}/(S^{(002)} + S^{\gamma}) \tag{16.1}$$

The average lateral crystallites size (L_a), which shows the in-plane dimension of crystalline carbon, and the staking height of crystallite (L_c) were calculated by Debye–Scherrer Eqs. (16.2) and (16.3). The carbon stacking layer spacing (d_{002}) was calculated by Braggs Eq. (16.4):

$$L_a = 1.84\lambda/^{1/2}h^{(002)} \times \cos\theta^{(002)} \tag{16.2}$$

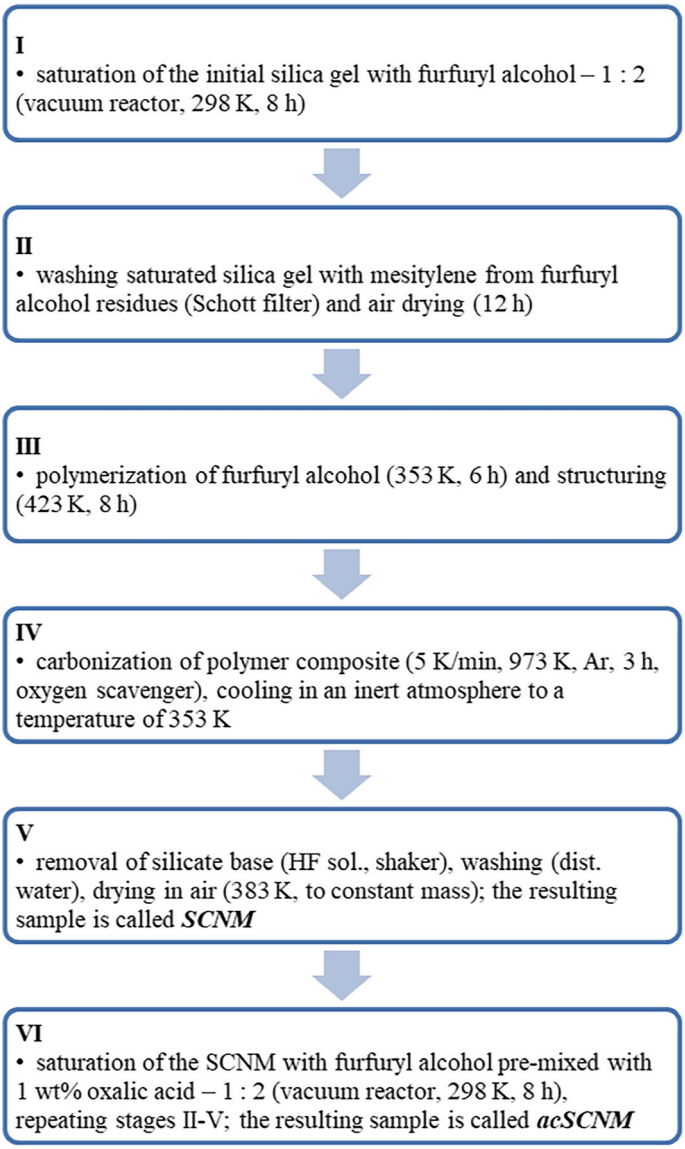

Fig. 16.1 Template synthesis scheme of samples

$$L_c = 0.89\lambda/^{1/2}h^{(100)} \times \cos\theta^{(100)} \tag{16.3}$$

$$d_{002} = \lambda/2 \times \sin\theta^{(002)} \tag{16.4}$$

OriginPro8.5.1 software was used for deconvolution of the diffractograms and Raman spectra (Gaussian function).

Fourier transform infrared (FTIR) spectroscopy (IRAffiniti-1 s, Shimadzu) was used to investigate the functional groups on the surface of the samples. The samples and KBr were pre-ground in an agate mortar and dried (383 K, during the night). Then they were mixed in a ratio of samples: KBr = 1: 800 and tableted using a press mold with vacuuming (10 tones).

Raman spectroscopy. Horiba LabRam HR800 Raman spectrometer equipped with a 100x lens (laser beam - 514.5 nm exciting line of a Ar-laser) have been successfully used to study the molecular structure of samples (the laser power was 1 mW, the average acquisition time for each spectrum was 45 s).

Atomic force microscopy (AFM). The surface morphology of the samples was evaluated using an AFM (NT-206 "Microtest machines") with a standard CSC37 probe and a cantilever stiffness of 0.3–0.6 N/m. Scanning was carried out in static contact mode at a speed of 10 μm/s and a step of 0.3 nm. Sample preparation was as follows: 4 mg of sample was ground in an agate mortar for 5 min and suspended in 5 ml of ethyl alcohol for 15 min, then 0.25 ml of the suspension was applied to a glass and dried at 50 °C to constant weight. The surface morphology of the samples was evaluated also using a **scanning electron microscope—SEM** (Phenom Pure—Thermo Scientific) with a secondary electron detector/backscatter electron detector (5 kV).

16.3 Results and Discussion

The diffractograms of the samples (Fig. 16.2) show two obvious peaks, bands 002 and 100, and the corresponding diffraction angles are around 26° and 47°, respectively. The former band is located in the neighborhood of the graphite band (002). The 002 band indicates the spacing of aromatic ring layers and corresponds to the microcrystals in the polycondensed aromatic rings [14]. On the left side of the 002 peak is the γ band (around 20°), which is caused by aliphatic hydrocarbon branch chains, various functional groups and alicyclic hydrocarbons connected to the condensed aromatic rings or attached to the edge of coal crystallites [15]. The γ band indicates the packing distance of saturated structures [14]. The area of the 002 and γ peaks indicates the number of aromatic carbon atoms and aliphatic carbon atoms, respectively.

The reduced $R^{ar/tot}$ value for the acSCNM sample shows that during the additional carbonization stage, the amount of aromatic carbon is reduced, i.e., disordered structures are added. Also, for sample acSCNM, a slight increase in the values of the average lateral crystallites sizes (L_a) and the carbon stacking layer spacing (d_{002}) by approximately 2.5% and a decrease in the stacking height of crystallite (L_c) by 10% compared to sample SCNM are observed.

Raman spectra of carbon materials are commonly divided into two regions—first- and second-order (600–2200 and 2000–3600 cm^{-1}, respectively). Graphite with perfect structure has only one band (G band) in the first-order region (Table 16.2). It

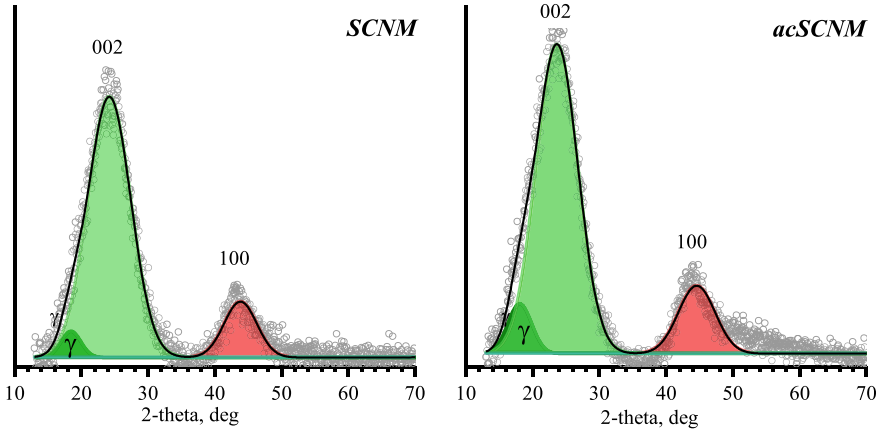

Fig. 16.2 The diffractograms of the samples

Table 16.1 XRD structural parameters of the samples

Sample	Peak position 2θ, deg			S, a.u		$R^{ar/tot}$	$^{1/2}$ h, a.u		d_{002}, nm	L_c, nm	L_a, nm
	γ	002	100	γ	002		002	100			
SCNM	18.5	24.2	43.2	166	3559	0.96	7.6	5.8	0.37	0.038	0.025
acSCNM	18.0	23.6	43.8	380	4108	0.92	7.4	6.5	0.38	0.039	0.023

corresponds to the stretching vibration mode in the aromatic layers of the graphite. For materials with disordered carbon, additional bands appear in the first-order region (D4, D1, D3 and D2 bands). They are induced by the defects in the microcrystalline lattices of carbon [16]. And in second-order range, all bands refer to overtone and combination of bands present in the first-order spectrum [17, 18].

The first-order spectra of the samples exhibit two broad and overlapping peaks corresponding to the D1 and G bands (Fig. 16.3). The ratio of the intensities of the D1 and G bands for both samples differs insignificantly. This means that the additional carbonization stage does not affect the crystallinity of the samples significantly. Substructures in the D bands (broad D4, D2 bands and less visible D3 band) are also observed. The intensities of D3 and D4 bands decrease after additional carbonization stage, while the D2 band increases. That is, there is a certain increase in both amorphous carbon structures and aromatics like graphene layers (Table 16.2). The additional carbonization stage also contributes to an increase in the width of the bands in the second-order region. The latter also indicates an increase in the number of disordered structures [18] in the acSCNM sample. It is also confirmed by the intensification of the bands of aliphatic groups in the IR spectrum of the acSCNM sample compared to SCNM (Fig. 16.4, Table 16.3).

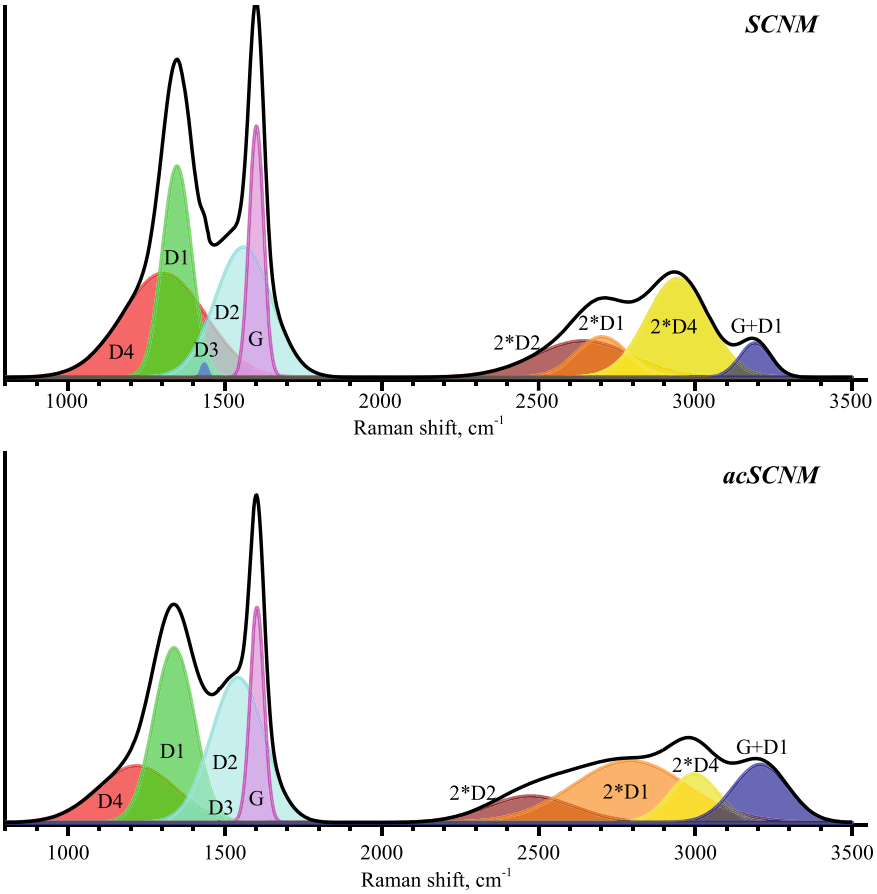

Fig. 16.3 Peaks derived by curve-fitting the curves of Raman spectra

Topographic characteristics of SCNMs can be estimated by AFM and SEM images (Fig. 16.5).

Analysis of AFM images of the samples (Fig. 16.5c, d) showed that both samples have nanoscale needle-like formations on the surface with a 2–9 and 2–12 nm height for SCNM and acSCNM, respectively, and trunk width at the base up to 0.4 μm. AFM images show the creation of a large number of new needle-like formations on the surface of the acSCNM, which were formed after an additional carbonization step during synthesis (Fig. 16.5a, b). The development of the acSCNM surface is also visible in SEM images (Fig. 16.5e, f).

Table 16.2 Assignment of the first-order Raman spectrum bands [18, 19]

Band position, cm^{-1}	Band name	Vibration mode and functional group	Bond type
1587–1599	G	Stretching vibration mode with E_{2g} symmetry in the aromatic layers of the graphite crystalline; double bond of alkenes	sp^2
1330–1368	D1	Graphitic lattice vibration mode with A_{1g} symmetry (in-plane imperfections, e.g., defects and heteroatoms); C–C between aromatic rings and aromatics with not less than 6 rings	sp^2
1540–1620	D2	Lattice vibration analogous to E_{2g} symmetry of the G band but involving graphene layers; amorphous carbon structures; aromatics with 3–5 rings	sp^2
1230, 1475–1538	D3	Amorphous sp^2-bonded carbon forms; aryl–alkyl ether; para-aromatics	sp^2, sp^3
1185–1250	D4	$C^{aromatic}$–C^{alkyl} at the periphery of crystallites and C=C stretching vibrations of polyene-like structures; aromatic /aliphatic ethers; C–C and C-H on hydroaromatic rings; hexagonal diamond carbon sp^3	sp^2, sp^3

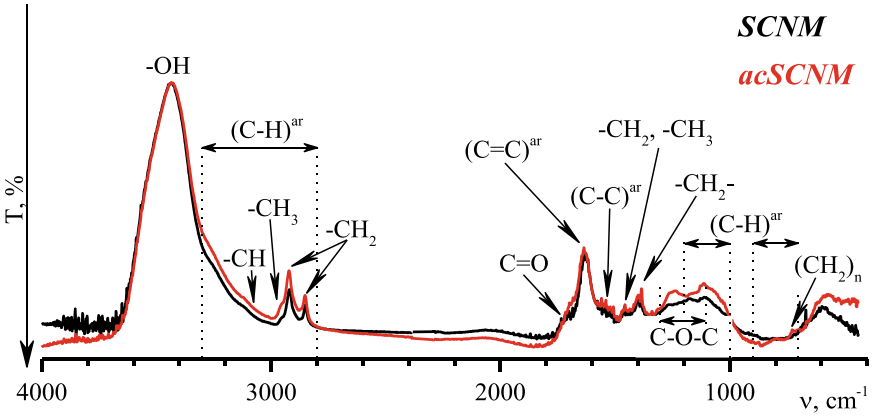

Fig. 16.4 The FTIR spectra of samples

16.4 Conclusions

It was determined the structure of SCNM produced by template synthesis and acSCNM produced according to an improved method with an additional post-carbonization stage, as well as the influence of the synthesis method on the properties of the external surface of SCNMs.

It has been established that the additional carbonization stage contributes to an addition of disordered structures and building-up of aromatic carbon crystallites in

Table 16.3 Band assignments for the FTIR spectra

Band position, cm^{-1}	Functional group	Type of vibration	References
3419−3359	− OH	Stretching vibration	[20, 21]
3080−3035	C−H aromatic nucleus	Stretching vibration	[20]
2975−2955	$-CH_3$ aliphatic	Asymmetric stretching vibration	[20]
2925−2919	$-CH_2$ aliphatic	Asymmetric stretching vibration	[20]
2848	$-CH_2$ aliphatic	Symmetric stretching vibration	[20]
2800−3300	C−H aromatic structure	Stretching vibration	[22]
1745−1730	C=O aliphatic (acid, ketone, aldehyde, lactone)	Stretching vibration	[20, 21]
1615−1585	C=C aromatic nucleus	Stretching vibration	[20, 22]
1500−1450	C−C aromatic nucleus	Stretching vibration	[20, 22]
1460−1450	$-CH_3$, $-CH_2$ aliphatic chains	Asymmetric deformation vibration	[20]
1380	$-CH_2-$	Symmetric deformation (bending)	[20]
1300−1000	C−O−C	Phenolic deformation (stretching)	[20]
730−720	$(CH_2)_n$, n > 4 alkanes side rings		[20]
700−900 1000−1200	C−H aromatic structure	Bending out of plane	[20]

SCNMs. Also, it was shown that the additional carbonization stage contributes to the development of SCNM's external surface. This indicates the expediency of using an additional carbonization stage in the synthesis of SCNMs to develop their external surface. It will be useful for complex use of SCNMs as a sorbents and catalysts/carriers.

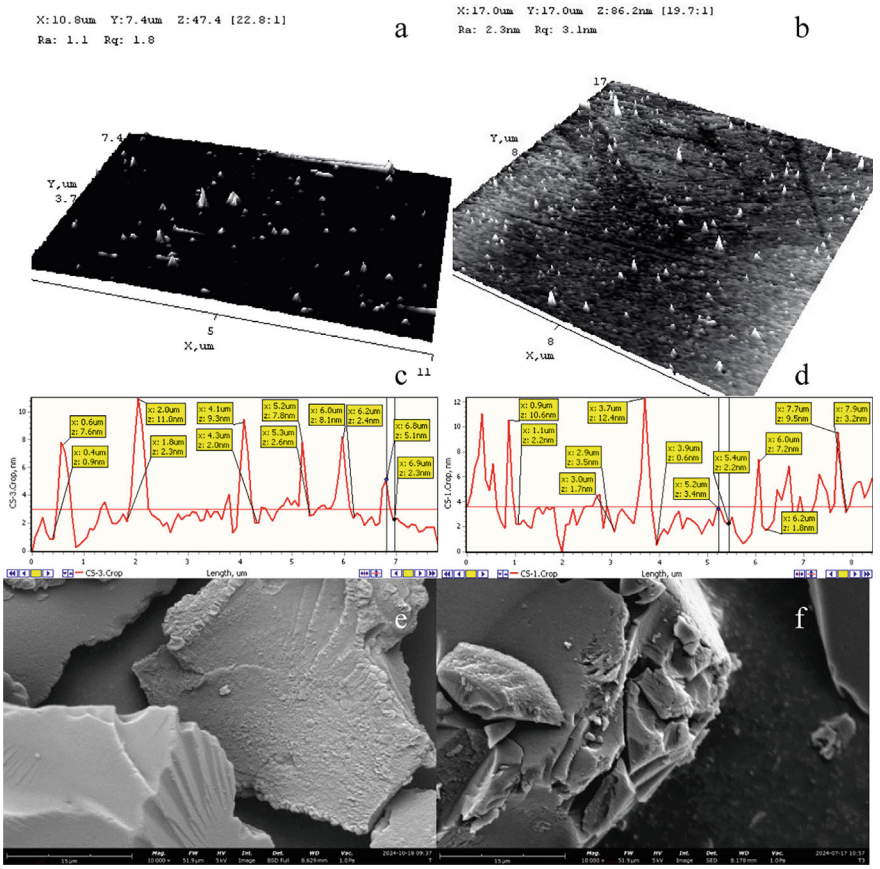

Fig. 16.5 AFM images with 3D surface height variations (**a**, **b**) and section analysis (**c**, **d**), and SEM images of the SCNM (**a**, **c**, **e**) and acSCNM (**b**, **d**, **f**)

Acknowledgements The authors express their gratitude to Ph.D. D.S. Kamenskih (V.P. Kukhar Institute of Bioorganic Chemistry and Petrochemistry of the NAS of Ukraine) for help in recording the XRD spectra of the samples, to prof. dr hab. inż. Ju. Mrowiec-Białoń, dr inż. K. Maresz and dr inż. A. Ciemięga (Institute of Chemical Engineering, Polish Academy of Sciences PAN) for help in recording the SEM foto of the sample, and also to the program «STUDY VISIT AT PAN» for Ukrainian scientists.

Disclosure of Interests The authors have no competing interests to declare that are relevant to the content of this article.

References

1. A. Azzouz, S.K. Kailasa, S.S. Lee, A.J. Rascón, E. Ballesteros, M. Zhang, K.-H. Kim, Review of nanomaterials as sorbents in solid-phase extraction for environmental samples. TrAC, Trends Anal. Chem. **108**, 347–369 (2018)
2. B. Gao, Q. Chang, J. Cai, Z. Xi, A. Li, H. Yang, Removal of fluoroquinolone antibiotics using actinia-shaped lignin-based adsorbents: role of the length and distribution of branched-chains. J. Hazard. Mater. **403**, 123603 (2021)
3. E. Santoso, R. Ediati, Y. Kusumawati, H. Bahruji, D.O. Sulistiono, D. Prasetyoko, Review on recent advances of carbon based adsorbent for methylene blue removal from waste water. Mater. Today Chem. **16**, 100233 (2020)
4. H. Sun, F.S. Cannon, X. He, Enhanced trifluoroacetate removal from groundwater by quaternary nitrogen-grafted granular activated carbon. Sci. Total. Environ. **660**, 577–585 (2019)
5. Y. Wang, Y. Zhang, S. Li, W. Zhong, W. Wei, Enhanced methylene blue adsorption onto activated reed-derived biochar by tannic acid. J. Mol. Liq. **268**, 658–666 (2018)
6. D. Xia, H. Yu, H. Li, P. Huang, Q. Li, Y. Wang, Carbon-based and carbon-supported nanomaterials for the catalytic conversion of biomass: a review. Environ. Chem. Lett. **20**, 1719–1744 (2022)
7. B. Louis, D. Bégin, M.-J. Ledoux, C. Pham-Huu, Advances in the use of carbon nanomaterials in catalysis, in *Ordered Porous Solids. Recent Advances and Prospects*, ed. by V, Valtchev, S. Mintova, M. Tsapatsis (Elsevier, 2009), pp. 621–649
8. R. Schlögl, Carbon in catalysis, in *Advances in Catalysis*, vol. 56, ed. by B.C. Gates, C. Jentoft (Academic Press, 2013), pp. 103–185
9. E. Pérez-Mayoral, V. Calvino-Casilda, E. Soriano, Metal-supported carbon-based materials: opportunities and challenges in the synthesis of valuable products. Catal. Sci. Technol. **6**, 1265–1291 (2016)
10. AG. Dyachenko, O.V. Ischenko, O.V. Prygunova, V.E. Diyuk, G.G. Tsapyuk, S.V. Gaidai, A.V. Yatsymyrskyi, T.M. Zakharova, E.O. Kostyrko, Ni–Fe, Co–Fe, and Co–Ni nanocomposites based on carbon nanotubes in the reaction of CO_2 methanation. Mol. Cryst. Liq. Cryst. **720**, 38–46 (2021)
11. P. Serp, M. Corrias, P. Kalck, Carbon nanotubes and nanofibers in catalysis. Appl. Catal. A **253**, 337–358 (2003)
12. V.A. Povazhnyi, Yu.G. Voloshyna, O.P. Pertko, O.V. Melnychuk, A.L. Kontsevoi, Enhancing the thermal stability of nanostructured carbonaceous materials using an improved method of template synthesis. Appl. Nanosci. **13**, 7491–7499 (2023)
13. T.F. Yen, J.G. Erdman, S.S. Pollack, Investigation of the structure of petroleum asphaltene by X-ray diffraction. Anal. Chem. **33**, 1587–1594 (1961)
14. S. Ergun, V.H. Tiensuu, Interpretation of the intensities of X-ray scattered by coals. Fuel **38**, 64–78 (1959)
15. O.O. Sonibare, T. Haeger, S.F. Foley, Structural characterization of Nigerian coals by X-ray diffraction Raman and FTIR Spectroscopy. Energy **35**(12), 5347–5353 (2010)
16. E. Quirico, J.-N. Rouzaud, L. Bonal, G. Montagnac, Maturation grade of coals as revealed by Raman spectroscopy: progress and problems. Spectrochim Acta Part A **61**, 2368–2377 (2003)
17. H. Rosen, T. Novakov, Identification of primary particulate carbon and sulfate species by Raman spectroscopy. Atmos. Environ. **12**(4), 923–927 (1978)
18. W. Dun, L. Guijian, S. Ruoyu, C. Shancheng, Influences of magmatic intrusion on the macromolecular and pore structures of coal: evidences from Raman spectroscopy and atomic force microscopy. Fuel **119**, 191–201 (2014)
19. X. He, L. Xianfeng, N. Baisheng, S. Dazhao, FTIR and Raman spectroscopy characterization of functional groups in various rank coals. Fuel **206**, 555–563 (2017)
20. W. Dun, L. Guijian, S. Ruoyu, F. Xiang, Investigation of structural characteristics of thermally metamorphosed coal by FTIR spectroscopy and X-ray diffraction. Energy Fuels **27**, 5823–5830 (2013)

21. M.S. Shafeeyan, W.M.A.W. Daud, A. Houshmand, A. Shamiri, A review on surface modification of activated carbon for carbon dioxide adsorption. J. Anal. Appl. Pyrol. **89**(2), 143–151 (2010)
22. B.S. Purwasasmita, F. Tafwidli, R. Septawendar, Synthesis and characterization of carbon nanocoil with catalytic graphitization process of Oryza Sativa pulp precursors. J. Aust. Ceram. Soc. **49**(1), 119–126 (2013)

Chapter 17
Carbon Materials Derived from Domestic Industrial Hemp Hurd

Bohdan Korinenko, Vladyslav Sokol, Tetiana Tkachenko, Dmytro Kamenskyh, Olha Haidai, Volodymyr Povazhnyi, Mariia Baran, Serhii Ruban, and Vitalii Yevdokymenko

Abstract Technical hemp has recently become a highly relevant and rapidly renewable raw material source. It's known that at least a quarter of hurd consists of lignin, which makes it a promising raw material for obtaining carbon materials. Therefore, the aim of our work was to study the possibility of obtaining different carbon materials from hemp hurd. Carbon materials were obtained by the method of activation at 800 °C with water vapour or alkaline. The obtained samples of carbon were studied by various physicochemical methods: low-temperature nitrogen sorption–desorption, SEM, XRD, XRF, FTIR-ATR, TGA and DSC. XRD pattern of the obtained carbons showed that the 2-theta region between 5° and 100° at long collection times indicates no crystalline peaks. Analysis of the FTIR-ATR spectra of the obtained materials show that they have absorption bands characteristic of carbon materials. There are two distinct mass loss steps in termograms (TGA). According to the thermograms, the decomposition of surface functional groups occurs continuously with an exothermic effect in the temperature range of 300–550 °C. At the same time, there is an increase in the specific surface area of the samples with alkaline activation by almost three times.

B. Korinenko · V. Sokol · T. Tkachenko (✉) · D. Kamenskyh · O. Haidai · V. Povazhnyi · M. Baran · V. Yevdokymenko
V.P. Kukhar Institute of Bioorganic Chemistry and Petrochemistry, NAS of Ukraine, Kyiv, Ukraine
e-mail: ttv13ttv@gmail.com

D. Kamenskyh
V. Bakul Institute for Superhard Materials, NAS of Ukraine, Kyiv, Ukraine

S. Ruban
LLC RPE «RD PRODUCTION GROUP», Kyiv, Ukraine

O. Fesenko and L. Yatsenko (eds.), *Functional Nanomaterials, Nanocatalysts, Nanotechnologies, and Their Applications*, Springer Proceedings in Physics 321,
https://doi.org/10.1007/978-3-031-99136-3_17

17.1 Introduction

Nowadays, more and more researches are directed towards obtaining carbon materials from renewable raw materials—biomass [1–16]. As a rule, this is thermal conversion of either the biomass itself or its waste (agriculture, forestry and stock farming, and urban waste) including common-used hydrothermal carbonization [3] pyrolysis [1, 4, 5], gasification [4] and torrefaction [1, 4–6]. Carbon materials or biochar obtained in this way are used as functional materials for remediation [7, 8], catalysts for biodiesel production [1], agriculture [2], water treatment [9–11], supercapacitors [12] sensors [9], biomedical applications [9], and carbon dioxide sequestration [13]. Lignin-rich biomass is the best precursor for obtaining biochar [11, 14–16].

Technical hemp has recently become a highly relevant and rapidly renewable raw material source [17–20]. However, in most cases, only fibre is in demand [21–24]. While the hurd turns out to be a multiton waste. There is information about the possibility of its use as a raw material for the production of environmentally safe insulation, as well as for mulching [25, 26]. At the same time, it's known that at least a quarter of hurd consists of lignin, which makes it a promising raw material for obtaining carbon materials [27].

The aim of our work to study the possibility of obtaining different carbon materials from domestic hemp hurd.

17.2 Experimental

17.2.1 Raw Materials

For research it was chosen domestic air-dry hemp hurd (humidity 8%), a waste of the technical hemp crop *Hlesia* varieties of the 2023 harvest, (fraction 20–50 mm) from Chernigiv's region of Ukraine. The composition of the raw materials is given in Table 17.1.

Table 17.1 The composition of the hemp hurd

	Mass fraction of components per completely dry substance (%)
Cellulose	48.4
Hemicellulose	25.8
Water-soluble substances	3.8
Lignin	20.9
Pitches and fats	0.7
Ash	2.7
Other	0.4

Table 17.2 Composition of initial industrial hemp hurd ash

Elements	Content %mass
SiO_2	29.299
K_2O	6.741
CaO	51.636
TiO_2	0.712
Fe_2O_3	3.655
SO_2	3.770
MnO_2	0.497
P_2O_5	1.920
Cl	1.771

The chemical composition of hemp hurd ash (inorganic components) determined by using XRF are shown in Table 17.2.

17.2.2 Methods

Hemp husk, which has undergone preliminary grinding and homogenization is granulated at a certain humidity. For samples that will be activated with alkali, the core is homogenized with a previously determined amount of alkali (25% (wt) of the raw material) and then pressed. Then the obtained "tablets" were introduced into the laboratory reactor of thermolysis. The reaction space was filled with an inert gas (argon) and further throughout the carbonation process, the system was blown with this gas. After that, the actual thermolysis took place. The heat treatment regime was step-by-step: up to 200 °C–1 h, 450 °C–1 h, and 800 °C–1 h. After entering the carbonation mode (800 °C) with steam activation, steam was supplied to the reaction space with inert gas for an hour. When activated with alkali (KOH), the reaction system was kept at 800 °C for 1 h in a stream of argon. After that, the heating was stopped and, if used, the supply of water vapour and the reaction system was cooled in an inert stream. The thermolysis reaction's products were collected in traps for further analysis, the carbon residue was unloaded after the reactor cooled down into a separate container. The resulting carbonaceous material was washed with distilled water to a neutral pH. The composition of thermolysis products is presented in the Table 17.3. Schematically, the entire process is presented in Fig. 17.1.

Table 17.3 Thermolysis products (%, wt.)

Activator	H_2O	Wax	C	Gas	KOH
Water vapour	20	25	25	30	–
Alkali	22	3	15	35	25

Fig. 17.1 Scheme of laboratory carbon obtaining

17.2.3 Characterization

The obtained samples of carbon were studied by various physicochemical methods: low-temperature nitrogen sorption–desorption, SEM, XRD, XRF, FTIR-ATR, TGA and DSC. The phase identification of the products was examined under X-ray diffraction using the MiniFlex 300/600 diffractometer (Rigaku, Japan). The diffraction patterns were recorded using Cu-Kα radiation (λ = 0.15418 nm) of 40 kV and 15 mA at a step 0.02° in the range 2–100° 2θ. FTIR analysis of the obtained silica was performed using IRAffinity-1S FTIR spectrometer (Shimadzu, Japan) equipped with a Quest ATR Diamond GS-10800X (Specac, UK) within the wavenumber range 4000–400 cm^{-1}. The carbon's surface area, average pore size, pore diameter, and total pore volume were measured by nitrogen adsorption using Nova 1200e (Quantachrome, USA). Prior to analysis, 0.23–0.24 g of sample was degassed at 120 °C for 3 h to remove previously adsorbed gases and dead space by vacuum pump to cool down the sample at room temperature. NovaWin 11.04 software was used to calculate the parameters of the porous structure, namely, the specific surface area of S_{BET} (multipoint BET method in the range of p/p_0 0.03–0.65); the specific surface area

without taking into account micropores S_t and the volume of micropores V_{tmicro}—by the t-method (V_α-S_{micro}—alpha-S method), as well as the specific surface area of micropores - by the formula $S_{tmicro} = S_{BET}—S_t$; some of these parameters were also calculated by the DFT method, as was the pore size distribution using selected models. Thermogravimetric analysis and differential scanning calorimetric analysis were performed with a PT1600 TG–DTA/DSC (STA Simultaneous Thermal Analysis, LINSEIS Messgeräte GmbH, Germany) by scanning from 15.8 to 1000 °C at the rate of 5 °C/min under the flow of air. The samples (13.0 ± 0.1 mg) were collected in a standard corundum pan. The sample was analysed three times. The scanning electron microscopy images were taken using Zeiss Evo-10 (Carl Zeiss Microscopy, USA) microscope working at 20.0 kV.

17.3 Results and Discussion

The diffractograms of the obtained carbon materials are shown in Fig. 17.2. The three main diffraction peaks of the carbon samples (Fig. 17.2) are located around 2θ—21–22, 43–44 and 80°. They are low and broad. The broad peak of 15–35° corresponds to the (002) plane of the graphite structure, which indicates the creation of a certain microcrystalline structure [28] in all the studied samples. During the activation of the carbon material, this peak becomes less intense but remains broad. Also, on the diffractograms of carbon material activated by water vapour, there is an intense narrow line 25.5° to the right of the broad (002) peak, which, according to literature data, may belong to quartz impurities [29]. A broad peak of low intensity of the C (002) line, described in the literature as belonging to a graphene nanosheet [30], has a structure intermediate between crystalline and amorphous. Therefore, the activation of the carbon material includes its greater amorphization. It is also worth noting that the activation process of carbon materials takes place in the presence of an oxidant (water vapour). Still, the peaks characteristic of graphene oxide [30] are not found in the diffractograms of the samples. This can be explained by the high activation temperature (800–900°C) and the course of the decarboxylation reaction [31].

The broad peak at 40–50° corresponds to the C (100) plane, and as well as C (002), it indicates that the samples have a turbostrate structure [29]. The low-intensity diffraction peak of carbon material activated by carbon material at about 80°, which corresponds to the C (110) plane, is characteristic of coal with high carbon content, such as anthracite and quasi-natural coke [32].

The studied carbon samples were analyzed in a FTIR analyzer (Fig. 17.3). Lines were assigned according to (Table 17.4).

The TGA-DTG results of the carbon samples are shown in Fig. 17.4a, b. TGA and DTG curves are shown in Fig. 17.4a for samples of activated carbon that have a typical carbon character [40]. Thus, up to 100 °C, there is a loss of sorbed water from the surface of all media, which is most clearly reflected on the differentiated thermogravimetric curves (DTG). The insignificant value of the peak indicates that

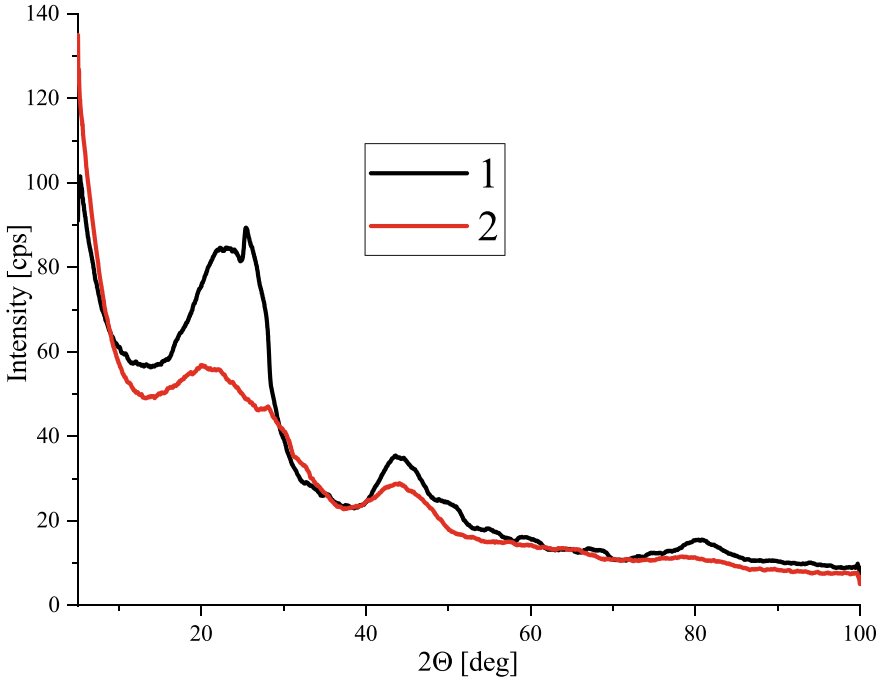

Fig. 17.2 XRD powder patterns of the activated carbons samples by water vapour (1) and alkali (2) obtained from hemp hurd

the samples were previously dried from water before the study. Common to all carbon materials is thermal stability up to 400 °C. The maximum mass loss ranges from 8% for steam-activated coal to 20% for alkali-activated coal (Fig. 17.4a). According to thermograms, the decomposition of surface functional groups occurs continuously with an exothermic effect in the temperature range of 400–600 °C (Fig. 17.4a). In this temperature range, the main weight loss of the samples is 92.5% for activated carbon with steam and 85% for activated carbon with alkali. At a temperature above 600 °C, the TGA, DTG and DSC curves are characterized by stability (Fig. 17.4). When the temperature is further increased to 1000 °C, there is an equalization of the residual mass at the level of 93.5% for activated carbon with steam and 85.5% for activated carbon with alkali.

Nitrogen adsorption–desorption isotherms and pore size distribution curves of the studied activated carbon samples are shown in Fig. 17.5. In the sample of adsorption activated by water vapour, the isotherm branch does not coincide with the desorption one (Fig. 5a). Such a curve is characteristic of type II isotherms and the hysteresis loop belongs to the H4-type [41], which passes into low-pressure hysteresis [42]. According to the works [43, 44] it is characteristic of materials with narrow pores. The isotherm of carbon material activated by alkali has a well-defined hysteresis

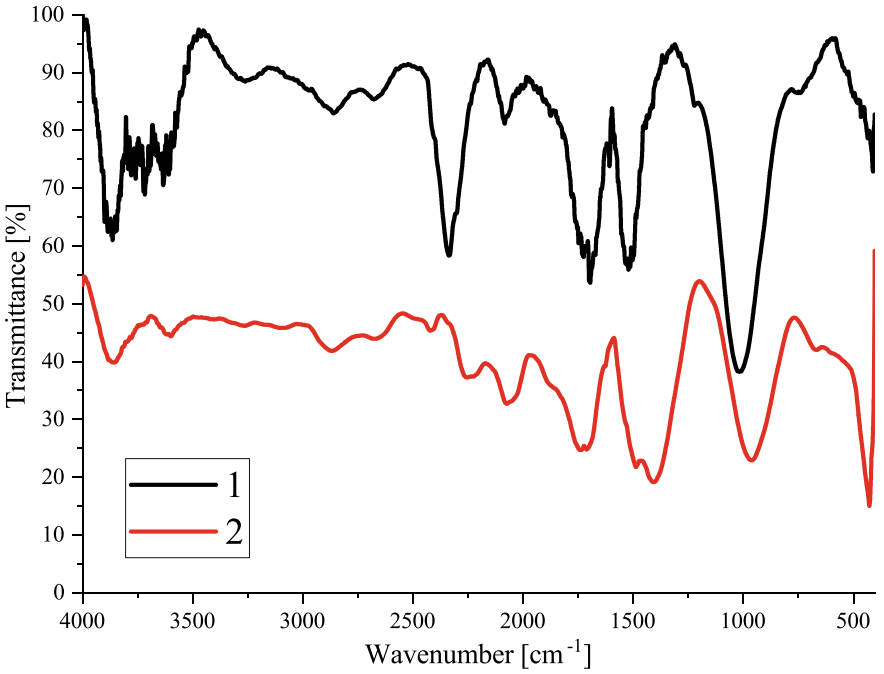

Fig. 17.3 FTIR spectra of the activated carbons samples by water vapour (1) and alkali (2) obtained from hemp hurd

loop at p/p_0 0.4–0.95. It is also characteristic of type II isotherms, and the hysteresis loop belongs to the H4-type.

The calculated parameters of the porous structure are shown in Table 17.5. Alkali activation results in an increase in the surface area and pore volume (Fig. 17.5a, b; Table 17.5) compared to the sample activated by steam. Alkali activation leads to the forming of a mesoporous sample with a specific surface area of more than 650 m^2/g. These may be due to the removal of carbon atoms from the ultramicropore walls [45]. The data presented in Table 17.5 can serve as confirmation of this.

SEM images can provide detailed information on the structure of materials and the shape of individual particles. The morphologies of the obtained carbon materials are presented in Fig. 17.6. These SEM images revealed a discernible trend in the morphology of the carbon after different conditions of the process.

17.4 Conclusions

In this work, the method of obtaining carbon materials from domestic hemp hurd with additional activation or steam or lye is considered. Samples of the obtained carbon materials were studied using XRD, FTIR, SEM, low-temperature N_2 ad(de)sorption

Table 17.4 Classification of FTIR spectrum lines of carbon samples [33–39]

Spectral data	Range (cm^{-1})
C−O in ethers (stretching)	1000–1300
Alcohols	1049–1276, 3200–3640
Phenol groups	
C−OH (stretching)	1000–1220
O−H	1160–1200, 2500–3620
Carbonates, carboxyl-carbonates	1100–1500, 1590–1600
-C−C- aromatic (stretching)	1585–1600
Quinones	1550–1680
Carboxylic acids	1120–1200, 1665–1760, 2500–3300
Lactones	1160–1370, 1740–1880
C−H (stretching)	2600–3000
N–H, C=N	1560–1570
Cyclic amides	646, 1461, 1546, 1685
C−N aromatic ring	1000, 1250, 1355
C−N	1190
C=C=N	2070–2040
N–O-	1300–1000

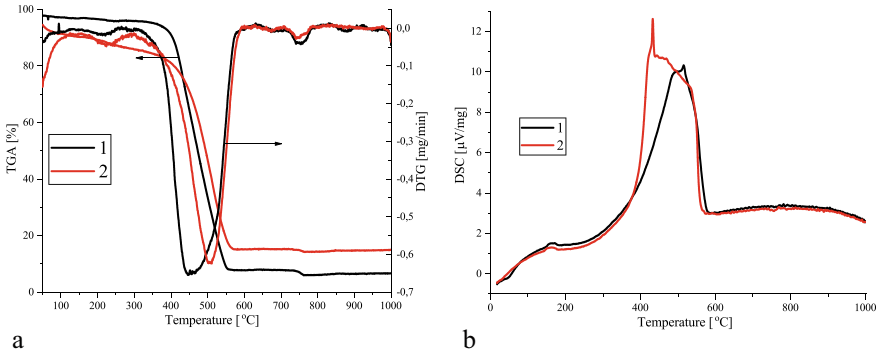

Fig. 17.4 TGA and DTG (**a**), and DSC (**b**) curves of the activated carbons samples by water vapor (1) and alkali (2) obtained from hemp hurd

and derivatography. In the carbonized samples activated by alkali, the development of the outer surface and mesoporosity in the nanoscale range of 1–5 nm was observed, as well as a decrease in the number of micropores. These had a positive effect on the material's heat resistance, which is confirmed by the shift of the maximum on the DTG curve by 50 °C. The increased thermal stability of the alkali-activated material

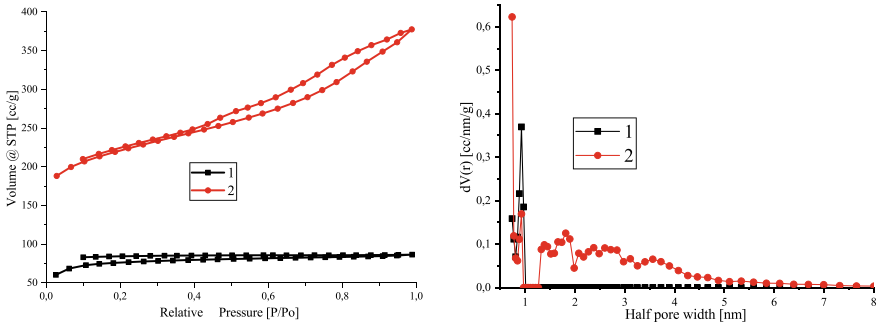

Fig. 17.5 Nitrogen adsorption–desorption isotherm (**a**) and DFT-calculated pore size distributions (**b**) curves of the activated carbons samples by water vapor (1) and alkali (2) obtained from hemp hurd

Table 17.5 Textural properties of activated carbons samples

Activator	S_{BET} (m^2/g)	S^t_{micro} (m^2/g)	V_{BJH} (cm^3/g)	V^t_{micro} (cm^3/g)	d_{BJH} (nm)
Water vapor	225.5	14.342	0.015	0.119	3.25
Alkali	673.8	0	0.276	0	3.262

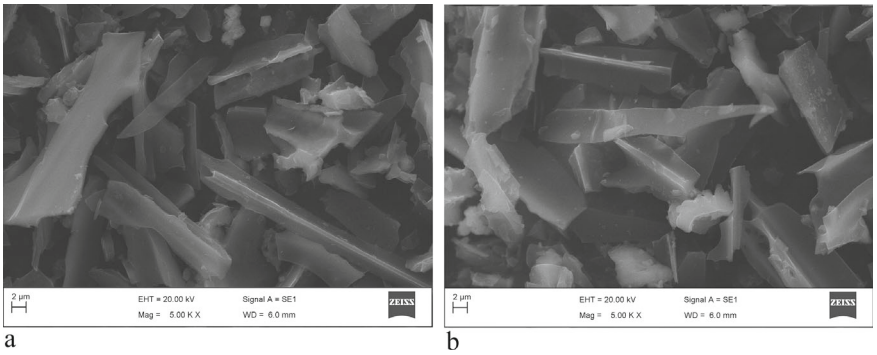

Fig. 17.6 SEM micrographs of the activated carbons samples by water vapor (**a**) and alkali (**b**) obtained from hemp hurd

was explained by a decrease in its microporosity. Thus, hemp hurd is a promising domestic source for obtaining activated carbon.

Acknowledgements The catalytic experiments and laboratory installation assembling have been funding by Target Complex Program of Scientific Research of NAS of Ukraine "Biofuel resources and bioenergy" 2022-2026. We thank the Armed Forces of Ukraine for safety to carry out this work. This work was only possible thanks to the resilience and courage of the Ukrainian Army. Our priceless thanks to the heroic soldiers of the Ukraine Army, who protect us from russian aggressor at the cost of their lives.

References

1. J.J. Villora-Picó, J. González-Arias, F.M. Baena-Moreno, T.R. Reina, Renewable carbonaceous materials from biomass in catalytic processes: a review. Materials **17**(3), 565 (2024). https://doi.org/10.3390/ma17030565
2. M. Freitas, L.P. da Silva, P.M.S.M. Rodrigues, J. Esteves da Silva, Sustainable technological applications of green carbon materials. Sustain. Chem. **5**(2), 81–97 (2024). https://doi.org/10.3390/suschem5020007, https://doi.org/10.1002/advs.202205557
3. T. Dai, N. Ye, S. Sævik, The effect of stick stiffness of friction models on the bending behavior in non-bonded flexible risers, in *Proceedings of the ASME 2017 36th International Conference on Ocean, Offshore and Arctic Engineering, vol. 5A, V05AT04A041. Pipelines, Risers, and Subsea Systems* (Trondheim, Norway, 2017). https://doi.org/10.1115/OMAE2017-62644
4. B. Prabir, *Biomass Gasification, Pyrolysis and Torrefaction. Practical Design and Theory*, 2nd edn (Academic Press, 2013). https://doi.org/10.1016/C2011-0-07564-6
5. P. Piersa, H. Unyay, S. Szufa, W. Lewandowska, R. Modrzewski, R. Ślężak, S. Ledakowicz, An extensive review and comparison of modern biomass Torrefaction reactors vs. biomass pyrolysis—Part 1. Energies, **15**(6), 2227 (2022). https://doi.org/10.3390/en15062227
6. J.S. Tumuluru, B. Ghiasi, N.R. Soelberg, S. Sokhansanj, Biomass torrefaction process, product properties, reactor types, and moving bed reactor design concepts. front. Energy Res. Sec. Bioenergy and Biofuels **9**(2021). https://doi.org/10.3389/fenrg.2021.728140
7. Y. Lijun, L. Chenghu, S. Fei, H. Mao, Z. Wenkun, D. Lichun, A critical review on the development of lanthanum-engineered biochar for environmental applications. J. Environ. Manage. **332** (2023). https://doi.org/10.1016/j.jenvman.2023.117318
8. Yuping, Z., S. Ahmad, M. Qamar, M. Qamar, H.M.N. Bilal, Iqbal: Sustainable remediation of hazardous environmental pollutants using biochar-based nanohybrid materials. J. Environ. Manage. **300** (2021). https://doi.org/10.1016/j.jenvman.2021.113762
9. H. Hongzhe, Z. Ruoqun, Z. Pengcheng, W. Ping, C. Ning, Q. Binbin, Z. Lian, Y. Jianglong, D. Baiqian, Functional carbon from nature: biomass-derived carbon materials and the recent progress of their applications. Adv. Sci. **10**(16) (2023). https://doi.org/10.1002/advs.202205557
10. S.S. Muhammad, Z.A. Faezrul, F. Halim, M.A. Aziz, M.A.M. Rahman, D.N.A. Amin, Chee: carbon-based material derived from biomass waste for wastewater treatment. Environ. Adv. **9** (2022). https://doi.org/10.1016/j.envadv.2022.100259
11. G. Eid, K. Al Bkoor, O. Alrawashdeh, Ø. Masek, A. Skreiberg, M. Corona, L. Zampilli, P. Wang, Q. Samaras, H. Yang, P. Zhou, F. Bartocci, Fantozzi: production and use of biochar from lignin and lignin-rich residues (such as digestate and olive stones) for wastewater treatment. J. Analyt. Appl. Pyrolysis **158**, (2021). https://doi.org/10.1016/j.jaap.2021.105263
12. S. Li, G. Youning, L. Delong, P. Chunxu, Biomass-derived porous carbon materials: synthesis, designing, and applications for supercapacitors. Green Chem. **24**, 3864–3894 (2022). https://doi.org/10.1039/D2GC00099G
13. Q. Cui, Z. Yingying, W. Jiawei, W. Chunfei, G. Ningbo: Biomass-based carbon materials for CO_2 capture: a review. J. CO_2 Utilization **68** (2023). https://doi.org/10.1016/j.jcou.2022.102373
14. E. Gul, K. Al Bkoor Alrawashdeh, O. Masek, Ø. Skreiberg, A. Corona, M. Zampil, L. Wang, P. Samaras, Q. Yang, H. Zhou, P. Bartocci, F. Fantozzi, Production and use of biochar from lignin and lignin-rich residues (such as digestate and olive stones) for wastewater treatment. J. Anal. Appl. Pyrol. **158**, 105263 (2021). https://doi.org/10.1016/j.jaap.2021.105263
15. K. Wang, J. Remón, Z. Jiang, W. Ding, Recent advances in the preparation and application of biochar derived from lignocellulosic biomass: a mini review. Polymers **16**(6), 851 (2024). https://doi.org/10.3390/polym16060851
16. A. Mukherjee, B.R. Patra, J. Podder, A.K. Dalai, Synthesis of biochar from lignocellulosic biomass for diverse industrial applications and energy harvesting: effects of pyrolysis conditions on the physicochemical properties of biochar. Front. Mater **9** (2022). https://doi.org/10.3389/fmats.2022.870184

17. A.T.M. Faiz Ahmed, Md. Zahidul Islam, Md. Sultan Mahmud, Md. Emdad Sarker, Md. R. Islam, Hemp as a potential raw material toward a sustainable world: a review. Heliyon **8**(1), (2022). https://doi.org/10.1016/j.heliyon.2022.e08753
18. Technical/Industrial Hemp. https://fhdau.org.ua/en/helpful-library/industry-interests/technical-industrial-hemp/
19. D.R. Enarevba, K.R. Haapala, The Emerging hemp industry: a review of industrial hemp materials and product manufacturing. AgriEngineering **6**(3), 2891–2925 (2024). https://doi.org/10.3390/agriengineering6030167
20. P. Ranalli, G. Venturi, Hemp as a raw material for industrial applications. Euphytica **140**, 1–6 (2004). https://doi.org/10.1007/s10681-004-4749-8
21. I. Elfaleh, F. Abbassi, M. Habibi, F. Ahmad, M. Guedri, M. Nasri, C. Garnier, A comprehensive review of natural fibers and their composites: An eco-friendly alternative to conventional materials. Results Eng. **19**, (2023). https://doi.org/10.1016/j.rineng.2023.101271
22. K.M. Mini, D. Sathyan, K. Jayanarayanan, 15 - Biofiber composites in building and construction, in *The Textile Institute Book Series, Advances in Bio-Based Fiber*, ed. by S. Mavinkere Rangappa, M. Puttegowda, J. Parameswaranpillai, S. Siengchin, S. Gorbatyuk (Woodhead Publishing, 2022), pp. 335–365. https://doi.org/10.1016/B978-0-12-824543-9.00019-0
23. J. Mariz, C. Guise, T.L. Silva, L. Rodrigues, C.J. Silva, Hemp: from field to fiber—A Review. Textiles **4**(2), 165–182 (2024). https://doi.org/10.3390/textiles4020011
24. A.G.D. Schumacher, S. Pequito, J. Pazour, Industrial hemp fiber: a sustainable and economical alternative to cotton. J. Clean. Prod. **268**, 122180 (2020). https://doi.org/10.1016/j.jclepro.2020.122180
25. V. Hemp. https://viteo.com.ua/en/viteo-hemp/
26. Exploring Hemp Hurd: Benefits and Versatile Uses. https://bulkhempwarehouse.com/exploring-hemp-hurd-its-versatile-uses-and-benefits/
27. G.G. Gramig, S.K. Hogstad, P.M. Carr, Can hemp hurd or paper mulch and biochar application improve weed management in matted-row strawberry production systems? Renewable Agric. Food Syst. **37**(3), 257–267 (2022). https://doi.org/10.1017/S1742170521000533
28. X. Baolin, Z. Chuantao, C. Yijun, H. Guangxu, L. Quanrun, Z. Chuanxiang, C. Zhengfei, Y. Guiyun, C. Lunjian, Y. Jianglong, Preparation of synthetic graphite from bituminous coal as anode materials for high performance lithium-ion batteries. Fuel Process. Technol. **172**, 162–171 (2018). https://doi.org/10.1016/j.fuproc.2017.12.018
29. J.M. Andrésen, C.E. Burgess, P.J. Pappano, H.H. Schobert, New directions for non-fuel uses of anthracites. Fuel Process. Technol. **85**(12), 1373–1392 (2004). https://doi.org/10.1016/j.fuproc.2003.05.001
30. Siburian R, Sihotang H, Raja SL, Supeno M, Simanjuntak CN (2018)New route to synthesize of graphene nano sheets. Orient. J. Chem. 34(1), 182–187. https://doi.org/10.13005/ojc/340120.
31. Tarkovskaya. I.A.: *Oxidized coal*. (Naukova Dumka, Kyiv, 1981).
32. S. Dangyu, Y. Cunbei, Z. Xiaokui, S. Xianbo, Z. Xiaodong, Structure of the organic crystallite unit in coal as determined by X-ray diffraction. Min. Sci. Technol. **21**(5), 667–671 (2011). https://doi.org/10.1016/j.mstc.2011.10.004
33. S. Wenzhong, L. Zhijie, L. Yihong, Surface chemical functional groups modification of porous carbon. Recent Patents Chem. Eng. **1**, 27–40 (2008). https://doi.org/10.2174/2211334710801010027
34. L.M.C. Blanco, A. Martínez-Alonso, J.M.D. Tascon, Microporous texture of activated carbon fibres prepared from nomex aramid fibres. Micropor Mesopor Mater. **34**, 171–179 (2000). https://doi.org/10.1016/S1387-1811(99)00171-7
35. X. Quan, X.T. Liu, L.L. Bo, S. Chen, Y.Z. Zhao, X.Y. Cui, Regeneration of acid orange 7-exhausted granular activated carbons with microwave irradiation. Water Res. **38**, 4484–4490 (2004). https://doi.org/10.1016/j.watres.2004.08.031
36. P.E. Fanning, M.A. Vannice, A DRIFTS study of the formation of surface groups on carbon by oxidation. Carbon **31**, 721–730 (1993). https://doi.org/10.1016/0008-6223(93)90009-Y
37. W. Tomaszewski, V.M. Gunko, J. Skubiszewska-Zieba, R. Leboda, Structural characteristics of modified activated carbons and adsorption of explosives. J. Colloid Interf. Sci. **266**, 388–402 (2003). https://doi.org/10.1016/S0021-9797(03)00633-7

38. A.N.A. El-Hendawy, Influence of HNO_3 oxidation on the structure and adsorptive properties of corncob-based activated carbon. Carbon **41**, 713–722 (2003). https://doi.org/10.1016/S0008-6223(03)00029-0
39. J. Przepiorski, M. Skrodzewicz, A.W. Morawski, High temperature ammonia treatment of activated carbon for enhancement of CO_2 adsorption. Appl. Surf. Sci. **225**, 235–242 (2004). https://doi.org/10.1016/j.apsusc.2003.10.006
40. D. Cuhadaroglu, O.A. Uygun, Production and characterization of activated carbon from a bituminous coal by chemical activation. Afr. J. Biotech. **7**(20), 3703–3710 (2008)
41. L. Xu, J. Zhang, J. Ding, T. Liu, G. Shi, X. Li, W. Dang, Y. Cheng, R. Guo, Pore structure and fractal characteristics of different shale lithofacies in the dalong formation in the western area of the lower Yangtze platform. Minerals **10**(1), 72 (2020). https://doi.org/10.3390/min10010072
42. G. Zelenková, T. Zelenka, M. Almáši, Characterizing mesoporosity in MOFs: a thermoporometry approach. J. Therm. Anal. Calorim. **20**(36), 2311990 (2024). https://doi.org/10.1007/s10973-024-13667-7
43. P. Schiller, M. Wahab, T.A. Bier, H.-J. Mögel, Low pressure hysteresis in materials with narrow slit pores. Colloids Interfaces. **2**(4), 62 (2018). https://doi.org/10.3390/colloids2040062
44. A.M. Silvestre-Albero, J.M. Juárez-Galán, J. Silvestre-Albero, F. Rodríguez-Reinoso, Low-pressure hysteresis in adsorption: an artifact? J. Phys. Chem. C **116**(31), 16652–16655 (2012). https://doi.org/10.1021/jp305358y10.1021/jp305358y
45. V.O. Kucherenko, Y.V. Tamarkina, O.O. Abakumov, Formation of long-flame coal microporous structure under alkali activation. Influence of temperature. Chem. Phys. Technol. Surface **15**(2), 241–254 (2024). https://doi.org/10.15407/hftp15.02.241

Chapter 18
Nanostructured Interpenetrating Polymer Networks Based on Polyurethane and a Copolymer of 2-Hydroxyethyl Methacrylate with Methacryloyloxyethylphosphorylcholine for Biomedical Application

L. V. Karabanova, N. V. Babkina, and O. M. Bondaruk

Abstract Interpenetrating polymer networks based on biocompatible components—polyurethane and copolymer of 2-hydroxyethyl methacrylate with methacryloyloxyethylphosphorylcholine (HEMA-MPC) were synthesized and thermodynamic parameters of interactions in the system, dynamic mechanical properties, porosity of the samples, morphology and physico-mechanical properties were investigated. The thermodynamic parameters of interactions between polymer components of the IPNs were calculated based on isotherms of methylene chloride vapors sorption by samples and it is shown that MPC plays the role of a compatibilizer in the system, increasing the thermodynamic compatibility between polyurethane and the HEMA-MPC copolymer at small amounts of the copolymer in the IPNs. As the amount of copolymer HEMA-MPC in the IPNs increases, the value of the free energy of the polyurethane and copolymer mixing moves to the positive value, which is associated with the formation of ionic clusters of MPC. By dynamic mechanical properties investigations have shown that created IPNs are two-phase systems with incomplete phase separation. The results of the morphology investigations of the IPNs samples are consistent with the data of the thermodynamic compatibility study of polymers during the formation of the IPNs. With a significant increase in the positive values of the free energy of the polyurethane and copolymer mixing in the IPNs with 41% and 51% of the copolymer content, a significant phase separation was observed in the IPNs, with phase inclusions ranging from 1 to 5 μm. Good physico-mechanical properties of the IPNs based on biocompatible components—polyurethane and copolymer of 2-hydroxyethyl methacrylate with methacryloyloxyethylphosphorylcholine and existence of transition pores of size from 26 to 35 Å allow to assume that created materials can be used as biomedical coatings.

L. V. Karabanova (✉) · N. V. Babkina · O. M. Bondaruk
Institute of Macromolecular Chemistry, National Academy of Sciences of Ukraine, Kyiv, Ukraine
e-mail: lyudmyla_karaban@ukr.net

O. Fesenko and L. Yatsenko (eds.), *Functional Nanomaterials, Nanocatalysts, Nanotechnologies, and Their Applications*, Springer Proceedings in Physics 321,
https://doi.org/10.1007/978-3-031-99136-3_18

18.1 Introduction

Polyurethanes, (PU)s, are widely used in the field of biomedical applications due to their excelent mechanical properties including very high flexural endurance compared to most elastomeres. Howerer, the blood compatibility of the PUs is relatively poor. Biofouling on the PU's surfaces occurs during contact with blood and it leads to the contamination of the surface and also it reduces mechanical properties of PUs [1–3]. Attempts of the surface modification of the PUs in order to improve the blood compatibility have been reported [4–14]. Among them there are physical methods of the surface modification such as corona, plasma and laser treatments [15]. In the presence of oxygen, high-energy photon treatment induces the radical sites formation at the surfaces. These radical sites react with atmosphere oxygen forming oxygenated functions [15]. Several studies of chemical modifications of the PUs, such as grafting or blending were carried out with aim to improve the blood compatibility [4–14].

2-Methacryloyloxyethyl phosphorylcholine (MPC) polymers are known as excellent blood compatible polymers [6, 9–12, 16–23]. The PUs have been modified with various MPC polymers by coating [6, 20], grafting [9] or blending [10, 11]. They effectively reduced protein adsorption and platelet adhesion compared with the neat PU. But such modification could not eliminate the elution of MPC polymers from the matrix of PU during long time been in human body.

Recently a lot of efforts have also been focused on improving the biocompatibility of polymers used in medical implants [24, 25]. One of the most powerful approaches that can be used to improve biocompatibility, enhance mechanical properties and resistance to degradation of polymers is the creation of interpenetrating polymer networks (IPNs) [26–32]. Interpenetrating polymer network structure could also inhibit the elution of polymer-guest from polymer-matrix [14].

Various IPN-based materials have been previously proposed for biomedical applications [33–35]. Among them the semi-IPNs based on PU and polyvinylpyrrolidone, based on PU and poly(2-hydroxyethyl methacrylate) (PHEMA) are proposed by our team [27, 28, 31]. In this study, the IPNs based on PU and copolymer of 2-hydroxyethyl methacrylate with 2-methacryloyloxyethyl phosphorylcholine were synthesized and investigated with a view of developing improved materials for biomedical applications by combining mechanical properties of PU with high biocompatibility of the copolymer.

18.2 Materials and Testing Methods

18.2.1 Materials

The IPNs were prepared on the basis of the polyurethane network (PU) and copolymer of 2-hydroxyethylmethacrylate (HEMA) and methacryloyloxyethylphosphorylcholine (MPC).

First the polyurethane network was synthesized by a two steps method. The first step was the preparation of the adduct of trimethylolpropane (TMP) and toluylene diisocyanate (TDI) both supplied by Bayer. Toluylene diisocyanate was distilled on a vacuum line. Trimethylol propane was dried at 308 K under vacuum. Then trimethylol propane was dissolved in ethylacetate supplied by Aldrich. The adduct of trimethylol propane and toluylene diisocyanate was prepared by reacting 1 equivalent of TMP with 1.5 equivalents of TDI at 338 K. The reaction was carried out until the theoretical isocyanate content was reached, which one was determined by di-n-butylamine titration method. The second step was the synthesis of the crosslinked polyurethane. The polyurethane network was obtained from poly(oxypropylene)glycol M_w = 2000 g mol^{-1} and adduct of trimethylolpropane and toluylene diisocyanate (ratio 1:2 g-equiv) at temperature 353 K in a nitrogen atmosphere during 48 h. The poly(oxypropylene)glycol was degassed at 343 K for 8 h under vacuum before use. Unreacted materials were extracted from the polyurethane network by Soxlhet extraction method using ethylacetate as a solvent. As result we have formed the polyurethane network depicted by the formula:

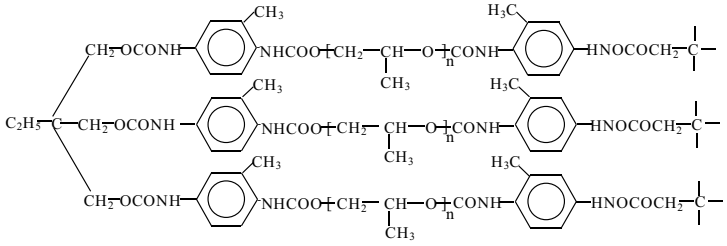

The second polymer component of IPNs was statistical copolymer of 2-hydroxyethylmethacrylate (HEMA) and methacryloyloxyethylphosphorylcholine (MPC), the content of MPC was 5% by weight. The HEMA was supplied by Sigma and MPC was supplied by LTD "Biocompatible" (United Kingdom). The IPNs were obtained by the sequential method. For this purpose, the polyurethane network was swollen with mixture of freshly distilled under vacuum monomer 2-hydroxyethylmethacrylate and MPC which contained Irgacure 651 as a photoinitiator. The swelling was carring out to the equilibrium state. Then the monomer mixture was photopolymerized in frame of matrix of polyurethane in a temperature-controlled chamber during one hour. The wavelength of UV light was 340 nm.

The obtained second polymer is statistical copolymer of 2-hydroxyethylmethacrylate (HEMA) and methacryloyloxyethylphosphorylcholine (MPC) wich presented by next chemical formula:

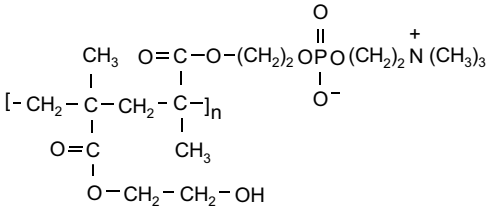

The prepared IPNs were then held in vacuum 10^{-5} Pa at 353 K during 36 h to reach the constant weight.

By this procedure the series of IPNs with a wide range of compositions were obtained.

18.2.2 Testing Methods

18.2.2.1 Vapour Sorption and Thermodynamic Calculations

The methylene chloride vapors sorption by PU, copolymer and IPNs samples was studied using a vacuum installation and a McBain balance [32]. The changes in partial free energy of methylene chloride by sorption (dissolution) were determined from the experimental data using Eq. 18.1:

$$\Delta\mu_1 = (1/\mathrm{M})\mathrm{RT}\ln(\mathrm{P}/\mathrm{P}_0), \tag{18.1}$$

where M is the molecular mass of methylene chloride, and P/P_o is the relative vapour pressure. The value $\Delta\mu_1$ changes with solution concentration from 0 to $-\infty$.

To calculate the free energy of mixing of the polymer components with the solvent, the changes in partial free energy of the polymers (native PU, copolymer, IPNs) needs to be determined. This requires the calculation of the difference between the polymer chemical potential in the solution of a given concentration and in pure polymer under the same conditions ($\Delta\mu_2$). $\Delta\mu_2$ for the polymer components were calculated using the Gibbs–Duhem equation:

$$\omega_1 \mathrm{d}(\Delta\mu_1)/\mathrm{d}\omega_1 + \omega_2 \mathrm{d}(\Delta\mu_2)/\mathrm{d}\omega_1 = 0, \tag{18.2}$$

where ω_1 and ω_2 are the weight fractions of a solvent and of a polymer. This can be rearranged to give Eq. 18.3:

$$\int d(\Delta\mu_2) = -\int (\omega_1/\omega_2)d(\Delta\mu_1) \tag{18.3}$$

Equation 18.3 allows the determination of $\Delta\mu_2$ for each polymer from the experimental data by integration over definite limits. The average free energy of mixing of solvent with the individual PU, copolymer and IPNs of various compositions for the solutions of different concentration, was then estimated using Eq. 18.4 and using computational analysis.

$$\Delta g^m = \omega_1 \Delta\mu_1 + \omega_2 \Delta\mu_2 \tag{18.4}$$

18.2.2.2 Dynamic Mechanical Analyses (DMA)

The dynamic mechanical analysis measurements were carried out using a Dynamic Mechanical Thermal Analyzer Type DMA Q800 from TA Instruments over the temperature range from −100 to + 220 °C and at fixed frequency of 10 Hz with a heating rate of 3 °C /min. The experiments were performed in the tension mode on rectangular speciments (35 mm × 5 mm × 1 mm). As the copolymer HEMA with MPC is a hydroscopic sample, all samples were dried at 80 °C for 48 h under vacuum before measurements. The samples were subsequently subjected to the following thermal cycle during DMA measurements: a first run from 20 °C up to 100 °C and then second run from −100 up to + 220 °C. The second run was used for analysis of the results.

18.2.2.3 Porosity by Method of Brunauer-Emmett-Teller (BET)

To estimate the porosity of the synthesized PU, copolymer and IPNs samples, the classical sorption method was chosen [36]. It consists in determining of the amount of vapors of low molecular weight liquid, which adsorbed by the sample at different vapor pressures, building of the sorption–desorption isotherms and subsequent calculations based on isotherms of the specific surface area, total pore volume and average pore size of the synthesized samples. The adsorption of the methanol vapors by samples of PU, copolymer and IPNs based on them was investigated at a temperature of 20 °C using a vacuum installation with McBain balances using molybdenum spirals with a sensitivity of 3–4 mg/mm [32, 37]. The specific surface area S_{spec} of the samples was calculated by the Brunauer-Emmet-Teller method (BET method) [37].

18.2.2.4 Scanning Electron Microscopy (SEM)

The morphology of IPNs samples based on polyurethane and the copolymer of HEMA-MPC was studied using scanning electron microscopy (SEM). Scanning electron microscopy was performed on a JEOL JSM 6060 LA (Tokyo, Japan) at an accelerating voltage of 30 kV and using a detector of secondary electrons. The samples were cut into the strips, before being submerged in liquid nitrogen for 5 min and then fractured. The samples were warmed to room temperature and fixed to an SEM stub. The fracture surface of samples was coated with gold in a vacuum to prevent accumulation of static charge and to increase the resolution. All measurements were done at 20 °C and at magnification of 10,000 times.

18.2.2.5 Mechanical Testing

Mechanical properties of the samples of polyurethane, the copolymer of HEMA-MPC and IPNs based on them were measured using a Series IX Automated Instron Materials Testing Systems. The samples were cut into micro dumb-bell shapes with gauge length of 20 mm, widths between 4 and 5 mm and thickness between 0.7 and 0.9 mm. Samples were processed at a continuous strain rate of 25 mm/min.

18.3 Results and Discussion

18.3.1 Thermodynamics of Interactions in the IPNs Based on Polyurethane and Copolymer of 2-Hydroxyethyl Methacrylate with Methacryloyloxyethylphosphorylcholine

Thermodynamic parameters of interactions in the system were calculated on the basis of experimental isotherms of methylene chloride vapors sorption by synthesized samples. In Fig. 18.1 the isotherms of methylene chloride vapors sorption at a temperature of 20° C by samples of polyurethane, copolymer of HEMA-MPC and IPNs which synthesized on the basis of these two polymer components, with a copolymer content of 17.76% are presented.

It can be seen that the sorption capacity of the components of the IPNs is significantly different: the sorption of methylene chloride vapors by polyurethane (curve 1) is an order of magnitude higher than the sorption of vapors by the copolymer sample (curve 2). The sorption isotherm for polyurethane has a typical form for polymers which are in an elastic state. The sorption isotherm of the copolymer is similar to the isotherms of sorption by the glassy polymers. The sorption isotherm of methylene chloride by the IPNs sample with a copolymer content of 17.76% (Fig. 18.1, curve

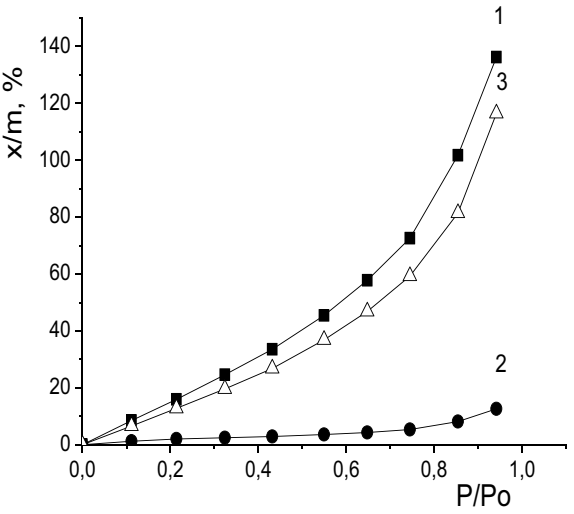

Fig. 18.1 Isotherms of methylene chloride vapors sorption at 20 °C by samples of native polymers and IPNs: PU (1), HEMA-MPC copolymer (2), IPNs with a copolymer content of 17.76% (3)

3) is located between the isotherms of individual components and has a form wich similar to the curve for polyurethane.

In Fig. 18.2 the isotherms of methylene chloride vapor sorptions at a temperature of 20 °C by samples of IPNs synthesized on the basis of polyurethane and HEMA-MPC copolymer, with a copolymer content from 17.76% to 51.26%. are presented.

It can be seen that the sorption capacity of the samples of interpenetrating polymer networks is lower than the sorption capacity of polyurethane (Fig. 18.1, curve 1), but significantly higher than the sorption capacity of the HEMA-MPC copolymer (Fig. 18.1, curve 2). The isotherms of methylene chloride vapors sorption by IPNs samples are quite close, the content of the copolymer has a small effect on the sorption capacity of the samples.

The application of thermodynamic methods to experimental data on the sorption of solvent vapors makes it possible to evaluate a number of system characteristics at a quantitative level. Based on the experimental data of the sorption isotherms of methylene chloride, the thermodynamic parameters of polyurethane and HEMA-MPC copolymer mixing were calculated according to the method described in publications [37, 38].

In Fig. 18.3 the calculated values of the average free energy of mixing Δg^m of individual components—polyurethane and HEMA-MPC copolymer, and IPNs with the solvent are presented. As can be seen, all investigated systems: PU—methylene chloride, HEMA-MPC copolymer—methylene chloride, IPNs—methylene chloride—are thermodynamically stable $\left(\frac{\partial^2 \Delta g^m}{\partial W_2^2} \rangle 0\right)$ [37]. At the same time, the affinity of methylene chloride to PU (Fig. 18.3, curve 1) is significantly higher than the affinity of this solvent to the HEMA-MPC copolymer (Fig. 18.3, curve 2). For IPNs, with an increase in the amount of the copolymer, the thermodynamic stability of the polymer mixture—solvent system decreases. (Δg^m becomes smaller) (Fig. 18.3, curves 3–7).

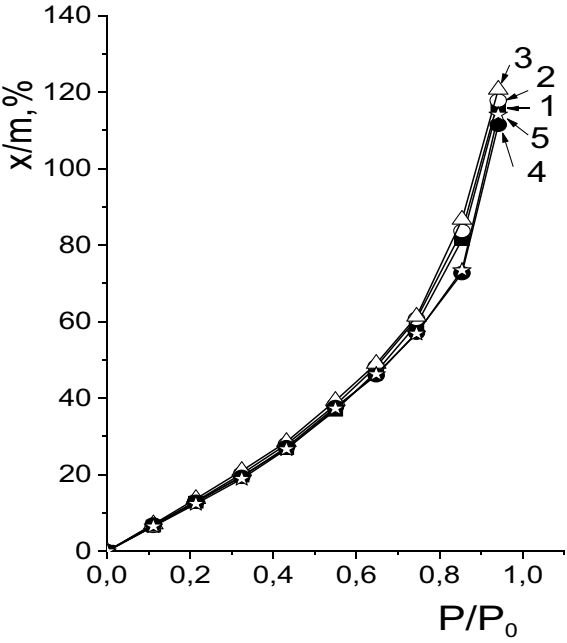

Fig. 18.2 Isotherms of methylene chloride vapors sorption at 20 °C by samples of the IPNs with a copolymer content of 17.76% (1), 21.08% (2), 30.33% (3), 41.72% (4), 51.26% (5)

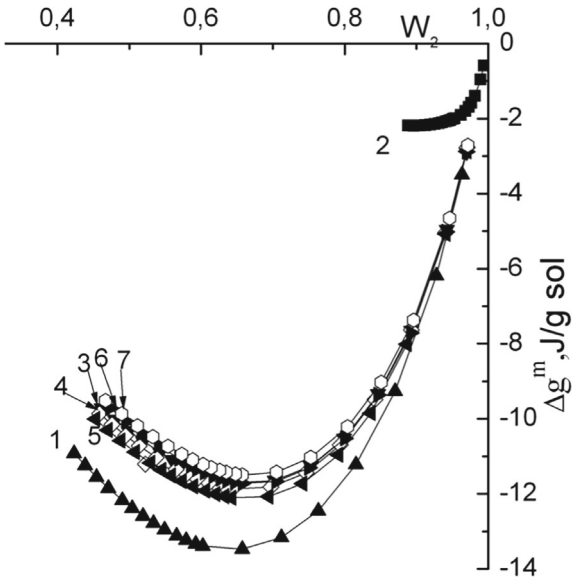

Fig. 18.3 Concentration dependence of the free energy of mixing in the polymer–solvent system for: PU (1), HEMA-MPC copolymer (2), IPNs containing 17.76% (3), 21.08% (4), 30, 33% (5), 41.72% (6), 51.26% (7) of the HEMA-MPC copolymer

Based on the concentration dependences of Δg^m—the average free energy of mixing of individual components (polyurethane and HEMA-MPC copolymer) and IPNs with methylene chloride, according to the thermodynamic cycles proposed by A.A. Tager with co-workers [38], the value of the free energy of polyurethane and the HEMA-MPC copolymer mixing during the formation of the IPNs was calculated.

The results of the calculations are presented in Table 18.1. It can be seen that the free energy of mixing of the studied samples with methylene chloride at the critical concentration (maximum dilution of the solution) for polyurethane is -106.27 J/g of polymer, for the HEMA-MPC copolymer this value is −10.34 J/g of polymer. So, the value is almost an order of magnitude smaller for the copolymer. The free energy of mixing IPNs samples with methylene chloride at the critical concentration changes from −85.95 J/g of polymer to −92.36 J/g of polymer, but this change occurs in non-monotonically way with the content of the copolymer.

Table 18.1 also shows the values of the free energy of polyurethane and copolymer mixing Δg_x during formation of interpenetrating polymer networks. It can be seen that at a small amount of HEMA-MPC copolymer (17.76%), the free energy of polyurethane and copolymer mixing is negative. This indicates that the two polymers which forming the IPNs at this concentration are thermodynamically compatible. When the copolymer content increases to 21.08%, the value of the free energy of polyurethane and copolymer mixing goes from negative to positive value.

A further increase in the copolymer content leads to an increase in the value of the free energy of polyurethane and copolymer mixing from + 2.9044 to + 28.5033. That is, when the content of the copolymer increases, the components of the IPNs become thermodynamically incompatible, and the incompatibility increases when approaching comparable concentrations of the components of the IPNs - polyurethane and the HEMA-MPC copolymer.

Table 18.1 Free energy of polyurethane and HEMA-MPC copolymer mixing during the formation of IPNs

Sample composition	The free energy of mixing with methylene chloride at a critical concentration, J/g of polymer	Free energy of polyurethane and copolymer mixing $\Delta g_{x,}$ J/g of polymer
PU	− 106.97	–
Copolymer HEMA-MPC	− 10.34	–
IPNs PU/copolymer 82.24/17.76	− 88.13	− 1.69
IPNs PU/copolymer 78.92/21.08	− 89.51	+ 2.90
IPNs PU/copolymer 69.67/30.33	− 92.36	+ 14.68
IPNs PU/copolymer 58.28/41.72	− 86.41	+ 19.74
IPNs PU/copolymer 48.74/51.26	− 85.95	+ 28.50

The synthesis of IPNs is usually occurs in thermodynamically non-equilibrium conditions. This process begins from a thermodynamically equilibrium state of a mixture of monomers or a polymer swollen in another monomer. During process of polymerization and crosslinking, there is a rapid decrease in the combinatorial entropy of mixing in the system. It is known that the entropy of polymers mixing is approximately 10^2 times lower than the entropy of mixing of low molecular weight substances, such as the monomers [39]. As a result, the energy of two polymers mixing ΔG (Gibbs energy) changes continuously during the process of synthesis. Since the mixing energy depends on the enthalpy and entropy of mixing ($\Delta G = \Delta H - T\Delta S$), due to the decrease of the mixing entropy, the Gibbs energy of mixing becomes positive, which leads to phase separation in the the system [40–42].

However, in this study, the value of the free energy of polyurethane and HEMA-MPC copolymer mixing during the formation of IPNs with a content of the latter of 17.76% turned out to be negative. This means that the contribution of the enthalpy of mixing in the studied system was significant and it outweighed the reduction of the entropy of mixing during the formation of the IPNs. The enthalpy of mixing is an energy component and it depends on the interactions that take place in the system.

Therefore, it can be concluded that the introduction of a small amount of MPC into the system radically changes the intermolecular interactions between the polyurethane and the copolymer. Apparently, negatively charged phosphoryl groups actively interact with urethane groups in polyurethane, and the positively charged nitrogen atom of MPC is capable to interact with the oxygen of the oligoether component in polyurethane. Thus, MPC plays the role of compatibilizer in the system, it increases the thermodynamic compatibility between polyurethane and copolymer. But with the increase in the content of the HEMA-MPC copolymer in the IPNs, the value of the free energy of polyurethane and the copolymer mixing became positive (Table 18.1).

This may mean that with an increase in the amount of MPC in the system, the interactions between negatively charged phosphoryl groups and positively charged nitrogen atoms of various MPC polymer chains arise, i.e., the number of intermolecular interactions (polyurethane and copolymer) decreases, while the number of intramolecular interactions (between different groups of MPC) is growing. At a certain concentration of MPC chains, the formation of ionic clusters can occur, and this leads to a situation where MPC ceases to play the role of a compatibilizer in the system. Wherein, interpenetrating polymer networks become thermodynamically incompatible, which leads to phase separation in the system.

18.3.2 Dynamic Mechanical Properties of the IPNs Based on Polyurethane and Copolymer of 2-Hydroxyethyl Methacrylate with Methacryloyloxyethylphosphorylcholine

The investigations of the dynamic mechanical properties of polyurethane, of copolymer of 2-hydroxyethyl methacrylate with methacryloyloxyethylphosphorylcholine and of interpenetrating polymer networks (IPNs) based on them, studying the peculiarities of the dynamics of glass transitions in the IPNs with variations in the content of components and phase separation in the system were carried out.

In Figure 18.4 the temperature dependences of the tangent of the mechanical loss angle (tanδ) for PU (curve 1), for copolymer HEMA with MPC (curve 2), and for IPNs with different copolymer content (curves 3-8) are presented. It can be seen that an abnormally wide glass transition with a maximum at −32 °C is observed for PU. The glass transition is also shown in Table 18.2.

The native copolymer of HEMA with MPC shows an intense maximum of tanδ at a temperature of + 145 °C. Two maxima of tanδ are observed for the IPNs. We could observe that the polyurethane maximum tanδ in IPNs decreases by amplitude compared to the native polyurethane. This could be explained by the suppressing effect of the copolymer on the segmental motions in the PU.

In more detail, the temperature position of the tanδ maxima and their intensity can be observed in Figure 18.5. It can be seen that the addition of the copolymer in the amounts up to 30 wt.% leads only to a decrease in the tanδ amplitude of PU without changing its temperature position. A further increase in the content of the copolymer to 41–51 wt.% also leads to a shift of the maximum tanδ of PU towards low temperatures.

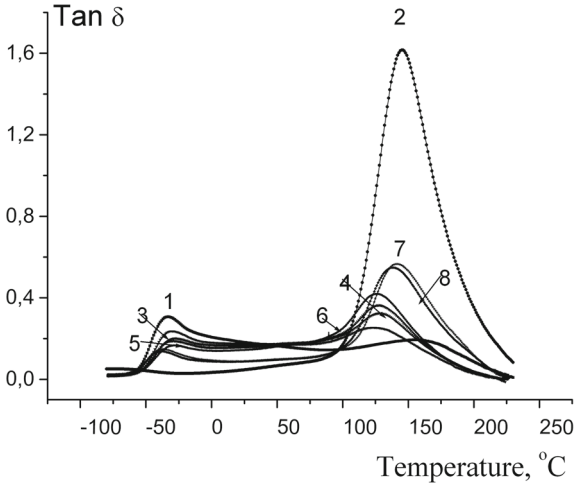

Fig. 18.4 The temperature dependences of the tangent of the mechanical loss angle (tanδ) at the DMA study at a frequency of 10 Hz for samples of PU (curve 1), copolymer HEMA with MPC (curve 2), and for IPNs with different content of copolymer: 10.04 (3), 17 0.76 (4), 21.08 (5), 30.33 (6), 41.72 (7), 51.26% (8)

Table 18.2 Glass transition temperature of polymer components and modulus of elasticity of the IPNs depending on the content of components

Sample	Glass transition temperature (maximum tanδ), °C		The modulus of elasticity at − 25 °C (MPa)	The modulus of elasticity at 0 °C (Mpa)
	PU	Copolymer		
PU	− 32.78	–	549	136
Copolymer HEMA with MPC		+ 145.82	4035	3636
IPNs PU/ copolymer 90/10	− 29.84	+ 124.22	989	259
IPNs PU/ copolymer 83/17	− 27.18	+ 128.89	1591	292
IPNs PU/ copolymer 79/21	− 28.47	+ 128.25	1321	415
IPNs PU/ copolymer 70/30	− 27.02	+ 126.57	1339	469
IPNs PU/ copolymer 59/41	− 36.83	+ 142.01	1624	607
IPNs PU/ copolymer 49/51	− 37.76	+ 138.69	1522	825

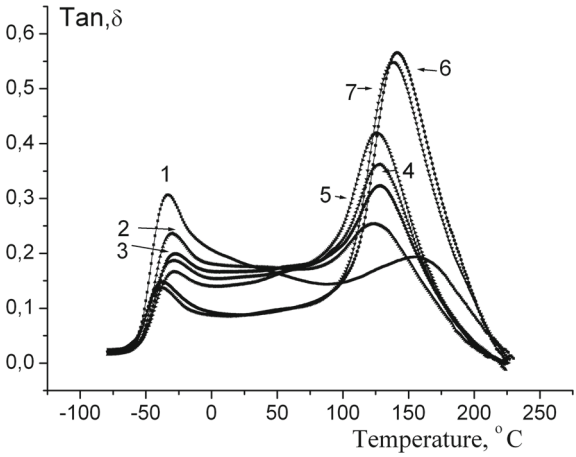

Fig. 18.5 The temperature dependences of the tangent of the mechanical loss angle (tanδ) at the DMA study at a frequency of 10 Hz for PU sample (curve 1) and for IPNs with different copolymer content: 10.04 (2), 17.76 (3), 21.08 (4), 30.33 (5), 41.72 (6), 51.26% (7)

For the maxima of tanδ of the copolymer HEMA with MPC in the IPNs, we could observe a significant decrease in the intensity and a shift along the temperature scale towards low temperatures in compare with the maximum of the native copolymer. At the same time, a more significant shift of the maxima tanδ of the copolymer towards low temperatures is observed at minimum amounts of the copolymer in the IPNs. Such behavior of the maxima of the tanδ copolymer in IPNs means that these IPNs are two-phase systems with incomplete phase separation [29, 30].

Also, a significant shift of the tanδ maxima of the copolymer towards low temperatures means the loss of the cooperativity of the segmental motion of the copolymer at its low contents in the IPNs.

In addition, it can be noted that in the IPNs with a copolymer content of 41 and 51 wt.%, the maximum depressing effect of the copolymer on the segmental motions in PU is observed (the intensity of tanδ peaks of PU is the lowest) (Fig. 18.5). At the same time, the tanδ maxima of the copolymer in the IPNs with a content of 41 and 51 wt.% of copolymer increase in compare with IPNs of other compositions, and a deepening of the bridge between the two peaks of tanδ (PU and copolymer) is observed.

At the qualitative level, it can be concluded that in the IPNs with a copolymer content of 41 and 51 wt.%, the phase separation between the components is more significant compared to the phase separation in the IPNs containing 7- 30 wt.% of copolymer.

In Table 18.2 the values of the modulus of elasticity of the investigated samples at – 25 and at 0 °C are presented. It can be seen that at −25 °C the modulus of elasticity of the copolymer HEMA with MPC is significantly higher than the modulus of elasticity of IPNs, at the same time the modulus of elasticity of IPNs regularly increases with the copolymer content. At 0 °C, there is a non-monotonic change in the modulus of elasticity of the IPNs with the copolymer content, but the values are significantly lower compared to the modulus of elasticity at −25 °C.

Figure 18.6 demonstrates the values of the modulus of elasticity for samples of PU (curve 1), copolymer (curve 2) and for IPNs with different copolymer content (curves 3–8). It could be seen that the maximal modulus of elasticity in all temperature range has the copolymer, and the minimal modulus has PU. For the IPNs, the modulus of elasticity increases with the copolymer content, this is especially noticeable in the temperature range from − 50 to + 50 °C.

As mentioned above, interpenetrating polymer networks based on polyurethane and copolymer HEMA with MPC are two-phase systems with incomplete phase separation [30]. For such systems, the degree of polymer components segregation α, which is a measure of phase separation, could be calculated. If $\alpha = 1$, this means the polymer system is completely phase separated. If $\alpha = 0$, this means that the polymer components are compatible at the molecular level [43, 44]. We have calculated the degree of polymer components segregation α in the IPNs with different PU and copolymer content, according to the method proposed by Yu.S. Lipatov and V.F. Rosovitsky [44]. Calculated parameters are given in Table 18.3.

As can be seen from Table 18.3, the calculated degree of polymer components segregation α increases with the content of copolymer HEMA with MPC. For IPNs

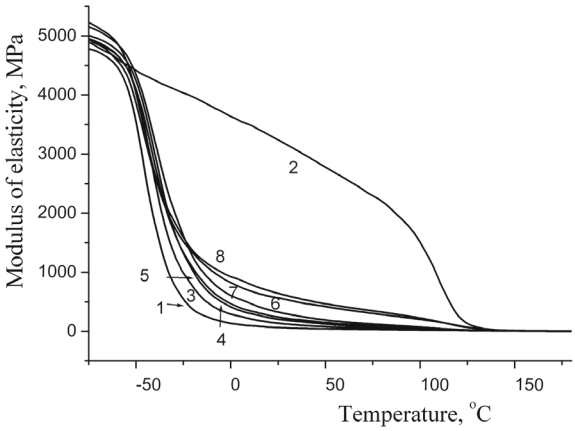

Fig. 18.6 Temperature dependences of elastic moduli at DMA investigations at a frequency of 10 Hz for samples of PU (curve 1), copolymer HEMA with MPC (curve 2) and for IPNs with different copolymer content: 10.04 (3), 17.76 (4), 21.08 (5), 30.33 (6), 41.72 (7), 51.26% (8)

Table 18.3 The degree of polymer components segregation α in the IPNs based on PU and copolymer HEMA with MPC

Sample	Maximum losses for components of phases 1 and 2		The shift of the corresponding maxima on the temperature scale		A parameter that takes into account the maximum shift	Degree of polymer components segregation
	h1	h2	l1	l2	λm	α
Copolymer HEMA with MPC		h_0 1.589				
PU	h_0 0.165					
IPNs PU/ copolymer 90/10	0.066	0.083	2.94	21.6	0.0111	0.079
IPNs PU/ copolymer 83/17	0.034	0.159	5.60	16.9	0.0162	0.101
IPNs PU/ copolymer 79/21	0.034	0.209	4.31	17.6	0.0214	0.126
IPNs PU/ copolymer 70/30	0.030	0.284	5.76	19.3	0.0316	0.161
IPNs PU/ copolymer 59/41	0.063	0.482	4.05	3.81	0.0117	0.304
IPNs PU/ copolymer 49/51	0.055	0.465	4.98	7.13	0.0201	0.285

with a low content of copolymer—10 wt.%, α is 0.079. For IPNs with a high content of copolymer—41 and 51 wt.%, α is 0.304 and 0.285, and for IPNs, containing 10–30 wt.% of copolymer, the degree of polymer components segregation α gradually increases from 0.079 to 0.161. We could observe that when the copolymer content increases to 41 wt.%, there is a sharp increase in the degree of polymer components

segregation α to 0.304. This allows us to conclude that the phase separation is more significant in IPNs containing high concentrations of copolymer HEMA with MPC, namely 41–51 wt.%.

The higher intensity of the tanδ maxima of the copolymer and the deeper bridge between the two peaks of the tanδ (PU and the copolymer HEMA with MPC) in the IPNs containing high concentrations of copolymer HEMA with MPC, namely 41–51 wt.% (Fig. 18.5), are also indicate that the phase separation is more significant in these IPNs. This may mean that with an increase in the amount of the copolymer HEMA with MPC, and therefore with an increase in the amount of methacryloyloxyethylphosphorylcholine in the system, interactions between negatively charged phosphoryl groups and positively charged nitrogen of various polymer chains of methacryloyloxyethylphosphorylcholine, i.e., the number of intermolecular interactions (polyurethane and copolymer) decreases, while the number of intramolecular interactions (between different groups of methacryloyloxyethylphosphorylcholine) increases. At a certain concentration of methacryloyloxyethylphosphorylcholine chains, the formation of ionic clusters can occur, and this leads to a situation when the phase separation in the IPNs system sharply increases.

18.3.3 Porosity of the IPNs Based on Polyurethane and Copolymer of 2-Hydroxyethyl Methacrylate with Methacryloyloxyethylphosphorylcholine

In this work, a study of the porosity of materials created for biomedical coatings based on polyurethane and a copolymer of hydroxyethyl methacrylate with methacryloyloxyethylphosphorylcholine synthesized on the principle of interpenetrating polymer networks (IPNs)) was carried out.

With a purpose to calculate the porosity and specific surface area of the created materials, the isothermal adsorption of methanol vapors by the created systems was investigated. The goal of the study was to evaluate the effect of the ratio of polyurethane and copolymer of hydroxyethyl methacrylate with methacryloyloxyethylphosphorylcholine on the porosity of materials for biomedical coatings.

The basis for the calculations were the experimental adsorption isotherms of methanol vapors by the created samples. The adsorption of methanol vapors by samples of the native polymers and by samples of IPNs was studied at 20 °C using a vacuum instalation with McBean balances [36].

Figure 18.7 shows the adsorption isotherms of methanol vapors by samples of polyurethane, copolymer, and IPNs with 10% and 18% of copolymer.

It can be seen that the adsorption isotherms of methanol vapors by the samples have the form of curves concave to the abscissa axis. The maximum value of methanol vapor adsorption for samples of IPNs with different copolymer content is in the range of 0.65–0.75 mmol/g.

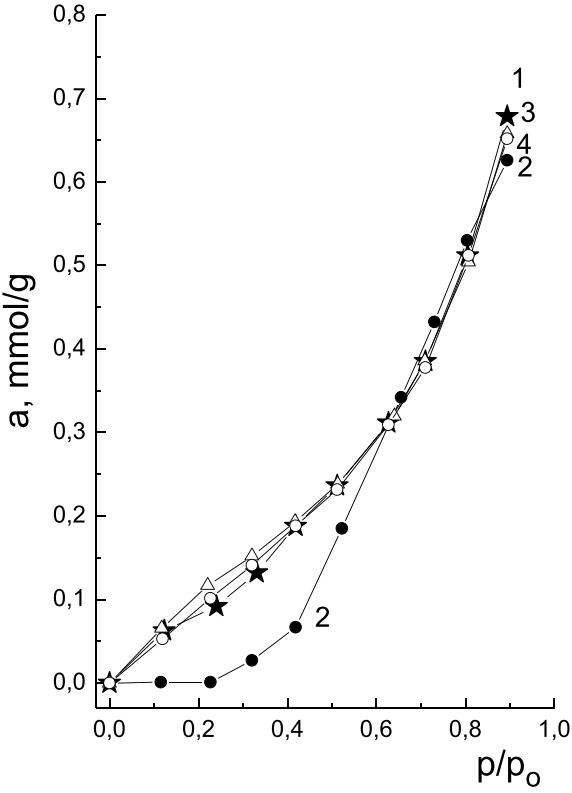

Fig. 18.7 Adsorption isotherms of methanol vapors at 20 °C by samples of the native polymers and IPNs: PU (1), copolymer HEMA with MPC (2), IPNs with copolymer content of 10% (3), IPNs with copolymer content of 18% (4)

Figure 18.8 shows the adsorption isotherms of methanol vapors by samples of IPNs containing 21, 30, 41, and 51% of the copolymer.

According to the Brunauer, Emmett, and Teller (BET) classification [45], the isotherms of methanol adsorption by polyurethane and IPNs samples belong to the third type. This means that the BET equation can be applied to such adsorption isotherms in the range of low vapor pressures [36] (Fig. 18.9).

Experimental adsorption isotherms of methanol vapors by samples of polyurethane, of copolymer and IPNs allowed to calculate the specific surface area, the total volume of the pores and the average radius of the pores of the created materials. The specific surface area was calculated using the BET method [46]. The BET equation was used in the form:

$$\frac{P/P_0}{a \cdot (1 - P/P_0)} = \frac{1}{C \cdot a_m} + \frac{C - 1}{C \cdot a_m} \cdot \frac{P}{P_0} \tag{18.5}$$

where P/P_0 is the relative vapour pressure of the sorbate;

a—the amount of adsorbed substance, mmol / g;

a_m—the amount of adsorbed substance in the monomolecular layer, mmol / g;

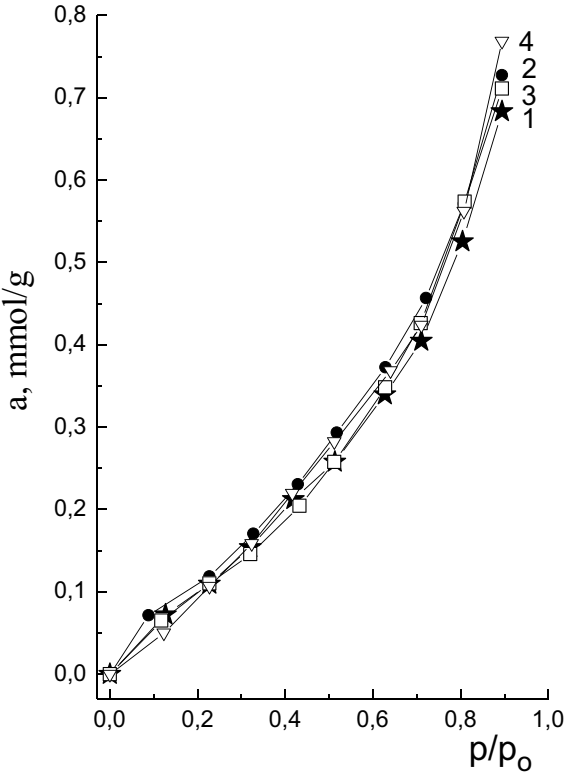

Fig. 18.8 Adsorption isotherms of methanol vapors at 20 °C by IPNs samples with copolymer content of 21% (1), 30% (2), 41% (3), 51% (4)

C—is a constant.

Experimental data were presented as a dependence:

$$\frac{P/P_0}{a \cdot (1 - P/P_0)} = f\frac{P}{P_0} \tag{18.6}$$

The tilt angle of the line and the length on the y-axis allowed to calculate C and $a_{m.}$

$a_m = 1/(k + b)$, where.

$k = tg\alpha$; b—segment on the y-axis.

Figure 18.10 shows the experimental data for PU, for copolymer and for IPNs of two compositions, which rearranged according to the BET Eq. (18.5).

It can be seen that in the range of low relative pressures of methanol vapor there are linear sections of the curves. The tangent of these linear sections and the axis segment on the ordinate allowed us to calculate $a_м$—the amount of sorbed substance in a monomolecular layer.

The specific surface area of the samples was calculated using the equation:

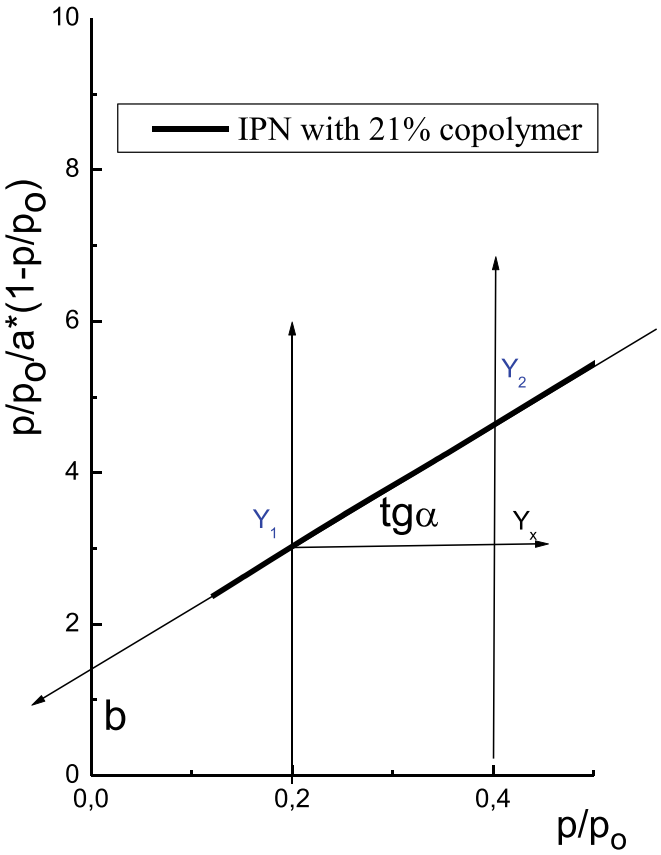

$a_m = 1/(k+b)$, where
$k = tg\alpha$; b – segment on the y-axis.

Fig. 18.9 Scheme for calculation of the amount of adsorbed substance in a monomolecular layer

$$S_{\text{spec}} = a_m \, \omega \, N_a \cdot 10^{-7} \tag{18.7}$$

where N_a—is the Avogadro's number;

ω—the area occupied by one sorbate molecule.

The area occupied by one sorbate molecule ω was calculated by the formula:

$$\omega = 4 \cdot 0.866 \cdot (M/4 \cdot \sqrt{2} \cdot d \cdot N_a)^{\frac{2}{3}}, \tag{18.8}$$

where

M—is the molecular weight of the sorbate;

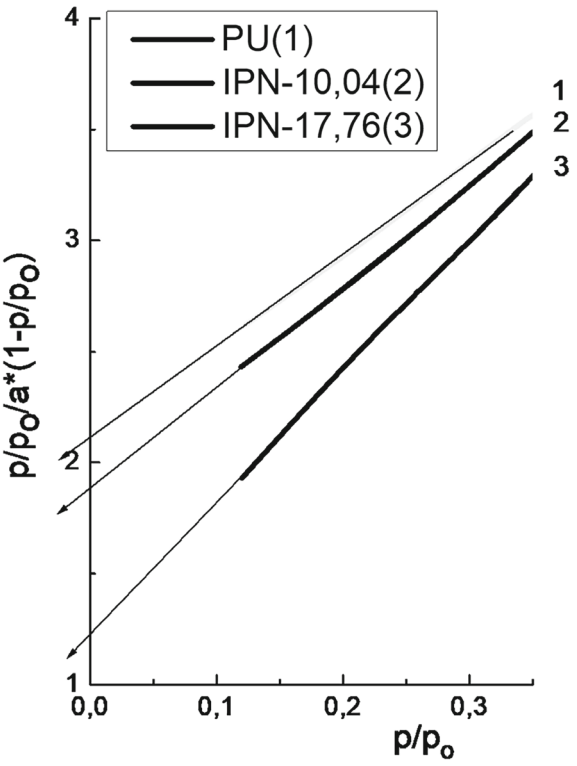

Fig. 18.10 Experimental data on the isothermal adsorption of methanol vapors at 20 °C by polyurethane and IPNs samples, presented in the form of the BET equation: PU (1), IPNs with content of copolymer 10% (2), IPNs with content of copolymer 18% (3)

d—is the density of the sorbate.

The results of the calculations are presented in Table 18.4.

Table 18.4 shows that the specific surface area of PU and IPNs samples based on PU and the copolymer of 2-hydroxyethyl methacrylate with methacryloyloxyethyl phosphorylcholine S_{sp} varies from 15.1 to 23.3 m^2/g. The specific surface area of the IPNs samples have a tendency of increasing with the copolymer content (from 15.1 to 23.3) m^2/g.

The specific surface area of polyurethane is 17.4 m^2/g. When adding a copolymer in the amount of 10% and 18%, the specific surface area decreases in compare with the polyurethane. But with a further increase in the amount of copolymer (21–51)%, the specific surface area of the IPNs increases from 19.1 m^2/g to 23.3 m^2/g.

Based on the adsorption isotherms of methanol vapors, the total pore volume in PU and IPNs samples based on PU and copolymer of 2-hydroxyethyl methacrylate with methacryloyloxyethylphosphorylcholine was also calculated.

The total pore volume in samples W_0 was avaluated using the maximum amount of methanol adsorbed by samples according to the formula [46]:

$$W_0 = aV, \tag{18.9}$$

Table 18.4 Porosity, specific surface area and total pore volume of IPNs samples based on polyurethane and copolymer of 2-hydroxyethyl methacrylate with methacryloyloxyethylphosphorylcholine

Sample	tgα	b	a_m, mmol/g	S_{sp}, m^2/g	a_{max}, mmol/g	W_0, cm^3/g	r_{av}, Å
PU	4.15	2.09	0.16026	17.4	6.79×10^{-1}	2.75×10^{-2}	31.67
IPNs 10% copolymer	5.90	1.26	0.13966	15.1	6.58×10^{-1}	2.66×10^{-2}	35.22
IPNs 18% copolymer	4.90	1.88	0.14749	16.0	6.52×10^{-1}	2.64×10^{-2}	33.04
IPNs 21% copolymer	3.90	1.78	0.17606	19.1	6.83×10^{-1}	2.76×10^{-2}	29.00
IPNs 30% copolymer	3.95	1.55	0.18182	19.7	7.27×10^{-1}	2.94×10^{-2}	29.89
IPNs 41% copolymer	3.65	2.12	0.17331	18.8	7.11×10^{-1}	2.88×10^{-2}	30.67
IPNs 51% copolymer	2.45	2.20	0.21505	23.3	7.69×10^{-1}	3.11×10^{-2}	26.73

where *a*—is the maximum amount of sorbate, absorbed by 1 g of sorbent, mol / g;

V—is the volume of one mole of sorbate.

The results of the calculations are shown in Table 18.4. It can be seen that the total pore volume W_0 of the samples varies from 2.66×10^{-2} cm^3/g to 3.11×10^{-2} cm^3/g. With the adding of a copolymer, the total pore volume in the IPNs increases with the increase in the amount of the second component.

The average pore radius of PU and IPNs samples based on PU and the copolymer of 2-hydroxyethyl methacrylate with methacryloyloxyethylphosphorylcholine was calculated according to the equation [37]:

$$r_{av} = (2W_0/S_{spec}) \cdot 10^4 (Å) \tag{18.10}$$

The results of the calculations are shown in Table 18.4. It can be seen that the average pore size in the studied samples of polyurethane and IPNs varies from 26 to 35 Å. According to Dubinin's classification [46], the studied samples belong to materials with transitional pores. According to this classification, materials with pore size up to 20 Å are classified as microporous, and those with pores larger than 200 Å are classified as macroporous. If the samples have pores with a size from 20 to 200 Å, such pores are classified as transition pores.

In addition, it can be seen from Table 18.4, that when the copolymer is added, the average pore size slightly increases in compare with polyurethane (for example, from 31 Å to 35 Å). But with a further increase in the amount of copolymer in the IPNs, there is a tendency of decreasing the average pore size (from 35 to 26) Å.

Therefore, it can be concluded that the IPNs based on PU and the copolymer of 2-hydroxyethyl methacrylate with methacryloyloxyethylphosphorylcholine belong to

materials with transition pores of size from 26 to 35 Å and can be used as biomedical coatings.

18.3.4 Morphology of IPNs Based on Polyurethane and Copolymer of 2-Hydroxyethyl Methacrylate with Methacryloyloxyethylphosphorylcholine

Figure 18.11 shows the microphotographs of the surface of fresh fractures of samples of the native polymers—polyurethane, HEMA-MPC copolymer and IPNs based on them with variation in the content of components at a magnification of 10,000 times. From the microphotographs it can be seen that the structure of polyurethane and the HEMA-MPC copolymer are significantly different.

The fracture of the polyurethane sample is similar to the fracture of a plastic material, while the fracture of the copolymer resembles a vitreous material. For IPNs containing 10 and 17% of copolymer, a homogeneous structure is observed without signs of phase separation.

But when moving to IPNs containing 21 and 30% of copolymer in the structure of IPNs the appearance of the second phase arise. SEM microphotographs recorded the presence of the inclusions with size of 0.5–1 μm. IPNs samples containing 41 and 51% of copolymer are significantly different in the structure from the previous samples. They show a significant phase separation, on the microphotographs the phase inclusions with a size of 1–5 μm are observed.

Therefore, the results of the morphology investigations of the samples of IPNs systems based on polyurethane and the HEMA-MPC copolymer, obtained by the SEM method, are consistent with the data of the study of the thermodynamic compatibility of polymers during the formation of IPNs systems. Exactly during the transition of the free energy of polyurethane and copolymer mixing from a negative value to a positive value, the signs of the beginning of phase separation are observed in the micrographs of the fractures of these samples. With a significant increase in the positive values of the free energy of polyurethane and the copolymer mixing in the IPNs with a content of 41 and 51% of the copolymer, a significant phase separation is observed, with phase inclusions ranging in size from 1 to 5 μm.

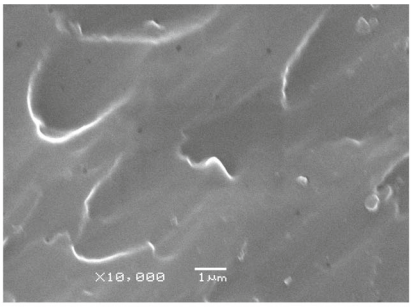

(a) PU

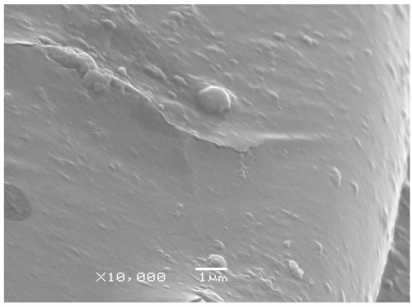

(b) Copolymer

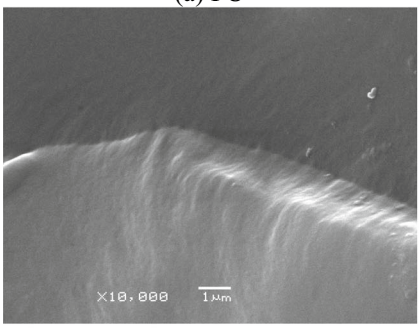

(c) 17% of Copolymer

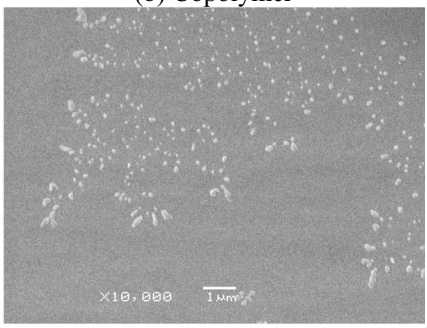

(d) 30 % of Copolymer

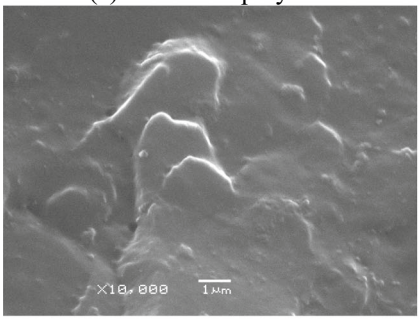

(e) 41% of Copolymer

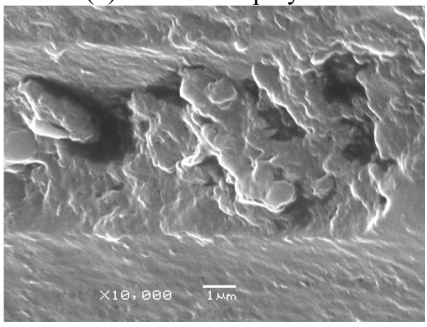

(f) 51% of Copolymer

Fig. 18.11 Microphotographs of polyurethane, of copolymer HEMA-MPC, and IPNs of different compositions with an increase of 10,000 time

18.3.5 Physical and Mechanical Properties of IPNs, Created from PU and Copolymer of 2-Hydroxyethyl Methacrylate with Methacryloyloxyethylphosphorylcholine

The physical and mechanical properties of the IPNs samples, which were synthesized in the form of films with a thickness of 0.7–0.9 mm, were studied using an automated Instron material testing system. The stress–strain curves for the samples based on polyurethane and copolymer of 2-hydroxyethyl methacrylate with methacryloyloxyethylphosphorylcholine, shown in Fig. 18.12a, b are averaged curves for three tests performed on each IPNs sample.

They indicate that the ultimate strength increases with increasing copolymer content in the IPNs. At the same time, the strain at break also increases with an increase in the copolymer content in the samples up to 30%. For the last two samples with 41 and 51% of copolymer content, the strain at break decreases dramatically, but the stress at break continues to increase for these samples.

Our assumption about the formation of ionic clusters in IPNs with a copolymer content of more than 30% [42] is confirmed by these results. Exactly the formation of ionic clusters in the IPNs could be the reason for the reduction of deformation when the system breaks (Fig. 18.12, curves 7, 8). Ionic clusters are composed of ionic groups from different polymer chains, and they can create additional "physical bonds" and, as a result, can limit the deformation of samples.

The detailed mechanical properties of the IPNs are shown in Table 18.5. They reflect the changes in the structure of the IPNs with an increase in the amount of copolymer of 2-hydroxyethyl methacrylate with methacryloyloxyethylphosphorylcholine in the system. Deformation at break has an extremum at 30% of copolymer. The tensile stress increases from 4.3 to 18.4 MPa with an increase in the amount of copolymer in the IPNs (Table 18.5).

It is important to note that Young's modulus increases from 14.5 to 324.4 MPa with increasing amount of copolymer in the system. A particularly sharp increase in the modulus is observed for IPNs with 30% or more copolymer in the samples. This is additional evidence of the formation of ionic clusters in the IPNs with a high content of copolymer. The formation of ionic clusters in the IPNs leads to strengthening of the samples.

18.4 Conclusion

Interpenetrating polymer networks based on biocompatible components—polyurethane and copolymer of 2-hydroxyethyl methacrylate with methacryloyloxyethylphosphorylcholine (HEMA-MPC) were synthesized and thermodynamic parameters of interactions in the system, dynamic mechanical properties, porosity of the samples, morphology and physico-mechanical properties were investigated. The

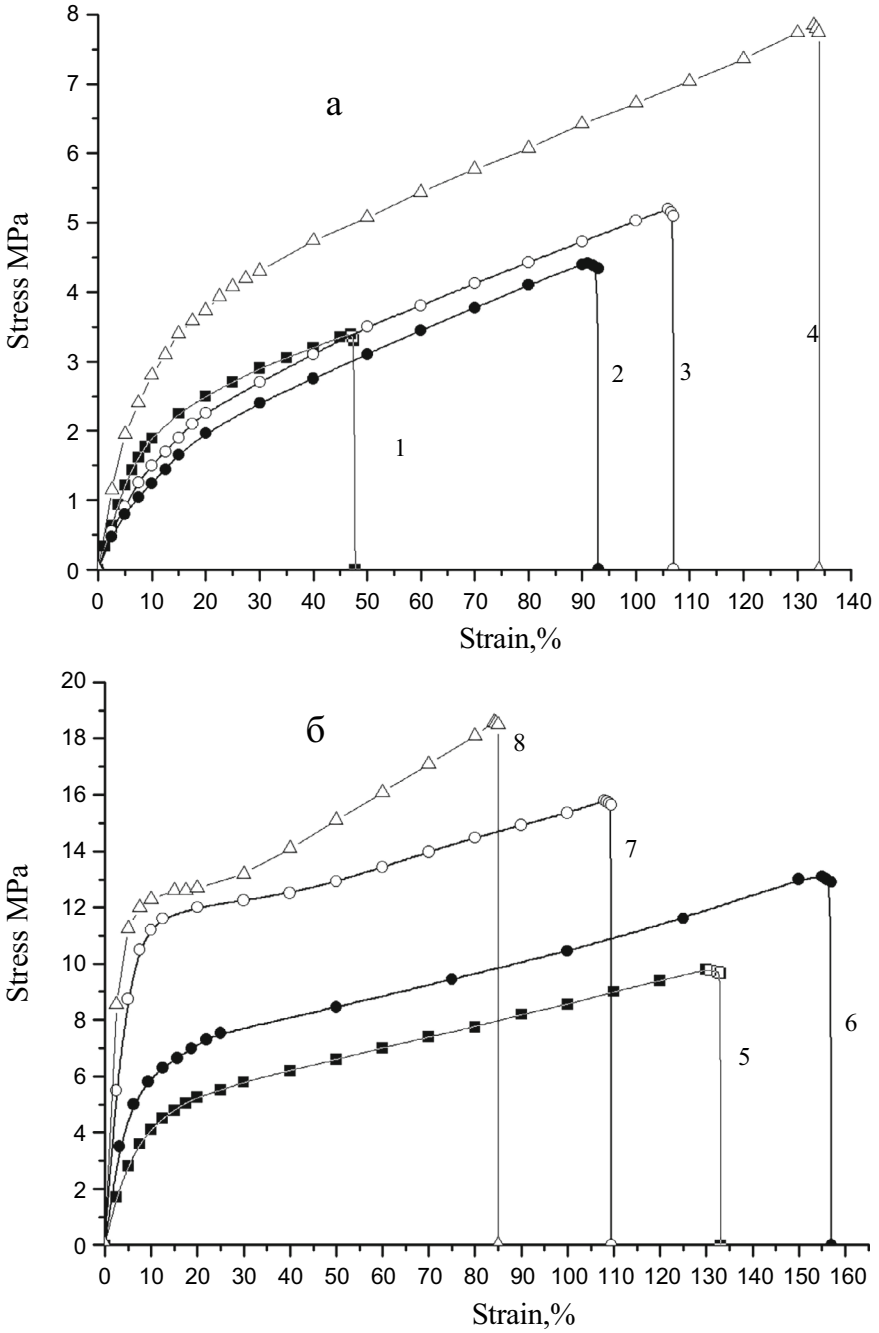

Fig. 18.12 Stress–strain curves for PU and IPNs films: 1- PU; 2- IPNs with 7% of copolymer; 3- IPNs with 10% of copolymer; 4- IPNs with 18% of copolymer; 5- IPNs with 21% of copolymer; 6- IPNs with 30% of copolymer; 7- IPNs with 41% of copolymer; 8- IPNs with 51% of copolymer

Table 18.5 Mechanical properties of interpenetrating polymer networks based on polyurethane and copolymer of 2-hydroxyethyl methacrylate with methacryloyloxyethylphosphorylcholine

Sample	Elongation at the peak (%)	Stress at the peak (MPa)	Elongation at break (%)	Stress at break (MPa)	Young's modulus(MPa)
PU	56.8	2.5	58.2	2.4	7.7
IPNs 7% copolymer	91.6	4.4	91.8	4.3	14.5
IPNs 10% copolymer	106.3	5.2	106.5	5.0	18.3
IPNs 18% copolymer	134.4	7.8	134.5	7.7	44.7
IPNs 21% copolymer	130.6	9.8	131.8	9.4	65.0
IPNs 30% copolymer	153.3	13.1	153.7	13.1	101.4
IPNs 41% copolymer	108.2	15.7	108.3	15.7	218.4
IPNs 51% copolymer	85.1	18.6	85.5	18.4	324.4

thermodynamic parameters of interactions between polymer components of the IPNs were calculated based on isotherms of methylene chloride vapors sorption by samples of the created polymer systems. It is shown that MPC plays the role of a compatibilizer in the system, increasing the thermodynamic compatibility between polyurethane and the HEMA-MPC copolymer at small amounts of the copolymer in the IPNs. As the amount of copolymer HEMA-MPC in the IPNs increases, the value of the free energy of the polyurethane and copolymer mixing moves to the positive value, what can be explained by the formation of ionic clusters of MPC. With an increasing of the amount of MPC in the system, interactions between the negatively charged phosphoryl groups and the positively charged nitrogen atom of various MPC polymer chains occur, i.e., the part of intermolecular interactions (polyurethane and copolymer) decreases, while the part of intramolecular interactions (between different groups of MPC) increases. By dynamic mechanical properties investigations the two maxima of tanδ were observed for the IPNs. The polyurethane maximum tanδ in the IPNs decreases by amplitude compared to the native polyurethane, that means the suppressing effect of the copolymer on the segmental motions in the PU. For the maxima of tanδ of the copolymer HEMA with MPC in the IPNs, a significant decrease in intensity and a shift along the temperature scale towards low temperatures in compare with the maximum of tanδ of the native copolymer was observed. Such behavior allow to conclude that these IPNs are two-phase systems with incomplete phase separation. The results of the morphology investigations of the IPNs samples are consistent with the data of the thermodynamic compatibility study of polymers during the formation of the IPNs. With a significant increase in the positive values of the free energy

of the polyurethane and copolymer mixing in the IPNs with 41% and 51% of the copolymer content, a significant phase separation is observed in the IPNs, with phase inclusions ranging from 1 to 5 μm. The results of physico-mechanical properties testing reflect the changes in the structure of the IPNs with an increase in the amount of copolymer of 2-hydroxyethyl methacrylate with methacryloyloxyethylphosphorylcholine in the system. The tensile stress increases from 4.3 MPa to 18.4 Mpa, the Young's modulus increases from 14.5 MPa to 324.4 MPa with an increase in the amount of copolymer in the IPNs. Deformation at break has an extremum at 30% of copolymer. A particularly sharp increase in the modulus is observed for IPNs with 30% or more copolymer in the samples. Results of porosity investigation allow to conclude that the IPNs based on PU and the copolymer of 2-hydroxyethyl methacrylate with 2-methacryloyloxyethylphosphorylcholine belong to materials with transition pores of size from 26 to 35 Å. The enough good physico-mechanical properties of the IPNs based on biocompatible components – polyurethane and copolymer of 2-hydroxyethyl methacrylate with methacryloyloxyethylyphosphorylcholine and existence of transition pores of size from 26 to 35 Å allow to assume that created materials can be used as biomedical coatings. The positive value for biomedical application also is that the nanostructured surface of the created IPNs samples could decrease the bacterial adhesion on the surface of such materials.

References

1. H. Durand, A. Whiteley, P. Mailey, G. Nonglaton, Combining chemistry and topography to produce antifouling surfaces, a review. ACS Appl. Bio Mater. **5**(10), 4718–4740 (2022). https://doi.org/10.1021/acsabm.2c00586
2. Y. Wang, F. Wang, H. Zhang, B. Yu, H. Cong, Y. Shen, Antibacterial material surfaces/interfaces for biomedical applications. Appl. Mater. Today **25**, 101–192 (2021). https://doi.org/10.1016/j.apmt.2021.101192
3. Q.H. Zhao, A.K. McNally, K.R. Rubin, M. Renier, Y.V. Wu, V. Rose-Caprara, A. Hiltner, P. Urabanski, K. Stokes, Human plasma α_2-macroglobulin promotes in vitro oxidative stress cracking of pellethane 2363–80A: in vivo and in vitro correlations. J. Biomed. Mater. Res. **27**(3), 379–388 (1993). https://doi.org/10.1002/jbm.820270311
4. C.M. Lim, M.X. Li, Y.K. Joung, Surface-modifying polymers for blood-contacting polymeric biomaterials. Biomimicked Biomaterials: Adv. Tissue Eng. Regenerat. Med. Adv Exp. Med. Biol. **1250**,189–198 (2020). H.J. Chun, R.L. Reis, A. Motta, G. Khang (eds.) *Advances in Experimental Medicine and Biology*(Springer, Singapore, 2020), pp 189–198. https://doi.org/10.1007/978-981-15-3262-7_13
5. I.K. Kang, O.H. Kwon, M.K. Kim, Y.M. Lee, Y.K. Sung, In vitro blood compatibility of functional group-grafted and heparin-immobilized polyurethanes prepared by plasma glow discharge. Biomaterials **18**(16), 1099–1107 (1997). https://doi.org/10.1016/s0142-9612(97)00035-5
6. K. Ishihara, H. Hanyuda, N. Nakabayashi, Synthesis of phospholipid polymers having a urethane bond in the side chain as coating material on segmented polyurethane and their platelet adhesion-resistant properties. Biomaterials **16**(11), 873–879 (1995). https://doi.org/10.1016/0142-9612(95)94150-j

7. R.G. Flemming, R.A. Proctor, S.I. Cooper, Bacterial adhesion to functionalized polyurethanes. J. Biomater. Sci. Polym. Edn. **10**(6), 679–697 (1999). https://doi.org/10.1163/156856299X00874
8. A.B. Mathur, T.O. Collier, W.J. Kao, M. Wiggins, M.A. Schubert, A. Hiltner, J.M. Anderson, In vivo biocompatibility and biostability of modified polyurethanes. J. Biomed. Mater. Res. **36**(2), 246–257 (1997). https://doi.org/10.1002/(SICI)1097-4636(199708)36:2%3c246::AID-JBM14%3e3.0.CO;2-E
9. F. Chen, D. Zhang, Q. Yang, J. Yong, G. Du, J. Si, F. Yun, X. Hou, Bioinspired wetting surface via laser microfabrication. ACS Appl. Mater. Interfaces **5**(15), 6777–6792 (2013). https://doi.org/10.1021/am401677z
10. K. Ishihara, S. Tanaka, N. Furukawa, K. Kurita, N. Nakabayashi, Improved bloodcompatibility of segmented polyurethanes by polymeric additives having phospholipid polar groups. I. Molecular design of polymeric additives and their functions. J. Biomed. Mater. Res. **32**(3), 391–399 (1996). https://doi.org/10.1002/(SICI)1097-4636(199611)32%3A3%3C391%3A%3AAID-JBM12%3E3.0.CO2-K
11. K. Ishihara, N. Shibata, S. Tanaka, Y. Iwasaki, T. Kurosaki, N. Nakabayashi, Improved blood compatibility of segmented polyurethane by polymeric additives having phospholipid polar group. II. Dispersion state of the polymeric additive and protein adsorption on the surface. J. Biomed. Mater. Res. **32**(3), 401–408 (1996). https://doi.org/10.1002/(SICI)1097-4636(199611)32:3%3C401%3A%3AAID-JBM13%3E3.0.CO%3B2-J
12. Y. Iwasaki, Y. Aiba, N. Morimoto, N. Nakabayashi, K. Ishihara, Semi-interpenetrating polymer networks composed of biocompatible phospholipid polymer and segmented polyurethane. J. Biomed. Mater. Res. **52**(4), 701–708 (2000). https://doi.org/10.1002/1097-4636(20001215)52:4%3c701::AID-JBM15%3e3.0.CO;2-6
13. H.W. Roh, M.J. Song, D.K. Han, D.S. Lee, J.H. Ahn, S.C. Kim, Effect of cross-link density and hydrophilicity of PU on blood compatibility of hydrophobic PS/hydrophilic PU IPNs. J. Biomater. Sci. Polym. Edn. **10**(1), 123–143 (1999). https://doi.org/10.1163/156856299X00324
14. J.H. Lee, Y.M. Ju, D.M. Kim, Platelet adhesion onto segmented polyurethane film surfaces modified by addition and crosslinking of PEO-containing block copolymers. Biomaterials **21**, 683–691 (2000). https://doi.org/10.1016/S0142-9612(99)00197
15. F. Abbasi, H. Mirzadeh, A.A. Katbab, Modification of polysiloxane polymers for biomedical applications: a review. Polym. Int. **50**(12), 1279–1287 (2001). https://doi.org/10.1002/pi.783
16. Y. Iwasaki, K. Ishihara, Cell membrane-inspired phospholipid polymers for developing medical devices with excellent biointerfaces. Sci. Technol. Adv. Mater. **13**(6), 064101 (2012). https://doi.org/10.1088/1468-6996/13/6/064101
17. K. Ishihara, K. Fukazawa, 2-Methacryloyloxyethyl phosphorylcholine polymer, in *Phosphorus-Based Polymers: From Synthesis to Applications,* Chapter ,. ed. by S. Monge, G. David, (RSC publishing, Cambridge, UK, 2014), pp. 68–96. https://doi.org/10.1039/9781782624523-00068
18. T.L. Nguyen, Y. Kawata, K. Ishihara, S. Yusa, Synthesis of amphiphilic statistical copolymers bearing methoxyethyl and phosphorylcholine groups and their self-association behavior in water. Polymers (2020). https://www.mdpi.com/2073-4360/12/8/1808
19. K. Ishihara, H. Nomura, T. Mihara, K. Kurita, Y. Iwasaki, N. Nakabayashi, Why do phospholipid polymers reduce protein adsorption? J. Biomed. Mater. Res. **39**(2), 323–330 (1998). https://doi.org/10.1002/(sici)1097-4636(199802)39:2%3c323::aid-jbm21%3e3.0.co;2-c
20. K. Ishihara, Y. Iwasaki, C. (2001) Phospholipid polymer biomaterials for making ventricular assist devices. J Conges Heart Circul Support 1(4):265–270. https://doi.org/10.1201/b14731-22
21. T. Yoneyama, K. Ishihara, N. Nakabayashi, M. Ito, Y. Mishima, Short-term in vivo evaluation of small-diameter vascular prosthesis composed of segmented poly(etherurethane)/2-methacryloyloxyethyl phosphorylcholine polymer blend. J. Biomed. Mater. Res. **43**(1), 15–20 (1998). https://doi.org/10.1002/(SICI)1097-4636(199821)43:1%3c15::AID-JBM2%3e3.0.CO;2-P
22. T. Yoneyama, M. Ito, K. Sugihara, K. Ishihara, N. Nakabayashi, Small diameter vascular prosthesis with a nonthrombogenic phospholipid polymer surface: preliminary study of a new

concept for functioning in the absence of pseudo- or neointima formation. Artif. Organs **24**(1), 23–28 (2000). https://doi.org/10.1046/j.1525-1594.2000.06433.x
23. K. Ishihara, H. Fujita, T. Yoneyama, Y. Iwasaki, Antithrombogenic polymer alloy composed of 2-methacryloyloxyethyl phosphorylcholine polymer and segmented polyurethane. J. Biomater. Sci. Polym. Edn. **11**(11), 1183–1195 (2000). https://doi.org/10.1163/156856200744264
24. A.W. Lloyd, R.G.A. Faragher, S.P. Denyer, Ocular biomaterials and implants. Biomaterials **22**(8), 769–785 (2001). https://doi.org/10.1016/s0142-9612(00)00237-4
25. A.B. Lowe, M. Vamvakaki, M.A. Wassall, L. Wong, N.C. Billingham, S.P. Armes, A.W. Lloyd, Well-defined sulfobetaine-based statistical copolymers as potential antibioadherent coatings. J. Biomed. Mat. Res. **52**(1), 88–94 (2000). https://doi.org/10.1002/1097-4636(200010)52:1<88::AID-JBM11>3.0.CO;2-%23
26. L.V. Karabanova, S.V. Mikhalovsy, L.M. Sergeeva, S.T. Meikle, M. Helias, A.W. Lloyd, Semi-interpenetrating polymer networks based on polyurethane and poly(vinyl pyrrolidone) obtained by photopolymerization: Structure-property relationships and bacterial adhesion. Polym. Eng. Sci. **44**(5), 940–947 (2004). https://doi.org/10.1002/pen.20085
27. L.V. Karabanova, L.V. Sergeeva, S.V. Mikhalovsky, J. Salvage, S. Butler, A.W. Lloyd, *Proceedings of the 9 International Conference "Polymers in Medicine and Surgery"*. Krems, Austria, September 13 (2000)
28. L.V. Karabanova, A. Lloyd, S. Mikhalovsky, M. Helias, G.P. Philips, S. Rose, L. Mikhalovska, G. Boiteux, L.M. Sergeeva, E.D. Lutsyk, A. Udovichenko, Polyurethane/poly(2-hydroxyethyl methacrylate) semi-IPN for biomedical materials applications. J. Mater. Sci. - Mater. Med. **17**(12), 1283–1296 (2006). https://doi.org/10.1007/s10856-006-0603-y
29. Y.S. Lipatov, L.V. Karabanova, *Advances in Interpenetrating Polymer Networks* (Technomic Publ, Company Inc, Lancaster, 1994), p.191
30. Y.S. Lipatov, *Advances in Interpenetrating Polymer Networks* (Technomic Publ, Company Inc, Lancaster, 1989), p.261
31. L.V. Karabanova, S.V. Mikhalovsky, A.W. Lloyd, G. Boiteux, L.M. Sergeeva, T.I. Novikova, E.D. Lutsyk, S. Meikle, Gradient semi-interpenetrating polymer networks based on polyurethane and poly(vinyl pyrrolidone). J. Mater. Chem. **15**(4), 499–507 (2005). https://doi.org/10.1039/B410178B
32. Y.S. Lipatov, L.V. Karabanova, L.M. Sergeeva, Thermodynamic state of reinforced interpenetrating polymer networks. Polym. Int. **34**(1), 7–13 (1994). https://doi.org/10.1002/pi.1994.210340102
33. M. Dror, M.Z. Elsabee, G.C. Berry, Interpenetrating polymer networks for biological applications. Biomater. Med. Devices Artif. Organs **7**(1), 31–39 (1979). https://doi.org/10.3109/10731197909119370
34. P. Predecki, A method for Hydron impregnation of silicone rubber. J. Biomed. Mater. Res. **8**(6), 487–489 (1974). https://doi.org/10.1002/jbm.820080615
35. P.D. Nair, V.N. Krishnamurthy, Polyurethane–poly(methyl methacrylate) interpenetrating polymer networks. I. Synthesis, characterization, and preliminary blood compatibility studies J. Appl. Polymer Sci. **60**(9), 1321–1327 (1996). https://doi.org/10.1002/(SICI)1097-4628(19960531)60%3A9%3C1321%3A%3AAID-APP7%3E3.0.CO%3B2-L
36. Gregg, S.J., Sing, K.S. *Adsorption, Specific Surface Area, Porosity*. (Mir, Moscow, 1970), p. 408 [in Russian]
37. A.A. Tager, *Phiziko-Chimiya Polimerov* (Khimiya, Moscow, 1978), p. 544 [in Russian]. ISBN 978-545-828-195-9
38. A.A. Tager, Thermodynamics of mixing of polymers and thermodynamic stability of polymer compositions. Vysokomol. Soed. A **19**(8), 1659–1669 (1977)
39. Y.S. Lipatov, L.V. Karabanova, T.S. Hramova, L.M. Sergeeva, Issledovaniye fiziko-khimicheskikh svoystv vzaimopronikayushchikh polimernykh setok na osnove poliuretana i poliuretanakrilata. Vysokomol. Soed. A **20**(1), 46–54 (1978). [in Russian]
40. Y.S. Lipatov, L.V. Karabanova, L.M. Sergeeva, E.Y. Gorichko, Issledovaniye sorbtsii i diffuzii vo vzaimopronikayushchikh polimernykh setkakh na osnove poliuretana i poliuretanovogo ionomera. Vysokomol. Soed. A **24910**, 110–116 (1982). [in Russian]

41. Y.S. Lipatov, L.V. Karabanova, L.M. Sergeeva, L.A. Gorbach, S.I. Skiba, Termodinamicheskoye issledovaniye vzaimopronikayushchikh polimernykh setok na osnove poliuretana i poliefirakrilata. Vysokomol. Soed. A **28**(4), 274–277 (1986). ([in Russian])
42. L.V. Karabanova, G. Boiteux, G. Seytre, I. Stevenson, A.W. Lloyd, S.V. Mikhalovsky, M. Helias, L.M. Sergeeva, E.D. Lutsyk, A. Svyatyna, Phase separation in the polyurethane/poly(2-hydroxyethyl methacrylate) semi-interpenetrating polymer networks synthesized by different ways. Polym. Eng. Sci. **48**(3), 588–597 (2008). https://doi.org/10.1002/pen.20965
43. L.E. Nielsen, *Mechanical Properties of Polymers and Composites* (Marcel Dekker Inc., New York, 1974). https://doi.org/10.1016/0032-3861(75)90022-1
44. Y.S. Lipatov, V.F. Rosovitsky, Physical chemistry of multicomponent polymer systems. Naukova dumka, Kyiv. **2**, 229–255 (1986). ([in Russian])
45. S. Brunauer, P.H. Emmett, E. Teller, Adsorption of gases in multimolecular layers. JACS **60**(2), 309–319 (1938). https://doi.org/10.1021/ja01269a023
46. M.M. Dubinin, The potential theory of adsorbtion of gases and vapors for adsorbents with energetically nonuniform surfaces. Chem. Rev. **60**(2), 235–241 (1960)

Chapter 19
Effect of Temperature on the Formation of Liquid Clathrates in Aqueous Solutions of Dyes

N. Atamas, G. Taranyik, and A. Makhinia

Abstract The molecular dynamics method was used to analyze the possibility of liquid clathrate formation in water solution of indigo carmine in the physiological temperature range. Based on the results of studying the effect of temperature on the processes of liquid clathrate formation in aqueous solutions of indigo carmine, it was found that liquid clathrate formation is possible at temperatures of T = 303 K, 305 K, 310 K, 313 K, 315 K, 318 K, 319 K.

19.1 Introduction

Indigo carmine ($C_{16}H_8N_2Na_2O_8S_2$) is a dye widely used in medical diagnostics and pharmacology [1]. Understanding its behavior in water, including its detection, degradation and removal, is of critical importance for environmental and health applications. In particular, indigo carmine (IC), used as a dye and viscosity marker, can serve as an indicator of physiological changes in the body under different temperature conditions. Therefore, understanding the dynamics of IC under different temperature conditions, including the physiological range of T = (300−323)K in aqueous solutions, can contribute to the assessment of its safety and possible side effects, which is especially important for minimizing risks in medical use. Current studies on aqueous solutions of indigo carmine are conducted using various experimental methods: the presence of indigo carmine can be effectively detected in water samples using square wave voltammetry (SWV) with a treated cathode boron doped electrode (BDD). This method provides a linear concentration range from 0.5 to 84.1 μmol

N. Atamas (✉)
Taras Shevchenko National University of Kyiv, Kyiv, Ukraine
e-mail: atamasphys@univ.kiev.ua

G. Taranyik
International European University, Kyiv, Ukraine

A. Makhinia
Vienna University, Vienna, Austria

O. Fesenko and L. Yatsenko (eds.), *Functional Nanomaterials, Nanocatalysts, Nanotechnologies, and Their Applications*, Springer Proceedings in Physics 321,
https://doi.org/10.1007/978-3-031-99136-3_19

L^{-1} with a detection limit of 0.058 μmol L^{-1}. The BDD electrode shows the best characteristics for the anodic response IC compared to other electrodes, making it a reliable tool for environmental monitoring [2]; the effect of temperature on the degradation processes of indigo carmine in water can be studied using advanced oxidation technologies (AOTs). The research results [3] show that the degradation of indigo carmine in water can be achieved using non-thermal plasma (NTP), ozone and hydrogen peroxide. It was found that the degradation process involves the formation of transient radicals OH, O and NO, which contribute to the change in the chemical properties of water, such as pH, conductivity and oxidation-reduction potential, which affects the structural and dynamic characteristics of water. However, the experimental methods described above leave open the question of what intermolecular interactions and how they affect the formation of macro-characteristics of aqueous solutions of IC at different temperatures. At the same time, with regard to aqueous solutions of dyes, special attention is paid to the possibility of the formation of liquid clathrates in them, which can have a significant effect on the dynamic, and therefore, physicochemical properties of IC solutions and their functional application. Therefore, the main issue within the framework of the presented study is to determine the effect of temperature in the physiological temperature range on the processes of clathrate formation in an aqueous solution of IC at the physiological range of temperature T = (300–323) K.

19.2 Methods

The molecular dynamics method (MD) implemented using DL_POLY_4.06 was used to study the effect of temperature on liquid clathrate formation in an aqueous solution of IC at T = (300–323)K. Intermolecular interactions in the studied systems were described by the sum of Lennard–Jones and Coulomb components [4]:

$$U = U_{L-J} + U_{Coulon} = \sum_{ij} 4\varepsilon_{ij}\left[\left(\frac{\sigma_{ij}}{r_{ij}}\right)^{12} - \left(\frac{\sigma_{ij}}{r_{ij}}\right)^{6}\right] + \sum_{ij}\frac{q_i q_j}{r_{ij}} \qquad (19.1)$$

where the values of the parameters $\sigma^{ab}{}_{ij}$, $\varepsilon^{ab}{}_{ij}$ are *L-J* parameters at the site *a* in molecule *i* and the site *b* in a molecule *j*, respectively, $r^{ab}{}_{ij}$ is the distance between sites a and b, $q^{a}{}_{i}$ and $q^{b}{}_{i}$ are the charges at sites a and b, respectively, and ε_0 is the vacuum permittivity. The OPLS force field calculations of IC were performed using the DLPOLY_FIELD package. The interactions between water molecules were modeled using the SPC/E potentials. The potential parameters $\sigma^{ab}{}_{ij}$ and $\varepsilon^{ab}{}_{ij}$ for the interaction between the atoms of the solute (IC) with the atoms of the water molecules are calculated using the Lorentz–Berthelot combination rule [4]. In the first step, the calculations were performed for a system consisting of one molecule of IC and 218 water molecules with a density equal to the density of water at T = 323 K. This configuration was equilibrated in the NPT ensemble for $1*10^6$ steps and

then re-equilibrated in the NVT ensemble using the Berendsen thermostat for $1*10^6$ steps. Electrostatic interactions were modeled taking into account the charges on the atoms, and long-range interactions were described using the Ewald summation. The configuration at T = 323 K was used as the initial one for the simulations at lower temperatures. The volume of the calculation box at each temperature was calculated based on the experimental data of the density of water at T = (300–323) K.

19.3 Results and Discussion

IC-water system can be treated as a mixture of large (ИК) and small (water) particles with a mass ratio of $\alpha_m = M_{large}/M_{small} = M_{indigo}/M_{water} > 25$ and the structural и dynamic properties in the IC-water systems at T = (300–323) K will be determined by the short-time diffusion. The dynamic properties of the system are determined by the temporal behavior of the mean-squared displacement (MSD) function $\langle\langle r^2(t)\rangle\rangle$, with represents the displacement vector of the center of mass of the i-th molecule between instants 0 and t and is described by [4]:

$$\langle r^2(t)\rangle = \left\langle \sum_{i=1}^{N} |\Delta r_i(t)|^2 \right\rangle / N \tag{19.2}$$

According to the Frenkel's theory and V-T formalism applied to the description of the particles' motion in liquid $\langle\langle r^2(t)\rangle\rangle$ can be represented as the following sum [5]:

$$\langle r^2(t)\rangle_D = \langle r^2(t)\rangle_{\text{vib-jamp}} + \langle r^2(t)\rangle_{tr} + \langle r^2(t)\rangle_{rw} + \langle r^2(t)\rangle_b \tag{19.3}$$

The interval at $0 < t_D$ is the time interval within which the motion can be described within different frameworks of the diffusion model representations. The crossover interval of diffusion at $t_D < t_{RW}$, $\langle r^2(t)\rangle_{rw}$ determines the transit random walk interval t_{RW}, within which the particle participates in the collective motion of the IC-water solutions. When analyzing the possibility of the formation of liquid clathrates, the greatest interest is aroused by $\langle r^2(t)\rangle_{rw}$, which in our case t_{RW} time is the time at which $\langle r^2(t)\rangle$ corresponds to the sub-diffused retarded motion of the "tracking" particle of IC in the collective motion of the water in the system. The t_D denotes the time when $\langle r^2(t)\rangle$ deviates from $\langle r^2(t)\rangle_{\text{vib - jamp}}$, as $\langle r^2(t)\rangle_{\text{vib - jamp}}$ interval only describes the vibrational-hopping mechanism of diffusion. Finally, the term $\langle r^2(t)\rangle_b$ determines the motion of IC or water due to ballistic collisions.

In the analysis of the temperature effect on clathrate formation processes in the systems under study, the main emphasis is placed on the analysis of the $\langle r^2(t)\rangle_{\text{rw}}$ interval, the existence of which can serve as an indicator of the existence of liquid clathrates formed by indigo carmine and surrounding water molecules, and the duration of this interval indicates the lifetime τ_c of these clathrates. In the work [6] when

studying the dynamic heterogeneity of IC in water, three temperature ranges were identified (T < 308 K; 310 K < T < 314 K, T > 318 K), in the area of which the temperature dependence of the diffusion coefficient of water differs, which deviates from linearity in the area of 310 K < T < 314 K. Moreover, it was established that the diffusion coefficient of IC decreases with increasing temperature also nonlinearly, namely, a change in the nature of the temperature dependence of IC is recorded at T = 303 K, T = 312 K and T = 318 K. In the temperature range 312 K < T < 318 K, the values of the diffusion coefficient of IC deviate from linearity and indicate a slowdown in the movement of IC in water. Analysis of the data (Fig. 19.1) shows that within the range T < 308 K, the formation of liquid clathrates is possible at T = 303 K and T = 305 K: within the second temperature range, the formation of clathrates is possible at T = 310 K, T = 313 K and T = 315 K; within the third temperature range, at T = 318 K and T = 319 K. Within the temperature range: 1) T < 308 K clathrates are formed at t = 930 ps (at T = 303 K, there are τ_c ~ 200 ps) and t = 300 ps (at T = 305 K, there are τ_c ~ 300 ps); 2) 308 K < T < 315 K clathrates are formed at t = 300 ps (at T = 310 K, there are τ_c ~ 650 pc), t = 700 ps (at T = 313 K, there are τ_c ~ 330 pc) and at t = 350 ps (at T = 315 K, there are τ_c ~ 400 ps); 3) T > 318 K clathrates are formed at t = 500 ps (at T = 318 K, there are τ_c ~ 200 pc), t = 450 ps (at T = 319 K, there are τ_c ~ 200 ps).

19.4 Conclusions

Based on the results of studying the temperature change on the processes of liquid clathrate formation in aqueous solutions of indigo carmine, it was found that liquid clathrate formation is possible at temperatures of T = 303K, T = 305K, T = 310K, T = 313K, T = 315K, T = 318K, T = 319K. The obtained results can be clarified by analyzing changes in the temperature dependences of the diffusion coefficients of the components of an aqueous solution of indigo carmine [6]. It is shown that at the boundaries of temperature intervals, cardinal changes occur in the nature of the movement of the components of the systems, which fixes a change in the slope of the temperature dependence of the diffusion coefficient of both water and indigo carmine. These changes are closely related to both changes in local structures in the region of the dissolved substance (indigo carmine) and changes in the predominant structures of water clusters under the influence of temperature, i.e. with the restructuring of the liquid. The greatest structural heterogeneity is recorded during the transition from one diffusion mode of liquid component motion to another; therefore, relatively long-lived systems of water and indigo carmine molecules cannot form at these temperatures. The lifetime of liquid clathrates within the first and second temperature ranges increases with increasing system temperature from τc ~ 170 ps (T = 303 K) to τ_c ~ 300 ps (T = 305 K) in the temperature region of the first range; τ_c ~ 330 pc (T = 313 K), τ_c ~ 400 ps (T = 313 K). Deviation from this trend is observed at temperature T = 310 K (τ_c ~ 650 ps), at which the longest lifetime of the liquid clathrate is recorded. This temperature is close to the temperature of 36 °C, at which the minimum specific

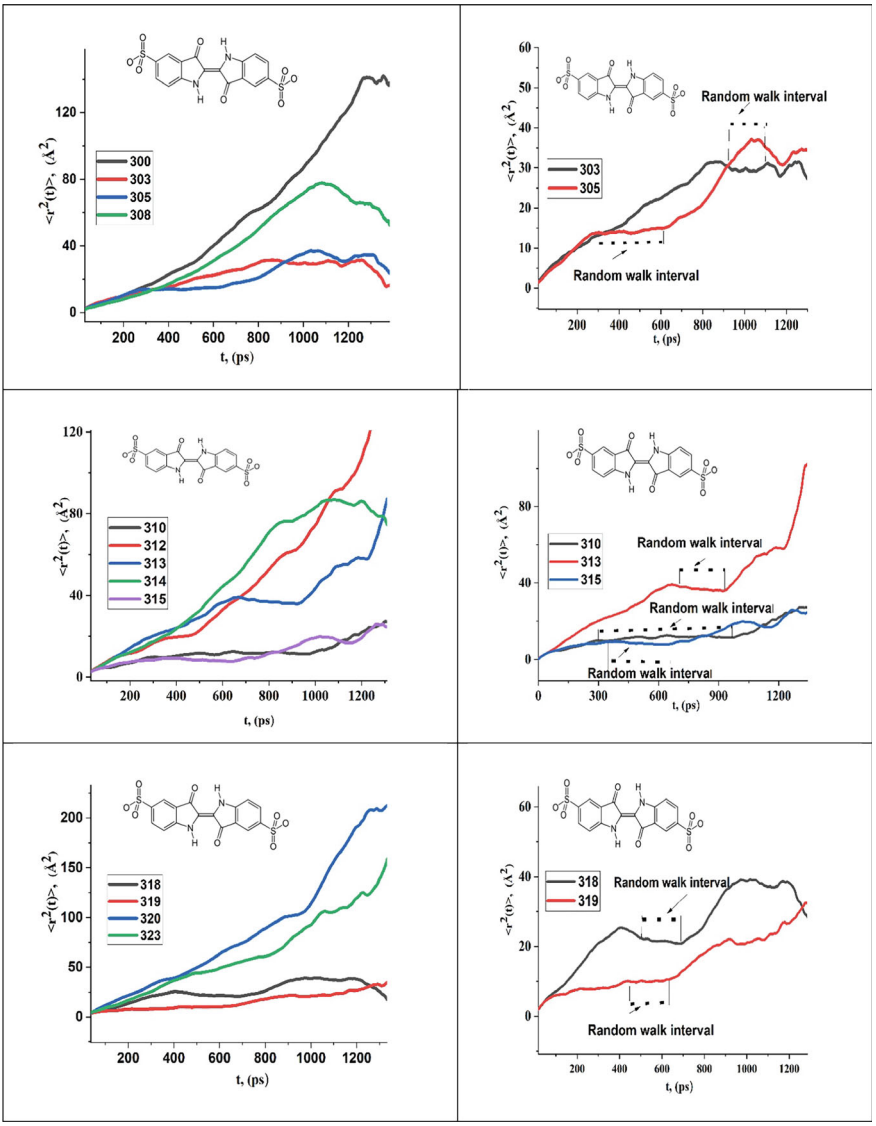

Fig. 19.1 Time dependence of the function MSD $\langle r^2(t)\rangle$ (left panel) and highlighted intervals $\langle r^2(t)\rangle_{\text{rw}}$ (right panel) of the MSD $\langle r^2(t)\rangle$ component of the center of mass of IC at temperatures T = (300–323) K

heat capacity (C_P) is recorded and water has anomalous properties [7]. Within the third temperature interval at T>318K the lifetime of liquid clathrates does not depend on temperature and is $\tau_c \sim 200$ ps. The time at which the presence of liquid clathrates begins to be recorded in the studied systems decreases within the first and third temperature intervals. Within the second temperature interval the dependence of the initial time of recording the existence of liquid clathrates is not observed, the reason for this may be the slowdown of dynamic processes in water, which is confirmed by the nonlinearity of the temperature dependence of the diffusion coefficient of water at these temperatures [8].

References

1. T. de Carvalho, Adsorption of indigo carmine from aqueous solution using coal fly ash and zeolite from fly ash. J. Radioanal. Nucl. Chem. **289**(2), 617–626 (2011)
2. T. Silva, Electroanalytical sensing of indigo carmine dye in water samples using a cathodically pretreated boron-doped diamond electrode. J. Electroanal. Chem. **769**, 28–34 (2016)
3. A. Crema, Degradation of indigo carmine in water induced by non-thermal plasma, ozone and hydrogen peroxide: a comparative study and by-product identification. Chemosphere **244**, 125502 (2019)
4. M.P. Allen, *Computer Simulation of Liquids* (Oxford University Press, 2017)
5. N.O. Atamas, Structure and dynamic inhomogeneity of liquids on the liquid-gas coexistence curve near the triple point. J. Phase Equilib. Diffus. **44**(6), 704–713 (2023)
6. N.O. Atamas, Competition between indigo carmine and water in the formation of dynamics behavior at different temperatures. Dyes Pigm. **226**, 112146 (2024)
7. V.P. Voronov, High-resolution adiabatic calorimetry of supercooled water. J. Phys. Conf. Ser. **1385**, 012008 (2019)
8. N. Atamas, Temperature and temporal heterogeneities of water dynamics in the physiological temperature range. J. Mol. Liq. **340**, 117201 (2012)

Chapter 20
Influence of the Structure of Amylose and Amylopectin on Their Dielectric Properties

M. O. Sosnovska, S. O. Alekseev, O. M. Alekseev, V. V. Klepko, S. D. Nesin, O. O. Mosia, K. S. Yablochkova, M. V. Lazarenko, N. M. Gregirchak, A. V. Varukha, D. A. Andrusenko, and M. M. Lazarenko

Abstract The paper examines the properties of amylose, high Mw amylose, low Mw amylose, and amylopectin obtained using dielectric spectroscopy and X-ray methods. We demonstrate that solid amylose exists in an amorphic state, whereas high Mw amylose, low Mw amylose, and amylopectin exist in an amorphocrystalline state. We report the presence of the dielectric relaxation in the high Mw amylose, low Mw amylose, and amylopectin and its absence in amylose. Such a result can be attributed to the presence of the crystalline phase in the former. The decrease in the polymerization degree and the branching in the amylose molecule leads to an increase in the relaxation intensity.

M. O. Sosnovska (✉) · O. M. Alekseev · K. S. Yablochkova · A. V. Varukha · D. A. Andrusenko · M. M. Lazarenko
Physical Faculty, Taras Shevchenko National University of Kyiv, Kyiv, Ukraine
e-mail: mariiasosnovska@knu.ua

S. O. Alekseev
Faculty of Chemistry, Taras Shevchenko National University of Kyiv, Kyiv, Ukraine

V. V. Klepko · S. D. Nesin
Department of Physics of Polymers, Institute of Macromolecular Chemistry of the National Academy of Sciences of Ukraine, Kyiv, Ukraine

O. O. Mosia
Educational Scientific Institute of High Technologies, Taras Shevchenko National University of Kyiv, Kyiv, Ukraine

M. V. Lazarenko
Faculty of Biotechnology and Environmental Control, Taras Shevchenko National University of Kyiv, Kyiv, Ukraine

N. M. Gregirchak
National University of Food Technologies of Ukraine, Kyiv, Ukraine

O. Fesenko and L. Yatsenko (eds.), *Functional Nanomaterials, Nanocatalysts, Nanotechnologies, and Their Applications*, Springer Proceedings in Physics 321,
https://doi.org/10.1007/978-3-031-99136-3_20

20.1 Introduction

Recent studies [1, 2] have shown that the dielectric properties of amylose and amylopectin, the two types of polysaccharides present in starches, are determined by their respective molecular structures. These dielectric properties determine how a molecule reacts to an external electric field and its ability to store and transfer electric energy. We have previously reported [3–9] that polysaccharides undergo a low-temperature dielectric relaxation, which may be caused by the conformational motion of the methylol groups in the surface layers of crystals or, according to [10] by a local chain rotation.

Amylose, according to [3, 11–13], is a linear polysaccharide, which consists of glucose units linked by α-1,4-glycosidic bonds. Its linear structure allows for a relatively free rotation of the glycosidic linkage, which results in relatively high values of the dielectric permittivity since this molecule can easily change the orientation of its dipoles when an external electric field is applied. In contrast, amylopectin is a branched polysaccharide, which has α-1,6-glycosidic bonds in addition to the α-1,4-glycosidic ones. The branching of the amylopectin creates a steric hindrance and lowers a molecule's ability to respond to the electric field. Thus, amylopectin has lower dielectric permittivity compared to amylose.

Both amylose and amylopectin can absorb water due to their hydrophilic properties [11, 14, 15]. Moisture content in starch can thus also impact the dielectric properties of its components, as the dielectric constant of water is high.

In the present manuscript, we describe how the molecular structure, the temperature of the sample, and the frequency of the external electric field impact the dielectric properties of amylose and amylopectin.

20.2 Materials and Methods

Amylopectin from maize (henceforth referred to as amylopectin) and amylose from potato (henceforth referred to as amylose) were purchased from Sigma-Aldrich. The samples were obtained in the form of white powders, whose particles did not stick together. The samples were additionally completely dried in «MX-50» and pressed into disks.

Samples of amyloses of different polymerization degrees (the high Mw amylose and the low Mw amylose), were prepared from potato starch and characterized according to procedures, described in detail in [16]. To get "high Mw amylose" (amylose-HMw) the starch was mixed with water to get 10% suspension, then an equal volume of 2 mol/l NaOH was added. The resulting viscous semi-transparent solution was mixed well for 20 min, neutralized by 1 mol/l HCl, and heated up to 85 °C. The n-butyl alcohol (n-BuOH) was added to the reaction mixture (15% vol); next the mixture was naturally cooled down under stirring and allowed to set for 24 h. The precipitate of amylose complex with n-BuOH was separated by

centrifugation, washed a few times with saturated aqueous solution of n-BuOH, and dissolved in hot (90–95 °C) water under intense stirring. Afterwards, the procedure of amylose complex precipitation and washing was repeated to purify it from amylopectin residues. Finally, the complex was mixed with an excess of methanol for a few hours to substitute n-BuOH with CH_3OH, then the methanol was substituted consequently by MTBE and hexane solvents. To remove the solvents the complex was dried at 1 mBar at 20 °C followed by 65 °C.

To prepare "low Mw amylose" (amylose-LMw) the starch (10% wt) was stirred at 85 °C in 0.01 mol/l HCl. As a result, an initially turbid and very viscous solution became fluid and transparent. Next, the solution was neutralized by NaOH, and the amylose was isolated from the reaction mixture identically to high Mw amylose.

The polymerization degrees of the amyloses, measured by viscometry of their solutions in 0.5 mol/l NaOH were found to be Dp = 3380 for amylose-HMw and Dp = 280 for amylose-LMw. Measurements of the light absorbance of iodine complexes demonstrated absorbance maxima near 650 nm, which correspond to amyloses with long (> 100 elementary units) unbranched sections of the amylose chain.

Wide-angle XRD patterns were obtained on a DRON—2.0 diffractometer, in copper anode radiation. Registration of the scattered intensity was carried out in the step scan mode of the scintillation detector for scattering angles between 3° and 33° (with ϑ being half of the scattering angle, and the wavelength of X-ray radiation λ equal to 0.154 nm). The details of the X-ray optical scheme used are described in detail in [17].

Dielectric properties were studied in the frequency range from 1 to 50 kHz and at temperatures between − 196 and 100 °C on an automated installation based on a P5083 AC bridge and a four-electrode thermostatic cell in which the thickness of the sample could be controlled [18].

20.3 Experimental Results

20.3.1 Dielectric Properties

Both the length of the chain and the presence of branches affect the thermal mobility of amylose, amylose-HMw, amylose-LMw, and amylopectin molecules. This, in turn, leads to a different intensity of the dipole relaxation polarization and the values of the dielectric properties of the samples. To gain insight into the processes of the relaxation in these molecules we have measured the variation of the real $\varepsilon'(T)$ and imaginary $\varepsilon''(T)$ parts of the complex dielectric permittivity with temperature. Figures 20.1 and 20.2 summarize this behaviour for all samples at frequencies 5, 10, 20, and 50 kHz.

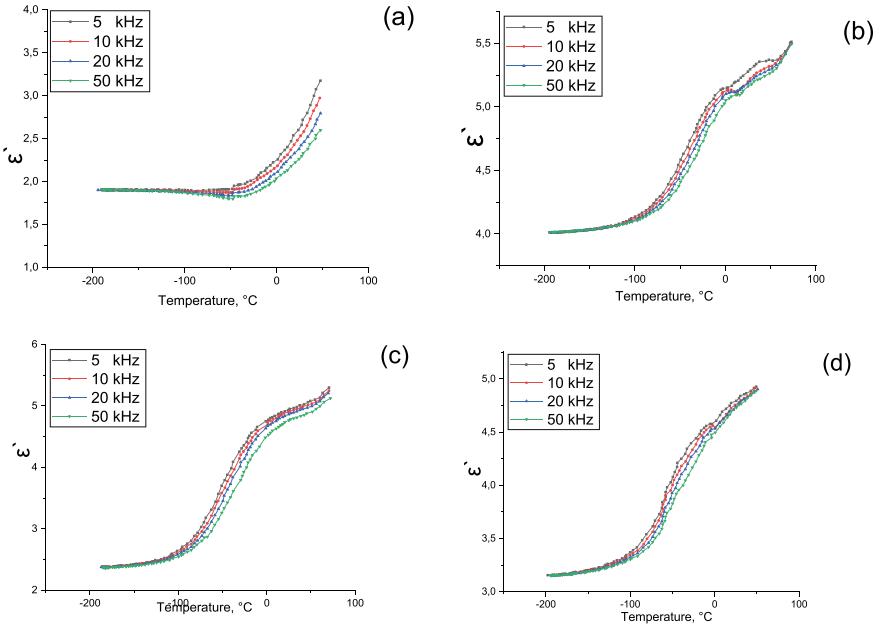

Fig. 20.1 Temperature dependencies of the real part ε′(T) of the complex dielectric permittivity of the amylose (**a**), amylose-HMw (**b**), amylose- LMw (**c**), and amylopectin (**d**) samples recorded at different frequencies

For all samples (Fig. 20.1b, c and d), except amylose (Fig. 20.1a), the real part of the dielectric permittivity grows steadily with increasing temperatures before levelling off. The inflection points shifts to higher temperatures with increasing frequency, indicating the presence of dielectric relaxation.

The imaginary part of the dielectric permittivity for all samples (Fig. 20.2b, c and d), except amylose (Fig. 20.2a), peaks in the region between − 200 °C and T = 60 °C. The position of this peak shifts towards higher temperatures at increasing frequencies, also indicating the presence of the relaxation processes in them.

To compare the relaxation processes in amylose-HMw, amylose-LMw and amylopectin, and to contrast their behaviour to that of amylose, in which no relaxation is observed, we can examine Figs. 20.3 and 20.4. These figures show the thermal dependencies of the increment of the real part of the dielectric permittivity (Fig. 20.3) and imaginary part of the dielectric permittivity (Fig. 20.4) at 10 kHz.

The different heights at which the graphs in Fig. 20.3 level off indicate that the intensity of the dielectric relaxation increases with the decreasing degree of amylose polymerization (amylose-HMw, amylose-LMw) and in the presence of branching in a molecule (amylopectin).

To gain further insight into the relaxation process occurring in the samples we can deduce its quantitative energy characteristics [8, 19–21], using the two-level

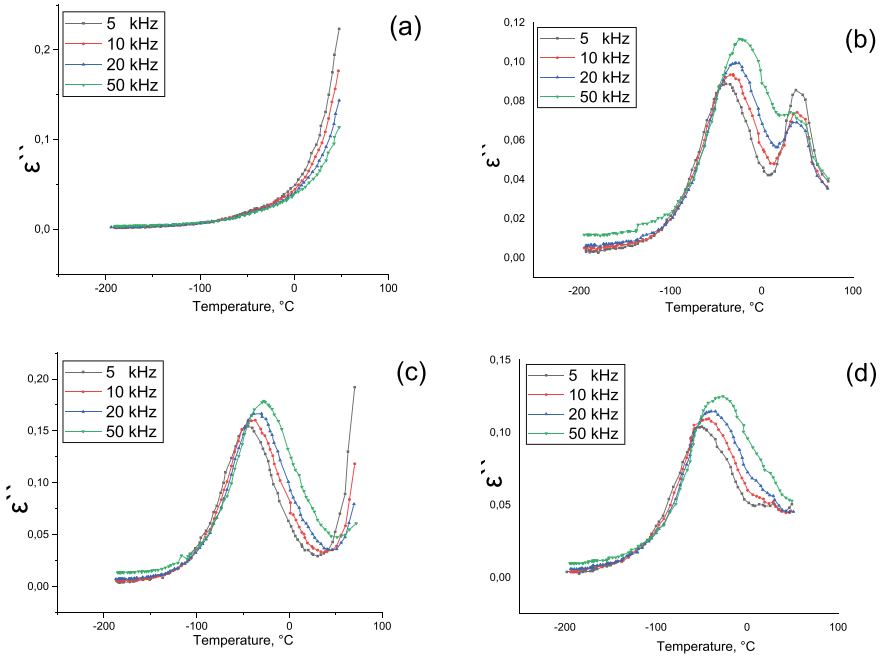

Fig. 20.2 Temperature dependencies of the imaginary part ε″(T) of the complex dielectric permittivity of the amylose (**a**), amylose-HMw (**b**), amylose-LMw (**c**), and amylopectin (**d**) samples recorded at different frequencies

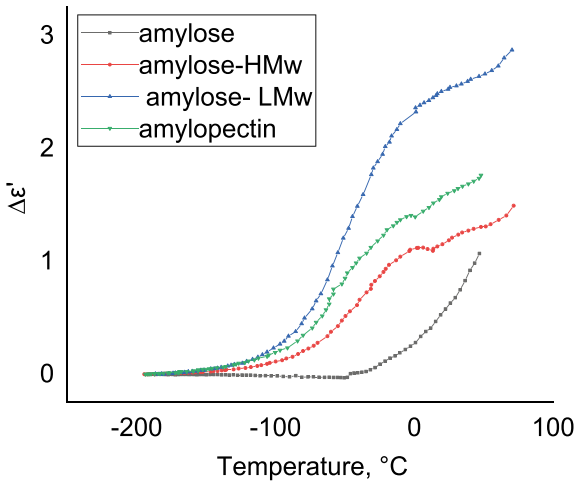

Fig. 20.3 Temperature dependencies of the increment of the real component of the dielectric permittivity for the amylose, amylose-HMw, amylose-LMw and amylopectin at frequency 10 kHz

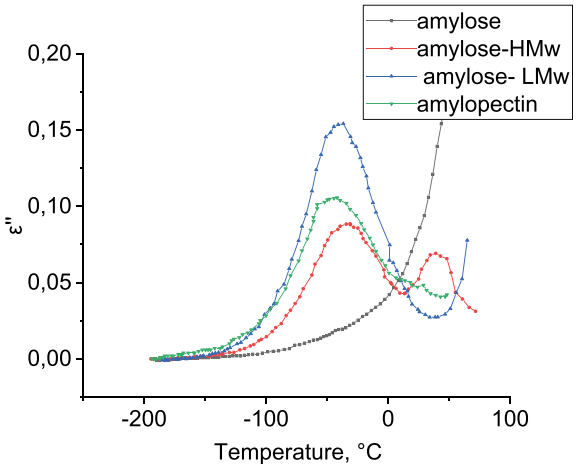

Fig. 20.4 Temperature dependencies of the imaginary component of the dielectric permittivity for the amylose, amylose-HMw, amylose- LMw and amylopectin at frequency 10 kHz

relaxation model. This model determines the dielectric losses caused by thermal polarization.

The temperature dependence of the increment of the dielectric permittivity can be fitted using the following relation:

The temperature dependence of the increment of the dielectric permittivity can be fitted using the following relation:

$$\Delta\varepsilon = \varepsilon_0 - \varepsilon_\infty = \frac{N\mu^2}{3kT\varepsilon_0} \frac{\exp\left(-V/kT\right)}{\left[1+\exp\left(-V/kT\right)\right]^2}, \tag{20.1}$$

where N is the relaxator concentration, μ^2 is the mean squared difference between the dipole moments of relaxators in positions 1 and 2, and V is the difference in relaxators' energies in positions 1 and 2. The data in Fig. 20.1 fitted with expression (20.1) yield the values of $N\mu^2$ and V, listed in Table 20.1.

The maximum of $\varepsilon''(T)$ relation corresponds to $\omega\tau = 1$, where

$$\tau = \tau_0 \exp\left(\frac{(U - T\Delta S)}{kT}\right). \tag{20.2}$$

Table 20.1 Relaxation processes energy characteristics

Sample	$N\mu^2$, 10–31 C^2/m	V, kJ/mol	U, kJ/mol	ΔS/k
Amylose	0	0	0	0
Amylose-HMw	26.51	10.01	77.35	73.92
Amylose-LMw	47.10	10.14	67.03	69.32
Amylopectin	6.97	6.76	56.29	64.93

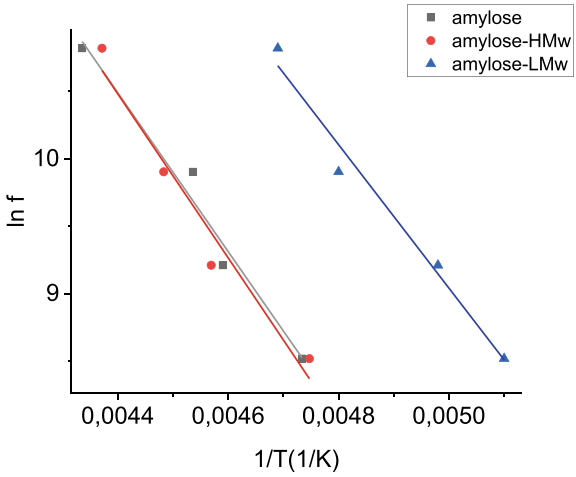

Fig. 20.5 Arrhenius equation: natural logarithm of the frequency as a function of the inverse temperature ln f(1/Tr) for the amylopectin, amylose-HMw, and amylose-LMw

$\omega = 2\pi f$ is the angular frequency of the external field oscillation, τ is the relaxation time, U is the activation energy, and ΔS is activation entropy. Thus, the following expression for the Arrhenius equation can be obtained:

$$\ln f = -\ln 2\pi\tau_0 + \frac{\Delta S}{k} - \frac{U}{kT}. \tag{20.3}$$

When the Arrhenius equation is plotted (ln f(1/T) in Fig. 20.5), the experimental data in Fig. 20.2 gives numerical values of U and ΔS, also listed in Table 20.1.

When the data for all samples are compared (Table 20.1), the following becomes apparent: as the length so the linear amylose chain decreases, the dielectric relaxation activation energy U increases, and the activation entropy ΔS decreases. This can be interpreted as follows: the increase in the number of end groups leads to an increase in the number of relaxators. The presence of the branching in the amylopectin molecules leads to a decrease in the number of relaxators and a decrease in the activation energy, as well as the activation entropy compared to amylose-HMw.

20.3.2 X-Ray Phase Analysis

The structure of the samples studied can be elucidated using X-ray phase analysis. Accordingly, we have obtained the dependencies of the intensity of X-ray diffracted radiation for the samples of amylopectin (Fig. 20.6), amylose (Figs. 20.6 and 20.7), amylose-HMw and amylose-LMw (Fig. 20.7).

The XRD pattern for amylose is, essentially, a broad featureless peak with a maximum at about 20°. Such a shape indicates the presence of the amorphous halo and suggests that the amylose in the sample is present in an amorphous form. This is

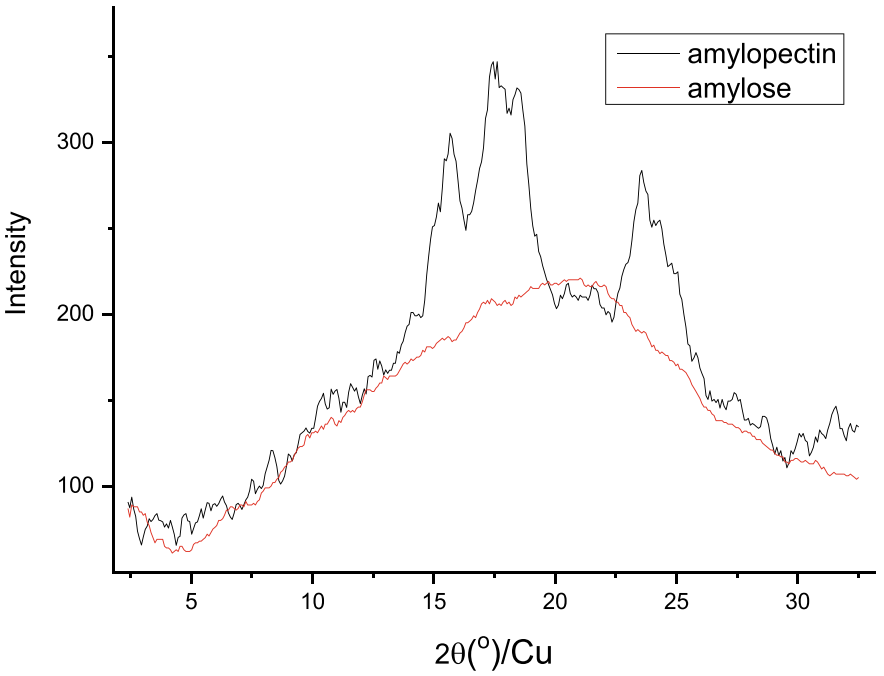

Fig. 20.6 XRD patterns for amylopectin and amylose samples

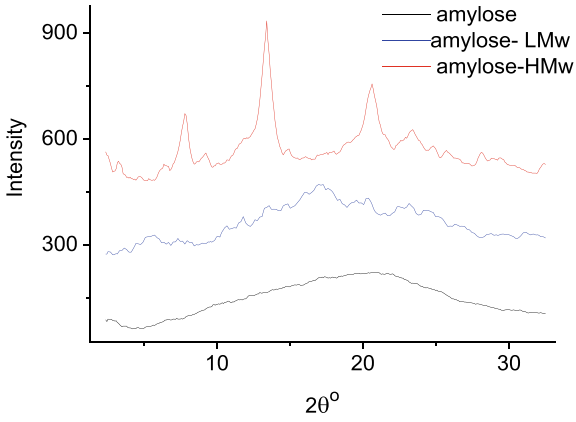

Fig. 20.7 XRD patterns for amylose, amylose-HMw, amylose- LMw

in contrast with results obtained by Myllärinen et al. [22] who reported two maxima on the amylose XRD pattern. We believe that the explanation for this could be traced to the difference in the methods by which amylose was obtained in these two studies.

Amylopectin demonstrates a different behaviour: on its XRD patterns, several peaks are observed at $2\theta = 15.7$, 17.5, 18.5, and 23.6°. Similarly, distinct peaks are observed on XRD patterns for amylose-HMw ($2\theta = 7.9$, 13.5, 20.6, and

23.4°) and amylose-LMw ($2\theta = 5.4$, 13.5, 17.2, 20, and 23°). Such results suggest that amylopectin, amylose-HMw, and amylose-LMw are all present samples in an amorphous-crystalline state.

20.4 Conclusions

The dielectric properties of amylose and amylopectin can be thus attributed to the following aspects of their structure and molecular assembly:

- The presence of the crystalline structure in amylose-HMw, amylose-LMw, as well as in amylopectin, explains why they undergo dielectric relaxation;
- A smaller polymerization degree in amylose-LMw, compared to that in amylose-HMw leads to an increase in the intensity of the dielectric relaxation; such result can be attributed to the increasing concentration of end groups;
- The branching in amylopectin (absent in amylose-LMw) leads to a decrease in the number of relaxators, as side radicals have only one end group.

References

1. C.Y. Beh et al., Dielectric properties of hydrothermally modified potato, corn, and rice starch. Agriculture **12**(6), 783 (2022)
2. K. Nishinari, E. Fukada, Viscoelastic, dielectric, and piezoelectric behavior of solid amylose. J. Polym. Science: Polym. Phys. Ed. **18**(7), 1609–1619 (1980)
3. R.A. Pethrick, M. Song, Dielectric studies of amylose, amylopectin and amylose–stearic acid complexes. Carbohydrate Polym. **92**(2), 1530–1538 (2013)
4. M.F. Butler, R.E. Cameron, A study of the molecular relaxations in solid starch using dielectric spectroscopy. Polymer **41**(6), 2249–2263 (2000)
5. O.M. Alekseev, K.M. Kovalov, M.M. Lazarenko, M.V. Lazarenko, Y.E. Grabovskii, S.Y. Tkachov, Nature of dielectric relaxation in microcrystalline cellulose. Cellul. Chem. Technol. **53**(1–2), 15–22 (2019)
6. R.V. Dinzhos, E.G. Privalko, V.P. Privalko, Enthalpy relaxation in the cooling/heating cycles of polyamide 6/organoclay nanocomposites. I. nonisothermal crystallization. J. Macromol. Science, Part B **44**(4), 421–430 (2005)
7. A.O. Sobchuk et al., Effects of molecular structure on the dielectric relaxation of substituted cellulose derivatives. Mol. Cryst. Liquid Cryst. **751**, 106–120 (2022)
8. M.M. Lazarenko et al., Topological solitons in chain molecular crystals with stoichiometric obstacles and hydrogen bonds. J. Phys. Chem. Solids **144**, 109514 (2020)
9. O.M. Alekseev, S.O. Alekseev, L.A. Bulavin, M.M. Lazarenko, O.M. Maiko, Phase transitions in chain molecular polycrystals of 1-octadecene. Ukr. J. Phys. **53**, 882–888 (2008)
10. K. Kaminski et al., Identifying the origins of two secondary relaxations in polysaccharides. J. Phys. Chem. B **113**(30), 10088–10096 (2009)
11. A.L. Lehninger, *Lehninger Principles of Biochemistry*, 5th edn. (W.H. Freeman, New York, 2008)
12. M.M. Green, G. Blankenhorn, H. Hart, Which starch fraction is water-soluble, amylose or amylopectin? J. Chem. Educ. **52**(11), 729 (1975)

13. V. Vamadevan, E. Bertoft, Structure-function relationships of starch components. Starch—Stärke **67**(1–2), 55–68 (2014)
14. K.M. Kovalov, O.M. Alekseev, M.M. Lazarenko, Y.F. Zabashta, Y.E. Grabovskii, S.Y. Tkachov, Influence of water on the structure and dielectric properties of the microcrystalline and nanocellulose. Nanoscale Res. Lett. **12**(1) (2017)
15. P. Ramasamy, A dielectric relaxation study of starch–water and starch–glycerol films. Ionics **18**(4), 413–423 (2011)
16. R. Manfred, Ausgewählte Methoden der Stärkechemie.: Isolierung, Charakterisierung und Analytik von Stärkepolysacchariden. Von Manfred Richter, Siegfried Augustat [und] Friedrich Schierbaum. Mit 81 zum Teil mehrfarbigen Abbildungen und 36 Tabellen. Stuttgart: Wissenschaftliche Verlagsgesellschaft (1968)
17. Rentgenographic methods of studying polymer systems. (Naukova dumka, Kyiv, 1982)
18. A.N. Alekseev, M.M. Lazarenko, M.V. Lazarenko, K.N. Kovalev, S.Y. Tkachev, Characterization of dielectric properties in liquid–solid phase transition. Inorg. Mater. **53**(15), 1473–1477 (2017)
19. M.M. Lazarenko et al., Topological solitons in aliphatic systems with a restricted translational mobility. Chem. Phys. **539**, 110959 (2020)
20. S.Y. Tkachev et al., Topological solitons in branched aliphatic molecules. Mol. Cryst. Liquid Cryst. **665**(1), 166–180 (2018)
21. K.I. Hnatiuk et al., Investigation of the structure and mechanisms of thermal motion in nanostructured undecylenic acid. Mol. Cryst. Liquid Cryst. **701**(1), 16–27 (2020)
22. P. Myllärinen, A. Buleon, R. Lahtinen, P. Forssell, The crystallinity of amylose and amylopectin films. Carbohydr. Polym. **48**(1), 41–48 (2002)

Chapter 21
Study of the Ferritization Process in MFe_2O4 Systems (M = Fe, Co, Ni, Mn, Zn) Under the Action of Contact Low-Temperature Non-equilibrium Plasma

Liliya Frolova

Abstract The processes of obtaining ferrites in MFe_2O_4 systems (M = Fe, Co, Ni, Mn, Zn) during the treatment of solutions with reduced pressure contact plasma were studied. The MEDUSA software package was used for the thermodynamic analysis of the deposition process. The zones of existence of ferrites were established using the Pourbaix diagram. The influence of the initial pH of the solution on the ferritization process was experimentally studied.

21.1 Introduction

Currently, the development and improvement of methods for obtaining spinel ferrites continues. Among the existing technologies for obtaining ferrites of the general formula MFe_2O_4 (M = Fe, Cu, Mn, Co, Ni, Zn), a special place is occupied by technologies that occur in the liquid phase. Co-precipitation is a method suitable for the synthesis of materials with a given composition and particle size, therefore, it is important to study the process of ferrite formation [1–4]. Despite the fact that the study of the method of hydrophase ferritization has recently been given much attention, there are discrepancies in the proposed mechanism of ferrite formation.

It is important that a rather promising raw material for obtaining transition metal ferrites is iron(II) sulfate and the corresponding metal sulfates. In this case, to obtain the final product, it is necessary to convert Fe^{2+} cations into Fe^{3+} using oxidizing agents. Oxidation of solutions of iron(II) salts and suspensions of hydroxides of the corresponding metals leads to the formation of poorly soluble nanodispersed iron(III) compounds. It has been established [5–8] that the phase and dispersion compositions

L. Frolova (✉)
Ukrainian State University of Science and Technologies, Dnipro, Ukraine
e-mail: 19kozak83@gmail.com

O. Fesenko and L. Yatsenko (eds.), *Functional Nanomaterials, Nanocatalysts, Nanotechnologies, and Their Applications*, Springer Proceedings in Physics 321,
https://doi.org/10.1007/978-3-031-99136-3_21

of these compounds depend on many synthesis parameters: temperature and pH of the reaction medium, concentration of iron(II) ions in the solution and $Fe(OH)_2$ in the suspension, nature of the salt anion and alkaline agent, activity of the oxidizing agent [8].

It is interesting to study the effect of low-temperature contact nonequilibrium plasma (CNP) on the dispersion medium. The effect of CNP on water and aqueous solutions has been considered by many researchers, but still remains insufficiently studied. The authors [9] believe that the main oxidizing agent is hydrogen peroxide. The literature provides a large set of possible reactions that occur under the action of CNP (Table 21.1). In a number of studies, it is believed that the main primary particles that are formed in the solution, regardless of the nature of the plasma-forming gas, are solvated electrons and ·OH radicals [10, 11]. The result of the dimerization of ·OH radicals is the formation of hydrogen peroxide. In addition, other particles should be formed in the liquid phase, for example, HO_2·, H· radicals, ions, etc.

The authors [9] also believe that the main chemically active particles formed in water under the action of the discharge are the OH_2· and OH· radicals and solvated electrons. When the discharge exposure time is up to 10 min, the formation of the hydroxyl radical is the most thermodynamically favorable, while with an increase in the exposure time, the advantage passes to the $\cdot OH_2$ radical. Therefore, when carrying out chemical processes, it can be expected that with a relatively short treatment time such processes will be initiated mainly by ·OH radicals. Thus, the impact of a glow discharge can be attributed to the Advanced Oxidation Process (AOP) group, which generates and uses powerful unstable radicals, mainly hydroxyl radicals ·OH ($E_0 = 2.80$ V) [12, 13]. In addition, it is possible to assume a large contribution of reactions 12 and 24, which are attributed to the Fenton process with the participation of UV radiation.

The modified Fenton process is a heterogeneous process involving iron(III) oxides and hydroxides. The homogeneous Fenton reagent is a mixture of Fe^{2+} and H_2O_2, and is one of the most active oxidation systems. This reactivity is due to the in situ generation of highly active oxidizing species, such as hydroxyl radicals, according to the process:

$$Fe^{2+} + H_2O_2 \rightarrow Fe^{3+} + OH^- + \cdot OH \tag{21.1}$$

Under these conditions, we can assume the catalytic action α-FeOOH, γ-FeOOH, Fe_3O_4, as well as the influence of the presence of Co, Mn, and Ni cations in the spinel structure for the generation of active radicals by the Fenton mechanism.

$$Co^{2+} + H_2O_2 \rightarrow Co^{3+} + OH^- + \cdot OH \tag{21.2}$$

$$Mn^{2+} + H_2O_2 \rightarrow Mn^{3+} + OH^- + \cdot OH \tag{21.3}$$

Heterogeneous reactions occur in neutral and alkaline media and additionally generate active radicals that contribute to the formation of the spinel structure.

Table 21.1 Reactions used in calculating concentration dependences in water during plasma discharge treatment [11]

No.	Reaction	Rate constant at 25 °C	No.	Reaction	Rate constant at 25 °C
1	$H_2O \rightarrow H\cdot + OH\cdot$	3.00×10^{-7} (8.00×10^{-6}) (s^{-1})	13	$2H\cdot \rightarrow H_2$	5.01×10^{9} ($l\ mol^{-1}\ s^{-1}$)
2	$OH\cdot + H_2 \rightarrow H_2O + H\cdot$	3.60×10^{7} ($l\ mol^{-1}\ s^{-1}$)	14	$H\cdot + OH^- \rightarrow H_2O$	2.19×10^{7} ($l\ mol^{-1}\ s^{-1}$)
3	$H_2O \rightarrow H^+ + OH\cdot$	2.63×10^{-8} (s^{-1})	15	$H\cdot + H_2O \rightarrow H_2 + OH^-$	6.17×10^{8} ($l\ mol^{-1}\ s^{-1}$)
4	$H_2O_2 \rightarrow OH\cdot + OH^-$	1.29×10^{10} (s^{-1})	16	$H\cdot + HO_2\cdot \rightarrow H_2O_2$	1.99×10^{10} ($l\ mol^{-1}\ s^{-1}$)
5	$H\cdot + H_2O_2 \rightarrow OH\cdot + H_2O$	5.01×10^{7} ($l\ mol^{-1}\ s^{-1}$)	17	$2HO_2\cdot \rightarrow H_2O_2 + O_2$	8.511×10^{5} ($l\ mol^{-1}\ s^{-1}$)
6	$H\cdot + H_2O \rightarrow OH\cdot + H_2$	10^{10} ($l\ mol^{-1}\ s^{-1}$)	18	$H^+ + OH^- \rightarrow H_2O$	1.48×10^{11} ($l\ mol^{-1}\ s^{-1}$)
7	$OH\cdot + H_2O_2 \rightarrow HO_2\cdot + H_2O$	2.69×10^{7} ($l\ mol^{-1}\ s^{-1}$)	19	$2H_2O \rightarrow H_2O_2 + H_2$	1.99×10^{6} ($l\ mol^{-1}\ s^{-1}$)
8	$OH\cdot + H_2 \rightarrow H\cdot + H_2O$	3.89×10^{7} ($l\ mol^{-1}\ s^{-1}$)	20	$H_2O \rightarrow H + OH^-$	1.78×10^{-5} (c^{-1})
9	$OH\cdot + OH\cdot \rightarrow H_2O_2$	5.50×10^{10} ($l\ mol^{-1}\ s^{-1}$)	21	$H\cdot + O_2 \rightarrow HO_2\cdot$	1.20×10^{10} ($l\ mol^{-1}\ s^{-1}$)
10	$H_2O_2 \rightarrow OH\cdot + OH\cdot$	3.55×10^{-9} (s^{-1})	22	$OH\cdot \rightarrow OH^-$	3.02×10^{10} (s^{-1})
11	$OH\cdot + HO_2\cdot \rightarrow O_2 + H_2O$	10^{10} ($l\ mol^{-1}\ s^{-1}$)	23	$H^+ \rightarrow H\cdot$	2.29×10^{10} (s^{-1})
12	$Fe^{2+} + HO_2\cdot \rightarrow Fe^{3+} + HO^-{}_2$	1.2×106 ($l\ mol^{-1}\ s^{-1}$)	24	$Fe^{2+} + HO\cdot \rightarrow Fe^{3+} + OH^-$	2.5×10^{8} ($l\ mol^{-1}\ s^{-1}$)

It is obvious that the coprecipitated heteropolyhydroxy complexes are converted to ferrite by replacing oxygen bridges with double bonds. The transformation schemes are unknown, although two plausible mechanisms are proposed: the first is dissolution–precipitation, the second is particle nucleation and growth [14]. The study of such systems is very complex, but the integrated use of theoretical and experimental studies allows us to study the mechanism of ferritization.

This work aims to construct Pourbaix diagram and study the kinetics of ferritization in MFe_2O_4 systems (M = Fe, Co, Ni, Mn, Zn) under the action of contact low-temperature non-equilibrium plasma.

21.2 Method

The starting reagents used in the work were $FeSO_4$ $7H_2O$, $NiSO_4$ $6H_2O$, $MnSO_4$ $7H_2O$, $CoSO_4$ $7H_2O$, $ZnSO_4$ $7H_2O$, NaOH.

For the research, aqueous solutions of iron(II) sulfate and sulfates of cobalt, nickel, zinc, manganese, and copper with a concentration of 0.5 mol/l were used. The range of concentrations of metal salts was adopted based on the following considerations: it is impractical to use solutions of low concentrations, the upper limit is due to the solubility of iron, cobalt, nickel, zinc, and copper salts in water. The initial concentration of sodium hydroxide varied from 0.4 to 1 mol/l.

The concentration of ferric cations in the solution was determined by three methods: permanganate, bichromate and in the case of the joint presence of ferric salts and cations of cobalt, zinc, manganese, copper, nickel, by weight using α-nitroso-β-naphthol.

Cobalt, nickel, manganese, zinc, copper were determined by the complexometric method.

The values of the redox potential and pH were measured by an ionometer and presented in the form of dependences pH (t), E (t), dE/dt (t).

The synthesis of ferrites was carried out under the action of CNP. The plasma installation and the principle of operation are described in detail in [15].

When studying oxidation under the action of contact low-temperature non-equilibrium plasma, the values of pH and redox potential were also determined. To evaluate the oxidation process, the integral indicator of pH change the duration of the first stage of oxidation $\tau_{1,}$ and the total oxidation time τ_{sum} were used.

21.3 Results and Discussion

21.3.1 Mechanism of the Ferritization Process Under the Action of Contact Low-Temperature Non-equilibrium Plasma. Pourbaix Diagrams

Since it is assumed that the precipitation reaction occurs at a certain pH, which corresponds to the redox reactions in the solution, which are described in the coordinates Eh = f(pH) on **Pourbaix diagram**, it is advisable to construct them taking into account the real concentrations of solutions. Pourbet diagrams for ferrites are unknown, but they are given for iron, nickel and zinc, manganese and copper in aqueous solutions. Comparing them and assuming that each metal cation reacts with the products of sonolysis of aqueous solutions of salts, it is possible to establish the optimal range of pH conditions for ferritization. To find the preliminary conditions for the formation of compounds in the presence of oxidizing agents, Pourbet

diagrams were used (Figs. 21.1 and 21.2). These diagrams reflect the thermodynamically stable forms of existence of ions, solid phase in solutions at different pH values and redox potential [16].

If we assume that the main oxidizing agent is peroxide radicals formed as a result of the destruction of hydrogen peroxide, and the pH of the synthesis varies in the range of 9–12, then the curve separating the region of possible ferritization will be above the potential values of 0.77 V. The formation of active radicals occurs as a result of the action of the CNP on the solution according to Eqs. (21.4–21.5). When creating Purbet diagrams for the studied systems, iron (II) sulfate and cobalt, manganese, copper, zinc sulfate and hydrogen peroxide should be considered as starting substances and ferritization processes occurring in a solution or suspension of divalent compounds. It is known that the reduction of hydrogen peroxide occurs according to the reactions:

$$H_2O_2 + 2H^+ + 2e \rightleftarrows 2H_2O \quad E^0 = 1.78\ \text{B} \tag{21.4}$$

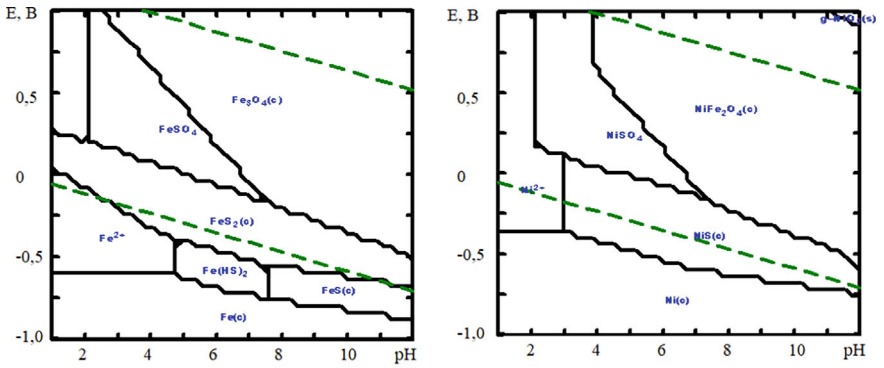

Fig. 21.1 Pourbaix diagrams of iron in the system Fe^{2+}–SO_4^{2-} (**a**) та Ni^{2+}–Fe^{2+}–SO_4^{2-}(**b**)

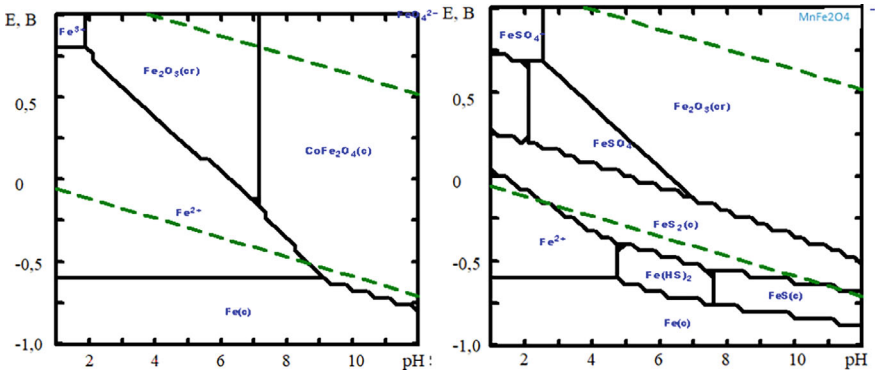

Fig. 21.2 Pourbaix diagrams of iron in the system Co^{2+}–Fe^{2+}–SO_4^{2-}(**a**) Mn^{2+}–Fe^{2+}–SO_4^{2-}(**b**)

$$HO_2^- + 3H^+ + 2e \rightleftarrows 2H_2O \quad E^0 = 2.12\ \text{B}. \tag{21.5}$$

That is, using Eqs. (21.6, 21.7), it is possible to determine the possibility of the ferritization process of polyhydroxycomplexes (PHC):

$$Fe^{2+} + H_2O_2 + 2H^+ = Fe^{3+} + 2H_2O \quad E^0 = 1.01\ \text{B} \tag{21.6}$$

$$Fe^{2+} + HO_2 = Fe^{3+} + 2H_2O \quad E^0 = 1.35\ \text{B} \tag{21.7}$$

Pourbaix diagrams clearly reflect thermodynamically stable forms of existence of ions, solid phase in solutions at different pH values and redox potential. In addition, the total area corresponding to the target product can characterize the tendency of this system to form a spinel phase.

Figures 21.1, 21.2 and 21.3 show the phase diagram for various metal ions in solution depending on pH. Let us consider the process of obtaining spinel oxide compounds of the type $MeFe_2O_4$ (Me = Fe^{2+}, Co^{2+}, Ni^{2+}, Mn^{2+}) from aqueous sulfate solutions using CNP. One of the most important stages in the application of this process is the correct selection of parameters, both the environment and the plasma discharge, which is the main processing tool.

This is due to the fact that the physicochemical mechanism of reactions is quite complex, and their course is accompanied by synergistic effects, the influence of which is imperfectly studied (cathode and anodic processes, photocatalytic processes under the influence of UV radiation, chemical transformations).

The study was carried out using the Hydra Medusa software package, which includes built-in reference databases for thermodynamic, physical and chemical properties of inorganic and organic substances, and calculation modules, in particular the module for calculating E-pH diagrams. The calculations considered the influence

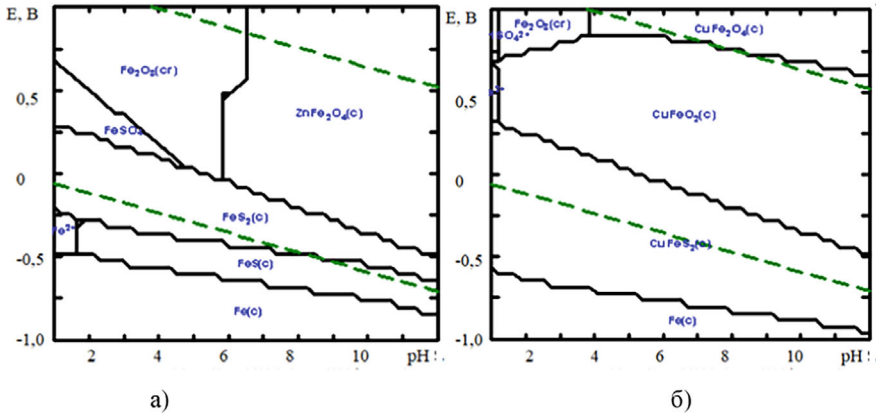

Fig. 21.3 Pourbaix diagrams of iron in the system Zn^{2+}–Fe^{2+}–$SO_4{}^{2-}$ (**a**), Cu^{2+}–Fe^{2+}–$SO_4{}^{2-}$ (**b**)

of pressure, concentrations and temperatures. As a result, it was noted that the most significant factors affecting the stability limits of complex and simple substances in solutions are their concentration and pH.

It is very important to study phase formation in aqueous solutions of sulfates (the ratio is stoichiometric as in ferrite) or suspensions of $Me_{1-x}Fe_x(OH)_2$ under the action of a glow discharge, at different molar ratios $n = OH^-/Me^{2+}$.

The choice of sulfate solutions for the study is due to their cheapness, simplicity, stability of composition and practically unlimited production volumes. The considered Pourbe diagrams of the studied systems allow us to assess the evolution of the stability regions of oxide, metal phases and solution forms. The use of these diagrams made it possible to assess the composition of solutions and, in particular, the stability of $CoFe_2O_4$, $MnFe_2O_4$, Fe_3O_4 та $ZnFe_2O_4$, $NiFe_2O_4$, $CuFe_2O_4$.

In the presence of oxidizing agents in acidic and neutral environments, Me^{3+} compounds are formed in the solution, in alkaline and strongly alkaline solutions, ferrites are formed.

At too low a pH, one type of cation is precipitated, while the formation of a non-stoichiometric precipitate is likely. At too high a pH, metal cations again begin to pass into the solution, which is associated with their amphoteric properties, and form a non-stoichiometric precipitate. The pH of precipitation of nickel and ferric hydroxides are similar, so the region of existence on the diagrams is larger. Since zinc hydroxide precipitates at a lower pH, and then dissolves mainly at a higher pH, the optimal pH range is from 9.2 to 10.4. In addition, the considered Pourbaix diagrams allowed us to assess the dependence of the stability regions of the oxide, metallic phases and soluble forms in the considered systems on the nature of the cation in ferrite.

The region of existence of $ZnFe_2O_4$ is in the pH range of 6–12 in an oxidizing environment. In the liquid phase, zinc can exist in the form of ions Zn^{2+}, $Zn(OH)^+$, $HZnO^{2-}$, $ZnO_2{}^{2-}$.

In the system Cu^{2+}–Fe^{2+}–$SO_4{}^{2-}$ in the solid phase, the existence of iron, copper(I) ferrite, copper(II) ferrite is possible. In the pH range of 1–12, iron is thermodynamically stable in a non-oxidizing environment, the region of existence of copper is absent on the diagram due to the fact that the oxidation potential of copper is much higher than the potential for hydrogen evolution from water. But iron and copper are easily oxidized, since the value of the oxygen reduction potential in the entire pH range is much higher than that required for the oxidation of copper and iron compounds. In the range of pH = 4–12, the formation of $CuFe_2O_4$ is thermodynamically possible, at lower values of pH = 2–4, a separate separation of non-magnetic oxide α-Fe_2O_3 is possible, a decrease in pH to 1–2 leads to the existence of soluble forms of iron and cuprum.

In a number of considered cations $Fe^{2+} > Zn^{2+} > Ni^{2+} > Co^{2+} > Mn^{2+}$, the region of existence of oxide compounds decreases accordingly. That is, the theoretically calculated regions of existence reflect the general regularities of the formation of ferrites. But it should be noted that the crystalline structure of ferrite particles is not formed immediately, but after a certain time. It is known that the structure of primary particles is amorphous [3]. Then, as a result of heterogeneous reactions, the

crystallization process occurs and nanodispersed crystalline particles are formed. Thus, the phase composition of the obtained crystalline particles is determined not only by the conditions of the formation of nuclei and the growth of amorphous particles, but also by the conditions of their crystallization. Therefore, additional experiments are needed to study the conditions of the formation of spinel ferrites.

21.3.2 Experimental Studies of the Ferritization Process Under the Action of Contact Low-Temperature Non-equilibrium Plasma

The oxidation processes of iron(II) compounds are the subject of many studies. The polyvalence of iron and the presence of a large number of allotropic forms lead to numerous contradictory results and discussions. During the oxidation of a suspension of iron(II) hydroxide, oxide, hydroxide and oxyhydroxide compounds of iron(III) are formed. Most iron oxide compounds are not magnetic. Obtaining iron compounds with a spinel structure at low temperatures is a rather complex technological task. The phase composition of the reaction product is determined by the nature of the oxidant used, the oxidation rate, the process temperature, the pH of the beginning of oxidation, the nature and concentration of the precipitant and the initial salt solution [17–20]. Previous studies on the production of ferrites under the action of ultrasound, CNP, and atmospheric oxygen made it possible to choose an effective ferritization technology. It is important to study the main regularities of the oxidation process of divalent iron compounds under the action of CNP, to establish the influence of the main synthesis parameters on the phase composition of the precipitate. Identification of the main regularities of the oxidation process will allow choosing the optimal conditions for its implementation.

Several series of experiments were performed. In the first series, the influence of the initial pH (or the ratio n) on the kinetics of the process was studied (Figs. 21.4, 21.5, 21.6, 21.7, 21.8, 21.9, 21.10, 21.11 and 21.12).

During the experiments, the dynamics of pH changes during the ferritization process in the systems Fe^{2+}–SO_4^{2-}–OH^-, Co^{2+}–Fe^{2+}–SO_4^{2-}–OH^-, Ni^{2+}–Fe^{2+}–SO_4^{2-}–OH^-, Zn^{2+}–Fe^{2+}–SO_4^{2-}–OH^-, Cu^{2+}–Fe^{2+}–SO_4^{2-}–OH^-, Mn^{2+}–Fe^{2+}–SO_4^{2-}–OH^-. were studied. The pH-dynamic mode was chosen as the oxidation mode, when the pH of the solution is brought to a certain value, and then its change is recorded. Figures 21.4 and 21.5 show how the pH changes in the Fe^{2+}–SO_4^{2-}–OH^- system during the treatment of CNP.

The system containing only iron(II) cations was chosen as the background in order to establish the influence not only of the acidity of the medium, but also of the presence of additional metal cations.

In Fig. 21.4, in the Fe^{2+}–SO_4^{-2}–OH^- system, there was initially a rapid change in pH, and then a more gradual decrease in pH with its subsequent stabilization. The drop in pH is a product of the oxidation of iron(II) to iron(III). Further establishment

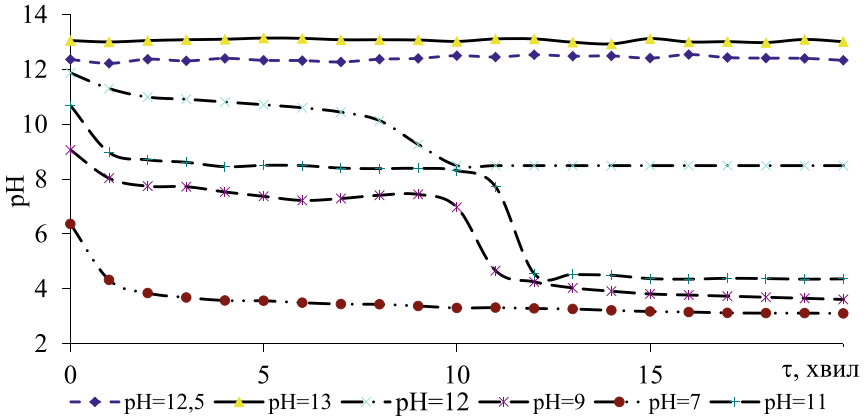

Fig. 21.4 Dependence of pH on the time of treatment of CNP for initial pH = 7–12 in the system Fe^{2+}–$SO_4{}^{-2}$–OH^-, C[$FeSO_4$] = 0.5 mol/l

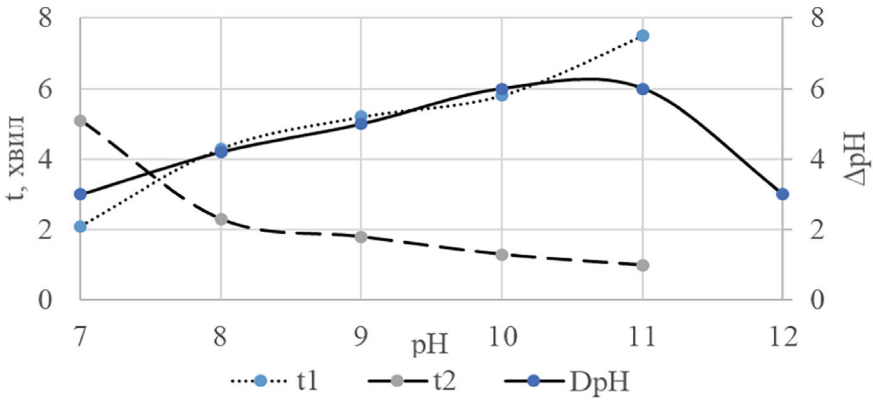

Fig. 21.5 Dependence of the time of complete oxidation for the first stage (1) and the second stage (2) and the total change in pH on the initial pH in the Fe^{2+}–$SO_4{}^{-2}$–OH^-

of these indicators at a constant level shows the achievement of an equilibrium state. During the experiments, it was found that characteristic extrema are observed on the differential curve of pH change during the oxidation process (Fig. 21.6 and 21.7).

In this case, the first corresponds to the beginning of the formation of the intermediate product, and the second to the formation of the final product. The time interval between these extremes can serve as a kinetic characteristic of the transformation of the intermediate product. The end of the oxidation process is the stabilization of pH in time. To describe the kinetics of oxidation, three quantities were introduced: oxidation time in the first stage (t_1), oxidation time in the second stage (t_2), the average rate of change of the pH indicator pH (θ_{sum} == $\Delta pH/\Delta t$),, which is defined as the ratio of the change in pH units to the treatment time. The dependence of the

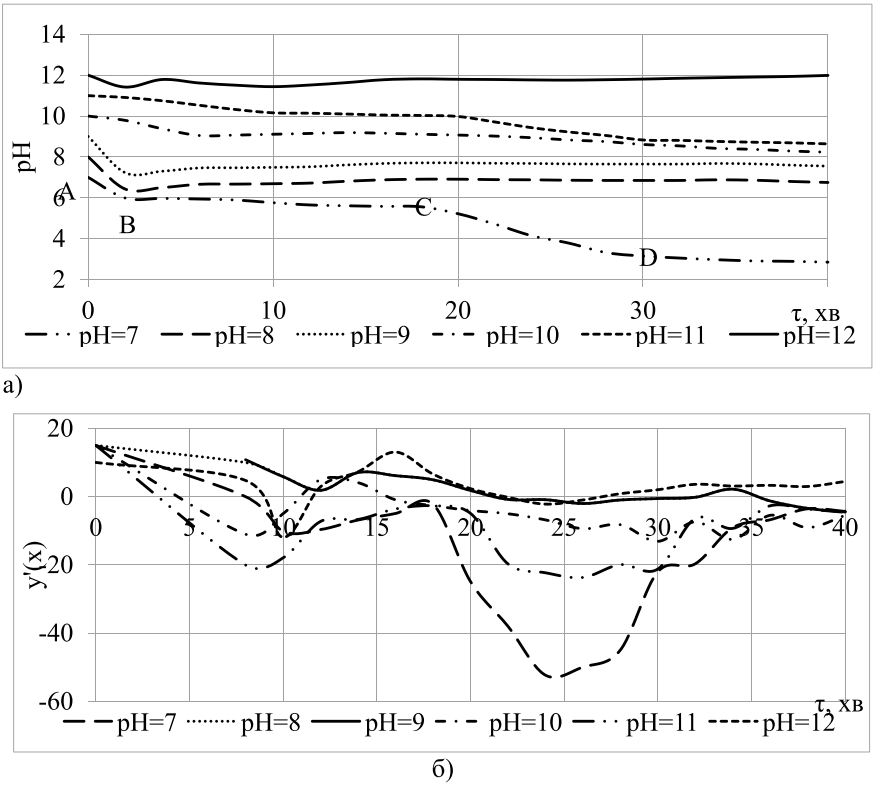

Fig. 21.6 Dependence of pH on the time of treatment of CNP for initial pH = 7–12 in the system Co^{2+}–Fe^{2+}–SO_4^{2-}–OH^-, $C[FeSO_4]/C[CoSO_4] = 2$ (**a**) and the corresponding differential curves (**b**)

value of the integral average rate of change of pH on the initial acidity of the solution is extreme, and at the same time, the maximum of the values of θ_{aver} corresponds to the maximum oxidation rate.

On the differential curve, the maximum corresponds to a certain transformation. Moreover, the first maximum corresponds to the formation of an intermediate, the second to the final product. The latter can be explained by the fact that at a certain stage of the process of transformation of intermediate products, the number of free H + groups is significant and in this region the rate of change is maximum. Accordingly, the shift of the maxima on the curve y/(x)—t to the left with an increase in the initial pH value reflects an increase in the rate of transformation of intermediate products.

Figure 21.6 shows the pH changes for the Fe^{2+}–Co^{2+}–SO_4^{2-}–OH^-system. The general process of oxidation of Fe^{2+} ions in solution and suspension consists of two clearly defined stages. In Fig. 21.6, the initial point A corresponds to the formation of heteropolyhydroxide $[Me_{0.33}Fe_{0.67}(OH)_2]n$. Point B indicates the transformation of HPG into an intermediate compound, the transformation of which is completed at

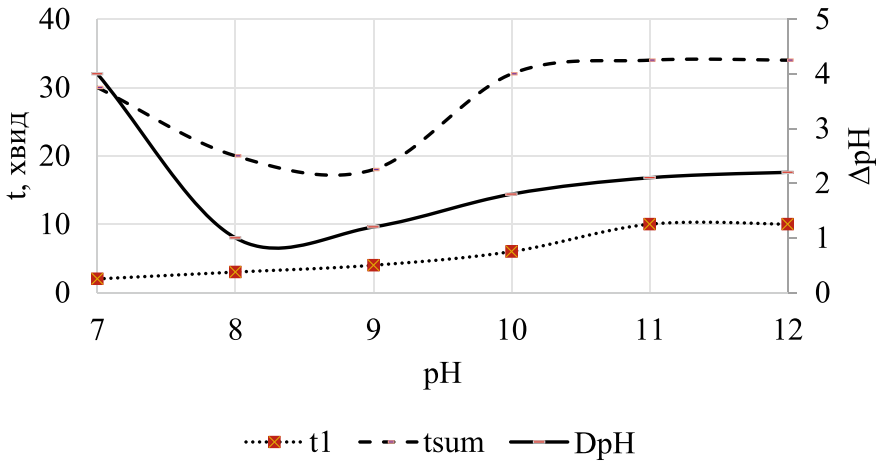

Fig. 21.7 Dependence of the time of complete oxidation for the first (1) and second stage (2) and the total pH change on the initial pH in the Co^{2+}–Fe^{2+}–SO_4^{2-}–OH system

point D. Point D corresponds to the transformation into a non-magnetic iron oxyhydroxide, a defective structure of the maghemite type or a spinel phase of ferrite. A constant pH value is ensured by the state of chemical equilibrium between the mother liquor and the reaction products. Complete oxidation of the iron(II) compounds leads to a sharp decrease in pH at point B, which indicates the end of all chemical reactions in the solution. Figure 21.6 shows two main stages, i.e. there are two stages of the transformation of $Me_{0.33}Fe_{0.67}(OH)_2$—the formation of the spinel structure, which corresponds to point D. The pH fluctuations in Figs. 21.4 and 21.6 are very similar to each other, and differ from the Ni^{2+}–Fe^{2+}–SO_4^{2-}–OH^- system, which is presented in Fig. 21.8.

This means that the overall oxidation reaction of the compound in solution consists of three different stages, which are characterized by the formation of an intermediate compound and the subsequent formation of iron(III) oxyhydroxide. The pH decreases rapidly during the formation of the intermediate compound with heteropolyhydroxides and remains constant during the formation of a goethite-like structure from heteropolyhydroxides. The heterogeneous reaction rate, which was calculated from the reaction time, is summarized in Fig. 21.7. However, the heterogeneous reaction rate for samples with initial pH = 7–8 was lower than for pH = 9–12. Experiments are needed to determine the phase composition of the formed compounds and their magnetic properties.

Common to all the systems considered is that a sharp decrease in the initial pH in the solution causes the formation of a goethite-like structure, instead of a spinel one. The possibility of goethite formation can be explained by the kinetics of hydroxide transformations (the first stage of the reaction). That is, the presence of unstable heteropolyhydroxy complexes promotes the formation of oxyhydroxides.

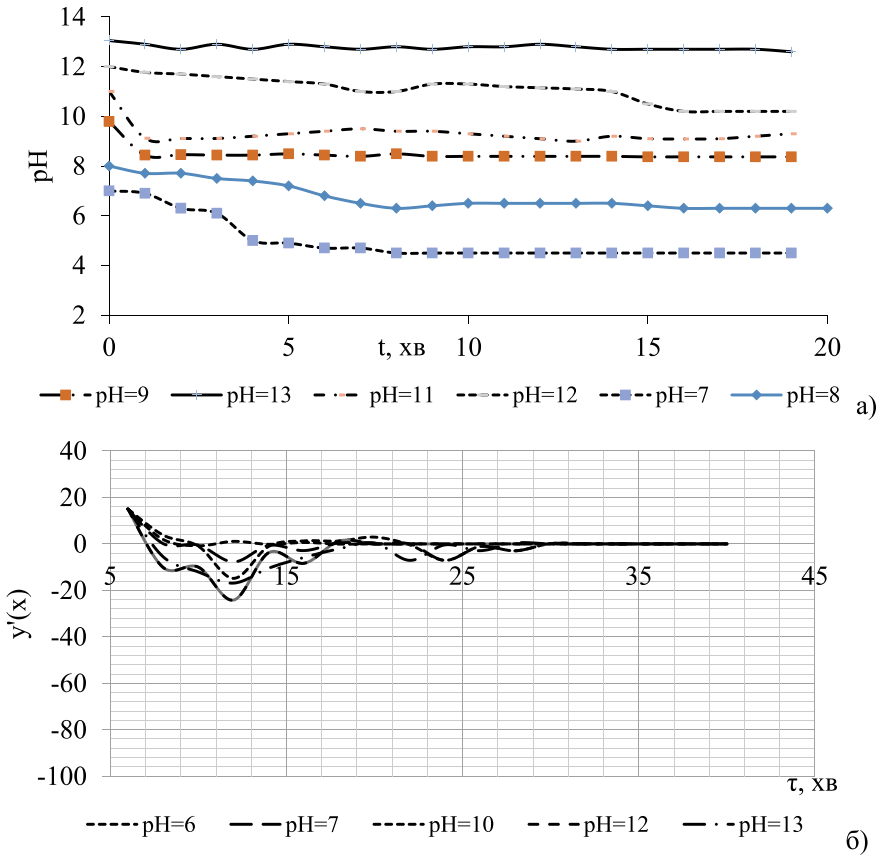

Fig. 21.8 Dependence of pH on the time of treatment of CNP for initial pH = 7–12 in the system Ni^{2+}–Fe^{2+}–SO_4^{2-}–OH^-, $C[FeSO_4]/C[NiSO_4] = 2$ (**a**) and the corresponding differential curves (**b**)

Secondly, goethite formation is also possible, which is caused by the slow rate of the second heterogeneous reaction, i.e. the limiting kinetics of the chemical transformation. It can be assumed that the formation of the spinel phase can be induced by regulating the oxidation rate. For example, the formation of the spinel phase could be increased by slow oxidation of Fe^{2+} ions in an alkaline medium, which depends on the stability of the previously formed compounds. It was found that an increase in pH in the solution leads to a decrease in the rate of the first heterogeneous reaction, as shown in Fig. 21.6a.

In particular, an increase in the reaction time t_1–t_2, for the conversion of HPC into oxyhydroxides was achieved at low pH as a result of the formation of unstable heteropolyhydroxy complexes in the composition of the starting material.

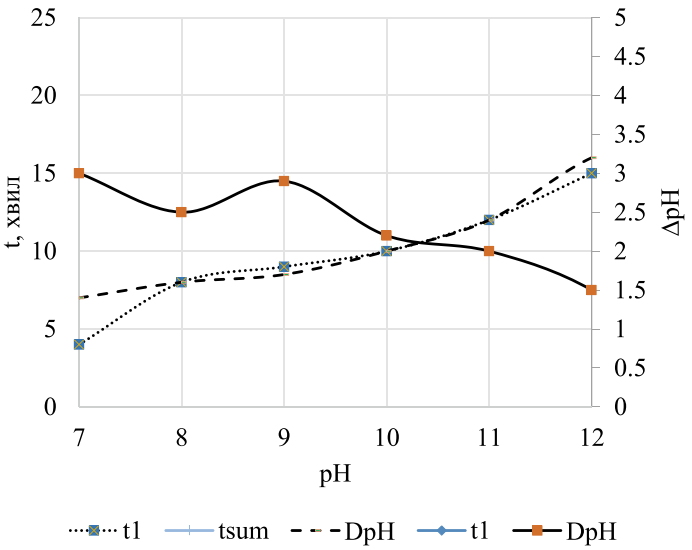

Fig. 21.9 Dependence of the time of complete oxidation for the first stage (1) and the second stage (2) and the total pH change on the initial pH in the system Ni^{2+}–Fe^{2+}–SO_4^{2-}–OH^-

Therefore, an increase in the reaction rate t_1 and a decrease in the rate of the heterogeneous reaction t_2 are prerequisites for the formation of iron(III) oxyhydroxide and an increase in the amount of goethite in the final product.

It was previously established [21, 22] that lepidocrocite and akagenite are formed by a very slow oxidation reaction of Fe^{2+} ions in an acidic medium. However, when the oxidation reaction of Fe^{2+} ions ends very quickly, lepidocrocite can also be formed as the final product. The reason is that sulfate ions are present in the structure of the PHC during the formation of iron(III) oxyhydroxide, since the rate of the oxidation reaction is too high compared to the internal diffusion processes to remove the SO_4^{2-} anions present in the composition of the basic salt.

The change of cations in the series $Fe^{2+} > Zn^{2+} > Ni^{2+} > Co^{2+} > Mn^{2+} > Cu^{2+}$ in the solution leads to an increase in the rate of the first reaction and a decrease in the time of the second reaction.

The given dependencies (Fig. 21.10 and 21.11) give an idea of the kinetics of processes in the Zn^{2+}–Fe^{2+}–SO_4^{2-}–OH^- system.

The total oxidation time and the oxidation time by stages also make it possible to determine some features of the pH oxidation process in the Zn^{2+}–Fe^{2+}–SO_4^{2-}–OH^- system depending on the pH of the medium.

Figures 21.11 present the oxidation time by the first stage (t_1) and the second (t_2) depending on the pH of the initial solution. In an acidic medium, the study of regularities has no applied value. That is, the lowest pH value was 7 and two characteristic segments were observed. In an alkaline medium, the time of the first stage increases significantly. That is, excess OH—groups in the solution play a significant role in

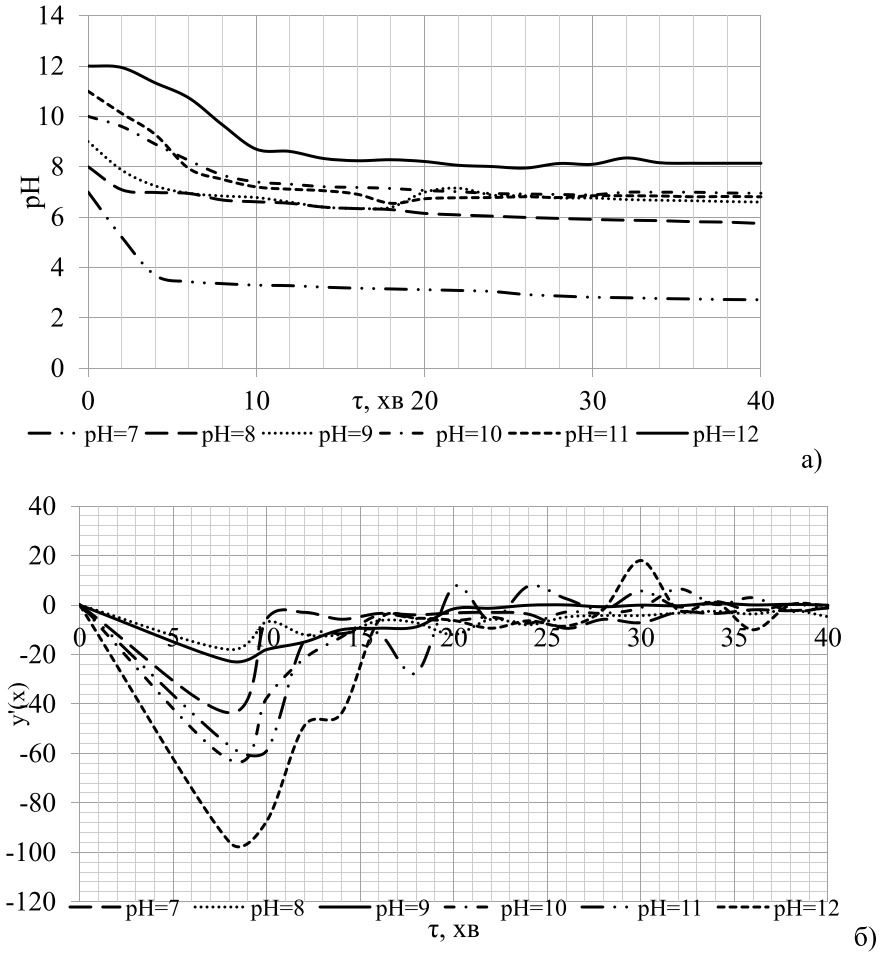

Fig. 21.10 Dependence of pH on the time of CNP treatment for initial pH = 7–12 in the system Zn^{2+}–Fe^{2+}–SO_4^{2-}–OH^-, C[$FeSO_4$]/C[$ZnSO_4$] = 2 (**a**) and the corresponding differential curves (**b**)

the formation of final products. Analyzing the pH change curves (Fig. 21.10), it can also be noted that low pH values are very sensitive to the influence of CNP and are characterized by a high slope. It was in such curves that a sharp change in pH for the first stage was noted.

For the system Cu^{2+}–Fe^{2+}–SO_4^{2-}–OH^-, the increase in pH during oxidation with time is special. This can be explained by the combination of oxidation and reduction processes of HPH with time.

The indicators characterizing the oxidation process are the oxidation time at the first stage and the total oxidation time in the systems Cu^{2+}–Fe^{2+}–SO_4^{2-}–OH^- and Zn^{2+}–Fe^{2+}–SO_4^{2-}–OH^-. Figures 21.12 and 21.13 show the total oxidation time

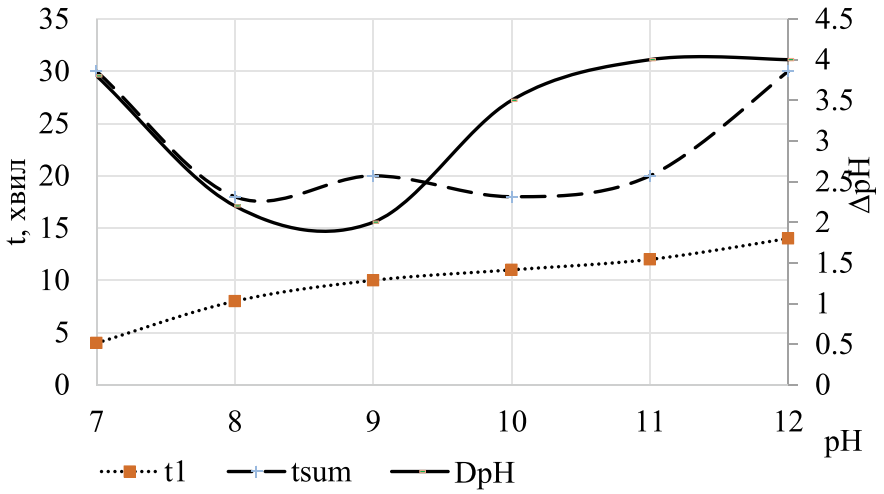

Fig. 21.11 Dependence of the time of complete oxidation for the first stage (1) and the second stage (2) and the total change in pH on the initial pH in the Zn^{2+}–Fe^{2+}–SO_4^{2-}–OH^- system

depending on pH. In this case, there is only one stage in the entire pH range. An anomalous increase in the value of ΔpH with increasing pH is observed.

That is, it is very important to be able to determine how the stability of heteropolyhydroxides changes depending on the pH of the solution. This is the main thing for determining the appropriate pH of the oxidation of the obtained heterohydroxy complexes. Numerous experimental data have shown that depending on the pH of the initial solution, different products are formed, which is primarily explained by the oxidation rate. Rapid oxidation leads to the formation of oxyhydroxides, which are not the target compounds. Oxidation at a pH corresponding to the most stable particles allows for obtaining crystalline ferrite particles with high magnetic characteristics. The second stage (Fig. 21.7, 21.8, 21.9, 21.10, 21.11 and 21.12) is almost insensitive to the initial pH, and we can conclude that it is the first stage that regulates the oxidation process and the phase composition of the formed compounds, which is observed in Fig. 21.10a.

That is, it is very informative to compare the results of studying the dependence of the stability of the formed hydroxo complexes on pH and the kinetics of oxidation on pH in order to determine the mechanism of ferritization.

Most of the proposed transformation chains relate to the formation of ferrites during hydrothermal treatment or oxidation. Calculated data are given on the possibility of coprecipitation in the system of Co–Zn ferrites, or Ni–Zn ferrites [6], based on the close pH values of the precipitation of the corresponding hydroxides. From this point of view, the formation of spinel phases from coprecipitated hydroxides observed in the systems $NiAl_2O_4$, and $CoAl_2O_4$ [23, 24]. The mechanism of spinel structure formation during precipitation of iron(II) hydroxides with sodium carbonate is explained by the course of a heterogeneous reaction, according to which crystalline

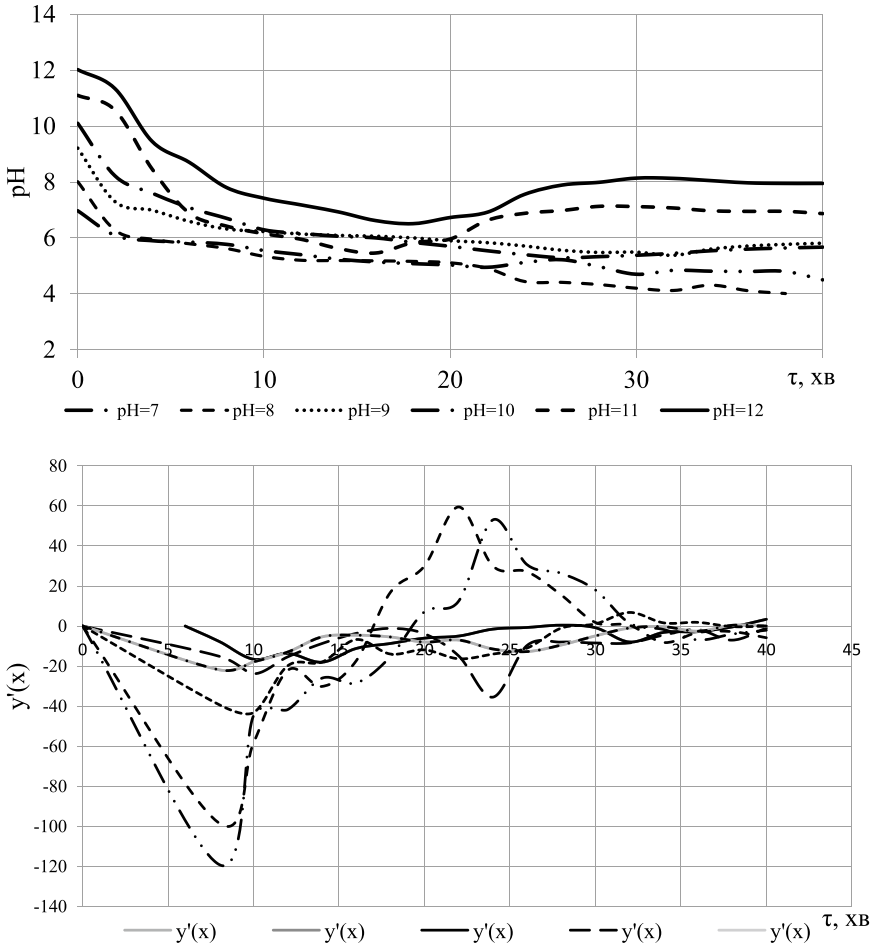

Fig. 21.12 Dependence of pH on the time of treatment of CNP for initial pH = 7–12 in the system Cu^{2+}–Fe^{2+}–SO_4^{2-}–OH^-, C[$FeSO_4$]/C[$CuSO_4$] = 2 (**a**) and the corresponding differential curves (**b**)

plates of iron(II) hydroxide carbonate are first formed, with the subsequent formation of Fe_3O_4/γ–Fe_2O_3. Ferrihydrite particles grow over time due to the dissolution of iron(II) hydroxide carbonate plates [25]. A similar mechanism of coprecipitation is proposed by the authors [26]. When there is a large difference in the solubility of trivalent and divalent metal hydroxides, the formation of DLH occurs by dissolving the trivalent hydroxide with subsequent precipitation of DLH. When the solubility products of two binary hydroxides are close, as in the case of the Zn–Al system, there is also the possibility of coprecipitation, which plays a major role in the formation of DLH. That is, at present, the main influencing factor is considered to be the solubility product of an individual hydroxide or the coincidence of the pH of precipitation.

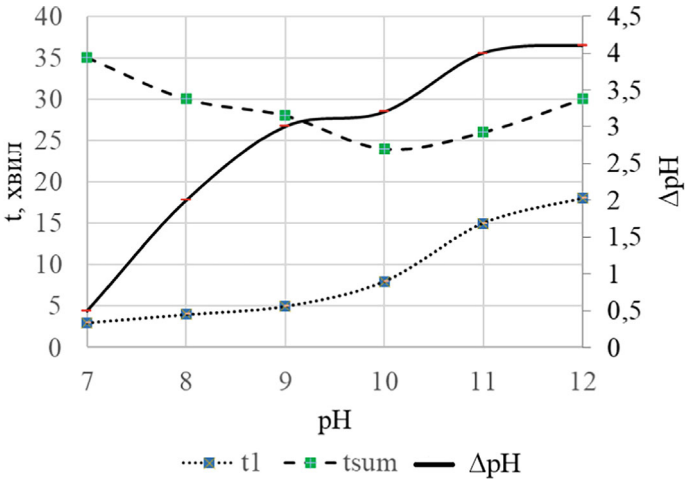

Fig. 21.13 Dependence of the time of complete oxidation for the first stage (1) and the second stage (2) and the total change in pH on the initial pH in the system Cu^{2+}–Fe^{2+}–SO_4^{2-}–OH^-

In [27], information is also provided on the interaction of Me^{2+} cations with ferrihydrite at a temperature of 60–70°, which can lead to the formation of a spinel phase. It was believed that nucleation occurs in the aqueous layer and then the particles are adsorbed on the surface of ferrihydrite. Growth occurs due to the dissolution of polyhydroxy complexes. However, there is no conclusion in the literature on the most significant factor determining the degree of coprecipitation. The degree of formation of the final ferrite is determined by the first main stage of the production technology—coprecipitation. Scientific groups have different views on this issue, but the dominant idea is that the similarity of the pH of precipitation, valences, and ionic radii of cations is significant. At high temperatures, under conditions of possible spontaneous oxidation of iron compounds, the formation of ferrites from coprecipitated hydroxides can be considered according to the goethite transformation mechanism. This mechanism is the most widely used and is most often used to explain the peculiarities of ferrite formation [28]. The following transformation scheme can be assumed:

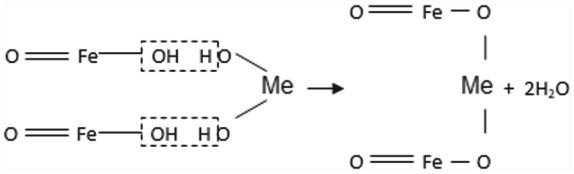

(21.8)

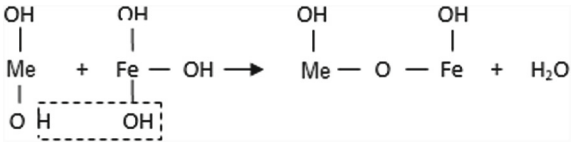

(21.9)

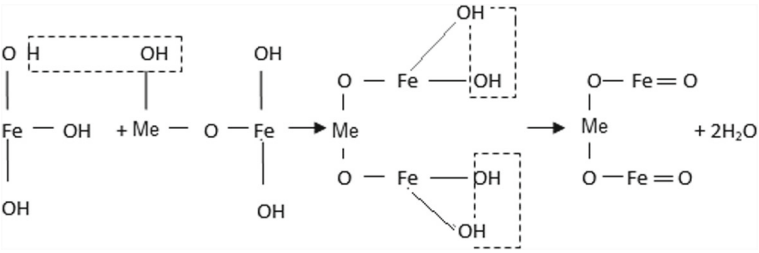

(21.10)

These equations show that in the process of spinel formation, intermediate compounds, hydroferrites, are initially formed. That is, the reaction of ferrite formation can be considered as the interaction of a polybasic base and an acid, and ferrite itself as a metal(II) ferrite.

But the mechanism of ferrite formation is much more complex and cannot be reduced to a purely topochemical reaction, especially for the multistage mechanism of formation from divalent salts. The study of reactions (21.8–21.10) is complicated by the fact that iron(II) compounds are unstable, prone to oxidation, and usually two parallel processes occur simultaneously: the formation of ferrites and the oxidation of iron(II) hydroxide to iron(III) oxyhydroxide. The rate of both reactions depends on the pH of the solution, temperature, the presence of impurities, and other conditions. The overall rate is determined by the rate of the limiting stage.

The scientific group [25] proposed a method for studying the mechanism of growth of iron hydroxide particles using an X-ray synchrophasotron at low temperatures. The work defines some parameters that influence the degree of coprecipitation of cations in iron(III) oxides, from the point of view of the similarity of the oxidation state and ionic radius of cations, the presence of structural defects, the determining conditions of synthesis (pH, temperature, $n = Me^{2+}/Fe^{3+}$). In the case of substitution of isomorphic cations in iron(III) oxyhydroxide, the nature of the cation determines the degree of coprecipitation.

Most authors believe that the mechanism of ferrite formation occurs by the adsorption mechanism, by embedding cations into the magnetite structure.

The possibility of coprecipitation and embedding into the crystal lattice of magnetite was studied [29] for small amounts of cations (< 1%) Co, Ni, Zn, Cu, Mn and Cd. Uniform distribution of various elements in magnetite crystals, investigated by the sequential precipitation-dissolution procedure, was found in the case of Co, Ni and Zn. However, Cu, Mn and Cd, as a rule, accumulated near the surface of magnetite particles. The authors explained this phenomenon by the lower electronegativity of Cu^{2+} and its ability to exhibit the Jahn–Teller effect and by the larger ionic radii of Mn^{2+} and Cd^{2+}, which may be the reason for their uneven distribution in magnetite crystals. Similar results were obtained for goethite and hematite when incorporating Cr^{3+}, Mn^{2+}, Ni^{2+} cations [30]. To explain the behavior of the introduction of a small amount of metals (1–15%), the authors [31] give the values of the covalence of these metals in the series Mn^{2+}, Co^{2+}, Ni^{2+}, Cu^{2+} та Zn^{2+}. Except Mn^{2+}, the considered metal ions stabilized ferrihydrite and increased the amount of hematite in the reaction product. The authors explained the stabilizing ability of these

ions with an increase in the covalence of these metals in the series. Having more than 15% of divalent metal ion, ferrihydrite transforms into spinel phase by dissolution–precipitation mechanism. The proposed mechanisms of ferrite formation cannot be used for the case of obtaining ferrites by precipitation technology with subsequent CNP treatment.

21.4 Conclusions

Pourbaix diagram and were constructed for iron in the systems Co^{2+}–Fe^{2+}–SO_4^{2-}, Ni^{2+}–Fe^{2+}–SO_4^{2-}, Zn^{2+}–Fe^{2+}–SO_4^{2-}, Mn^{2+}–Fe^{2+}–SO_4^{2-},Cu^{2+}–Fe^{2+}–SO_4^{2-}, which showed that in a number of the considered cations the region of existence of oxide compounds decreases as follows $Fe^{2+} > Zn^{2+} > Ni^{2+} > Co^{2+} > Mn^{2+} > Cu^{2+}$. Theoretically calculated regions of existence reflect the general regularities of ferrite formation. The possibility of obtaining spinel ferrites by the hydrophase method under the action of CNP is shown.

Experimental study of the oxidation process under the action of CNP in the systems Fe^{2+}–SO_4^{2-}–OH^-,Co^{2+}–Fe^{2+}–SO_4^{2-}–OH^-, Ni^{2+}–Fe^{2+}–SO_4^{2-}–OH^-, Zn^{2+}–Fe^{2+}–SO_4^{2-}–OH^-,Cu^{2+}–Fe^{2+}–SO_4^{2-}–OH, Mn^{2+}–Fe^{2+}–SO_4^{2-}–OH^- showed that the ferritization process and the phase composition of the final products in systems containing several metal cations are determined by the stability of the formed heteropolyhydroxides. A general multi-stage mechanism of ferritization under the action of CNP has been established, which includes the formation of hydroferrites and intramolecular dehydration due to the formation of double bonds.

References

1. A.K. Nikumbh, R.A. Pawar, D.V. Nighot, G.S. Gugale, M.D. Sangale, M.B. Khanvilkar, A.V. Nagawade, Structural, electrical, magnetic and dielectric properties of rare-earth substituted cobalt ferrites nanoparticles synthesized by the co-precipitation method. J. Magn. Magn. Mater. **355**, 201–209 (2014)
2. P.A. Shaikh, R.C. Kambale, A.V. Rao, Y.D. Kolekar, Structural, magnetic and electrical properties of Co–Ni–Mn ferrites synthesized by co-precipitation method. J. Alloy. Compd. **492**(1–2), 590–596 (2010)
3. M.P. Gonzalez-Sandoval, A.M. Beesley, M. Miki-Yoshida, L. Fuentes-Cobas, J.A. Matutes-Aquino, Comparative study of the microstructural and magnetic properties of spinel ferrites obtained by co-precipitation. J. Alloy. Compd. **369**(1–2), 190–194 (2004)
4. P. Iranmanesh, S.T. Yazdi, M. Mehran, S. Saeednia, Superior magnetic properties of Ni ferrite nanoparticles synthesized by capping agent-free one-step coprecipitation route at different pH values. J. Magn. Magn. Mater. **449**, 172–179 (2018)
5. T. Jahanbin, M. Hashim, K.A. Matori, S.B. Waje, Influence of sintering temperature on the structural, magnetic and dielectric properties of $Ni_{0.8}Zn_{0.2}Fe_2O_4$ synthesized by co-precipitation route. J. Alloy. Compd. **503**(1), 111–117 (2010)

6. X. Huang, J. Zhang, W. Wang, T. Sang, B. Song, H. Zhu, C. Wong et al., Effect of pH value on electromagnetic loss properties of Co–Zn ferrite prepared via coprecipitation method. J. Magn. Magn. Mater. **405**, 36–41 (2016)
7. S. Krehula, S. Popović, S. Musić, Synthesis of acicular α-FeOOH particles at a very high pH. Mater. Lett. **54**(2), 108–113 (2002)
8. B. Morgan, O. Lahav, The effect of pH on the kinetics of spontaneous Fe(II) oxidation by O_2 in aqueous solution–basic principles and a simple heuristic description. Chemosphere **68**(11), 2080–2084 (2007)
9. A.V.Kravchenko, V.S.N Kublanovskyi, A.A. Pyvovarov, V.P. Pustovoitenko, Nyzkotemperaturnыi plazmennыi elektrolyz: Teoryia y praktyka. Monohrafyia.: OOO «Aktsent PP»: Dnepropetrovsk, 222 s (2012)
10. L.A.Kuz'micheva, Y.V. Titova, A.I. Maksimov, A.S. Vashurin, S.G. Pukhovskaya, Effect of the cathode material on the accumulation of hydrogen peroxide in a plasma-solution system. Surf. Eng. Appl. Electrochem. **49**(6), 485–487 (2013)
11. V.V. Rybkin, D.A. Shutov, Atmospheric-pressure electric discharge as an instrument of chemical activation of water solutions. Plasma Phys. Rep. **43**(11), 1089–1113 (2017)
12. P.Bruggeman, C. Leys, Non-thermal plasmas in and in contact with liquids. J. Phys. D. Appl. Phys. **42**(5), 053001 (2009)
13. A.R. Denaro, K.O. Hough, Glow-discharge electrolysis of sulphuric acid solutions. Electrochim. Acta **17**(3), 549–559 (1972)
14. J. Baumgartner et al., Nucleation and growth of magnetite from solution. Nat. Mater. **12**(4), 310–314 (2013)
15. L.A. Frolova, M.P. Derhachov, The effect of contact non-equilibrium plasma on structural and magnetic properties of $Mn_XFe_{3-X}O_4$ spinels. Nanoscale Res. Lett. **12**(1), 505–515 (2017)
16. M.Pourbaix, Atlas of electrochemical equilibria in aqueous solution. NACE, 307 (1974)
17. F.G. Stickland, Thermal formation of ferrites from amorphous precipitates. J. Phys. Chem. **67**(11), 2504–2505 (1963)
18. L.A. Frolova, Production conditions of iron oxide black from pickle liquors. Metall. Min. Ind. (4), 65–69 (2014)
19. L.A. Frolova, T.V. Hrydnieva, Influence of various factors on the ferric oxyhydroxide synthesis. J. Chem. Technol. **28**(1), 61–67 (2020)
20. L.A. Frolova, et al., Recuperation of etching solutions with obtaining pigments on the basis of ferrum oxide. in *2017 IEEE 7th International Conference Nanomaterials: Application & Properties (NAP)*. IEEE, pp 01NNPT09-1–01NNPT09-4 (2017)
21. A.E. Chastukhin, A.D. Izotov, I.G. Gorichev, A.M. Kutepov, Analysis of Fe_2O_3 and Fe_3O_4 dissolution kinetics in terms of the chain mechanism model. Theor. Found. Chem. Eng. **37**, 398–406 (2003)
22. E.R.Encina, M. Distaso, R.N. Klupp Taylor, W. Peukert, Synthesis of goethite α-FeOOH particles by air oxidation of ferrous hydroxide Fe $(OH)_2$ suspensions: insight on the formation mechanism. Cryst. Growth Des. **15**(1), 194–203 (2015)
23. Фролова, Л. А.; Півоваров, О. А. Дослідження умов синтезу вихідних речовин одержання алюмінату кобальту. Nanosyst. Nanomater. Nanotechnologies **11**(2), с 303–312 (2013)
24. L. Frolova, T. Butyrina, Investigation of the conditions of synthesis of Alumo-Nickel spinel. in *Nanocomposites, Nanostructures, and Their Applications. NANO 2018*, vol. 221 eds by O. Fesenko, L. Yatsenko (Springer Proceedings in Physics. Springer, Cham, 2019), pp. 243–250
25. A.P. LaGrow, M.O. Besenhard, A. Hodzic, A. Sergides, L.K. Bogart, A. Gavriilidis, N.T.K. Thanh, Unravelling the growth mechanism of the co-precipitation of iron oxide nanoparticles with the aid of synchrotron X-Ray diffraction in solution. Nanoscale **11**(14), 6620–6628 (2019)
26. A.V. Radha, P.V. Kamath, Aging of trivalent metal hydroxide/oxide gels in divalent metal salt solutions: Mechanism of formation of layered double hydroxides (LDHs). Bull. Mater. Sci. **26**(7), 661–666 (2003)
27. S.Mann, N.H.C. Sparks, S.B. Couling, M.C. Larcombe, R.B. Frankel, Crystallochemical characterization of magnetic spinels prepared from aqueous solution. J. Chem. Soc. Faraday Trans. 1 **85**(9), 3033–3044 (1989)

28. J. Hu, S. Li, J. Chu, S. Niu, J. Wang, Y. Du, Z. Li, X. Han, P. Xu, Understanding the phase-induced electrocatalytic oxygen evolution reaction activity on FeOOH nanostructures. ACS Catal. **9**(12), 10705–10711 (2019)
29. P.S. Sidhu, R.J. Gilkes, A.M. Posner, The synthesis and some properties of Co, Ni, Zn, Cu, Mn and Cd substituted magnetites. J. Inorg. Nucl. Chem. **40**(3), 429–435 (1978)
30. B. Singh, D.M. Sherman, R.J. Gilkes, M.A. Wells, J.F. Mosselmans, Incorporation of Cr, Mn and Ni into goethite (α-FeOOH): mechanism from extended X-ray absorption fine structure spectroscopy. Clay Miner. **37**(4), 639–649 (2002)
31. R. Giovanoli, R.M. Cornell, Crystallization of metal substituted ferrihydrites. Zeitschrift für Pflanzenernährung und Bodenkunde. **155**(5), 455–460 (1992)

Chapter 22
Application of Nanotechnology for Natural and Marine Waters Monitoring

Svitlana Kyrii and Tetiana Dontsova

Abstract This article provides an overview of recent advancements in nanomaterials usage such as quantum dots, noble metals, carbon nanostructures (graphene and carbon nanotubes), magnetic nanoparticles, etc. for monitoring natural and marine waters. It highlights the application of nanomaterial-based sensors, including electrochemical nanosensors and optical sensors, for detecting various pollutants such as bacteria, chemical oxygen demand (COD), heavy metals (e.g., Pb^{2+}, Cu^{2+}, Cd^{2+}, Cr^{6+}, Cr^{3+}, Ni^{2+}), and arsenic. Additionally, the paper explores different types of nanobiosensors and their role in identifying heavy metals in surface and marine waters. It also discusses using nanostructured membranes as contaminant indicators for microplastic detection.

22.1 Introduction

Natural and marine water monitoring for different contaminants is critical for guaranteeing environmental and economic security, sustainable use of marine resources, and biodiversity conservation. In the current context of Russian aggression, which is causing unprecedented environmental contamination, as well as anthropogenic pressure and climate change, monitoring of water bodies, mainly natural and marine waters, is critical and strategically important. Timely monitoring makes it possible to quickly identify harmful substances and take specific measures to prevent their negative impact on ecosystems.

The natural water and marine environment is subject to significant negative impacts daily due to various natural and anthropogenic pollution. The most common pollutants of natural and marine waters are oil products [1, 2], heavy metals [3–6],

S. Kyrii (✉) · T. Dontsova
National Technical University of Ukraine "Igor Sikorsky Kyiv Polytechnic Institute", Kyiv, Ukraine
e-mail: kyrii.svitlana@lll.kpi.ua

O. Fesenko and L. Yatsenko (eds.), *Functional Nanomaterials, Nanocatalysts, Nanotechnologies, and Their Applications*, Springer Proceedings in Physics 321,
https://doi.org/10.1007/978-3-031-99136-3_22

phosphates and nitrates [7–10], antibiotics [11, 12], pesticides and herbicides [13–15], various organic contaminants [16, 17], microplastic [18–20] etc. These pollutants seriously threaten human health, marine ecosystems and biodiversity daily. In the context of military conflicts, natural and marine waters can be additionally contaminated by a wide range of pollutants, including metals (iron, lead, cadmium, mercury, etc.), chemicals (explosives and their decomposition products, oil products), microplastics, etc. The primary sources of marine pollution attributable to hostilities include submerged warships, aircraft, UAVs and other equipment, emissions of oil products, heavy metals, remnants of mines and ammunition, and chemical contamination from explosives etc. [21].

Monitoring natural and marine water bodies is an integral and effective part of environmental protection and sustainable development. It ensures early pollution detection, assesses environmental risks, and creates the basis for effective environmental protection measures [22].

A wide range of modern high-performance materials, including nanomaterials, are used to ensure effective monitoring. Due to their large specific surface area and high reactivity [23, 24], nanomaterials demonstrate incredible performance and can be used as excellent sensors [25], adsorbents [26, 27], photocatalysts [24, 28], etc.

Nanostructured electrodes have been actively used as sensors for various environmental applications [29]. Nanomaterial-based sensors, with their superior properties, are recognised for their precision, sensitivity, and selectivity, providing a reliable tool for environmental monitoring. Moreover, nanomaterials can significantly increase the sensitivity of sensors, ensuring accurate detection even at low concentrations [30]. This precision and sensitivity offer reassurance about the accuracy of the monitoring process, instilling confidence in the data collected.

The growing interest in sensors based on nanomaterials is evidenced by the analysis of Scopus publications (Fig. 22.1). The graph shows that the number of studies for nanomaterial-based sensors is increasing yearly.

Thus, nanomaterial-based sensors are promising tools for monitoring the natural water and marine environment and detecting a wide range of pollutants, offering hope for a more effective and sustainable approach to environmental protection.

22.2 Using Nanomaterial-Based Sensors

Sensors are specialised devices that are used to detect changes in environmental parameters, concentrations of compounds, or molecules' characteristics. They are characterised by compact size, high reliability, and the ability to integrate with other electronic systems, such as computer processors. This allows for data storage and real-time monitoring [31, 32]. In addition, sensors can detect even very small concentrations of pollutants. They can quantify, qualify, and monitor various environmental pollutants or environmental changes [33].

As modern analytical tools, nanosensors are highly adaptable and effective in real-life conditions, instilling confidence in their versatility. This adaptability has led to

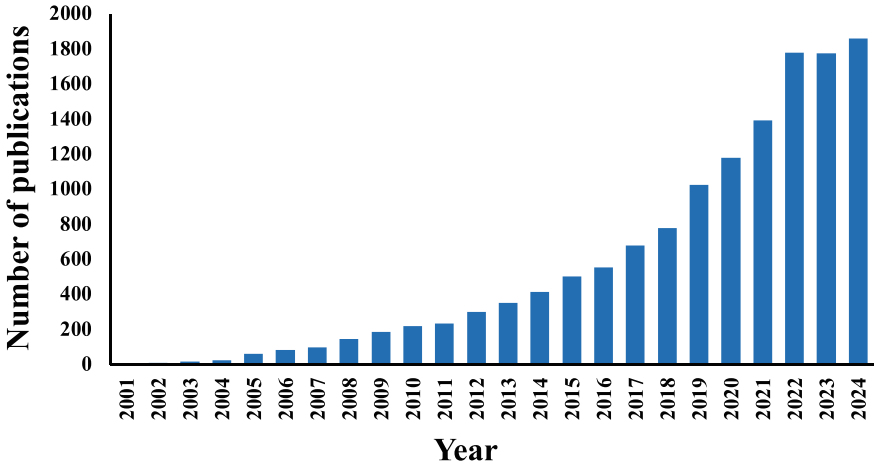

Fig. 22.1 Number of publications reported in Scopus with keywords "nanomaterials and sensors" in the period 2001–2024 (November 2024)

the widespread use of nanomaterials in developing sensors for various applications, including environmental monitoring.

Today, new nanomaterials have various characteristics, such as a wide absorption band in the visible range, high electrical conductivity, good mechanical properties, etc., making them suitable for use in sensors for various applications. A variety of nanomaterials with specified characteristics and controlled nanoscale are widely used. Such materials include metal nanoparticles, magnetic nanospheres, quantum dots, nanotubes, nanowires, nanorods, nanofibres, etc. In addition, nanocomposites, nanofilms, nanopolymers, and nanoplatelet materials that demonstrate unique physical and chemical properties have attracted considerable interest [34]. For example, nanosensors based on various nanomaterials with excellent optical, electrochemical, magnetic, etc. properties have been developed to the present day. In particular, materials such as noble metals (Ag or Au), carbon nanostructures (graphene and carbon nanotubes), quantum dots, magnetic nanoparticles, etc., are able to detect pathogens, organic and inorganic pollutants [35, 36]. At the same time, researchers [37] have found that nanosensors are three to four orders of magnitude more sensitive than thin-film sensors due to their high signal-to-noise ratio. In addition, nanosensors demonstrate excellent properties for water quality monitoring. They can detect extremely low concentrations of pollutants and perform rapid analysis, which can be used, for example, in water quality management [38–40].

22.2.1 Electrochemical Nanosensors

Electrochemical nanosensors detect changes in resistance in a nanomaterial when an analyte is bound due to changes in scattering, emptying, or overflowing of charge carriers. The fundamental principle of an electrochemical sensor is the electrocatalytic reaction between the electrodes and the analyte in the test sample.

Zhou et al. have developed an ultra-sensitive electrochemical sensor for detecting single-cell bacteria based on target-triggered click chemistry and fast scan voltammetry. The linear range and limit of quantification are 1–108 CFU·mL^{-1} and 1 CFU·mL^{-1}, respectively. The sensor's efficiency was demonstrated during the analysis of *E. coli* in seawater and milk samples, with a recovery rate of 94–110%. This approach to detection is actively used, opening up new opportunities for developing methods for identifying single-celled bacteria [41].

Ai et al. developed an electrocatalytic sensor for chemical oxygen demand (COD) determination using an electrode modified with PbO_2 nanoparticles. Organic compounds in the water samples underwent electrocatalytic oxidation, accompanied by the generation of an oxidation current, which served as the basis for recording the sensor signal. The developed sensor demonstrated a linear range of 5–3000 ppm and a detection limit of 2.5 ppm. This type of sensor was characterised by low analysis time, ease of use, and no need for sample preparation. Additionally, the authors noted that the sensor remained stable for 20 days when measuring COD in wastewater [42].

Nanosensors for detecting metals in water have become extremely popular. In particular, the inexpensive copper-based chemical sensor e62800 was developed to detect lead ions by modifying the surface of copper electrodes, as described by the authors in [43]. The sensor's sensitivity allowed a detection limit of 21 nM (4.4 ppb) in real water samples. For the quantitative determination of Pb^{2+} ions in water, researchers [44] used ferroxide@polyaniline (Fe_3O_4@PANI) nanoparticles. This sensor demonstrated significantly increased sensitivity due to the large specific surface area of Fe_3O_4 and the high electrical conductivity of polyaniline. Under optimal conditions, a linear detection range from 0.1 to 104 nmol·L^{-1} was observed, and the detection limit was 0.03 nmol·L^{-1} [44]. Al-Gethami et al. [45] developed a nanosensor based on $CoFe_2O_4$/Ca-alginate nanocomposite to determine Pb^{2+} ions in aqueous solutions at different temperatures. The lowest limit of detection of Pb^{2+} ions was 125 ng. In addition, the authors noted that their sensor has high sensitivity, stability, and rapid detection.

Wu et al. developed a nanosensor for the simultaneous detection of Pb^{2+} and Cu^{2+} ions. This sensor was based on monodisperse spherical Fe_2O_3 nanoparticles with a diameter of 80–100 nm synthesised by a new emulsion hydrothermal meth-od and subsequent annealing in an Ar atmosphere. The authors found that the detection limits of this nanosensor are 9.48 nM and 38.31 nM for Pb^{2+} and Cu^{2+}, respectively [46].

Scientists have also developed various sensors to detect Cd in water. Ruigang et al. developed an electrochemical sensor for cadmium detection using nanostructured carbon electrodes based on soot-naphtha-glassy carbon. The fabricated sensor

exhibited a linear response range between 6 and 1000 nM for selective electrolytic determination of cadmium, with a detection limit of 8 nM (0.9 $\mu g \cdot L^{-1}$) in water [47]. Using a spin-coating method, Taneja et al. [48] coated a nanocomposite of single-walled carbon nanotubes and beeswax onto the sensor. The resulting sensor demonstrated excellent sensitivity with a very low detection limit of 5.2 ppb in an aqueous medium [48]. Al-Qasmi et al. [49] used synthesised cuprospinel nanoparticles in their nanosensor to detect low-concentration Cd^{2+} ions in aqueous solutions. Such a nanosensor detected traces of Cd^{2+} ions with a concentration of about 3.6 $ng \cdot L^{-1}$. For the ultrasensitive potentiometric detection of Cd^{2+} ions, Singh et al. used a CNT-Cu-MOF electrochemical sensor based on multi-walled carbon nanotubes and a copper metal–organic framework [50]. Such a sensor demonstrated stability, selectivity for Cd^{2+} ions, and repeatability of results.

Mohammadzadeh et al. developed a colourimetric nanosensor to detect Cd^{2+} and Ni^{2+} ions [51]. This sensor was based on synthesised silver nanoparticles and demonstrated good selectivity, sensitivity, and linearity. In addition, it achieved satisfactory recoveries ranging from 90.57 to 113.61%.

Various scientists have also paid considerable attention to detecting chromium ions in water by sensors. For example, Salimi et al. [52] developed an electrochemical sensor for the detection of Cr^{3+} using a nanocomposite containing chitosan and multi-walled carbon nanotubes as a platform for immobilising electrodeposited nanostructured manganese oxide. This sensor showed excellent electrocatalytic activity for Cr^{3+} oxidation in solutions with neutral pH. The sensor's detection limit, sensitivity and linear range were 0.3 μM, 18.7 $nA \cdot \mu M^{-1}$ and 3–200 μM, respectively.

To simultaneously detect and remove Cr^{6+}, Roy et al. [53] created a nanosensor based on copper-doped bemite nanomaterial. The nanosensor demonstrated sensitivity with a detection limit of around 6.24 μM and selectivity for Cr^{6+} ions. The sensor also showed versatility in the adsorption removal of Cr^{6+} from wastewater, with an extremely high adsorption rate of around 85% in 5 min.

Thus, studies of electrochemical nanosensors detecting various pollutants in different water environments demonstrate significant potential for their application in monitoring, including marine waters.

22.2.2 Optical Sensors Based on Nanomaterials

The development of optical nanosensors using nanomaterials with different properties has shown the possibility of detecting various pollutants, including heavy metals [54], pesticides [55] and other chemical substances [56]. Optical nanosensors are chemical sensors that use electromagnetic radiation to generate an analytical signal in a transducer element. The interaction of the sample with the radiation results in a change in a specific optical parameter that can be correlated with the analyte concentration [57]. An optical sensor typically consists of transducer components that act as indicators of the optical signal and detection elements that can interact specifically with the target analyte [58]. The principle of operation of such sensors is based on

the change in optical characteristics, such as absorption, transmission, emission, or lifetime, which occurs due to the binding of an immobilised indicator to an analyte [59].

Colourimetric methods, due to their high sensitivity, low cost, simple design, and the possibility of quick and easy determination without special equipment, are currently attracting considerable interest among optical nanosensors [60]. For example, gold-based nanomaterials demonstrate a unique ability to physically adsorb a variety of biological compounds through functional groups containing sulfur or nitrogen, such as antibodies or nucleic acid probes, making them promising for the development of, for example, fluorescent biosensors [61]. Amin et al. have developed a fluorescent lab-in-a-tube sensor for detecting *E. coli* using FRET-based on gold nanoclusters (AuNCs), and AuNPs conjugated with antibodies [62, 63]. The results showed that the system provided both qualitative analysis (visual inspection with the naked eye) and quantitative analysis (using a smartphone with a LOD of 4.0 $CFU \cdot mL^{-1}$).

Jing et al. found that polymeric nanomaterials can enhance fluorescence signals due to the delocalisation and rapid diffusion of excitons through their structure [62, 64]. This assumption was confirmed by Kumar et al. when they presented a copolymer in which, due to the presence of several functional groups on the copolymer chain, several analytes can be detected with high selectivity. Their work used copolymer P(MMA-co-Dansyl-Ala-HEMA) synthesised by RAFT copolymerisation to detect nitroaromatic compounds. In addition, the authors noted the long-term stability of polymeric nanomaterials, which ensured stable and reliable operation of the developed sensor [65].

Pankaew et al. have developed colourimetric sensors for the detection of copper (II) ions (Cu^{2+}) with high sensitivity and selectivity based on incorporated carbon dots of polyethyleneimine polymer for environmental and forensic applications [66]. The authors found that UV sensitivity could be significantly increased by adding poly(vinylpyrrolidone) with MW 10,000 or poly(N-vinyl formamide) 18,000 $g \cdot mol^{-1}$ to DA assemblies. The presence of these polymers also causes a colour change at a much longer UV irradiation time compared to the system made of pure polydiacetylene [66]. To detect Cu^{2+} ions, Jeevika [67] developed a chemosensor based on a PVA hydrogel impregnated with safranin. The operation of such a sensor is based on the change in colour of safranin from the basic red to yellow with a shift in the absorption peak to the blue side due to the formation of a complex between Cu^{2+} and safranin. The LOD of the chemosensor probe was calculated and found to be 8.6×10^{-6} M $\pm$ 0.004 with a linear coefficient of $R^2 = 0.986$. As a result, the author notes that the developed chemosensor demonstrates good selectivity, sensitivity, and reproducibility and can be used for real-time monitoring of Cu^{2+} in water.

Another effective and relatively inexpensive colourimetric strip sensor based on a polymeric hydrogel was developed by Das and Sarkar [68] for the detection of arsenate, including in the field. The developed strip sensor works based on a reduction reaction between arsenate ion and ammonium molybdate. To create it, we used the encapsulation of ammonium molybdate in a polymeric hydrogel consisting of polyvinyl alcohol, glutaraldehyde and acrylamide. The method was based on the

formation of a blue arsenomolybdate complex under reducing conditions, which can be visually identified at a detection limit of up to 10 ppb [68]. Also, Xu et al. proposed ultrasensitive colourimetric nanoprobes for arsenic detection using unmodified gold nanoparticles and rhodamine-B as a colour indicator [69]. This technique is based on inhibiting the catalytic oxidation reaction between rhodamine-B and sodium borohydride with the participation of AsO^{2-} ion, which causes a change in colour and absorbance peak. The proposed assay demonstrates high selectivity to interfering ions and provides sensitivity with a detection limit of 0.64 ppb, which is lower than the WHO recommended level of arsenic in drinking water.

A new direction in the development of nanomaterials is the development of quantum dots. These materials can be used to detect heavy metals. Hydrophilic graphene quantum dots were used to detect Hg^{2+}, Cd^{2+}, and Pb^{2+} in the study by Anusuya et al. [70]. The authors used an optical nanosensor designed in such a way that the detection limit of 1.171 μM, 2.455 μM and 2.011 μM for Hg^{2+}, Cd^{2+} and Pb^{2+} ions, respectively. In the work of Sui et al. [71], a probe based on CdTe/ZnS quantum dots coated with L-cysteine was synthesised with CdTe as a core template and a ZnS shell. The detection limit of Ni^{2+} was 5.9 × 10–10 mol·L^{-1} with a Ksv value of 3.09 × 106 mol·L^{-1}. This development was tested for tracking Ni^{2+} ions in surface drinking and river water samples with recoveries in the 87.6–117.1% range.

22.3 Nanobiosensors

A biosensor is an analytical device that uses biomolecular interactions on its surface to detect any biochemical changes and rejects non-specific, unintended signals [72]. A biosensor consists of two parts: a sensing element and a bioelement. The bioelement can be tissue, living cells, enzymes, antibodies, etc., while the sensing element can be impedance, electric current, electric potential or electrical conductivity. The sensing element converts the biochemical signal into another form of signal, and the bioelement is responsible for the detection of a specific analyte [73]. Depending on the type of biological signalling mechanism and signal transmission mechanism, there are four different categories of biosensors: potentiometric biosensors, amperometric biosensors, conductometric biosensors, and impedimetric biosensors. A potentiometric biosensor measures the potential difference between an indicator electrode and a reference electrode in a system, with the potential being directly related to the concentration of the target analyte. These sensors are based on the selective recognition of specific molecules by a biological component and the transduction of this recognition event into an electrical signal. An amperometric biosensor measures the current generated by the oxidation or reduction of an electroactive species at an electrode surface. The current produced is directly proportional to the concentration of the target analyte in the sample. A conductometric biosensor measures changes in the solution's electrical conductivity due to a biochemical reaction. These changes occur because of the production or consumption of ions during the analyte interaction with the biological recognition element. A conductometric biosensor uses two

noble metal electrodes immersed in a solution to measure its conductivity. Enzymatic reactions serve as a mechanism for converting neutral substrates into charged products that change the conductivity of the medium. Despite the limited distribution of such sensors, this method is widely used to determine the salinity of marine ecosystems [74]. For example, a study [75] examined the impact of Cr^{6+} pollution by inhibiting thiosulfate-oxidising bacteria. The analysis was carried out by measuring electrical conductivity, pH and sulphate formation due to thiosulphate oxidation. These bacteria use thiosulfate as an electron donor, forming sulfate accompanied by decreased pH and increased electrical conductivity. This makes it possible to determine Cr^{6+} concentrations in dissolved water of less than 100 $\mu g \cdot L^{-1}$. In addition, Qambrani et al. also used thiosulfate-oxidising bacteria to detect Cr^{6+} with a detection limit of 100 $\mu g \cdot L^{-1}$ and used sulfur-oxidising bacteria to determine both Cr^{3+} and Cr^{6+} [75]. In the study by Çevik et al., a $PdRuO_2$/PVP nanomaterial was synthesised and used as an ionophore in potentiometric sensor electrodes for detecting Cr^{3+} ions. The potentiometric characteristics of the sensor were investigated within the concentration range of 1×10^{-6}—1.0×10^{-1} M. The detection limit of this sensor was exceptionally low, at 8.6×10^{-8} M. The potentiometric measurements demonstrated the high efficiency of the $PdRuO_2$/PVP ionophore for Cr^{3+} detection across a wide pH range (2.0–8.0) and confirmed its stability, which remained effective for over one year [76]. Caroline et al. demonstrated the quantification of chromium in groundwater using an enzymatic amperometric biosensor, where cytochrome c3 (Mr 13,000) from D. norvegicum (DSM 1741) was evaluated for pH, temperature and ionic strength [77]. Nepomuscene et al. [78] developed a sol–gel immobilisation sensor for detecting chromium in water, utilising enzyme inhibition activity, and assessed the effects of both free and immobilised enzymes on biosensor performance. For chromium concentrations up to 50 $mg \cdot L^{-1}$, a current change of approximately 200 μA was observed. The activity of immobilised urease, inhibited by chromium ions, was restored by soaking the sensor chip in a buffer solution containing ethylenediaminetetraacetic acid. Additionally, kinetic parameters were evaluated, demonstrating that the biosensor's activity and stability remained consistent after six uses over four days [78].

22.4 Nanostructured Membranes for Concentrating Contaminants

Modern advances in materials science and engineering have led to the development of new membrane materials with improved properties and increased selectivity. The use of innovative membranes based on nanomaterials is of great interest due to their potential to solve urgent problems related to water scarcity and environmental pollution, which are becoming increasingly important in the global context. In particular, ceramic membranes made of nanostructured materials have demonstrated

high potential for improving the efficiency and selectivity of membrane technologies [79–83].

The integration of nanomaterials into the structure of membranes can be achieved by two main approaches: surface deposition or incorporation into the membrane matrix. These methods significantly improve the physical and chemical characteristics of membranes and increase their efficiency. Such approaches make it possible to functionalise the surface of membranes to provide them with properties such as increased selectivity, long-term operational stability and improved permeability, allowing them to solve various separation applications. In addition, introducing nanomaterials into membranes has opened up new prospects for developing highly efficient solutions in areas such as water purification or pollutant detection [84]. That is, highly selective membranes responsible for the selective concentration (separation) of target analytes or their molecular recognition can be the basis for highly sensitive sensors [84].

The procedure for using membranes to detect certain contaminants can be as follows: The water samples are collected in a large container, separated using a pump, filtered, and collected using an autosampler [85]. Since the collected water is to be filtered, the choice of pore size of the filter membranes is crucial.

Specific membranes can be successfully used to detect micro- and nanoplastics in water. There are three main approaches to detecting and treating water-containing microplastics: density separation, membrane filtration and sieving, and visual sorting. The density separation method, which is based on the difference in density between plastic and sediment, is promising for the quantification and identification of microplastics. However, its application is limited by the small volume of the analysed sample [86].

Therefore, membrane technology is an effective tool for microplastic detection by size separation. Particles of different sizes are separated by filtration through membranes with 1–2 μm diameter pores, usually under vacuum. This method allows for particle size classification and can be integrated with various chemical analytical techniques such as FTIR spectrophotometry, Raman spectroscopy, infrared spectroscopy, scanning electron microscopy etc. [87].

In addition, membranes can be used as part of a biosensing mechanism, performing various roles: mechanical support, transmission component, filter for concentration or dilution of pathogens, and a basis for immobilisation of active proteins [88].

22.5 Conclusions

Monitoring of surface and marine waters is critical due to the growing impact of anthropogenic and natural factors that threaten ecosystems and human health. Intensive urbanisation and industrial, agricultural, and transport development lead to water pollution caused by toxic substances, including heavy metals, pesticides, microplastics, oil hydrocarbons, and organic compounds. The effects of shipping, resource extraction and waste disposal further complicate the situation in marine waters. In

addition, military operations can be an additional pollution factor, causing additional pollution with heavy metals, nitrogen-containing compounds, oil products, etc.

Regular monitoring allows for timely identification of sources and extent of pollution, assessment of water's ecological status, and development of effective strategies for water conservation and restoration. This approach is a key element of sustainable management of aquatic ecosystems and maintaining environmental safety.

It has been determined that using nanomaterials and nanotechnologies is an up-and-coming area for high-quality, efficient and rapid monitoring of surface and marine waters. It has been established that for the monitoring of a wide range of pollutants, there are several areas of application of such nanomaterials as quantum dots, noble metals, carbon nanostructures (graphene and carbon nanotubes), magnetic nanoparticles, etc., in chemical sensors, biosensors and membranes.

Thanks to nanomaterials, modern sensors provide an increased active surface area, improved conductivity and high catalytic activity, which allows for the effective detection of a wide range of pollutants, even at low concentrations. Their compact size and the ability to be integrated with portable systems make them suitable for field research and offline monitoring. The prospects of using such nanosensors also lie in the possibility of their adaptation to work in challenging marine environments, such as high salinity, temperature variability and the presence of multicomponent pollutants. Further research and optimisation of their design can contribute to developing sustainable, cost-effective and highly efficient surface and marine water monitoring systems.

Acknowledgements We are grateful for project of fundamental scientific research, applied research and scientific and technical (experimental) developments of young scientists of Ministry of Education and Science of Ukraine for funding the project 0124U001100 "Novel selective indicator systems for assessing the state of the marine environment in Ukraine" and the project of applied scientific research 0124U001095 "Chemically modified membranes for the rapid detection of nitrogen-containing compounds in natural waters as markers of explosives".

References

1. L.F. Chuah, K.W. Chew, A. Bokhari et al., Biodegradation of crude oil in seawater by using a consortium of symbiotic bacteria. Environ. Res. **213**, 113721 (2022). https://doi.org/10.1016/j.envres.2022.113721
2. E. Bani-Hani, M. Tawalbeh, A. Al-Othman et al., Rheological study on seawater contaminated with oil components. Pol. J. Environ. Stud. **28**(4), 2585–2591 (2019). https://doi.org/10.15244/pjoes/92121
3. S. Mahboob, Z. Ahmed, M.F. Khan et al., Assessment of heavy metals pollution in seawater and sediments in the Arabian Gulf, near Dammam, Saudi Arabia. J. King Saud Univ.—Sci. **34**(1), 101677 (2022). https://doi.org/10.1016/j.jksus.2021.101677
4. I. Trus, M. Gomelya, Effectiveness of nanofiltration during water purification from heavy metal ions. J. Chem. Technol. Metall. **56**(3), 615–620 (2021)
5. I. Trus, M. Gomelya, V. Vorobyova et al., Effectiveness of complexation-nanofiltration during water purification from copper ions. J. Chem. Technol. Metall. **56**(5), 1008–1015 (2021)

6. T.M. Ansari, I.L. Marr, N. Tariq, Heavy metals in marine pollution perspective–a mini review. J. Appl. Sci. **4**, 1–20 (2004). https://doi.org/10.3923/jas.2004.1.20
7. M.D. Patey, M. Rijkenberg, P. Statham, Determination of nitrate and phosphate in seawater at nanomolar concentrations. TrAC, Trends Anal. Chem. **27**(2), 169–182 (2008). https://doi.org/10.1016/j.trac.2007.12.006
8. T. Tyrrell, C. Law, Low nitrate: phosphate ratios in the global ocean. Nature **387**, 793–796 (1997). https://doi.org/10.1038/42915
9. L.M. Mosley, G.L. Aalbersberg William, Nutrient levels in sea and river water along the 'Coral Coast' of Viti Levu, Fiji. S. Pac. J. Nat. Appl. Sci. **21**, 35–40 (2003). https://doi.org/10.1071/SP03007
10. M. Ishizu, K.J. Richards, Relationship between oxygen, nitrate, and phosphate in the world ocean based on potential temperature. J. Geophys. Res. Oceans **118**, 3586–3594 (2013). https://doi.org/10.1002/jgrc.20249
11. M. Litynska, S. Kyrii, O. Nosovska, N. Ryzhenko, Problem of antibiotics in natural water: a review. Water Purif. Technol. Sci. Tech. News, **31**(3), 26–34 (2021). https://doi.org/10.20535/2218-930032021247159
12. D. Dasí, M.L. Camaró-Sala, A. González et al., Antibiotic resistance in seawater samples from East Coast of Spain. Appl. Sci. **14**(5), 1965 (2024). https://doi.org/10.3390/app14051965
13. P. Mercurio, J.F. Mueller, G. Eaglesham et al., Herbicide persistence in seawater simulation experiments. PLoS One. **10**(8): e0136391 (2015). https://doi.org/10.1371/journal.pone.0136391
14. C. Ojemaye, C. Onwordi, D. Pampanin et al., Presence and risk assessment of herbicides in the marine environment of Camps Bay (Cape Town, South Africa). Sci. Total. Environ. **738**, 140346 (2020). https://doi.org/10.1016/j.scitotenv.2020.140346
15. L. Wang, M. Zheng, H. Xu et al., Fate and ecological risks of current-use pesticides in seawater and sediment of the Yellow Sea and East China Sea. Environ. Res. **207**, 112673 (2022). https://doi.org/10.1016/j.envres.2021.112673
16. Litynska, M. Persistent organic pollutants: sources, migration in ecosystems, removal methods in wastewater treatment and remediation of soils and natural water. Water Purif. Technol. Sci. Tech. News. **37**(3), 40–49 (2024). https://doi.org/10.20535/2218-930032023309558
17. M.C. Vagi, A.S. Petsas, M.N. Kostopoulou, Potential effects of persistent organic contaminants on marine biota: a review on recent research. Water **13**(18), 2488 (2021). https://doi.org/10.3390/w13182488
18. S. Kyrii, T. Dontsova, O. Karaschuk, O. Yanushevska, State of the art of microplastic and nanoplastic pollution: origin and removal methods. in *Nanomaterials and Nanocomposites, Nanostructure Surfaces, and Their Applications*, eds. by O. Fesenko, L. Yatsenko, vol. 279 (Springer Proceedings in Physics, 2023), pp. 229–241. https://doi.org/10.1007/978-3-031-18096-5_125_12
19. M. Litynska, Microplastics in natural water: sources and determination. Water Purif. Technol. Sci. Tech. News, **34**(3), 3–9 (2022). https://doi.org/10.20535/2218-930032022277748
20. A. Alfaro-Núñez, D. Astorga, L. Cáceres-Farías et al., Microplastic pollution in seawater and marine organisms across the Tropical Eastern Pacific and Galápagos. Sci Rep **11**, 6424 (2021). https://doi.org/10.1038/s41598-021-85939-3
21. S. Kyrii, M. Litynska, A. Misevych, The war impact on Ukraine's marine environment. Water & Water Purif. Technologies. Sci. Tech. News. **38**(1), 52–61 (2024). https://doi.org/10.20535/2218-930012024316112
22. T. Mitchenko, I. Kosogina, S. Kyrii, The local solutions for water security in Ukraine. in *Proceedings of the NATO Advanced Research Workshop on Physical and Cyber Safety in Critical Water Infrastructure, Sub-Series D: Information and Communication Security*, vol. 56 (2019). pp. 99–106. https://doi.org/10.3233/NICSP190044
23. S. Kyrii, T. Dontsova, I. Kosogina et al., Effect of yttrium and niobium oxide modifiers on physicochemical and photocatalytic properties of titanium (IV) oxide. East.-Eur. J. Enterp. Technol. **4** (112), 67–74 (2021). https://doi.org/10.15587/1729-4061.2021.238347

24. T.A. Dontsova, A.S. Kutuzova, K.O. Bila et al., Enhanced photocatalytic activity of TiO_2/SnO_2 binary nanocomposites. J. Nanomater. **2020**, 1–13 (2020). https://doi.org/10.1155/2020/8349480
25. I. Dimitrievska, P. Paunovic, A. Grozdanov, Recent advancements in nano sensors for air and water pollution control. Material Sci Eng. **7**(2), 113–128 (2023). https://doi.org/10.15406/mseij.2023.07.00214
26. T. Dontsova, S. Kyrii, O. Yanushevska et al., Physicochemical properties of TIO_2, ZrO_2, Fe_3O_4 nanocrystalline adsorbents and photocatalysts. Chem. Pap. **76**(12), 7667–7683 (2022). https://doi.org/10.1007/s11696-022-02433-4
27. S. Kyrii, A. Tyvonenko, I. Kosogina et al., A comparison of carbon-containing and clay sorption materials and (nano)composites based on them. Nor. J. Dev. Int. Sci. **25**(2018), 19–27 (2018)
28. A. Feliczak-Guzik, Nanomaterials as photocatalysts-synthesis and their potential applications. Materials (Basel) **16**(1), 193 (2022). https://doi.org/10.3390/ma16010193
29. B. Bethi, S.H. Sonawane, Nanomaterials and its application for clean environment. Nanomater. Green Energy, Micro Nano-Technol. 385–409 (2018). https://doi.org/10.1016/B978-0-12-813731-4.00012-6
30. N. Jamil, F. Jameel, S.Z. Bajwa et al., Potential carbon nanotube–metal oxide hybrid nanostructures for gas-sensing applications. Met. Oxide-Carbon Hybrid Mater. 459–474 (2022). 00https://doi.org/10.1016/B978-0-12-822694-0.00012-0
31. S. Tilak, N.B. Abu-Ghazaleh, W. Heinzelman, A taxonomy of wireless micro-sensor network models. SIGMOBILE Mob. Comput. Commun. Rev. **6**(2), 28–36 (2002). https://doi.org/10.1145/565702.565708
32. F.G. Mustafa, M. Shahzeb Khan, M.I Asif et al., Water pollutants and nanosensors, in *Aqua-nanotechnology: Applications of Nanomaterials for Water Purification*, pp. 105–133 (2021). https://doi.org/10.1016/B978-0-12-821141-0.00018-5
33. K. Martinez, J.K. Hart, R. Ong, Environmental sensor networks. Computer **37**(8), 50–56 (2004). https://doi.org/10.1109/MC.2004.91
34. F. Arduini, S. Cinti, V. Scognamiglio, D. Moscone, Nanomaterial-based sensors. in *Handbook of Nanomaterials in Analytical Chemistry: Modern Trends in Analysis*, 329–359 (2020). https://doi.org/10.1016/B978-0-12-816699-4.00013-X
35. X.Y. Xue, R. Cheng, L. Shi et al., Nano materials for water pollution monitoring and remediation. Environ. Chem. Lett. **15**(1), 23–27 (2017). https://doi.org/10.1007/s10311-016-0595-x
36. K.K. Singh, Role of nanotechnology and nanomaterials for water treatment and environmental remediation. Int. J. New. Chem. **9**(3), 373–398 (2022). https://doi.org/10.22034/ijnc.2022.3.6
37. S. Khan, M. Naushad, A. Al-Gheethi et al., Engineered nanoparticles for removal of pollutants from wastewater: current status and future prospects of nanotechnology for remediation strategies. J. Environ. Chem. Eng. **9**(5), 106160 (2021). https://doi.org/10.1016/j.jece.2021.106160
38. K. Jain, A.S. Patel, V.P. Pardhi et al., Nanotechnology in wastewater management: a new paradigm towards wastewater treatment. Molecules **26**(6), 1797 (2021). https://doi.org/10.3390/molecules26061797
39. E.F. Mohamed, Nanotechnology: future of environmental air pollution control. Environ. Manag. Sustain. Dev. **6**(2) (2017). https://doi.org/10.5296/emsd.v6i2.12047
40. X.Y. Xue, R. Cheng, L. Shi et al., Nano materials for water pollution monitoring and remediation. Environ. Chem. Lett. **15**(1), 23–27 (2017). https://doi.org/10.1007/s10311-016-0595-x
41. G. Zhou, H. Guo, W. Hao et al., Electrochemical sensor for single-cell determination of bacteria based on target-triggered click chemistry and fast scan voltammetry. Food Chem. **417**, 135906 (2023). https://doi.org/10.1016/J.FOODCHEM.2023.135906
42. S. Lambertz, M. Franke, M. Stelter, P. Braeutigam, Determination of chemical oxygen demand with electrochemical methods: a review. Chemical Engineering Journal Advances **18**, 100615 (2024). https://doi.org/10.1016/J.CEJA.2024.100615

43. W. Kang, X. Pei, C.A. Rusinek et al., Determination of lead with a copper-based electrochemical sensor. Anal. Chem. **89**(6), 3345–3352 (2017). https://doi.org/10.1021/acs.analchem.6b03894
44. F. Kong, Ying, T. Wu et al., An electrochemical sensor based on Fe_3O_4@PANI nanocomposites for sensitive detection of Pb^{2+} and Cd^{2+}. Anal. Meth. 10 (39): 4784–4792 (2018). https://doi.org/10.1039/C8AY01245H.
45. W. Al-Gethami, D. Alhashmialameer, N. Al-Qasmi et al., Design of a novel nanosensors based on green synthesized $CoFe_2O_4$/Ca-Alginate nanocomposite-coated QCM for Rapid Detection of Pb(II) Ions. Nanomaterials **12**(20), 3620 (2022). https://doi.org/10.3390/nano12203620
46. W. Wu, W. Xiong, H. Li, Insights into the Fe oxidation state of sphere-like Fe_2O_3 nanoparticles for simultaneous Pb^{2+} and Cu^{2+} detection. J. Alloy. Compd. **934**, 167863 (2023). https://doi.org/10.1016/j.jallcom.2022.167863
47. R. Attaallah, A. Amine, An ultrasensitive and selective determination of cadmium ions at ppt level using an enzymic membrane with colorimetric and electrochemical detection. Biosensors (Basel). **12**(5), 310 (2022). https://doi.org/10.3390/bios12050310
48. P. Taneja, V. Manjuladevi, R. Gupta, R.K. Gupta, Detection of cadmium ion in potable water using quartz crystal microbalance. Macromol. Symp. **376**, 1600207 (2017). https://doi.org/10.1002/masy.201600207
49. N. Al-Qasmi, W. Al-Gethami, D. Alhashmialameer et al., Evaluation of green-synthesized cuprospinel nanoparticles as a nanosensor for detection of low-concentration Cd(II) ion in the aqueous solutions by the quartz crystal microbalance method. Materials, **15**(18), 6240 (2022). https://doi.org/10.3390/ma15186240
50. S. Singh, A. Numan, H.H. Somaily et al., A novel, eco-friendly multi-walled carbon nanotubes functionalized copper metal-organic framework for ultrasensitive potentiometric detection of cadmium ions. J. Environ. Chem. Eng. **9**(6), 106534 (2021). https://doi.org/10.1016/j.jece.2021.106534
51. S.E. Mohammadzadeh, F. Faghiri, F. Ghorbani, Green synthesis of phenolic capping Ag NPs by green walnut husk extract and its application for colorimetric detection of Cd^{2+} and Ni^{2+} ions in environmental samples. Microchem. J. **179**, 107475 (2022). https://doi.org/10.1016/j.microc.2022.107475
52. A. Salimi, B. Pourbahram, S. Mansouri-Majd, R. Hallaj, Manganese oxide nanoflakes/multi-walled carbon nanotubes/chitosan nanocomposite modified glassy carbon electrode as a novel electrochemical sensor for chromium (III) detection. Electrochim. Acta **156**, 207–215 (2015). https://doi.org/10.1016/j.electacta.2014.12.146
53. S. Roy, S. Bardhan, D.K. Chanda et al., Development of a Cu(II) doped boehmite based multifunctional sensor for detection and removal of Cr(VI) from wastewater and conversion of Cr(VI) into an energy harvesting source. Dalton Trans. **49**, 6607–6615 (2020). https://doi.org/10.1039/D0DT00888E)
54. S. Gupta, N. George, M. Yadav et al., Optical detection of heavy metal contaminants: advancements with bio-functionalized gold nanoparticles in environmental monitoring. Chem. Pap. **78**, 699–714 (2024). https://doi.org/10.1007/s11696-023-03145-z
55. S. Rajat, P. Thakur, A. Thakur et al., Colorimetric sensing approaches of surface-modified gold and silver nanoparticles for detection of residual pesticides: a review. In J Environ Anal Chem. **1**, 1–16 (2019). https://doi.org/10.1080/03067319.2020.1715382
56. J. Xiao, C. Jiang, L. Li et al., UV–vis spectrophotometer and smartphone RGB dual mode detection of inorganic arsenic based on hydride generation iodine–starch system. Microchem. J. **186**, 108298 (2023). https://doi.org/10.1016/j.microc.2022.108298
57. N. Ullah, M. Mansha, I. Khan, A. Qurashi, Nanomaterial-based optical chemical sensors for the detection of heavy metals in water: recent advances and challenges. TrAC, Trends Anal. Chem. **100**, 155–166 (2018). https://doi.org/10.1016/j.trac.2018.01.002
58. P.A. Lieberzeit, F.L. Dickert, Sensor technology and its application in environmental analysis. Anal. Bioanal. Chem. **387**, 237–247 (2007). https://doi.org/10.1007/s00216-006-0926-z
59. P. Gruber, M.P.C. Marques, N. Szita, T. Mayr, Integration and application of optical chemical sensors in microbioreactors. Lab Chip **17**, 2693–2712 (2017). https://doi.org/10.1039/C7LC00538E

60. V.S.A. Piriya, P. Joseph, S.C.G.K. Daniel et al., Colorimetric sensors for rapid detection of various analytes. Mater. Sci. Eng. C, Mater. Biol. Appl. **78**, 1231–1245 (2017). https://doi.org/10.1016/j.msec.2017.05.018
61. J. Zhang, L. Mou, X. Jiang, Surface chemistry of gold nanoparticles for health-related applications. Chem. Sci. **11**(4), 923–936 (2020). https://doi.org/10.1039/C9SC06497D
62. S. Jampasa, W. Khamcharoen, S. Wirojsaengthong et al., Recent advances and trends in the applications of nanomaterials in optical sensing platforms. TrAC, Trends Anal. Chem. **180**, 117914 (2024). https://doi.org/10.1016/J.TRAC.2024.117914
63. N. Amin, A.S. Torralba, R. Álvarez-Diduk et al., Lab in a tube: point-of-care detection of Escherichia coli. Anal. Chem. **92**(6), 4209–4216 (2020). https://doi.org/10.1021/acs.analchem.9b04369
64. X. Jing, F. Yu, W. Lin, Monitoring cysteine level changes under LPS or H_2O_2 induced oxidative stress using a polymer-based ratiometric fluorescent probe. Anal. Chim. Acta **1174**, 338738 (2021). https://doi.org/10.1016/j.aca.2021.338738
65. V. Kumar, B. Maiti, M.K. Chini et al., Multimodal fluorescent polymer sensor for highly sensitive detection of nitroaromatics. Sci. Rep. **9**(1), 7269 (2019). https://doi.org/10.1038/s41598-019-43836-w
66. A. Pankaew, N. Traiphol, R. Traiphol, Tuning the sensitivity of polydiacetylene-based colorimetric sensors to UV light and cationic surfactant by co-assembling with various polymers. Colloids Surf A Physicochem Eng Asp **608**, 125626 (2021). https://doi.org/10.1016/j.colsurfa.2020.125626
67. A. Jeevika, A simple colorimetric sensor for the recognition of copper ions based on safranin impregnated poly vinyl alcohol hydrogels. Opt. Mater. **105**, 109971 (2020). https://doi.org/10.1016/J.OPTMAT.2020.109971
68. J. Das, P. Sarkar, A new dipstick colorimetric sensor for detection of arsenate in drinking water. Environ. Sci. Water Res. Technol. **2**(4), 693–704 (2016). https://doi.org/10.1039/C5EW00276A
69. C. Xu, D. Liu, D. Zhang et al., Ultrasensitive point-of-care testing of arsenic based on a catalytic reaction of unmodified gold nanoparticles. New J. Chem. **42**(18), 14857–14862 (2018). https://doi.org/10.1039/C8NJ03259A
70. T. Anusuya, V. Kumar, Hydrophilic graphene quantum dots as turn-off fluorescent nanoprobes for toxic heavy metal ions detection in aqueous media. Chemosphere **282**, 131019 (2021). https://doi.org/10.1016/j.chemosphere.2021.131019
71. C.X. Sui, Y.F. Liu, P.A. Li, D. Zhang, F. Xia, Determination of IO^{4-} and Ni^{2+} ions using L-cysteine-CdTe/ZnS quantum dots as pH-dependent fluorescent probes. Anal. Methods **5**(7), 1695–1701 (2013). https://doi.org/10.1039/C3AY26426B
72. S.P. Mohanty, E. Kougianos, Biosensors: a tutorial review. IEEE Potentials **25**(2), 35–40 (2006). https://doi.org/10.1109/MP.2006.1649009
73. S. Borgmann, A. Schulte, S. Neugebauer, W. Schuhmann, Amperometric biosensors. bioelectrochemistry: fundamentals. Appl. Recent. Dev. **13**, 1–83 (2012). https://doi.org/10.1002/9783527644117.CH1
74. P. Biswas, A.K. Karn, P. Balasubramanian, P.G. Kale, Biosensor for detection of dissolved chromium in potable water: a review. Biosens. Bioelectron. **94**, 589–604 (2017). https://doi.org/10.1016/J.BIOS.2017.03.043
75. N.A. Qambrani, B.S. Shin, J.S. Cho, S.E. Oh, Assessment of chromium-contaminated groundwater using a thiosulfate-oxidizing bacteria (TOB) biosensor. Chemosphere **104**, 32–36 (2014). https://doi.org/10.1016/J.CHEMOSPHERE.2013.10.032
76. K. Çevik, İ Yildiz, A. Yildiz et al., $PdRuO_2$/PVP nanomaterial as a highly selective, stable, and applicable potentiometric sensor for the detection of Cr^{3+}. Microchim. Acta **191**, 467 (2024). https://doi.org/10.1007/s00604-024-06543-6
77. C. Michel, F. Battaglia-Brunet, C.T. Minh et al., Amperometric cytochrome c3-based biosensor for chromate determination. Biosens Bioelectron. **19**(4):345–52 (2006). https://doi.org/10.1016/S0956-5663(03)00191-X

78. N.J. Nepomuscene, D. Daniel, A. Krastanov, Biosensor to detect chromium in wastewater. Biotechnol. Biotechnol. Equip. **21**(3), 377–381 (2007). https://doi.org/10.1080/13102818.2007.10817477
79. D. Aydin, İ.H. Gübbük, M. Ersöz, Recent advances and applications of nanostructured membranes in water purification. Turk. J. Chem. **48**(1), 1–20 (2023). https://doi.org/10.55730/1300-0527.3635
80. N.H. Othman, N.H. Alias, N.S. Fuzil et al., A review on the use of membrane technology systems in developing countries. Membranes **12**(1), 30 (2021). https://doi.org/10.3390/membranes12010030
81. O. Vovk et al., Antibacterial properties of ceramic membranes with TiO_2 selective layer. J. Chem. Technol. **32**(2), 351–362 (2024). https://doi.org/10.15421/jchemtech.v32i2.298738
82. S. Kyrii, Materials and methods for ceramic membrane synthesis. Short review. Water Water Purif. Technologies. Sci. Tech. News. **35**, 6–40 (2023). https://doi.org/10.20535/2218-930012023281034
83. V.K. Sharma, C. Jinadatha, E. Lichtfouse, Environmental chemistry is most relevant to study coronavirus pandemics. Environ. Chem. Lett. **18**(4), 993–996 (2020). https://doi.org/10.1007/s10311-020-01017-6
84. S. Mondal, M. Malankowska, A.H. Avci et al., Membrane sensors for pollution problems. in *Current Trends and Future Developments on (Bio-) Membranes: Membrane Technologies in Environmental Protection and Public Health: Challenges and Opportunities*, pp. 335–361 (2023). https://doi.org/10.1016/B978-0-12-824103-5.00004-8
85. J. Sun, X. Dai, Q. Wang, Microplastics in wastewater treatment plants: detection, occurrence and removal. Water Res. **152**, 21–37 (2019). https://doi.org/10.1016/j.watres.2018.12.050
86. V. Hidalgo-Ruz, L. Gutow, R.C. Thompson, M. Thiel, Microplastics in the marine environment: a review of the methods used for identification and quantification. Environ. Sci. Technol. **46**, 3060–3075 (2012). https://doi.org/10.1021/es2031505
87. M. Malankowska, C. Echaide-Gorriz, J. Coronas, Microplastics in marine environment: a review on sources, classification, and potential remediation by membrane technology. Environ. Sci.: Water Res. Technol. **7**, 243–258. https://doi.org/10.1039/D0EW00802H
88. R. van den Hurk, S. Evoy, A review of membrane-based biosensors for pathogen detection. Sensors (Switzerland) **15**, 14045–14078 (2015). https://doi.org/10.3390/s150614045

Chapter 23
The Conductivity of Polymer Composites Based on with Nanocarbon Fillers of Different Structure Under Thermal Load

Iryna V. Ovsiienko, Lyudmila L. Vovchenko, Lyudmila Yu. Matzui, Tetiana A. Len, Tatiana L. Tsaregradskaya, Oleh V. Turkov, and Yurii Yu. Moiseienko

Abstract The results of investigations of electrical conductivity of polymer composites based on epoxy resin with different types of nanocarbon filler under thermal load have been investigated. Nanocarbon materials with different structure and shape of particles (different *aspect ratio*) have been used as fillers in the preparation of polymer composites. A study of the temperature dependence of the electrical resistance of polymer composites with a content of up to 10% of different types of nanocarbon fillers in the temperature range from 77 to 293 K has been carried out. It is shown that that the temperature dependence of the electrical conductivity of polymer composites with nanocarbon fillers is formed as a result of the interaction of several factors among them the conductivity of the nanocarbon filler itself, the shape (*aspect ratio*) of the nanocarbon filler particles and the structural and morphological state of its surface and also the ratio between the values of coefficients of thermal expansion for the polymer matrix and nanocarbon filler particles. It has been revealed that for nanocarbon filler particles with large *aspect ratio* the effect of thermal expansion of the polymer on the contact resistance between the filler particles is levelled off, while for nanocarbon fillers with a small *aspect ratio* value the difference between the CLTE values has the main effect on the contact resistance.

I. V. Ovsiienko · L. L. Vovchenko · L. Yu. Matzui · T. A. Len · T. L. Tsaregradskaya · O. V. Turkov · Y. Yu. Moiseienko (✉)
Department of Physics, Taras Shevchenko National University of Kyiv, Kyiv, Ukraine
e-mail: window7.uriy@gmail.com

O. Fesenko and L. Yatsenko (eds.), *Functional Nanomaterials, Nanocatalysts, Nanotechnologies, and Their Applications*, Springer Proceedings in Physics 321,
https://doi.org/10.1007/978-3-031-99136-3_23

23.1 Introduction

Polymer composites play an important role in modern life due to their advantages compared to other materials, in particular, metals due to their low density, resistance to corrosion and aggressive environments, low cost and ease of production. Among the many materials used as fillers in polymer composites (metals, ceramics), it is necessary to single out nanocarbon structures, which, thanks to the variety of forms, a wide range of properties, and practically unlimited possibilities of modification, give polymer composites new functional properties. Thus, the use of carbon nanotubes (CNTs) as fillers in polymer composites, which have a large *aspect ratio* value, leads to a significant improvement in the mechanical properties of the polymer composite. CNTs give the composites stiffness, which is due to their high value of the modulus of elasticity under tension (1 TPa) [1]. CNTs have a high elastic deformation (up to 5%), which increases the tensile strength of the polymer composite by an order of magnitude compared to conventional polymers. CNTs have the highest values of specific strength and stiffness [2]. This means that noticeable improvements in the properties of polymer composites are achieved with smaller amounts of CNTs compared to other fillers. In addition, by using high volume concentrations of CNTs, it is possible to obtain composites with properties that cannot be achieved with other fillers [3–5].

When making electrically conductive composites with a dielectric matrix and an electrically conductive filler, three factors are important: the intrinsic conductivity of the filler, the amount of filler introduced and the shape of the filler particles. When electrically conductive particles of the same substance are introduced, the conductivity of the composite changes depending on the amount of filler introduced. When the concentration corresponding to the percolation threshold is reached (~30% for isometric metal particles), when the filler creates continuous clusters throughout the polymer composite, the conductivity of the polymer composite begins to increase sharply. Nanocarbon particles with a large aspect ratio form electrically conductive channels at much lower concentrations and significantly lower the percolation threshold [6–10].

Polymer composites with nanocarbon fillers can be used to create films to remove electrostatic charges [11, 12]

Polymer composites with nanocarbon filler are also one of the most promising materials for shielding microwave radiation. The electrodynamic parameters of the polymer composite can be widely varied by changing the concentration, type, concentration and distribution of the nanocarbon filler [13, 14].

The use of nanocarbon as a filler also improves the thermal properties of the polymer composite. The addition of CNTs to the polymer makes it possible to expand the operating temperature range of polymer composites due to the increase in the transition temperature to the glassy state [15, 16].

23.2 Experimental

23.2.1 Characteristic of Nanocarbon Filler

In the work polymer composites based on ED-20 epoxy resin with different types of nanocarbon filler have been investigated.

Nanocarbon materials with different structure, shape of particles (*aspect ratio*) and morphological state of surface have been used as fillers in the preparation of polymer composites. These nanocarbon materials are multiwalled carbon nanotubes (MWCNTs), thermoexfoliated graphite (TEG), TEG with next treatment (TEG(2) and TEG(2)d) and graphite nanoplatelets (GNPs). The structure, phase and morphological features of nanocarbon materials used as fillers were studied in detail in the works [17–19].

Table 23.1. shows the methods of obtaining and the main structural and morphological characteristics of nanocarbon materials used as fillers.

Please provide a definition for the significance of 'italics' in theTables 21.1–21.4'.In Table 23.1-23.4 Aspect ration (A) charactarizes the shape of particles A=l /d, where l-length and d-diameter of particles

As can be seen from the above Table, all nanocarbon fillers used to obtain polymer composites, depending on the shape and internal structure of the filler particles, surface morphology, and the value of the aspect ratio, can be divided into three groups: fillers with plate-shaped particles, worm-shaped particles and cylindrical shape particles.

Fillers with worm-shaped particles are characterized by a complex internal particle structure, high values of internal porosity and a highly developed particle surface. The particle sizes can vary in a wide range from 5 mm (TEG) to 250 mcm (TEG2).

Another group with an aspect ratio from 1 to 50 consists of nanocarbon fillers with plate-shaped particles. The composition of this group is quite heterogeneous. This group includes fillers with disk-shaped particles with a flat undeveloped surface and a complete lack of internal porosity (dispersed graphite, GNPs) and fillers whose particles have a lamellar shape, but at the same time retain a certain heterogeneity and development of the surface and a certain part of closed pores (TEG(2)d).

The last group includes nanocarbon fillers with cylindrical particles (CNTs). A distinctive feature of these fillers is a very high value of the aspect ratio of the particles (~ 1000).

Table 23.2 presents the main structural and morphological characteristics of various groups of nanocarbon fillers.

The given classification of nanocarbon fillers according to the structural and morphological features of the filler particles allows for a detailed analysis of the electrical and transport properties of the obtained polymer composites. Nanocarbon fillers with particles with different structural and morphological features have different mechanical, thermal and electrophysical properties. It is obvious that the shape, internal structure, and surface condition of the particles of this or that nanocarbon filler also determine the nature of the interaction of the filler particles with the

Table 23.1 Methods of obtaining and the main structural and morphological characteristics of nanocarbon fillers

Filler	Obtaining method	Structure	Surface	Internal porosity, pore size	Size ($l \times d$)	*Aspect ratio, A = l/d*
MWCNTs	Decomposition of benzene in the presence of ferrocene in a tube furnace	Cylindrical		The absence of open pores	10 nm × 10 mcm	~ 1000
TEG	Thermal shock in a cyclone furnace of GICs based on natural graphite with H_2SO_4	Worm-shaped openwork, cellular	Significant ribbing	Significant porosity, up to 95%, (5–10) mcm	(50–100) mcm × (3–5) mm	~ 100
TEG(2)	Repeated intercalation of TEG with next thermal shock at a temperature of 1000–1200 K	Worm-shaped shortened	Bumpy, wavy	Porosity ~ 40% (4–8) mcm	(30–70) mcm × (1–2) mm	~ 50–70
TEG(2)d	Sonication of TEG(2) in acetone solution for 3 h	Worm-shaped chopped	Longitud. Indenta-tions	Porosity ~ 40% Reduction of the share of open pores	(30–50) × (250–600) mcm	~ 10–20
GNPs	Sonication of TEG(2) in acetone solution for 20 h	Platelets	Large number of defects	The absence of open pores	(10–30) × 300 nm	~ 10

Table 23.2 Main structural and morphological characteristics of various groups of nanocarbon fillers

Group number	The shape of the particles	Particle surface morphology	Internal porosity, micropore size	*Aspect ratio, A*	Materials
I	Worm-shaped	Developed, ribbed	Cellular structure, significant internal porosity	50–100	TEG (~100), TEG2 ~ 10cg
II	Platelets	Flat, the presence of a certain number of defects is possible	Internal porosity is almost absent	10–50	Dispersed graphite, GNPs
		Not flat, developed, structured	Insignificant internal porosity, the presence of only closed pores	10–50	TEG2(d)
III	Cylindrical	A minor defect may be present	Internal cavities	~ 1000	MWCNTs

polymer matrix, the degree of dispersion and uniform distribution of the filler particles in the polymer, thereby affecting the mechanical, thermal, and electrical transport properties of the polymer composite.

Let's in the terms of the proposed classification of types of nanocarbon fillers, evaluate the limits and conditions of stability of the electro-transport properties of polymer composites with nanocarbon filler.

23.2.2 Preparation of Polymer Composites with Different Types of Nanocarbon Filler

Composites based on epoxy resin have been studied in presented work. The source materials for obtaining epoxy polymers are epoxy oligomers, which contain in their molecules at least one epoxy group capable of entering into a polymerization or polycondensation reaction. Epoxy resin is a viscous liquid with a density of (1150–1210) kg/m^3, which dissolves well in polar (ketones) and non-polar (toluene) solvents. Epoxy resin does not dissolve in water and is resistant to acid and alkali solutions. The viscosity of low-molecular epoxy resins is not less than 8 Pa s at a temperature of 25 °C and increases sharply with increasing molecular mass of the epoxy resin. Plasticizers, which are high molecular compounds, are used to reduce the viscosity of epoxy resin. Molecules of plasticizers fill the gaps between chains of

epoxy resin macromolecules when forming a three-dimensional molecular network. In other words, plasticizers loosen the structure of the epoxy resin as it cures, making it more plastic.

To obtain polymer composites with epoxy resin at the first stage, it is necessary to use solvents. Low molecular mass compounds are used as solvents, most commonly acetone, which evaporates as the resin cures. The viscosity of the liquid polymer and the kinetics of its drying process are regulated by the use of an appropriate combination of solvents. With the wrong choice of solvents, the polymer composite will break down into phases during the drying process, making it impossible to form a strong structure.

Polycondensation of epoxy oligomers with the formation of an epoxy polymer occurs with the use of special substances—hardeners. A wide variety of substances are used as epoxy oligomer hardeners, in particular, amines, carboxylic acid anhydrides, amides and amino amides, isocyanates, modified carboxylic acid anhydrides, and others. Depending on the selected components, curing can begin immediately after mixing the components ("cold" curing hardeners) or when the components are heated to initiate the curing process ("hot" curing hardeners). Cold curing hardener—polyethylene polyamine (PEPA) is most often used as a cross-linking reagent.

The process of obtaining polymer composites with nanocarbon filler consisted of the following stages.

First stage: preparation of a solution of epoxy resin in acetone. The mass ratio of epoxy resin and acetone is determined by the type and content of carbon filler in the composite.
Second stage: impregnation of nanocarbon filler particles with a solution of epoxy resin in acetone. The nanocarbon filler powder was introduced into a solution of epoxy resin in acetone and the mixture was kept at a temperature of 20 °C with periodic stirring until the acetone completely evaporated. The exposure time of the mixture is determined by the type of carbon filler and can vary from several hours to several days. At the same time, the more porous the filler, the longer the exposure time.
Third stage: adding to mixture a plasticizer (dibutyl phthalate DBF) to give the final product plastic characteristics and a hardener (polyethylene polyamine PEPA) at a certain stage of infiltration.
Fourth stage: final drying of the mixture within 4 h with a gradual increase in temperature from 50 to 80 °C (by 10 °C every hour) in the oven until the complete evaporation of the acetone.

As a result, the polymer composites with different types of nanocarbon filler have been obtained. The concentration of the filler in the obtained composites varied from 5 to 10% mass. Note that for all specimens of polymer composites the concentration of the nanocarbon filler is much higher than the percolation threshold. The detailed method of obtaining polymer composites is given in [20].

23.2.3 Measurement of Electrical Resistance of Polymer Composites with Nanocarbon Filler

To determine the stability and regularities of changes in the transport properties of polymer composite materials under thermal load conditions, a study of the temperature dependence of the electrical resistance of composites based on epoxy resin with a content of up to 10% of different types of nanocarbon fillers in the temperature range from 77 to 293 K has been carried out. To measure electrical resistance, specimens of polymer composites in the form of rectangular parallelepipeds with dimensions of 15 × 3 × 1 mm were produced. Depending on the concentration and structural and morphological features of the filler, bulk specimens of nanocarbon-polymer were obtained by one of two methods:

(1) method of cold pressing of carbon powders impregnated with epoxy resin using a hydraulic press (filler content 10% by mass).
(2) the method of pouring liquid mixtures of carbon-ED20 into appropriate Teflon molds followed by stepwise drying (filler content 0.5% up to 10% by mass).

The measurements of temperature dependences of electrical resistance for bulk specimens of polymer composites depending on the value of electrical resistance have been made by with standard two- probe and four-probe methods in direction perpendicular to pressure axis. The resistivity measurement error did not exceed 0.5%.

23.2.4 Temperature Dependences of Conductivity of Polymer Composites with Different Carbon Filler

The temperature dependences of normal conductivity σ/σ_{77} for polymer composites with different carbon filler are presented in Fig. 23.1.

As can be seen from the Figure, the temperature dependences of normalized conductivity $\sigma/\sigma_{77}(T)$ for polymer composites with nanocarbon fillers can be divided into three types. The first type includes increasing temperature dependences $\sigma/\sigma_{77}(T)$ or those in which a small local minimum is observed at a temperature close to the maximum measurement temperature. Such temperature dependences have composites with TEG and CNTs fillers regardless of the concentration of the filler, as well as the composite with TEG(2) with the maximum concentration for which the studies were conducted. The second type includes dependencies $\sigma/\sigma_{77}(T)$ that have a wide maximum in the temperature range of (200–250) K. Such temperature dependences are typical for polymer composites with TEG(2) and with fillers TEG2(d) and GNPs with the maximum concentration for which the dependences were performed. The third type of $\sigma/\sigma_{77}(T)$ dependence is a decreasing dependence, or a dependence that has a small maximum at low temperatures. This type of temperature dependence $\sigma/\sigma_{77}(T)$ is observed for polymer composites with filler TEG(2)d with a minimum

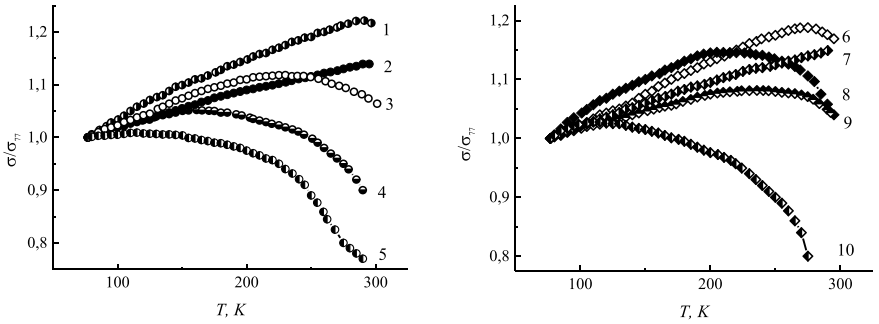

Fig. 23.1 Temperature dependences of normal conductivity $\sigma/\sigma_{77}(T)$ for polymer composites with different carbon fillers: 1—TEG (7.8% mass), 2—TEG (5% mass), 3—TEG(2)d (10% mass), 4—GNP (8.5% mass), 5—TEG(2)d (5% mass), 6—TEG(2) (10% mass), 7—CNTs (5% mass), 8—GNP (10% mass), 9—TEG(2) (5% mass), 10—GNP (5% mass)

concentration and composites with filler GNP with all concentrations except 10%. Therefore, polymer composites with fillers with maximum values of aspect ratio (CNTs – *aspect ratio* up to 1000, TEG, respectively, up to 100) have an increasing temperature dependence regardless of the concentration of the nanocarbon filler. For polymer composites with fillers with smaller *aspect ratio* values, the following trend is observed. As the filler concentration in the composite increases, there is a gradual transition from a decreasing temperature dependence $\sigma/\sigma_{77}(T)$ to a dependence with a pronounced maximum, and the smaller the value of the aspect ratio for the filler particles, the greater the filler concentration should be for the transition from a decreasing to an increasing temperature dependence of conductivity.

Table 23.3 shows the features of the temperature dependence of normalized conductivity for polymer composites with different types of nanocarbon filler.

As follows from the Table, there is a full correlation between the shape of the filler particles and their aspect ratio and the character of the electrical conductivity temperature dependence for polymer composite with this filler. The larger the value of the *aspect ratio* for the nanocarbon filler particles, the higher the temperature of the maximum in the temperature dependence of the conductivity $\sigma/\sigma_{77}(T)$ for polymer composite with this filler. For one type of nanocarbon filler, the greater the filler concentration, the higher the maximum temperature in dependence $\sigma/\sigma_{77}(T)$.

23.3 Results and Discussion

Let's consider what causes the connection between the type of nanocarbon filler and the conductivity of the polymer composite with such filler.

Table 23.3 Features of the temperature dependence of normalized conductivity for polymer composites with different types of nanocarbon filler

Characteristics of the filler			C, % mass	$\sigma_{(293)}/\sigma_{(77)}$	Dependence $\sigma/\sigma_{77}(T)$	T_{max}, K
Type	Filler	Aspect ratio				
Cylindrical	MWCNTs	~ 1000	5.0	1.15	Increases monotonically	
Worm-shaped	TEG	~ 100	7.8	1.21	Increases, with a slightly pronounced *max* at high temperatures	300
			5.0	1.14		295
	TEG(2)	~ 50–70	10.0	1.04	With a broad *maximum*	272
			5.0	1.17		235
	TEG2(d)	~ 10–20	10.0	1.07	With a broad *maximum*	227
			5.0	0.77	Weakly expressed *max* at low temperatures, decreases	114
Platelets	GNPs	~ 10	10.0	0.90	With a broad *maximum*	213
			8.5	1.08	Weakly expressed *max* at low temperatures, decreases	150
			5.0	0.70		113

The temperature dependence of the conductivity of the composite material is determined, in the first approximation, by the change with temperature of three parameters: 1) the electrical resistance of the nanocarbon filler particles R_f; 2) contact electrical resistance between nanocarbon filler particles R_c; 3) the number of continuous conductive chains (current paths) N_{ch} through the sample.

Let us consider in more detail the changes with temperature of all the specified parameters.

23.3.1 Temperature Dependences of Resistivity of Different Nanocarbon Fillers

The Fig. 23.2 show the temperature dependence of the resistivity $\rho(T)$ for bulk pressed nanocarbon materials that have been used as fillers in polymer composites [21, 22].

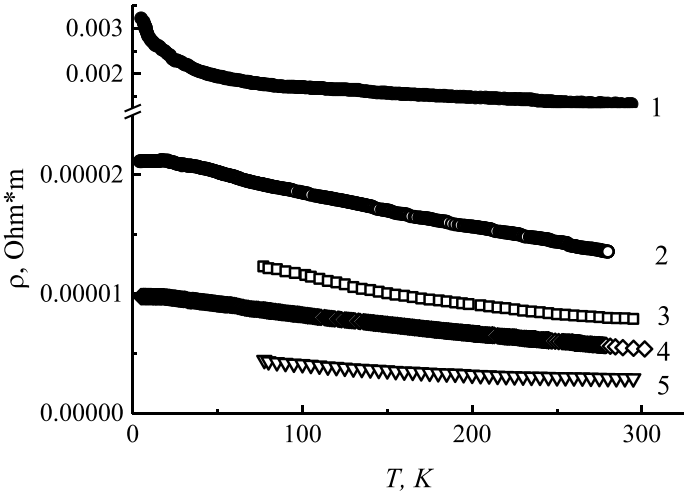

Fig. 23.2 Temperature dependence of resistivity $\rho(T)$ for bulk pressed nanocarbon materials: 1—CNTs, 2—GNP, 3—TEG(2)d, 4—TEG, 5—TEG(2)

As can be seen from the above Figures, the resistivity decreases with temperature for all nanocarbon fillers. The ratio $\rho_{4.2}/\rho_{293}$ for all nanocarbon fillers has approximately the same values and does not exceed 2 except MWCNTs. The values of resistivity for bulk samples of nanocarbon are different, which is primarily related to the features of the surface state of nanocarbon particles and, as a result, the contact resistance between separated nanocarbon particles. For nanocarbon particles with a developed surface (TEG, TEG(2), TEG2(d)), the contact resistance between the particles is lower, while for nanocarbon particles with a flat or smooth small-defect surface, the contact resistance increases significantly, which causes a significant increase in the resistance of the a bulk sample in general. Thus, it is not possible to determine the value of the resistivity of the nanocarbon filler on the base of measurements in the bulk sample without estimating the value of the contact resistance. However, the character of the temperature dependence of the resistivity can be established from such measurements.

The temperature dependence of the resistivity of the nanocarbon filler is determined by the temperature dependence of the concentration of charge carriers and the mobility of charge carriers. At low temperatures (up to 50–77 K), the concentration of charge carriers in the nanocarbon materials does not depend on temperature, since there is a slight overlap of the valence and the conduction bands. Above the degeneration temperature, the concentration of charge carriers in nanocarbon materials increases with temperature. As for the mobility of charge carriers, its temperature dependence is determined by the prevailing mechanisms of charge carrier scattering in the nanocarbon. For all investigated nanocarbon materials, the predominant mechanism of charge carrier scattering is temperature-independent charge carrier scattering

at crystallite boundaries. Thus, for all investigated nanocarbon fillers, at low temperatures, the resistivity does not depend on temperature, and at temperatures above (50–77) K, the resistivity decreases with temperature. The exception is MWCNTs, for which at low temperatures an abnormal increase in resistivity is observed, which is associated with the manifestation of the effect of weak localization and interaction of charge carriers for these nanocarbon materials.

23.3.2 Contact Electrical Resistance Between Nanocarbon Filler Particles and the Number of Continuous Conductive Chains

The character of the temperature dependence of the contact electrical resistance between the particles of the nanocarbon filler is determined by the temperature dependence of the nanocarbon filler itself (it decreases with increasing temperature) and the change with temperature of the radius of the contact spot. Depending on the ratio between the coefficients of linear thermal expansion (CLTE) for the nanocarbon fillers and epoxy resin, its size may not change or increase or decrease with increasing temperature. That is, the temperature dependence of the contact resistance is quite complex, since it is determined by the change with temperature of several parameters, the temperature dependence of which cannot be interpreted unambiguously.

As you know, depending on the ratio between the radius of the contact spot r and the length of the free path of charge carriers l, contact resistances R_c are divided into two types. At $r >> l$ (Holm-type contact), the contact resistance is defined as

$$R_c = \frac{\rho}{2r}, r \gg l. \tag{23.1}$$

If $r << l$ (Sharvin-type contact), the contact resistance can be presented as:

$$R_c = \frac{\rho l}{4r^2}, r \ll l, \tag{23.2}$$

where ρ is the resistivity of nanocarbon particles.

As follows from the formulas, for contacts of the Sharvin type, the dependence of the contact resistance on the size of the contact spot is more pronounced. Thus, if Sharvin-type contacts are implemented in the composite material between the filler particles, the contribution of the contact resistance to the total resistance of the composite will be more significant. Therefore, if the size of the contact spot between the nanocarbon particles changes significantly under thermal load, and Sharvin-type contacts are realized between the nanocarbon particles, then the contact resistance will be an additional significant factor affecting the character of the temperature dependence of the composite.

Let's analyze what type of contacts occurs for the investigated nanocarbon fillers. As a first approximation, we will assume that the size of the contact spot cannot exceed the size of the nanocarbon particles, although for particles with a highly developed surface (for example, TEG) this statement is not accurate. As indicated above, for all nanocarbon materials used as fillers in polymer composites, the main mechanism of scattering of charge carriers is temperature-independent scattering at crystallite boundaries. That is, the length of the free path of the charge carriers for all nanocarbon fillers is equal to the size of the crystallites in them and, accordingly, is smaller than the size of the nanocarbon particles, and, therefore, smaller than the size of the contact spot between the nanocarbon particles. Thus, the electrical contact between individual nanocarbon particles of the filler is described within the terms of the Holm contact resistance model, for which the contact resistance is inversely proportional to the size of the contact spot.

Another one important parameter that determines the electrical conductivity of the polymer composite is the number of continuous conductive chains (current paths) N_{ch} through the sample. A change in the number of such conductive chains through the sample under thermal load will cause a change in the electrical conductivity of the polymer composite as a whole.

The number of continuous nanocarbon particles chains along the entire length of the sample is determined by the total number of nanocarbon filler particles n_f and the number of filler particles in one chain $n_{f\text{-}ch}$:

$$n_{f-ch} = \frac{L\gamma}{d}, N_{Ch} = \frac{n_f}{n_{f-ch}} = \frac{V}{\gamma\pi dh}, \tag{23.3}$$

where L is the specimen's length, γ is some multiplier varying from 1 to 2, V is the volume of the specimen, φ is the volume part of nanocarbon filler in the specimen, d is the linear size of the nanocarbon particle along the graphite planes, i.e., along the direction in which charge transfer occurs in the nanocarbon particle. For TEG and nanocarbon particles based on TEG this is diameter of particle and h is the, respectively, length of particle. For MWCNTs on the contrary, d is the length of tubes, h is their diameter.

Among all chains of nanocarbon particles formed in polymer composites, electric current can flow only along those in which the polymer interlayers between individual nanocarbon particles do not exceed 2–3 nm. With such a thickness of the polymer layer, conductivity is through the tunneling mechanism. Such a chain is excluded from the process of electrical conductivity (so-called dead-end branches of a cluster of filler particles). The number N'_{ch} of carbon nanoparticle chains through which charge transfer is possible is related to the total number of N_{ch} carbon nanoparticle chains by the following ratio:

$$N'_{ch} = C \times N_{ch}, \tag{23.4}$$

where the coefficient C can have a value from 0 (the state of the polymer composite before percolation) to 0.3 (all particles of the nanocarbon filler form continuous chain

structures). In fact, *C* is the part of the nanocarbon particles chains through which an electric current passes.

Thus, if the coefficients of linear thermal expansion (CLTE) for particles of nanocarbon filler and polymer matrix are different, it can lead to the increase in the size of the polymer layer between particles or chains of nanocarbon filler with increasing temperature As a result, such chains are excluded from the charge transfer process In other words, under certain conditions, the number of conductive channels in the composite material will change with increasing temperature. Thus, the study of the CLTE is very important for establishing the stability of the transport properties of polymer composites.

23.3.3 Temperature Dependences of the Coefficient of Linear Expansion of Different Types of Nanocarbon Filler

The study of the CLTE of the bulk composites based on TEG has been carried out using the dilatometric method with an accuracy of (5–7)%. Measurement of the linear dimensions of the samples under thermal load was made using an optical microscope with a micrometric nozzle. The CLTE of bulk specimens of TEG has been measured along the axis of specimens pressing, depending on the density of the composite.

Since all nanocarbon fillers, except for MWCNTs, were obtained on the basis of TEG, the study of the CLTE of the bulk samples of TEG with different densities gives an idea of the value of the CLTE for nanocarbon fillers obtained from TEG during the destruction of its structure by the methods of repeated expansion and dispersion.

Pressing TEG to obtain bulk samples with high density values is accompanied by the destruction of the worm-like structure of TEG, the particles of which in this process acquire a structure similar to the structure of TEG(2), TEG2(d) and GNP, respectively.

The dependence of the CLTE of the TEG bulk samples on the sample's density $\alpha(\rho)$ is presented in Fig. 23.3.

As can be seen from the Figure, with an increase in the material density, an increase in the value of CLTE is observed. When the density changes from 0.4 g/cm^3 to 1.9 g/cm^3, the CLTE value increases by more than 2 times [5]. Further growth of the material density leads to a sharp decrease in the CLTE value.

The value of the CLTE for bulk nanocarbon samples, the change of the CLTE with the composite density changes and during thermal loading are determined by several reasons that depend on the structure of the nanocarbon. Firstly, it is the ability of the material to transmit the thermal expansion of microcrystallites, secondly, it is the thermal expansion of the "framework", which is formed by nanocarbon particles during the formation of the composite.

The expansion of microcrystallites occurs mainly along the C-axis microcrystallites, since the value of the CTLE along the graphite layer in the studied temperature

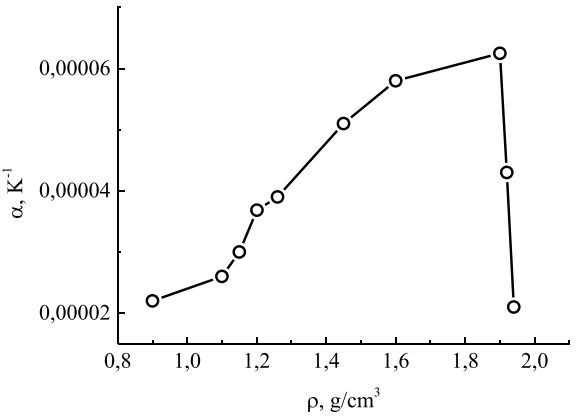

Fig. 23.3 Dependence of the CLTE on the sample density (α(ρ)) for the TEG bulk samples

range is almost 2 orders of magnitude smaller than the corresponding value of the CTLE along the C-axis.

At low densities of composites, when "worm-like" TEGs particles are slightly deformed during pressing, and microcrystallites form something like rings, their expansion can be transmitted in the direction of open pores, which coincide with the direction of expansion of crystallites.

As the density of bulk samples increases, the number of closed pores oriented parallel to the pressing axis increases (TEG2, TEG2(d)), and the thermal expansion of crystallites will lead to an increase in the volume of the bulk samples as a whole.

Since the CTLE is determined by the additive contribution of both the thermal expansion of graphite crystallites and the thermal expansion of the "framework", the value of the CTLE in this range of densities is several times higher than the value of the CTLE along the C axis of natural graphite, the CTLE of which is determined mainly by the thermal expansion of the "framework".

At bulk sample densities close to 2 g/cm^3, the worm-like structure of TEG particles is destroyed (GNPs). In bulk samples, there is a low concentration of pores and a fairly high degree of orderly arrangement of graphite layers in a plane perpendicular to the pressing axis. The value of CTLE along the pressing axis at these densities is similar to the value of CTLE along the C axis in natural graphite.

As for the CLTE for MWCNTs, its value is very small and amounts to ~ 1.2×10^{-5} K^{-1} [23].

The values of CLTE for particles of nanocarbon fillers with different structure are presented in the Table 23.4.

As can be seen from the Table, for all nanocarbon fillers the values of CLTE are smaller compared to the CTLE for epoxy resin. For worm-shaped nanocarbon fillers, the CLTE is 5 times smaller, while for other nanocarbon fillers, CLTE is 15–25 times smaller than CLTE for epoxy resin. It is obvious that such a difference in the value of CTLE for different nanocarbon fillers will significantly affect the temperature dependence of the contact resistance R_c.

Table 23.4 CLTE for different nanocarbon fillers

The shape of the particles	*Aspect ratio, A*	Filler	α_f, K^{-1}
Worm-shaped	50–100	TEG, TEG2	~ 6×10^{-5}
Platelets	10–50	TEG2(d), GNPs	~ 2×10^{-5}
Cylindrical	~ 1000	MWCNTs	~ 1.2×10^{-5}
Epoxy			~ $(25–30) \times 10^{-5}$

23.3.4 Peculiarities of Changes in Parameters Determining Electrical Conductivity for Different Types of Nanocarbon Fillers

The conducted experimental and theoretical studies revealed that in order to establish the regularities of changes in the electrical conductivity of polymer composites with nanocarbon fillers of various types, it is necessary to take into account the structural and morphological state of the nanocarbon filler (the size and aspect ratio of the filler particles), as well as the condition of the surface of the filler, the concentration of the filler (the number of particles that form a conductive cluster), character of interphase interaction (contact resistance of filler particles and resistance of polymer interlayer, conductive properties of filler).

Table 23.5 shows the characteristics of the parameters that determine the electrical conductivity of polymer composites with different types of nanocarbon fillers.

As can be seen from the Table, the temperature dependence of the electrical conductivity of the polymer composite is formed as a result of the complex interaction of several factors, for which the temperature dependences can differ significantly. As showed above, the electrical conductivity of all nanocarbon materials used in the polymer composites as filler increases with temperature. Therefore, when analysing the temperature dependence of the conductivity of a polymer composite, the main attention should be paid to the mechanisms of contact resistance change with temperature.

There are several mechanisms that determine the temperature dependence of the contact resistance between nanocarbon filler particles. Temperature dependence of contact resistance between particles of a nanocarbon filler depends not only on the ratio between the temperature coefficients of linear expansion for the filler and the polymer matrix, but also on the *aspect ratio* and shape of the filler particles.

For a polymer composite with a CNT filler, the contact resistance decreases with temperature, as does the resistance of the CNTs themselves throughout the temperature range in which the studies were conducted, although the CLTE for the epoxy resin is much larger than the CLTE for the CNTs. Obviously, such temperature dependence of contact resistance can be explained by the fact that CNTs, which have the greatest *aspect ratio* value, form a branched conductive structure in the composite even at low filler concentrations. The CNTs concentration (5% mass) in studied polymer composites is far beyond the percolation threshold. And with such

Table 23.5 Parameters that determine the electrical conductivity of polymer composites with different types of nanocarbon fillers

Type of nanocarbon filler / Parameters	Cylindrical, l/d ~ 1000	Worm-like, l/d ~ 100	Worm-like, l/d ~ 10–50	Platelets l/d ~ 10
Resistivity of the nanocarbon filler, R_f	It decreases with temperature due to the increase in the concentration of charge carriers with temperature-independent scattering of charge carriers			
Electrically conductive structure	Branched frame	Branched frame	Minor conductive clusters	Individual conductive clusters
The number of contacts between filler particles	Small	Relatively small	Significant	Very large
CLTR of the polymer (α_p) and the nanocarbon filler (α_f)	$\alpha_p >> \alpha_f$	$\alpha_p > \alpha_f$	$\alpha_p > > \alpha_f$	$\alpha_p >> \alpha_f$
Contact resistance, R_c	$R_c(T) \sim R_f(T)$	$R_c(T) \sim R_f(T)$	It increases significantly with temperature due to a decrease in the size of the contact spot and an increase in the thickness of the polymer layers between individual nanoparticles	
The number of current-conducting channels, N_{ch}	It is large, number practically does not change with temperature, $N_{ch} \neq f(T)$	It is large, number varies slightly with temperature	Number is limited, as the temperature increases, N_{ch} decreases due to the exclusion of individual chains from the conductive network, the polymer layer between which becomes larger than the critical size of ~ 2 nm	
Correlation between factors determining electrical resistance	$R_f > R_c$ in the entire studied temperature range	$R_f > R_c$ in the entire studied	$R_f > R_c$, at $T <$ 240 K $R_f < R_c$, at $T >$ 240 K	$R_f > R_c$, at $T <$ 150 K $R_f < R_c$, at $T >$ 150 K

filler concentration, a slight change in the number of conductive clusters, which can occur due to an increase in the polymer layer between individual CNTs, practically does not affect the conductivity of the polymer composite as a whole. A decreasing dependence of the contact resistance with increasing temperature is also observed for composites in which TEG is used as a filler. On the one hand, the *aspect ratio* for TEG particles is smaller compared to CNTs. On the other hand, TEG, due to its cellular structure and the presence of closed pores, has the largest value of CTLE among all the investigated nanocarbon fillers. Therefore, during heating, there is no significant increase in the contact resistance between the TEG particles due to the increase in the polymer layer and the decrease in the contact spot.

For polymer composites with nanocarbon fillers, for which the *aspect ratio* has small values, and the CLTE is significantly smaller than the CLTE for epoxy resin, the contact resistance between the filler particles during heating increases very significantly due to the reduction of the contact spot and reduction of number of conductive clusters during growth polymer layer between individual filler particles. Thus, the resistance of nanocarbon filler particles decreases with increasing temperature, and the contact resistance between the filler particles increases, which leads to the appearance of a minimum in the temperature dependence of resistance and, accordingly, a maximum in the temperature dependence of conductivity. The temperature of the maximum in the temperature dependence of the conductivity will be smaller, the smaller the *aspect ratio* and the CLTE for the nanocarbon filler particles. Moreover, for the appearance of a maximum in the temperature dependence of electrical conductivity, a combination of both of these factors is necessary. For CNTs, the CLTE is even smaller than for GNPs. However, a high value of the *aspect ratio* for CNTs practically eliminates the effect of significant temperature expansion of the polymer. Also, the increase in the concentration of the nanocarbon filler contributes to the shift of the maximum temperature towards higher temperatures.

23.4 Conclusion

Thus, the carried-out research made it possible to reveal the patterns of changes in the electrical conductivity of polymer composites based on epoxy resin with different types of nanocarbon filler under thermal load. It has been found that the temperature dependence of the specific electrical conductivity of polymer composites with nanocarbon fillers is formed as a result of the interaction of several factors. The first, it is the conductivity of the nanocarbon filler itself, due to the peculiarities of its crystalline, and therefore, band structure. Secondly, the shape (*aspect ratio*) of the nanocarbon filler particles and the structural and morphological state of its surface are essential for determining the type of the temperature dependence of the polymer composite also. In addition, the ratio between the values of CLTE for the polymer matrix and nanocarbon filler particles is important.

It is obvious that a significant contribution to the temperature dependence of the conductivity of the polymer composite is given by the temperature dependence of the conductivity of the nanocarbon material used as a filler. For the absolute majority of carbon materials, which are conductors, the temperature coefficient of resistance is negative, which causes by the weak temperature dependence of the charge carriers' mobility due to the preferential scattering of charge carriers at the boundaries of crystallites.

As with other factors, particularly those that determine the temperature dependence of contact resistance, a comprehensive approach to their analysis is important. Thus, it has been revealed that for nanocarbon filler particles with large *aspect ratio* (CNTs, TEG), the effect of thermal expansion of the polymer on the contact resistance between the filler particles is levelled off, while for nanocarbon fillers with

a small *aspect ratio* value (GNPs, dispersed graphite), the difference between the CLTE values has the main effect on the contact resistance. The significant expansion of the polymer on heating compared to the nanocarbon filler for the low aspect ratio filler results in the elimination of a large number of conductive paths through the sample and a reduction in the size of the contact area. This, in turn, leads to an increasing temperature dependence of the contact resistance and, as a result, a change in the sign of the temperature coefficient of resistance for the polymer composite as a whole. For polymer composites with a nanocarbon fillers with a small value of the *aspect ratio*, the temperature dependence of the conductivity, as a rule, has a pronounced maximum, and the smaller the value of the *aspect ratio* for the filler particles, the lower the temperature at which the transition from increasing to decreasing temperature dependence occurs conductivity.

Authors acknowledge the financial support from National Research Foundation of Ukraine, grant: NRFU2023-03/193 and Ministry of Education and Science of Ukrain, grants 24BF051-01 M, 24BF051-04, 22BF051-11.

References

1. Y. Min-Feng, O. Lourie, M.J. Dyer, K. Moloni, T.F. Kelly, R.S. Ruoff, Strength and breaking mechanism of multiwalled carbon nanotubes under tensile load. Science **287**(5453), 637–640 (2000). https://doi.org/10.1126/science.287.5453.637
2. B. Arash, Q. Wang, V.K. Varadan, Mechanical properties of carbon nanotube/polymer composites. Sci. Rep. **4**, 6479 (2014). https://doi.org/10.1038/srep06479
3. M. Tarfaoui, K. Lafdi, A. El Moumen, Mechanical properties of carbon nanotubes based polymer composites. Compos. Part B Eng. **103**, 113–121 (2016). https://doi.org/10.1016/j.compositesb.2016.08.016
4. A. Kumar, K. Sharma, A.R. Dixit, A review on the mechanical properties of polymer composites reinforced by carbon nanotubes and graphene. Carbon Lett. **31**, 149–165 (2021). https://doi.org/10.1007/s42823-020-00161-x
5. H.G. Chae, T.V. Sreekumar, T. Uchida, S. Kumar, A comparison of reinforcement efficiency of various types of carbon nanotubes in polyacrylonitrile fiber. Polymer **46**(24), 10925–10935 (2005)
6. G.J. Hu, C.G. Zhao, S.M. Zhang, M.S. Yang, Z.G. Wang, Low percolation thresholds of electrical conductivity and rheology in poly(ethylene terephthalate) through the networks of multiwalled carbon nanotubes. Polymer **47**(1), 480–488 (2006)
7. V. Bavastrello, V. Erokhin, S. Carrara, F. Sbrana, D. Ricci, C. Nicolini, Morphology and conductivity in poly(ortho-anisidine)/carbon nanotubes nanocomposite films. Thin Solid Films **468**(1–2), 17–22 (2004); H.S. Shko, A.R. Dlzar, Open Access J. Phys. **2**(2), 5–10 (2018)
8. S. Barrau, P. Demont, A. Peigney, C. Laurent, C. Lacabanne, DC and AC conductivity of carbon nanotubes-polyepoxy composites. Macromolecules **36**(14), 5187–5194 (2003)
9. K. Miyasaka, K. Watanabe, E. Jojima, K. Aida, M. Sumita, K. Ishikawa, Electrical conductivity of carbon-polymer composites as a function of carbon content. J. Mater. Sci. **17**, 1610–1616 (1982). https://doi.org/10.1007/BF00540785
10. Y. Wang, S. Lu, W. He, S. Gong, Y. Zhang, X. Zhao, Y. Fu, Z. Zhu, Modeling and characterization of the electrical conductivity on metal nanoparticles/carbon nanotube/polymer composites. Sci. Rep. **12**, 10448 (2022). https://doi.org/10.1038/s41598-022-14596-x
11. J.G. Smith Jr., J.W. Connell, D.M. Delozier, P.T. Lillehei, K.A. Watson, Y. Lin, B. Zhou, Y.-P. Sun, Space durable polymer/carbon nanotube films for electrostatic charge mitigation. Polymer **45**(3), 825–836 (2004). https://doi.org/10.1016/j.polymer.2003.11.024

12. Z.V. Quiñones-Jurado, M.Á. Waldo-Mendoza, J.M. Mata, C.A. Ávila-Orta, Transparent low electrostatic charge films based on carbon nanotubes and polypropylene. Polymers **10**(1), 55 (2018). https://doi.org/10.3390/polym10010055
13. J.-M. Thomassin, C. Jérôme, T. Pardoen, C. Bailly, I. Huynen, C. Detrembleur, Polymer/carbon based composites as electromagnetic interference (EMI) shielding materials. Mater. Sci. Eng. R. Rep. **74**(7), 211–232 (2013). https://doi.org/10.1016/j.mser.2013.06.001
14. R. Banerjee, A. Gebrekrstos, J.T. Orasugh, S.S. Ray, Nanocarbon-containing polymer composite foams: a review of systems for applications in electromagnetic interference shielding, energy storage, and Piezoresistive sensors. Ind. Eng. Chem. Res. **62**(5) (2023). https://doi.org/10.1021/acs.iecr.3c00089
15. Z. Han, A. Fina, Thermal conductivity of carbon nanotubes and their polymer nanocomposites: a review. Prog. Polym. Sci. **36**(7), 914–944 (2011). https://doi.org/10.1016/j.progpolymsci.2010.11.004
16. A.G. Jineesh, S. Mohapatra, Thermal properties of polymer–carbon nanocomposites. Springer Ser. Polym. Compos. Mater. 235–270 (2018). https://doi.org/10.1007/978-981-13-2688-2_7
17. Yu.S. Perets, I.V. Ovsiienko, L.L. Vovchenko, L.Y. Matzui, O.A. Brusilovetz, I.P. Pundyk, Characterization of nanodispersed graphite. Ukr. J. Phys.J. Phys. **57**(2), 219–223 (2012)
18. I.V. Ovsiienko, T.A. Len, L.Y. Matzui, O.A. Golub, Yu.I. Prylutskyy, P. Eklund, The effect of thermal and chemical treatment on the structural and phase composition of nanocarbon materials. Mater. Sci. Eng. C **26**(5–7), 1180–1184 (2006). https://doi.org/10.1016/j.msec.2005.09.063
19. I.V. Ovsiienko, T.A. Len, L.Y. Matzui, O.A. Lazarenko, F.L. Normand, Features of microstructure of chemically obtained graphene-like particles. Ukr. J. Phys. **63**(8), 759–766 (2018). https://doi.org/10.15407/ujpe63.8.759
20. Y. Perets, L. Matzui, L. Vovchenko, I. Ovsiienko, O. Yakovenko, O. Lazarenko, A. Zhuravkov, O. Brusylovets, Influence of ultraviolet/ozonolysis treatment of nanocarbon filler on the electrical resistivity of epoxy composites. Nanoscale Res. Lett. **11**(370) (2016). https://doi.org/10.1186/s11671-016-1577-4
21. I.V. Ovsiienko, T.A. Len, L.Y. Matzui, Yu.I. Prylutskyy, U. Ritter, P. Scharff, F.L. Normand, P. Eklund, Resistance of a nanocarbon material containing nanotubes. Mol. Cryst. Liq. Cryst. **468**(1), 289–297 (2007). https://doi.org/10.1080/15421400701231582
22. I.V. Ovsiienko, T.A. Len, O.A. Syvolozhskyy, L.Y. Matzui, I.G. Mirzoiev, V.V. Andrievskii, E.Y. Beliayev, Magnetoresistance of graphite nanoplatelets with different structure. Low Temp. Phys. **47**(10), 854–862 (2021). https://doi.org/10.1063/10.0006066
23. K. Shirasu, A. Nakamura, G. Yamamoto, T. Ogasawara, Y. Shimamura, Y. Inoue, T. Hashida, Potential use of CNTs for production of zero thermal expansion coefficient composite materials: an experimental evaluation of axial thermal expansion coefficient of CNTs using a combination of thermal expansion and uniaxial tensile tests. Compos. A Appl. Sci. Manuf. **95**, 152–160 (2017). https://doi.org/10.1016/j.compositesa.2016.12.027

Chapter 24
Technology and Knowledge Transfer for Nanotechnology Industry

Artem Artyukhov, Nadiia Artyukhova, and Jan Krmela

Abstract This paper investigates the critical aspects of effective technology transfer in nanotechnology. It highlights the challenges of translating laboratory research into real-world applications, including the need for robust intellectual property protection, strong industry-academia collaborations, and comprehensive risk assessment. The study introduces a novel framework for assessing the readiness of nanotechnology innovations for commercialization. This framework integrates various readiness levels, including Technology Readiness Level (TRL), Innovation Readiness Level (IRL), Intellectual Property Readiness Level (IPRL), and Sustainability Readiness Level (SRL), alongside market, customer, and business readiness considerations. Furthermore, the paper emphasizes the importance of iterative development, feedback mechanisms, and continuous improvement in the product development cycle. By incorporating these elements, researchers and industries can make informed decisions, mitigate risks, and accelerate the translation of nanotechnology research into impactful and beneficial applications. This framework provides a valuable tool for academia, industry, and government stakeholders to navigate the complex landscape of nanotechnology development and ensure its responsible and sustainable integration into society.

A. Artyukhov (✉) · N. Artyukhova
Bratislava University of Economics and Business, Bratislava, Slovakia
e-mail: a.artyukhov@pohnp.sumdu.edu.ua

Sumy State University, Sumy, Ukraine

A. Artyukhov
WSEI University, Lublin, Poland

J. Krmela
Alexander Dubcek University of Trencin, Puchov, Trencin, Slovakia

O. Fesenko and L. Yatsenko (eds.), *Functional Nanomaterials, Nanocatalysts, Nanotechnologies, and Their Applications*, Springer Proceedings in Physics 321,
https://doi.org/10.1007/978-3-031-99136-3_24

24.1 Introduction

Nanotechnology, a field with immense potential, demands efficient technology transfer to bridge the gap between academic research and industrial application. Effective technology transfer in nanotechnology involves a complex interplay of intellectual property protection, collaborative partnerships, technology readiness assessment, knowledge transfer mechanisms, and ethical considerations.

Securing patents for inventions and protecting original works through copyright is crucial to safeguarding intellectual property rights and attracting potential licensees. Protecting confidential information, such as proprietary manufacturing processes or formulations, is essential.

Fostering collaborations between academia and industry through partnerships, consortia, and joint ventures facilitates knowledge exchange, resource sharing, and accelerating research and development.

Assessing the technology readiness level (TRL) ensures that technologies are mature enough for commercialization while iterative development and risk management mitigate potential challenges.

Knowledge transfer mechanisms, such as licensing agreements, spin-off companies, consultancy services, and training programs, facilitate the dissemination of knowledge and the commercialization of nanotechnology innovations.

Finally, ethical considerations, including environmental impact, health and safety, and social responsibility, must be carefully considered to ensure nanotechnology's sustainable and beneficial development.

By effectively applying these principles, researchers, universities, and industry can accelerate nanotechnology innovation and address pressing global challenges, such as climate change, healthcare, and energy.

24.2 Background

The successful transfer of knowledge and technology from the laboratory to the industry remains a critical challenge in nanotechnology [1]. Collaborative networks and technology clusters play a crucial role in facilitating the commercialization of nanotechnology innovations [2, 3]. Researchers have highlighted the importance of co-patenting, co-authorship, and geographic proximity in fostering knowledge exchange and technology transfer [4, 5]. The involvement of institutional entrepreneurs and policy initiatives can also significantly influence the dynamics of knowledge transfer in the nanotechnology industry [6, 7].

Several mechanisms have been identified for transferring knowledge in the nanotechnology domain. University-industry collaborations, the mobility of skilled personnel, and the licensing and commercialization of patents are some key pathways [8, 9]. However, nanotechnology's interdisciplinary nature and complexity pose unique challenges regarding knowledge integration and transfer [10, 11].

Factors such as public funding, regulatory frameworks, and educational initiatives significantly impact the diffusion and adoption of nanotechnology [12, 13]. Adequate public funding and supportive policy environments can catalyze the development and commercialization of nanotechnology applications [13, 14]. At the same time, the lack of standardized risk assessment methods and regulatory guidelines has been identified as a barrier to the widespread adoption of nanotechnology [7, 12].

Emerging trends in nanotechnology, such as advancements in artificial intelligence and computational tools, the internationalization of knowledge flows, and the increasing emphasis on sustainability and environmental impact, will likely shape the future of knowledge transfer in this domain [9, 15]. Effective governance frameworks and stakeholder engagement strategies will ensure nanotechnology's responsible and socially beneficial development [16, 17].

Supportive policy environments that encourage pre-competitive research, inter-firm collaboration, and university-industry partnerships have been instrumental in driving nanotechnology's development and commercialization [2, 18, 19].

Educational initiatives and workforce development programs are also essential for enhancing the diffusion and adoption of nanotechnology [20–22]. Improving public awareness and understanding of nanotechnology and fostering the necessary skills and expertise can contribute to the responsible and socially beneficial development of this emerging field [2, 23, 24].

Intellectual property rights and technology transfer policies can also influence the dynamics of knowledge transfer in the nanotechnology industry [9, 18]. Societal concerns and public perception regarding nanotechnology's potential risks and ethical implications can further hinder its commercialization and societal acceptance [25–27].

The literature highlights the multifaceted and complex nature of knowledge transfer in the nanotechnology industry. A comprehensive understanding of the interplay between technological, organizational, and institutional factors is essential for enhancing the efficiency and effectiveness of knowledge transfer and driving the successful commercialization of nanotechnology innovations [5, 7, 28, 29].

Developing robust technology transfer models is essential to address these challenges and accelerate the translation of nanotechnology research into real-world applications. These models should incorporate a comprehensive understanding of the readiness levels of nanotechnology innovations, enabling the identification of critical milestones and the allocation of appropriate resources. This research aims to develop and evaluate a comprehensive technology transfer model for nanotechnology innovations based on product readiness levels to facilitate the smooth transition of nanotechnology research from the laboratory to the market.

24.3 Model of Product Complex Readiness and Assessment Levels for the Nanotechnology Industry

The Technology Readiness Level (TRL) [30] is a widely used metric to assess the maturity of a technology. In the context of nanotechnology, TRL helps gauge the readiness of a nanomaterial or nanotechnology-based product for commercialization. A higher TRL indicates a more advanced stage of development, with TRL 9 representing a fully validated and market-ready product.

The Innovation Readiness Level (IRL) is a more nuanced approach considering factors beyond technological maturity. It assesses the readiness of an innovation to be adopted and diffused in the market. IRL considers market demand, regulatory environment, and intellectual property protection [31].

The Intellectual Property Readiness Level (IPRL) [32] focuses explicitly on protecting intellectual property rights associated with nanotechnology innovations. This includes patents, trademarks, and copyrights. A higher IPRL indicates stronger protection and a more robust intellectual property portfolio.

The System Readiness Level (SRL) assesses the maturity of a system or platform incorporating nanotechnology. ARL includes the integration of nanomaterials or devices into larger systems, such as electronic devices, medical devices, or energy storage systems. A higher SRL signifies a more advanced and reliable system [33].

The Market Readiness Level (MRL) evaluates the readiness of a market to adopt a nanotechnology-based product or service. It considers factors like market demand, consumer awareness, regulatory compliance, and distribution channels. A higher MRL indicates a more receptive market [34].

The Adoption Readiness Level (ARL) assesses the readiness of potential adopters to embrace nanotechnology innovations. ARL includes factors such as the willingness to adopt new technologies, the availability of training and support, and the perceived benefits of nanotechnology. A higher ARL indicates a greater willingness to adopt [35].

Risk level assessment (RLA) is a critical component of technology transfer. It involves identifying and evaluating potential risks associated with nanotechnology, including technical, market, regulatory, and environmental risks. Organizations can develop mitigation strategies by assessing risks and making informed decisions about resource allocation and investment [36].

The Business Readiness Level (BRL) is a crucial concept that complements TRL to assess the overall readiness of an innovation for market launch. While TRL focuses on the technological maturity of innovation, BRL evaluates the business aspects such as market demand, financial viability, and commercialization strategy. By considering TRL and BRL, innovators can ensure their technology is technically feasible and commercially viable. This holistic approach enhances the likelihood of successful technology commercialization [37].

Assessing its quality and maturity is crucial to ensure the effective sharing and utilization of data. Data Readiness Levels (DRLs) provide a standardized framework for evaluating data derived from experiments or models. Like TRLs, DRLs

classify data based on its quality and reliability, facilitating its use in analytical methods, model validation, and comparisons with historical datasets. However, DRLs are further enhanced by metadata qualifiers, which offer additional context, such as measurement techniques, computational methods, and data provenance. This combination of DRLs and metadata enables researchers to share data more effectively, cite it in publications, and accelerate the translation of research into practical applications [38].

The Sustainability Readiness Level (SRL) assesses the environmental and social impact of nanotechnology products and processes throughout their lifecycle. It considers energy efficiency, resource consumption, waste generation, and human health and safety. A higher SRL indicates a more sustainable product or process with minimal negative environmental and social impacts [39].

The Product Readiness Level (PRL) evaluates the maturity of a nanotechnology-based product. It considers product performance, reliability, safety, and regulatory compliance factors. A higher PRL signifies a more advanced product closer to market readiness [39].

The Supply Chain Readiness Level (SCRL) assesses the maturity of the supply chain for nanotechnology materials and components. It considers factors such as the availability of raw materials, suppliers' reliability, and manufacturing processes' efficiency. A higher SCRL indicates a more robust and resilient supply chain [39].

By considering these various readiness levels, organizations can make informed decisions about the timing and resources required to bring nanotechnology innovations to market. A comprehensive understanding of these levels can help accelerate the commercialization of nanotechnology and maximize its societal and economic impact.

Figure 24.1 illustrates a conceptual framework for technology and knowledge transfer in nanotechnology, emphasizing product development's iterative and feedback-driven nature.

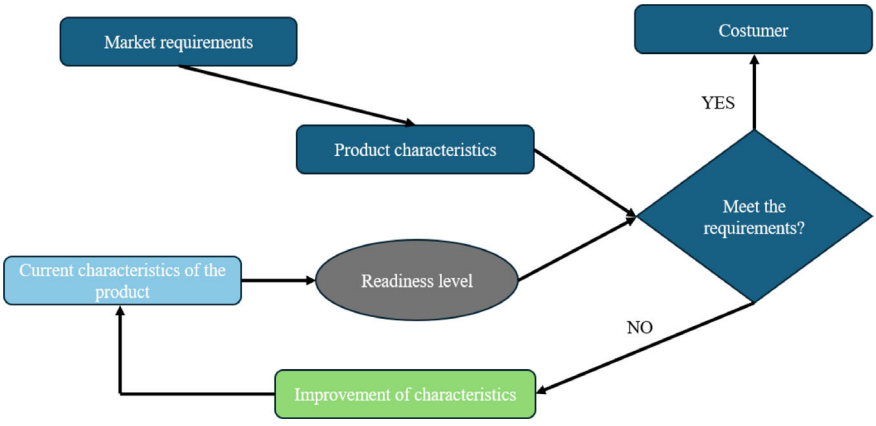

Fig. 24.1 Technology and knowledge transfer in nanotechnology

Figure 24.1 shows the technology and knowledge transfer in nanotechnology. It consists of the below-mentioned blocks.

1. Market requirements represent the market's needs, expectations, or demands. These could include functionality, performance, cost, compliance with standards, or other features desired by customers or industry trends. These requirements directly influence the next step—product characteristics.
2. Product characteristics translate the market requirements into specific product features or attributes. These characteristics are measurable or qualitative attributes of the product, such as its design, quality, usability, and performance. This step ensures the product aligns with what the market expects. The product characteristics are then compared to customer requirements in the next step.
3. The decision node "Meet the Requirements?" evaluates whether the product characteristics, as defined in step 2, satisfy the initial market requirements and the customer's specific needs.

- two possible outcomes:
  - YES: if the product characteristics meet the requirements, the process moves to the customer node, indicating that the product is ready to be delivered or launched.
  - NO: if the product does not meet requirements, the process flows to improve the characteristics to refine the product.

4. Customer represents the endpoint for a successful product. If the product characteristics align with market and customer requirements, it is ready to be delivered to the customer.
5. Improvement of characteristics is a feedback mechanism triggered when the product does not meet the requirements. This stage involves modifying, optimizing, or redesigning the product to address the gaps identified in the previous step. Improvements might include enhancing functionality, increasing durability, reducing costs, or refining usability. The improved product characteristics feed into the next step – the current characteristics of the product.

24.4 Conclusions

Nanotechnology represents a transformative field with the potential to address some of the most pressing global challenges, including climate change, healthcare, and sustainable energy. However, its successful integration into real-world applications relies heavily on effective knowledge and technology transfer frameworks. This study has emphasized the importance of comprehensive readiness assessments and multidisciplinary approaches to bridge the gap between laboratory research and industrial application.

The integration of various readiness level models, such as the Technology Readiness Level (TRL), Innovation Readiness Level (IRL), and Sustainability Readiness

Level (SRL) etc., provides a holistic framework for evaluating nanotechnology innovations. These models enable researchers and industries to systematically identify critical milestones, allocate resources efficiently, and address barriers to commercialization. Similarly, licensing agreements, spin-offs, and collaborative partnerships between academia and industry facilitate the dissemination and practical application of nanotechnology innovations.

Furthermore, the feedback-driven model of product readiness underscores the iterative nature of nanotechnology development, ensuring that market and customer needs remain at the forefront. Ethical considerations, including environmental sustainability, health and safety, and social responsibility, are essential for fostering public trust and ensuring the responsible development of nanotechnology.

Incorporating robust intellectual property management, supply chain readiness, and risk assessment into technology transfer strategies can further enhance the efficiency of commercialization pathways. Evaluating Data Readiness Levels (DRLs) and integrating metadata qualifiers are critical in fostering data transparency, reproducibility, and effective collaboration.

By leveraging these frameworks and strategies, academia, industry, and government stakeholders can collectively accelerate nanotechnology's adoption and societal impact. The advancement of nanotechnology innovations, driven by effective technology transfer and knowledge dissemination, has the potential to revolutionize industries and contribute significantly to global economic and social well-being. Future research should continue to refine these frameworks, incorporate emerging trends, and address the unique challenges posed by the interdisciplinary nature of nanotechnology to maximize its transformative potential.

Acknowledgements This research was funded by a European Union grants "NextGenerationEU through the Recovery and Resilience Plan for Slovakia" (No. 09I03-03-V01-00130) and "Immersive Marketing in Education: Model Testing and Consumers' Behavior" (No. 09I03-03-V04-00522/2024/VA) and a grant from the Ministry of Education and Science of Ukraine under project "Modeling and forecasting of socio-economic consequences of higher education and science reforms in wartime" (reg. no. 0124U000545).

References

1. C. Genet, K. Errabi, C. Gauthier, Which model of technology transfer for nanotechnology? A comparison with biotech and microelectronics. Technovation **32**(3–4), 205–215 (2012)
2. K. Pandža, T. Wilkins, E. Alfoldi, Collaborative diversity in a nanotechnology innovation system: evidence from the EU framework programme. Technovation **31**(9), 476–489 (2011)
3. M. Roco, B. Harthorn, D. Guston, P. Shapira, Innovative and responsible governance of nanotechnology for societal development. J. Nanopart. Res. **13**(9), 3557–3590 (2011)
4. K. Zalewska-Kurek, Understanding researchers' strategic behaviour in knowledge production: a case of social science and nanotechnology researchers. J. Knowl. Manag. **20**(5), 1148–1167 (2016)

5. L.G. Zucker, M.R. Darby, J.S. Armstrong, Commercializing knowledge: university science, knowledge capture, and firm performance in biotechnology. Manage. Sci. **48**(1), 138–153 (2002)
6. D. Hristozov, S. Gottardo, E. Semenzin, A. Oomen, P. Bos, W. Peijnenburg, M. van Tongeren, B. Nowack, N. Hunt, A. Brunelli, J.J. Scott-Fordsmand, L. Tran, A. Marcomini, Frameworks and tools for risk assessment of manufactured nanomaterials. Environ. Int. **95**, 36–53 (2016)
7. O. Renn, M. Roco, Nanotechnology and the need for risk governance. J. Nanopart. Res. **8**(2), 153–191 (2006)
8. Y. Gökuç, S. Turunç, Use of nanotechnological building materials in the Turkish construction industry. J. Sustain. Constr. Mater. Technol. **4**(1), 296–305 (2019)
9. N. Islam, Trends in nanotechnology knowledge creation and dissemination. Int. J. Nanotechnol. Mol. Comput. **3**(4), 47–64 (2011)
10. S. Dwivedi, Q. Saquib, A.A. Al-Khedhairy, J. Musarrat, Understanding the role of nanomaterials in agriculture. in *Microbial Inoculants in Sustainable Agricultural Productivity*, eds. by D. Singh, H. Singh, R. Prabha (Springer, New Delhi), pp. 271–288
11. A. Zhidebekkyzy, S. Kupeshova, A. Yesmurzayeva, Project management in nanotechnology: a systematic literature review. Montenegrin J. Econ. **15**(3), 227–244 (2019)
12. J. Chen, C. Sun, Nanoparticles: aspects of safety and risk management. Adv. Mater. Res. **113–116**, 222–225 (2010)
13. F. Mollá, C. Fito-López, J. Alvaro, F. Huertas-López, New tools to support the risk assessment process of nanomaterials in the insurance sector. Int. J. Environ. Res. Public Health **18**(13), 6985 (2021)
14. L. Zucker, M. Darby, J. Furner, R. Liu, Minerva unbound: knowledge stocks, knowledge flows and new knowledge production. NBER Working Paper Series, p. 12669 (2006)
15. S.Y. Paik, D.M. Zalk, P. Swuste, Application of a pilot control banding tool for risk level assessment and control of nanoparticle exposures. Ann. Occup. Hyg. **52**(6), 419–428 (2008)
16. P.J.M. Bartos, Nanotechnology in construction: a roadmap for development, in *Nanotechnology in Construction 3*. ed. by Z. Bittnar, P.J.M. Bartos, J. Němeček, V. Šmilauer, J. Zeman (Springer, Berlin, Heidelberg, 2009), pp.15–26
17. R. DiSanto, V. Subramanian, Z. Gu, Recent advances in nanotechnology for diabetes treatment. Wiley Interdiscip. Rev. Nanomedicine Nanobiotechnology **7**(4), 548–564 (2015)
18. J. Woolley, R. Rottner, Innovation policy and nanotechnology entrepreneurship. Entrep. Theory Pract. **32**(5), 791–811 (2008)
19. P. Shapira, J. Wang, From lab to market? Strategies and issues in the commercialization of nanotechnology in China. Asian Bus. Manag. **8**(4), 461–489 (2009)
20. A. Anderson, D. Brossard, D. Scheufele, The changing information environment for nanotechnology: online audiences and content. J. Nanopart. Res. **12**(4), 1083–1094 (2010)
21. N. Elmarzugi, E. Keleb, A. Mohamed, H. Benyones, N. Bendala, A. Mehemed, A. Eid, Awareness of Libyan students and academic staff members of nanotechnology. J. Appl. Pharm. Sci. **4**(06), 110–114 (2014)
22. E.A. Şenocak, A survey on nanotechnology in the view of the Turkish public. Sci. Technol. Soc. **19**(1), 79–94 (2014)
23. C.-H. Wang, P.-Y. Chien, Exploring the nanotechnology alliances of nanotechnology firms: the roles of network position and technological uncertainty. Sci. Technol. Soc. **18**(2), 139–164 (2013)
24. H. Diefes-Dux, M. Dyehouse, D. Bennett, P. Imbrie, Nanotechnology awareness of first-year food and agriculture students following a brief exposure. J. Nat. Resour. Life Sci. Educ. **36**(1), 58–65 (2007)
25. M. Jones, G. Gardner, M. Falvo, A. Taylor, Precollege nanotechnology education: a different kind of thinking. Nanotechnol. Rev. **4**(1), 117–127 (2015)
26. M. Siegrist, C. Keller, Labeling of nanotechnology consumer products can influence risk and benefit perceptions. Risk Anal. **31**(11), 1762–1769 (2011)
27. S. Smith, H. Hosgood, E. Michelson, M. Stowe, Americans' nanotechnology risk perception: assessing opinion change. J. Ind. Ecol. **12**(3), 459–473 (2008)

28. N. Kamarulzaman, K. Lee, K. Siow, M. Mokhtar, Psychological and sociological perspectives for good governance of sustainable nanotechnology development in Malaysia. J. Nanopart. Res. **21**(7), 164 (2019)
29. A. Ryszko, Interorganizational cooperation, knowledge sharing, and technological eco-innovation: the role of proactive environmental strategy—empirical evidence from Poland. Pol. J. Environ. Stud. **25**(2), 753–764 (2016)
30. S. Yfanti, N. Sakkas, Technology Readiness Levels (TRLs) in the era of co-creation. Appl. Syst. Innov. **7**, 32 (2024)
31. S. Ozcan, A. Stornelli, C. Simms, A product innovation readiness level framework. IEEE Trans. Eng. Manag. **71**, 9920–9937 (2024)
32. IPR Readiness Level—IPRL https://kthinnovationreadinesslevel.com/wp-content/uploads/sites/9/2021/02/IPR-Readiness-Level_E.pdf
33. S. Yasseri, H. Bahai, System readiness level estimation of oil and gas production systems. Int. J. Coast., Offshore Environ. Eng. **3**(2), 31–44 (2018)
34. Understanding market readiness level: From idea to IP. https://iuk-business-connect.org.uk/perspectives/understanding-market-readiness-level/
35. Adoption Readiness Levels (ARL) framework. https://www.energy.gov/technologytransitions/adoption-readiness-levels-arl-framework
36. Balancing acts: exploring risk and luck through lens of gender and decision-making. https://dadsinbusiness.co.uk/blog/risk-and-luck/
37. Business Readiness Level—BRL. https://kthinnovationreadinesslevel.com/wp-content/uploads/sites/9/2018/10/Business-readiness-Level.pdf
38. N.D. Lawrence (2017, May 5). Data readiness levels. https://arxiv.org/abs/1705.02245
39. Sustainability Readiness Level—SRL. https://infrasweden.nu/wp-content/uploads/2024/04/Sustainability-Readiness-Level_1.0.pdf

Chapter 25
Electron-Beam Evaporation–condensation Technology for Applying Heat-Protective Coatings to the Blades of Gas Turbine Engines with Boride Nanoparticles in the Outer Ceramic Layer

M. Grechanyuk, V. Grechanyuk, V. Chornovol, O. Matsenko, and I. Grechanyuk

Abstract The article extensively explores protective thermal barrier coating technologies for gas turbines, emphasizing their significance in enhancing turbine efficiency and longevity. The authors conducted experiments involving the application of protective coatings on gas turbine blades of various purposes using electron beam physical vapor deposition of alloys and ceramics. The research revealed that thermal barrier coatings contribute to raising gas temperatures ahead of the turbine or increasing the durability of the blades, leading to enhanced efficiency and fuel savings. Optimal parameters for different types of coatings, including layer composition and structure, were established to improve heat resistance and overall coating longevity. Laboratory and industrial electron beam facilities for coating application are described in detail, ensuring optimal conditions for material melting and application. Special attention is given to the advanced L-9 setup, which distinguishes itself from previous ones by utilizing a cold cathode for electron beam heaters, enhancing stability and durability. Additionally, the article details the technical peculiarities of the installations, their design, and capabilities for applying various types of coatings. Information regarding the control systems for these installations and the operational

M. Grechanyuk
Department of Abrasion—and Corrosion-Resistant Powder Construction, Materials Institute for Problems of Material Sciences NAS of Ukraine, Kyiv, Ukraine

V. Grechanyuk · V. Chornovol (✉) · O. Matsenko · I. Grechanyuk
Department of Chemistry, Kyiv National University of Construction and Architecture, Ave of Air Forces, Kyiv, Ukraine
e-mail: missvik@ukr.net

V. Grechanyuk
E.O. Paton Electric Welding Institute of the National Academy of Sciences, Kyiv, Ukraine

O. Fesenko and L. Yatsenko (eds.), *Functional Nanomaterials, Nanocatalysts, Nanotechnologies, and Their Applications*, Springer Proceedings in Physics 321,
https://doi.org/10.1007/978-3-031-99136-3_25

principles of the state-of-the-art setup, applicable for depositing different protective coatings, including novel micro-layered silicide coatings, is presented. With this comprehensive overview of technologies and installations, the article showcases the direction of research and development in the field of protective thermal barrier coatings, aiming to augment the reliability and effectiveness of gas turbines.

25.1 Introduction

The development of efficient and reliable gas turbines is a complex problem that has arisen in the course of gas turbine development. The key aspects of this complexity are the turbine's impeller and nozzle blades, whose materials and design are essential for the permissible gas temperature upstream of the turbine and, therefore, affect the technical and economic characteristics of gas turbine engines (GTEs). At present, technological challenges associated with the further development of convective blade cooling and the state of heat-resistant alloy metallurgy indicate the need to improve GTE cycle parameters. This requires the development of a new system for protecting gas turbine blades and the transition from heat-resistant multicomponent coatings to thermal protection coatings (TPC). Attempts to create protective heat coatings for gas turbines were made more than 60 years ago. However, interest in these technologies has recently increased significantly, as modern GTDs operate at very high temperatures, which poses new challenges for heat protection materials and technologies.

25.2 Experimental Part

At RPE 'Eltechmash', protective coatings on gas turbine blades were applied by electron beam evaporation of MeCrAlY (where Me–NiCoFe), MeCrAlYHfSiZr alloys, and ceramics based on ZrO_2 stabilised by Y_2O_3 and subsequent condensation of the vapour phase on the surface of gas turbine blades for various purposes [1]. (Fig. 25.1).

Studies have shown that the use of heat-shielding coatings with a thickness of 250 μm and thermal conductivity of 1 W/m^{2}K on two turbine stages allows for one of two possibilities [2–7]:

1. At a constant operating temperature of the blade material, increase the gas temperature in front of the turbine by about 100 °C, which will lead to an increase in efficiency and fuel economy by more than 13%;
2. Without changing the gas temperature in front of the turbine, increase the service life of the blades by about 4 times due to a decrease in their operating temperature.

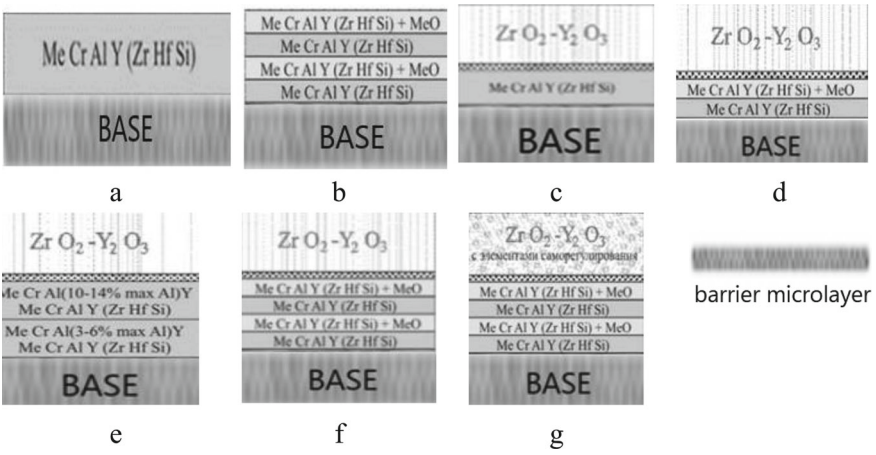

Fig. 25.1 Schemes of heat-resistant and heat-protective coatings obtained by electron beam deposition: **a**—single-layer metallic types MeCrAlY, MeCrAlY(HfSiZr); **b**—single-layer composite micro-layer types with alternating layers of MeCrAlY (MeCrAlYHfSiZr)/MeCrAlY (MeCrAlY-HfSiZr) + MeO where MeO is Al_2O_3 or ZrO_2 + 6… 8 wt% Y_2O_3; **c**—two-layer coatings with an inner metal MeCrAlY (MeCrAlYHfSiZr) and an outer ceramic layer; **d**—two-layer coatings with an inner composite MeCrAlY(MeCrAlYHfSiZr) + MeO of dispersion-hardened or micro-layer types and an outer ceramic (ZrO_2–Y_2O_3) layer; **e**—three-layer coatings with inner and intermediate metal layers based on MeCrAlY (MeCrAlYHfSiZr) alloys and an outer layer based on ceramics (ZrO_2–Y_2O_3); **f**—three-layer coatings with inner metal MeCrAlY (MeCrAlYHfSiZr), intermediate composite MeCrAlY (MeCrAlYHfSiZr) + MeO of dispersion-strengthened or micro-layer types and outer ceramic (ZrO_2–Y_2O_3) layers; **g**—three-layer coatings with internal metal MeCrAlY (MeCrAlYHfSiZr), intermediate composite MeCrAlY (MeCrAlYHfSiZr) + MeO of dispersed or micro-layer types and external ceramic (ZrO_2–Y_2O_3) layers with nanodispersed boride particles, which, when oxidised, heal microcracks in the outer ceramic layer that occur during heating and cooling thermal cycles

The total thickness of single-layer heat-resistant coatings does not exceed 150 μm, two-layer heat-protective coatings—200 μm, three-layer heat-protective coatings—300 μm. The thickness of the damping inner layer with a reduced Al content (3–6% by weight) in three-layer heat-shielding coatings ranges from 30 to 50 μm, the thickness of the intermediate heat-resistant layer is 50–80 μm, and the outer ceramic layer is 80–120 μm. The concentrations of chromium, aluminium, yttrium in the heat-resistant layer are 18–24% by weight, 10–130% by weight, 0.4–1.8% by weight, respectively, and zirconium, hafnium, and silicon are from 0.05 to 0.2% by weight.

25.3 Results and Discussion

Additional alloying of MeCrAlY alloys with zirconium, hafnium and silicon made it possible, on the one hand, to increase the heat resistance of single-layer multicomponent and composite heat-resistant coatings, and on the other hand, when these alloys are used as materials for the internal damping and intermediate heat-resistant layer, to slow down the diffusion processes at the interface between the base—damping layer, intermediate heat-resistant layer—outer ceramic layer and thereby increase the overall service life of the coating.

An even greater slowdown of diffusion processes in the coating is observed when an intermediate heat-resistant layer is used in a micro-layer version. Optimal parameters are achieved when the thickness of the alternating metal and composite layers is from 0.5 to 1 μm and the concentration of dispersed refractory particles (ZrO_2–Y_2O_3, Al_2O_3) in the composite microlayer is from 0.3 to 1% by weight.

In the design of thermal protective coatings (TPC), the formation of a barrier microlayer at the interface between the intermediate heat-resistant layer and the outer ceramic layer is of great importance. Typically, a 1–5 μm thick metal-ceramic layer based on complex spinels of Al_2O_3, ZrO_2, Y_2O_3, CrO_3 and MeCrAlY alloy is produced using special technological methods. Such a barrier layer inhibits the formation of an oxide (Al_2O_3) film at the interface between the intermediate and outer layers of the heat-shielding coating.

If the thickness of the Al_2O_3 film reaches 10–15 μm, delamination of the outer ceramic layer ZrO_2–Y_2O_3 is observed.

The two-layer metal/ceramic coatings (Fig. 25.1c) obtained by the two-stage technology are widely used at Zorya-Mashproekt (Mykolaiv, Ukraine) and provide a service life of the first stage turbine blades of gas turbine units for gas pumping of up to 25,000 h. Currently, the company is optimising the technology for applying two-layer heat-shielding coatings with an inner composite layer of micro-layer type with alternating layers of CoCrAlY/CoCrAlY + (ZrO_2–Y_2O_3) and an outer ceramic layer of ZrO_2–Y_2O_3. Such coatings are applied in one technological cycle and should provide a service life of up to 32,000 h.

It is advisable to increase the durability of fuel assemblies by changing the design of the coatings, since there is no need to make any changes to the process scheme, which is associated with significant energy costs.

Adjustments in the design scheme of the TZP are not limited by the capabilities of electron beam technology. In three-layer coatings (Figs. 25.1e, f, and g), as mentioned earlier, MeCrAlY and MeCrAlYSiHfZr alloys are used as an internal damping layer with a ratio of components that provides high plasticity (relative elongation at break $\delta = 2.5\%$) and sufficient heat resistance. This layer is used to reduce stresses in the concrete mixtures, as well as to inhibit and block cracks developing from the surface to the depth of the base.

The intermediate layer is a composite of increased heat resistance and thermal stability. The third outer ceramic layer is formed on the basis of zirconium dioxide stabilised with yttrium oxide. One or more borides with a concentration of 5–10%

by weight and a nanoparticle size of 10–20 nm are additionally introduced into the outer ceramic layer. These nanoparticles, when oxidised, heal microcracks that occur in the outer ceramic layer.

The latest modification of the TFP for the protection of the first stage turbine blades of fifth-generation military engines. Such work is being carried out for Ukrainian enterprises operating in the field of gas turbine construction (SE Ivchenko-Progress and JSC Motor-Sich in Zaporizhzhia).

Laboratory and industrial electron beam equipment has been developed to apply heat-resistant and heat-protective coatings. Figure 25.2 shows the appearance of the universal laboratory electron beam unit L-2 for melting and evaporation of materials in a vacuum [8]. Schemes of technological processes are shown in Fig. 25.3, technical characteristics of the installation are given in Table 25.1.

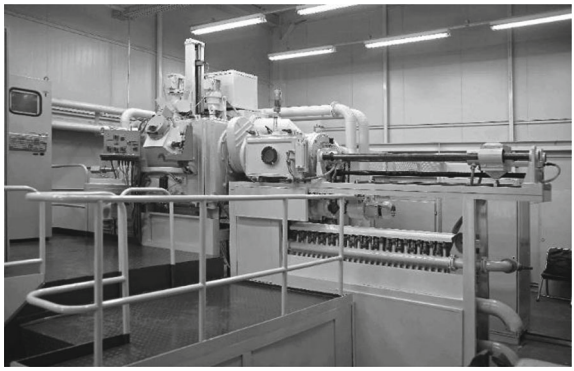

Fig. 25.2 Exterior view of the universal laboratory electron beam machine L-2

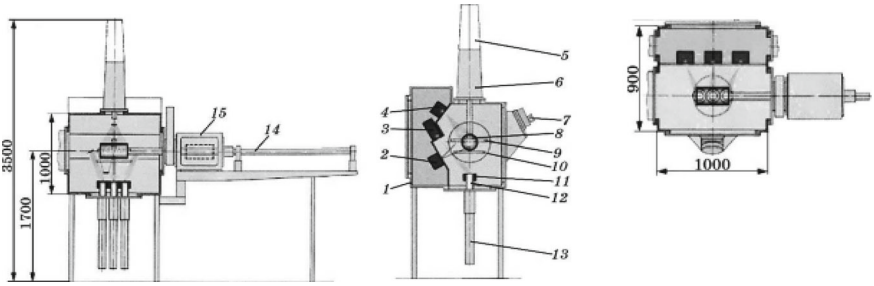

Fig. 25.3 Schemes of technological processes of the L-2 unit: 1—working chamber; 2—electron beam (EB) gun for heating products from below; 3—EB gun for evaporation of materials; 4—EB gun for heating products from above; 5—vertical mechanism for feeding the billet for fusion; 6—mechanism for suspension and rotation of the product; 7—inspection system; 8—dimension of the cylindrical product; 9—dimension of the disc product; 10—damper; 11—crucible; 12—ingot; 13—ingot feeding mechanism for evaporation; 14—horizontal product feeding mechanism; 15—airlock chamber

Table 25.1 Technical characteristics of the L-2 unit

1	Installed capacity, kW	300
2	Acceleration voltage, kV	20
3	Size of ingots to be evaporated, mm	
	- Diameter	70
	- Length	400
4	Size of workpieces to be fused, mm	
	- Diameter	80
	- Length	390
5	Size of ingots to be smelted, mm	
	- Diameter, section	70
	- Length	400
6	Condensation surface size, mm	
	- Rectangular flat	350 × 350
	- Round flat (diameter)	400
	- Cylindrical	
	Diameter	150
	Length	350
7	Number of crucibles, pcs	3
8	Inner diameter of crucibles	70, 74
9	Horizontal rod lifting capacity, kg	30
10	Horizontal rod lifting capacity, kg	50
11	Number and rated power of electron guns, n × kW	
	- For evaporation of materials	3 × 60
	- For heating products	2 × 60
	- For remelting	(3 × 60)
12	Degree of vacuum in the working chamber, Pa	6×10^{-3} to 1×10^{-2}
13	Cooling water flow rate, m^3/h	10
14	Area occupied by the unit, m^2	100

The system consists of a working and auxiliary chambers for loading and unloading the products to be coated. The plant is equipped with 5 electron beam guns with hot cathodes of its own design. The plant is designed for:

- remelting of metals and alloys for refining and production of cylindrical ingots;
- production of special alloys, including intermetallics, such as Ni3Al, Ti3Al, TiAl, etc.;
- deposition of corrosion-resistant, heat-protective, structural coatings on flat and rotating surfaces, including gas turbine blades;
- deposition of particularly hard wear-resistant coatings from pure metal-like compounds and their mixtures, including micro-layer coatings;

- synthesis of refractory compounds (carbides, borides, silicides) during the deposition of steam streams,
- borides, silicides) and production of thin and thick coatings;
- production of dispersion-strengthened microlayer and microporous materials in the form of coatings and massive blanks separable from the substrate;
- production of coatings from equilibrium phases of carbon.

For industrial use, a universal electron beam unit L-9 was created [9]. The general view of the installation and the coating scheme are shown in Fig. 25.4. Technical characteristics are given in Table 25.2.

The plant is a block of vacuum chambers with mechanisms, devices and systems that ensure the technological process of coating various products in a vacuum. A block of crucibles is docked to the lower flange of the working chamber, which includes four mechanisms for feeding evaporated ingots. The ingots of evaporated materials are fed into the mechanisms from above through the crucibles. A special feature of the plant's design is its equipment with a new power supply with stabilised accelerating voltage and electric beam heaters with a cold cathode.

The use of a cold cathode made of a low-alloy aluminium-based alloy eliminates any distortion, which makes it possible to obtain a stable electron beam for 250 h of

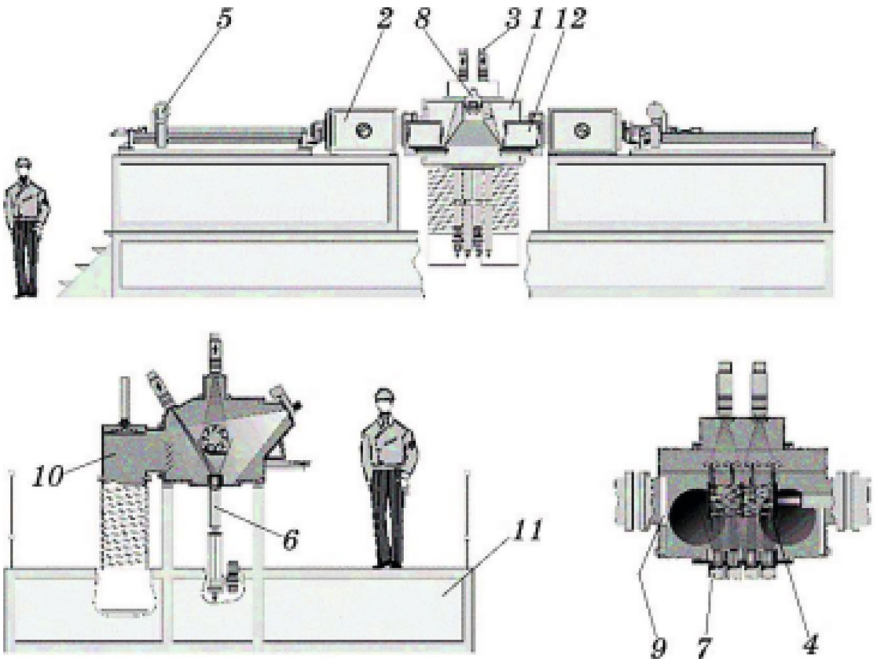

Fig. 25.4 General view of the L-9 unit and coating scheme: 1—process chamber; 2—gateway chamber; 3—electron gun; 4—cassette; 5—cassette (product) feeding mechanism; 6—ingot feeding mechanism; 7—crucible; 8—inspection system; 9—damper; 10—vacuum system; 11—service platform; 12—control panel

Table 25.2 Technical characteristics of the L-9 unit

1	Installed capacity, kW	400
2	Acceleration voltage, kV	25
3	Size of evaporating ingots, mm	
	- Diameter	70
	- Length	500
4	Dimensions of the cassette with sprayed shovels, mm	
	- Diameter	250
	- Length	500
5	Number of crucibles, pcs	4
6	Load capacity of the cassette feed rod, kg	50
7	Number and rated power of electronic guns, n x kW	6×60
8	Vacuum degree in the working chamber, Pa	6×10^{-3} to 1×10^{-2}
9	Cooling water flow rate, m^3/h	15
10	Area occupied by the unit, m^2	140

operation of the facility without replacing it. On the other hand, cold cathode electron beam heaters are capable of stable operation at a vacuum of 10 Pa, while hot strip cathode electron beam heaters operate in a vacuum of at least 5×10^{-2} Pa.

The use of cold cathode electron beam heaters involves the injection of oxygen into the zirconium dioxide vapour cloud and ensures the stoichiometric composition of the outer layer of the heat shielding coating.

The four cold cathode electron beam guns are used to evaporate the feedstock from the crucibles and are arranged in such a way that each electron gun designed to evaporate an ingot from a particular crucible can also be used to evaporate material from an adjacent crucible. This may be necessary if the number of crucibles or their arrangement is changed to meet the requirements of the process. Two synchronously operating dampers are designed to shield the products during the heating of the evaporated materials and products until the process conditions are stabilised. Two similar electron guns mounted on top of the process chamber are used to heat the products. Two gateway chambers are used for reloading the coated products.

The volumes of the process and gateway chambers are separated by two vacuum gates. The gateway chambers are equipped with devices for ionic cleaning of products before coating. The presence of two auxiliary chambers increases the productivity of the plant. Coatings are applied to the products fed alternately from the gateway chambers without depressurising the working chamber where the coatings are deposited. The horizontal feeding mechanism is used to move the products from the airlock chambers to the spraying chamber and back, as well as to rotate the products. The rods are equipped with devices for receiving signals from thermocouples mounted on cassettes with blades. The design of the system uses separate sources for each electron gun with an accelerating voltage of 30 kV.

The plant control system performs:

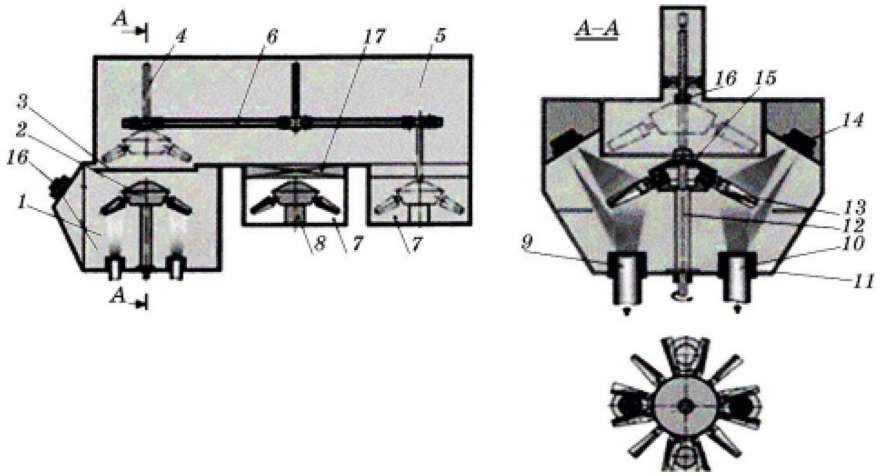

Fig. 25.5 Schematic of an advanced electron beam unit for applying protective coatings: 1—working chamber; 2—planetary mechanism of product (blades) rotation; 3—flap; 4—manipulator; 5—transition chamber; 6—rails; 7—sluice chambers; 8—stand; 9—ceramic ingot; 10—metal ingot; 11—crucible; 12—rotating support; 13—product (blade); 14—electron gun; 15—drive gear; 16—gripper; 17—shutter

- monitoring the technical condition of all plant systems;
- automatic preparation of the plant for the technological process;
- control of plant components from the operator's console during the process;
- processing, display and storage of process parameters and cyclograms in real time.

Currently, work is underway to develop design documentation for a fundamentally new industrial electron beam equipment for deposition of protective coatings. The unit (Fig. 25.5) is a block consisting of four interconnected vacuum chambers: the process chamber 1, the transition chamber 5 and two gateway chambers 3.

Inside the process chamber 1, water-cooled crucibles 11 are installed, in which ingots 9,10 of evaporated materials are placed. Beams of electron guns 14 evaporate the ingot material, which condenses in the form of steam on the products 13. The number of crucibles used can vary depending on the required composition and design (two- or three-layer, micro-layer) of the coating.

All types of protective coatings can be deposited at this facility, including new types of micro-layer silicide coatings.

It should be noted that the company has implemented a closed cycle of deposition of coatings on turbine blades, including the smelting of all types of ingots on nickel, cobalt and iron bases using ceramic ingots.

25.4 Conclusions

The use of electron beam installations for applying protective coatings to gas turbine blades shows significant potential for improving the efficiency of these engines. According to the studies, the L-9 unit with cold cathodes demonstrates stable operation for 250 h without the need to replace cathodes, which is a significant improvement over previous models. The successful introduction of these technologies into industry demonstrates the ability of electron beam facilities to provide up to 30 kV of accelerating voltage for each electron gun. This allows for stable deposition of coatings on the surface of turbine blades, ensuring their protection and long service life. Refined technical indicators, such as a reduction in vacuum requirements by 10 Pa for cold cathode electron beam heaters compared to 5×10^{-2} Pa for hot strip cathodes, indicate an improvement in the efficiency of the new technologies. This makes it possible to optimise the coating process under vacuum conditions, ensuring the stability and quality of the coating. Studies also show that electron beam installations allow deposition of various protective coatings, including new types of micro-layer silicide coatings, which opens up broad prospects for improving the reliability and service life of gas turbine engines. Thus, the results of research and practical implementation of electron beam installations for applying protective coatings to gas turbine blades indicate their great potential for improving the technical characteristics of these engines, in particular, increasing their efficiency and reliability.

References

1. V.A. Akrymov, I.M. Hrechaniuk, Yu. O. Smashniuk, V.H. Hrechaniuk, M.P. Liubarenko Promyslova Tekhnolohiia Nanesennia Dvosharovykh Plazmovykh Teplozakhysnykh Pokryttiv na Soplovi Lopatky Hazovykh Turbin [Industrial technology of applying two-layer plasma heat-protective coatings on the nozzle blades of gas turbines] (Sovremennaia elektrometallurhyia, (4), 28–31 (2020) (in Ukrainian) https://doi.org/10.37434/sem2020.04.05
2. I.M. Grechanyuk, M.I. Grechanyuk, G.A. Bagliuk, V.G. Grechanyuk, O.V. Khomenko, O.V. Dudnik, V.I. Gots, Powder Metall. Met. Ceram. **61**, 459 (2022). https://doi.org/10.1007/s11106-023-00333-0
3. M.I. Grechanyuk, I.M. Grechanyuk, Y.N.Yevterev, V.G. Grechanyuk, T.O. Prikhna, G.A. Bagliuk, V.I. Gots, O.V. Khomenko, O.V. Dudnik, O.V. Powder Metall. Met. Ceram. **61**, 328 (2022) https://doi.org/10.1007/s11106-022-00320-x
4. T.O. Prikhna, I.M. Grechanyuk, M.V. Karpets, M.I. Grechanyuk, G.A. Bagliuk, V.G. Grechanyuk, O.V. Khomenko, Powder Metall. Met. Ceram. **2022**(61), 230 (2022). https://doi.org/10.1007/s11106-022-00310-z
5. T.O. Prikhna, I.M. Grechanyuk, M.V. Karpets, M.I. Grechanyuk, G.A. Bagliuk, I.M. Grechanyuk, V.A. Chornovol, Powder Metall. Metal Ceramics **61**, 70 (2022). https://doi.org/10.1007/s11106-022-00296-8
6. N.I. Grechanyuk, V.G. Grechanyuk, A.F. Manulyk, J. Mater. Sci. Technol. Res. **8**, 19 (2021). https://doi.org/10.31875/2410-4701.2021.08.3
7. N.I. Grechanyuk, V.G. Grechanyuk, A.F. Manulyk, J. Mater. Sci. Technol. Res. **8**, 24 (2021). https://doi.org/10.31875/2410-4701.2021.08.4
8. N.I. Grecyanyuk, G.A. Baglyuk, P.P. Kucherenko, A.G. Melnik, I.N. Grechanyuk V. G. Grechanyuk, Y.A. Smashnyuk, Laboratory electron-beam multipurpose installation L-2 for

producing alloys, composites, coatings, and powders. Powder Metall. Met. Ceram. **56**(1), 113 (2017)
9. N.I. Grecyanyuk, P.P. Kucherenko, A.G. Melnik, I.N. Grechanyuk, Y.A. Smashnyuk, Industrial electron-beam installation L-4 for melting and vacuum refining of metals and alloys. Powder Metall. Met. Ceram. **55**(7–8): 489 (2016). https://doi.org/10.1007/s11106-016-9831-y

Chapter 26
Preparation and Problem-Solving in Si/SiO_2 Anode Materials for High-Performance Lithium-Ion Batteries

Akbar Avvalboev, Mirtemir Kurbanov, Ilkhom Ashurov, Sardor Tulaganov, Usmon Choriev, and Lyudmila Andriyko

Abstract Despite several challenges, Si/SiO_2-based lithium-ion batteries (LIBs) show potential to replace widely used carbon-based LIBs due to their higher capacity and higher energy density. The high abundance of silicon in the Earth's crust and the possibility of synthesizing SiO_2 nanoparticles from copper slag at low cost and with high energy efficiency enable maintaining a lower production cost for LIBs. By optimizing the concentration of Si/SiO_2/C/PVDF and reducing the average particle size of the materials to 140–160 nm, it was possible to minimize degradation in the anode material. The prepared anode material was studied using SEM and XRD methods, while its electrochemical properties, long-cycle charge–discharge behavior, and voltammetric characteristics were recorded. High economic efficiency was achieved by optimizing experimental conditions and ensuring the substitution and regeneration of reagents used during the process.

26.1 Introduction

Current trends demand the development of new types of energy storage devices and the optimization of existing ones, as the demand for chargeable batteries is growing rapidly. Today, the most widely used rechargeable batteries are lithium-based, and their active materials are built on graphite [1]. In lithium-ion batteries (LIBs), the

A. Avvalboev (✉) · M. Kurbanov · I. Ashurov · S. Tulaganov · U. Choriev
Arifov Institute of Ion-Plasma and Laser Technologies of Academy of Sciences, Tashkent, Uzbekistan
e-mail: avvalboev@iplt.uz

A. Avvalboev
National University of Uzbekistan, Tashkent, Uzbekistan

L. Andriyko
Chuiko Institute of Surface Chemistry of NASU, Kyev, Ukraine

O. Fesenko and L. Yatsenko (eds.), *Functional Nanomaterials, Nanocatalysts, Nanotechnologies, and Their Applications*, Springer Proceedings in Physics 321,
https://doi.org/10.1007/978-3-031-99136-3_26

primary research is conducted on the anode and electrolyte components because carbon-based cathodes can sufficiently accept and release lithium ions during charge and discharge processes [1, 2]. The theoretical capacity of the graphite-based anode in these batteries is 372 mAh/g, and in practice, this capacity has almost been fully utilized [2, 3]. Therefore, new materials are being explored as active components for lithium-ion batteries. Silicon (Si) and its oxides are highly promising for this purpose due to their theoretical capacities: 4200 mAh/g for Si, 2767 mAh/g for SiO, and 1872 mAh/g for SiO_2. These values enable the achievement of higher capacity and energy density for LIBs [4].

Anode materials based on silicon (Si) in LIBs also present several challenges. One of the major issues is volumetric expansion, which has been observed to reach 350–400% for Si and 80–150% for SiO_2 [5]. This rapid expansion accelerates the mechanical degradation of the battery, effectively eliminating the possibility of creating a stable and durable structure [5, 6]. In classical graphite-based LIBs, the electrical conductivity is 10^5 S m^{-1}, allowing a significant reduction in charging time. However, pure Si and SiO_2 exhibit much lower electrical conductivity (see Table 26.1). Therefore, it is necessary to create composite materials by combining them with elements that possess higher electrical conductivity [5].

In comparison, SiO_2 offers moderate improvements in specific capacity (1965 mAh g^{-1}) but still faces challenges with volume expansion (100%) and lower electrical conductivity (< 10^{-1} S m^{-1}) [2, 7]. On the other hand, graphite exhibits superior electrical conductivity (105 S m^{-1}) and minimal volume change (10%), ensuring stable performance and higher initial coulombic efficiency (90–95%) [5]. The findings highlight the need to develop composite materials or structural modifications for Si and SiO_2 to mitigate their drawbacks while leveraging their high energy storage potential [8].

As in typical LIBs, in Si and SiO_2-based systems, irreversible reactions during the initial charge/discharge cycles cause a significant drop in Coulombic efficiency (CE) [9, 10]. During the first few cycles, reactions such as (26.1), (26.2), (26.3), and (26.4) lead to lithium ions being trapped within the structure, preventing their release [10].

$$5SiO_2 + 4Li^+ + 4e^- \rightarrow 2Li_2Si_2O_5 + Si \tag{26.1}$$

Table 26.1 Provides a comparative overview of the main characteristics of silicon (Si), silicon dioxide (SiO_2), and graphite (C) as anode materials for lithium-ion batteries (LIBs) [2, 6]

Anode material	Si	SiO_2	C (graphite)
Volume change (%)	350–400	100	10
Electrical conductivity (S m^{-1})	10^{-1}	< 10^{-1}	10^5
Initial theoretical specific capacity (mAh/g)	4200	1965	372
Typical initial coulombic efficiency (%)	70–85	52.38	90–95

$$3SiO_2 + 4Li^+ + 4e^- \rightarrow 2Li_2SiO_3 + Si \quad (26.2)$$

$$2SiO_2 + 4Li^+ + 4e^- \rightarrow Li_4SiO_4 + Si \quad (26.3)$$

$$SiO_2 + 4Li^+ + 4e^- \rightarrow 2Li_2O + Si \quad (26.4)$$

In general, the reactions involving lithium ions occur in two stages. In the first stage, an active electrochemical phase ($Li_2Si_2O_5$) and inactive electrochemical phases (Li_4SiO_4, Li_2SiO_3, and Li_2O) are formed. In the second stage, newly formed silicon interacts with lithium ions to produce LixSi compounds [9, 11]. Conversely, during the delithiation process, the remaining inactive phases (Li_4SiO_4, Li_2SiO_3, and Li_2O) result in a lower initial Coulombic efficiency (CE) for SiO_2 due to their inability to restore the original charge capacity effectively [6, 12].

Understanding the role of the Solid Electrolyte Interphase (SEI) layer in silicon (Si) and silicon dioxide (SiO_2)-based lithium-ion batteries is crucial [13]. The volumetric expansion of silicon electrodes caused by their reaction with lithium ions significantly affects the stability and quality of the SEI layer. Silicon oxide additives can help manage this process by reducing silicon expansion and improving the SEI layer [8, 13]. The primary function of the SEI layer is to allow lithium-ion transport while preventing electron transfer [14]. This layer ensures the battery operates safely and efficiently. However, the formation of the SEI layer on silicon electrodes can be complex because silicon's expansion and contraction may damage this layer [12, 15]. To enhance SEI layer stability, electrolyte composition is optimized, and nanoscale materials or additives are employed. A stable SEI layer is critical for improving the battery's lifespan and efficiency [16]. Therefore, silicon and silicon oxide materials require modifications and optimizations to ensure the SEI layer's effective performance in lithium-ion batteries [17]. Experiments have shown that several issues encountered in Si and SiO_2-based LIBs, such as SEI stability, volumetric expansion, and low electrical conductivity in the anode, can be addressed by utilizing materials with sizes in the range of 100–200 nm [18–20]. Additionally, using various carbon modifications and polymer-based compounds in the preparation of composite materials for the anode has also demonstrated significant effectiveness in resolving these challenges [21, 22].

26.2 Methods and Materials

The main materials used in this study include copper slags from AMMC, ammonium fluoride (NH_4F, 98.5%) supplied by Guangzhou Yijia Supply Chain Co. Ltd, Super P carbon powder (99%), polyvinylidene fluoride (PVDF), and the organic solvent N-Methylpyrrolidone (NMP, 99.0%).

26.2.1 Synthesis of SiO_2 Nanoparticles

Nano-sized particles obtained from the processing of copper slag from AMMC were used as a source of SiO_2. An analysis of the elemental composition of the copper slag revealed its high SiO_2 content (see Table 26.2).

The fluorination process enables the extraction of SiO_2 particles with controllable dispersion, alongside metal concentrates as the primary product. The procedure involves mixing copper slag with NH_4F in the fluorination reactor and maintaining the mixture at 30–200 °C for approximately two hours. This method offers an efficient route to utilize copper slag for advanced material synthesis (see Fig. 26.1) [23–26].

In the second stage of the reactor, at temperatures between 200 and 400 °C, sublimation of SiO_2 bonded with fluorine is observed, leaving metal concentrates at the bottom. In the desublimator, HFSA (Hexafluoroammonium) ($(NH_4)_2SiF_6$) is formed. Using the sol–gel method, HFSA enables the synthesis of controlled and monodisperse SiO_2 particles. This approach provides an efficient pathway for creating high-quality SiO_2 particles with desired properties. (see Fig. 26.2).

In the second stage of the reactor, temperatures are raised to 200–400 °C, facilitating the sublimation of fluorinated SiO_2 from the metal concentrates. This results in

Table 26.2 Elemental composition of copper slag used as a source of SiO_2

SiO_2	Fe_{total}	Al_2O_3	CaO	Cu	MgO	Zn
29.8–40.0	30.7–41.4	4.2–6.0	1.8–2.6	0.06–0.9	0.5–1.3	0.9–1.2

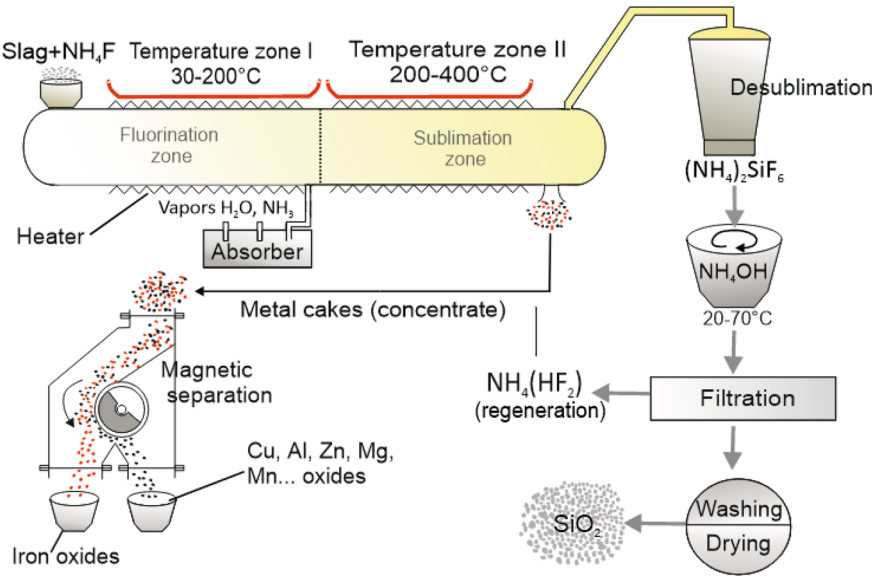

Fig. 26.1 Schematic of the fluorination process for copper slag to synthesize SiO_2 particles

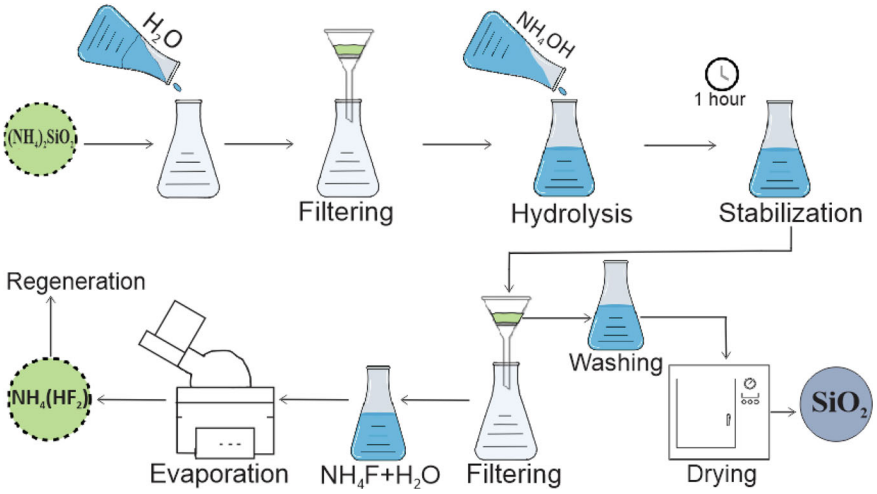

Fig. 26.2 Schematic of the SiO_2 nanoparticles from HFSA using the sol–gel method

the formation of HFSA ($(NH_4)_2SiF_6$) in the desublimator, while metal concentrates remain at the bottom. Using the sol–gel method, HFSA can be further processed to synthesize controlled and monodisperse SiO_2 particles, offering precise material properties for advanced applications. In this technology, (see Figs. 26.1 and 26.2) it is possible to control the dispersity of SiO_2 nanoparticles by influencing several parameters of the hydrolysis process. By adjusting the hydrolysis temperature, ammonia content, pH level, and concentration, the size of the resulting particles can be precisely controlled. Using the developed technology, SiO_2 nanoparticles with an average size of 145 nm were synthesized. One of the main achievements of this technology is that the purity of the produced SiO_2 exceeds 99.97%, while also being cost-effective and employing an environmentally friendly process.

26.2.2 Preparation of Si

Silicon is the second most abundant element in nature, making up 27.6% of the Earth's crust by mass. This provides a cheap and abundant raw material source for LIBs. However, in preparing composite materials for anodes, crystalline silicon cannot be directly used. Its size must be reduced to 150 nm. For this purpose, it was ground in a ball mill for 22 h. Structural analysis revealed that the resulting particle sizes were close to the desired dimensions.

Metallurgical-grade silicon (Si) can be produced through high-temperature carbothermal reduction of silicon dioxide (SiO_2), which is obtained from copper slag. However, due to the fine powder nature of SiO_2 from copper slag—characterized by low gas permeability and a tendency to carry over small particles—it is unsuitable

for direct smelting in an electric arc furnace. To address this issue, the material is converted into briquettes using a binder. Sodium liquid glass with the formula $Na_2O(SiO_2)n$ and a density of 1.34 g/cm^3 is used as the binder. A 2.5% aqueous solution of liquid glass at the specified density effectively produces briquettes with sufficient mechanical strength.

26.2.3 The Method for Preparing SiO_2/C and Si/C Nanocomposites

The nanocomposite serving as the active anode material was synthesized using SiO_2 or Si, Super P (pure carbon), and polyvinylidene fluoride (PVDF) in specific weight ratios: 30–70% SiO_2 or Si, 20–60% Super P, and 10% PVDF across all samples. NMP was used as the solvent. The mixture was stirred at 1500 rpm for 12 h at room temperature with a magnetic stirrer, applied to a copper foil, and then dried under vacuum at 80 °C for 12 h to ensure NMP evaporation.

26.2.4 Electrochemical Measurements

Electrochemical measurements were carried out using a coin cell (CR2032) assembled in an argon-filled glovebox, with the oxygen content maintained at 40–45 ppm. (see Fig. 26.3) The working LIB cell consisted of a lithium iron phosphate ($LiFePO_4$) cathode with a diameter of 15 mm, a single-layer microporous polypropylene film (Celgard 2400) with a diameter of 20 mm as the separator, and an active anode material made from a silicon-carbon mixture applied onto copper foil and cut into 15 mm diameter discs. The total mass of the active anode material was 3 mg.

The electrolyte used was 1 mol L^{-1} $LiPF_6$ dissolved in a mixture of ethylene carbonate (EC) and diethyl carbonate (DEC) in a 1:1 weight ratio. The electrochemical properties of the obtained materials were evaluated using cyclic voltammetry and

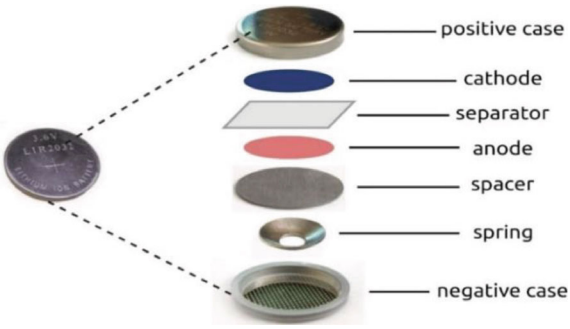

Fig. 26.3 Diagram of the assembly of a lithium-ion cell

galvanostatic charge/discharge methods. Galvanostatic charge/discharge tests were conducted at room temperature (25 °C) within a potential range of 0–4.2 V and a current range of 8–10 mA, using a Neware BTS4000 multichannel battery testing system.

26.3 Results and Discussion

26.3.1 Materials' Physical and Chemical Characteristics

The elemental composition and purity of the prepared Si and SiO_2 for composite material production were analyzed. The SiO_2 nanoparticles synthesized using the sol–gel method were found to have high purity, as confirmed by mass spectrometry (ICP MS 7700). The elemental composition of SiO_2 was recorded to be above 99.97%. The trace amounts of metal elements in the material did not negatively affect the properties of the anode material. On the contrary, a slight improvement in electrical conductivity was observed due to their presence. (see Table 26.3).

It is known that pure Si and SiO_2 have very poor electrical conductivity. Therefore, carbon (C) was added in varying proportions during the preparation of the composite material, with optimal concentrations being carefully selected. Higher proportions of carbon led to a decrease in capacity, necessitating the selection of alternative proportions. The electrical conductivity of the composite material was studied using the four-point probe method. (see Table 26.4) These conductivity values were found to be the most optimal, and experiments confirmed their suitability for achieving the best charge–discharge cycle speeds and charge density values.

The particle size of SiO_2 used in the fabrication of the anode material was studied using NANOSIGHT, revealing an average size of approximately 140–145 nm. The dispersion of particles can be controlled by influencing the hydrolysis process through

Table 26.3 Purity of SiO_2 nanoparticles synthesized using the sol–gel method

Elements	SiO_2	Fe	Al	K	Ca	Cu	Zn	Mg
Composition (%)	99.97	0.014	0.006	0.003	0.002	0.001	0.001	0.001

Table 26.4 Electrical resistivity and electrical conductivity of the anode material measured using the four-probe method

	Electrical resistivity, Ω·m	Electrical conductivity, 1/Ω·m
Si/PVDF/C-50/10/40	0.01382	72.35
SiO_2/PVDF/C-50/40/10	0.04319	20.35
Si/PVDF/C-70/10/20	0.01925	51.94
SiO_2/PVDF/C-70/40/20	0.02986	33.49

factors such as temperature, pH, concentration, and the level of ammonia. A correlation was observed in the results (see Fig. 26.4). The particles also exhibited high dispersity, which was controlled as described in process 2.1.

Figure 26.5 presents the X-ray diffraction (XRD) patterns of SiO_2 nanoparticles (see Fig. 26.6a) and the SiO_2/C composite material with a 50:50 SiO_2-to-carbon ratio (see Fig. 26.6b). In Fig. 26.10a, the broad diffraction peak observed between 20° and 25° confirms the amorphous nature of the SiO_2 nanoparticles.

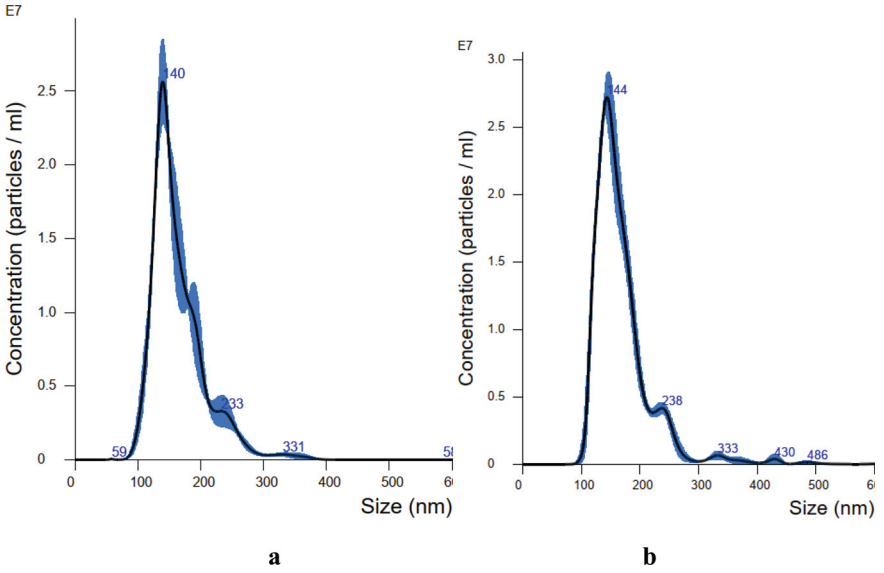

Fig. 26.4 The size of SiO_2 particles synthesized using the sol–gel method. Particles hydrolyzed under 10% ammonia conditions (**a**) and particles hydrolyzed under 20% ammonia conditions (**b**)

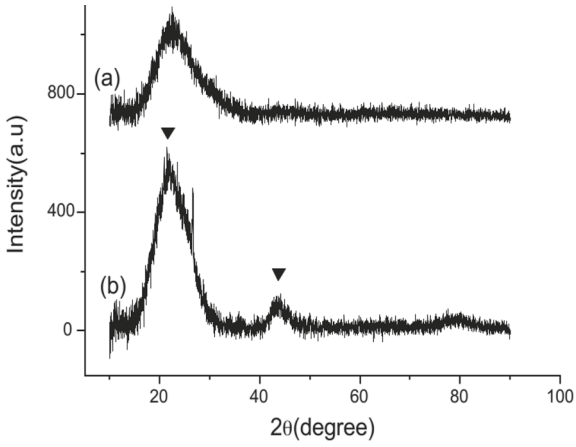

Fig. 26.5 X-ray diffraction patterns of SiO_2 nanoparticles (**a**) and SiO_2 nanoparticles with carbon coating at $SiO_2 = 50{:}50\%$ ratio (**b**)

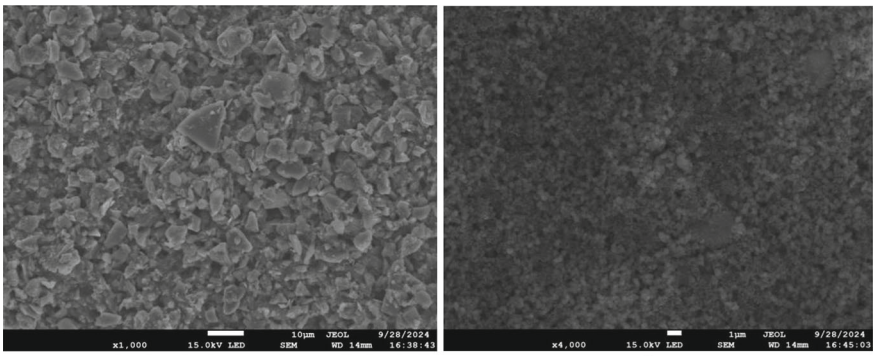

a b

Fig. 26.6 The SEM image of the anode material based on Si/PVDF/C with a ratio of 70/10/20 (**a**) and the SEM image of the anode material based on SiO_2/PVDF/C with the same ratio (**b**)

In Fig. 26.5b**,** the broad peaks around 22° and 43° correspond to the amorphous structure of the carbon layer coated on the SiO_2 nanoparticles. Notably, no peaks corresponding to silicon are detected, indicating that SiO_2 has not been reduced to elemental silicon. This is attributed to the fact that the reduction of SiO_2 to silicon using carbon requires extremely high temperatures, exceeding 1500 °C.

26.3.2 SEM

The SEM images of composite materials prepared with Si/PVDF/C and SiO_2/PVDF/C in proportions of 70/10/20, respectively, were analyzed (see Fig. 26.6). Upon examining the structure of the composite material made of Si, it was observed that strong bonds were not formed with C and PVDF. However, this did not significantly impact the electrochemical parameters of the structure. This phenomenon can be explained by the defects introduced during the grinding process of Si (see Fig. 26.7). From the SEM images of Si, it is also evident that the monodispersity index of Si particles is low. On the other hand, the SiO_2 particles exhibit uniformity in shape and dispersity, closely aligning with the dimensions of the materials used. As a result, they introduce fewer defects into the anode structure (see Fig. 26.6).

26.3.3 Charging and Discharging Process

Several experiments were conducted to determine the optimal proportions of Si and SiO_2 for fabricating the anode material. Increasing the proportion of Si and SiO_2 in the structure enhances the capacity but reduces electrical conductivity. Conversely, increasing the amount of C and PVDF improves electrical conductivity but decreases

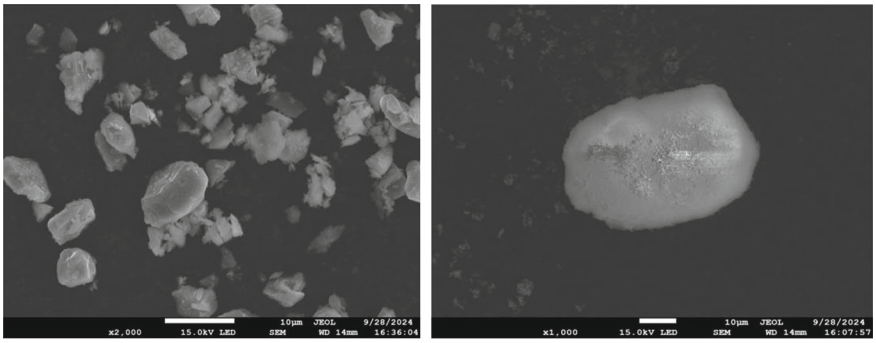

Fig. 26.7 The SEM images of Si (**a**) and SiO_2 (**b**) used for preparing the anode material

the capacity. Therefore, anode materials with Si and SiO_2 proportions ranging from 30 to 70% were fabricated, and their electrical capacity was studied (see Fig. 26.8).

The composite material consisting of Si/PVDF/C in a ratio of 70/10/20 was confirmed as an optimal choice based on its balance of electrical conductivity and capacity. Long-term cycling tests demonstrated the material's capacity retention under extended usage conditions, as shown in the provided graph.

The provided data illustrates the charge and discharge capacities of the Si based anode material over multiple cycles. (see Fig. 26.9) Initially, the material demonstrates a high specific capacity, with a charge capacity of 2382.6 mAh/g and a discharge capacity of 3302.3 mAh/g during the first cycle. This high initial capacity is typical for new materials due to lithium ions being absorbed into the structural layers, leading to irreversible capacity losses. As the cycling progresses, both charge and discharge capacities gradually decline. By the 10th cycle, the charge capacity decreases to 1256.8 mAh/g, and the discharge capacity falls to 1273.7 mAh/g. This

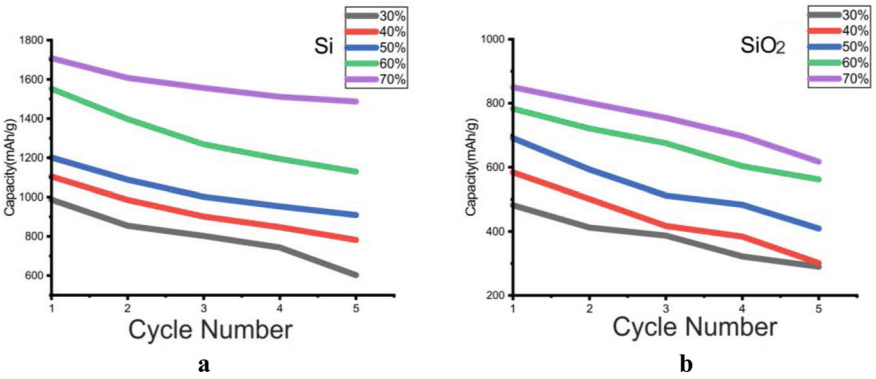

Fig. 26.8 The capacity of the anode material made with 30–70% Si (**a**) and SiO_2 (**b**) combined with C and PVDF

trend continues, with capacities reducing to 794.5 mAh/g (charge) and 825.3 mAh/g (discharge) by the 54th cycle. This capacity fading can be attributed to factors such as mechanical or electrochemical degradation of the material, particle cracking, electrolyte decomposition, or the formation of a solid electrolyte interphase (SEI) layer. From around the 15th cycle, the rate of capacity decline slows, indicating that the material enters a more stable phase. However, the gradual capacity loss over extended cycling suggests that the long-term performance of the material is still affected. The total capacity retention from the 1st to the 54th cycle is approximately 66.6%, highlighting significant degradation. Despite this, the difference between charge and discharge capacities narrows in later cycles, reflecting an improvement in Coulombic efficiency and better energy utilization.

Figure 26.10a illustrates the cyclic voltammetry (CV) behavior of the SiO_2-based anode material (60% SiO_2) over the first two charge/discharge cycles. In the initial cycle, the solid line shows prominent current peaks, which are attributed to the initial lithium-ion intercalation and the formation of the solid electrolyte interphase (SEI) layer. The low-voltage peak (0–0.5 V) corresponds to lithium insertion into the SiO_2 structure, accompanied by some irreversible capacity loss—a characteristic common to silicon-based anodes. During the second cycle, represented by the dashed line, the current peaks are reduced, indicating SEI stabilization and improved reversibility of lithium intercalation. The consistent shape between the first and second cycles reflects the material's ability to maintain its structural integrity and electrochemical performance after SEI formation. This behavior aligns with findings that highlight

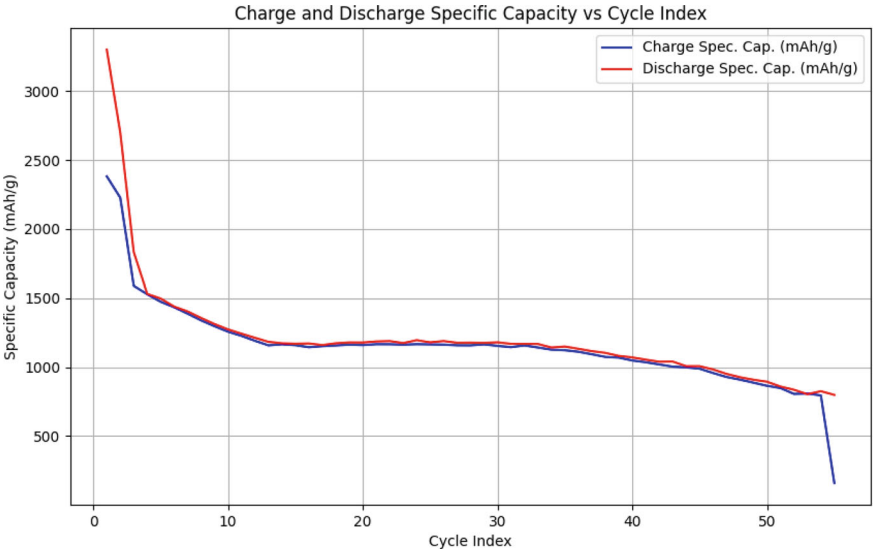

Fig. 26.9 The charge–discharge process of the LIB anode material fabricated with Si/C/PVDF in 70/20/10 ratio at the 50th cycle demonstrates the material's electrochemical performance

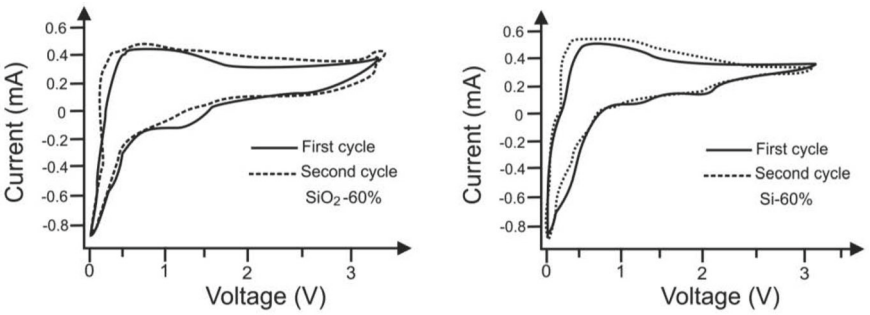

Fig. 26.10 Cyclic voltammetry (CV) of the SiO_2-60% (**a**) and Si-60% (**b**) anode materials for the first two charge–discharge cycles

the stable cycling performance of SiO_2-based anodes, confirming their potential for enhanced capacity retention in lithium-ion batteries.

Figure 26.10b depicts the CV curves for the Si-based anode material containing 60% silicon (Si-60%) over two consecutive cycles. During the first cycle, a sharp current increase near 0.2 V marks the lithiation process, with a distinct peak between 0.1 V and 0.3 V associated with lithium intercalation and SEI formation, leading to some capacity loss. As the voltage increases, the current decreases, signaling the completion of lithiation. During delithiation, partial reversibility of the redox reactions is observed.

In the second cycle, the reduction peak decreases, indicating additional capacity loss due to SEI stabilization and structural changes. However, the overall curve retains a similar shape, suggesting that the material stabilizes after the initial changes. A slight shift in peak positions suggests further structural modifications that contribute to reduced lithiation capacity in subsequent cycles. These CV results show that while SEI formation plays a dominant role during the first cycle, the material demonstrates good redox reversibility and stabilizes after the initial capacity loss, offering valuable insights into the cycling stability and capacity retention of the Si-60% anode.

26.4 Conclusions

This study focused on the controllable synthesis of SiO_2 dispersions and their application as anode materials for lithium-ion batteries (LIBs). The optimization of reagent proportions and their impact on the quality of the anode material were carefully investigated. The primary causes of degradation, including volumetric changes and the breakdown of interfacial bonds, were analyzed, and strategies to mitigate these issues were identified. SEM images revealed that the particle sizes of residual reagents during the grinding of Si were closely uniform, which significantly contributed to the improvement of electrode material quality. In the synthesized SiO_2, the formation of

bonds involving C and PVDF was observed, enhancing the electrical conductivity of the anode material.

Additionally, the capacity retention after 50 cycles remained high, demonstrating the stability of the material. The use of inexpensive and readily available sources for the synthesis reagents further supports the feasibility of scaling this method for industrial applications. These findings open new opportunities for the production of high-performance anode materials for LIBs.

References

1. C. Li, Z. Hu, H. Guo, J. Li, SiO_2/C composites with tunable core-shell structures as anode materials for lithium-ion batteries. J. Power. Sources **204**, 67–72 (2012). https://doi.org/10.1016/j.jpowsour.2012.01.051
2. K. Xu, Electrolytes and interphases in Li-ion batteries and beyond. Chem. Rev. **114**(23), 11503–11618 (2014). https://doi.org/10.1021/cr500003w
3. W. Zhang, M. Gong, H. Niu, X. Wang, SiO_2/C composites derived from rice husks as anode materials for lithium-ion batteries. Mater. Lett. **164**, 605–608 (2016). https://doi.org/10.1016/j.matlet.2015.11.099
4. J.M. Tarascon, M. Armand, Issues and challenges facing rechargeable lithium batteries. Nature **414**(6861), 359–367 (2001). https://doi.org/10.1038/35104644
5. B. Scrosati, J. Garche, Lithium batteries: status, prospects, and future. J. Power. Sources **195**(9), 2419–2430 (2010). https://doi.org/10.1016/j.jpowsour.2009.11.048
6. M. Yoshio, H. Wang, K. Fukuda, Influence of carbon coating on the electrochemical performance of SiO anodes for lithium-ion batteries. Solid State Ionics **152–153**, 373–379 (2002). https://doi.org/10.1016/S0167-2738(02)00318-3
7. S. Wang, M. Li, P. Xu, Z. Zhang, J. Xiao, J. Meng, Preparation of nanosilicon from SiO_2 and its application as anode material for lithium-ion batteries. Electrochim. Acta **215**, 594–600 (2016). https://doi.org/10.1016/j.electacta.2016.08.110
8. Z. Chen, M. Gao, Y. Wang, Recent progress on silicon-based anode materials for next-generation lithium-ion batteries. Nano Energy **41**, 110–120 (2017). https://doi.org/10.1016/j.nanoen.2017.09.047
9. N. Akram et al., Comprehensive modeling of charge transport in LIB electrodes. Chem. Phys. **540**, Article 110974 (2021). https://doi.org/10.1016/j.chemphys.2020.110974
10. K. Ashurov, K. Akhunov, H. Ashurov, G. Wang, P. Wang, M. Ji, Kurbanov, Appl. Solar Energy **60**(1), 90–126 (2024). https://doi.org/10.3103/S0003701X23601801
11. X. Liu et al., Hazards in LIB electrode materials and recycling approaches. J. Hazard. Mater. **373**, 397–412 (2019). https://doi.org/10.1016/j.jhazmat.2019.03.103
12. V. Kumar, G. Singh, S. Kumar Dwivedi, Geomicrobiological insights on LIB material recovery. Geomicrobiol. J. **39**(3–5), 186–200 (2022). https://doi.org/10.1080/01490451.2021.1956648
13. J.B. Goodenough, K.S. Park, The Li-ion rechargeable battery: a perspective. J. Am. Chem. Soc. **135**(4), 1167–1176 (2013). https://doi.org/10.1021/ja3091438
14. X. Zhou, S. Cui, H. Li, X. Qu, Advances in solid electrolytes for lithium-ion batteries. Chem. Rev. **121**(23), 15115–15144 (2021). https://doi.org/10.1021/acs.chemrev.1c00209
15. H. Wu, Y. Cui, M.T. McDowell, Nanostructured materials for silicon-based lithium-ion battery anodes. Energy Environ. Sci. **7**(5), 1436–1450 (2014). https://doi.org/10.1039/C3EE43182G
16. C.F. Lux et al., The mechanism of SEI formation on graphite in organic electrolytes. Electrochim. Acta **220**, 337–349 (2016). https://doi.org/10.1016/j.electacta.2016.10.102
17. Manthiram, A reflection on lithium-ion battery cathode chemistry. Nat. Commun. **11**, article 1550 (2020). https://doi.org/10.1038/s41467-020-15355-0

18. Y. Idota et al., Tin-based amorphous oxide: a high-capacity lithium-ion storage material. Science **276**(5317), 1395–1397 (1997). https://doi.org/10.1126/science.276.5317.1395
19. P. Simon, Y. Gogotsi, B. Dunn, Where do batteries end and supercapacitors begin? Science **343**(6176), 1210–1211 (2014). https://doi.org/10.1126/science.1249625
20. M. Kurbanov, A. Avvalboev, I. Ashurov, U. Choriev, Kh. Ashurov, P. Ji, Utilizing copper waste to develop silicon-carbon anode materials for lithium-ion batteries. Uzb. Phys. J. https://doi.org/10.52304/.v26i3.538
21. K.T. Lee et al., Metal–air batteries with high energy density: Li–air versus Zn–air. Energy Environ. Sci. **4**(9), 3371–3380 (2011). https://doi.org/10.1039/C1EE01598F
22. M. Armand, J.M. Tarascon, Building better batteries. Nature **451**(7179), 652–657 (2008). https://doi.org/10.1038/451652a
23. M. Kurbanov, L. Andriyko, J. Panjiev, S. Tulaganov, V. Gun'ko, A. Marynin, S. Pikus, Resource-saving synthesis of nanoscaled silicon dioxide and its textural characteristics. J. Nanopart. Res. **25**, 202 (2023). https://doi.org/10.1007/s11051-023-05852-w
24. M. Kurbanov, S. Tulaganov, M. Ernazarov, L. Andriyko, A. Marinin, A. Shevchenko. Amorphous silica properties, synthesized from slags of the copper-smelting production. J. Nano Electron. Phys. **13**(6), 06024(6pp) (2021). https://doi.org/10.21272/jnep.13(6).06024
25. M. Kurbanov, S. Tulaganov, U. Nuraliev, L. Andriyko, O. Goncharuk, N. Guzenko, Y. Nychyporuk, A. Marynin. Comparative characteristics of the structure and physicochemical properties of silica synthesized by pyrogenic and fluoride methods. Silicon, 1221–1233 (2023). https://doi.org/10.1007/s12633-022-02087-7
26. L. Andriyko, M. Kurbanov, I. Siora, I. Petrika, A. Marynin, S. Tulaganov, The influence of the aqueous media acidity on the electrokinetic potential, aggregation and adsorption properties of silica nanoparticles synthesized from metallurgical wastes. J. Mol. Liq. **392** (2023). https://doi.org/10.1016/j.molliq.2023.123513
27. H. Duan et al., Graphene-coated silicon as high-performance anodes for lithium-ion batteries. Nat. Nanotechnol. **14**, 179–185 (2019). https://doi.org/10.1038/s41565-018-0346-7

Chapter 27
Influence of Preliminary Thermal Oxidation and Gas Nitriding on Phase Composition and Thickness of Oxide-Ceramic Coatings on VT1-0 Alloy

Iryna Pohrelyuk, Volodymyr Posuvailo, Ihor Koval'chuck, Iryna Ivasenko, and Roman Iurkevych

Abstract The influence of preliminary oxidation and gas nitriding of titanium alloy on the process of plasma electrolytic synthesis of oxide-ceramic coatings was investigated. PEO was carried out in the electrolyte KOH (5 g/l), Na_2SiO_3 (5 g/l). The phase composition, thickness and porosity of the obtained oxide-ceramic coatings were determined. It was shown that after preliminary oxidation the number of pores increases more than 2 times compared to the gas nitriding alloy. Preliminary gas nitriding leads to the formation of plasma discharges of a significantly larger pore size of 1.66 e−12 m^2 compared to 7.74 e−13 m^2 for the preliminary oxidized alloy. This indicates a significantly higher power of plasma discharges that arise on titanium nitride. These results correlate with the phase composition and thickness of oxide-ceramic coatings. Based on the analysis of X-ray diffraction patterns, it was established that the main phases in the surface layers are titanium oxides: rutile, brookite and anatase. Titanium nitride contributes to the formation of a significantly larger amount of high-temperature titanium oxides rutile and brookite in the PEO process.

I. Pohrelyuk · V. Posuvailo (✉) · I. Koval'chuck · I. Ivasenko
Karpenko Physico-Mechanical Institute of the NASU, Lviv, Ukraine
e-mail: posuvaylo@ipm.lviv.ua

I. Ivasenko
Lviv Polytechnic National University, Lviv, Ukraine

R. Iurkevych
Hetman Petro Sahaidachnyi National Army Academy, Lviv, Ukraine

O. Fesenko and L. Yatsenko (eds.), *Functional Nanomaterials, Nanocatalysts, Nanotechnologies, and Their Applications*, Springer Proceedings in Physics 321,
https://doi.org/10.1007/978-3-031-99136-3_27

27.1 Introduction

One of the key tasks of modern science and technology is the development of new technologies for applying highly effective and reliable coatings to metals and alloys, which provide protection and strengthening of metal products, increasing their operational properties.

Many methods are known for improving the operational characteristics of metals and alloys, such as anodizing, mechanical pulse treatment, vacuum spraying, plasma electrolytic oxidation (PEO), chemical-thermal treatment [1–9] and others. These technologies allow not only to influence the wear resistance of alloys, but also their surface layers, which opens up opportunities for creating materials with new, improved properties, in particular, with increased corrosion resistance, strength and biocompatibility. Thanks to the use of such methods, it is possible to form coatings with different microstructures, which in turn significantly affect their physicochemical and mechanical characteristics. For example, coatings obtained by vacuum deposition, anodizing, or PEO can have an amorphous, nanocrystalline, or crystalline structure, which provides high hardness and wear resistance, as well as improves their ability to be used in electronics and medical applications.

These surface treatment methods are actively used to form coatings on titanium alloys. Since titanium alloys have unique physicochemical properties—low density, high melting point, low thermal conductivity. But along with this, they have low wear resistance and cannot be used in friction units without additional surface treatment. To increase the wear resistance and strength of titanium parts, they are subjected to preliminary thermal chemical treatment (TCT), which allows diffusion saturating and strengthening the treated surface. Nitrogen is mainly used for TCT of titanium alloys. The increased temperature creates conditions for better diffusion of nitrogen into the crystal lattice of the titanium matrix, which has a positive effect on the formation of strengthened nitride layers.

Titanium nitrides have a low coefficient of thermal expansion and a low level of residual stresses. This minimizes the risk of cracking or destruction of the surface layer of the material.

However, the nitriding process has certain difficulties. In particular, the diffusion of nitrogen atoms into the crystal lattice of α- and β-modifications of titanium is slower than that of oxygen atoms. Therefore, to form a thicker diffusion layer, the nitriding process is carried out at higher temperatures and longer exposure in a nitrogen atmosphere. This promotes the growth of nitride crystallites in the titanium matrix, which leads to an increase in the strength of nitrided parts [10, 11].

The priority direction of materials science for coatings on titanium alloys is both the search for ways to intensify process to ensure the formation of high-quality hardened layers, preserving the mechanical properties of the base material, and the development of new coatings with bioactive and semiconductor properties for medical and electronic applications.

One of the promising methods for processing titanium alloys is PEO. This technology allows to create multifunctional oxide-ceramic coatings on valve metals,

such as aluminum, magnesium, titanium, zirconium and tantalum. The advantages of using the PEO method for titanium alloys are that titanium oxides have unique properties and are used as semiconductors and LEDs. Titanium oxides are also widely used in electronics, acting as catalysts for chemical reactions [12, 13]. Due to their high corrosion resistance and biocompatibility, titanium-based coatings formed by the PEO method are used as implants in medicine [14–16].

The aim of the work is to study the processes of forming oxide-ceramic layers with specified properties on titanium alloys. For this purpose, it is necessary to study in detail the influence of various pre-treatment methods on the properties and formation mechanism of coatings obtained by the PEO method. This will not only improve the surface treatment technologies of titanium alloys, but also ensure their wider application in industries such as aviation, shipbuilding, biomedicine, and electronics.

27.2 Methods and Materials

Preliminary oxidation of titanium alloy VT 1-0 (Ti—99.7; Fe—0.2; Si—0.1) was carried out in air at a temperature of 650 °C for 1 h. Gas nitriding was carried out according to the standard method [3]. The synthesis of PEO coatings was carried out in an electrolyte (KOH (5 g/l), Na_2SiO_3 (5 g/l)) with a holding time of 5 min [17]. The elemental composition of the obtained coatings was studied by scanning electron X-ray microscopy on a microscope (Zeiss EVO-40XVP). X-ray structural phase analysis of plasma electrolytic coatings was carried out on a DRON-3.0 X-ray diffractometer using CuKα radiation. The crystallographic parameters of all phases present in the coatings were refined by the full profile Rietveld method using the FuLLProf program [18]. The thickness of the coatings was determined on transverse sections of oxidized samples using a LOMO METAM RV-21 optical microscope. Their porosity was investigated by analyzing micrographs of PEO coatings obtained on a Zeiss EVO-40XVP scanning electron microscope with a magnification of × 1000 according to the method [19].

27.3 Results and Discussions

The work investigated the influence of preliminary oxidation and gas nitriding on the phase composition and structure of oxide-ceramic coatings based on titanium alloy VT1-0. Also, the phase composition of the surface layers, the crystal structure of the formed compounds and the distribution of elements in the oxide layers were determined by X-ray structural analysis and scanning electron microscopy.

Figure 27.1 shows micrographs of the surface of titanium alloy VT1-0 after oxidation (a) and gas nitriding (b).

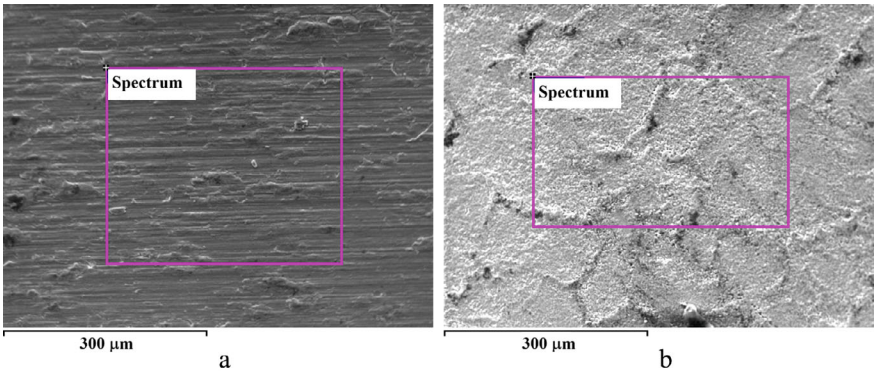

Fig. 27.1 Micrograph of the surface of titanium alloy VT 1-0 preliminary oxidation (**a**) and gas nitriding (**b**)

By the method of plasma electrolytic oxidation for 2 h, it was possible to synthesize quite porous oxide layers. It was established that on the pre-oxidized titanium alloy VT 1-0 within 5 min of synthesis, an oxide-ceramic coating with a thickness of 15–20 μm is formed, and on the nitrided one, under the same conditions, 30–40 μm.

Figure 27.2 shows micrographs of the surface of oxide-ceramic coatings synthesized on the titanium alloy VT 1-0 after preliminary oxidation (a) and gas nitriding (b).

The porosity of the obtained coatings was investigated by the method of segmentation of surface micrographs. To solve such problems, both classical segmentation methods and machine learning methods are actively used [20–28].

Image segmentation was performed by determining the threshold value of the image intensity function. The thresholding operation consists in comparing the value of the intensity function of each pixel of the image with a given threshold value. Selecting the appropriate value allows you to select a certain type of area in the image.

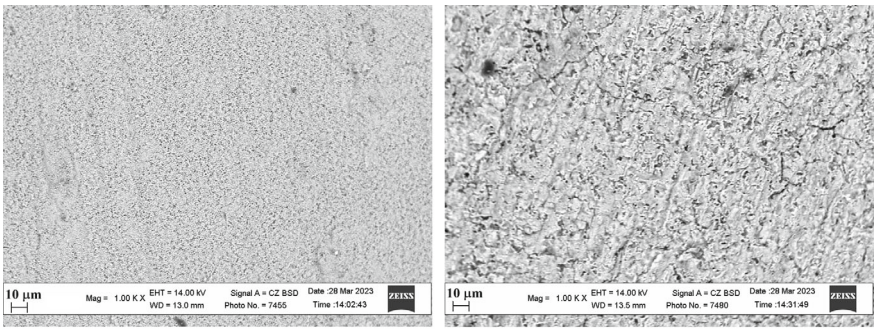

Fig. 27.2 Surface micrographs of oxide-ceramic coatings synthesized on titanium alloy VT 1-0 after preliminary oxidation (**a**) and gas nitriding (**b**)

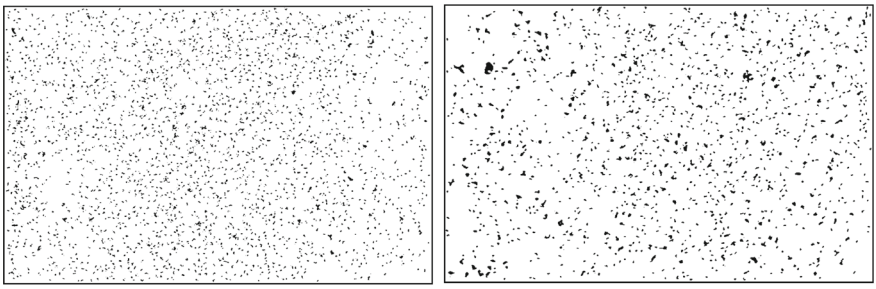

a b

Fig. 27.3 Results of surface segmentation of oxide-ceramic coatings on titanium alloy VT 1-0 after preliminary oxidation (**a**) and gas nitriding (**b**)

In the binarization process, the initial halftone image, which has 256 Gy levels, is converted to black and white, where the background pixels have the value 1, and the pore pixels have the value 0 (see Fig. 27.3). In the case of a noisy background, a filtering procedure or retinex transformation can be applied before segmentation to smooth the background [29, 30].

After the segmentation procedure, the total number of defects N is determined; the defect area S_{def}; the ratio of the number of defects to the total area N/S_{sur}; the ratio of the defect area to the total area S_{def}/S_{sur}; the minimum defect size S_{min}; the maximum defect size S_{max}; the average defect size S_{avg}. The surface area is $S_{sur} =$ 4.680332e−08 m^2. The defect parameters are given in Table 27.1.

Figure 27.3 shows the corresponding segmented images of the surface of oxide-ceramic coatings.

It was found that after preliminary oxidation, the number of pores increases more than 2 times, but the total area of pores (isolated by the object segmentation method) is almost the same. Preliminary gas nitriding leads to the formation of a significantly larger size of plasma discharge pores. This is explained by the fact that preliminary gas nitriding promotes the formation of more powerful spark discharges, which correlates well with the results of the study of transverse sections of oxide-ceramic coatings.

Table 27.1 Results of surface segmentation of oxide ceramic coatings

Parameters	VT 1-0-pre-oxidation	VT 1-0-TiN
N	2913	1361
S_{def}	2.256094e−09 m^2	2.269460e−09 m^2
N/S_{sur}	6.223917e+10 1/m^2	2.907913e+10 1/m^2
S_{def}/S_{sur}	0.04820372	0.04848929
S_{min}	6.925208e−14 m^2	6.925208e−14 m^2
S_{max}	5.609418e−12 m^2	2.894737e−11 m^2
S_{mean}	7.74225869e−13 m^2	1.66627007e−12 m^2

By the method of full-profile Rietveld analysis of X-ray diffractograms, it was possible to determine the phase composition and crystal structure of compounds in the surface PEO layers [18, 31].

Figure 27.4 shows X-ray diffractograms of oxide-ceramic coatings after 5 min of PEO treatment of titanium alloy VT 1-0 with preliminary oxidation (a) and nitriding (b).

Tables 27.2 and 27.3 show the crystallographic parameters and contents for each of the phases present in the X-ray diffraction patterns determined using the full-profile Rietveld method.

Based on the analysis of X-ray diffraction patterns, it was established that the main phases in the surface layers are titanium oxides: rutile, brookite and anatase. In particular, the determined lattice parameters and the ratio of these phases allow us to draw conclusions about the mechanical and physical properties of the studied samples and analyze the processes of formation of oxide-ceramic coatings.

It was established that the pre-oxidized VT 1-0 diffractogram has intense α-Ti reflexes. This correlates with the small thickness of the oxide-ceramic coating (~ 15 μm) through which X-rays penetrate to the base metal. The coating itself mainly consists of brookite and approximately the same amount of anatase and rutile. Anatase is stable at temperatures up to 600 °C and at elevated temperatures

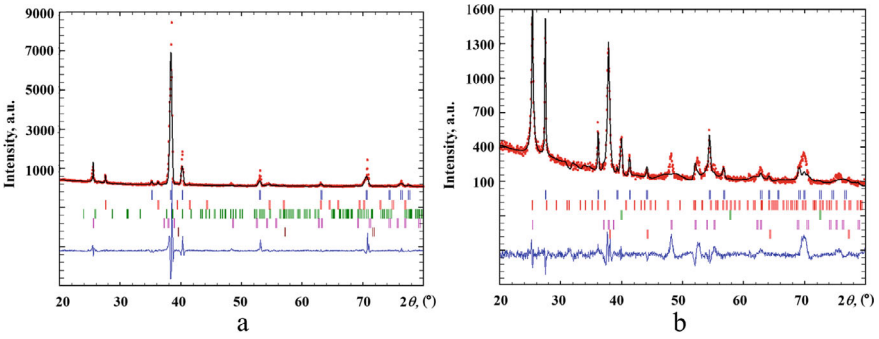

Fig. 27.4 X-ray diffraction patterns of oxide-ceramic coatings on titanium alloy VT 1-0 with preliminary oxidation (**a**) and gas nitriding (**b**)

Table 27.2 Phase composition and crystallographic parameters of the oxide-ceramic coating obtained on pre-oxidized titanium alloy VT 1-0

Phase content	a, Å	b, Å	c, Å	SG	%
α-Ti	2.9461(6)	2.9461(6)	4.6960(6)	P63/mmc	74.34
TiO_2 (rutile)	4.5726(6)	4.5726(6)	2.9489(5)	P 4_2/mmn	5.39
TiO_2 (brookite)	8.9669(2)	7.4353(5)	4.3377(9)	P c a b	11.94
TiO_2 (anatase)	3.7492(6)	3.7492(6)	9.4917(5)	I 4_1/amd	8.10
α′-Ti	3.2313(8)	3.2313(8)	3.2313(8)	Im3m	0.22

Table 27.3 Phase composition and crystallographic parameters of the oxide-ceramic coating obtained on gas nitriding titanium alloy VT 1-0

Phase content	a, Å	b, Å	c, Å	SG	%
TiO_2 (rutile)	4.5898(7)	4.5898(7)	2.9578(8)	P 4_2/mmn	29.78
TiO_2 (brookite)	6.1098(1)	6.4471(3)	5.7662(4)	P c a b	7.85
α′-Ti	3.1932(1)	3.1932(1)	3.1932(1)	Im3m	5.18
TiO_2 (anatase)	3.7802(4)	3.7802(4)	9.5119(1)	I 4_1/amd	56.70
β-Ti	4.0987(5)	4.0987(5)	4.0987(5)	Fm3m	0.49

transforms into rutile. The fact of detecting brookite in oxide-ceramic coatings is interesting, since brookite occurs at temperatures above 800 °C and high pressures, which can occur in oxide-ceramic coatings due to an increase in the volume of titanium oxide.

PEO coating on gas nitriding titanium consists of anatase, rutile and a small amount of brookite and α′-Ti and traces of β-Ti. Due to the significant thickness of the coating (30–40 μm), α-Ti reflexes are not observed in the diffractogram.

Rutile (SG P 42/mmn) is the most stable high-temperature phase of TiO_2.

Anatase (SG I 41/amd) is a low-temperature modification of TiO2, which is thermodynamically stable up to 600 °C and at higher temperatures gradually transforms into rutile.

Brookite (SG P c a b)—is formed at temperatures above 800 °C under high pressure conditions. In our samples, its presence can be explained by the influence of significant mechanical stresses and an increase in the volume of titanium oxide during the formation of the coating, which creates conditions for the stabilization of this phase.

The phase composition of the oxide ceramic coating formed on gas nitriding titanium is somewhat different from that of the pre-oxidized samples. The main three phases are: anatase; rutile and a small amount of brookite. In addition, impurity phases α′-Ti and β-Ti were detected. This is explained by the fact that various modifications of titanium are formed during pre-nitriding. Due to the formation of a thicker oxide ceramic coating on TCTed titanium (30–40 μm), the reflections from the main α-phase of titanium in the diffractogram are no longer present.

27.4 Conclusions

The influence of preliminary oxidation and gas nitriding on the phase composition and structure of oxide-ceramic coatings based on titanium alloy VT1-0 is analyzed. The phase composition of the surface layers, the crystal structure of the formed compounds and the distribution of elements in the oxide layers were determined by X-ray structural analysis and scanning electron microscopy methods.

The results obtained confirm that the ratio of the rutile, anatase and brookite phases significantly affects the properties of the surface layers of oxide-ceramic coatings based on titanium alloys. In particular, the presence of brookite affects the temperature and mechanical properties of the coating formation.

It was established that preliminary oxidation leads to a uniform distribution of small pores over the entire surface. Gas nitriding, in turn, leads to a much smaller number of pores, but their significantly larger size and the formation of a network of microcracks around them. Preliminary gas nitriding contributes to a significant increase in the growth rate of the oxide-ceramic coating (6–8 μm/min) compared to the thermally oxidized surface (3–4 μm/min). This is due to the higher power of plasma discharges, which correlates with the pore area. Compliance with these synthesis conditions allows the formation of oxide-ceramic coatings with a given phase composition and corresponding physicochemical properties on the surface of the titanium alloy. These coatings can be used both to improve the mechanical characteristics of the material, in particular to increase its strength and wear resistance, and to solve problems in the electronics and chemical industries.

References

1. M.V. Diamanti, B. Del Curto, M.P. Pedeferri, Anodic oxidation of titanium: from technical aspects to biomedical applications. J. Appl. Biomater. Biomech. **9**(1), 55–69 (2011)
2. X. Liu, P.K. Chu, C. Ding, Surface modification of titanium, titanium alloys, and related materials for biomedical applications. Mater. Sci. Eng. R. Rep. **47**(3–4), 49–121 (2004)
3. IM Pohrelyuk, S.M Lavrys, Thermal stability of the deformed surface layer of VT22 titanium alloy in a nitrogen-containing medium. Mater. Sci. **57**(1), 43–47 (2021)
4. R.O. Hussein, P. Zhang, X. Nie, Y. Xia, D.O. Northwood, The effect of current mode and discharge type on the corrosion resistance of plasma electrolytic oxidation (PEO) coated magnesium alloy AJ62. Surf. Coat. Technol. **206**(7), 1990–1997 (2011)
5. B. Nagarajan, S.C. Mathalai, Evaluation of different electrolytic solution composition on the microstructure and corrosion study on AZ31 magnesium alloy using PEO method. Phys. Scr. **99**(12), 125003 (2024)
6. Y. Cheng, Z. Xue, Q. Wang, X.Q. Wu, E. Matykina, P. Skeldon, G.E. Thompson, New findings on properties of plasma electrolytic oxidation coatings from study of an Al–Cu–Li alloy. Electrochim. Acta **107**, 358–378 (2013)
7. A.S. Kuprin, V.D. Ovcharenko, A. Gilewicz, G.N. Tolmachova, I.V. Kolodiy, R.L. Vasilenko, T. Kuznetsova, V. Lapitskaya, B. Warcholinski, Structural, mechanical and tribological properties of Cr-V-N coatings deposited by cathodic arc evaporation. Tribol. Int. **165**, 107246 (2022)
8. V. Kyryliv, O. Maksymiv, V. Gurey, I. Hurey, Y. Kyryliv, O. Zvirko, The mode deformation effect on surface nanocrystalline structure formation and wear resistance of steel 41Cr4. Coatings **12**(2), 249 (2023)
9. V.I. Kyryliv, B.P. Chaikovs'kyi, O.V. Maksymiv, A.V. Shal'ko, P.Y. Sydor, Serviceability of 60Kh2M roll steel with surface nanostructure. Mater. Sci. **52**(6), 848–853 (2017)
10. D. Toboła, J. Morgiel, L. Maj, TEM analysis of surface layer of Ti-6Al-4V ELI alloy after slide burnishing and low-temperature gas nitriding. Appl. Surf. Sci. **51515**, 145942 (2020)
11. C. Zhang, K. Wen, Y. Gao, Columnar and nanocrystalline combined microstructure of the nitrided layer by active screen plasma nitriding on surface-nanocrystalline titanium alloy. Appl. Surf. Sci. **61730**, 156614 (2023)

12. S.M. Lam, J.C. Sin, A.Z. Abdullah, A.R. Mohamed, Photocatalytic TiO_2/carbon nanotube nanocomposites for environmental applications: an overview and recent developments fullerenes. Nanotub. Carbon Nanostructures **22**, 471–509 (2014)
13. M. Landmann, E. Rauls, W.G. Schmidt, The electronic structure and optical response of rutile, anatase and brookite TiO_2 J. Phys.: Condens. Matter **24**, 195503 (2012)
14. O.V. Tkachuk, I.M. Pohrelyuk, R.V. Proskurnyak, J. Morgiel, M. Faryna, A. Goral, Morphology and corrosion resistance of hydroxyapatite coatings formed on commercially pure titanium. J. Mater. Eng. Perform. **24**, 11040–11049 (2023)
15. R.I.M. Asri, W.S.W. Harun, M. Samykano, N.A.C. Lah, S.A.C. Ghani, F. Tarlochan, M.R. Raza, Corrosion and surface modification on biocompatible metals: a review. Mater. Sci. Eng. C Mater. Biol. Appl. **77**, 1261–1274 (2017)
16. H. Ji, X. Xie, Z. Jiang, X. Wu, Wear and corrosion of titanium alloy spinal implants in vivo. Sci. Rep. **14**, 16847 (2024)
17. M. Student, I. Pohrelyuk, J. Padgurskas, V. Posuvailo, V. Hvozdets'kyi, K. Zadorozhna, H. Chumalo, H. Veselivska, I. Kovalchuk, A. Kychma, Influence of plasma electrolytic oxidation of cast Al-Si alloys on their phase composition and abrasive wear resistance. Coatings **13**(3), 637 (2023)
18. J. Rodríguez-Carvajal, *Program FullProf.2k. Version 2.20*. (Laboratoire Léon Brillouin, France, 2002) (CEA–CNRS)
19. M.M. Student, V.M. Posuvailo, H.H. Veselivs'ka, Y.Y. Sirak, R.A. Yatsyuk, Corrosion resistance of plasma-electrolytic layers on alloys and coatings of the Al–Cu–Mg system for various modes of heat treatment. Mater. Sci. **53**(6), 789–795 (2018)
20. M. Kaseem, S. Fatimah, N. Nashrah, Y.G. Ko, Recent progress in surface modification of metals coated by plasma electrolytic oxidation: principle, structure, and performance. Prog. Mater. Sci. **117**, 100735 (2021)
21. T.W. Clyne, S.C. Troughton, A review of recent work on discharge characteristics during plasma electrolytic oxidation of various metals. Int. Mater. Rev. **64**, 127–162 (2019)
22. G. Barati Darband, M. Aliofkhazraei, P. Hamghalam, N. Valizade, Plasma electrolytic oxidation of magnesium and its alloys: mechanism, properties and applications. J. Magnes Alloy **5**, 74–132 (2017)
23. Z. Bergant, J. Grum, Porosity evaluation of flame-sprayed and heat-treated nickel-based coatings using image analysis. Image Anal. Ster. **30**(1), 53–62 (2011)
24. X.C. Zhang, B.S. Xu, F.Z. Xuan, H.D. Wang, Y.X. Wu, S.T. Tu, Statistical analyses of porosity variations in plasma-sprayed Ni-based coatings. J. Alloy. Compd. **467**(1–2), 501–508 (2009)
25. P. Elia, E. Nativ-Roth, Y. Zeiri, Z.E. Porat, Determination of the average pore-size and total porosity in porous silicon layers by image processing of SEM micrographs. Microporous Mesoporous Mater. **225**, 465–471 (2016)
26. P. Karlova, M. Serdechnova, C. Blawert, X. Lu, M. Mohedano, D. Tolnai, B. Zeller-Plumhoff, M.L. Zheludkevich, Comparison of 2D and 3D plasma electrolytic oxidation (PEO)-based coating porosity data obtained by X-ray tomography rendering and a classical metallographic approach. Materials **15**, 6315 (2022)
27. H. Zhang, R. Zhang, D. Sun, F. Yu, Z. Gao, S. Sun, Z. Zheng, Analyzing the pore structure of pervious concrete based on the deep learning framework of Mask R-CNN. Constr. Build. Mater. **318**, 125987 (2022)
28. P.K. Nalajam, V. Ramesh, Microstructural porosity segmentation using machine learning techniques in wire-based direct energy deposition of AA6061. Micron **151**, 103161 (2021)
29. R. Vorobel, O. Student, I. Ivasenko, P. Maruschak, H. Krechkovska, O. Zvirko, O. Berehulyak, T. Mandziy, I. Tsybailo, P. Solovei, Development of a method for computer processing of fractographic images to assess the cohesion of inclusions to the matrix in the weld metal after its operational degradation and hydrogenation. Materialia **34**, 102074 (2024)
30. T. Mandziy, I. Ivasenko, O. Berehulyak, R. Vorobel, Influence of colour restoration on rust image segmentation. in *IEEE 3rd Ukraine Conference on Electrical and Computer Engineering*, UKRCON 2021, 26–28 Aug 2021 (Lviv, Ukraine, 2021), pp. 68–73

31. E.P. Meagher, G. Lager, A: Polyhedral thermal expansion in TiO, polymorfs: refinement of the crystal structure of rutile and brookite at high temperature. Can. Mineral. **17**, 77–85 (1979)

Chapter 28
Binding Energy of an Exciton Quasimolecule from Ge/Si Double Quantum Dots: Theory

Serhii I. Pokutnii, Taras Yu. Gromovy, and Valeriia M. Ovdenko

Abstract The theory of excitonic quasimolecules (formed from spatially separated electrons and holes) in a nanosystem consisting of double quantum dots of germanium synthesized in a silicon matrix is presented. It is shown that the binding energy of the singlet ground state of the quasimolecule of an exciton is considerably larger than the binding energy of biexciton in a silicon single crystal by almost two orders of magnitude.

28.1 Introduction

At present the optical properties of Ge/Si heterostructures with germanium quantum dots (QD) are the subject of the intense study. In Ge/Si heterostructures structures that have self-assembled Ge/Si nanoislands are promising in the implementation of effective sources of infrared radiations, since the photoluminescence signal of such nanostructures, in the spectral range

$$(0.20 - 1.14)\text{eV}, \tag{28.1}$$

is observable all the way to room temperatures [1, 2]. In order to create new Ge/Si-based heterostructures with new effective optoelectronic devices, the mechanism of light absorption in such nanoheterostructures must be studied [1–5]. Ge/

S. I. Pokutnii (✉) · T. Yu. Gromovy
Chuiko Institute of Surface Chemistry of National Academy of Sciences of Ukraine, Kyiv, Ukraine
e-mail: pokutnyi.serg@gmail.com

S. I. Pokutnii · V. M. Ovdenko
Institute of Physics of National Academy of Sciences of Ukraine, Kyiv, Ukraine

V. M. Ovdenko
Department of Macromolecular Chemistry, Taras Shevchenko National University of Kyiv, Kyiv, Ukraine

O. Fesenko and L. Yatsenko (eds.), *Functional Nanomaterials, Nanocatalysts, Nanotechnologies, and Their Applications*, Springer Proceedings in Physics 321,
https://doi.org/10.1007/978-3-031-99136-3_28

Si heterostructures with germanium QDs are classified as heterostructures of the second type. Such nanoheterostructures are characterized by the presence of significant gaps in the valence and conduction bands. The ground electron state therein is located in the silicon matrix, and the ground hole level is in the volume of the germanium QD. The significant gap in the valence band causes hole localization in the QD volume. A significant gap in the conduction band is the potential barrier for electrons (electrons move throughout the matrix and do not penetrate into the QD volume) [1–5]. Study of the optical properties of Ge/Si heterostructures with germanium QDs in Ref. [1] was the first to discover the spatial separation between electrons and holes, as a result of which the electrons localized on the QD surface, and the holes moved through the QD volume.

The energy of the Coulomb interaction of electron with hole form is a potential well, in which the electron is localized above the surface of the QD. In the volume of the QD there is a hole, while the electron is localized above the spherical surface of the QD-matrix interface [6, 7].

In [7–20] it is theoretically analyzed the exciton transitions in double vertically conjugated QD of germanium, separated by silicon layer d thickness. The QD of germanium was in the form of pyramids, in which the ratio of the height h to the lateral dimension $l = (10, 15, 20)$ nm was (≈ 0.1). The spatial structure of excitons and the oscillator is the theoretically studied [8]. The ground state of the exciton in a single germanium QD corresponded to the configuration in which the hole was in the ground state in germanium QD, and an electron moving in the silicon matrix was localized near the apex of the pyramidal QD. It is shown that for small distances (d < 3 nm) between QDs, the electron configuration is analogous to the case of single QDs. It is found that with the increase of the distance d to the values ($d = ((3.0 - 3.5)$ nm) for $l = (10, 15)$ nm, the oscillator strength for the interband transition with the formation of the ground state of the exciton can be much larger (up to a factor of 5) than the analogous value in single QD. In [8] in contrast to the present work, when studying the occurrence of exciton states between the QD surfaces, the exchange interaction between electrons was not taken into account. Such exchange interaction, as it will be shown in the present paper, gives the main contribution to the binding energy of the exciton quasimolecule.

In [6] the theory of the exciton formed by spatially separated electron and hole is developed (the hole moves in the bulk of a germanium QD and the electron is localized above the spherical interface between the QD and the silicon matrix). It was found that the binding energy of an exciton in such nanosystem is much higher (almost an order of magnitude) than the binding energy of an exciton in the silicon single crystal. In [6], in the framework of classical electrodynamics, an expression was obtained that describes the Coulomb interaction between an electron and hole. In [6], the exciton appeared as a result of the Coulomb interaction between the electron and hole, which, in contrast to [1, 2, 8], was depended on the dielectric permittivities of the QD and the matrix. The energy spectrum of the exciton, as a function of the radius of the germanium QD, was obtained in [6] for radii of QDs exceeding 3 nm. This is due to the fact that the study of exciton states in the nanosystem containing germanium QD with radii a less than 3 nm in the framework of approach in which

the expression describing the Coulomb interaction between the electron and hole was obtained by the methods of classical electrodynamics is incorrect.

The convergence of two QDs up to the certain critical value D_c between surfaces of QD leads to overlapping of the electron wave functions and the emergence of exchange interactions [9]. As a result, the conditions for the formation of quasi-molecules from QDs can be created [1, 2, 8, 9]. One can also assume that the above conditions of formation of quasimolecules can be provided by external physical fields. This assumption is evidenced by results of [10, 11], in which the occurrence of the effective interaction between QDs at considerable distances under conditions of electromagnetic field was observed experimentally. In [12–19] energies of the ground state of "vertical" and "horizontal" located pair of interacting QDs ("molecules" from two QDs) were determined as a function of the steepness of the confining potential and the magnetic field strength. The quantum part of nanocomputer, which was implemented on a pair of QDs ("molecules" from two QDs) with charge states is n qubits [14]. The first smoothly working quantum computer has been on QDs with two electron orbital states as qubits, described by a pseudospin (½). As a single cell was taken as a couple of asymmetric pair QDs with different sizes and significantly different energy. The electron is injected into the heterostructure from the channel occupied the lower level. That is, it was located in a QD with larger size.

In [3] heterostructures which are linear chains of QDs germanium on Si substrates were obtained by electron-beam lithography method. The average sizes of the QD Ge is less than 60 nm. With increasing concentration of Ge QDs linear chains in the average distance between the surfaces decreases QDs [3]. In such nanostructures at distances D_c between the surfaces of QD (which is about a_e, where ($a_e = 0.63$ nm) is the Bohr radius of the electron in a silicon matrix) must take into account the interaction between the surfaces of the quantum dots. In this case the overlap integral of the electron wave functions takes a significant value. As a result, the conditions for the formation of the excitonic quasi-molecules from of double QDs can be created.

Therefore, in the present paper, which is a continuation of research [6], using the variational method, we obtain the binding energy of the excitonic quasimolecule singlet ground state in such system as a functions of the spacing between the QD surfaces and of the QD radius. We show that the excitonic quasi-molecule formation is of the threshold character and possible in a nanosystem, where the distance D between the surfaces of QD is given by the condition $D_c^{(1)} \leq D \leq D_c^{(2)}$ (where $D_c^{(1)}$ and $D_c^{(2)}$ are some critical distance). A significant increase in the binding energy of the singlet ground state of excitonic quasi-molecule (of spatially separated electrons and holes) in a nanosystem that consist of germanium QDs grown in a silicon matrix has been predicted; the effect is almost two orders of magnitude larger than the binding energy of biexciton in a silicon single crystal. It is shown that the major contribution to the excitonic quasi-molequle binding energy is made by the energy of the exchange interaction of electrons with holes and this contribution is much more substantial than the contribution of the energy of Coulomb interaction between the electrons and holes.

28.2 The Binding Energy of the Singlet Ground State of Exciton Quasimolecule

Consider a model of nanosystem that consists of two spherical germanium quantum dots: QD(A) and QD(B) with radius a, grown in a matrix of silicon with a dielectric constant ($\varepsilon_1 = 11.7$) (D is the distance between the surfaces of the QD). The QDs contain germanium with the dielectric constant of ($\varepsilon_2 = 16.3$) in their volume. For simplicity, we assume that holes $h(A)$ and $h(B)$ with the effective mass $((m_h/m_0) = 0.39)$ are located at the centers of QD(A) and QD(B), and electrons $e(1)$ and $e(2)$ with effective mass $((m_e^{(1)}/m_0) = 0.98)$ are localized above the surfaces of QD(A) and QD(B) in a matrix of silicon, respectively (m_0 is the electron mass in free space; $r_{A(1)}$ is the distance of the electron $e(1)$ from the QD(A) center; $r_{B(2)}$ is the distance of the electron $e(2)$ from the QD(B) center; $r_{A(2)}$ is the distance of the electron $e(2)$ from the QD(A) center; $r_{B(1)}$ is the distance of the electron $e(1)$ from the QD(B) center). Let us assume that there is an infinitely high potential barrier on a spherical interface (QD-matrix). In the nanosystem the holes do not therefore escape from the volume of the QD while the electrons do not enter the QD. Therefore, the proposal in which the holes $h(A)$ and $h(B)$ located at the centers QD(A) and QD(B), in the studied model nanosystems, is justified [18–20].

Let us now use this model to consider the possibility of the formation of excitonic quasimolecule from spatially separated electrons and holes (the holes are located at the centers of QD(A) and QD(B) and electrons are localized near their spherical surfaces). Using adiabatic approximation and the effective mass approximation, the Hamiltonian of the excitonic quasimolecule (of spatially separated electrons and holes) can be written in the form [18–20]:

$$\hat{H} = \hat{H}_{A(1)} + \hat{H}_{B(2)} + \hat{H}_{int} \tag{28.2}$$

where $\hat{H}_{A(1)}$ and $\hat{H}_{B(2)}$ are the Hamiltonians of the excitons of spatially separated hole $h(A)$ and electron $e(1)$ and hole $h(B)$ and electron $e(2)$, respectively.

The contribution of the energy of polarization interaction with the surface of QD to the Hamiltonians of the excitons $\hat{H}_{A(1)}$ and $\hat{H}_{B(2)}$ can be, as a first approximation neglected [6, 7]. Thus the exciton Hamiltonian $\hat{H}_{A(1)}$ takes the form [8, 9]:

$$\hat{H}_{A(1)} = -\frac{\hbar^2}{2\mu}\Delta_{(1)} + V_{e(1)h(A)}\left(\boldsymbol{r}_{\boldsymbol{A}(1)}, \boldsymbol{r}_{\boldsymbol{h}(\boldsymbol{A})}\right) + E_g, \tag{28.3}$$

where the first term is the exciton kinetic energy operator and the energy of Coulomb interaction $V_{e(1)h(A)}$ between electron $e(1)$ and hole $h(A)$ is given be the following expression [6, 7]:

$$V_{e(1)h(A)} = -\frac{1}{2}\left(\frac{1}{\varepsilon_1} + \frac{1}{\varepsilon_2}\right)\frac{e^2}{\boldsymbol{r}_{\boldsymbol{A}(1)}} \tag{28.4}$$

and E_g is the bandgap energy of the germanium ($E_g = 0.661$eV). The Hamiltonian $\hat{H}_{B(2)}$ is of the same form as $\hat{H}_{A(1)}$ (28.2). In the first approximation we can neglect the contributions to the Hamiltonian $\hat{H}_{int}$ of the interaction energies of the electrons $e(1)$ and $e(2)$ and the holes $h(A)$ and $h(B)$ with polarization fields induced by these charge carriers on the surfaces of QD (A) and QD (B) [6]. Thus, the Hamiltonian $\hat{H}_{int}$ incorporates only the energies of Coulomb interaction of electron $e(1)$ with hole $h(B)$, and electron $e(2)$ with hole $h(A)$, as well as that between electrons $e(1)$ and $e(2)$, and holes $h(A)$ and $h(B)$ [8, 9].

Under the assumption that the spins of the electrons $e(1)$ and $e(2)$ are antiparallel let us write down the normalized wave function of the ground singlet state of the exciton quasimolecule as a symmetric linear combination of wave functions $\Psi_1\left(r_{A(1)}, r_{B(2)}\right)$ and $\Psi_2\left(r_{A(2)}, r_{B(1)}\right)$ [9]:

$$\begin{aligned}&\Psi_s\left(r_{A(1)}, r_{A(2)}, r_{B(1)}, r_{B(2)}\right)\\&= \left[2\left(1 + S^2(D, a)\right)\right]^{-1/2}\left[\Psi_1\left(r_{A(1)}, r_{B(2)}\right) + \Psi_2\left(r_{A(2)}, r_{B(1)}\right)\right]\end{aligned} \tag{28.5}$$

where $S(D, a)$ is the overlap integral of single-electron wave functions. Assuming that the electrons $e(1)$ and $e(2)$ move independently from each other, let us represent the wave functions $\Psi_1(r_{A(1)}, r_{B(2)})$ and $\Psi_2(r_{A(2)}, r_{B(1)})$ (28.5) as a product of single-electron wave functions $\varphi_{A(1)}\left(r_{A(1)}\right)$ and $\varphi_{B(2)}\left(r_{B(2)}\right)$, as well as $\varphi_{A(2)}\left(r_{A(2)}\right)$ and $\varphi_{B(1)}\left(r_{B(1)}\right)$, respectively [18–20]. Let us also represent the single-electron wave functions as variational functions of Coulomb type [18–20]:

$$\begin{aligned}\varphi_{A(1)}\left(r_{A(1)}\right) &= \tilde{A}\exp\left(-\overline{\mu}(\tilde{a})\left(r_{A(1)}/a_{ex}^{2D}\right)\right),\\ \varphi_{B(2)}\left(r_{B(2)}\right) &= \tilde{A}\exp\left(-\overline{\mu}(\tilde{a})\left(r_{B(2)}/a_{ex}^{2D}\right)\right),\\ \varphi_{A(2)}\left(r_{A(2)}\right) &= \tilde{A}\exp\left(-\overline{\mu}(\tilde{a})\left(r_{A(2)}/a_{ex}^{2D}\right)\right),\\ \varphi_{B(1)}\left(r_{B(1)}\right) &= \tilde{A}\exp\left(-\overline{\mu}(\tilde{a})\left(r_{B(1)}/a_{ex}^{2D}\right)\right).\end{aligned} \tag{28.6}$$

where $\overline{\mu}(\tilde{a})$ is a variational parameter, $\tilde{a} = \left(a/a_{ex}^{2D}\right)$, where $a_{ex}^{2D} = (2\varepsilon_1\varepsilon_2/(\varepsilon_1 + \varepsilon_2))\cdot\left(\hbar^2/\mu_0 e^2\right)$ is the Bohr radius of two-dimensional (2D) exciton localized over the flat interface between the germanium and the matrix of silicon, $\mu_0 = m_e^{(1)}m_h/\left(m_e^{(1)} + m_h\right)$ is the reduced mass of the 2D exciton (of spatially separated electrons and holes) [18–20].

In the framework of the variational method, the energy of the excitonic quasimolecule ground singlet state, as a first approximation, is given by the mean value of the Hamiltonian $\hat{H}$ (28.2) over the states described by the wave functions of the zeroth approximation Ψ_s (28.5) [18–20]:

$$E(D, \overline{\mu}(a, D), a) = \Psi_s(r_{A(1)}, r_{A(2)}, r_{B(1)}, r_{B(2)})\left|\hat{H}\right|\Psi_s\left(r_{A(1)}, r_{A(2)}, r_{B(1)}, r_{B(2)}\right). \tag{28.7}$$

With the explicit form of the wave functions (28.5), (28.6), the energy functional of the exciton quasimolecule singlet ground state takes the form

$$E_0\left(\widetilde{D},\overline{\mu}\left(\tilde{a},\tilde{D}\right),\tilde{a}\right) = 2E_{ex}(\tilde{a},\overline{\mu}(\tilde{a})) + \frac{J\left(\widetilde{D},\overline{\mu}\left(\tilde{a},\tilde{D}\right),\tilde{a}\right) + K\left(\widetilde{D},\overline{\mu}\left(\tilde{a},\tilde{D}\right),\tilde{a}\right)}{1 + S^2\left(\widetilde{D},\overline{\mu}\left(\tilde{a},\tilde{D}\right),\tilde{a}\right)}, \tag{28.8}$$

Here, $E_{ex}(\tilde{a},\overline{\mu}(\tilde{a}))$ is the energy functional of the exciton ground state (for the exciton formed from an electron and a hole spatially separated from the electron):

$$E_{ex}(\tilde{a},\overline{\mu}(\tilde{a})) = \varphi_{A(1)}\left(r_{A(1)}\right)\left|\hat{H}_{A(1)}\right|\varphi_{A(1)}\left(r_{A(1)}\right). \tag{28.9}$$

The second term in (28.8) is a functional $E_{\text{в}}(D, a)$ representing the binding energy of singlet ground state of excitonic quasimolecule. In the functional determined by formula (28.8), $J\left(\widetilde{D},\overline{\mu}\left(\tilde{a},\tilde{D}\right),\tilde{a}\right)$ is determined by the expression (here ($\tilde{D} = \left(D/a_{ex}^{2D}\right)$).

$$J\left(\widetilde{D},\overline{\mu}\left(\tilde{a},\tilde{D}\right)\tilde{a}\right) = \varphi_{A(1)}\left(r_{A(1)}\right)\varphi_{B(2)}\left(r_{B(2)}\right)|H_{int}|\varphi_{A(1)}\left(r_{A(1)}\right)\varphi_{B(2)}\left(r_{B(2)}\right). \tag{28.10}$$

The functional $J\left(\widetilde{D},\overline{\mu}\left(\tilde{a},\tilde{D}\right),\tilde{a}\right)$ (28.10) can be represented as the algebraic sum of the functionals of the average energies of Coulomb interaction [18–20]. In the functional described by (28.8), $K\left(\widetilde{D},\overline{\mu}\left(\tilde{a},\tilde{D}\right),\tilde{a}\right)$ is determined by the formula

$$K\left(\widetilde{D},\overline{\mu}\left(\tilde{a},\tilde{D}\right),\tilde{a}\right) = \varphi_{B(1)}\left(r_{B(1)}\varphi_{A(2)}\left(r_{A(2)}\right)\right)\left|\hat{H}_{int}\right|\varphi_{A(1)}\left(r_{A(1)}\right)\varphi_{B(2)}\left(r_{B(2)}\right). \tag{28.11}$$

The functional $K\left(\widetilde{D},\overline{\mu}\left(\tilde{a},\tilde{D}\right),\tilde{a}\right)$ (28.11) can be represented as the algebraic sum of the functionals of the average energies of the exchange interaction [18–20].

Within the framework of the variational method at the first approximation the total energy of ground singlet state of excitonic quasimolecule is determined by average value of the Hamiltonian $\hat{H}$ (28.2) for states, which are described by wave functions of the zero approximation $\Psi_s\left(r_{A(1)}, r_{A(2)}, r_{B(1)}, r_{B(2)}\right)$ (28.5) [18–20]:

$$E_0\left(\tilde{D},\tilde{a}\right) = 2E_{ex}(\tilde{a}) + E_{\text{в}}\left(\tilde{D},\tilde{a}\right), \tag{28.12}$$

where $E_{\text{в}}\left(\tilde{D},\tilde{a}\right)$ is the binding energy of the ground singlet state of the excitonic quasimolecule and $E_{ex}(\tilde{a})$ is the binding energy of the ground state of the exciton (consisting of spatially separated electron and hole) localized over the surface of QD, which was worked out in [6, 7].

28.3 Results and Discussion

Figure 28.1 presents the results of the variational calculations of the binding energy $E_{\text{в}}\left(\tilde{D},\tilde{a}\right)$ studied in [18–20] of the excitonic quasimolecule ground state in a nanosystem with QD germanium of the mean radius $\overline{a}_1 = 12.8\text{nm}$, grown in a

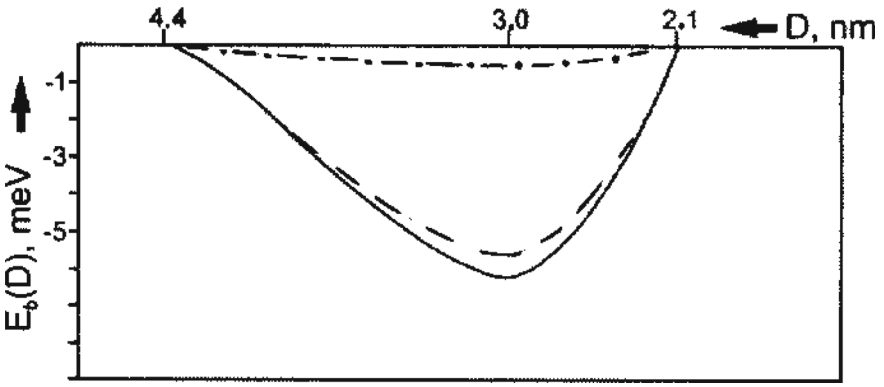

Fig. 28.1 The dependence of the binding energy of the ground singlet state $E_ß(D, \overline{a}_1)$ of the excitonic quasimolecule (continuous line) in a nanosystem made up of two spherical germanium quantum dots QD(A) and QD(B) with the mean radius $\overline{a}_1 = 12.8$ nm, on the distance D between the surfaces of QD(A) and QD(B). Dependence of the exchange interaction energy of the electrons and holes (dashed line) and the energy of the Coulomb interaction between electrons and holes (dot dashed line) on the distance D between the surfaces of the quantum dots

matrix of silicon (the Bohr radius of the 2D exciton $a_{ex}^{2D} = 2.6$ nm). The variational method that we used for the calculation of the excitonic quasimolecule ground state binding energy $E_ß\left(\tilde{D}, \tilde{a}\right)$ is applicable provided that iis much smaller than the binding energy of the exciton ground state $E_{ex}(\tilde{a})$, i.e. the following condition must be fulfilled [18–20]:

$$\left(E_ß\left(\tilde{D}, \tilde{a}\right)/E_{ex}(\tilde{a})\right) \ll 1 \tag{28.13}$$

The binding energy $E_ß\left(\tilde{D}, \tilde{a}\right)$ of the excitonic quasimolecule ground state in a nanosystem with QD germanium of the mean radius $\overline{a}_1 = 12.8$ nm has a minimum $E_ß^{(1)}(D_1, \overline{a}_1) \approx -6.1$ meV (at the distance $D_1 \cong 3.1$ nm) (Fig. 28.1) ($E_ß^{(1)}$ corresponds to the critical temperature $T_c \approx 71$ K). As it follows from Fig. 28.1, the excitonic quasimolecule appears in the nanosystem at distances $D \geq D_c^{(1)} \cong 2.1$nm between the surfaces of QD. The formation of such excitonic quasimolecule has of the threshold character and can occur in a nanosystem with quantum dots of the mean radius $\overline{a}_1$, where the distance D between the surfaces of QD exceeds a certain critical value $D_c^{(1)}$. The existence of such distance $D_c^{(1)}$ arises from quantum size effects in which the decrease in the energies of interaction of the electrons and holes entering into the Hamiltonian (Eq. (28.2)) of the excitonic quasimolecule with decrease of the distance D between the surfaces of the QD cannot compensate for the increase in the kinetic energy of the electrons and holes.

The binding energy of the exciton $E_{ex}(\tilde{a})$ amounts to $E_{ex}(\overline{a}_1) \cong -64$meV [8, 9], with the energy of the excitonic quasimolecule ground state (28.12) taking the value $E_0\left(\tilde{D}_1, \overline{a}_1\right) \approx -134.1$meV. It should be emphasized that the criterion (28.13)

of the applicability of the variational method for the calculation of the exciton quasimolecule binding energy $E_ß(\tilde{D}, \tilde{a})$ is fulfilled ($\left(E_ß^{(1)}(D_1, \overline{a}_1)/E_{ex}(\overline{a}_1)\right) \cong 0.09$). At larger distances D between the surfaces of QD: $D \geq D_c^{(2)} \cong 4.4$nm, the excitonic quasimolecule breaks down into two excitons (consisting of spatially separated electrons and holes), localized over QD surfaces (Fig. 28.1). Thus, the excitonic quasimolecule can be formed in a nanosystem where $D_c^{(1)} \leq D \leq D_c^{(2)}$ (see Fig. 28.1). Furthermore, a excitonic quasimolecule can exist only at temperatures lower than the critical temperature $T_c = 71$ K. In the germanium monocrystal with the binding energy $E_ß = 0.34$ meV [18–20] (which corresponds to the temperature 4 K) the exciton binding energy $E_ß^{(1)}$ is almost two orders of magnitude.

As follows from the results of the variational calculations, the major contribution to the excitonic quasimolecule binding energy is from the energy of exchange interaction of electrons and holes, which by far surpasses that from their Coulomb interaction (i.e. the ratio ≤ 0.08) (see Fig. 28.1). Since the calculations of the excitonic quasimolecule ground state binding energy $\left|E_ß(\tilde{D}, \tilde{a})\right|$ in the nanosystem are variational, the values of $\left|E_ß(\tilde{D}, \tilde{a})\right|$ and $\left|E_ß^{(1)}\right|$ can be somewhat underestimated.

As such, the interband electron electron transitions between the quantum-level of the hole located in the valence band of the germanium QD, and the quantum-level of the excitonic quasi-molecule located in the conduction band of the silicon matrix cause a significant absorption of radiation in the infrared wavelength region. In the considered energy intervals, located in the spectral range (1), where the absorption in the experiments from Refs. [1, 2] was observed, the indicated transitions ensure the significant experimentally- observed blurring of the absorption edge, all the way up to room temperatures.

In [8] the energy of the Coulomb interaction between electron and hole decreased (from 28.8 meV to 24.4 meV) with increasing the lateral size l (from $l = 10$ nm to $l = 20$ nm) of pyramidal germanium QD. In [6] exciton from spatially separated electron and hole (the hole was moving in QD, and the electron was localized over spherical surface seperataion (QD-matrix)) arose as a result of the Coulomb interaction V_{eh} (28.4) between electron and hole, which, in contrast to [1, 2, 8], was depended on the dielectric permittivities of the QD and matrix. In [6] nanosystem consisting of spherical shape germanium QD was studied, as well. It was shown in [6] that the energy of the Coulomb interaction between electron and hole decreased (from 94 to 26 meV) with increasing the radius a of germanium QD (from $a = 3$ nm to $a = 5$ nm). Since in [6] the expression V_{eh} (28.4), which describes the Coulomb interaction between electron and hole, was obtained in in the framework of classical electrodynamics, the study of exciton states in nanosystem containing a QD with radii a less than 3 nm is incorrect.

28.4 Conclusions

Thus, it has been shown that the exciton quasimolecule formation is of the threshold character and possible in a nanosystem, where the distance D between the surfaces of QD is given by the condition $D_c^{(1)} \leq D \leq D_c^{(2)}$ (where $D_c^{(1)}$ and $D_c^{(2)}$ are some critical distance). A significant increase in the binding energy of the singlet ground state of excitonic quasi-molecule (of spatially separated electrons and holes) in a nanosystem that consists of germanium QDs grown in a silicon matrix has been predicted; the effect is almost two orders of magnitude larger than the binding energy of biexciton in a silicon single crystal. It is shown that the major contribution to the exciton quasi-molecule binding energy is made by the energy of the exchange interaction of electrons with holes and this contribution is much more substantial than the contribution of the energy of Coulomb interaction between the electrons and holes (see Fig. 28.1).

The fact that the energy of the ground state singlet excitonic quasi-molecule is in the infrared range of the spectrum, presumably, allow the use of a quasi-molecule to create new elements silicon infrared nano-optoelectronics [21, 22].

References

1. S.A. Rudin, V. Zinovyev, J.V. Smagina et al., J. Appl. Phys. **131**, 035302 (2022)
2. S.A. Rudin, V. Zinovyev, J.V. Smagina et al., J. Cryst. Growth **593**, 126763 (2022)
3. J.V. Smagina, V. Zinovyev, A.F. Zinivieva et al., J. Lumines. **249**, 119033 (2022)
4. A.I. Yakimov, A.A. Bloshkin, A.V. Dvurechenskii, JETP Lett. **90**, 569 (2009)
5. A.F. Zinovieva, V.A. Zinovyev, A.I. Nikiforov et al., JETP Lett. **104**, 823 (2016)
6. Z.V. Smagina, A.V. Dvurechenskii, V.A. Seleznev, Semiconductors **49**, 749 (2015)
7. S.I. Pokutnyi, Phys. B Phys. Condens. Matter **616**, 4130598 (2021)
8. S.I. Pokutnyi, Low Temp. Phys. **42**, 1151 (2016)
9. S.I. Pokutnyi, Low Temp. Phys. **44**, 819 (2018)
10. S.I. Pokutnyi, Eur. Phys. J. Plus. **135**, 74 (2020)
11. S.I. Pokutnyi, Phys. Solid Stat. **39**, 634 (1997)
12. S.I. Pokutnyi, Phys. Solid Stat. **39**, 528 (1997)
13. S.I. Pokutnyi, Y.N. Kulchin, V.P. Dzyuba, J. Nanophoton. **10**, 036008 (2016)
14. V.G. Klyuev, D.V. Volykhin, O.V. Ovchinnikov et al., J. Nanophoton. **10**, 033507 (2016)
15. S.I. Pokutnyi, Physica Status solidi (b) **173**, 607 (1992)
16. S.I. Pokutnyi, Semiconductors **30**, 1015 (1996)
17. S.I. Pokutnyi, Semiconductors **47**, 791 (2013)
18. S.I. Pokutnyi, Semiconductors **47**, 1626 (2013)
19. S.I. Pokutnyi, Opt. Eng. **56**(9), 091603 (2017)
20. S.I. Pokutnyi, Opt. Eng. **56**(6), 067104 (2017)
21. D.K. Efimkin, Y.E. Lozovik, A.A. Sokovik, Phys. Rev. B **86**(11), 115436 (2012)
22. Y.E. Lozovik, Adv. Phys. Sci. **57**(4), 653 (2014)

Chapter 29
The Role of Electrostatic and Electron-Deformation Interaction in the Formation of the Semiconductor Quantum Dot—HSA Bionanocomplexes

O. V. Kuzyk, O. O. Dan'kiv, A. I. Stolyarchuk, and I. D. Stolyarchuk

Abstract The addition of the human serum albumin (HSA) to a colloidal solution of nanoparticles (NPs) leads to a decrease in optical density and blurring of the exciton structure in the absorption spectra. This behavior indicates the interaction between the semiconductor nanoparticles and the HSA, with the formation of the corresponding bionanocomplexes. The albumin molecule contains about one hundred pairs of positive and negative charges. Thus, as a result of electrostatic interaction between quantum dot (QD) and albumin molecules (their attraction), the mechanical pressure arises on the surface of QD, which as a result of self-consistent electron-deformation interaction leads to a change in its band structure. A model of QD interacting with HSA molecules has been developed. The proposed model takes into account the interaction of dipolar HSA molecules with QDs through its polarization and electron-deformation interaction in a self-consistent manner. Theoretical calculations performed within the framework of the self-consistent electron-deformation coupling method are in good agreement with the results of thermodynamic analysis of experimental data on the photoluminescence intensity decay of the CdTe QD–HSA biocomplex.

29.1 Introduction

Semiconductor quantum dots (QDs) have become the subject of active research in medicine due to their unique optical and electronic properties [1–4]. They can be used in areas such as visualization, diagnostics and therapy. However, there are a number of problems that limit their widespread use. First, the toxicity of some materials [5, 6] from which quantum dots are obtained can cause inflammatory reactions in the body.

O. V. Kuzyk (✉) · O. O. Dan'kiv · A. I. Stolyarchuk · I. D. Stolyarchuk
Drohobych Ivan Franko State Pedagogical University, Drohobych, Ukraine
e-mail: olehkuzyk@dspu.edu.ua

O. Fesenko and L. Yatsenko (eds.), *Functional Nanomaterials, Nanocatalysts, Nanotechnologies, and Their Applications*, Springer Proceedings in Physics 321,
https://doi.org/10.1007/978-3-031-99136-3_29

Second, instability in biological environments leads to the loss of their functional properties.

The introduction of albumin, in particular human serum albumin (HSA), into the composition of biocomplexes with quantum dots can significantly improve their characteristics [7, 8]. Albumin has natural biocompatible properties that reduce the toxicity of quantum dots, as well as increase their stability in biological media [9, 10]. In addition, albumin can act as a transporter, ensuring more efficient delivery of active substances to cells and tissues [11, 12]. This opens up new opportunities for the use of quantum dots in the therapy of various diseases, including cancer, where precise drug delivery is critically important. As a result, the combination of quantum dots with albumin creates new avenues for the development of safe and effective medical technologies.

A number of researches on the QD and albumin biocomplexes have already been described in the scientific literature. In particular, a number of researches focus on methods for synthesizing QDs, which are modified with the help of albumin [13], studying their optical properties [14], stability in biological systems, and effects of interaction with albumin [15]. Many works are devoted to assessing the biocompatibility of the QD–HSA systems. Researches have shown that the addition of albumin reduces the toxicity of quantum dots and increases their safety for cell cultures. The potential of such biocomplexes for targeted drug delivery was analyzed in [16]. QDs modified with albumin demonstrate improved efficacy in the delivery of anticancer drugs, due to the ability of albumin to bind to cells.

The conducted researches [17] indicate the possibility of using the QD–albumin complexes in medical visualization. Albumin increases the contrast of images, which allows for more accurate detection of pathologies. The mechanisms of absorption and excretion of biocomplexes from the body were also researched, which is critically important for their use in therapy. The results show that albumin can contribute to a longer stay of QDs in the body.

Another very important effect is that albumin, as the main serum protein, acts as a transporter for many drugs, affecting their bioavailability, distribution, metabolism and excretion [18]. Therefore, binding to albumin can protect drugs from metabolic degradation, which prolongs their duration of action. Albumin can regulate the release of drugs, allowing therapeutic blood concentrations to be reached smoothly and gradually. Binding to albumin can reduce the toxic effects of drugs by reducing their activity before they are delivered to target cells.

When using colloidal QDs as fluorescent markers in in vitro and in vivo researches, there is a need for bioconjugation. It should be noted that the surface area of the nanoparticle (NP) is sufficient for simultaneous binding to it of several biomolecules, for example, several antibodies. The surface of the QD is a platform for conjugation. The possibility of conjugating semiconductor nanoparticles with protein molecules, for example, human serum albumin (HSA) [8] or bovine serum albumin (BSA) [19], has been experimentally tested.

The conducted researches in [8, 19–21] indicate the formation of the NP–albumin biocomplexes with a predominance of electrostatic attraction. They quickly form the so-called “protein corona” by adsorption with proteins in biological liquids. Among

proteins, the HSA is the most abundant, accounting for about 60% of total protein concentration in blood plasma. The addition of the HSA to a colloidal solution of nanoparticles leads to a decrease in optical density and blurring of the exciton structure in the absorption spectra. However, it was shown in [22] that depending on the type of ligand used and the sign of the QD charge, either the formation of a biocomplex is possible or the agglomeration of nanoparticles into clusters of different sizes occurs. Among the main interactions associated with protein adsorption, hydrophobic force, Van der Waals force and hydrogen bond, electrostatic interaction are distinguished, however, the main mechanism of binding is not currently understood.

Elucidation of the mechanisms of interaction between QD and HSA will allow choosing the optimal characteristics of QD in order to reduce their toxicity, which is important for their application in medicine. The interaction of HSA with QD can reduce the negative effects on cells, making these systems more biocompatible. Establishing the mechanisms by which HSA interacts with QD can help in creating more effective drug delivery systems. The QD–HSA biocomplex provides targeted delivery of active substances to affected tissues. Understanding the interaction between QD and HSA will contribute to the development of technologies that allow controlling the release of drugs from biocomplexes, which is important for achieving stable therapeutic effects.

The mechanical deformation is an important factor influencing the optical and electrical properties of QD with multilayer shell. Ligands that "envelop" the QD also exert additional pressure. Biochemical investigations have shown that most of the ionized atomic groups in serum albumin are on the surface of the protein globule. These groups cause a significant charge of the protein macromolecule, and, consequently, its electrostatic properties in solution. The albumin molecule contains about one hundred pairs of positive and negative charges. Thus, as a result of electrostatic interaction between QD and albumin molecules (their attraction), the mechanical pressure arises on the surface of QD, which as a result of self-consistent electron-deformation interaction leads to a change in its band structure. Therefore, the development of a model of strained QD with a multilayer shell that interacts with HSA molecules is an urgent task and has practical value.

29.2 Thermodynamic Approach for Analyzing the Interaction of QD and HSA

The procedure for analyzing the interaction of QD and HSA is as follows [23]. First, the fluorescence intensity of human serum albumin (HSA) is measured at different quencher (QD) concentrations. Визначаємо максимум інтенсивності фотолюмінесценції без гасника (без КТ) F_0 та з гасником F.

The Stern–Volmer equation is used to analyze fluorescence quenching:

$$\frac{F_0}{F} = 1 + K_{SV}[C], \tag{29.1}$$

where F_0 is the fluorescence intensity without the quencher; F is the fluorescence intensity in the presence of the quencher; K_{SV} is the Stern–Volmer quenching constant; $[C]$ is the quencher concentration.

We construct $\frac{F_0}{F}$ depending on $[C]$. If the relationship is nonlinear, it may indicate a static or mixed quenching mechanism, requiring modified equations.

The experiment is repeated at different temperatures T. The quenching constant K_{SV} is calculated for each temperature. If K_{SV} increases with temperature, dynamic quenching dominates. If K_{SV} decreases, static quenching (complex formation) is predominant.

The relationship between the binding constant K and temperature follows the Van't Hoff equation:

$$\ln K = -\frac{\Delta H}{RT} + \frac{\Delta S}{R}, \tag{29.2}$$

ΔH is the enthalpy change; ΔS is the entropy change.

Next, we plot the dependence of $\ln K$ on $1/T$. The slope of the straight line gives $-\Delta H/R$, and the intercept gives $\Delta S/R$. From these values, ΔH and ΔS are calculated.

The Gibbs free energy change is then determined using:

$$\Delta G = \Delta H - T\Delta S. \tag{29.3}$$

The essence of the thermodynamic analysis of the interaction between QDs and human serum albumin HSA lies in studying the energetic aspects of this interaction. Change in Gibbs free energy ΔG determines whether the interaction is spontaneous. A negative ΔG value indicates a thermodynamically favorable binding process. Change in enthalpy ΔH) indicates whether the interaction is exothermic (heat-releasing) or endothermic (heat-absorbing). This helps identify the dominant forces driving the interaction, such as hydrogen bonding, van der Waals forces, or hydrophobic interactions. Change in entropy ΔS reflects changes in system disorder. A positive ΔS often suggests an increase in randomness, which may result from the release of water molecules from the hydration shell upon binding. Binding constant K can be determined using the Van't Hoff equation. It characterizes the strength of the interaction between QDs and HSA.

In this work, the colloidal CdTe QDs were selected to analyze the interaction of QDs with HSA molecules. The results of measurements of the photoluminescence intensity depending on the QD concentration, temperature, and radius are given in [24]. This work shows that the interaction between CdTe QDs and HSA has a static character and leads to the formation of bionanocomplexes. It was also established that the quenching constant increases with increasing QD size and decreases with increasing temperature of the QD–HSA solution. The results of calculations of thermodynamic parameters based on formulas (29.1)–(29.3) are presented in Table 29.1.

Electrostatic interactions between charged particles or molecules are usually exothermic, since the attraction of opposite charges lowers the energy of the system.

Table 29.1 Thermodynamic parameters of the CdTe QD–HSA interaction

R_0 (nm)	ΔS (kJ/K·mol)	ΔH (kJ/mol)	ΔG (kJ/mol)		
			T = 293 K	T = 303 K	T = 309 K
2.8	0.048	− 6.4	− 20.4	− 20.95	− 21.23
2.9	0.0505	− 6.2	− 21	− 21.5	− 21.8
3.2	0.053	− 6.17	− 21.7	− 22.23	− 22.55

The negative enthalpy change indicates that the interaction between albumin (which has a large dipole moment) and CdTe quantum dots is energetically favorable. If the interaction is electrostatic, it can lead to desorption of the protein, which increases the entropy of the system [25, 26]. In addition, electrostatic attraction can cause conformational changes in the protein, which also contributes to an increase in entropy. Thus, the above calculations confirm that electrostatic interaction is the main mechanism of interaction in the formation of the CdTe QD–HSA biocomplexes.

29.3 Model of the QD–HSA Bionanocomplex

As previously mentioned, during the formation of quantum dot–HSA biocomplexes with predominant electrostatic attraction, the so-called "protein corona" is observed (Fig. 29.1). Biochemical studies have shown that most of the ionized atomic groups in serum albumin are located on the surface of the protein globule. These groups contribute to the substantial charge of the macromolecule, thereby influencing its electrostatic properties in solution. The HSA molecule contains approximately one hundred pairs of positive and negative charges, and its dipole moment is about 500 D [27]. As a result of electrostatic interactions between QDs and albumin molecules, an attractive force arises, leading to mechanical pressure on the QD surface. This pressure, in turn, induces a self-consistent electron-deformation interaction, ultimately modifying the band structure of the quantum dot.

The strong dipole moment of the HSA molecule can polarize the QD, leading to charge redistribution within the QD. This results in the formation of an effective electric potential on the QD surface, enhancing the electrostatic attraction between the QD and HSA. Electron-deformation interaction: The mechanical pressure exerted by albumin on the QD surface can induce structural deformation, modifying its band structure. This alteration leads to charge redistribution within the QD, giving rise to an additional dipole-electron-deformation interaction, which further strengthens the interaction between the QD and HSA (Fig. 29.2). Both mechanisms may operate simultaneously, reinforcing each other.

Thus, the electric charge in the QD is redistributed not only under the action of the electric field of the HSA dipole, but also due to localization in certain regions caused by the nonuniform deformation of the QD.

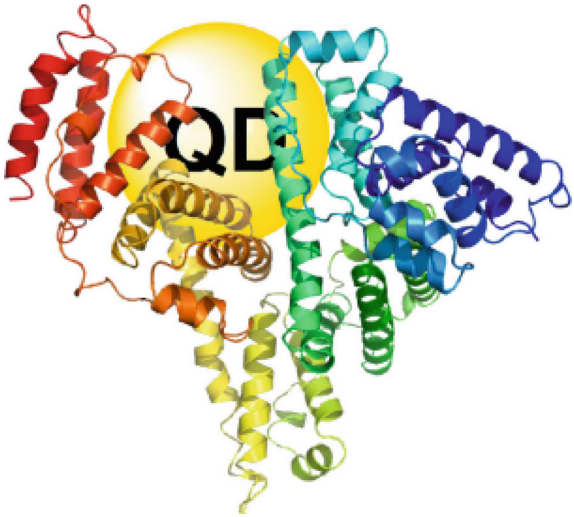

Fig. 29.1 Image of HSA protein interacting with the quantum dot surface, forming a QD–HSA biocomplex

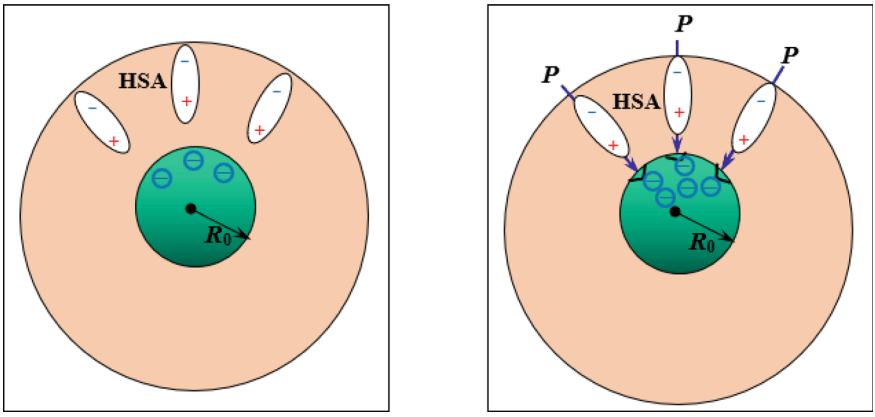

Fig. 29.2 Model of QD interacting with albumin molecules

Consider a spherical QD with radius R_0, which interacts with albumin molecules through an electric field. The electric field strength created by one molecule with dipole moment p along the dipole axis at a distance z from its center:

$$E_{HSA} = \frac{p}{2\pi\varepsilon_0 z^3}.$$

Then the interaction energy of albumin molecules and QS:

$$W_{el} = -\frac{p^2 R_0^3}{2\pi\varepsilon_0}\frac{\varepsilon - 1}{\varepsilon + 2}\frac{\theta N_{\max}}{(R_0 + l)^6}, \tag{29.4}$$

where ε is the dielectric constant; θ is the fraction of coating of the QD surface by HSA molecules; $N_{\max}$ is the number of possible states on the QD surface for HSA molecules (per 1 mol); l is the distance from the QD surface to the center of the HSA dipole.

The interaction force does generate a mechanical pressure on the quantum dot's (QD's) surface. The force represents the net attractive interaction between the dipole (from the albumin molecule) and the QD. When this force is applied, it acts over the contact area between the dipole and the QD, effectively creating a pressure.

This pressure can lead to a local deformation of the QD. Such deformation may alter the QD's band structure and its other electronic properties.

In [21] it is shown that this pressure can be determined by the formula:

$$P = \frac{N}{4\pi V R_0^2} p \frac{\mathrm{d}E}{\mathrm{d}r}_{|r=R_0}, \tag{29.5}$$

where N is the number of HSA molecules on the QD surface; E is the resulting electric field strength created both by dipolar HSA molecules and as a result of self-consistent spatial redistribution of electric charge.

Taking into account electron-deformation effects, the interaction energy between HSA molecules and QD can be determined as follows:

$$W_{int} = -pE\theta N_{\max}. \tag{29.6}$$

To determine the electric field strength E, we use the method of self-consistent electron-deformation coupling [21]. In what follows, we will consider the QD doped with a donor impurity with an average electron concentration n_0.

To find the deformation $\varepsilon^{(i)}$ of materials of quantum dot, the concentration of conduction electrons $n^{(i)}(r)$, the electric field strength and the electrostatic potential $\varphi^{(i)}(r)$, the self-consistent system of the following equations was solved:

(1) The equation for determining the displacements of atoms $u_r^{(1)}$ in the materials of the QD

$$\vec{\nabla}\mathrm{div}\,\vec{u} = 0 \tag{29.7}$$

with corresponding boundary conditions [28]

$$\sigma_{rr|r=R_0} + P_L(R_0) = -P, \tag{29.8}$$

where σ_{rr} is mechanical strain; $P_L(R_0) = \frac{2\gamma}{R_0}$ is the Laplace pressure, $\gamma = \frac{\gamma_{bulk}}{1+2\sigma/R_0}$.

The mechanical strain σ_{rr} in the QD is determined by the formula:

$$\sigma_{rr} = \frac{Y}{(1+\nu)(1-2\nu)}\big((1-\nu)\varepsilon_{rr} + \nu\big(\varepsilon_{\varphi\varphi} + \varepsilon_{\theta\theta}\big)\big), \tag{29.9}$$

where Y is Young's modulus; ν is Poisson's ratio.

Knowing the displacement, we determine the components of the deformation tensor of the materials of QD:

$$\varepsilon_{rr} = \partial u_r/\partial r, \quad \varepsilon_{\varphi\varphi} = \varepsilon_{\theta\theta} = u_r/r, \quad \varepsilon = \varepsilon_{rr} + \varepsilon_{\varphi\varphi} + \varepsilon_{\theta\theta}. \tag{29.10}$$

(2) The stationary Schrödinger equation

$$\left(-\frac{\hbar^2}{2m^*}\Delta - e\varphi(r) + a_c\varepsilon\right)\psi_n(r) = E_n\psi_n(r), \tag{29.11}$$

where m^* is the effective mass of the electron; a_c is the constant of hydrostatic deformation potential of the conduction band [29].

(3) The equation that determines the concentration of electrons $n^{(i)}(r)$

$$n(r) = \Sigma_n \frac{\psi_n^*(r)\,\psi_n(r)}{\exp(\beta_0(E_n - \mu)) + 1}, \tag{29.12}$$

where $\beta_0 = \frac{1}{k_B T}$; μ is the chemical potential.

(4) The Poisson equation, from which the electrostatic potential $\varphi(r)$ is determined,

$$\Delta\varphi(r) = \frac{e}{\varepsilon_d\varepsilon_0}(n(r) - n_0), \tag{29.13}$$

where ε_d is the relative dielectric permittivity of the QD.

(5) The law of conservation of electric charge.

$$\frac{1}{V}\int_V n(r)\mathrm{d}V = n_0. \tag{29.14}$$

Thus, the system of Eqs. (29.5), (29.7)–(29.14) makes it possible to find the spatial distribution of the charge concentration in QD and the electrostatic field in a self-consistent manner and, accordingly, to determine the interaction energy between QD and HSA molecules under the condition of the formation of a bionanocomplex.

29.4 Results of Calculations and Discussion of Results

Figure 29.3 shows the results of modeling the distribution of electric charge (in relative units) in a QD that forms a bionanocomplex with HSA molecules for different values of the QD radius and different values of the fraction of coating of the QD surface by HSA molecules.

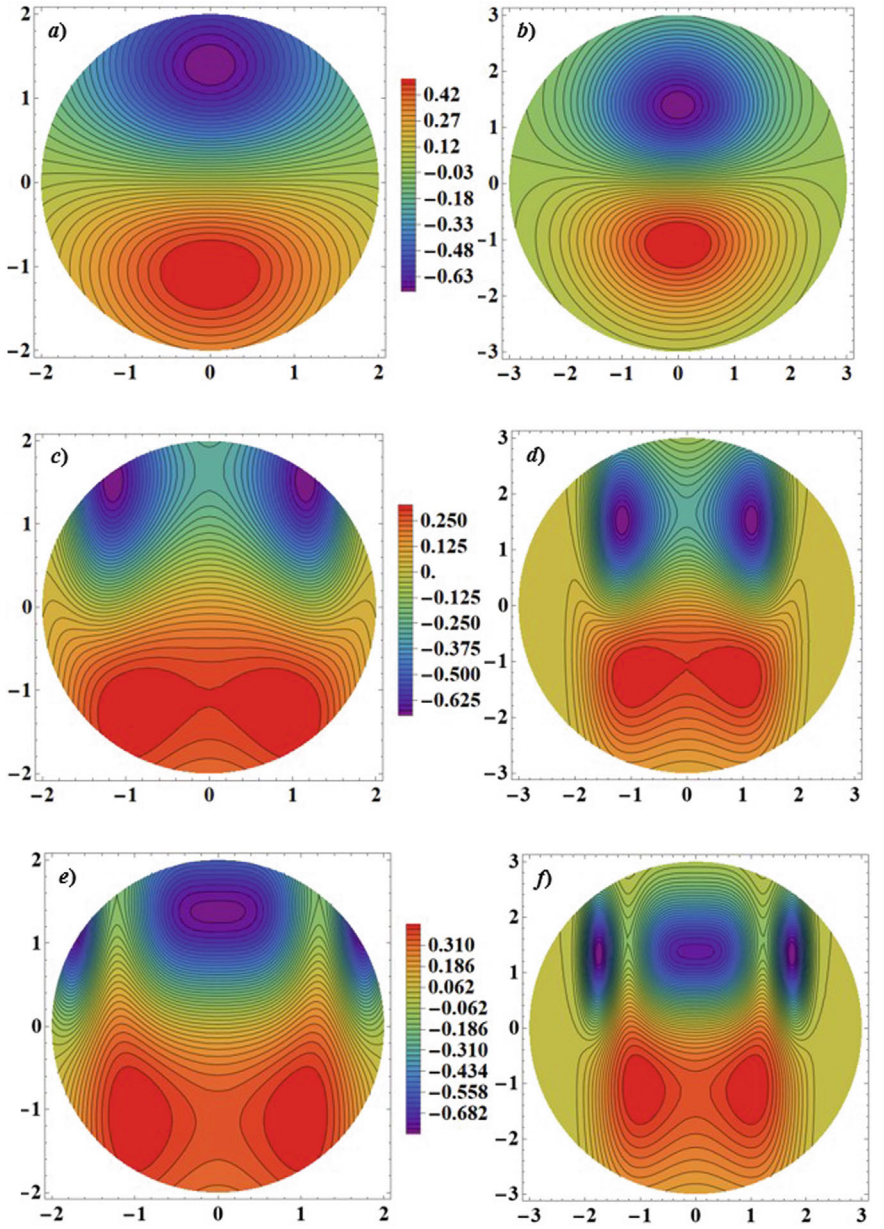

Fig. 29.3 Distribution of electric charge (in relative units) in a QD forming a bionanocomplex with HSA molecules at $R_0 = 2$ nm (**a**, **c**, **e**), 3 nm (**b**, **d**, **f**) and different values of the fraction of coating of the QD surface by HSA molecules: $\theta = 0.1$ (**a**, **b**); $\theta = 0.3$ (**c**, **d**); $\theta = 0.4$ (**e**, **f**)

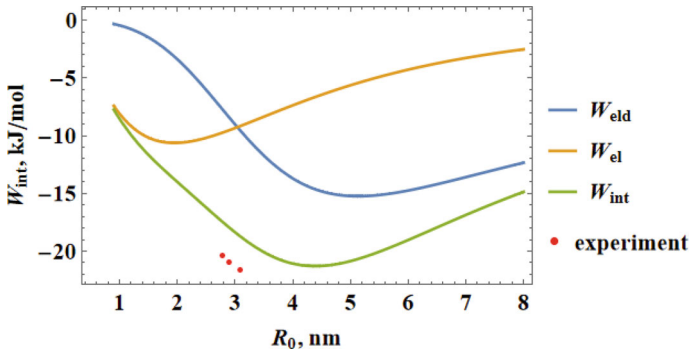

Fig. 29.4 Dependence of the interaction energy between QD and HSA on the radius of QD ($\theta = 0.4$)

Calculations were performed for CdTe QDs at $n_0 = 8 \cdot 10^{18}$ cm^{-3}. Increasing the QD radius from 2 to 3 nm leads to greater charge localization. This is due to the increased role of electron-deformation effects [21]. Increasing the number of HSA molecules involved in the forming of the bionanocomplex leads to the formation of several different regions with negative charge localization in the QD–HSA contact region. This is explained by the highly nonuniform distribution of deformation near the QD–HSA contact region. Electrons are localized in the region of relative stretching [21].

Figure 29.4 shows the dependence of the interaction energy W_{int} between the QD and HSA on the radius of the QD, calculated by Formula (29.6) taking into account the self-consistent electron-deformation interaction. In addition, a similar dependence W_{el} (calculated by Formula (29.4)) is given, which assumed only the interaction of the HSA dipole with the induced electric charge in the QD (without taking into account the electron-deformation interaction).

The contribution of the electron-deformation interaction W_{eld} was calculated as the difference $W_{eld} = W_{in} - W_{el}$. This figure also presents the experimental values of the change in free energy (Table 29.1).

As we can see, the value of W_{el} differs significantly from the experimental values. Even if we assume that there are additional charges on the QD surface, the character of the $W_{el}(r)$ dependence will still remain opposite. Namely, the experiment demonstrates that in the range of QD radii up to 3.1 nm, the value of the free energy decreases. And theoretical calculations according to Formula (29.4) show that already for radii greater than 1.6 nm, the free energy should increase. Taking into account the electron-deformation interaction gives a good match both qualitatively and quantitatively. The insignificant difference between the experimental and theoretical values can be explained by the presence of additional electric charges on the QD surface and the presence to a small extent of other mechanisms (for example, Van der Waals forces or hydrophobic interactions), except for the electrostatic one.

The role of the electron-deformation interaction increases with increasing QD radius, and becomes especially noticeable at radii larger than 2 nm.

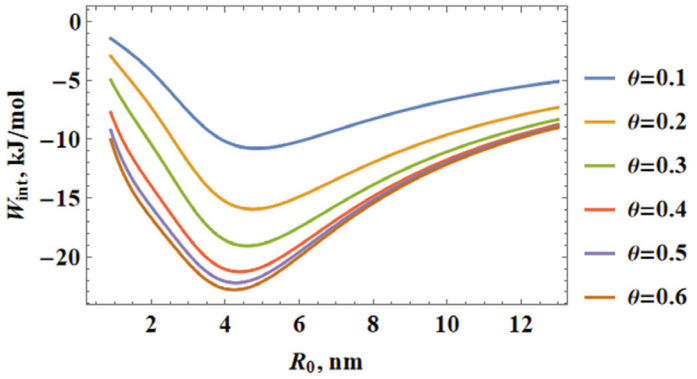

Fig. 29.5 Dependence of the interaction energy between QD and HSA on the QD radius at different values of the coating fraction of the QD surface by HSA molecules

Figure 29.5 shows the dependence of the interaction energy between QD and HSA on the QD radius at different values of the coating fraction of the QD surface by HSA molecules. As we can see, this dependence has a monotonic character with minima that shift towards smaller radii. From this we can conclude that when many molecules are bound to the QD surface for their radii greater than 4 nm, the formation of a bionanocomplex becomes energetically disadvantageous. But this fact requires additional experimental verification. Also, when the coating fraction of the QD surface by HSA molecules is increased, higher than 0.4, the interaction energy value practically does not change.

Figure 29.6 presents the graphical dependence of the electron-deformation component (a) and the purely electrostatic component (b) of the interaction energy between QD and HSA on the QD radius at different average electron concentration values in QD. The dependence of the electron-deformation interaction energy and the position of the minimum of the $W_{eld}(r)$ function on the electron density have a non-monotonic character (Fig. 29.6a). At low electric charge density, its increase leads to an increase in the interaction energy. On the contrary, at high electron concentration, an increase in the electric charge density leads to a decrease in the interaction energy. This fact is explained by the competing action of two factors: the redistribution of electrons under the action of the electric field and under the action of nonuniform deformation [30].

On the contrary, an increase in the electron density leads to a monotonic decrease in the electrostatic interaction energy between QD and HSA (Fig. 29.6b). The radius of the QD, at which the electrostatic interaction energy is minimal, is practically independent of the electron concentration in the QD.

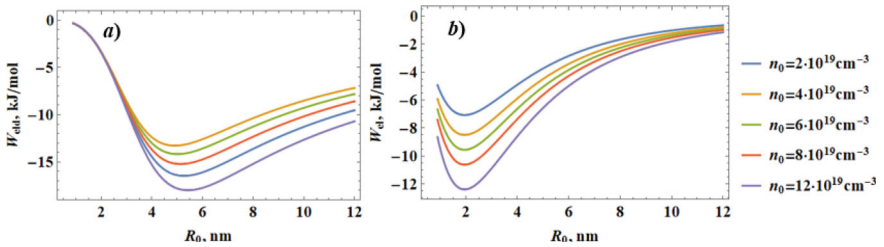

Fig. 29.6 Dependence of the electron-deformation component (**a**) and the purely electrostatic component (**b**) of the interaction energy between QD and HSA on the QD radius at different average values of the electron concentration in the QD

29.5 Results and Conclusions

The addition of the HSA to a colloidal solution of nanoparticles leads to a decrease in optical density and blurring of the exciton structure in the absorption spectra. This behavior indicates the interaction between the semiconductor nanoparticles and the HSA, with the formation of the corresponding bionanocomplexes. Moreover, the increase in the radius of nanoparticles leads to a corresponding increase in the biocompatibility of albumins with semiconductor quantum dots, which is manifested in the spectral dependences of the respective biocomplexes.

A model of QD interacting with HSA molecules has been developed. The proposed model takes into account the interaction of dipolar HSA molecules with QD through their polarization and electron-deformation interactions in a self-consistent manner.

Within the framework of the developed model, the dependence of the interaction energy of CdTe QD and HSA on the QD radius was investigated for different values of the electron concentration in the QD and the coating fraction of the QD surface by HSA molecules. The results of theoretical calculations are in good agreement with experimental data.

It has been shown that increasing the radius of CdTe QD to 4 nm leads to an increase in the probability of biocomplex forming.

The role of electron-deformation interaction in the formation of the CdTe QD–HSA bionanocomplex has been established. It has been shown that this interaction plays a crucial role at QD radius greater than 2 nm.

References

1. M. Akbari, M. Rahimi-Nasrabadi, S. Pourmasud, M. Eghbali-Arani, CdTe quantum dots prepared using herbal species and microorganisms and their anti-cancer, drug delivery and antibacterial applications; a review. Ceram. Int. **46**, 9979 (2020). https://doi.org/10.1016/j.ceramint.2020.01.051
2. A. Kumari, A. Sharma, R. Sharma, U. Malairaman, R.R. Singh, Biocompatible and fluorescent water based NIR emitting CdTe quantum dot probes for biomedical applications. Spectrochim.

Acta Part A Mol. Biomol. Spectrosc. **248**, 119206 (2021). https://doi.org/10.1016/j.saa.2020.119206
3. W. Liu, L. Wang, C. Zhang, Progress in quantum dot-based biosensors for microRNA assay: a review. Anal. Chim. Acta **1278**, 341615 (2023). https://doi.org/10.1016/j.aca.2023.341615
4. M.H. Elkomy, A.A. Ali, H.M. Eid, Chitosan on the surface of nanoparticles for enhanced drug delivery: a comprehensive review. J. Control. Release **351**, 923 (2022). https://doi.org/10.1016/j.jconrel.2022.10.005
5. J.G. Paithankar, S. Kushalan, S. Nijil, S. Hegde, S. Kini, A. Sharma, Systematic toxicity assessment of CdTe quantum dots in Drosophila melanogaster. Chemosphere **295**, 133836 (2022). https://doi.org/10.1016/j.chemosphere.2022.133836
6. A. Valizadeh, H. Mikaeili, M. Samiei, S.M. Farkhani, N. Zarghami, M. Kouhi, A. Akbarzadeh, S. Davaran, Quantum dots: synthesis, bioapplications, and toxicity. Nanoscale Res. Lett. **7**, 480 (2012). https://doi.org/10.1186/1556-276X-7-480
7. S. Chinnathambi, N. Abu, N. Hanagata, Biocompatible CdSe/ZnS quantum dot micelles for long-term cell imaging without alteration to the native structure of the blood plasma protein human serum albumin. RSC Adv. **7**(5), 2392 (2017). https://doi.org/10.1039/C6RA26592H
8. R. Wojnarowska-Nowak, J. Polit, A. Zięba, I.D. Stolyarchuk, S. Nowak, M. Romerowicz-Misielak, E.M. Sheregii, Synthesis and characterisation of human serum albumin passivated CdTe nanocrystallites as fluorescent probe. Micro Nano Lett **13**(3), 326 (2018). https://doi.org/10.1049/mnl.2017.0054
9. M. Diaz-Gonzalez, A. Escosura-Muniz, M. Fernandez-Arguelles, F. Alonso, J. Costa-Fernandez, Quantum dot bioconjugates for diagnostic applications. Top. Curr. Chem. **378**(2), 35 (2020). https://doi.org/10.1007/s41061-020-0296-6
10. A.N. Traverso, D.J. Fragale, D.L. Viale, O. Garate, P. Torres, G. Valverde, A. Berra, A.V. Torbidoni, J.S. Yakisich, M. Grasselli, Two-step preparation of protein-decorated biohybrid quantum dot nanoparticles for cellular uptake. Pharmaceutics **15**(6), 1651 (2023). https://doi.org/10.3390/pharmaceutics15061651
11. E.N. Hoogenboezem, C.L. Duvall, Harnessing albumin as a carrier for cancer therapies. Adv. Drug Deliv. Rev. **30**, 73 (2018). https://doi.org/10.1016/j.addr.2018.07.011
12. M. Kiarashi, S. Yasamineh, Albumin nanoparticles are a promising drug delivery system in dentistry. BioMed Eng. **23**, 122 (2024). https://doi.org/10.1186/s12938-024-01318-9
13. R. Yan, B.Q. Yu, M.M. Yin, Z.Q. Zhou, X. Xiang, X.L. Han, Y. Liu, F.L. Jiang, The interactions of CdTe quantum dots with serum albumin and subsequent cytotoxicity: the influence of homologous ligands. Toxicol. Res. (Camb). **7**(2), 147 (2018). https://doi.org/10.1039/c7tx00301c
14. J. Simon, S. Udayan, V.P.N. Nampoori, M. Kailasnath, Investigations on nonlinear optical properties and thermal diffusivity of gold nanoparticle embedded protein complex. Opt. Laser Technol. **138**, 106859 (2021). https://doi.org/10.1016/j.optlastec.2020.106859
15. N. Le, M. Zhang, K. Kim, Quantum dots and their interaction with biological systems. Int. J. Mol. Sci. **23**(18), 10763 (2022). https://doi.org/10.3390/ijms231810763
16. D. Kunachowicz, M. Ściskalska, M. Jakubek, R. Kizek, M. Kepinska, Structural changes in selected human proteins induced by exposure to quantum dots, their biological relevance and possible biomedical applications. NanoImpact **26**, 100405 (2022). https://doi.org/10.1016/j.impact.2022.100405
17. N. Le, K. Kim, Current advances in the biomedical applications of quantum dots: promises and challenges. Int. J. Mol. Sci. **24**(16), 12682 (2023). https://doi.org/10.3390/ijms241612682
18. A. Spada, J. Emami, J.A. Tuszynski, A. Lavasanifar, The uniqueness of albumin as a carrier in nanodrug delivery. Mol. Pharmaceutics **18**, 1862 (2021). https://doi.org/10.1021/acs.molpharmaceut.1c00046
19. W. Bai, K. Zhang, S. Yu, J. Zhang, L. Jin, The preparation of MnO_2/BSA/CdTe quantum dots complex for ratiometric fluorescence/T1-weighted MRI detection of H_2O_2. Talanta **252**, 123774 (2023). https://doi.org/10.1016/j.talanta.2022.123774
20. T.P.H. Hutapea, K.A. Madurani, M.Y. Syahputra, M.N. Hudha, A.N. Asriana, S.F. Kurniawan, Albumin: source, preparation, determination, applications, and prospects. J. Sci. Adv. Mater. Devices **8**, 00549 (2023). https://doi.org/10.1016/j.jsamd.2023.100549

21. O.V. Kuzyk, I.D. Stolyarchuk, O.O. Dan'kiv, R.M. Peleshchak, Baric properties of quantum dots of the type of core (CdSe)-multilayer shell (ZnS/CdS/ZnS) for biomedical application. Appl. Nanosci. **13**, 4727 (2023). https://doi.org/10.1007/s13204-022-02604-5
22. L. Lai, C. Lin, Z.-Q. Xu, H.-L. Han, Spectroscopic studies on the interactions between CdTe quantum dots coated with different ligands and human serum albumin. Spectrochim. Acta Part A Mol. Biomol. Spectrosc. **97**, 366 (2012). https://doi.org/10.1016/j.saa.2012.06.025
23. Q. Wang, W.Q. Chen, X.Y. Liu, Y. Liu, F.L. Jiang, Thermodynamic implications and time evolution of the interactions of near-infrared PbS quantum dots with human serum albumin. ACS Omega **6**(8), 5569 (2021). https://doi.org/10.1021/acsomega.0c05974
24. I.D. Stolyarchuk, A.I. Savchuk, R. Wojnarowska, J. Polit, Characterization of the interaction of CdTe quantum dots with human serum albumin by optical spectroscopic techniques. Sens. Electron. Microsyst. Technol. **12**(3), 40 (2015). http://nbuv.gov.ua/UJRN/seimt_2015_12_3_6
25. H.X. Zhou, X. Pang, Electrostatic interactions in protein structure, folding, binding, and condensation. Chem. Rev. **118**(4), 1691 (2018). https://doi.org/10.1021/acs.chemrev.7b00305
26. L. Jia, Y. Wang, Q. Nie, B. Liu, E. Liu, X. Hu, J. Fan, Aqueous-synthesis of $CuInS_2$ core and $CuInS_2$ /ZnS core/shell quantum dots and their optical properties. Mater. Lett. **200**, 27 (2017). https://doi.org/10.1080/15533174.2013.763275
27. W. Scheider, H.M. Dintzis, J.L. Oncley, Changes in the electric dipole vector of human serum albumin due to complexing with fatty acids. Biophys. J. **16**, 417 (1976). https://doi.org/10.1016/S0006-3495(76)85698-6
28. O. Kuzyk, O. Dan'kiv, R. Peleshchak, I. Stolyarchuk, Baric properties of CdSe-core/ZnS/CdS/ZnS-multilayer shell quantum dots. Phys. E Low-Dimensional Syst. Nanostruct. **143**, 115381 (2022). https://doi.org/10.1016/j.physe.2022.115381
29. Ch.G. Van de Walle, Band lineups and deformation potentials in the model-solid theory. Phys. Rev. B **39**, 1871 (1989). https://doi.org/10.1103/PhysRevB.39.1871
30. R.M. Peleshchak, O.V. Kuzyk, O.O. Dan'kiv, The deformation-diffusion mechanism of the formation of n-n+-transitions in semiconductors under the influence of pulsed laser irradiation. Roman. Rep. Phys. **73**, 506 (2021). https://rrp.nipne.ro/2021/AN73506.pdf

Chapter 30
Morphology of Nanostructure Formation on the Surface of CdI_2 Crystals

I. Rovetskii and H. Klym

Abstract The morphology and nanostructures of CdI_2 crystal surfaces have been studied. The surface features a hexagonal close-packed atomic arrangement. Atomic force microscopy revealed micro- and nanoscale structures, including steps, spirals, and channel-like depressions. Steps along basal planes likely result from edge dislocations and dislocation walls formed during crystal growth, while spirals arise from screw dislocations due to uneven impurity distribution causing local stress and lattice shifts. Prolonged air exposure leads to nanopore and nanocluster formation specifically on van der Waals surface steps. This suggests that the nanoscale dislocation relief in the basal anion plane is crucial for nanostructure formation.

30.1 Introduction

The surface morphology of crystals plays a pivotal role in determining their physicochemical properties and their suitability for applications in nanotechnology [1–5]. Among layered materials, cadmium iodide (CdI_2) crystals have attracted significant attention due to their unique structure and potential as templates for nanoscale systems [6–8]. The CdI_2 belongs to the family of layered transition metal halides, characterized by a hexagonal crystal structure with strong intralayer ionic-covalent bonding and weak interlayer van der Waals (vdW) interactions [9–12]. This structural anisotropy facilitates the exfoliation of CdI_2 into ultrathin layers and provides a versatile platform for studying surface phenomena and nanostructure formation [13–16].

The morphology of CdI_2 crystal surfaces, including features such as terraces, step edges, dislocations, and other defects, is known to significantly influence the nucleation, growth, and arrangement of nanostructures. These surface irregularities act

I. Rovetskii
Lviv State University of Life Safety, Lviv, Ukraine

H. Klym (✉)
Lviv Polytechnic National University, Lviv, Ukraine
e-mail: halyna.i.klym@lpnu.ua

O. Fesenko and L. Yatsenko (eds.), *Functional Nanomaterials, Nanocatalysts, Nanotechnologies, and Their Applications*, Springer Proceedings in Physics 321,
https://doi.org/10.1007/978-3-031-99136-3_30

as active sites for adsorption and self-assembly, playing a crucial role in the formation of functional nanostructures with desirable properties [17–19]. Several studies have highlighted the importance of controlling surface morphology to optimize the characteristics of nanostructures for applications in optoelectronics, catalysis, and sensing [20, 21].

The CdI_2 surfaces also exhibit unique electronic and optical properties that depend on their morphology [19, 22–24]. The presence of atomic steps and defects can modify the local electronic structure, impacting charge carrier dynamics and interaction with external stimuli. Recent advancements in surface-sensitive techniques, such as atomic force microscopy (AFM), scanning tunneling microscopy (STM), and X-ray photoelectron spectroscopy (XPS), etc. have enabled detailed characterization of these morphological features at the nanoscale [25–30]. These techniques have provided valuable insights into the relationship between surface structure and functional properties, paving the way for designing advanced nanodevices.

Furthermore, the formation of nanostructures on CdI_2 surfaces has been the subject of extensive research, as it holds promise for creating hybrid systems with tailored functionalities. Studies on the deposition of metals, semiconductors on CdI_2 surfaces have demonstrated the feasibility of engineering nanoscale systems with enhanced optical performance [31–33]. The ability to manipulate the surface morphology of CdI_2 provides a powerful tool for tuning the properties of these systems.

In this work, we focus on a comprehensive investigation of the morphological features of CdI_2 crystal surfaces and their role in the formation of nanostructures. By integrating experimental techniques, we aim to elucidate the mechanisms governing surface morphology and its impact on nanostructure formation. The findings of this study will contribute to the fundamental understanding of surface-driven phenomena and provide practical insights for the development of advanced nanomaterials.

30.2 Experimental

The studied CdI_2 single crystals were grown from the melt using the Bridgman-Stockbarger method and from the gas phase. The crystals obtained from the melt were in the form of cylindrical blocks with a diameter of 20 mm and a height of up to 50 mm. The raw materials used for crystal growth were further purified from impurities by the vertical zone melting method [10, 13].

When the salt was heated in a vacuum-sealed quartz tube to a temperature 80–100 °C below its melting point, crystal growth of cadmium iodide occurred on the cooler end of the tube from the gas phase. These crystals formed as thin plates with lateral dimensions of approximately 10 mm and a thickness of several tens of microns.

As demonstrated by X-ray diffractometry, CdI_2 exhibited intense diffraction reflections from the basal planes (001), (002), (003), (004), (005), and (006) of the hexagonal lattice of the CdI_2 single crystal (Fig. 30.1a). The interplanar spacing values were used to calculate the lattice c-parameter, with the true value determined

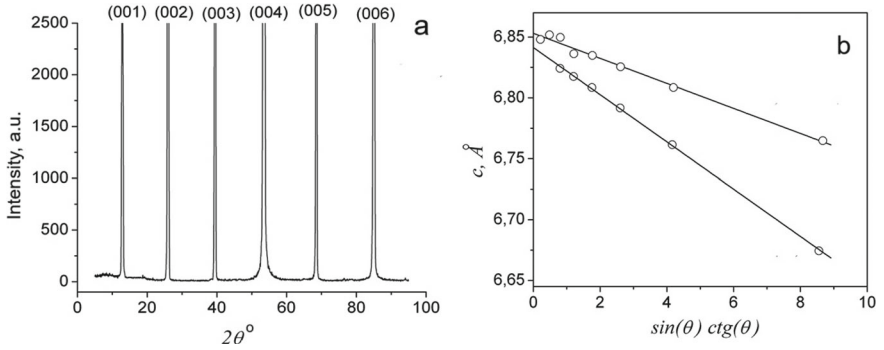

Fig. 30.1 X-ray diffraction patterns of CdI_2 crystals (**a**) and determination of the lattice c-parameter by the extrapolation method (**b**)

by graphical extrapolation using the Nelson–Riley function $f(\theta) = \sin(\theta)\cdot\cot(\theta)$ (Fig. 30.1b).

The value of the lattice c-parameter lies in the range of 6.841… 6.853 Å (Fig. 30.1b), indicating the formation of 2H polytypes of CdI_2. It is known [34] that when crystals are grown from the melt, the 4H polytype of CdI_2 always forms, whereas in crystals obtained from the gas phase, the formation of various polytypes, including the 2H structure, is possible.

The formation of the 2H polytype in CdI_2 crystals grown from the melt can be explained by a 4H → 2H phase transition, which occurs during prolonged storage of the crystals (longer than two years) [35].

The dependence of the lattice c-parameter value may be associated with the influence of uncontrolled impurities localized within the triple I-Cd-I layer or in the van der Waals (vdW) gaps [36]. The physical reason for the dependence of the c-parameter value on the impurity content lies in the weak interaction between the anions of two adjacent layers, which significantly affects the distance between them under the influence of external physical fields, such as temperature and mechanical stress [13].

For microscopic studies, samples were cleaved along the cleavage planes of CdI_2 crystals, forming flat, parallel plates with dimensions of 5 × 5 mm and a thickness not exceeding 1 mm. Both the surfaces and fresh cleavages of the obtained samples were studied. The surfaces were allowed to age in air for a certain period of time, while fresh cleavages were prepared by removing the top layers using adhesive tape. Single-crystal CdI_2 plates obtained from the gas phase were not subjected to prior mechanical processing.

For the study of the morphology and local properties of the sample surfaces, an AFM Solver P47-PRO was used. During the experiments, semi-contact probe sensors with rectangular cantilevers of stiffness 11.8 H/m were employed. The radius of curvature of the probe tip did not exceed 10 nm. The height resolution of the instrument was 0.1 nm [10, 13, 19].

AFM measurements of the morphology of micro- and nanostructures were performed in the semi-contact mode of the microscope. Electron microscopic images were obtained using the JSM-T220A microscope.

30.3 Results and Discussion

The surface morphology of freshly cleaved CdI_2 crystals is characterized by a hexagonal close packing of atoms, the distance between which within one layer (the a-lattice parameter) is 0.35 nm (Fig. 30.2), which is in good agreement with the XRD data.

The statistical characteristics of the crystal surface can be determined using the autocorrelation function of its digital microscopic image, which is calculated according to the following relation:

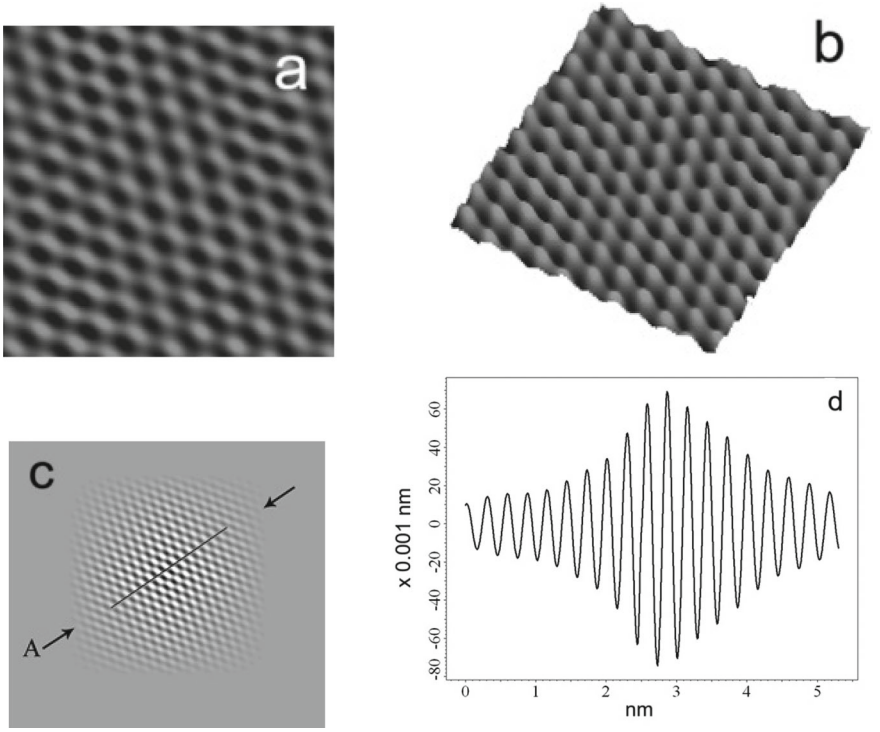

Fig. 30.2 AFM images of the surface morphology of CdI_2 crystals grown from the melt (**a**, **b**); (area sizes: 3 × 3 nm; height range: 3 nm) (**c**, **d**) autocorrelation function and its profile plotted along the A line

$$C(x, y) = \frac{1}{S} \int_S z(x, y) z(x + x', y + y') \mathrm{d}x\mathrm{d}y, \tag{30.1}$$

where z is the height distribution function; x, y are the coordinates of the point; S is the surface area.

The correlation function can be calculated numerically by the equation [37]:

$$C(x, y) = F^{-1}\{F^{-1}[z(x, y)]F[z(x, y)]\}, \tag{30.2}$$

where F and F^{-1} describe the forward and inverse discrete Fourier transforms.

In the case of a Gaussian distribution of irregularities, the statistical characteristics of the surface can be estimated by approximating the autocorrelation function of the surface by a Gaussian curve in the form:

$$C(\mathrm{r}) = \delta^2 e^{-r^2/\sigma^2}, \tag{30.3}$$

where δ and σ are the surface roughness and correlation length.

The autocorrelation function of the CdI_2 surface (Fig. 30.2c) is periodic with a period of ~ 0.3 nm (Fig. 30.2c, d), and its profile shows that the surface roughness value does not exceed 0.3 nm (Fig. 30.2d). The obtained value is less than the value of the c-parameter of the crystal lattice, so we can assume that the surface of the crystals is atomically smooth, which will be called the VdW surface in the future.

Atomic force microscopy methods revealed micro- and nanoscale structures formed in cadmium iodide crystals: steps of complex configuration (Fig. 30.3a, b), growth spirals (Fig. 30.4a, b) and channel-like depressions (Figs. 30.5 and 30.6).

The morphological features of the steps are nanoscale height and length, which reaches micron values. For example, the height of step A (Fig. 30.3b) is 6 nm, which is approximately 9 layer packages of I-Cd-I, and its length reaches 12 μm. The steps

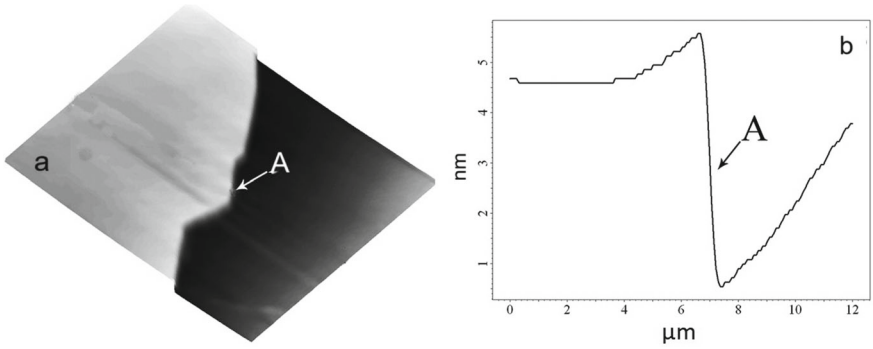

Fig. 30.3 AFM image of a nanoscale step formed in melt-grown CdI_2 crystals (**a**); step profile (area size: 12 × 12 μm; height range: 6 nm) (**b**)

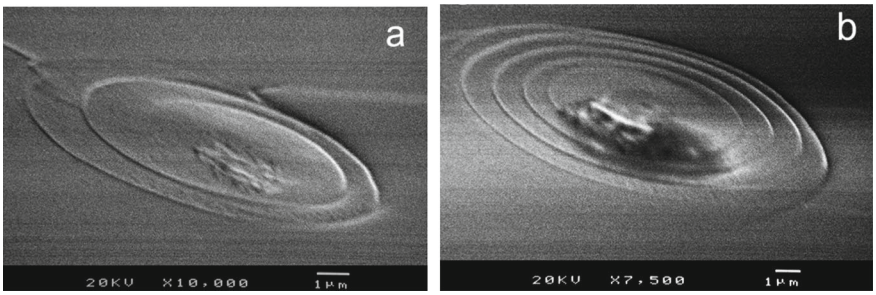

Fig. 30.4 Electron microscopic images of growth spirals formed in melt-grown CdI_2 crystals

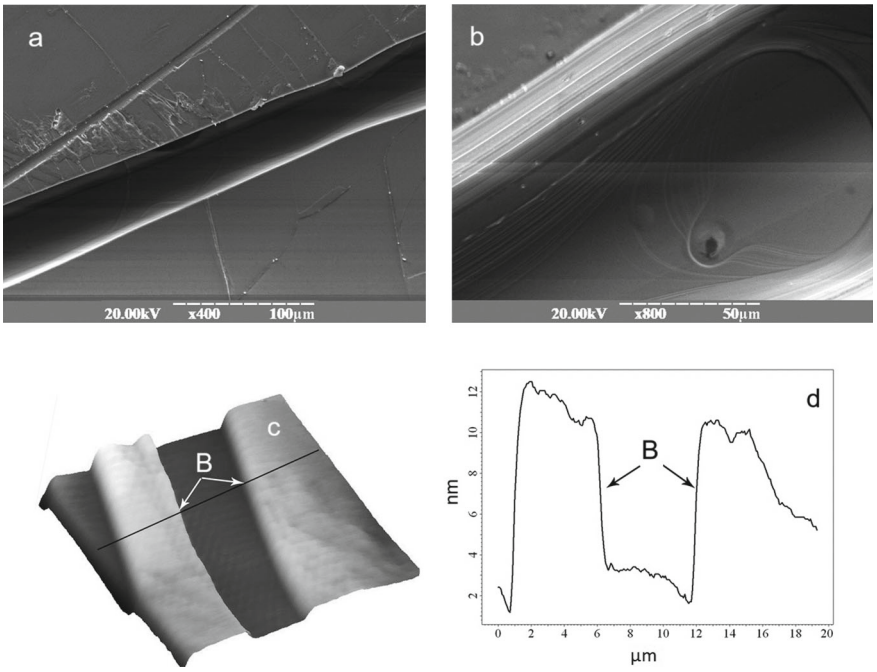

Fig. 30.5 Microscopic images of pores formed in melt-grown CdI_2 crystals: **a**, **b** SEM image of a micropore (**a**, **b**); AFM image of a nanopore and its profile; (area size: 20 × 20 µm; height range: 24 nm) (**c**, **d**)

intersect at angles that are multiples of 60°, which is characteristic of the hexagonal close-packed atoms of a layered crystal.

Figure 30.4a, b shows SEM images of growth spirals, which were first discovered in crystals grown from the melt. They consist of steps twisted into a spiral, the length of which is 4–5 µm, and the distance between them is 1 µm [15].

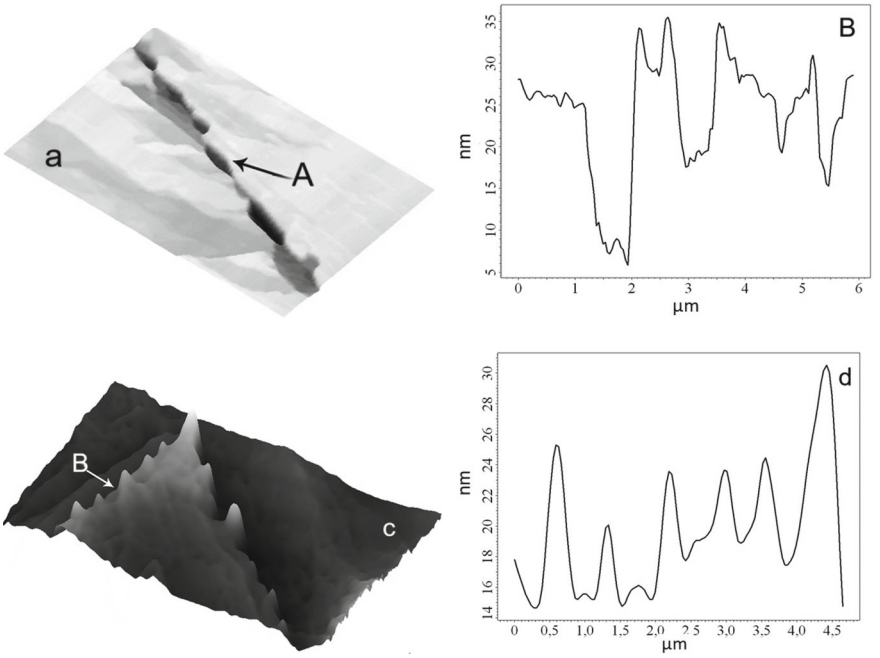

Fig. 30.6 Nanopores (**a**) and nanoclusters (**c**) formed on the steps of the vdW surface of CdI_2 crystals grown from the melt after long-term aging of the latter in an air atmosphere; **b**, **d** profiles of nanopores and nanoclusters; (area sizes: **a**—5.4 × 3.5 μm, **c**—5 × 9 μm; height range: **a**—44 nm, **c**—34 nm)

In the studied crystals, channel-shaped micro- and nanopores were found, formed in cadmium iodide crystals grown from the melt (Fig. 30.5). The lateral dimensions (length, width) of the micropores are 300 and 30 μm, respectively (Fig. 30.5a, b). The depth and width of the nanopores are 8 nm and 5 μm, respectively (Fig. 30.5c, d).

Steps formed along the CdI_2 basal planes most likely arise at the exits of edge dislocations and/or dislocation walls formed during crystal growth [10, 15]. Since the I-Cd-I basal planes at the defect exit points are held together not only by molecular but also by electrostatic forces, during crystal cleavage its delamination occurs mainly along planes with minimal defects, between which the bonding forces are the weakest [15, 29].

Growth spirals most likely arise at the exits of screw dislocations formed during crystal growth. The mechanism of their formation is associated with the influence of a number of factors (e.g., uneven distribution of uncontrolled impurities), which cause local internal stresses, under the action of which one part of it shifts relative to the other and the appearance of a step on the crystal surface. The step caused by a screw dislocation remains fixed at the dislocation exit point on the crystal surface,

and therefore it can move only by rotating around the dislocation axis, resulting in its twisting into a growth spiral [15].

AFM methods have established that when CdI_2 crystals are kept in air for a long time (30 days or more), nanostructures in the form of nanopores (Fig. 30.6a, b) and nanoclusters (Fig. 30.6c, d) are formed on the steps of the vdW surface.

Nanopores have a nanoscale depth within 5–30 nm, lateral dimensions that reach submicron values within 500–900 nm (Fig. 30.6b), and a shape close to hexagonal, characteristic of the hexagonal dense packing of atoms of cadmium iodide crystals.

Nanoclusters have a nanoscale height within 5–10 nm and submicron lateral dimensions within 300–500 nm (Fig. 30.6c, d). The steps on which nanostructures are formed intersect at an angle of ~ 60° (Fig. 30.6c).

To establish the mechanism of nanostructure formation, the morphology of the vdW surface of CdI_2 crystals was studied after their long-term exposure in an air atmosphere (Figs. 30.7 and 30.8).

Figure 30.7a shows an AFM image of the morphology of the vdW surface of CdI_2 crystals grown from the gas phase, aged in an air atmosphere for 30 days, on which the evolution of the formation of nanostructures is observed. At the first stage, nanosized pores are formed on the steps of the crystal surface (A in Fig. 30.8a). The

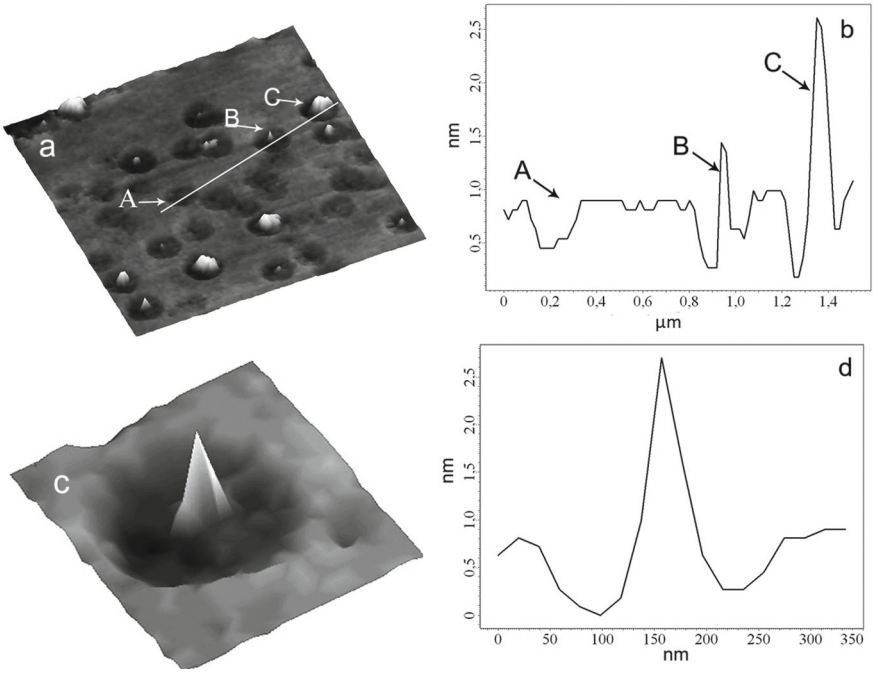

Fig. 30.7 AFM images of the morphology of the VdV surface of CdI_2 crystals grown from the gas phase, aged in an air atmosphere for a long time (30 days or more); **a** nanostructures: A—nanopore; B, C—nanoclusters; **b** nanocluster formed in a nanopore and their profiles (**c**); (area sizes: **a**—2 × 2 µm; **c**—320 × 350 nm; height range: **a**, **c**—3 nm)

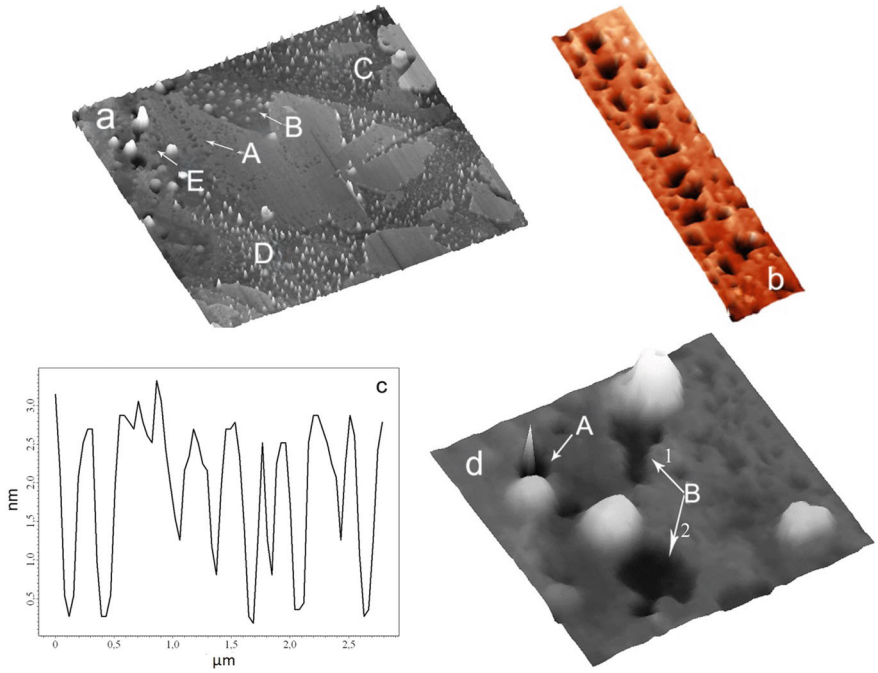

Fig. 30.8 AFM images of the morphology of the vdW surface of melt-grown CdI_2 crystals, aged in air for 30 days (**a**); **b**, **c** nanopores formed in area A and their profile; **d** nanocluster formed in a nanopore (A) and nanopores (B) (area sizes: **a**—10 × 10 µm, **b**—3.2 × 0.6 µm, **d**—2 × 2 µm; height range: **a**—30 nm, **b**—5 nm, **d**—30 nm)

average values of the diameters and depths of the formed nanopores are ~ 250 and ~ 0.5 nm (Fig. 30.7b), respectively [15]. At the next stage of formation, nanoclusters are nucleated in the nanopores (B, C in Fig. 30.7a, c). Their diameter at this stage does not exceed ~ 100 nm, and their height is ~ 2.5 nm (Fig. 30.7b, d).

Figure 30.8a shows an AFM image of the morphology of the vdW surface of CdI_2 crystals grown from the melt, aged in an air atmosphere for 30 days, on which the evolution of the formation of nanostructures is observed (areas A, B, C, D, E).

A characteristic feature of the morphology of area A is the presence of nanosized pores on it (Fig. 30.8a,b). The profile of the formed nanopores indicates that their depth and diameter do not exceed ~ 3 and 200 nm, respectively.

Nanocluster systems are observed in areas B, C, D (Fig. 30.8a). Analysis of their numerical characteristics (Table 30.1) indicates that they are at different stages of their evolution. The density of nanostructures formed in areas B, D does not exceed $13 \cdot 10^8$ cm^{-2} with cluster sizes of 70 nm.

Area D (Fig. 30.8c) is particularly interesting in the sense that it records the formation of a cluster with a diameter of 116 nm and a height of 30 nm on the boundary of

Table 30.1 Numerical characteristics of nanostructures formed on the surface of CdI_2 grown from the melt (areas B, C, D, and E in Fig. 30.8)

Area	B	C	D	E
Quantity	27	54	54	4
Average height (nm)	3	5	7	14
Average radius (nm)	51	34	39	140
Average height (nm)	300	200	200	800
Roughness (nm)	1.3	1.5	1.7	3.5

a pore with a diameter of ~ 230 nm and a depth of 8 nm (A in Fig. 30.7,c). In addition, this area contains "pure" nanopores without nanostructures (B in Fig. 30.7,c), similarly to area A (Fig. 30.7a, b).

The values of the surface roughness of the areas B, C, D, and E (Fig. 30.8) are given in Table 30.1, from which it can be seen that with an increase in the density of nanostructures and their sizes, the surface roughness of the areas also increases.

30.4 Conclusions

The morphology of the surface and micro- and nanostructures formed in CdI_2 crystals was studied. It was shown that it is characterized by a hexagonal close-packed arrangement of atoms, the distance between which within one layer is nm. Atomic force microscopy methods revealed micro- and nanoscale structures formed in CdI_2 crystals in the form of steps of complex configuration, spirals and channel-like depressions. The lateral dimensions (length, width) of the formed micropores are 300 and 30 μm, and the depth and width of the nanopores are 8 nm and 5 μm, respectively. The steps formed along the basal planes of CdI_2 most likely arise at the exits of edge dislocations and/or dislocation walls, which are formed during the crystal growth process. Growth spirals arise at the exits of screw dislocations, which are formed during the crystal growth process. The mechanism of their formation is associated with the influence of the uneven distribution of uncontrolled impurities, which cause local internal stresses, under the action of which one part of it shifts relative to the other and the appearance of a step on the crystal surface.

It is shown that during the exposure of CdI_2 crystals in air for a long time, nanopores and nanoclusters are formed on the steps of the vdW surface. Nanopores have a nanoscale depth within 5–30 nm, lateral dimensions that reach submicron values within 500–900 nm. Nanoclusters have a nanoscale height within 5–10 nm and submicron lateral dimensions within 300–500 nm. It has been established that the formation of nanostructures occurs only on the steps of the vdW surface of cadmium iodide, which implies that the nanoscale dislocation relief of the vdW surface, formed by a system of dislocations located in the basal plane of anions, is decisive for their formation.

Acknowledgements Authors would like to thanks the Ministry of Education and Science of Ukraine for providing support.

References

1. Y. Gao, W. Song, J. Yang, X. Ji, N. Wang, X. Huang, T. Wang, H. Hao, Crystal morphology prediction models and regulating methods. Crystals **14**(6), 484 (2024). https://doi.org/10.3390/cryst14060484
2. Z. Ahmad, A. Mishra, Growth of $PbBr_2$ microrods with unique structure and surface morphology. J. Mater. Sci. Mater. Electron. **31**(6), 4672–4676 (2020). https://doi.org/10.1007/s10854-020-03019-0
3. H. Klym, A. Ingram, O. Shpotyuk, O. Hotra, A.I. Popov, Positron trapping defects in free-volume investigation of Ge–Ga–S–CsCl glasses. Radiat. Meas. **90**, 117–121 (2016). https://doi.org/10.1016/j.radmeas.2016.01.023
4. S. Kaur, V.K. Chalotra, R. Jasrotia, V. Bhasin, Suman, S. Kumari, S. Thakur, J. Ahmed, A. Mehtab, T. Ahmad, R. Singh, S.K. Godara, Spinel nanoferrite ($CoFe_2O_4$): the impact of Cr doping on its structural, surface morphology, magnetic, and antibacterial activity traits. Opt. Mater. **133**, 113026 (2022). https://doi.org/10.1016/j.optmat.2022.113026
5. H. Klym, A. Ingram, O. Shpotyuk, Free-volume nanostructural transformation in crystallized GeS_2–Ga_2S_3–CsCl glasses. Materialwiss. Werkstofftech. **47**(2–3), 198–202 (2016). https://doi.org/10.1002/mawe.201600476
6. B. Kumar, N. Sinha, Micromorphology of pure and PbI_2-doped CdI_2 dendritic single crystals. Cryst. Res. Technol. J. Exp. Ind. Crystallogr. **40**(9), 887–892 (2005). https://doi.org/10.1002/crat.200410451
7. Z. Yan, K. Yin, Z. Yu, X. Li, M. Li, Y. Yuan, X. Li, K. Yang, X. Wang, L. Wang, Pressure-induced band-gap closure and metallization in two-dimensional transition metal halide CdI_2. Appl. Mater. Today **18**, 100532 (2020). https://doi.org/10.1016/j.apmt.2019.100532
8. S. Kawabata, H. Nakagawa, Life-time resolved emission spectra in CdI_2 crystals. J. Lumin. **126**(1), 48–52 (2007). https://doi.org/10.1016/j.jlumin.2006.05.006
9. L. Niu, Y. Li, M. Zhao, Z. Liu, M. Zhang, C. Ding, Z. Dou, Y. She, K. Zhang, Z. Luo, L. Zhang, S. Wang, Van der Waals template-assisted low-temperature epitaxial growth of 2D atomic crystals. Adv. Func. Mater. **32**(35), 2202580 (2022)
10. I.M. Bolesta, I.N. Rovetskyj, M.V. Partyka, I.D. Karbovnyk, B.Y. Kulyk, Formation of nanostructures on the VdW-surface of CdI_2 crystals. Ukr. J. Phys. **58**(5), 490–496 (2013). https://doi.org/10.1002/adfm.202202580
11. X. Bai, Q. Jiang, P. Song, Z.P. Jia, S. Lu, Z.K. Gao, S.H. Lang, H. Cui, R. Feng, Z.Y. Liang, Q. Kang, H.K. Yuan, Study of electronic and optical properties of CdI_2 modulated by electric field: a first-principles study. Opt. Express **31**(19), 31504–31521 (2023). https://doi.org/10.1364/OE.497833
12. Z. Shao, X. Wang, H. Qiu, H. Sun, Y. Cao, X. Wu, X. Chen, Phonon mode softening and band convergence induced significant enhancement of thermoelectric performance in strained CdI_2-type SnI_2 monolayer. Results Phys. **58**, 107541 (2024). https://doi.org/10.1016/j.rinp.2024.107541
13. I.M. Bolesta, I.N. Rovetskii, Z.M. Yaremko, I.D. Karbovnyk, S.R. Velgosh, M.V. Partyka, N.V. Gloskovskaya, V.M. Lesivtsiv, On the mechanism of nanostructure growth on the surface of CdI_2 crystals. Ukr. J. Phys. **60**(11), 1143–1143 (2015)
14. N. Sallacan, R. Popovitz-Biro, R. Tenne, Nanoparticles of CdI_2 with closed cage structures obtained via electron-beam irradiation. Solid State Sci. **5**(6), 905–908 (2003). https://doi.org/10.1016/S1293-2558(03)00110-9

15. I.M. Bolesta, I.N. Rovetskii, I.D. Karbovnik, S.V. Rykhlyuk, M.V. Partyka, N.V. Gloskovskaya, Formation and optical properties of CdI_2 nanostructures. J. Appl. Spectrosc. **82**, 84–90 (2015). https://doi.org/10.1007/s10812-015-0068-1
16. M.I. Miah, J. Kasperczyk, Cu-doping effects in CdI_2 layered nanostructures: the role of photoinduced electron-phonon anharmonic interactions. Appl. Phys. Lett. **94**(5), 053117 (2009). https://doi.org/10.1063/1.3077171
17. R. Popovitz-Biro, N. Sallacan, R. Tenne, CdI_2 nanoparticles with closed-cage (fullerene-like) structures. J. Mater. Chem. **13**(7), 1631–1634 (2003). https://doi.org/10.1039/B302505E
18. I. Aguiar, A. Olivera, M. Mombrú, H.B. Pereira, L. Fornaro, Novel bismuth tri-iodide nanostructures obtained by the hydrothermal method and electron beam irradiation. J. Cryst. Growth **457**, 244–249 (2017). https://doi.org/10.1016/j.jcrysgro.2016.06.024
19. I.M. Bolesta, I.N. Rovetskii, S.R. Velgosh, S.V. Rykhlyuk, I.D. Karbovnyk, N.V. Gloskovskaya, Morphology and optical properties of nanostructures formed in non-stoichiometric CdI_2 crystals. Ukr. J. Phys. **63**(9), 816–816 (2018)
20. K. Zhang, C. Ding, B. Pan, Z. Wu, A. Marga, L. Zhang, H. Zeng, S. Huang, Visualizing van der Waals epitaxial growth of 2D heterostructures. Adv. Mater. **33**(45), 2105079 (2021). https://doi.org/10.1002/adma.202105079
21. M. Ghanbari, F. Ansari, M. Salavati-Niasari, Simple synthesis-controlled fabrication of thallium cadmium iodide nanostructures via a novel route and photocatalytic investigation in degradation of toxic dyes. Inorg. Chim. Acta **455**, 88–97 (2017). https://doi.org/10.1016/j.ica.2016.10.015
22. I.A. Kariper, Structural, optical and porosity properties of CdI_2 thin film. J. Market. Res. **5**(1), 77–83 (2016). https://doi.org/10.1016/j.jmrt.2015.10.005
23. Q.J. Liu, Z.T. Liu, L.P. Feng, Calculations of structural, elastic, electronic, and optical properties of trigonal CdI_2. Phys. Status Solidi B **248**(7), 1629–1633 (2011). https://doi.org/10.1002/pssb.201046481
24. I.M. Bolesta, N.V. Gloskovskaya, M.R. Panasyuk, I.N. Rovetskii, L.I. Yaritskaya, Extrinsic luminescence centers in CdI_2 crystals doped with PbI_2 (10^{-4} to 1 mol%). Inorg. Mater. **49**, 214–218 (2013). https://doi.org/10.1134/S0020168513020039
25. A. Majid, M. Bibi, A. Majid, M. Bibi, Cadmium-based nanomaterials, in Cadmium Based II-VI Semiconducting Nanomaterials: Synthesis Routes and Strategies (2018), pp. 7–41. https://doi.org/10.1007/978-3-319-68753-7_2
26. I. Karbovnyk, I. Borshchyshyn, Y. Vakhula, I. Lutsyuk, H. Klym, I. Bolesta, Impedance characterization of Cr^{3+}, Y^{3+} and Zr^{4+} activated forsterite nanoceramics synthesized by sol–gel method. Ceram. Int. **42**(7), 8501–8504 (2016). https://doi.org/10.1016/j.ceramint.2016.02.075
27. Q. Liu, H. Hua, W. Wei, X. Huang, J. Yang, Q. Lu, H. Lu, Y. Liu, Efficient interfacial charge separation in graphene quantum dots/tin disulfide hybrids for improved photoelectrochemical performance. Ionics **30**(9), 5611–5621 (2024). https://doi.org/10.1007/s11581-024-05647-6
28. H. Klym, I. Karbovnyk, S. Piskunov, A.I. Popov, Positron annihilation lifetime spectroscopy insight on free volume conversion of nanostructured $MgAl_2O_4$ ceramics. Nanomaterials **11**(12), 3373 (2021). https://doi.org/10.3390/nano11123373
29. I. Karbovnyk, I. Bolesta, I. Rovetskii, S. Velgosh, H. Klym, Studies of CdI_2-Bi_3 microstructures with optical methods, atomic force microscopy and positron annihilation spectroscopy. Mater. Sci.-Pol. **32**, 391–395 (2014). https://doi.org/10.2478/s13536-014-0215-z
30. H. Klym, I. Karbovnyk, A. Luchechko, Y. Kostiv, V. Pankratova, A.I. Popov, Evolution of free volumes in polycrystalline $BaGa_2O_4$ ceramics doped with Eu^{3+} ions. Crystals **11**(12), 1515 (2021). https://doi.org/10.3390/cryst11121515
31. P. Tyagi, A.G. Vedeshwar, N.C. Mehra, Thickness dependent optical properties of CdI_2 films. Phys. B **304**(1–4), 166–174 (2001). https://doi.org/10.1016/S0921-4526(01)00392-1
32. I.S. Yahia, M. Shapaan, Y.A. Ismail, A.M. Aboraia, E.R. Shaaban, Thickness dependence of structural and optical properties of cadmium iodide thin films. J. Alloy. Compd. **636**, 317–322 (2015). https://doi.org/10.1016/j.jallcom.2015.02.181
33. R.S. Rawat, P. Arun, A.G. Vedeshwar, P. Lee, S. Lee, Effect of energetic ion irradiation on CdI_2 films. J. Appl. Phys. **95**(12), 7725–7730 (2004). https://doi.org/10.1063/1.1738538

34. S.K. Chaudhary, H. Kaur, Study of cracks and phase transitions in cadmium iodide crystals using X-ray diffraction. J. Phys. Conf. Ser. **226**(1), 012017 (2010). https://doi.org/10.1088/1742-6596/226/1/012017
35. V.S. Harutyunyan, Analytic dependence of the madelung constant on lattice parameters for 2D and 3D metal diiodides (MI_2) with CdI_2 (2H polytype) layered structure. Mater. Res. Express **7**(2), 026301 (2020). https://doi.org/10.1088/2053-1591/ab6fa9
36. M. Zhao, S. Yang, K. Zhang, L. Zhang, P. Chen, S. Yang, T. Zhai, A universal atomic substitution conversion strategy towards synthesis of large-size ultrathin nonlayered two-dimensional materials. Nano-Micro Lett. **13**, 1–13 (2021). https://doi.org/10.1007/s40820-021-00692-6
37. R. Strzalka, I. Buganski, J. Wolny, Statistical approach to diffraction of periodic and non-periodic crystals. Crystals **6**(9), 104 (2016). https://doi.org/10.3390/cryst6090104

Chapter 31
Diagnostics of Nanoscale Defects in Single Crystals by X-Ray Acoustic Method

V. B. Molodkin, G. I. Nizkova, T. P. Vladimirova, Y. V. Vasylyk, A. O. Bilotska, I. I. Demchik, L. I. Makarenko, S. V. Lizunova, V. V. Molodkin, I. M. Zabolotnyy, and V. V. Lizunov

Abstract A semi-phenomenological model of the dependence of the total integrated intensity of dynamical diffraction on the ultrasonic amplitude was proposed and X-ray acoustic diagnostics of the characteristics of microdefects in single crystals was performed using it. It is shown that tthe dependences of the coherent and diffuse components of the total integrated intensity of dynamical diffraction on the ultrasonic amplitude can be significantly different.

31.1 Introduction

Since most modern nanosystems are multi-parametrical and contain defects of many types simultaneously, it is necessary to use the theory of multiple (dynamical) scattering to establish the characteristics of the defect structure for such systems.

Unlike the kinematical theory, the sum and ratio of the diffuse and Bragg components of the total integrated intensity of dynamical diffraction, according to the dynamical theory, become dependent on both the parameters of the defect structure and the diffraction conditions. Moreover, the dependences of the Bragg and diffuse components of the total integrated intensity of dynamical diffraction on the both parameters of defects and diffraction conditions are fundamentally different. This provides the diagnostic capabilities of the total integrated intensity dynamical diffraction method.

In [1], the general physical nature of phenomena and effects that provide improved sensitivity and informativeness of diagnostics during the transition from kinematical diffraction to dynamical one was established and investigated. In [2], theoretical foundations of dispersion multiparametrical diagnostics based on phase-variable principles were created.

V. B. Molodkin · G. I. Nizkova · T. P. Vladimirova · Y. V. Vasylyk · A. O. Bilotska · I. I. Demchik · L. I. Makarenko · S. V. Lizunova (✉) · V. V. Molodkin · I. M. Zabolotnyy · V. V. Lizunov
G.V. Kurdyumov Institute for Metal Physics of the N.A.S. of Ukraine, Kyiv, Ukraine
e-mail: svetlana.lizunova@gmail.com

O. Fesenko and L. Yatsenko (eds.), *Functional Nanomaterials, Nanocatalysts, Nanotechnologies, and Their Applications*, Springer Proceedings in Physics 321,
https://doi.org/10.1007/978-3-031-99136-3_31

As shown by a detailed analysis of solutions of homogeneous equations for dynamical Bragg and inhomogeneous equations for dynamical diffuse waves, the influence of both structural imperfections and diffraction conditions on the Bragg component due to the dispersion mechanism is fundamentally different from their influence on the diffuse component. Therefore, the total integrated intensity of dynamical diffraction from a crystal with defects (TIIDD) differs by orders of magnitude from the integrated intensity of dynamical diffraction (IIDD) from an ideal crystal. In addition, it was found that, unlike the kinematical case, the diffraction conditions (wavelength, object thickness, geometry, and asymmetry angles) determine the nature of the effect of defects. This allows, by purposefully changing the diffraction conditions, to control the relative contributions of the Bragg and diffuse components, as well as contributions from imperfections of various types, i.e., to control the nature of the influence of imperfections on the scattering pattern by changing the diffraction conditions.

Thus, the main principle of solving the problem of unambiguous multiparametric (phase-variant) diagnostics, developed on the basis of the dynamic dispersion mechanism, is to selectively ensure maximum amplification of the manifestation of each of the many types of defects and other imperfections of crystals in the scattering patterns by controlled changes in diffraction conditions.

31.2 X-Ray Acoustic Method for Diagnostics of Defects in Single Crystals

The ultrasonic wave field in a single crystal creates a sinusoidal deformation field of atomic displacements. This field is characterized by the displacement amplitude W, which determines the degree of crystal distortion, and the wavelength λ_s, with W and λ_s easily varying over wide ranges. In the classic work [3], an increase in the number and brightness of spots on the Lauegram was first observed, which was enhanced with an increase in the amplitude of oscillations W, under the influence of ultrasonic, excited piezoelectrically in a quartz crystal plate, at frequencies close to resonant ones.

In this case, the condition for mechanical resonance of the sample is the equality $n\lambda_s/2 = T$, where T is the sample thickness.

To explain this phenomenon, the crystal under the influence of ultrasonic vibrations was considered as a perfect crystal with a modified lattice [4–6]. For small amplitudes of an ultrasonic wave ($|HW| < 1$, where $\mathbf{H}$ is the reciprocal lattice vector), the problem of X-ray diffraction was solved within the framework of perturbation theory, which made it possible to establish the amplitude dependences of integral reflections, the nature of the change in the extinction length, etc.

Although perturbation theory is not applicable for strong lattice distortions ($|HW| \gg 1$), in this case the amplitude dependences of integral reflections were also calculated and the intensity values at the kinematic scattering limit ($|HW| >$

$(\pi T/\Lambda)^2$, where Λ is the extinction length) were shown [7, 8]. When this criterion is met, the reciprocal lattice contains a system ~ 2 $|HW|$ of satellites $H \pm nK_s$, for each of which the extinction length exceeds the crystal thickness. Summing the integral reflections of the satellites leads to the well-known expression for the intensity of the integral reflection of a perfectly mosaic crystal. In strongly excited crystals for any λ_s, the main mechanism for increasing intensity is the emergence of higher-order satellites.

The fact theoretically established in [8] that at small amplitudes of the electrical signal on the piezoelectric transducer, the nature of the change in the $I(x)$ profiles with increasing ultrasonic amplitude in the short-wave case is significantly different from the resonant and long-wave cases was experimentally confirmed in [9]. At the same time, for the resonant and long-wavelength cases, the behavior of the experimental dependences $I(x)$ turned out to be similar in general terms. For $\lambda_s < \Lambda$, the X-ray beam localizes the superlattices created by ultrasonic, and the main mechanism for increasing the intensity is the emergence of satellites and the growth of their structural factors. The increase in the reflex intensity in the ultrasonic-distorted crystal occurs along most of the base of the Bormann delta. For $\lambda_s > \Lambda$, the increase in $I(x)$ is observed only in its central part, while on the periphery of the Bormann delta the intensity decreases. The indicated differences in the $I(x)$ curves gradually disappear with further increase in the ultrasonic amplitude.

Another dependence of $I(x)$ is observed in the region of X-ray acoustic resonance. Acoustic vibrations, whose wavelength is equal to the extinction length, lead to a strong increase in the intensity of the diffracted radiation in a narrow angular region in the center of the Bormann delta, which can be interpreted as focusing of the X-ray beam by X-ray acoustic resonance [10]. The resonance here is due to the interferometric amplification of interband scattering when the quasi-momentum conservation law is fulfilled $K_S = \Delta K_0$ (therefore, $\lambda_s = \Lambda$), where K_S is the ultrasonic wave vector; $K_S = 2\pi/\lambda_S$; ΔK_0 is the minimal splitting of the dispersion surface; $\Delta K_0 = 2\pi/\Lambda$.

It should be noted that in an acoustically excited crystal there are two competing mechanisms of influence of ultrasonic vibrations on the X-ray intensity (an increase in the angular reflection region and an increase in the level of X-ray absorption). It is believed that the second mechanism prevails at small values W and is pronounced in conditions of X-ray acoustic resonance.

It was shown in [11] that the experimental separation of the contributions of Bragg and diffuse scattering can be performed by using the dependence of the reflection intensity on the amplitude of ultrasonic excited in the crystal under conditions of X-ray acoustic resonance, i.e. when the wavelength of the transverse ultrasonic field λ_S is equal to the extinction length Λ.

Under conditions of X-ray acoustic resonance, the Bormann effect in a sufficiently thick absorbing crystal is almost completely suppressed even by weak oscillations with the amplitude W by order 10^{-10} cm. The authors of [11] assumed that, since the angular interval of diffuse scattering is much larger than the angular interval of both Bragg dynamical diffraction and the diffraction region formed by ultrasonic action, ultrasonic excitation should not affect the intensity of diffuse scattering. However,

the effect of ultrasonic vibrations on the diffuse component of the total integrated intensity of dynamical diffraction (TIIDD) can be significant and also different for different types of microdefects that may be present in real single crystals.

31.3 The Theoretical Model of the Dependences of the Total Integrated Intensity of Dynamical Diffraction on the Ultrasonic Amplitude

To describe the deformation dependence of the total integrated intensity of dynamical diffraction of single crystals with microdefects, the authors proposed a semi-phenomenological model in [12]:

$$R = R^{\mathrm{coh}} + R^{\mathrm{dif}}(1 + 1.65(\alpha'/\alpha)BT + 1.6(\beta'/\beta)B^2T^2)\exp(-6.97 \cdot 10^{12}(\gamma'/\gamma)\left|1/r\right|^2\sqrt{M_0} + \mu_0 l\Lambda\delta/r), \quad (31.1)$$

where r is the radius of curvature of an elastic bending, BT is an effective deformation, M_0 is the absorption. The values of the coefficients α, β, γ, δ and α′, β′, γ′, δ′ are selected by fitting the dependencies calculated using model (31.1) to the theoretical and experimental deformation dependences of integrated intensity of dynamical diffraction.

In [12] the following phenomenological relations were found for the coefficients α, β, γ, δ and α′, β′, γ′, δ′:

$$\begin{aligned} \alpha'/\alpha &= 0, \\ \beta'/\beta &= 0,73(R_{\max}/\Lambda)/L, \\ \gamma'/\gamma &= 0,0779/L, \\ \delta'/\delta &= 75,1 \cdot 10^5(R_{\max}/\Lambda)^{3/2}, \end{aligned} \quad (31.2)$$

where $R_{\max}$ is the the largest of the values of the average cluster radii R_{cl}, loop radii R_{l} and small loop radii $R_{\mathrm{sm.l.}}$, L is Krivoglaz factor (static Debye–Waller factor).

To adapt the proposed model to the case of X-ray acoustic diagnostics, by analyzing the experimental dependences of the TIIDD on the ultrasonic amplitude obtained for single crystals with different defect structures in the "thin" and "thick" crystal approximations, the expression was empirically established that allows us to correlate the voltage on the piezoelectric transducer with the radius of the cylindrical bending of the sample.

The established expression has the form:

$$1\ \mathrm{V} = 0.1887 \cdot 10^7/\left(r\cos^2\theta_{\mathrm{B}}\right)\left(\mu\mathrm{m}^{-1}\right), \quad (31.3)$$

where θ_{B} is the Bragg angle.

Figures 31.1, 31.2, 31.3 and 31.4 illustrate the results of the specified analysis.

It was considered Si samples with thickness 7110 μm. Clusters Cu_3Si were formed in the silicon sample under study as a result of copper decoration of dislocation loops that were present in it after growth. To observe the distribution (topography) of dislocations in crystals, the fact that dislocations in some cases are centers of precipitation in supersaturated solid solutions is used. The dislocation structure is decorated with precipitates during appropriate heat treatment of the crystal, into which an excess of an impurity is introduced (specifically for this purpose) by additive solution methods, the solubility of which is either completely insignificant or significantly dependent on temperature. The purpose of such decoration is to increase the contrast of the images of the specified dislocation loops on the X-ray topograms of dynamically scattering single crystals. But introducing copper into a sample with the aim of detecting defects already existing in it leads to the formation of new defects.

The example of the studied sample shows that the influence of decorating defects on the value of the TIIDD depends on the initial defect structure of the sample. The concentration of decorating clusters Cu_3Si formed in the sample is proportional to

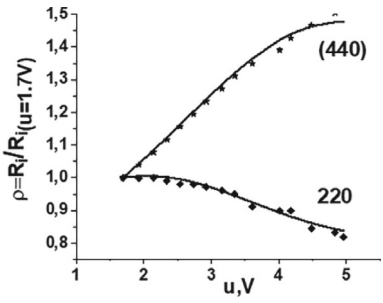

Fig. 31.1 The dependences of total integrated intensity of dynamical diffraction normalized to the intensity value at u = 1.7 V on an ultrasonic vibration amplitude, (AgK_α, (220) and (440) reflections)

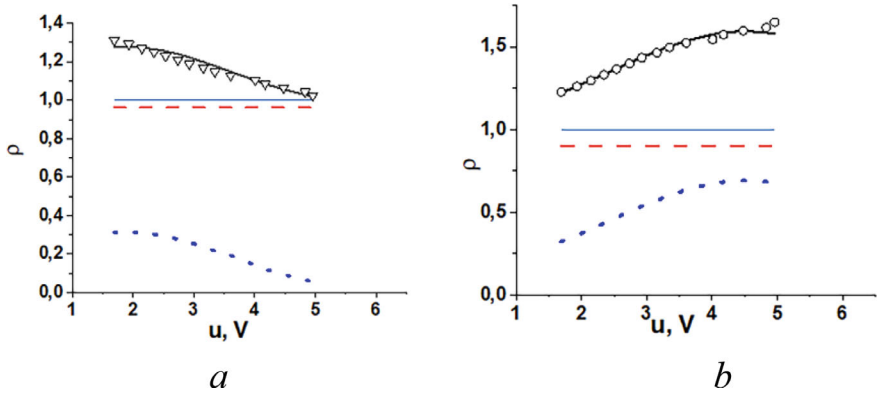

Fig. 31.2 The dependences of TIIDD and its components normalized to the dependences of the integrated intensity of dynamical diffraction of a perfect crystal on an ultrasonic amplitude: **a** AgK_α, (220) reflection, **b** AgK_α, (440) reflection

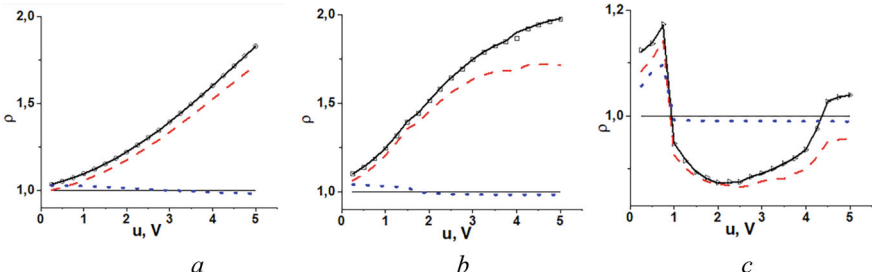

Fig. 31.3 The dependences of the normalized TIIDD on an ultrasonic amplitude: MoK_α (440) reflection (**a**), MoK_α (660) reflection (**b**), MoK_α (880) reflection (**c**); the area 1 of the sample

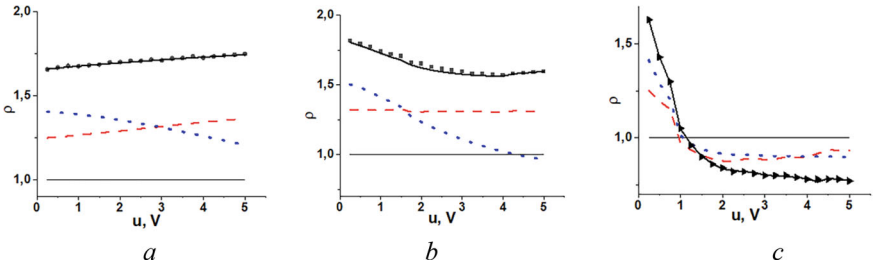

Fig. 31.4 The dependences of the normalized TIIDD on an ultrasonic amplitude: MoK_α (440) reflection (**a**), MoK_α (660) reflection (**b**), MoK_α (880) reflection (**c**); the area 2 of the sample

the sum of the lengths of the loop circles present in 1 cm^3 of the sample, namely, for an area 1: 3.103×10^7 μm, for an area 2: 36.51×10^7 μm. In this work, the values of the parameters of two types of defects were obtained for each of the areas.

Figure 31.1 shows the dependences of total integrated intensity of dynamical diffraction on an ultrasonic vibration amplitude for Si sample with thickness 7110 μm with using characteristic radiation AgK_α, (220) and (440) reflections. The curves presented in Fig. 31.1 (solid lines) are calculated according to models (31.1)–(31.2) assuming that the sample contains dislocation loops with parameters: $R_l = 3.54$ μm, $c_l = 1.67 \cdot 10^{-18}$. Markers are experimental data [13].

Figure 31.2 shows the dependences of the total integrated intensity of dynamical diffraction and its components normalized to the dependences of the integrated intensity of dynamical diffraction of a perfect crystal on an ultrasonic amplitude for Si sample with thickness 7110 μm. Lines correspond to the dependences calculated by models (31.1)–(31.2) assuming that the sample contains dislocation loops with parameters: $R_l = 3.524$ μm, $c = 1.719 \cdot 10^{-18}$. Thin solid line corresponds to the dependences calculated for normalized integrated intensity of dynamical diffraction for perfect crystal. Solid line corresponds to the dependences of the TIIDD, the dashed line corresponds to the dependence of the coherent component of the TIIDD, the dotted line corresponds to the dependence of the diffuse component of the TIIDD. Markers are experimental data [13].

Figures 31.3 and 31.4 show the dependences of the TIIDD on an ultrasonic amplitude for different reflections, namely MoK_α (440) reflection (*a*), MoK_α (660) reflection (*b*), MoK_α (880) reflection (*c*) for two areas of the sample. Thin solid lines correspond to the dependences calculated for normalized integrated intensity of dynamical diffraction for perfect crystal. The bold solid lines presented on Fig. 31.3 are calculated according to models (31.1)–(31.2) assuming that there are two dominant types of defects in the sample ($R_{cl\ Cu3Si} = 0.0686$ μm, $c_{cl\ Cu3Si} = 2.173 \times 10^{-15}$, $R_{large\ 1} = 3.4$ μm, $c_{large\ 1} = 2.905 \times 10^{-17}$). The dashed lines presented on Fig. 31.3 correspond to the calculated dependences of the TIIDD if there are only large loops in the sample ($R_{large\ 1} = 3.4$ μm, $c_{large\ 1} = 2.905 \times 10^{-17}$). The dotted lines presented on Fig. 31.3 correspond to the calculated dependences of the TIIDD if there are clusters Cu_3Si only in the sample ($R_{cl\ Cu3Si} = 0.0686$ μm, $c_{cl\ Cu3Si} = 2.173 \times 10^{-15}$). Markers are experimental data [13].

The bold solid lines on Fig. 31.4 correspond to the calculated dependences of the TIIDD if there are two dominant types of defects in the sample ($R_{cl\ Cu3Si} = 0.0686$ μm, $c_{cl\ Cu3Si} = 2.56 \times 10^{-14}$, $R_{large\ 1} = 1.425$ μm, $c_{large\ 1} = 8.156 \times 10^{-16}$). The dashed lines on Fig. 31.4 correspond to the calculated dependences of the TIIDD if there are only large loops in the sample ($R_{large\ 1} = 1.425$ μm, $c_{large\ 1} = 8.156 \times 10^{-16}$). The dotted lines presented on Fig. 31.4 correspond to the calculated dependences of the TIIDD if there are clusters Cu_3Si in the sample only ($R_{cl\ Cu3Si} = 0.0686$ μm, $c_{cl\ Cu3Si} = 2.56 \times 10^{-14}$). Markers are experimental data [13].

Figures 31.3 and 31.4 show that the dependences of the normalized TIIDD on the ultrasonic amplitude (bold solid lines) for both studied areas of the sample do not intersect with similar dependences for perfect crystal (thin solid lines). This indicates the predominant influence on the value of the TIIDD multiplier describing the reflectivity of the diffuse component of the TIIDD. The indicated dominance is also observed for the TIIDDs calculated assuming the presence in the sample under study of only Cu_3Si clusters or only large dislocation loops. In addition, the dashed and dotted lines do not intersect with the experimentally obtained (markers) dependences of the normalized TIIDD on the ultrasonic amplitude. This illustrates the inability to determine the parameters of Cu_3Si clusters and large dislocation loops.

From Fig. 31.3 it is clear that the contribution of Cu_3Si clusters to the TIIDD values measured at the area 1 can be detected only when using the (880) reflection. At the same time, it is clear from the figure that Cu_3Si clusters make the predominant contribution to the TIIDD values measured at the area 2.

At u = 2–2.5 V, calculations for large loops coincide with the experiment, which allows us to determine their parameters. The parameters of Cu_3Si clusters are determined at u = 0 V, using the already known values of the parameters of large loops.

When calculating taking into account the contributions of all defects, as well as taking into account the contribution of only clusters, the average radius of defects that have the predominant influence on the value of the TIIDD, namely, clusters $R_{cl\ Cu3Si} = 0.0686$ μm, is substituted into formula (31.2).

When calculating taking into account the contribution of only large loops, their average radius $R_{big\,1} = 1.425$ μm is substituted into formula (31.2).

At u = 1.5 V, the calculations for large loops coincide with the experiment, which allows us to determine their parameters. The parameters of the Cu_3Si clusters are determined at u = 0 V, using the already known values of the parameters of large loops.

At u = 2–2.5 V, calculations for Cu_3Si clusters agree with the experiment, which allows us to determine their parameters. The parameters of large loops are determined at u = 0 V, using the already known values of the parameters of Cu_3Si clusters.

By computer processing of experimentally obtained (markers) dependences of the normalized TIIDD on the ultrasonic amplitude, the following values of the parameters of defects of two types were obtained for the two studied areas of the sample:

For area 1: $c_{cl\,Cu3Si} = 2.173 \times 10^{-15}$, $R_{large\,1} = 3.4$ μm, $c_{large\,1} = 2.905 \times 10^{-17}$.
For area 2: $c_{cl\,Cu3Si} = 2.56 \times 10^{-14}$, $R_{large\,1} = 1.425$ μm, $c_{large\,1} = 8.156 \times 10^{-16}$.

31.4 Diagnostics of a Single Crystal Containing Defects of Three Dominant Types by X-ray Acoustic Method

In this section, calculations were performed for a silicon sample with a thickness of 13,010 μm, which was annealed at a temperature of 1100 °C for 6.5 h. Laue reflection (220) was used [3]. The wavelength of the used continuous spectrum radiation is λ = 0.404 Å. According to research data [14], after such annealing, SiO_2 clusters with a concentration of $c_{cl\,SiO2} = 1.6 \times 10^{-14}$ were formed in the sample.

Figure 31.5 shows the calculated by models (31.1)–(31.2) dependences of the TIIDD on an ultrasonic amplitude. Thin solid lines correspond to the dependence calculated for integrated intensity of dynamical diffraction for perfect crystal. Bold solid lines correspond to the calculated dependences of TIIDD if there are all three dominant types of defects ($R_{cl\,SiO2} = 0.097$ μm, $c_{cl\,SiO2} = 1.6 \times 10^{-14}$, $R_{sm.l} = 0.07$ μm, $c_{sm.l} = 1.06 \times 10^{-11}$, $R_{large\,1} = 2$ μm, $c_{large\,1} = 8.4 \times 10^{-17}$). The dashed lines correspond to the calculated dependences of TIIDD if there are only clusters in the sample ($R_{cl\,SiO2} = 0.097$ μm, $c_{cl\,SiO2} = 1.6 \times 10^{-14}$). The dotted lines correspond to the calculated dependences of TIIDD if there are only large loops in the sample ($R_{big\,1} = 2$ μm, $c_{big\,1} = 8.4 \times 10^{-17}$). The dash-dotted lines correspond to the calculated dependences of TIIDD if there are only small loops in the sample ($R_{sm.l} = 0.07$ μm, $c_{sm.l} = 1.06 \times 10^{-11}$). Markers are experimental data [11].

Figure 31.5 shows that the experimental dependence of the TIIDD at different values of ultrasonic amplitude coincide with the theoretical dependences calculated for small loops, clusters, and large loops.

Figure 31.6 demonstrates that at large ultrasonic amplitudes, the calculated theoretical dependences of the coherent component of the TIIDD R_{icoh} coincide with the experiment (Fig. 31.6a), while the contribution of the diffuse component of the TIIDD R_{idif} practically disappears (Fig. 31.6c). At small ultrasonic amplitudes, the

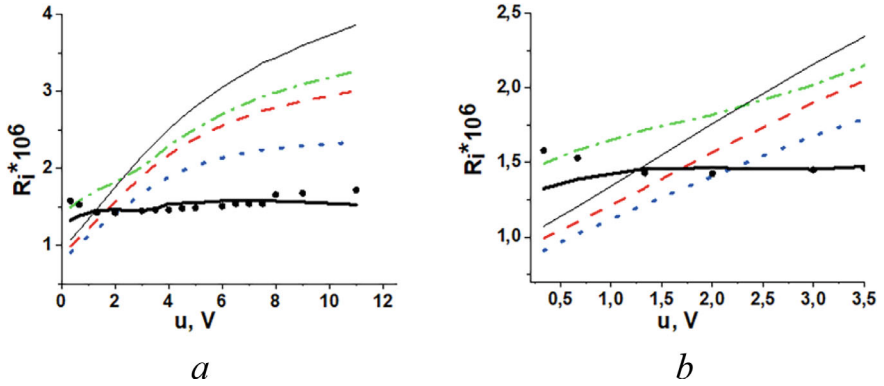

Fig. 31.5 The dependences of the TIIDD on an ultrasonic amplitude, MoK_α (220) reflection (**a**) and the same zoomed in for range u = 0.5–3.5 V (**b**)

contribution of the diffuse component is practically commensurate with the contribution of the coherent component, which ensures the coincidence of the total TIIDD with the experiment. Figure 31.6b, d show that with increasing ultrasonic amplitude, the value of the coherent component of the EIDD R_{icoh} increases (Fig. 31.6b), and the value of the diffuse component of the TIDD R_{idif} decreases (Fig. 31.6d). In addition, it is clear that, unlike the kinematical case, the course of the dependences of the components of the TIIDD for different types of defects is different.

Figure 31.7 illustrates even more clearly the possibility of separating the contributions of defects of different types simultaneously present in the sample, due to the fact that, unlike the kinematical case, in dynamical diffraction for the total integrated intensity, the ratio of the diffuse and Bragg components changes depending on the type of defects.

By fitting the experimental dependence of the TIIDD on the amplitude of ultrasonic vibrations to a similar dependence of the TIIDD calculated using models (31.1)–(31.2), the parameters of the three dominant types of defects present in the sample were obtained: clusters SiO_2 ($R_{cl\ SiO2} = 0.097$ μm, $c_{cl\ SiO2} = 1.6 \times 10^{-14}$), small dislocation loops ($R_{sm.l} = 0.07$ μm, $c_{sm.l} = 1.06 \times 10^{-11}$) and large loops ($R_{large\ 1} = 2$ μm, $c_{large\ 1} = 8.4 \times 10^{-17}$).

31.5 Conclusions

A semi-phenomenological model of the dependence of the total integral intensity of dynamical diffraction on the amplitude of ultrasonic vibrations was proposed. By using the established relationship between the parameters of the dependence of the diffuse component of the TIIDD on the ultrasonic amplitude and the parameters of defects, the possibility of separating the contributions of defects of different types simultaneously present in the sample has been demonstrated, due to the fact that,

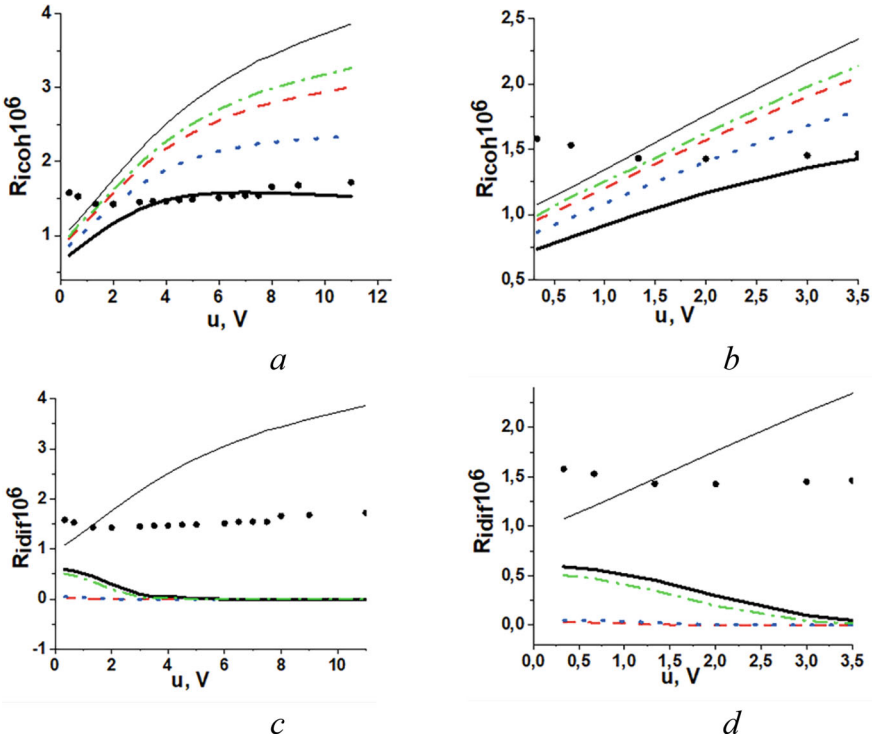

Fig. 31.6 The dependences of the coherent (**a**, **b**) and the diffuse (**c**, **d**) components of the TIIDD on an ultrasonic amplitude (Fig. 31.6b, d are the zoomed in areas of Fig. 31.6a, c for range u = 0.5–3.5 V). Thin solid lines correspond to the dependence calculated for integrated intensity of dynamical diffraction for perfect crystal. Bold solid lines correspond to the calculated dependences of the TIIDD if there are all three dominant types of defects ($R_{cl\ SiO2} = 0.097$ μm, $c_{cl\ SiO2} = 1.6 \times 10^{-14}$, $R_{sm.l} = 0.07$ μm, $c_{sm.l} = 1.06 \times 10^{-11}$, $R_{large\ l} = 2$ μm, $c_{large\ l} = 8.4 \times 10^{-17}$). The dashed lines correspond to the calculated dependences of the TIIDD if there are only clusters in the sample ($R_{cl\ SiO2} = 0.097$ μm, $c_{cl\ SiO2} = 1.6 \times 10^{-14}$). The dotted lines correspond to the calculated dependences of the TIIDD if there are only large loops in the sample ($R_{big\ l} = 2$ μm, $c_{big\ l} = 8.4 \times 10^{-17}$). The dash-dotted lines correspond to the calculated dependences of the TIIDD if there are only small loops in the sample ($R_{sm.l} = 0.07$ μm, $c_{sm.l} = 1.06 \times 10^{-11}$). Markers are experimental data [11]

unlike the kinematical case, in dynamical diffraction for the full integrated intensity, the ratio of the diffuse and Bragg components changes depending on the type of defects.

X-ray acoustic diagnostics of the characteristics of microdefects in single crystals was carried out using it.

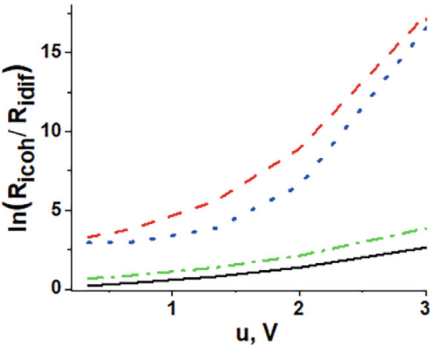

Fig. 31.7 Dependences of the logarithm of the ratio of the coherent component of the TIIDD to its diffuse component on the amplitude of ultrasonic. Solid line corresponds to calculation by the models (31.1)–(31.2) assuming the presence of three types of defects in the sample ($R_{cl\ SiO2} = 0.097$ μm, $c_{cl\ SiO2} = 1.6 \times 10^{-14}$, $R_{sm.l} = 0.07$ μm, $c_{sm.l} = 1.06 \times 10^{-11}$, $R_{large\ l} = 2$ μm, $c_{large\ l} = 8.4 \times 10^{-17}$). The dashed lines correspond to the calculated dependences of TIIDD if there are only clusters in the sample ($R_{cl\ SiO2} = 0.097$ μm, $c_{cl\ SiO2} = 1.6 \times 10^{-14}$). The dotted lines correspond to the calculated dependences of TIIDD if there are only large loops in the sample ($R_{big\ l} = 2$ μm, $c_{big\ l} = 8.4 \times 10^{-17}$). The dash-dotted lines correspond to the calculated dependences of TIIDD if there are only small loops in the sample ($R_{sm.l} = 0.07$ μm, $c_{sm.l} = 1.06 \times 10^{-11}$)

References

1. M.A. Krivoglaz, *X-Ray and Neutron Diffraction in Nonideal Crystals* (Springer, Berlin, 1996)
2. V.V. Lizunov, V.B. Molodkin, S.V. Lizunova et al., The phenomenon of amplification by orders of magnitude of the manifestation of defects in the pattern of multiple scattering and its dispersion nature. Metallofiz. Noveishie Tekhnol. **36**, 857–870 (2014)
3. G.W. Fox, H.P. Carr, The effect of piezoelectric oscillation intensity of X-ray reflections from quartz. Phys.Rev. **37** (1931)
4. I.R. Entin, On the suppression of X-ray anomalous transmisssion by acoustic oscillation. Phys. Status Solidi B **132**, 355–364 (1985)
5. I.R. Entin, I.A. Smirnova, The effect of X-ray beam intensity oscillations as a function of the amplitude of ultrasonic excited in a crystal. Phys. Status Solidi A **106**, 339–350 (1988)
6. I.A. Smirnova, I.R. Entin, Extinction length variation in a distorted crystal. Phys. Status Solidi B **147**, 459–469 (1988)
7. R. Kohler, W. Mohling, H. Peibst, Mean acoustoelectric frequencies as determined by X-ray diffraction. Ibid **56**, K21–K23 (1973)
8. I.R. Entin, Dynamical and kinematical X-ray diffraction in crystals strongly distorted by ultrasonic vibrations. Phys. Status Solidi A **106**, 25–30 (1988)
9. V.I. Khrupa, I.R. Entin, To the question of the influence of ultrasonic on the intensity of X-ray diffraction reflexes. Metallofiz. Noveishie Tekhnol. **12**, 80–84 (1990)
10. I.R. Entin, Theoretical and experimental study of X-ray acoustic resonans in perfect silicon crystal. Phys. Status Solidi B **90**, 575–584 (1978)
11. I.R. Entin, V.I. Khrupa, L.I. Datsenko, Bragg and diffuse components of X-ray reflection measured using acoustic excitation of Si crystal with oxide precipitates. J. Appl. Crystallogr. **23**, 355–358 (1990)
12. V.B. Molodkin, G.I. Nizkova, T.P. Vladimirova et al., X-ray diagnostics of nanoscale defects in single crystals by deformation dependencies method for total integrated intensity of dynamical diffraction. Springer Nature **312**, 209–225 (2024)

13. D.O. Grigoriev, L.I. Datsenko, V.F. Machulin, V.I. Khrupa, The influence of the order of Laue diffraction on the dependence of the reflective ability of a real crystal on the amplitude of ultrasonic oscillations. Ukr. J. Phys.. Phys. **38**, 1393–1397 (1993)
14. A. Borghesi, B. Pivac, A. Sassella, A. Stella, Oxygen precipitation in silicon. J. Appl. Phys. **77**, 4169–4244 (1995)

Chapter 32
Nanomaterials in Detection of Fe(II) and Fe(III) in Water

Viktor Kurylenko, Marta Litynska, and Khrystyna Hutsul

Abstract The paper analyzed the usage and efficiency of different nanomaterials in detection of iron species in water. The content of iron ions in the majority of natural waters of Ukraine significantly exceeds the maximum permissible level for consumption due to geological conditions and contamination of water bodies with metals as a result of military operations. It is also a common problem when clean water after the drinking water treatment plant is significantly contaminated with iron during transportation through pipes. Fast and effective determination of total iron content is extremely relevant both in the field of water resources management, and in quality monitoring after water treatment. There are a lot of different methods, which can effectively detect iron content in water in situ, including, electrochemical, spectrophotometric, fluorometric, etc. But these methods are often expensive, not selective enough, or require lengthy sample preparation, which makes them inconvenient to use, especially in the field. In the paper various compositions and application of detection methods are observed.

32.1 Introduction

Iron, in particular in the forms Fe(II) and Fe(III), is an essential trace element involved in key processes such as oxygen transport and energy metabolism [1]. But despite its importance, iron can be toxic under certain conditions or cause equipment damage [2, 3]. According to the Ukrainian regulations, the maximum permissible concentration (MPC) of iron is 0.2 mg/L for drinking water and 0.3 mg/L for water bodies, but

V. Kurylenko · M. Litynska (✉) · K. Hutsul
Igor Sikorsky Kyiv Polytechnic Institute, Kyiv, Ukraine
e-mail: m.litynska-2017@kpi.ua

V. Kurylenko
e-mail: vi.kurylenko@kpi.ua

K. Hutsul
e-mail: x_gucul1997@ukr.net

O. Fesenko and L. Yatsenko (eds.), *Functional Nanomaterials, Nanocatalysts, Nanotechnologies, and Their Applications*, Springer Proceedings in Physics 321,
https://doi.org/10.1007/978-3-031-99136-3_32

in natural waters the concentration is often much higher [1, 4]. Iron compounds most often enter natural waters as a result of leaching from rocks and minerals [1]. Another source of iron compounds can be the decomposition of biomass, since iron is an essential element for plants and animals. Iron compounds mainly enter the seas and oceans with river runoff [5]. In the case of Ukraine, in addition to natural factors, military operations actively affect the content of iron compounds in natural waters due to leaching from sunken military equipment, ships, shells, ammunition, missiles, mines, etc. [4, 6–8]. That is, rapid determination of iron content in surface waters and the marine environment allows us to assess the impact of the war on water quality and draw conclusions about the need to search for sunken military equipment and other metal objects.

Drinking water can also be contaminated with iron compounds due to contact of water with corroding pipes or violation of water purification conditions when using iron-containing reagents [9–11]. Such water can lead to rapid breakdown of water heating equipment.

All this makes the development of fast and inexpensive methods for determining the iron content in water an extremely urgent task.

Traditional methods for detecting iron, although accurate, are expensive, require complex sample preparation and take a long time. Currently, in Ukraine, the determination of iron content is most often carried out by quite imprecise photometric methods using sulfosalicylic acid [12] or 1,10-phenanthroline [13], since such highly sensitive methods as ICP-MS or AAS are extremely expensive. Therefore, nanomaterials have recently gained more and more attention as an innovative solution for fast, accurate and environmentally friendly iron detection. Nanomaterials, such as graphene quantum dots, carbon nanoparticles, and metal nanoparticles, exhibit unique physical and chemical properties. They enable analysis with high sensitivity and selectivity, which is critical for the determination of iron in complex environments. In addition, the use of environmentally friendly synthesis, such as using plant extracts, makes these methods even more attractive.

There are several analytical methods for detecting Fe(III) and Fe(II) ions. These include fluorometry, a spectrometric method that measures changes in fluorescence intensity caused by the interaction between nanomaterials and the target ions, enabling high sensitivity and selectivity. Colorimetry, another widely used approach, relies on visible color changes in the presence of iron ions, facilitated by the optical properties of nanostructures like gold or silver nanoparticles. Additionally, electrochemical methods have emerged as a powerful tool for iron detection, utilizing nanomaterials such as gold nanoparticles, carbon-based electrodes, or metal oxides to improve electron transfer, enhance catalytic activity, and achieve ultralow detection limits. Each of these methods provides unique advantages, with nanomaterials playing a pivotal role in advancing their sensitivity, selectivity, and applicability in complex matrices.

32.2 Methods of Iron Ions Detection

32.2.1 Fluorometry

Chemically modified fluorescent graphene quantum dots (GQDs) were employed [14] for selective quantification of Hg^{2+} and Fe^{3+} ions in real water samples using a fluorescence spectroscopy and trained a machine learning (ML) algorithm for the selective quantification. Urea-modified GQDs (uGQDs) were obtained following a modified electrochemical synthesis from graphene foam and then functionalized with 1-nitroso-2-naphthol. The functionalized GQDs exhibited a detection limit of 0.003 mg/L for Fe^{3+} ions, dynamic concentration range was between 0.003 and 0.1 mg/L. The NN-functionalized GQDs demonstrated strong selectivity, with minimal interference from Cu^{2+}, Zn^{2+}, or Hg^{2+} ions and relative error in distinguishing Fe^{3+} and Hg^{2+} in mixed samples was less than 5%. Emission spectra exhibited distinct quenching behaviors for Fe^{3+} and Hg^{2+}, which enabled precise quantification even in the presence of competing ions.

Nitrogen-doped carbon nanoparticles (N-CNPs) were synthesized [15] via a quick, green, and low-cost method for selective and sensitive detection of Fe^{3+} ions in water. N-CNPs, prepared with dextrose and urea, can be used for sensitive detection of Fe(III) ions in the range of 1–30 ppm, detection limit for Fe^{3+} ions was found to be 1 ppm. Minimal fluorescence response was observed for competing ions such as Al^{3+}, Zn^{2+}, Cu^{2+}, and Pb^{2+} (< 2%). Correlation coefficient $R^2 = 0.9945$ indicates that the N-CNPs have a very high sensitivity towards Fe(III) ions. Fe(III) sensing with N-CNPs was tested several times and only negligible deviations ($\leq 4\%$) were observed.

The determination approaches of Fe(III) in biological samples were developed by authors in article [16], that created a novel water-soluble silicon nanoparticles (SiNPs). The SiNPs were synthesized by a facile microwave-assisted method. The fluorescence intensities of SiNPs were gradually quenched with Fe(III) concentration increasing from 2.0 to 50 μmol/L ($R^2 = 0.9974$). The detection limit of the established method was 0.56 μmol/L and the precision for eleven replicate detections of 20 μmol/L Fe(III) was 3.2% (relative standard deviation, RSD). The spiked recoveries were 99.0–104.5%. SiNPs were successfully applied in the determination of Fe(III) in different environmental waters and human serum.

Water soluble carbon nanoparticles (CNPs) is described [17] for selective and sensitive detection of Fe(III) ions in water. The CNPs were synthesized by acid treatment of naturally occurring d-glucose followed by heating at 80 °C. The limit of quantification and limit of detection of Fe^{3+} ions were found to be 18 ppm and as 56 ppb, respectively. Interference from ions such as Pb^{2+}, Hg^{2+}, and Zn^{2+} was minimal (< 1%), highlighting the selectivity of the sensor. The method was validated against ICP-OES, showing consistent results for Fe^{3+} detection in real samples.

Phosphorus-doped carbon quantum dots (PCQDs) [18] have emerged as a highly effective fluorescent probe for the detection of Fe^{3+} ions. Synthesized via a

hydrothermal method, these PCQDs demonstrated exceptional sensitivity and selectivity, with a detection limit of 9.5 nM and a linear concentration range extending from 20 nM to 3.0 μM. The fluorescence quenching observed in the presence of Fe^{3+} was attributed to a static quenching mechanism, resulting from the formation of a fluorescent inactive complex (PCQDs − Fe^{3+}). Selectivity tests confirmed minimal interference from other metal ions, including Zn^{2+}, Cu^{2+}, and Hg^{2+}, with interference levels remaining below 3%. The fluorescence quantum yield of PCQDs was determined to be 16.1%, reflecting their efficiency in generating a strong signal upon interaction with Fe^{3+} ions. Validation of this fluorescent assay in real-world samples, such as raw and treated water from reverse osmosis plants, showed excellent recovery rates exceeding 95%, underscoring the practical applicability of PCQDs for environmental monitoring.

Rhodamine-based fluorescent polyacrylic nanoparticles (RhAcL-3) were developed [19] for rapid and selective detection of Fe^{2+} and Fe^{3+} in water. These nanoparticles were synthesized via semi-continuous emulsion polymerization, incorporating Rhodamine B ethylenediamine acrylate into a poly(methyl methacrylate-co-glycidyl methacrylate) matrix. The sensor demonstrated low detection limits of 2.63 μM for Fe^{2+} and 2.5 μM for Fe^{3+}, with a wide linear dynamic range from 4 to 320 μM. The fluorescence intensity increased significantly, up to 2.2 fold, upon interaction with Fe^{3+} ions, due to the chelation-induced spirolactam ring-opening mechanism in the Rhodamine moiety. Importantly, interference from other common metal ions, such as Mg^{2+}, Cu^{2+}, and Zn^{2+}, was negligible, ensuring high selectivity for iron ions. The sensor performed effectively under neutral pH conditions, enhancing its applicability for real-world water quality monitoring.

32.2.2 Colorimetry

A simple colorimetric assay for Fe(III) based on hydroxamic acid functionalized gold nanoparticles was developed [20], enabling visible detection of Fe(III) ions. This highly selective sensor allows a direct quantitative assay of Fe(III) with a UV–visible spectroscopy detection limited to 45.8 nM. Colorimetric changes were observable to the naked eye, transitioning from red to blue in the presence of Fe(III). The dynamic concentration range for Fe(III) detection extended from 45.8 nM to 10 μM. The sensor demonstrated high selectivity for Fe(III) ions, with negligible interference from Mg^{2+}, Ca^{2+}, and Hg^{2+} ions (< 1%). The method proved effective for Fe(III) quantification in real water samples, with recovery rates above 95%.

A novel colorimetric sensor using methylene blue-modified gold nanoparticles (MB-AuNPs) was developed [21] for the detection of Fe(II) and Cr(III) ions. The AuNPs were prepared using methylene blue (MB) as the capping agent and sodium borohydride as the reducing agent in the aqueous medium. The MB-AuNPs were employed as colorimetric for Cr(III) and Fe(II) ions at pH range of 3–8, at room temperature in aqueous solution. Upon aggregation, the surface plasmon absorption band red-shifts so that the nanoparticle solution appears a blue color. The MB-AuNPs

were found to be highly sensitive, detection limit for Fe(II) was determined to be 11.21 nM, with a quantification range extending up to 0.5 μM under optimized conditions in the aqueous medium. The MB-AuNPs exhibited strong selectivity for Fe(II) ions in the presence of competing ions such as Ni^{2+}, Mn^{2+}, and Pb^{2+} (< 1.5%). The method was validated in environmental samples, achieving recovery rates between 92 and 102%.

N-acetyl-L-cysteine-stabilized silver nanoparticles (NALC–AgNPs) were synthesized [22] as a highly sensitive colorimetric probe for Fe(III) ions. The Ag NPs were successfully synthesized through a simple method using sodium borohydride as reducing agent and N-acetyl-L-cysteine as protecting ligand. The synthesized silver nanoparticles show a strong surface plasmon resonance (SPR) around 400 nm and the SPR intensity decreases with the increasing of Fe^{3+} concentration in aqueous solution. Silver nanoparticles can be used for the sensitive and selective detection of Fe^{3+} ions in water with a linear range from 80 nM to 80 mM and a detection limit of 80 nM. The detection mechanism was attributed to an oxidation–reduction interaction between Fe(III) and AgNPs. Selectivity tests confirmed negligible interference from competing ions such as Pb^{2+}, Zn^{2+}, and Cu^{2+} (< 2%). The method demonstrated robust performance in detecting Fe(III) in real water samples, with recovery rates exceeding 95%.

Green synthesized silver nanoparticles (AgNps) capable of distinguishing Fe^{2+} and Fe^{3+} ions were synthesized [23] for simple naked eye detection. A visible color change from yellow to orange was observed upon interaction with Fe(II). Sapindus mukorossi pericarp extract was used as both reducing and stabilizing agent for the synthesis of eco-friendly AgNps within 10 min by means of ultrasound assistance. The proposed AgNps was successfully explored as a potential colorimetric probe for selective, sensitive, rapid detection and distinction of Fe^{2+} and Fe^{3+} ions over various other metal ions. The detection limit for Fe(II) was 0.3 ppb, with a linear range extending from 0.3 to 7.0 ppb. The sensor exhibited excellent selectivity, showing minimal interference from Fe(III) ions (< 5%). The recovery rates in real environmental samples ranged from 97 to 105%.

Green synthesized gold nanoparticles (CA-AuNPs) using green bell pepper Capsicum annuum extract were applied [24] as a sensitive colorimetric sensor for Fe(II) detection. Importantly, the fabricated CA-AuNPs based colorimetric sensor functioned linearly in the range of 0.3–7.0 ppb Fe^{2+}, based on increasing absorption intensity with R^2 value of 0.9938 using UV–Vis spectrometry. The limit of detection (LOD) and limit of quantification (LOQ) for Fe^{2+} were estimated as 0.036 and 0.12 ppb, respectively. The CA-AuNPs exhibited strong selectivity for Fe(II) ions, with interference from Fe(III) ions limited to < 4%. The method showed excellent reproducibility, with recovery rates for real water samples ranging from 96 to 103%. Finally, the sensor was effectively tested for determination of Fe^{2+} in some locally collected real water samples.

32.2.3 Electrochemical Detection

A dual-nanomaterial-based electrode incorporating titanium carbide nanoparticles (TiCNPs) and platinum nanoflowers (PtNFs) was developed [25] for the voltammetric stripping determination of Fe(II) in coastal waters. TiCNPs served as a structural template, facilitating the controlled growth of PtNFs with a three-dimensional flower-like morphology, which increased the active surface area of the electrode. Nafion, used as a conducting matrix, further enhanced the stability and electron transfer efficiency of the modified electrode. The electrode exhibited a remarkable detection limit of 0.03 nmol/L and a dynamic linear range from 1 nmol/L to 6 μmol/L for Fe(II). The use of 2,2′-bipyridyl as a complexing agent significantly improved the selectivity of the sensor by minimizing interference from other ions in the matrix. This approach proved highly effective in real-world applications, demonstrating precise and reproducible detection of Fe(II) in complex coastal water samples.

A carbon paste electrode (CPE) modified with gold nanoparticles and dithiodianiline was developed [26] for the electrochemical detection of Fe(II) ions in aqueous solutions. This electrode demonstrated a detection limit of 0.05 nmol/L and a broad linear range, enabling precise quantification of trace Fe(II). The gold nanoparticles provided enhanced electron transfer kinetics, while dithiodianiline contributed to selective complexation of Fe(II), ensuring high sensitivity and minimal interference from competing ions such as Cu^{2+}, Zn^{2+}, and Pb^{2+}. This modified electrode was successfully applied to the analysis of real water samples, achieving recovery rates between 94 and 102%.

32.2.4 Comparison of Different Detection Methods

The reviewed methods for detecting Fe(III) and Fe(II) ions utilizing nanomaterials in different analytical methods, including: fluorometry, colorimetry, and electrochemical techniques. Each method offers specific advantages in terms of sensitivity, selectivity, and detection limits, often dictated by the nanomaterials employed. Table 32.1 summarizes the key characteristics of these methods, highlighting the type of nanomaterial used, detection range, sensitivity (limit of detection), selectivity, and notable features, providing a comprehensive comparison of their performance.

Among all compared methods, electrochemical method using Pt-containing electrode [25] and colorimetry using biosurfactant modified silver nanoparticles [23] or green synthesized with Capsicum annuum gold nanoparticles [24] are the most sensitive and demonstrate detection range about 0.001–6 μM and 0.005–0.125 μM, respectively. Golden and silver nanoparticle syntheses are eco-friendly, but a disadvantage is the high cost of the gold or silver compounds used to synthesize these nanomaterials. Platinum compounds for the synthesis of nanoparticles for electrode modification are even more expensive.

Table 32.1 Comparison of methods for iron ions detection in water

Method	Nanomaterial	Target ion	Detection limit	Detection range	Key features	References
Fluorometry	Graphene quantum dots (GQDs)	Fe(III)	0.003 mg/L	0.003–0.1 mg/L	Machine learning-enhanced analysis for real samples	[14]
Fluorometry	N-doped carbon nanoparticles (N-CNPs)	Fe(III)	1 ppm	1–30 ppm	Cost-effective, eco-friendly synthesis	[15]
Fluorometry	Silicon nano-particles (SiNPs)	Fe(III)	0.56 μM	2.0–50 μM	Applied in environmental and biological samples	[16]
Fluorometry	Carbon nano-particles (CNPs)	Fe(III)	56 ppb	0.056– 10 ppm	Green synthesis using d-glucose, validated with ICP-OES	[17]
Fluorometry	Phosphorus-doped carbon quantum dots (PCQDs)	Fe(III)	9.5 nM	0.02–3 μM	High fluorescence quantum yield (16.1%), validated in RO water samples	[18]
Fluorometry	Rhodamine-based polyacrylic nanoparticles (RhAcL-3)	Fe(II), Fe(III)	2.63 μM (Fe^{2+}), 2.5 μM (Fe^{3+})	4–320 μM	Rapid response, chelation-induced fluorescence emission	[19]
Colorimetry	Gold nanoparticles (AuNPs), Hydroxamic acid functionalized	Fe(III)	45.8 nM	0.0458–10 μM	Visible color change, simple and rapid assay	[20]
Colorimetry	Gold nanoparticles (AuNPs), Methylene blue modified	Fe(II)	11.21 nM	0.01121–0.5 μM	Stable across a wide pH range	[21]
Colorimetry	Silver nanoparticles (AgNPs), Stabilized with N-Acetyl-L-Cysteine	Fe(III)	80 nM	0.080–80 μM	Based on redox interaction	[22]
Colorimetry	Silver nanoparticles (AgNPs), Biosurfactant modified	Fe(II), Fe(III)	0.3 ppb (Fe^{2+})	0.3–7.0 ppb (Fe^{2+})	Eco-friendly synthesis	[23]
Colorimetry	Gold Nanoparticles (AuNPs), Green synthesized with capsicum annuum	Fe(II)	0.3 ppb	0.3–7.0 ppb	Eco-friendly synthesis	[24]

(continued)

Table 32.1 (continued)

Method	Nanomaterial	Target ion	Detection limit	Detection range	Key features	References
Electro-chemistry	TiCNPs/PtNFs Modified electrode	Fe(II)	0.03 nM	0.001–6 μM	High active surface area, applied in coastal water samples	[25]
Electro-chemistry	Carbon paste electrode, Gold nanoparticle modified	Fe(II)	0.05 nM	Broad linear range	Reproducible and stable performance in real water analysis	[26]

32.3 Conclusions

Monitoring of water resources, especially to assess the impact of war, and testing of the quality of drinking water are significant reasons for the need to develop modern, cheap and effective detection methods.

Currently, in Ukraine, the determination of iron content is most often carried out by quite imprecise photometric methods using sulfosalicylic acid or 1,10-phenanthroline, since such highly sensitive methods as ICP-MS or AAS are extremely expensive. Therefore, nanomaterials have recently gained more and more attention as an innovative solution for fast, accurate and environmentally friendly iron detection. Among all compared methods, electrochemical method using Pt-containing electrode and colorimetry using silver nanoparticles or gold nanoparticles are the most sensitive and demonstrate detection range about 0.001–6 μM and 0.005–0.125 μM, respectively. These syntheses of golden or silver nanoparticle are eco-friendly, but a disadvantage is the high cost of the gold or silver compounds used to synthesize these nanomaterials. Platinum compounds for the synthesis of nanoparticles for electrode modification are even more expensive.

Therefore, it is more appropriate to use carbon nanoparticles, since these syntheses are much cheaper. Although the sensitivity of methods using carbon nanoparticles is much lower, it is sufficient to detect iron content exceeding the maximum permissible concentration in water.

Acknowledgements We are grateful for project of fundamental scientific research, applied research and scientific and technical (experimental) developments of young scientists of Ministry of Education and Science of Ukraine for funding the project 0124U001100 "The novel selective indicator systems for assessing the state of the marine environment in Ukraine".

References

1. W. Stumm, G.F. Lee, The chemistry of aqueous iron. Schweiz. Z. Hydrol. **22**(1), 295–319 (1960)
2. V. Fedin, V. Vorobyova, M. Skiba, I. Trus, Assessment of the efficiency of the stabilization treatment for water of various mineralization. J. Chem. Technol. **32**(4), 1109–1118 (2024)
3. T. Mitchenko, I. Kosogina, S. Kyrii, The local solutions for water security in Ukraine, in *Proceedings of the NATO Advanced Research Workshop on Physical and Cyber Safety in Critical Water Infrastructure, Sub-Series D Information and Communication Security* (vol. 56, 2019), pp. 99–106
4. M. Litynska, O. Pelekhata, The influence of the war on the content of some components in the rivers of Ukraine. IOP Conf. Ser. Earth Environ. Sci. **1415**, 012094 (2024)
5. R. Krachler, F. Jirsa, S. Ayromlou, Factors influencing the dissolved iron input by river water to the open ocean. Biogeosciences **2**(4), 311–315 (2005)
6. I. Astrelin, M. Litynska, O. Sanginova, N. Tolstopalova, T. Mitchenko, A. Arkhipova, Water utilities' risk assessment, in *Proceedings of the NATO Advanced Research Workshop on Physical and Cyber Safety in Critical Water Infrastructure, Sub-Series D Information and Communication Security* (vol. 56, 2019), 99–106.

7. K. Gebka, J. Beldowski, M. Beldowska, The impact of military activities on the concentration of mercury in soils of military training grounds and marine sediments. Environ. Sci. Pollut. Res. **23**, 23103–23113 (2016)
8. A. Myroshnychenko, V. Loboichenko, M. Divizinyuk, A. Levterov, N. Rashkevich, O. Shevchenko, R. Shevchenko, Application of up-to-date technologies for monitoring the state of surface water in populated areas affected by hostilities. Bull. Georg. Natl. Acad. Sci. **16**, 50–59 (2022)
9. M. Litynska, T. Dontsova, O. Yanushevska et al., Development of iron-containing sorption materials for water treatment from arsenic compounds. East. Eur. J. Enterp. Technol. **10**(110), 35–42 (2021)
10. M. Litynska, N. Tolstopalova, I. Astrelin et al., Influence of foreign ions on the adsorption of arsenate on iron(III) oxides and hydroxides. Voprosy Khimii i Khimicheskoi Tekhnologii **3**, 22–29 (2019)
11. M. Litynska, T. Dontsova, A. Gusak, Nanostructured iron-based sorption materials for drinking water and wastewater treatment. Springer Proc. Phys. **279**, 243–255 (2023)
12. P. Komadel, Quantitative assay of minerals for Fe^{2+} and Fe^{3+} using 1,10-phenanthroline: III. A rapid photochemical method. Clays Clay Miner. **36**(4), 379–381 (1988)
13. J. Kozak, N. Jodlowska, M. Kozak, P. Koscielniak, Simple flow injection method for simultaneous spectrophotometric determination of Fe(II) and Fe(III). Anal. Chim. Acta **702**(2), 213–217 (2011)
14. M. Llaver, S.D. Barrionuevo, J.M. Núñez, A.L. Chapana, R.G. Wuilloud, M.H. Aguirre, F.J. Ibañez, Fluorescent graphene quantum dots-enhanced machine learning for the accurate detection and quantification of Hg^{2+} and Fe^{3+} in real water samples. Environ. Sci. Nano. **11**, 2703–2715 (2024)
15. A. Molkenova, Y. Amangeldinova, D. Aben, S. Sayatova, TSh. Atabaev, Quick synthesis of fluorescent nitrogen-doped carbon nanoparticles for selective and sensitive Fe(III) detection in water. Sens. Bio-Sens. Res. **23**, 100271 (2019)
16. H.-L. Ye, Y. Shang, H.-Y. Wang, Y.-L. Ma, X.-W. He, W.-Y. Li, Y.-H. Li, Y.-K. Zhang, Determination of Fe(III) ion and cellular bioimaging based on a novel photoluminescent silicon nanoparticles. Talanta **230**, 122294 (2021)
17. V. Singh, A.K. Mishra, Green and cost-effective fluorescent carbon nanoparticles for the selective and sensitive detection of iron (III) ions in aqueous solution: mechanistic insights and cell line imaging studies. Sens. Actuators, B Chem. **227**, 467–474 (2016)
18. G. Kalaiyarasan, J. Joseph, P. Kumar, Phosphorus-doped carbon quantum dots as fluorometric probes for iron detection. ACS Omega **5**, 22278–22288 (2020)
19. S. Ghezelsefloo, J. Keyvan Rad, M. Hajiali, A.R. Mahdavian, Rhodamine-based fluorescent polyacrylic nanoparticles: a highly selective and sensitive chemosensor for Fe(II) and Fe(III) cations in water. J. Environ. Chem. Eng. **9**, 105082 (2021)
20. C. Karami, A. Alizadeh, M.A. Taher, Z. Hamidi, B. Bahrami, UV-visible spectroscopy detection of iron(III) ion on modified gold nanoparticles with a hydroxamic acid. J. Appl. Spectrosc. **83**, 687–693 (2016)
21. F. Salimi, M. Kiani, C. Karami, M.A. Taher, Colorimetric sensor of detection of Cr (III) and Fe (II) ions in aqueous solutions using gold nanoparticles modified with methylene blue. Optik **158**, 813–825 (2018)
22. X. Gao, Y. Lu, S. He, X. Li, W. Chen, Colorimetric detection of iron ions (III) based on the highly sensitive plasmonic response of the N-acetyl-l-cysteine-stabilized silver nanoparticles. Anal. Chim. Acta **879**, 118–125 (2015)
23. K. Dayanidhi, N.S. Eusuff, Distinctive detection of Fe^{2+} and Fe^{3+} by biosurfactant capped silver nanoparticles via naked eye colorimetric sensing. New J. Chem. **45**, 9936–9943 (2021)
24. P. Siyal, A. Nafady, R. Sirajuddin Memon, S. Tufail Hussain Sherazi, J. Nisar, A. Ali Siyal, M. Raza Shah, S. Ahmed Mahesar, S. Bhagat, Highly selective, sensitive and simpler colorimetric sensor for Fe^{2+} detection based on biosynthesized gold nanoparticles. Spectrochim. Acta Part A Mol. Biomol. Spectrosc. **254**, 119645 (2021)

25. M. Lin, D. Pan, Y. Zhu, X. Hu, H. Han, C. Wang, Dual-nanomaterial based electrode for voltammetric stripping of trace Fe(II) in coastal waters. Talanta **154**, 127–133 (2016)
26. Y. Zhu, D. Pan, X. Hu, H. Han, M. Lin, C. Wang, An electrochemical sensor based on reduced graphene oxide/gold nanoparticles modified electrode for determination of iron in coastal waters. Sens. Actuators, B Chem. **243**, 1–7 (2017)

Chapter 33
Comparison of the Properties of Nanosized $TiO_2(ZnO)/WO_3$ and $TiO_2(ZnO)/MoO_3$ Composites Synthesized by Ultrasonic and Mechanochemical Methods in the Decomposition of Metronidazole

Ye. V. Zabolotnii, O. V. Kiziun, and V. O. Zazhigalov

Abstract Mechanochemical and sonochemical modification of complexe oxides mixtures ZnO/MoO_3, ZnO/WO_3, TiO_2/MoO_3 and TiO_2/WO_3 with equimolar ratio of the initial oxides was realized. The formation of new phase $ZnWO_4$ at mechanochemical treatment of the mixture oxides was shown. XRD method was established that mechanochemical treatment leads to an essential decrease of the composites particles size in contrary to sonochemical treatment where in the most cases an increase of the particles dimensions was observed. The data obtained by XRD method were confirmed by SEM results. It was shown that an increase of particles size composites at sonochemical treatment accompanied by an increase of their photocatalytic activity in metronidazole decomposition in water solution which can be connected with an decrease of the electron–hole rate recombination.

33.1 Introduction

The pharmaceutical industry's development and human health problems are accompanied by an increase in the production of drugs and their consumption, which leads to an increase in the amount of waste in the environment, including wastewater. It should be noted that when medical preparations have expired, they are not disposed of, but rather enter the environment, where they gradually penetrate wastewater under the effect of atmospheric factors. Antibiotics (AB) are one

Ye. V. Zabolotnii (✉) · O. V. Kiziun · V. O. Zazhigalov
Institute for Sorption and Problems of Endoecology, National Academy of Sciences of Ukraine, Kyiv, Ukraine
e-mail: evgeniy2019q@ukr.net

O. Fesenko and L. Yatsenko (eds.), *Functional Nanomaterials, Nanocatalysts, Nanotechnologies, and Their Applications*, Springer Proceedings in Physics 321,
https://doi.org/10.1007/978-3-031-99136-3_33

of the most dangerous pharmacological compounds, which include metronidazole (2-methyl-5-nitromidazole-1-ethanol, MNZ) [1–6].

Metronidazole is a commonly detected contaminant in the environment. Also MNZ has been widely used as a typical antiprotozoal and antibacterial drug in recent years. It has the potential ability to inhibit the growth of the anaerobic bacteria. Residues of MNZ in the environment could cause animal-derived food contamination. In addition, with its neural toxicity, MNZ has the potential to harm human body. The compound is classified as poorly biodegradable and highly soluble in water. Heterogeneous photo-catalysis is the most promoted water purification method due to the possibility of using UV-light and small amounts of a catalyst needed for the process [7, 8].

Titanium dioxide has been applied as one of the most effective photocatalysts for eliminating organic contaminants because of its non-toxicity, high photoactivity, and stability. Zinc oxide is also a potential photocatalyst. Despite its less interest, ZnO possesses promising applications due to its photocatalytic activity and low cost in contrast to TiO_2. In some studies, ZnO exhibited even more photoactivity than TiO_2 for the photodegradation of organics [4, 8].

It is known that molybdenum (VI) [4–8] and tungsten (VI) [9–13] oxides and their compositions [14–18] are good photocatalysts for the degradation of organic substances.

The aim of this study was to evaluate the removal efficiency of metronidazole by heterogeneous photocatalysis using different types of semiconductors (TiO_2, ZnO) and their mixtures with WO_3 and MoO_3 synthesized by ultrasonic and mechanochemical methods.

33.2 Experimental

33.2.1 Sample Preparation and Synthesis

Initial mixtures of ZnO/MoO_3, ZnO/WO_3, TiO_2/MoO_3 and TiO_2/WO_3 systems with an equimolar content of reagents (1:1) were prepared by mixing the corresponding components. TiO_2 (p.a., China), ZnO (pharm., Peru), MoO_3 (p.), WO_3 (p.a.) were used as initial oxides. Synthesis of nanosizedpowders was performed by mechanochemical and ultrasonic methods.

Mechanochemical treatment of samples was subjected to intense mechanical treatment in Fritsch high-energetic planetary ball mill (Pulversitte-6). Zirconia vessel (250 mL) and balls ($Ø = 5$ mm) were used for the treatment of 10 g of the oxides mixture. The duration of the treatment was 1 h in air at 500 rpm, and balls-to-powder weight ratio (BPR) was 10:1.

Ultrasonic treatment of samples was performed in an aqueous environment for 30 min in an ultrasonic generator with an operating frequency of 20 kHz and a power of 80 W. After ultrasonic treatment, the obtained suspensions were dried in air.

33.2.2 Characterization Methods and Techniques

X-ray powder diffractograms of initial and sonoactivated samples were determined by using a D8 ADVANCE diffractometer (Bruker). The patterns were run with Cu Kα radiation with Ni filter and working in continuous mode with a step size 0.05° 2Θ in combination with the Inorganic Crystal Structure Database (ICSD), for example, ZnO phases with wurtzite structure (JCPDS 1314-13-2), TiO_2 with anatase structure (JCPDS 21-1272), WO_3 (JCPDS 72-0677) monoclinic modification, α-MoO_3 orthorhombic modification (ICSD—005-008). Scanning was performed in the range of 10–90°.The average crystallite size (L) was calculated according to the Debye–Scherrer equation:

$$L = \frac{K\lambda}{\beta \cos \Theta}, \tag{33.1}$$

The porous structure of the samples was determined from isotherms of low-temperature nitrogen adsorption on the Quantachrome NOVA-2200e instrument.

The UV–vis absorption studies were performed in the wavelength range of the 190–800 nm on a Shimadzu UV-2450 spectrometer. Photocatalytic oxidative degradation of metronidazole (15 mg/L) in water in the presence of the studied samples (for up to 5 h) was performed in a glass reactor at room temperature. During irradiation, the solutions were intensively stirred by an electromagnetic stirrer to establish adsorption equilibrium (1 h) in the photocatalyst/adsorbate system. The lamp with 125 W Hg (Optima) was used as the light source. The standard conditions of the typical process were next: 0.150 g of photocatalyst was dispersed into a beaker, which was filled with 300 mL of dye solution, in particular, the catalyst concentration of 0.5 g/L. The absorption spectra of the selected samples were recorded every hour to monitor the progress of the process. The efficiency of the reaction was evaluated by the change in the maximum optical density of the solution of the active substance, namely, metronidazole (λ = 320 nm). The photocatalytic degradation of metronidazole is a pseudo-first-order reaction and its kinetic can be expressed according to Eqs. (33.2 and 33.3):

$$Kd = \ln\left(\frac{D}{D_0}\right)/\Delta t, \tag{33.2}$$

where D_0 and D are optical densites of the initial solutions and after its irradiation for a certain period Δt.

$$G = \frac{D_0 - D}{D_0} \times 100\ \ \%, \tag{33.3}$$

where G is the degree of photocatalytic destruction.

The optical properties of powdered samples were studied on a Shimadzu UV-2450 spectrometer in the wavelength range of 200–800 nm. The absorption edge

was determined by extrapolation of the linear section of the absorption band edge to the abscissa axis in the coordinates $\alpha^{1/r} = f(h\nu)$ (where α is the absorption coefficient of the material, ν is the energy, 1/r is the nature of the transition). This method can be used to determine the band gap with an accuracy of ± 0.02 eV. At the same time, each sample was studied several times while thoroughly mixing. The relative error in these measurements was 0.01 eV. The absorption spectra were obtained from the corresponding reflection spectra according to the Kubelka–Munk Formula (33.4):

$$F(R\infty) = \frac{(1 - R/R\infty)^2}{2(R/R\infty)} = \alpha/S, \tag{33.4}$$

33.3 Results and Discussion

Results of XRD analysis of the $TiO_2(ZnO)/WO_3$ and $TiO_2(ZnO)/MoO_3$ samples are presented in Fig. 33.1.

The X-ray pattern of $TiO_2/MoO_3 = 1{:}1$ (Fig. 33.1a–c) shows the characteristic titanium oxide peaks of anatase crystal structure and reflexes of α-MoO_3. From $TiO_2/WO_3 = 1{:}1$ (Fig. 33.1d–f) shows the characteristic titanium oxide peaks of anatase crystal structure and reflexes of WO_3 (monoclinic modification). After sonochemical activation of the $ZnO/MoO_3 = 1{:}1$ (Fig. 33.1h) sample the diffractogram contains the reflexes of initial compound α-MoO_3 and new phase – α-$ZnMoO_4$ triclinic modification (JCPD card 01-072-1486). From $ZnO/MoO_3 = 1{:}1$ (Fig. 33.1i, g) shows the characteristic ZnO phases peaks of wurtzite structure and reflexes of α-MoO_3. After mechanochemical activation of the $ZnO/WO_3 = 1{:}1$ (Fig. 33.1m) sample the diffractogram contains the reflexes of WO_3, and new phase—monoclinic $ZnWO_4$ (JCPDS 73-0554) with reflexes at 2θ values of 18.8° (100), 30.45° (111), 64.6° (311). The most intense reflections correspond to interplanar distances d = 0.25 ZnO; 0.35 TiO_2; 0.35 and 0.33 α-MoO_3; 0.37 and 0.38, 0.39 nm WO_3.

The intensity of composites synthesized by mechanochemical method reflections sharply decreases and their expansion occurs indicating a decrease in the size of primary particles of the oxide, besides size of MoO_3 particles $TiO_2/MoO_3 = 1{:}1$. The intensity of composites synthesized by ultrasonic reflections slight decreases and a decrease in the size is observed ($ZnO/MoO_3 = 1{:}1$; TiO_2 of $TiO_2/MoO_3 = 1{:}1$; ZnO of $ZnO/WO_3 = 1{:}1$), too. The change in the size of modified initial composites is confirmed by calculations based on the Scherrer equation, the results of which are shown in Table 33.1.

According to the results obtained by scanning electron microscopy, presented in Fig. 33.2, for example, the results for TiO_2/WO_3 and ZnO/WO_3, there are quite large particles of initial oxide WO_3, The micrometric particles of ZnO and TiO_2 are agglomerates consisting of nanosized particles of these oxides. The UST of the mixture practically does not affect the size of particles, which can be seen in detail in the image obtained in the BSE mode. The MCT of mixtures leads to a significant

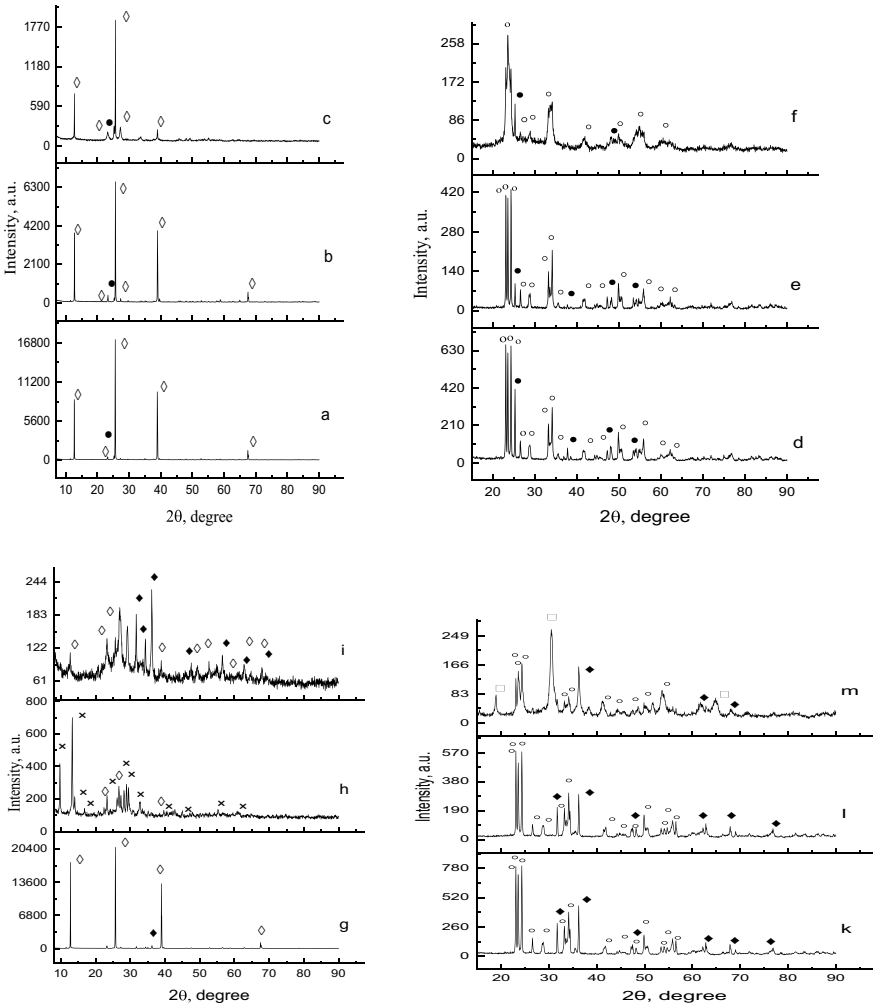

Fig. 33.1 X-ray diffractograms of the samples TiO_2/MoO_3 = 50:50 (**a**—initial, **b**—after 30 min UST, **c**—after 1 h of MChT); TiO_2/WO_3 = 50:50 (**d**—initial, **e**—after 30 min UST, **f**—after 1 h of MChT); ZnO/MoO_3 = 50:50 (**g**—initial, **h**—after 30 min UST, **i**—after 1 h of MChT); ZnO/WO_3 = 50:50 (**k**—initial, **l**—after 30 min UST, **m**—after 1 h of MChT) ● TiO_2, ◊ α-MoO_3, ◆ ZnO, ○WO_3, □ $ZnWO_4$, × α-$ZnMoO_4$

grinding of particles, as shown in Fig. 33.2c, f when compared to the initial mixtures (Fig. 33.1a, d) and samples after UST (Fig. 33.2b, e).

The synthesis samples by mechanochemical method leads to an increase in the specific surface area of the mixture, besides ZnO/MoO_3, where the specific surface area at UST is lower than initial sample.

It was established that the destruction of larger diameter particles occurs during MChT, which leads to a decrease in the average diameter of pores of the obtained

Table 33.1 Properties of synthesized and initial oxide compositions

Sample	Treatment	L (nm)		d (nm)		S_{BET} (m^2/g)	V_Σ (cm^3/g)	R_{pore} (nm)	Eg (eV)	Photoactivity		
										k_d (h^{-1})	G_{5h} (%)	G_{1h} (%)
ZnO	–	42	–	0.25	–	6	0.02	29	3.29	1.97	95	83
	MCT	28	–	0.25	–	7	0.04	19	3.32	0.44	99.7	22
	UST	44	–	0.25	–	4	0.02	28	3.29	2.07	99	88
ZnO/ WO_3	–	45	48	0.25	0.37	5	0.02	9	3.27	0.91	98	60
	MCT	21	24	0.25	0.37	16	0.05	7	3.36	0.41	95	34
	UST	43	51	0.25	0.39	8	0.03	8	3.31	0.93	96	20
ZnO/ MoO_3	–	68	63	0.25	0.35	4	0.01	5	3.27	0.55	96	79
	MCT	27	21	0.25	0.35	3	0.01	7	3.51	0.16	70	15
	UST	–	26	–	0.33	9	0.04	10	4.44	0.59	96	17
TiO_2	–	38	–	0.35	–	10	0.41	40	3.20	1.14	90	78
	MCT	36	–	0.35	–	15	0.17	23	3.22	0.33	83	28
	UST	46	–	0.35	–	9	0.11	35	3.14	1.51	99	55
TiO_2/ MoO_3	-	59	65	0.35	0.35	4	0.06	35	3.25	0.14	61	29
	MCT	25	86	0.35	0.35	10	0.08	16	3.30	0.04	42	4
	UST	45	64	0.35	0.35	5	0.04	16	3.18	0.14	59	13
TiO_2/ WO_3	-	49	48	0.35	0.39	5	0.04	14	3.18	0.39	59	32
	MCT	31	10	0.35	0.38	7	0.03	9	3.12	0.08	41	8
	UST	54	55	0.35	0.37	6	0.03	9	2.65	0.39	59	15

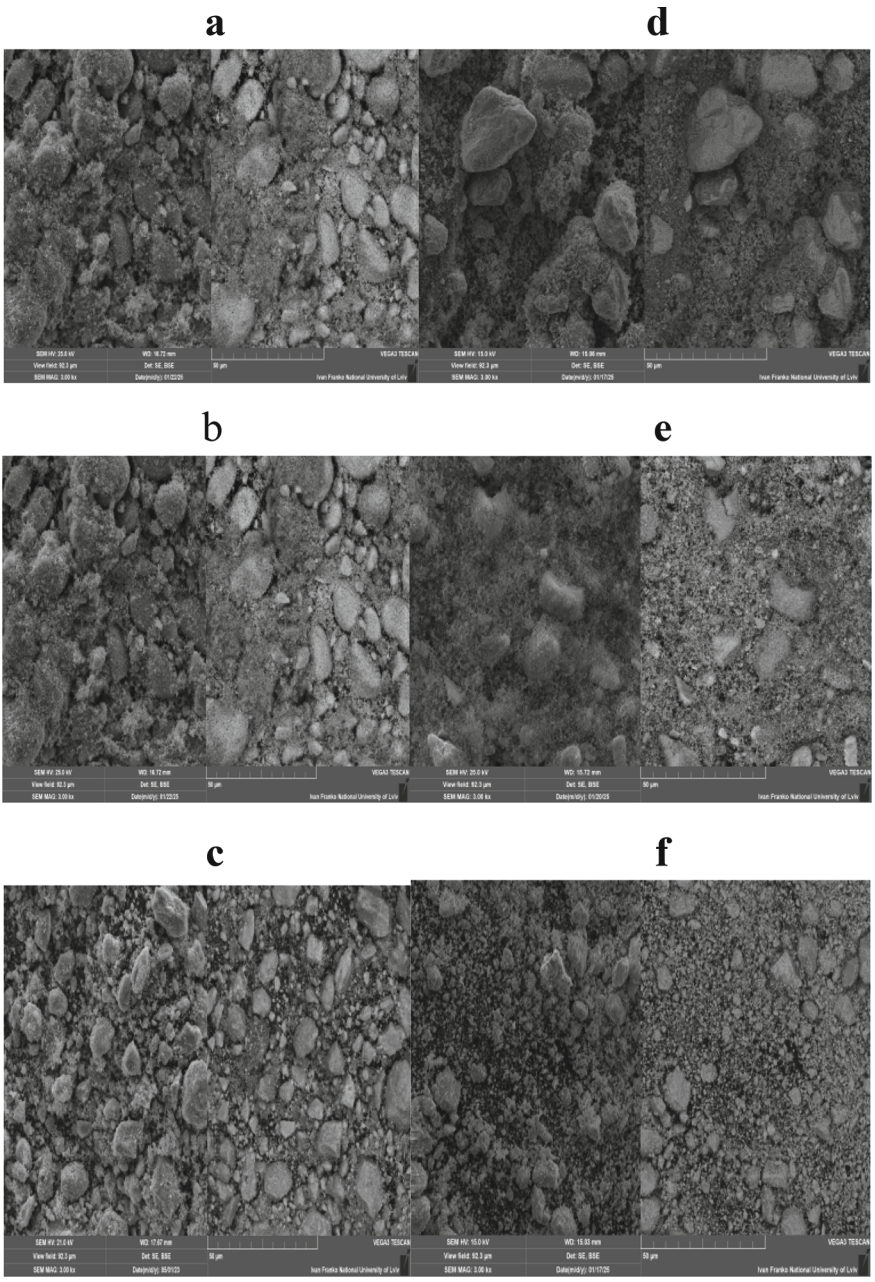

Fig. 33.2 SEM images of TiO_2/WO_3 and ZnO/WO_3 (**a**, **d**—initial samples; **b**, **e**—after UST; **c**, **f**—after MCT)

samples, besides ZnO/MoO_3, where R_{pore} is higher than initial sample. For others samples after UST almost doesn't change or increases. It's may be associated with the formation of small agglomerates between nanosized particles of the MoO_3 or WO_3.

According to the data shown in Table 33.1 the band gap values practically don't differ from the values for initial samples after the UST of samples The analysis of the absorption spectra of samples and the band gap values determined from them shows that the band gap values practically don't differ from the values for initial samples after the UST of samples, besides ZnO/MoO_3 and TiO_2/WO_3, but after MCT the band gap values of the obtained samples almost leads to a increase, besides ZnO/MoO_3 and TiO_2/WO_3, too.

The results of the study of photocatalytic activity in the reaction of oxidative degradation of metronidazole are presented in Table 33.1. It was established that addition of the MoO_3 or WO_3 to the TiO_2 or ZnO photoactive catalysts a molar ratio of 1:1 (initial mixture) leads to formation of less photoactive catalysts: a decrease in the photoreaction rate constant value was observed. This effect can be explained by the fact that introduction MoO_3 or WO_3 decreases the concentration of the photocatalytic oxides (TiO_2 or ZnO) at a constant concentration of the catalyst in the reaction medium. This effect was observed and explained early in [1]. The mechanochemcal and sonochemical teatments of the oxide mixtures lead to the change their photocatalytic characteristics. In the case of mechanochemistry the decrease of their activity was observed which can be connected with a decrease of particles dimensions but sonochemistry where an increase of particles sizes was established leads to an increase of photocatalytic activity of the samples. Analogous result was observed in [19] for the samples ZnO synthesized by different methods and was explained by electron–hole recombination rate decreases with an increase of particles dimensions [19–21].

33.4 Conclusion

It was shown that mechanochemical and sonochemical modifications of complex oxides mixtures ZnO/MoO_3, ZnO/WO_3, TiO_2/MoO_3 and TiO_2/WO_3 with molar ratio of the initial oxides 1:1 lead to the change of the size particles of composites. XRD and SEM methods demonstrate that mechanochemical treatment leads to an essential decrease of the composites particles size in contrary to sonochemical treatment where in the most cases an increase of the particles dimensions was observed. The formation of new phase $ZnWO_4$ at mechanochemical treatment of the mxture ZnO and WO_3 oxides was shown. It was established that an increase of particles size composites at sonochemical treatment accompanied by an increase of their photocatalytic activity in metronidazole decomposition in water solution which can be connected with an decrease of the electron–hole rate recombination.

Acknowledgements This work was financially supported by National Academy of Sciences of Ukraine Programs: project "Development of alternative methods for the preparation of nanosized

oxide catalysts and composites based on Mo, Ti, Zr, Nb and Sn" No. 0118U003420 and project "Nanodisperse complex oxide catalysts and composites: synthesis and their application in ecological and productive catalysis" No. 0123U100427.

References

1. V.O. Zazhigalov, E.V. Zabolotnii, V.M. Kordan, M.M. Kurmach, Influence of particle sizes of zinc and titanium oxides on their activity in metronidazole photocatalytic oxidative degradation in water. Theoret. Exp. Chem. **60**(2), 1–8 (2024)
2. O.S. Ayanda, B.O. Adeleye, O.H. Aremu et al., Photocatalytic degradation of metronidazole using zinc oxide nanoparticles supported on acha waste. Indones. J. Chem. **23**(1), 158–169 (2023)
3. F. Ghribia, M. Sehailiaa, L. Aoudjit et al., Solar-light promoted photodegradation of metronidazole over ZnO-$ZnAl_2O_4$ heterojunction derived from 2D-layered double hydroxide structure. J. Photochem. Photobiol. A Chem. **397**, 112510 (2020)
4. M.L. Tran, C.-C. Fu, R.-S. Juang, Removal of metronidazole by TiO_2 and ZnO photocatalysis: a comprehensive comparison of process optimization and transformation products. Environ. Sci. Pollut. Res. (2018)
5. B. Wu, T. Zhang, J. Li, Y. Ye, H. Chen, The photodegradation of metronidazole in the presence of coexisting pharmaceuticals. Water Sci. Technol. **66**, 4 (2012)
6. H. Derikvandia, A. Nezamzadeh-Ejhieh, Increased photocatalytic activity of NiO and ZnO in photodegradation of a model drug aqueous solution: effect of coupling, supporting, particles size and calcination temperature. J. Hazard. Mater. (2016)
7. K. Stando, P. Kasprzyk, E. Felis, S. Bajkacz, Heterogeneous photocatalysis of metronidazole in aquatic samples. Molecules **26**(7612), 1–16 (2021)
8. C. Ding, K. Fu, Y. Pan, J. Liu, H. Deng, J. Shi, Comparison of Ag and AgI-modified ZnO as heterogeneous photocatalysts for simulated sunlight driven photodegradation of metronidazole. Catalysts **10**(1097), 1–26 (2020)
9. S. Surendhiran, K.S.G. Jagan, A. Karthik, V. Rajendran, Biogenic fabrication of α-h phase 2D-MoO_3 nanomaterials: comprehensive analysis of physicochemical and impedance properties for biological and photocatalytic applications. J. Mol. Struct. **1324**, 140811 (2025)
10. R.K. Dharman, A. Mariappan, T.H. Oh, Engineering bandgap energy of MoO_3 nanorod heterostructure using $AgVO_3$ for efficient photocatalytic degradation of antibiotic pollutant. Environ. Res. **268**, 120829 (2025)
11. L. Zhao, Y.-F. Yu, H.-W. Wang, Q. Cai, X.-Y. Zhou, B. Zhang, Y.W. Wu, Q. Lu, Insights into the effect of Cd on simultaneous removal of NO_x and dioxins over V_2O_5-MoO_3/TiO_2 catalyst: a combination of experimental and DFT study. Sep. Purif. Technol. **268**, 130159 (2025)
12. S. Boobesh, P. Sanjeevi, G. Kalpana, C. Sivaraj, M. Elango, Structural, morphological, and photocatalytic studies of Co-doped MoO_3 on SiO_2: a multifunctional material for environmental remediation. J. Environ. Nanotechnol. 13(4), 326–331 (2024)
13. M.S.H. Fathima Afridha, S. Hari Prakash, S.M. Roopan, MoO_3 based nanocomposites for the photocatalytic degradation of colourants—a review. J. Taiwan Inst. Chem. Eng. 166, 105354 (2025)
14. X. Cao, B. Tan, B. Zhang, G. Huang, H. Xu, Z. Song, J. Yan, Integration of silver nanoparticles into carbon-encapsulated tungsten oxide promoting visible-light-driven photocatalytic degradation efficiency. Appl. Surf. Sci**. 678**, 161112 (2025)
15. V. Zazhigalov, E. Zabolotnii, Modification of oxide composition TiO_2/WO_3 and its properties in processes of photodegradation drugs in water medium. Ukrainian Chem. J. **91**(2), 39–54 (2025)

16. S. Velusamy, S. Sakarapani, K. Palani, P. Natarajan, M. Ashagurajan, Cellulose acetate membranes loaded with WO_3/g-C_3N_4: a synergistic approach for effective photocatalysis. Nanotechnology **35**(47), 475401 (2024)
17. S. Dong, J. Dai, Y. Yang, A. Zada, K. Qi, Extended interfacial charge transference $CoFe_2O_4$/WO_3 nanocomposites for the photocatalytic degradation of tetracycline antibiotics. Molecules **29**(19), 4561 (2024)
18. P. Nisha, D. Gokulnath, G. Vijayakumar, et al., Exploration of morphological, structural, and photocatalytic behaviours of MoS_2/WO_3 nanocomposites. Inorg. Chem. Commun. **167**, 112730 (2024)
19. V.O. Zazhigalov, D.V. Brazhnyk, O.V. Sachuk, O.V. Kiziun, I.V. Bacherikova, I. Alessandri, L.E. Depero, Photocatalytic properties of zinc oxide prepared by combustion of jellied precursor. Theor. Exp. Chem. **59**(1), 25–31 (2023)
20. H.I. Yoo, C.R. Song, D.K. Lee, Electronic carrier mobilities of $BaTiO_3$. J. Eur. Ceram. 24(6), 1259–1263 (2004)
21. J.L. Giocondi, G.S. Roher, Hydrogen production using highly active titanium-oxide-based catalysts. Top. Catal. **49**(1–2), 18–23 (2008)